Carburized Ethylene Pyrolysis Tubes – An Analysis of the Relationship between Microstructure, Creep Performance, and Magnetic Response

---

A thesis

submitted in partial fulfilment

of the requirements for the Degree of

DOCTOR OF PHILOSOPHY IN MECHANICAL ENGINEERING

IN THE

UNIVERSITY OF CANTERBURY

by

AMY CHARLOTTE MCLEOD

University of Canterbury

2016

Preface

This thesis is submitted as a partial requirement for the degree of Doctor of Philosophy in Mechanical Engineering in the University of Canterbury. This research was conducted under the supervision of Professor Milo V. Kral in the Department of Mechanical Engineering, University of Canterbury, between April 2011 and April 2016.

Acknowledgements

I would like to acknowledge the following people and organizations that have made this research possible:

- Professor Milo V. Kral for supervision of the thesis and for his support, critique, and advice throughout this research program;
- Dr. Catherine Bishop for co-supervision of the thesis, for her patience, enthusiasm, and advice, and for many valuable discussions;
- Dr. Kevin Stevens (Quest Integrity Group Ltd.) for co-supervision of the thesis, and for the discussions and advice over the course of this research;
- Quest Integrity Group Ltd, in particular Charles Thomas and Andy Saunders-Tack, for the supply of material and data and for generously funding this research;
- The Ministry of Science and Innovation of New Zealand, for generously funding the project;
- Members of the Materials Engineering Group (MEG): Mike Flaws, Kevin Stobbs, and fellow MEG students, both past and present;
- Technical staff of the Department of Mechanical Engineering, in particular Ken Brown, Julian Phillips, Scott Amies, David Read, Gary Cotton, and Paul Southward, in addition to the numerous administration staff for their skill, knowledge, and assistance;
- Last but certainly not least, my parents Brenda and Glen, my partner Timothy, and my family and friends for their continual support throughout this project.

Abstract

High alloy Fe-Cr-Ni austenitic stainless steels have become the industry standard alloys for use in ethylene pyrolysis furnaces in the petrochemical industry. Each pyrolysis furnace contains a large array of vertically oriented pyrolysis tubes through which various hydrocarbon feedstocks are flowed and converted into ethylene. The pyrolysis tubes are typically operated at temperatures of 850 – 1100°C, at low pressure (< 0.5 MPa) and short residence times (< 1.0 s).

The HP (25%Cr-35%Ni) and ET45 (35%Cr-45%Ni) alloys are the latest in a series of high alloy, heat resisting stainless steels developed in order to provide the strength, ductility, corrosion, and oxidation resistance necessary in the carbon, hydrogen and oxygen rich environment typical of ethylene pyrolysis furnaces. However, the thermal pyrolysis, or cracking, of hydrocarbon molecules creates free carbon, and at the elevated service temperatures the diffusion of carbon into the tube material occurs rapidly. Alloying elements, in particular chromium, are pulled from the matrix to combine with the carbon, resulting in the formation of new carbides and contributing to growth of existing ones. Carburization is the life-limiting mechanism of ethylene pyrolysis tubes, and its effects on tube life manifest in a number of ways, including reducing ductility and the ability of the pyrolysis tube to withstand thermal cycles, and creating internal stresses that result in increases in creep rate.

Plant operators prefer to replace tubes at planned outages in order to minimise downtime, but there is currently no reliable end-of-life indicator by which tube replacement decisions can be made. Knowing the level of carburization of an in-situ tube can assist in remaining life estimates based on finite element analysis (FEA) modelling, thermography, and fracture mechanics. There is therefore great interest in the non-destructive detection and monitoring of the level of carburization of in-situ tubes. Due to the changes in microstructure and magnetic properties of the tubes over their service life, the level of carburization can be detected non-destructively using eddy current probes. There is, however, industry demand for automated systems and more accurate remaining life estimation. Quest Integrity Group has recently developed an automated eddy current tube crawler system, and are in the process of developing FEA models for a variety of pyrolysis furnace geometries in order to simulate service conditions over a number of thermal cycles and assist in predicting remaining life. In order to improve the interpretation of the eddy current non-destructive testing results and improve the accuracy of the material property data necessary for the FEA models, fundamental research of carburized tubes is necessary. In the present work, detailed characterization of carburized microstructures has been performed, and the effects of carburized microstructures on the mechanical properties and magnetic response analysed in order to better understand the relationship between the factors that influence the remaining life estimates of ethylene pyrolysis tubes.

Extensive detailed characterization of phase fractions and phase distributions in the ex-service tubes demonstrated the wide range of phases present and phase transformations that can occur during service in pyrolysis furnaces. It was determined that the primary chromium-rich carbides are the main contributors to the depletion of chromium in the austenite matrix, but that other phase transformations that produce chromium-containing phases, such as the transformation of NbC or (Nb,Ti)C to η-carbide, and the precipitation of σ-phase, also contribute, particularly in those tubes with minimal microstructural coarsening. The depletion of chromium in the austenite matrix in HP-Nb and HP-Micro alloys was shown to be directly proportional to the increase in the concentration of chromium in the primary precipitate network.

The growth of the primary precipitate network was demonstrated to be the main contributor to the reduction in creep resistance of carburized tubes. The steady state creep rate was determined to be dependent on the volume fraction of the primary precipitate network, with highly carburized tubes displaying steady state creep rates an order of magnitude higher than moderately carburized tubes, and up to two orders of magnitude higher than tubes with little to no carburization. The relative importance of phase transformation in determining the differences in creep behaviour was in some case uncertain, due to more than one phase transformation typically occurring.

The chromium concentration in the austenite matrix was compared to available data for magnetic permeability in order to predict the amount of ferromagnetic material in each sample, to enable analysis of the eddy current NDT results. An increase in the amount of ferromagnetic material resulted in both an increase in normalised probe inductance and an increase in the range of normalised probe inductance across the test frequencies. The analysis of the eddy current NDT results demonstrated that measurement of the magnetic permeability of Fe-Cr-Ni compositions with chromium concentrations between 15 wt% (in the range of the chromium-depleted austenite matrix material) would enable more accurate interpretation and better insight into the relationship between chromium concentration and magnetic response.

Deputy Vice-Chancellor's Office
Postgraduate Office

UNIVERSITY OF CANTERBURY
Te Whare Wānanga o Waitaha
CHRISTCHURCH NEW ZEALAND

Co-Authorship Form

This form is to accompany the submission of any thesis that contains research reported in co-authored work that has been published, accepted for publication, or submitted for publication. A copy of this form should be included for each co-authored work that is included in the thesis. Completed forms should be included at the front (after the thesis abstract) of each copy of the thesis submitted for examination and library deposit.

Please indicate the chapter/section/pages of this thesis that are extracted from co-authored work and provide details of the publication or submission from the extract comes:

Select results from chapters 4, 5, and 7 have been published in the following journal article:

McLeod, A.C.; Bishop, C.M.; Stevens, K.J. and Kral M.V. (2015) *Microstructure and Carburization Detection in HP Alloy Ethylene Pyrolysis Tubes,* Metallography, Microstructure and Analysis, 4 (4): 273-285.

Please detail the nature and extent (%) of contribution by the candidate:

Aside from the collection of the eddy current NDT data, all data collection and analysis was performed by the candidate. The journal article was written by the candidate and edited by co-authors. The extent of contribution to the article by the candidate was 90%.

Certification by Co-authors:

If there is more than one co-author then a single co-author can sign on behalf of all.

The undersigned certifies that:

- The above statement correctly reflects the nature and extent of the PhD candidate's contribution to this co-authored work
- In cases where the candidate was the lead author of the co-authored work he or she wrote the text

Name: *Prof. Milo Kral* Signature: 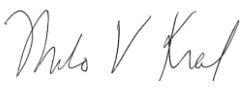 Date: *28/04/2016*

Deputy Vice-Chancellor's Office
Postgraduate Office

UNIVERSITY OF CANTERBURY
Te Whare Wānanga o Waitaha
CHRISTCHURCH NEW ZEALAND

Co-Authorship Form

This form is to accompany the submission of any thesis that contains research reported in co-authored work that has been published, accepted for publication, or submitted for publication. A copy of this form should be included for each co-authored work that is included in the thesis. Completed forms should be included at the front (after the thesis abstract) of each copy of the thesis submitted for examination and library deposit.

Please indicate the chapter/section/pages of this thesis that are extracted from co-authored work and provide details of the publication or submission from the extract comes:

Select results from chapters 4, 5, and 7 have been published in the following journal article:

McLeod, A.C; Bishop, C.M.; Stevens, K.J. and Kral, M.V. (2016) *Microstructural Characterization and Image Analysis in Ex-Service HP alloy Stainless Steels Tubes for Ethylene Pyrolysis,* Metallography, Microstructure and Analysis, article in press.

Please detail the nature and extent (%) of contribution by the candidate:

Aside from the collection of the eddy current NDT data, all data collection and analysis was performed by the candidate. The journal article was written by the candidate and edited by co-authors. The extent of contribution to the article by the candidate was 90%.

Certification by Co-authors:

If there is more than one co-author then a single co-author can sign on behalf of all

The undersigned certifies that:

- The above statement correctly reflects the nature and extent of the PhD candidate's contribution to this co-authored work
- In cases where the candidate was the lead author of the co-authored work he or she wrote the text

Name: *Prof. Milo Kral* Signature: 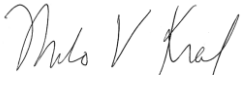 Date: *28/04/2016*

Contents

List of Figures

List of Tables

Chapter 1: Introduction

Heat resistant, high alloy Fe-Cr-Ni austenitic stainless steels have become the industry standard alloys for use in ethylene pyrolysis furnaces. Large arrays of hundreds of vertically oriented pyrolysis tubes are used in pyrolysis furnaces to convert various hydrocarbon feedstocks, such as ethane or naphtha, into ethylene. The pyrolysis tubes operate at temperatures of 850 – 1100 °C, with low pressures (<0.5 MPa) and short residence times (<1.0 s). The pyrolysis reaction for the conversion of ethane (C_2H_6) into ethylene (C_2H_4) is described by Equation 1.1:

$$C_2H_6 \rightarrow C_2H_4 + H_2 \qquad \textbf{Equation 1.1}$$

The heat resisting (H-series) austenitic alloys were developed in order to provide the high temperature strength, ductility, and oxidation and corrosion resistance necessary to withstand extended service in the carbon, hydrogen, and oxygen rich environment typical of pyrolysis furnaces. Initially, the centrifugally cast HK alloy (25% Cr – 20% Ni) replaced the wrought HT alloy (18% Cr – 37% Ni), providing comparable creep resistance at a lower cost due to the reduced Ni content. Industry demands for a material that could withstand more aggressive operating conditions resulted in the HK alloy being superseded by the HP alloy series (25% Cr – 35% Ni), which provides greater corrosion and creep resistance. A shift in pyrolysis furnace design to shorter residence times and higher operating temperatures pushed the operating conditions of some furnaces beyond the capabilities of the HP series, leading to the development of the ET45-type alloys (35% Cr – 45% Ni), which provide oxidation resistance up to 1150 °C whilst still providing sufficient creep strength. Recently, the HT-E alloy (30% Cr – 45% Ni – 4% Al), an alumina-forming alloy, has come in to use, which reportedly has greater resistance to coke deposition than the chromia-forming alloys such as the HP and ET45-type alloys.

The thermal cracking (pyrolysis) of hydrocarbon molecules creates free carbon, as described by Equation 1.2:

$$C_2H_4 \rightarrow CH_4 + C \qquad \textbf{Equation 1.2}$$

At the elevated service temperatures, the diffusion of free carbon into the tube material occurs rapidly. Alloying elements, in particular chromium, are pulled from the matrix to combine with the carbon, forming new carbides and contributing to the growth of existing ones. The effects of carburization on remaining tube life manifest in a number of ways, including decreases in ductility and the ability of

the tubes to withstand thermal cycles, alloy embrittlement, and the creation of internal stresses causing increases in creep rate. As a result, carburization is the life-limiting mechanism for pyrolysis tubes.

Plant operators prefer to replace tubes at planned outages in order to minimize downtime of the plant. The expensive costs of the high-alloy tubes and the costs of unplanned shutdowns mean that unexpected failures are highly undesirable. Unexpected temperature drops can also cause damage to tubes, if the tubes have not been decoked first. However, there is currently no reliable end-of-life indicator by which to make tube replacement decisions. There is, therefore, great interest in the non-destructive detection and monitoring of the level of carburization of in-situ ethylene pyrolysis tubes throughout their service life in order to estimate remaining tube life.

The detection of carburization by eddy current non-destructive testing (eddy current NDT) has been developed by Quest Integrity Group and elsewhere [1-10]. In the as-cast condition, the austenite matrix of Fe-Cr-Ni alloys is paramagnetic at room temperature. The precipitation and growth of chromium carbides in the alloy during service results in chromium being depleted from the austenite matrix. The composition of the matrix progressively shifts from the ternary Fe-Cr-Ni composition towards the binary Fe-Ni composition. Below a critical chromium content, the austenite matrix shifts from being paramagnetic to being ferromagnetic at room temperature, and with continued chromium depletion the amount of ferromagnetic matrix material and its relative magnetic permeability increases. Eddy current NDT systems measure the changes in bulk magnetic permeability associated with increased amounts of ferromagnetic material. However, in order to interpret the eddy current results, the system needs to be calibrated on carburized tubes that have had their microstructure, mechanical properties, and magnetic properties characterized. Additionally, there are no current criteria by which to use the data to make decisions on tube replacements, except for Finite Element modelling.

Manual eddy current NDT inspection systems have been developed; however, there is industry demand for automated systems and for more accurate remaining life estimations. Quest Integrity Group has recently developed a tube crawler system to allow for automated eddy current NDT inspection [10], and are in the process of developing finite element analysis (FEA) models for each pyrolysis furnace geometry in order to simulate the service conditions and stresses experienced over multiple thermal cycles and assist in remaining life estimation. Inputs to the FEA model include materials properties such as creep rate and thermal expansion coefficients, determined from observations of carburized microstructures and mechanical tests. The FEA model, in combination with the eddy current crawler, presents a unique market opportunity for ethylene pyrolysis furnace inspection and tube life estimation. However, in order to improve the interpretation of the eddy current NDT results and the accuracy of the material property data input into the FEA model, and therefore improve the accuracy of remaining life estimates, more fundamental research is necessary. Detailed characterization of carburized microstructures is required, and the effects of carburized

microstructures on the mechanical properties and magnetic response need to be determined, in order to better understand the relationship between the factors that influence remaining life estimates. These requirements were the primary motivation for the current project.

1.1 Research Background

The microstructure of a typical ethylene pyrolysis tubes consists of an austenitic matrix with a primary network of chromium-rich and niobium-rich carbides. Carbon diffusion into the tube during service results in chromium being drawn from the austenite matrix to combine with carbon, precipitating new chromium carbides and contributing to the growth of existing ones. With continued carbon ingress, the primary chromium carbide network coarsens and coalesces, and the carbide volume fraction increases.

An increase in the volume fraction of hard, brittle carbides results in significant decreases in tube ductility and a continuous network of chromium carbides provides an easy path for crack propagation, and thus a tube's ability to withstand thermal cycles without rupture is reduced with increased carburization. The increase in internal volume as a result of carbide precipitation and growth induces internal stresses, which contribute to increases in the longitudinal creep rate of the tubes. Longitudinal lengthening (creep) of the tubes due to self-weight eventually necessitates the tubes to be shortened and re-welded; however, heavily carburized tubes may be too brittle to re-weld without cracking.

There are a number of studies of ex-service ethylene pyrolysis tubes presented in the literature, [1-3, 8, 9, 11-13]; however, few studies fully identify the phases present in the tubes and their distributions, simply stating "chromium carbides" or "niobium carbides" without determining crystal structure or reporting composition. There are a wide number of phases that can be present, and phase transformations that can occur, in ethylene pyrolysis tubes depending on the alloy composition and service conditions. Of particular interest for this project are the chromium-containing phases, as the growth of these phases during service is likely to contribute to chromium depletion of the austenite matrix, and thus the change in magnetic properties. There are multiple chromium carbides with varying chromium-to-carbon ratios that can be present in ex-service tubes, as well as other chromium-containing phases that can be formed during service exposure.

The precipitation and growth of chromium carbides during service exposure results in the adjacent austenite matrix being depleted of chromium, and with continued chromium depletion the austenite matrix shifts from being paramagnetic at room temperature to being ferromagnetic at room temperature. Eddy current NDT systems measure the changes in bulk magnetic permeability associated with increased amounts of ferromagnetic material. Although the precipitation and growth of chromium carbides is reportedly the most significant contributor to matrix chromium depletion, there are other phase transformations that occur during service that may also contribute – for example

the transformation of niobium carbides to the chromium-containing η-carbide, or the formation of chromium nitrides due to the exposure to flue gases at elevated temperatures.

Multi-frequency eddy current NDT systems enable the magnetic response at different locations across tube walls to be analyzed, as the depth of eddy current penetration is dependent on frequency [14]. Different levels of carburization have been demonstrated to elicit different magnetic responses when multi-frequency eddy current NDT is used. For example a tube moderately carburized across the entire wall exhibits a moderate magnetic response across all frequencies, where as a tube highly carburized at the inner wall exhibits a high magnetic response at low frequencies but a low magnetic response at high frequencies [8, 9]. However, likely due to commercial sensitivities, there is, to the best of the author's knowledge, minimal information in the literature directly comparing the distribution of the individual phases present in the microstructure and the associated chromium depletion of the matrix with the corresponding eddy current NDT response.

There is a reasonable amount of data published in literature regarding the creep properties of aged HP alloys [15-17]; however, this data is not entirely applicable to ethylene pyrolysis tubes. The HP alloy series is also widely used for steam reformer furnace tubes, which do not experience carburization during service, and the operating conditions of which (850 – 1050 °C, 1 - 2.5 MPa internal pressure) are not directly comparable to these experienced by ethylene pyrolysis tubes (850 – 1050 °C, <0.5 MPa internal pressure). Thus the results of accelerated creep rupture tests as published in the literature, while they may representative of the service conditions experienced by reformer tubes over their service life, are not representative of the life of ethylene pyrolysis tubes as they do not accurately represent the thermal cycling and progressive carburization that ethylene pyrolysis tubes experience. There is currently no information in literature on the steady state creep performance of carburized ethylene pyrolysis alloys.

1.2 Research Overview and Scope

In the present work, six ex-service ethylene pyrolysis tubes have been studied. Five of the tubes are HP alloys (25% Cr – 35% Ni), and one is an ET45-type alloy (35% Cr – 45% Ni). The present work can be split into three categories: characterization of microstructure, characterization of mechanical properties, and characterization of magnetic response.

The collection of the magnetic response data has been carried out by Quest Integrity Group, using an earlier hand-held system and now the automated eddy current NDT crawler system recently developed [10]. The crawler measures the magnetic response of a tube at a particular location over a range of frequencies, and measurements are taken at set intervals around the circumference of the tube and set intervals along the tube length. Due to the penetration depth increasing with decreasing frequency [14], multi-frequency measurements allows the change in magnetic response across the tube

wall cross-section to be quantified. The mechanical and microstructural characterization of the tubes has been completed at the University of Canterbury, and has been designed to coincide with the eddy current testing locations on the tubes to enable analysis of the relationship between microstructure, mechanical properties, and magnetic response.

Due to the minimal information regarding the distribution of chromium-containing phases in ex-service tubes presented in the literature, it was deemed necessary to characterize the phase distributions in the ex-service tubes studied in this project. As such, the phases present in the tubes needed to be identified. This was achieved using a combination of imaging in the scanning electron microscope (SEM), energy dispersive x-ray spectroscopy (EDS), and electron back-scattered diffraction (EBSD). Characterization of the phase distributions was then achieved using a combination of SEM imaging and image analysis.

Characterization of mechanical properties, in particular the creep performance of carburized material, was considered an important facet to the project, as the data presented in the literature to date is not representative of the complex thermal cycling and progressive carburization that ethylene pyrolysis tubes experience during service. The steady state creep rate (secondary creep rate) was deemed the most relevant measure of creep performance for the purposes of this project, due to the short-term nature of the thermal cycles. Hardness testing of the metallographic samples was completed for comparison with the microstructural characterization and creep performance.

Upon collection of the microstructural data, mechanical properties, and magnetic response, integration and analysis of the results was performed in order to determine the nature of the relationships between the three factors. A summary of the project is shown in Figure 1.1.

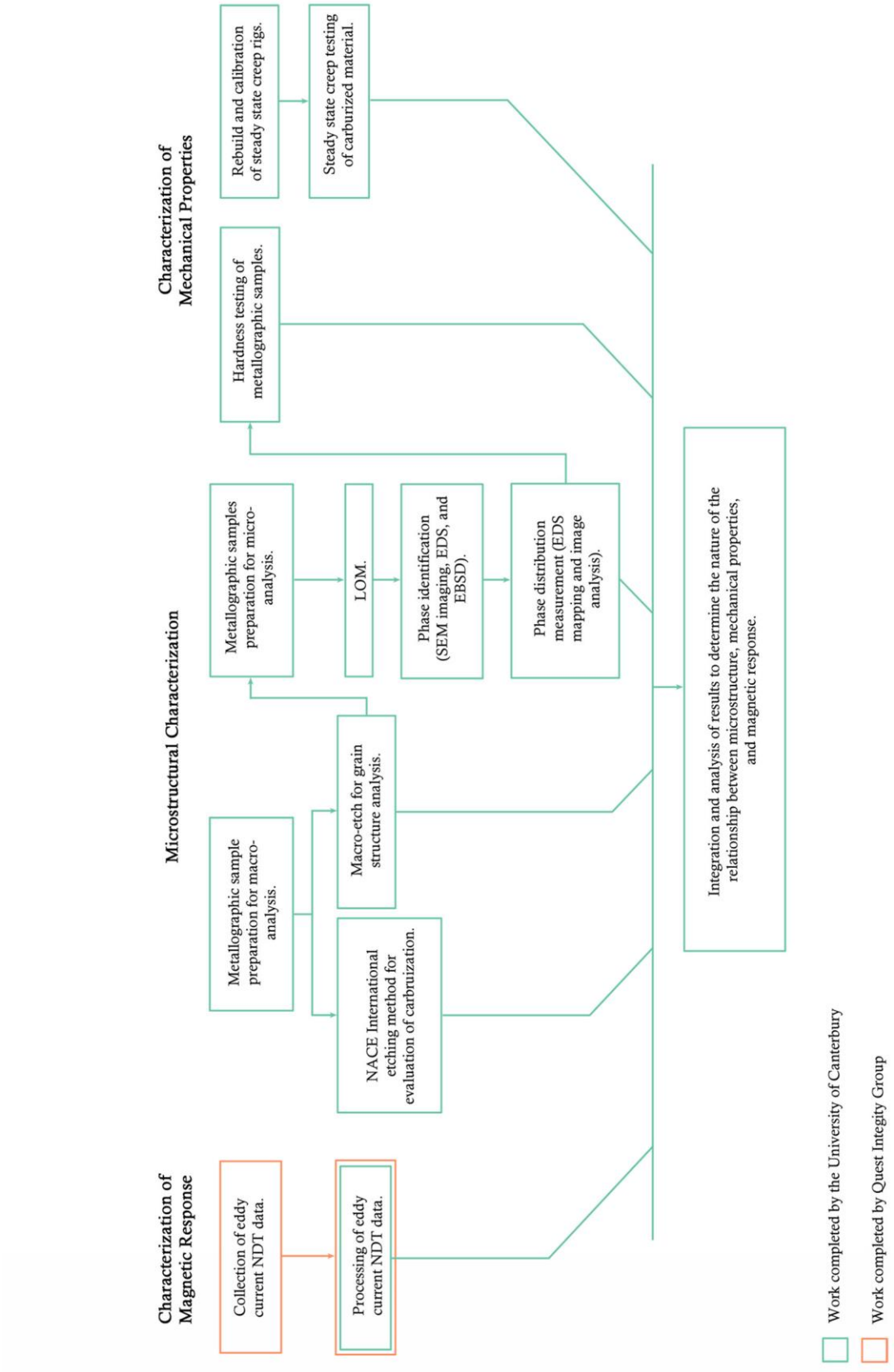

Figure 1.1 - Schematic of the experimental process, detailing the eddy current non-destructive testing (eddy current NDT), microstructural characterization, and characterization of mechanical properties presented in this thesis. LOM – Light optical microscopy, SEM = scanning electron microscope, EDS = energy dispersive x-ray spectroscopy, EBSD = electron backscatter diffraction.

1.3 Format of Thesis

The content of the eight chapters in this thesis can be briefly summarized.

Chapter 1 (current chapter) discusses the background, overview, and scope of the research presented in this thesis.

Chapter 2 presents a review of the literature to date, addressing the development of alloys for reformer and ethylene pyrolysis tubes, the conditions of ethylene pyrolysis furnaces that influence tube life, previous metallurgical studies of reformer and ethylene pyrolysis tube alloys, and the development of eddy current NDT for carburization detection.

Chapter 3 discusses the experimental techniques used to prepare metallographic samples for light optical microscopy (LOM) and scanning electron microscopy (SEM). The equipment used for the energy dispersive x-ray spectroscopy (EDS) and electron backscatter diffraction (EBSD) analyses and the standard operating conditions for each piece of equipment are also presented.

Chapter 4 presents the phase identification results for the ex-service tubes studied.

Chapter 5 presents the detailed microstructural analysis of the ex-service tubes studied. The distributions of the phases identified in the tubes and the phase transformations that occur during service are discussed.

Chapter 6 presents the results of the mechanical tests performed, including steady-state creep and hardness tests. The apparatus and conditions of the creep tests are discussed.

Chapter 7 presents the response of the six ex-service tubes to eddy current non-destructive testing, and discusses the microstructural factors that influence the response.

Chapter 8 concludes this thesis with a summary of the academic achievements and the industry relevance of the knowledge gained from the current research project.

Appendix A contains copies of the journal papers published during the course of the research presented in this thesis.

1.4 Research Achievements

1. **McLeod, A.C.; Bishop, C.M.; Stevens, K.J. and Kral M.V.** (2012) *The Effects of Microstructure upon Remaining Life of Carburized Ethylene Pyrolysis Tubes,* presented at the TMS 141st Annual Meeting and Exhibition, Orlando, Florida, USA.

2. **McLeod, A.C.; Bishop, C.M.; Stevens, K.J. and Kral M.V.** (2013) *The Effects of Microstructure upon Remaining Life of Carburized Ethylene Pyrolysis Tubes,* presented at the 26th New Zealand Conference on Microscopy, Christchurch, New Zealand
3. Awarded the ProSciTech Trans-Tasman Bursary for outstanding contribution to microscopy and microanalysis, at the 26th New Zealand conference on Microscopy, Christchurch, New Zealand (2013).
4. **McLeod, A.C.; Bishop, C.M.; Stevens, K.J. and Kral M.V.** (2013) *The Effects of Microstructure upon Remaining Life of Carburized Ethylene Pyrolysis Tubes,* presented at Non-Destructive Measurement of Microstructural Evolution, 8th Pacific Rim International Conference on Advanced Materials and Processing (PRICM-8), Waikoloa, Hawaii, USA.
5. **McLeod, A.C.; Bishop, C.M.; Stevens, K.J. and Kral M.V.** (2013) *The Effects of Microstructure upon Remaining Life of Carburized Ethylene Pyrolysis Tubes,* presented at NZCCME 2013, Auckland, New Zealand
6. **McLeod, A.C.; Bishop, C.M.; Stevens, K.J. and Kral M.V.** (2014) *The Effects of Microstructure upon Remaining Life of Carburized Ethylene Pyrolysis Tubes,* presented at ACMM2014, Adelaide, Australia.
7. **McLeod, A.C.; Bishop, C.M.; Stevens, K.J. and Kral M.V.** (2015) *Microstructural Characterization and Image Analysis in Ex-Service Ethylene Pyrolysis Tubes,* presented at the 27th New Zealand Conference on Microscopy, Dunedin, New Zealand.
8. Awarded the Keith Williamson Medal for excellence in microscopy research, at the 27th New Zealand Conference on Microscopy, Dunedin, New Zealand (2015).
9. **McLeod, A.C.; Bishop, C.M.; Stevens, K.J. and Kral M.V.** (2015) *Microstructure and Carburization Detection in HP Alloy Ethylene Pyrolysis Tubes,* Metallography, Microstructure and Analysis, 4 (4): 273-285.
10. **McLeod, A.C; Bishop, C.M.; Stevens, K.J. and Kral, M.V.** (2015) *Microstructural Characterization and Image Analysis in Ex-Service Ethylene Pyrolysis Tubes*, presented at M&M 2015, Portland, Oregon, USA.
11. **McLeod, A.C; Bishop, C.M.; Stevens, K.J. and Kral, M.V.** (2016) *Microstructural Characterization and Image Analysis in Ex-Service HP alloy Stainless Steels Tubes for Ethylene Pyrolysis,* Metallography, Microstructure and Analysis, 5(3); 178-187.

Select microstructural characterization and eddy current non-destructive testing results for samples from tubes 1-3 have been published in the journal papers detailed in points 9 and 11. These journal papers have been appended in Appendix A.

Chapter References

[1] da Silva, I.C., da Silva, R.S., Rebello, J.M.A., Bruno, A.C., and Silveira, T.F. *Characterization of carburization of HP steels by non destructive magnetic testing.* NDT & E International, 2006. **39**(7): p. 569-577.

[2] Silva, I.C., Rebello, J.M.A., Bruno, A.C., Jacques, P.J., Nysten, B., and Dille, J. *Structural and magnetic characterization of a carburized cast austenitic steel.* Scripta Materialia, 2008. **59**(9): p. 1010-1013.

[3] Silva, I.C., Silva, L.L., Silva, R.S., Rebello, J.M.A., and Bruno, A.C. *Carburization of ethylene pyrolysis tubes determined by magnetic measurements and genetic algorithm.* Scripta Materialia, 2007. **56**(4): p. 317-320.

[4] Stevens, K.J., Ingham, B., Ryan, M., Luzin, V., and Cheong, K. *Carbide composition and stress measurement in ethylene pyrolysis tubes*. in *34th Annual Condensed Matter and Materials Meeting*. 2010. Waiheke Island, New Zealand.

[5] Stevens, K.J. and Minchington, I.E. *A portable system for through-wall carburisation detection in hydro-carbon cracking tubes*. in *NDTA Workshop 2000 - New Zealand Non Destructive Testing Association*. 2000. Rotorua, New Zealand.

[6] Stevens, K.J., Parbhu, A., and Soltis, J. *Magnetic force microscopy and cross-sectional transmission electron microscopy of carburised surfaces.* Current Applied Physics, 2004. **4**(2-4): p. 304-307.

[7] Stevens, K.J., Parbhu, A., Soltis, J., and Stewart, D. *Magnetic force microscopy of a carburized ethylene pyrolysis tube.* Journal of Physics D (Applied Physics), 2003. **36**(2): p. 164-8.

[8] Stevens, K.J., Tack, A.J., Thomas, C.W., and Stewart, D. *Through-wall carburization detection in ethylene pyrolysis tubes.* Journal of Physics D (Applied Physics), 2001. **34**(5): p. 814-22.

[9] Stevens, K.J. and Trompetter, W.J. *Calibration of eddy current carburization measurements in ethylene production tubes using ion beam analysis.* Journal of Physics D (Applied Physics), 2004. **37**(3): p. 501-9.

[10] Quest Integrity Group. *Ethylene Pyrolysis Tube Inspection System*. [cited 27/05/2015; Available from: http://www.questintegrity.com/services/inspection-services/ethylene-pyrolysis-tube-inspection.

[11] Guan, K., Xu, H., and Wang, Z. *Analysis of failed ethylene cracking tubes.* Engineering Failure Analysis, 2005. **12**(3): p. 420-431.

[12] Khodamorad, S.H., Haghshenas Fatmehsari, D., Rezaie, H., and Sadeghipour, A. *Analysis of ethylene cracking furnace tubes.* Engineering Failure Analysis, 2012. **21**(0): p. 1-8.

[13] Ul-Hamid, A., Tawancy, H.M., Al-Jaroudi, S.S., Mohammed, A.I., and Abbas, N.M. *Carburisation of Fe-Ni-Cr alloys at high temperatures.* Materials Science Poland, 2006. **24**(2): p. 319-331.

[14] García-Martín, J., Gómez-Gil, J., and Vázquez-Sánchez, E. *Non-Destructive Techniques Based on Eddy Current Testing.* Sensors, 2011. **11**(3): p. 2525-2565.

[15] de Almeida Soares, G.D., de Almeida, L.H., da Silveira, T.L., and Le May, I. *Niobium additions in HP heat-resistant cast stainless steels.* Materials Characterization, 1992. **29**(4): p. 387-96.

[16] Ribeiro, A.F., Borges, R.M.T., and de Almeida, L.H. *Phase transformation in heat resistant steel observed by STEM. (NbTi)C - NiNbSi (G-phase).* Acta Microscopica, 2002. **11**(1): p. 59-63.

[17] Buchanan, K.G. *The Effects of Long-Term Isothermal Ageing on the Microstructure of HP-Nb and HP-NbTi Alloys - Doctoral Dissertation*. 2013, University of Canterbury: Christchurch, New Zealand.

Chapter 2: Literature Review

The following chapter provides an overview of the previous work conducted on ethylene pyrolysis tube alloys, and the application of eddy current non-destructive testing (eddy current NDT) to the detection of carburization.

It will begin by discussing the use of high temperature, austenitic stainless steels for ethylene pyrolysis furnaces. The emphasis is on the latest generations of ethylene pyrolysis tube alloys – the HP and ET45 series. Service factors that influence the life of ethylene pyrolysis tubes will be discussed, followed by a summary of the metallurgical history of the alloys. A review of the evolution of the microstructure and properties of the alloys with respect to the ageing or service conditions will be presented.

The basic theory behind eddy current NDT systems for a variety of applications will be presented. The properties of ethylene pyrolysis tubes that enable carburization to be detected by eddy current NDT will be discussed, and the use of eddy current NDT for carburization detection and recent work in this field will be presented.

The primary microstructural objective for this project was to characterize the microstructure of carburized ex-service ethylene pyrolysis tubes. The HP alloy series, which is widely used in ethylene pyrolysis furnaces, is also widely used for steam reformer furnaces. Although the conditions experienced by reformer tubes (850 - 1050 °C, 1 - 3.5 MPa internal pressure) are not directly comparable to those experienced by ethylene pyrolysis tubes (850 - 1050 °C, <0.5 MPa internal pressure, carburizing environment), the microstructural evolution of these tubes and of laboratory aged samples is nevertheless important to the understanding of the microstructural evolution of ethylene pyrolysis tubes, which experience ageing as well as carburization during service. Therefore, literature pertaining to ex-service reformer tubes and laboratory aged samples has been included in this literature review alongside that pertaining to ethylene pyrolysis tubes.

2.1 The Use of Austenitic Stainless Steel Tubes in Ethylene Pyrolysis Furnaces

Ethylene is produced industrially by the thermal cracking, or pyrolysis, of more complex hydrocarbons in the presence of steam within the radiant tubes of a pyrolysis furnace. Typical hydrocarbon feedstocks include naphtha and ethane. The principal arrangement of a pyrolysis furnace is shown in Figure 2.1. The feedstock and steam mixture initially passes through the convection

section of the furnace, where it is preheated, before passing through the radiant section where the cracking reaction occurs.

The radiant section is composed of hundreds of vertically oriented tubes which are heated externally by burners to reach tube skin temperatures in the range of 850 – 1100 °C, depending on the feedstock. The residence time of the feedstock-steam mixture within these tubes is extremely short (maximum 1.0 s), and the tubes are operated at minimal pressures (<0.5 MPa) [1-3]. Radiant box heights of up to 15 m and widths of 2-3 m are fairly standard, and the tubes within the radiant box can be heated with wall or floor mounted burners, or a combination of the two. The length of the radiant box is determinant on the total production rate of ethylene desired, and the residence time of the cracking operation. This also determines the number of individual radiant tubes needed, as shorter residence times will require more tubes than longer residence times to achieve the same production capacity. Tubes are typically in the range of 15-20 m long. Individual tubes can be the same diameter along the length, or swaged to larger diameters one or multiple times along the total tube length, as shown in Figure 2.2. As a result of the number of variables, there are many different radiant tube designs implemented in industry, and the designs are typically considered proprietary information. Ethylene pyrolysis tubes can therefore come in many different lengths, diameters, and wall thicknesses [3].

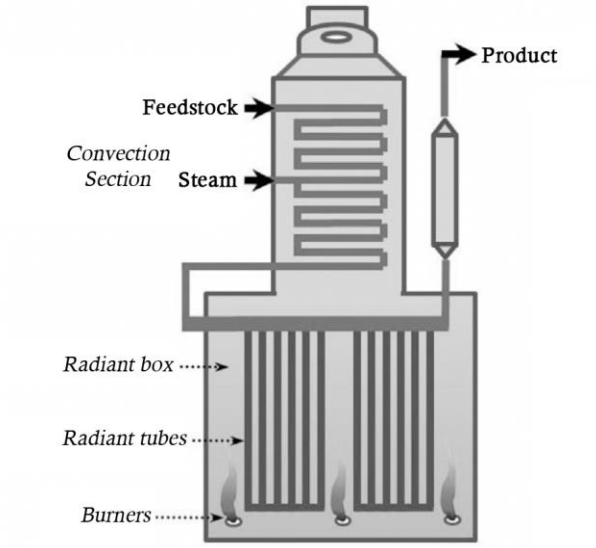

Figure 2.1 - Schematic of a typical ethylene pyrolysis unit (adapted from [2]).

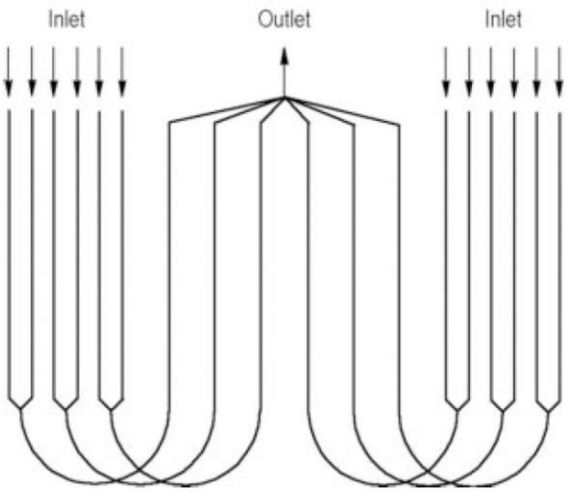

Figure 2.2 - An example of a two-pass, split tube, short residence time radiant tube arrangement [3].

The cracking reaction for the production of ethylene (C_2H_4) from ethane (C_2H_6), one of the more common feedstocks, can be summarized by Equation 1.1:

$$C_2H_6 \rightarrow C_2H_4 + H_2 \qquad \textbf{Equation 2.1}$$

The cracking reaction is also known to produce free carbon, which proceeds according to Equation 1.2:

$$C_2H_4 \rightarrow CH_4 + C \qquad \textbf{Equation 2.2}$$

The free carbon formed as a result of the cracking reaction has high mobility in the tube alloys at the elevated service temperatures and is able to diffuse into the radiant tubes, resulting in carburization and a corresponding loss in ductility, oxidation and corrosion resistance, creep resistance, and ability to withstand thermal cycles. A layer of coke forms on the inside surfaces of the radiant tubes, limiting heat transfer to the process stream, requiring higher tube skin temperatures in order to maintain the same cracking efficiency. The coke layer also promotes a high carbon activity environment at the inner diameter of the tubes, further promoting carburization. As a result, the coke layer must be burned or spalled off periodically in order to retain the desired heat transfer rate within the furnace [2, 4, 5]. Consequently, carburization is the major life-limiting factor for ethylene pyrolysis tubes. The aggressive environment that these tubes experience during service necessitates the use of high alloy austenitic stainless steels that have the ability to form chromia layers (such as the HK and HP alloy series), in an effort to balance the corrosion protection afforded by chromia films with other high-temperature mechanical properties such as creep resistance [2, 6].

Plant operators prefer to replace tubes during planned outages, as unexpected failures result in the shutdown of the furnace, costing millions of dollars a day. Large, un-expected temperature drops can also result in the rupture of further tubes, if the tubes contract around an intact coke plug upon cooling. However, the timing of tube replacements in order to avoid on-line failures is problematic, as there is currently no known reliable indicator that a tube is near to its end of life. As such, there is a strong interest in the non-destructive detection and monitoring of the extent of carburization in ethylene pyrolysis tubes throughout their operating life. This would ideally enable plant operators to order replacement tubes 6 - 12 months in advance, and replace tubes well in advance of a failure when the furnace is on-line, thus avoiding potentially severe economic losses and the possibility of further damage to the plant [7-9].

The detection of carburization using non-destructive eddy current techniques (eddy current NDT) has been developed by Quest Integrity Group and elsewhere [7-16]. However, the eddy current NDT systems require calibration against ex-service tubes that have had their microstructure, mechanical properties, and magnetic response characterized [7-9]. The need for an understanding of the relationship between the microstructure, mechanical properties, and magnetic response of carburized ethylene pyrolysis tubes led to the initiation of the current project.

2.2 Factors that Influence the Life of Ethylene Pyrolysis Tubes

It should be noted that the chromium-rich carbides in ethylene pyrolysis tubes, although dominantly chromium, can also contain small amount of other metals, and are thus often termed M_7C_3 and $M_{23}C_6$ (where M = Cr, Fe, Ni). $M_{23}C_6$ is typically an almost pure chromium carbide with minimal other metals; however, the exact composition of the M_7C_3 carbide can vary significantly, with different proportions of iron and chromium making up the metal component [17-19]. In order to avoid confusion, the chromium rich carbides will henceforth be termed M_7C_3 and $M_{23}C_6$ in this thesis.

2.2.1 Carburization

Carburization is the major degradation mechanism of ethylene pyrolysis tubes [5, 9, 20]. High carbon potentials or concentrations present at the inner diameter of the tubes due to the cracking reaction combined with high tube temperatures results in the diffusion of carbon into the tubes, where it combines with chromium and other carbide-forming elements to grow existing carbides and create new ones. The carbides undergo chemical and morphological changes, initially coarsening and coalescing, followed by phase transformation. Carburization attack of high temperature alloys is almost always internal, as the solubility and rate of diffusion in these alloys is high, and the outward diffusion of carbide-forming elements is much slower [21, 22].

Microstructural Evolution during Combined Oxidation and Carburization at the Inner Diameter

The mixed oxidant attack model presented by Chun *et al.* [2], Ramanarayanan *et al.* [22], and Petkovic-Luton *et al.* [23] describes the evolution of the tube microstructure at the inner diameter as oxidation and carburization start and progress during service, and has been validated by comparison with ex-service microstructures. Four stages of evolution are described – initial oxidation, oxidation in a carburizing environment, direct carburization, and internal oxidation. A schematic of the microstructural evolution at the inner diameter is shown in Figure 2.3.

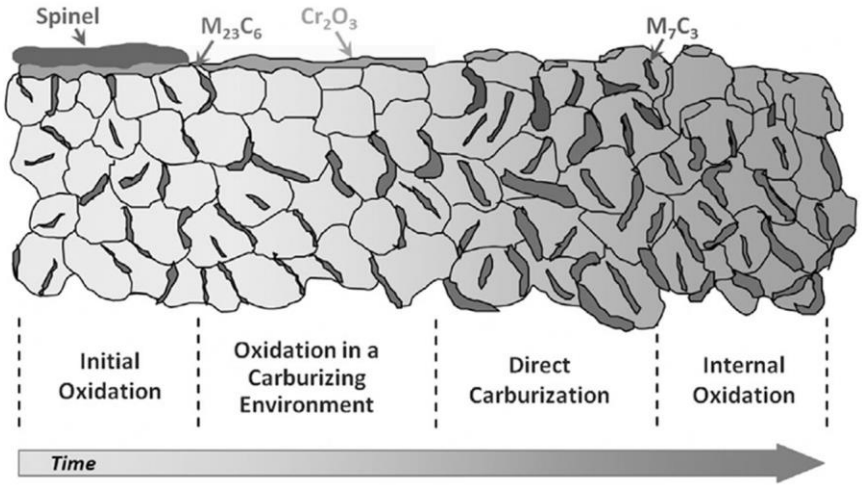

Figure 2.3 - Schematic representation of the sequential stages of mixed oxidation-carburization [1].

The tubes in pyrolysis furnaces are typically brought up to process temperature in a predominantly oxidizing environment. During this initial oxidation stage, over the 550 – 950 °C range, surface oxidation of the alloy at the inner diameter results in the formation of a two-layer oxide morphology, consisting of an outer layer of spinel (Fe, Cr, and Ni), and an inner oxide layer of Cr_2O_3 [2, 22, 23].

Upon the introduction of the hydrocarbon feedstock and steam, the environment at the inner diameter changes from one that is predominantly oxidizing to one that is characterized by both carbon and oxygen activities, resulting in oxidation in a carburizing environment. The ratio of hydrocarbon feedstock to steam is typically high enough that coke is deposited on the tube wall, resulting in a carbon activity of $a_c \sim 1$ at the interface between the coke deposit and the tube. With the levels of steam typical of ethylene pyrolysis, the oxygen activity is high enough to keep a Cr_2O_3 layer thermodynamically stable, and the Cr_2O_3 surface layer grows with intermittent spalling [2, 22, 23]. While the Cr_2O_3 layer is intact, the tube is protected from carbon ingress as Cr_2O_3 has negligible solubility for carbon [2, 22, 24]. However, due to the continual process of growth and regeneration of the Cr_2O_3 layer, there is continual chromium depletion in the sub-surface region of the tube. The depletion leads to the dissolution of the chromium-rich carbides in the sub-surface region (typically $M_{23}C_6$, where M is usually Cr), and a carbide-free zone is developed that advances into the tube interior. When the chromium-rich carbides dissolve, the chromium released diffuses to the surface to

form more Cr_2O_3, whereas the carbon released diffuses into the tube interior, where it contributes to the growth of existing carbides and the precipitation of new ones [2, 22, 23]. During this stage, structural defects present in the Cr_2O_3 layer, such as cracks formed as a result of thermal cycling, can allow carbon diffusion into the tube material [5].

The chromium content in the sub-surface region of the tube eventually reaches a critical value below which further Cr_2O_3 formation is not possible, and the depth of the chromium depleted zone is too large to facilitate the diffusion of chromium from the bulk of the tube. In ethylene pyrolysis environments, the critical chromium content in the sub-surface region has been reported as approximately 10 wt% chromium [2, 22], and the critical thickness of the chromium depleted zone is reported as approximately 200 μm [5]. This stage is the direct carburization stage, and from this point onwards, carbon has an unrestricted path into the tube interior, and it rapidly diffuses into the tube. M_7C_3 type carbides rapidly precipitate in the region that was previously the carbide-free zone (due to their lower ratio of chromium to carbon), and beyond this region the $M_{23}C_6$ carbides coarsen. The direct carburization stage has a short duration and thus is rarely observed before the next stage of microstructural evolution commences [2, 22, 23].

The final stage is internal oxidation. In principle, in the third stage (direct carburization), both oxygen and carbon can diffuse into the tube interior causing internal attack; however, due to the higher diffusivity of carbon, carburization occurs first. During the internal oxidation stage, an oxidizing front moves in, following the carburization front. The chromium rich carbides at the inner diameter are converted to chromium rich oxides by the ingress of oxygen [2, 22, 23]. Carbon still has free access to the alloy interior, thus carburization continues to progress.

With continued carbon ingress in to the tube, the carbides continue to coarsen and agglomerate. The $M_{23}C_6$ carbides are initially present across the entire tube wall; however, the high carbon content at the inner wall region necessitates the transformation to M_7C_3 [11, 21, 25]. The $M_{23}C_6$-to-M_7C_3 transformation front progresses into the tube wall as carbon continues to diffuse into the tube, moving from the inner diameter towards the outer diameter. A continual increase in the volume of hard, brittle carbides results in an increasingly brittle alloy with decreasing ductility, and a continuous carbide network that favours crack propagation. The increase in internal volume due to the precipitation and growth of the chromium carbides induces internal stresses in the tube [5].

2.2.2 Creep

Creep is the time-dependent deformation of a material when it is subject to temperatures in excess of 40% of its melting point. Creep failure is said to have occurred when a component exhibits deformation that interferes with its function, or when the component fractures as a result of the creep process (creep rupture). Creep tests are conducted in order to determine the creep response of a material. This is typically achieved by the application of a constant load to a tensile specimen, which

is maintained at a constant temperature. The extension, or strain, of the specimen, is measured as a function of time [26].

The typical relationship between time and deformation is shown in Figure 2.4. At the very beginning of the test, there is an initial strain due to the elastic, and possibly plastic, deformation of the material. The strain rate, $\dot{\varepsilon} = d\varepsilon/dt$, progressively decreases during this primary stage, until it reaches a relatively constant value, at which point the primary creep stage is said to end and the secondary creep stage begins. The slope of the curve during the secondary creep stage is termed the secondary creep rate, but this is often called the steady-state creep rate, the minimum creep rate, or simply the creep rate. At the end of the secondary creep stage, the strain rate increases until the point of rupture. This third stage is termed the tertiary creep stage. Generally, the secondary creep stage represents the largest portion of the creep test duration

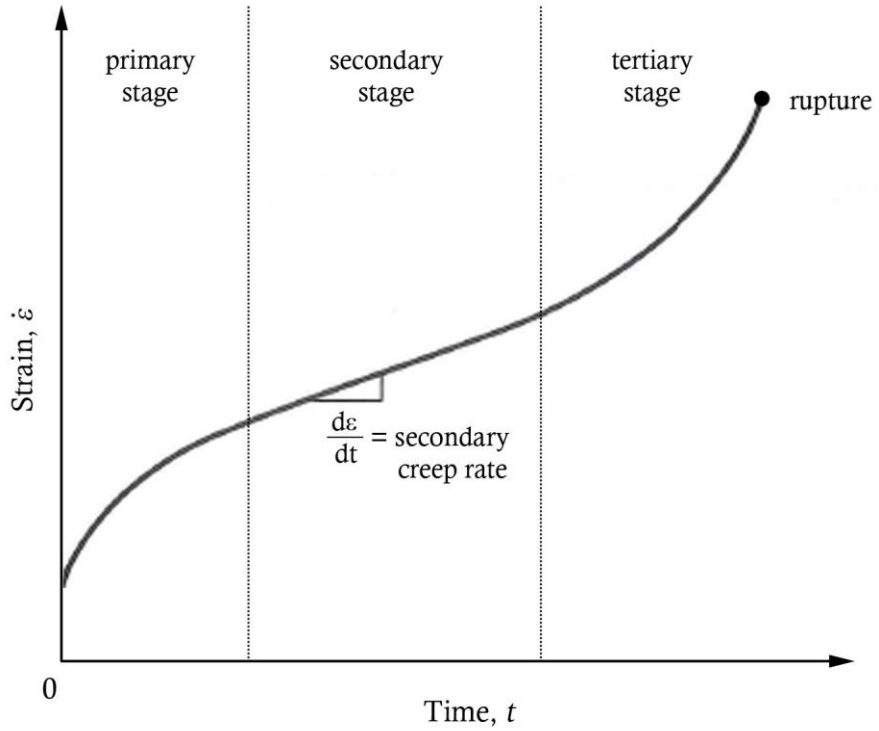

Figure 2.4 - Strain versus time behaviour for creep under constant load, showing the three stages of creep (adapted from [26]).

Creep tests are typically performed on short timescales (1,000 hours being common), thus in order for test data to be applicable to longer service times, extrapolation parameters are necessary. Various approaches using time-temperature parameters to extrapolate data have been proposed, including the Shelby-Dorne and Larson-Miller parameters. Of these, the latter is more common for petrochemical applications such as reformer and ethylene pyrolysis tubes. The Larson-Miller parameter (LMP) is a combination of time and temperature given by Equation 2.3:

$$LMP = T(\log t_r + C) \qquad \textbf{Equation 2.3}$$

where T = absolute temperature in K, t_r is the time to rupture in hours, and C is a constant that is specific to the alloy. Once the constant, C, has been calculated experimentally, the time to rupture can then be estimated for a variety of test conditions [26]. Manufacturers typically present a material's creep performance in terms of LMP, as shown in Figure 2.5.

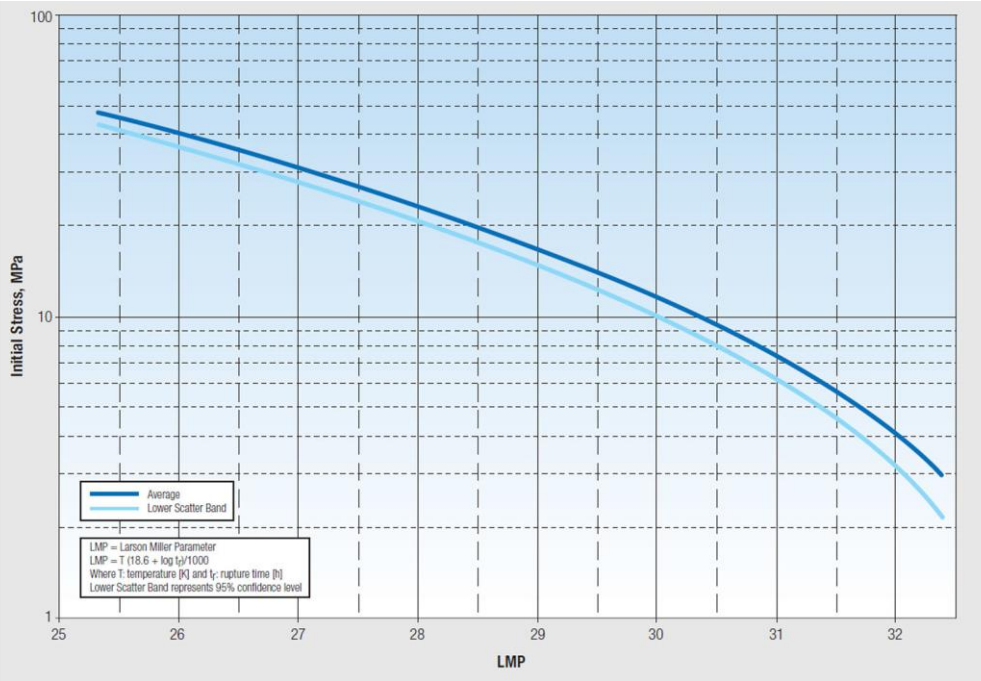

Figure 2.5 - Plot of Larson-Miller parameter (LMP) versus stress for an HP-Nb alloy [27].

Pyrolysis tubes experience creep in the longitudinal direction due to the self-weight of the tubes, and hoop creep strain as a result of decoking processes. The as-cast microstructure of the HP and ET45 alloys, an austenitic matrix with a discontinuous primary network of carbides, is well-suited to providing resistance to creep deformation. The primary carbide network has been reported to play an important role in preventing grain boundary sliding and the secondary carbide distribution that forms as a result of ageing at elevated temperatures acts to restrict dislocation motion [28, 29]. However, as carburization progresses, more carbides form, the secondary carbide network dissolves in favour of the primary network, and the primary network coarsens and coalesces, resulting in a less fragmented network and a low-resistance path for crack propagation. Internal volume increases due to the formation of new carbides and the growth of existing ones creates internal stresses, which adversely affect the creep properties of the tube, causing an increase in creep rate. Carburization has been shown to be a major contributor to increases in longitudinal creep rate, and thus shortening of tube life [5, 30].

Although pyrolysis tubes typically do not fail as a direct result of creep (i.e. due to rupture of the tubes), high longitudinal creep rates result in lengthening of the pyrolysis tubes which can cause warping and bowing, creating further stresses that lead to further increases in creep rate, eventually leading to a point where the tubes need to be shortened. Circumferential temperature distributions can also cause the tubes to become elliptical, resulting in un-even carburization profiles and tube bowing, and blockages due to coking can cause excessive tube deformation. Shortening is achieved by removing a section of the tube, and welding the cut ends back together. Whether a tube can be welded without cracking is dependent on the level of carburization – tubes with low levels of carburization will have retained much of their as-cast ductility, but highly carburized tubes are brittle due to the large volume of brittle carbides, and are at high risk of cracking due to thermal gradients induced during welding [6, 31-33]. Excessive deformation can make the cutting and re-welding process difficult. Economic factors also have to be taken into account when deciding whether a tube is to be shortened or replaced, as there is little point in a tube remaining in service if it has minimal remaining life [31].

As a result of frequent decoking procedures and plant shutdowns, ethylene pyrolysis tubes experience a number of thermal cycles over their lifetimes. The thermal cycling is expected to result in tube damage that accumulates with every cycle, but determining the effect of cyclic stresses as a result of thermal cycling on the remaining life of ethylene pyrolysis tubes is a complex problem. Creep ductility exhaustion has been proposed as a method by which to quantify the damage accumulation as a result of cyclic stresses [5, 34]. The concept of creep ductility exhaustion assumes that a fraction of the material's creep ductility (typically defined as the creep strain at failure) is consumed during each thermal cycle. Once the material's creep ductility is consumed then failure of the tube occurs. Previous work by Thomas et al. [34] has attempted to quantify the effect of cyclic stresses on the life of HP-Nb reformer tubes based on this concept.

The use of the creep ductility exhaustion method to quantify the effects of thermal cycling and cyclic stresses on remaining life is relatively complex. It requires an understanding of the creep ductility and stress relaxation properties of the alloy with respect to temperature, stress, exposure time, and, in the case of ethylene pyrolysis tubes, the extent of carburization. In addition, the service conditions of the tube need to be accurately known, namely the number of thermal cycles, and the heating/cooling rates. The creep ductility of high temperature alloys varies significantly when comparing the as-cast and aged conditions (reported values for HP-Nb range from 3-19% as-cast, 17-39% aged [34, 35]), and despite there currently being no data reported in the literature regarding the creep ductility of carburized tubes, it is expected that there would be great variation depending on the level of carburization. Thus, further understanding of the creep and stress relaxation properties of the alloys in various microstructural conditions is necessary to be able to accurately predict the effects of thermal cycling and cyclic stresses on remaining life using creep ductility exhaustion.

2.2.3 Coking, Decoking and Thermal Cycling

Over the course of pyrolysis operation, a layer of coke is deposited on the inside of the radiant tubes, limiting heat transfer to the process stream and thus requiring an increase in the tube temperature, as coke acts as an insulator [2, 4, 5]. At the end of run, such coke layers can be up to 20 mm thick.

The coke deposits are burned or spalled off periodically using steam or a steam-air mixture, typically called a "decoking" operation. A decoking cycle involves the furnace being taken off-line and the residual hydrocarbon feedstock being purged downstream. Steam or a steam-air mixture is then introduced to the radiant tubes and the furnace brought back on-line to burn, gasify, or spall the coke layer. Once the decoking process is complete (typically after 20 – 35 hours), the furnace is reset back to normal operating conditions [2, 4, 5].

During the change between normal operation and decoking, a temperature drop occurs. The thermal expansion coefficient of the tube metal (~19 $x10^{-6}$ K^{-1}) is much higher than that of the coke (~4 $x10^{-6}$ K^{-1}), and coke has a high compressive strength, thus it is not crushed but rather restrains the contraction of the tube, leading to high tensile stresses in the tube [5]. If the tube has enough ductility these stresses will then relax during the decoking procedure. However, carburized tubes are very brittle, and a temperature drop can result in the tube cracking. The risk of cracking in carburized tubes upon a temperature drop is dependent on a number of factors. The severity of the temperature drop is important, as larger temperature drops lead to greater thermal contraction of the tube, and therefore the tube experiences higher tensile stresses as a result of the coke layer restraining the contraction. The thickness of the coke layer determines whether the thermal contraction of the tube will be restrained or not – thinner layers are more likely to be crushed, but thicker layers will restrain tube contraction. Lastly, the level of carburization of the tube, and therefore its ductility, is significant, as increasing levels of carburization results in decreasing ductility, and therefore increased risk of cracking. Unexpected furnace shutdowns/furnace trips that result in extreme temperature drops can therefore be destructive. The most risky time for brittle failures are when the pyrolysis tubes are a few years old (aged and carburized, and therefore embrittled) and when the furnace is in the second half of its operation run (thicker coke layers). This is demonstrated schematically in Figure 2.6. The frequency of decoking cycles is a delicate balance – too frequent decoking cycles accelerate thermal damage of the tubes, but infrequent decoking promotes carburization of the tube material, and leaves tubes at a higher risk of cracking during thermal cycling due to thicker coke layers [5, 30]. This provides some motivation for the development of coke-resistant furnace alloys, such as the alumina-forming HT-E alloy [36], which could allow for longer production runs in between decoking cycles [2, 37].

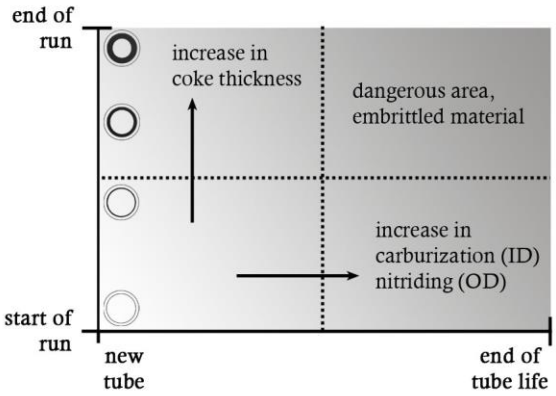

Figure 2.6 - "Dangerous area" for brittle cracking of ethylene pyrolysis tubes (adapted from [5]).

2.2.4 Oxidation at the Outer Diameter

The outer diameter of the tubes is subject to a primarily oxidizing environment, due to exposure to flue gases and air at service temperatures. HK and HP alloy ethylene pyrolysis tubes experience many of the same microstructural changes seen at the inner diameter as a result of oxidation [38, 39]. A Cr_2O_3 surface layer grows and spalls periodically, and while it is intact the alloy is protected from internal attack; however, once the sub-surface chromium content is below the critical level to form Cr_2O_3, further scale formation is impossible and the alloy is susceptible to attack. The growth of the chromium-rich scale is accompanied by the depletion of chromium and the dissolution of secondary, and eventually primary, chromium carbides in the sub-surface region. Internal oxidation is also typically observed at the exposed outer surface. A thin, continuous layer of silicon oxides is typically observed directly under the Cr_2O_3 scale, with large interdendritic silicon oxides penetrating into the sample along dendrite and grain boundaries. The silicon oxides are typically identified as SiO_2, and appear to take the place of the dissolved chromium carbides in the chromium depleted zone. Large voids are often observed near the outer surface; the formation of these voids in ex-service reformer tubes is attributed to the Kirkendall effect [40].

2.2.5 Nitridation

At the outer diameter of the tubes, internal attack is typically nitridation, due to nitrogen ingress as a result of the exposure to flue gases and air at service temperatures. Nitrogen ingress into the tube occurs through cracks and pores in the oxide layer, and the nitrogen reacts with chromium to form nitrides or carbonitrides. The nitridation sequence typically starts with the conversion of chromium carbides (usually $M_{23}C_6$ at the outer diameter) into carbonitrides, $M_2(C,N)$, M(C,N), and/or $M_6(C,N)$, which then grow with uptake of nitrogen and chromium. The changes in mechanical properties as a result of nitridation are similar to those caused by carburization; both cases result in internal stresses, chromium depletion, and embrittlement [5].

Buchanan [35] observed carbonitrides of the type $Cr_2(C,N)$ along columnar grain boundaries at the mid wall region of an HP-Nb alloy sample aged in air at 1100 °C for 10,000 hours. These $Cr_2(C,N)$ mid wall carbonitrides were observed at a distance of 2.5 mm ahead of the $M_{23}C_6$-to-$Cr_2(C,N)$ transformation interface that occurred at the surface of the sample. It is currently unknown why $Cr_2(C,N)$ precipitates were located at such a large distance ahead of the transition interface.

2.3 Metallurgical History of Heat-Resistant Alloys for Reformer and Pyrolysis Tubes

The aggressive environment of reformer and pyrolysis furnaces requires the use of high temperature, austenitic stainless steels. Up until the 1960's, the alloy in use for reformer and pyrolysis tubes was the expensive wrought HT alloy (Table 2.1) [41]. In order to reduce the cost of the furnaces, the centrifugally cast HK alloy series was introduced in the early 1960's to replace the HT alloys. The HK alloy tubes displayed comparable creep performance at a reduced cost, due to reduced production costs and a lower Ni content (Table 2.1).

The high carbon content of the HK alloy series (typically 0.4 wt%) results in the formation of chromium-rich M_7C_3 carbides along the grain boundaries and dendrite arm boundaries, improving the creep properties when compared to low-carbon stainless steels with similar chromium and nickel content [42]. During service at elevated temperatures, the primary M_7C_3 carbides transform to $M_{23}C_6$, and a distribution of secondary $M_{23}C_6$ precipitates intragranularly [41]. The combination of both primary and secondary carbides initially increases the alloy's creep resistance, but due to continual coarsening of the carbides during service this increase is progressively lost and the alloy becomes embrittled. Despite this, the HK alloy series became the industry standard, as it was the only available alloy that displayed reasonable creep strength up to 1000 °C whilst being comparatively inexpensive [43]. Machining of the inner diameter of the tubes was introduced, in order to remove the non-metallic inclusions that typically segregate to the inner diameter during centrifugal casting, thus reducing the possibility of crack initiation [43].

Subsequent developments to the high temperature alloys focused on composition. In the early 1970's International Nickel Ltd. developed alloy IN519 – a modified HK alloy with niobium additions and increased nickel content [43, 44]. Niobium is a strong carbide former, and its addition to alloy IN519 (Table 2.1) resulted in a mixed network of primary carbides in the as-cast condition. The NbC carbides partially replaced the M_7C_3 carbides, creating alternating groups of M_7C_3 and NbC lamellae [43, 44], resulting in significant increases in the creep rupture strength and creep ductility in comparison to the un-modified alloy (Figure 2.7).

Increasing demand from the petrochemical industry for materials that could withstand increasingly more aggressive service conditions led to the development of the HP alloy series (Table 2.1) [42, 43].

The un-modified HP alloy displayed similar creep strength to the un-modified HK alloy, as shown in Figure 2.7. Niobium was immediately introduced to the HP composition, in the range of 0.5-1.5 wt%, and, as with the HK-Nb alloy, this resulted in alternating groups of NbC and M_7C_3 lamellae in the as-cast structure. As with the HK alloy series, the HP-Nb alloy experiences the transformation of M_7C_3 to $M_{23}C_6$, the precipitation of secondary $M_{23}C_6$ carbides, and subsequent carbide coarsening during ageing. The HP-Nb alloy was seen to have superior creep strength and carburization resistance up to 1050 °C, leading to it becoming the industry standard for reformer and pyrolysis furnaces [43].

The instability of the primary NbC precipitates and their transformation to G-phase ($Ni_{16}Nb_6Si_7$) [45-47] during service raised concerns regarding the long-term effectiveness of the niobium additions. The continual coarsening of the primary and secondary $M_{23}C_6$ precipitates was also of concern. Thus, in order to increase the microstructural stability of the HP alloy, and to further increase the creep strength, manufacturers began to produce "micro-alloyed" HP compositions which contained varying combinations of niobium, titanium, zirconium, tungsten, rare earth elements, or other proprietary combinations. The addition of multiple alloying elements is largely based on the work of Hou and Honeycombe [44], who used combined additions of niobium, titanium and zirconium to significantly increase the creep strength of the IN519 alloy. The use of micro-alloying additions in the HP alloy further increased the creep strength in comparison to the HP-Nb alloy (Figure 2.7). A number of studies conducted on micro-alloys commonly report the combined use of niobium (up to 1.5 wt%) and titanium (up to 0.1 wt%) [29, 42, 48, 49]. The increase in the creep strength of HP-Micro when compared to HP-Nb is typically attributed to the increased complexity of the precipitate networks combined with their increased stability at service temperatures [29, 48].

Although the creep and carburization resistance of HP-Micro was improved compared to its predecessors, a change in the typical design of ethylene pyrolysis furnaces to shorter residence times and higher operating temperatures (up to 1150 °C) pushed the operating conditions beyond the capabilities of HP-Micro. Higher nickel grades were experimented with, and the ET45-Micro alloy (Table 2.2) was seen to be oxidation resistant up to 1150 °C, while still retaining sufficient creep strength (Figure 2.7). The metallurgy of this alloy went straight to the micro-alloyed version, based on previous experience with HP-Micro [43, 50, 51]. Recent studies on ET45-type alloys report the combined use of niobium (up to 1.5 wt%) and titanium (up to 0.1 wt%), similar to the micro-alloying additions reported for the HP-Micro alloy [30, 51, 52]. The industry standard today for centrifugally cast tubes for ethylene pyrolysis furnaces is ET45-Micro or HP-Micro alloys for the hot outlet tubes, sometimes combined with HP-Nb alloy for the colder inlet tubes [43].

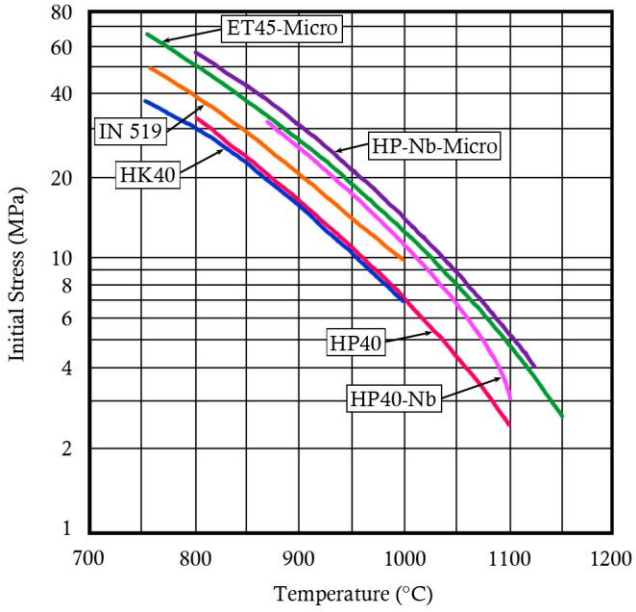

Figure 2.7 - Comparison of the 1000-hour rupture strength of several heat-resistant alloys (adapted from [35, 43]).

Table 2.1 - Composition of selected heat-resistant stainless steels.

wt%	C	Cr	Ni	Si	Mn	Fe	Ref.
HT	0.35-0.75	13-17	33-37	2.50	-	Bal.	[42]
HK	0.2-0.6	24-38	18-22	1.75	1.0	Bal.	[42]
IN519	0.3-0.4	23-24	24-25	0.7-0.8	0.5-0.7	Bal.	[44]
HP	0.35-0.75	24-28	33-37	1.5	1.5	Bal.	[42]

Table 2.2 - Composition of selected micro-alloyed heat-resistant stainless steels (Add. = additions).

wt%	C	Cr	Ni	Si	Mn	Fe	Nb	Ti	Zr	Rare Earths	Ref.
HP-Nb-Micro	0.45	25	35	1.5	1.0	Bal.	1.5 max	0.1 max	-	-	[29, 42, 48, 49, 53]
ET45-Micro	0.45	35	Bal.	1.6	1.0	16	1.0	Add.	Add.	Add.	[43, 54]

2.4 Metallurgy of HP and ET45 Alloys

2.4.1 Macrostructure

The cross-section of centrifugally cast pyrolysis and reformer tubes typically consists of three distinct regions – small equiaxed chill grains at the outer diameter (A), followed by columnar grains at the mid wall (B), and equiaxed grains at the inner diameter (C) (Figure 2.8) [48, 55]. The equiaxed chill grains are formed first upon solidification. The proportion of columnar and inner equiaxed grains is dependent on the casting parameters, namely the melt pouring temperature, the mould material, and the rotational speed of the mould. Tubes with almost entirely columnar grains can be produced if the cooling rate is high enough. Due to the centrifugal forces generated during casting, impurities and inclusions are segregated to the inner diameter of the tubes, where they are subsequently removed by machining [43, 48]. As a result of the improvement in purity and creep properties, as well as lower productions costs in comparison to static casting, the centrifugal casting technique has become the industry standard for the production of pyrolysis and reformer tubes.

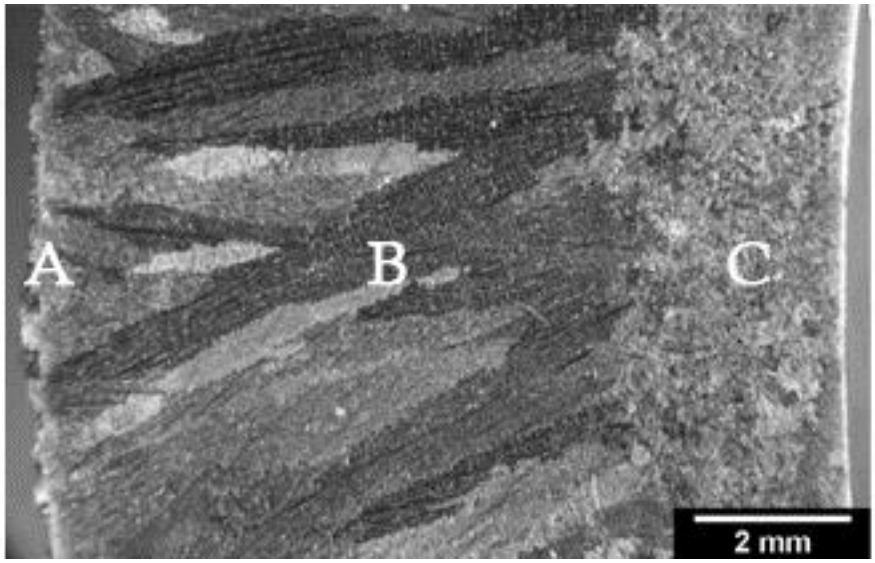

Figure 2.8 – Cross-section of a typical HP alloy tube displaying the macrostructure due to the centrifugal casting method [56].

The optimum columnar/equiaxed grain ratio with respect to creep strength of the material is unclear, at least in the widely published literature, and advances in casting practice are known to be kept as industrial secrets [56]. Manufacturers report that, for reformer tubes, an equiaxed structure that comprises 30% of the wall thickness as measured from the inner wall is ideal, stating that creep damage typically starts in the inner third of the wall where the combined thermal and hoop stresses peak [43]. An equiaxed grain structure at the inner wall is reportedly more resistant to creep crack propagation than a columnar structure. However, little evidence was found in the literature to support this theory. In addition, the creep damage experienced by pyrolysis tubes will not necessarily be concentrated at

the inner wall, due to complex stress profiles across the wall as a result of internal volume increases and thermal cycling.

There are a limited number of studies characterizing the effects of grain structure on the creep properties of HK and HP alloys that have been reported in literature [55, 57-59]. Wu *et al.* [57] modified the grain structure of two separately cast HK alloy tubes by using graphite (low cooling rate) and cast iron (high cooling rate) molds, while keeping the rotational speed constant. A third tube was cast in a cast iron mold while magnetically stirring the melt during solidification. Creep samples were machined from the three tubes and subjected to uni-axial creep testing at 871 °C and 950 °C over a range of stresses between 25 - 100 MPa. Tests on creep samples where the gauge length was either 100% columnar (cast iron mold) or 100% equiaxed (graphite mold) grain structures showed no significant difference in the creep rupture life when comparing the two. The creep rupture life of the tube that was magnetically stirred during solidification was increased by approximately 53% compared to the other two tubes. This increase was partially attributed to refinement of the columnar and equiaxed grains; however, the magnetic stirring during solidification also increased the volume fraction of primary carbides in both the columnar and equiaxed zones. Thus the effects of grain structure on the creep properties were unable to be quantified, due to the interdependence of the grain structure and carbide volume fraction.

Zaghloul *et al.* [55] modified the cooling rate during solidification by using different mold materials (graphite, cast iron and copper) combined with varying mold rotation speeds (1400 – 1700 rpm). The ratio of columnar to equiaxed grains, the columnar grain size, the carbide morphology, and the refinement of the primary carbide network are all determined by the cooling rate during solidification. Generally, the average size of the columnar grains and the proportion of the tube wall composed of columnar grains increased with increased cooling rate. Uni-axial creep rupture tests were performed over a range of temperatures. For rupture tests performed at 950 °C, the rupture life was relatively unaffected by the cooling rate during casting. However, for rupture tests conducted at 1000 °C and 1100 °C, the rupture life increased (by ~30% and ~300% respectively) for those tubes which experienced higher cooling rates during casting (804 °C/min versus 240 °C/min). Although the grain size increased with increased cooling rate during casting, the volume fraction of primary precipitates decreased (5% to 2.2%). The number of secondary precipitates increased with cooling rate, while the average size decreased (0.35 μm to 0.3 μm), resulting in a refinement of the secondary precipitate network, which would provide a superior dispersion strengthening effect and thus a contribution to increased creep rupture life. Therefore, as casting conditions affect both the grain size/shape and the precipitate distribution, it is difficult to isolate the effect of grain size/shape on the creep properties of centrifugally cast HK and HP alloys.

The study that focused on the accumulation of creep damage (i.e. creep voids) in ex-service HP alloy reformer tubes found that the level of creep damage was lowest within the equiaxed region of the tube

[59]. Three dimensional reconstruction of serial sectioning data from the columnar and equiaxed regions of the tube revealed that the creep void density and accumulated creep void volume was lowest in the equiaxed region at the inner wall of the tube, and highest in the columnar region at the outer wall.

2.4.2 Microstructural Evolution of HP-Nb

As-Cast Condition

Niobium is added to the HP composition in order to modify the primary carbide network. Niobium is a stronger carbide former than chromium, thus the addition causes the partial replacement of the as-cast chromium carbides in the primary network with niobium carbides. Representative optical and scanning electron micrographs of a HP-Nb alloy in the as-cast condition are shown in Figure 2.9. The as-cast microstructure is typically composed of an austenitic matrix with alternating interdendritic groups of primary chromium (M_7C_3) and niobium (NbC) carbides. Due to atomic number contrast in electron backscattered images, as in Figure 2.9 (b), the chromium carbides appear dark grey and the niobium carbides appear white. The matrix is typically considered to be free of precipitates.

Relatively high cooling rates during the centrifugal casting process result in the formation of the meta-stable M_7C_3 carbide, and a matrix supersaturated in carbon [47]. However, niobium additions can cause a change in the stoichiometry of the primary chromium carbides, as seen in statically cast HP-Nb alloys where $M_{23}C_6$ precipitates were identified as the primary chromium carbide for niobium concentrations greater than 1.97 wt% [29, 45-47]. In addition to the partial replacement of the M_7C_3 carbides by niobium carbides, niobium additions to the HP composition have been shown to fragment and refine the primary carbide network [29, 45-47]. The amount of replacement, refinement, and fragmentation is a function of the niobium content [60].

Accelerated creep testing showed that niobium-modified HP alloys have increased rupture life and lower minimum creep rates in comparison to the un-modified HP composition [43, 46, 60]. The improvement in creep properties is partially attributed to the refinement and fragmentation of the primary carbide network, due to the absence of a continuous path for crack propagation along the precipitate/matrix interface [29, 45-47].

The as-cast primary niobium carbides are typically reported to obtain a lamellar "Chinese Script" morphology, identical to NbC precipitates in the HK-Nb alloy [29, 44-47]. However, recent high-magnification observations of NbC precipitates in two as-cast HP-Nb alloys by Buchanan *et al.* [35, 60] revealed the existence of two significantly different morphologies of individual plate lamellae. Type I lamellae, shown in Figure 2.10 (a), obtain a relatively planar interface with the matrix. Type II lamella, shown in Figure 2.10 (b), exhibit undulations along the surface of the lamellae. Buchanan *et al.* confirmed that both the Type I and type II morphologies have the FCC NbC ($Fm\bar{3}m$) crystal structure. Small precipitates rich in chromium and carbon were observed at the interface between the

Type II lamellae and the austenitic matrix, as shown in Figure 2.11, and were subsequently identified as Cr_7C_3. Buchanan *et al.* believe that the interfacial Cr_7C_3 is independent of the primary Cr_7C_3 network (i.e. not caused by two-dimensional sectioning effects).

Deep etching using glyceregia by Buchanan *et al.* clearly revealed the differences in the two morphologies and their three-dimensional structure, as shown in Figure 2.12. The Type I lamellae were revealed as smooth, solid plates, with the faces exhibiting varying degrees of curvature. The Type II lamellae were revealed to have a web-like, or reticulated, structure, with the fragmentation observed in two dimensions corresponding to the three-dimensional pores within the plane of the plates visible in three dimensions.

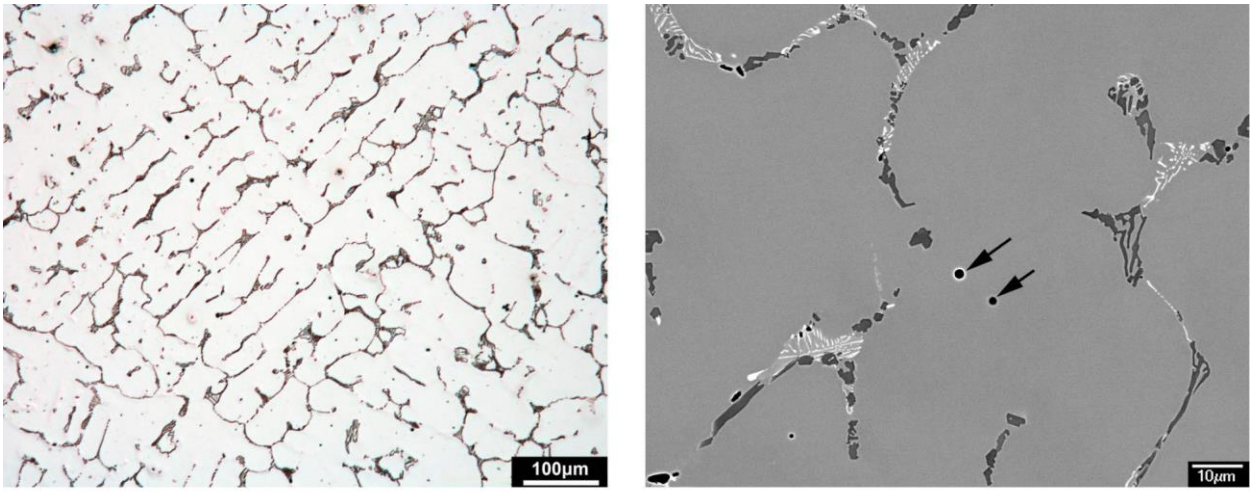

Figure 2.9 - (a) optical and (b) backscattered electron micrographs of an as-cast HP-Nb alloy [35]. The arrows in (b) indicate manganese sulfide inclusions.

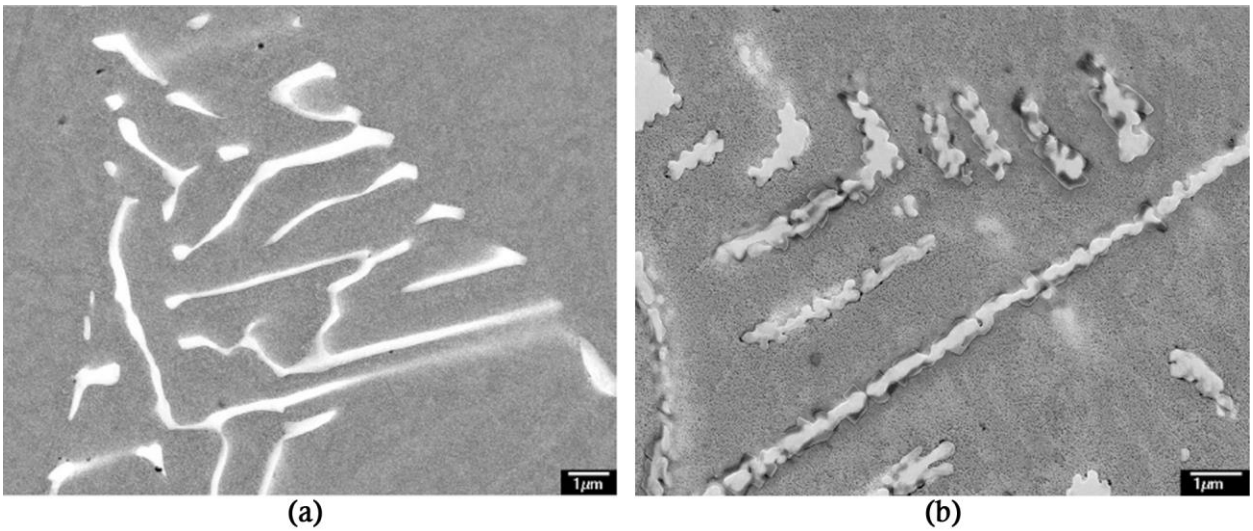

Figure 2.10 – Scanning electron micrographs showing the two-dimensional morphology of (a) Type I lamellae and (b) Type II lamellae [35].

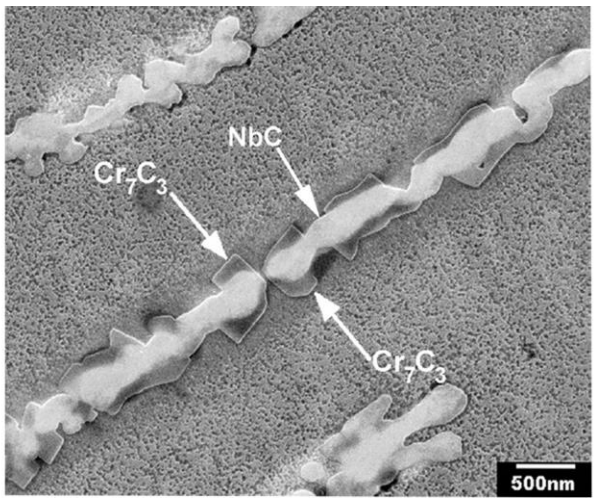

Figure 2.11 - Scanning electron micrograph showing the Cr_7C_3 located on the precipitate/matrix interface of the Type II lamellae [35].

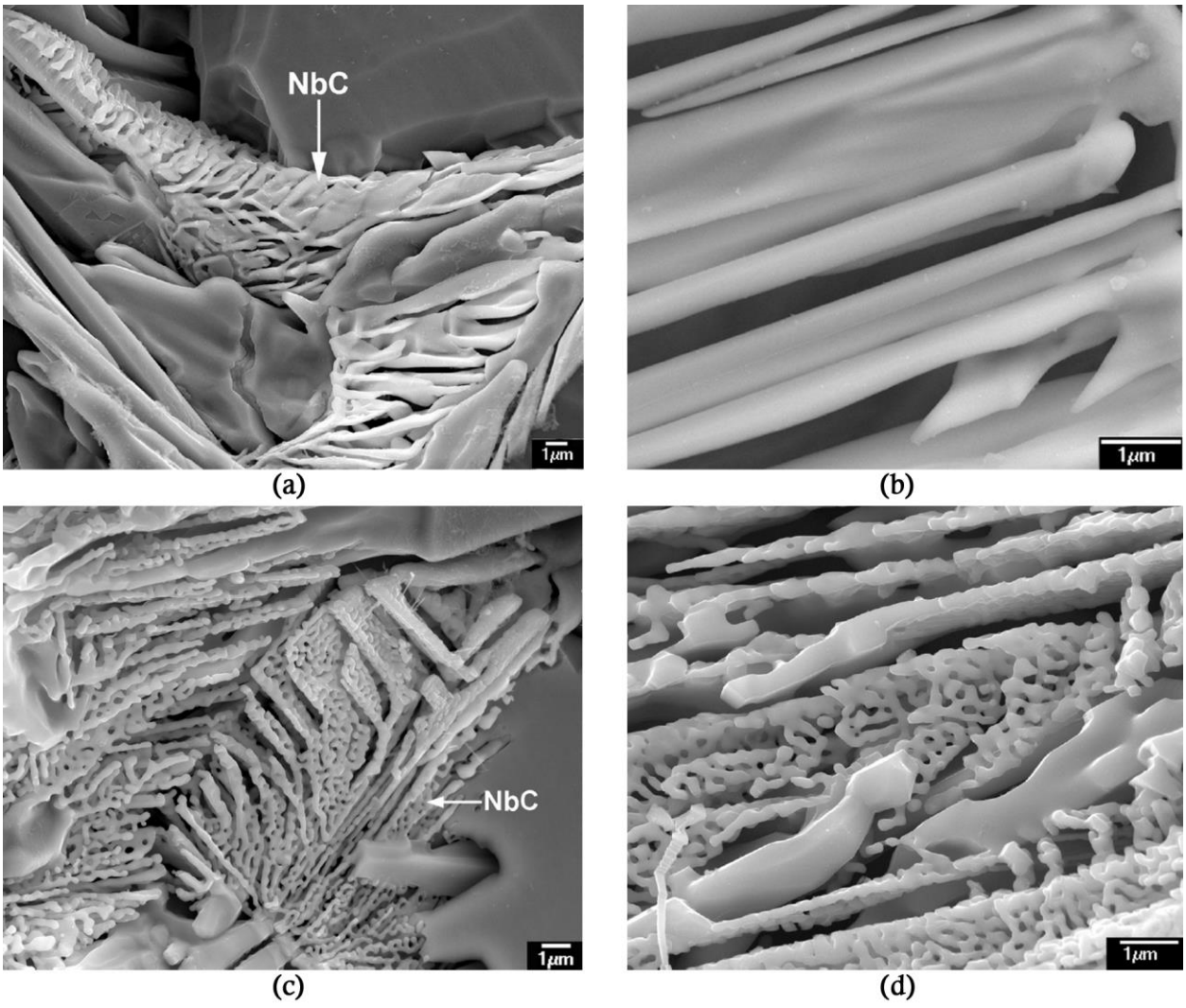

Figure 2.12 - Secondary electron micrographs showing the three-dimensional morphology of (a)-(b) Type I lamellae and (c)-(d) Type II lamellae [35].

The primary NbC carbides in the HK-Nb alloy were shown by Hou and Honeycombe [44] to obtain a cube-cube orientation relationship (OR) with the matrix:

$$\langle 100 \rangle_{\mathrm{NbC}} \parallel \langle 100 \rangle_{\gamma}$$

$$\{100\}_{\mathrm{NbC}} \parallel \{100\}_{\gamma}$$

Buchanan *et al.* confirmed that all the Type I lamellae in the HP-Nb alloys characterized conformed to this cube-cube OR with the matrix, on all sides of the lamella. In cases where the lamella was located on a grain boundary, it exhibited a cube-cube OR with the grain that contained the lamella, i.e. the grain where nucleation of the lamella occurred. TEM (transmission electron microscopy) trace analysis revealed that the Type I lamellae exhibit a {100} habit plane. After performing a similar analysis on the Type II lamellae, Buchanan *et al.* concluded that although the Type II lamellae typically adhered to an overall growth plane, they exhibited no crystallographically rational habit plane, and did not obtain a consistent, rational orientation relationship with the matrix. The Type II lamellae were more prevalent than the Type I, particularly in the alloy which contained higher niobium content.

Based on these observations, Buchanan *et al.* concluded that the difference in morphology between the two types is due to the solidification conditions experienced by each type. In the case of the Type I lamellae, nucleation likely occurs on the existing austenite dendrite, setting the NbC/austenite orientation relationship, followed by eutectic growth of the lamellae with the austenite. The {100} habit plane allows the NbC precipitates to obtain a high surface area while minimizing the total free energy associated with the boundary. The Type II lamellae likely nucleate in the liquid ahead of the γ/L interface, prior to the formation of the Type I lamellae, and the effects of local melt thermodynamics on the growth of the lamellae result in the undulations of the plates and overall planar growth.

Evolution of Microstructure during Ageing and Carburization

Exposure of the HP-Nb alloy to temperatures above 700 °C results in the primary network of M_7C_3 transforming to the more stable $M_{23}C_6$ carbide, with complete transformation typically occurring within the first 1000 hours of exposure [35, 45, 46]. During prolonged ageing (>1000 hours), the primary $M_{23}C_6$ coarsens, with coarsening rate generally increasing with ageing temperature. The $M_{23}C_6$ precipitates are typically composed of numerous grains, and typically obtain a $[100]_{M23C6}//[100]_{\gamma}$ with the austenite matrix [35].

Carbon diffusion into the tube results in chromium, a strong carbide former, being pulled from the austenitic matrix and combining with the carbon to grow the existing chromium-rich carbides and also form new ones. With continued carbon diffusion, the primary carbide network continues to coarsen and coalesce, eventually leading to an almost continuous primary network. Typically two

chromium carbide zones are observed; $M_{23}C_6$ is initially present across the entire tube wall; however, high amounts of carbon at the inner wall necessitate the transformation to M_7C_3 [11, 21, 25]. The $M_{23}C_6$-to-M_7C_3 transformation is reported to occur by the rejection of metal from the carbide [17, 21]:

$$M_{23}C_6 \rightarrow M_7C_3 + M \qquad \textbf{Equation 2.4}$$

The $M_{23}C_6$-to-M_7C_3 transformation front continues to progress into the tube wall with the continual supply of carbon from the cracking reaction at the inner diameter. An example of the $M_{23}C_6$-to-M_7C_3 transition in an HK40 alloy is shown in Figure 2.13.

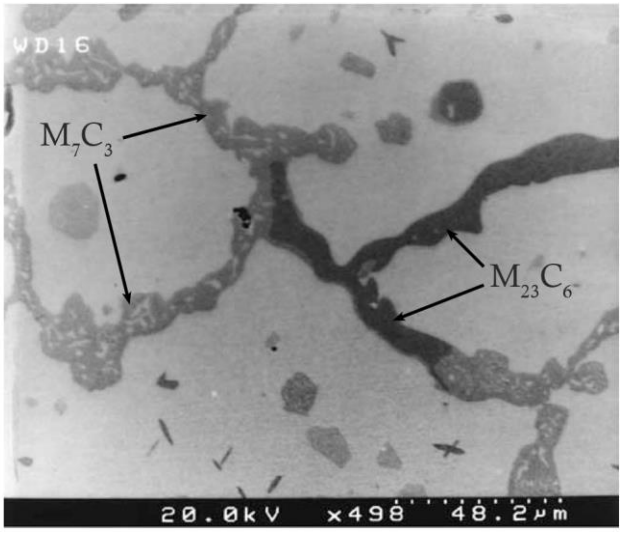

Figure 2.13 - Scanning electron micrograph of the $M_{23}C_6$-to-M_7C_3 transformation in an HK40 alloy [61].

Fine distributions of secondary carbides form in the austenitic matrix during exposure to elevated temperatures, and the distribution is typically concentrated adjacent to the interdendritic and grain boundary primary carbide network [35, 45, 46]. The secondary precipitates are generally $M_{23}C_6$; however, a small number of secondary NbC precipitates similar in size to the secondary $M_{23}C_6$ have been observed in laboratory aged HP-Nb alloys [35]. The density of the secondary precipitate distribution decreases with increasing distance from the primary precipitates. The preferential formation of secondary precipitates adjacent to the primary network reportedly occurs as a result of the high density of dislocations in these regions, induced by the primary precipitates during the casting process [35, 44, 46]. In service, the secondary carbides adjacent to the grain boundaries are believed to inhibit the creep deformation that is also typically concentrated in this area [48].

The secondary $M_{23}C_6$ carbides typically have a cuboidal morphology, and obtain a cube-cube OR ($[100]_{M23C6}//[100]_\gamma$) with the austenitic matrix [29]. A Widmanstätten (needle-like) morphology can be obtained; however, this is less common than the cuboidal morphology – Buchanan [35] estimated that for a HP-Nb alloy aged at 1000 °C for 1000 hours, the Widmanstätten morphology represented

less than 1% of the secondary precipitate population. The Widmanstätten morphology reportedly occurs when there is an excess of chromium in solution with respect to carbon; however, the exact chromium to carbon ratio necessary to cause the formation of the Widmanstätten morphology is unclear as it is also influenced by the niobium content [45, 46].

Prolonged exposure to elevated temperatures (>1000 hours) results in Ostwald ripening of the secondary precipitate distribution. The distribution coarsens as ageing progresses, and the coarsening occurs at a more rapid rate at higher temperatures. The secondary precipitates do not become comparable in size to the primary precipitates, and thus the Gibbs-Thomson effect [62] eventually causes the dissolution of the secondary precipitates in favour of the growth of the primary precipitates. With sufficient time, the secondary precipitate distribution completely dissolves in favour of the primary network [35].

A comparison between the carbide networks of HP-Nb alloys in the as-cast, aged, and carburized conditions is shown in Figure 2.14.

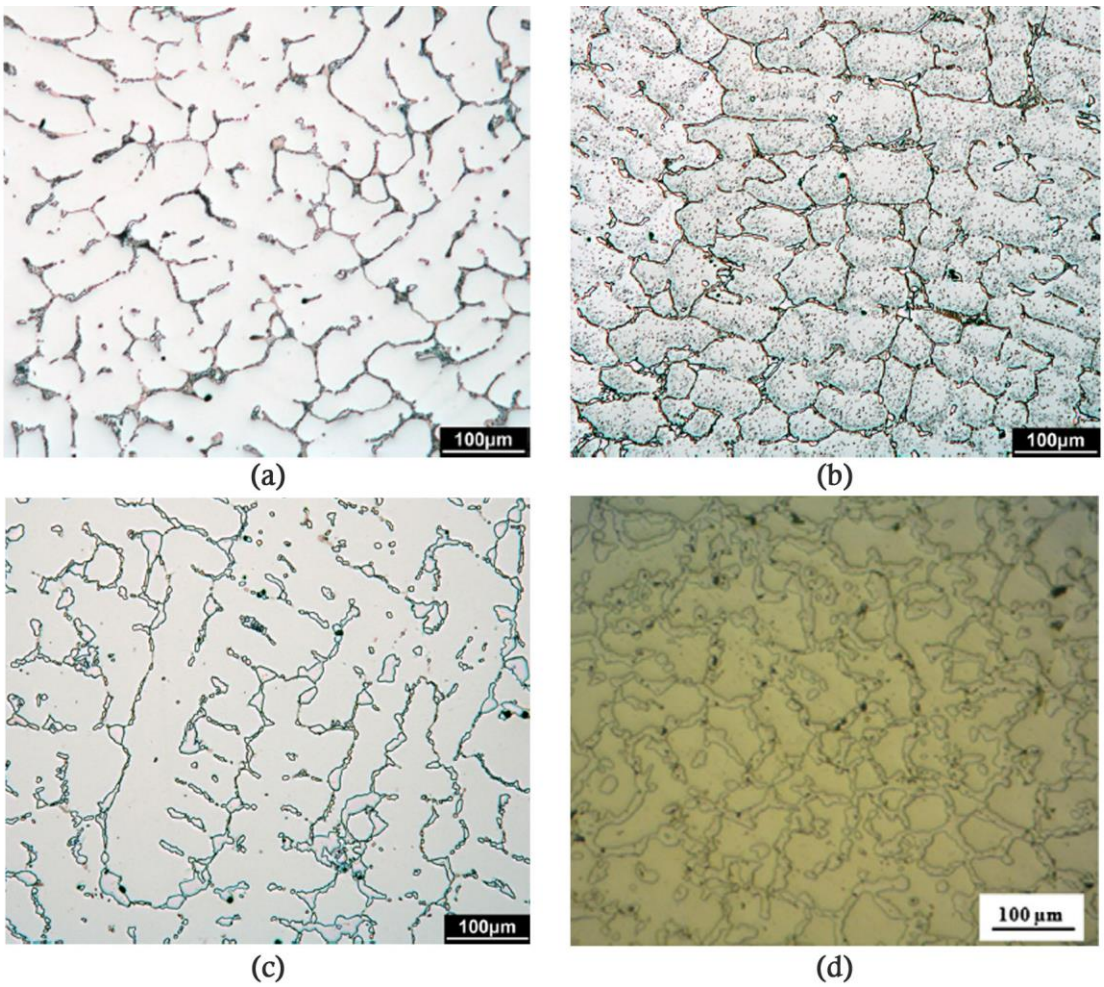

Figure 2.14 - Optical micrographs displaying (a) as-cast HP-Nb alloy [33], (b) HP-Nb alloy aged for 1000 hours at 1100 °C [33], (c) HP-Nb alloy aged for 10,000 hours at 1100 °C [33], and (d) carburized region of an ex-service HP alloy tube after approximately 44,000 hours in service with a maximum working temperature of 1100 °C [39].

Exposure of HP-Nb alloys between 700 - 1000 °C can, depending on the silicon and niobium content, cause the transformation of the primary niobium carbides to one of two silicide phases – a Ni-Nb-Si silicide, or a Cr-Ni-Nb-Si silicide. The instability of NbC precipitates in HP alloys during exposure to temperatures between 700 – 1050 °C, and their subsequent transformation, is well documented in literature [35, 46, 47, 50, 63-65].

The composition of the face centered cubic ($Fm\bar{3}m$) nickel-niobium-silicon silicide is typically reported in literature to be $Ni_{16}Nb_6Si_7$, and it is commonly known as G-phase [29, 45-47]. The transformation of the primary niobium carbides to G-phase is typically complete after 1000 hours, and it is observed that the G-phase retains the prior lamellar morphology of the niobium carbide. Ageing for longer than 1000 hours causes growth of G-phase regions and an eventual loss of the lamellar morphology. The transformation of NbC to G-phase is believed to occur by the rejection of carbon from and the diffusion of silicon and nickel to the existing NbC precipitate [29, 45, 46, 65]. The rate

of transformation is dependent on the ageing temperature, as well as the relative contents of silicon, niobium and nickel. An increase in silicon content increases the transformation rate for a given temperature [47]. Increases in nickel and niobium content also increase the transformation rate, but the effect is much less pronounced than that of silicon. $Cr_{23}C_6$ carbides are often found in close contact with G phase and are believed to form as a result of the rejection of carbon from the transforming NbC to the surrounding matrix [46, 47]. Secondary G-phase has also been observed at the $Cr_{23}C_6$/matrix interface [29, 46].

The diamond-cubic ($Fd\bar{3}m$) chromium-nickel-niobium-silicon silicide is commonly referred to as η-carbide, and has been identified in HP-Nb alloys after laboratory ageing [35, 49] and in ex-service material that had experienced ageing during service [50, 63, 64]. The chromium content of η-carbide is typically reported to be 30-35% [35, 49, 64], significantly higher than that reported for G-phase (typically <5%) [29, 46, 47].

G-phase was identified in laboratory aged HP-Nb alloys by de Almeida Soares *et al.* [46] and Ibañez *et al.* [47], after a number of different HP-Nb alloys with varying niobium and silicon contents were aged at temperatures between 700 – 1100 °C. Regardless of the alloy composition, G-phase was the only phase seen in association with the NbC precipitates after ageing between 700 – 1000 °C for up to 1000 hours. The NbC precipitates remained stable after ageing at 1100 °C, indicating that the maximum temperature limit for the transformation of NbC to G-phase lies between 1000 – 1100 °C. Time-temperature-transformation (TTT) curves were constructed from the ageing data, and were used to predict an upper limit for the NbC-to-G-phase transformation between 1000 – 1050 °C.

Buchanan [35] conducted a series of laboratory ageing experiments on two HP-Nb alloys, at temperatures between 900 – 1100 °C, and ageing times of 500 - 10,000 hours. G-phase was not observed in the two alloys after ageing at 1000 and 1050 °C, suggesting that the upper temperature limit for the NbC-to-G-phase transformation may differ between alloys. In order to directly compare with the studies conducted by de Almeida Soares *et al.* and Ibañez *et al.,* Buchanan aged samples at 900 °C for 1000 hours, observing that the NbC carbides partially transformed to a mixed network of G-phase and η-carbide. Transformation of the NbC colonies to solely G-phase or solely η-carbide was not observed; rather the G-phase and η-carbide precipitates within an individual colony were located adjacent to one another.

Although there are a limited number of studies on laboratory aged HP-Nb in literature, there are numerous studies published on ex-service HP-Nb alloys which have experienced ageing during service (typically steam reformer tubes), e.g. [40, 49, 50, 63, 64, 66]. As with the laboratory aged alloys, the transformation product of the NbC carbides varied depending on the tube temperature. In tubes exposed to temperatures of 815 °C and 890 °C, only the NbC-to-G-phase transformation was observed. In tubes exposed to temperatures of 920 – 1100 °C, the NbC-to-η-carbide transformation

was dominant. Mixed NbC/G-phase/η-carbide networks were observed in tubes exposed to 875 – 905 °C.

Based on the preceding results, Buchanan [35] concluded that, in aged HP-Nb alloys, the transformation product of the NbC carbides is determined by the ageing temperature. The NbC-to-G-phase transformation is expected to be favoured at temperatures below 875 °C, whereas the NbC-to-η-carbide transformation is expected to be favoured at temperatures above 920 °C. At temperatures between 875 – 920 °C, the G-phase and η-carbide transformations occur in parallel, with the relative amounts of the two phases depending on the ageing temperature and time. The η-carbide volume fraction would be expected to increase with ageing temperature, until the NbC-to-η-carbide transformation becomes dominant. However, these stated temperature ranges are approximations based on data from a limited number of laboratory-aged and ex-service samples. Additionally, the ex-service HP-Nb alloy materials studied typically come from steam reformer tubes, which undergo ageing during service but not carburization. The effects of carburization (for example compositional gradients in the matrix and carbides across the tube wall, and the $M_{23}C_6$-to-M_7C_3 phase transformation) are likely to alter the temperature ranges over which the NbC-to-G-phase and NbC-to-η-carbide transformations occur in carburized HP-Nb alloy tubes.

2.4.3 Microstructural Evolution of HP-Micro

The HP-Micro (or HP-MA) alloy is an HP alloy modified with combined additions of niobium and titanium. The HP-Micro designation is also often applied to alloys with combined additions of niobium, titanium, and other micro-alloying elements (W, Zr, Y).

As-Cast Condition

Combined additions of niobium and titanium, have been added to the HP alloy composition in order to further increase the alloy's creep resistance. Similar to the HP-Nb alloy, the as-cast microstructure of HP-Micro alloys (Figure 2.15) is composed of an austenitic matrix with a primary network of chromium carbides (dark grey) and MC carbides (white), where M represents the total amount of the combination of niobium and titanium. The MC carbides are therefore often termed (NbTi)C carbides.

The chromium-rich primary carbides in separately-cast HP-Micro alloys have been reported to obtain either solely the M_7C_3 (orthorhombic) crystal structure [35, 49, 67] or solely the $M_{23}C_6$ (FCC) crystal structure [29, 68].

The addition of titanium is reported to cause further fragmentation of the primary carbide network [29, 48]. The MC carbides in HP-Micro alloys have been reported to obtain a blocky morphology, as opposed to the lamellar morphology seen in the HP-Nb alloy. In the Ti and Nb modified HK alloy, the change in morphology from lamellar to blocky is attributed to the addition of titanium causing a higher interfacial energy between the MC carbide and austenite matrix, causing the MC precipitates

to obtain a blocky morphology to minimize the surface area [44, 69]. Cuboidal TiC precipitates have been reported within the austenite matrix of HP-Micro alloys [35, 44].

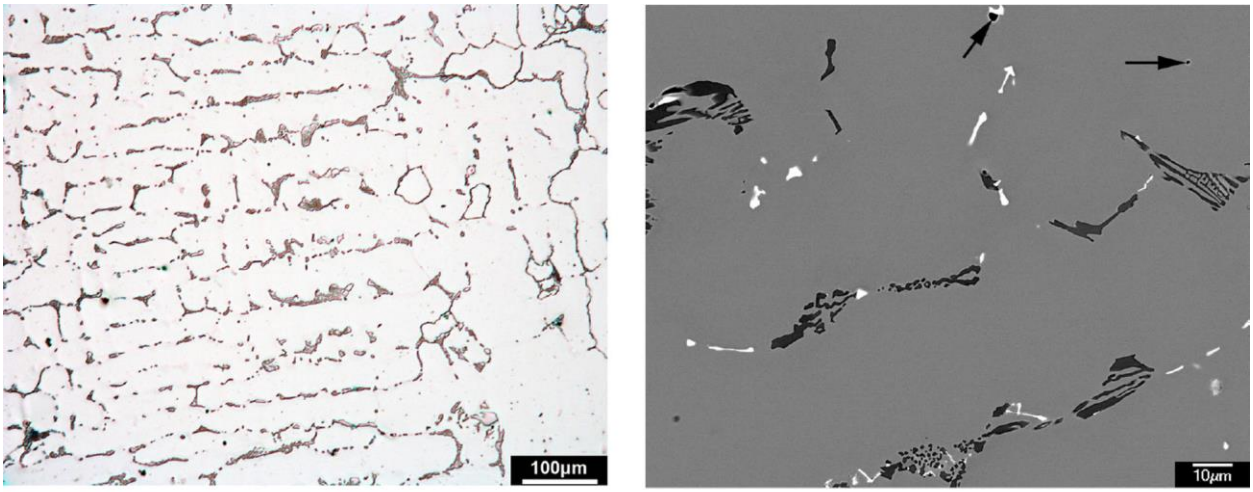

Figure 2.15 - (a) optical and (b) backscattered electron micrographs of an as-cast HP-Micro alloy [35]

As with the HP-Nb alloys, recent detailed observations of MC precipitates in two HP-Micro alloys by Buchanan [35] revealed the existence of two distinctly different morphologies. (NbTi)C precipitates with the typical blocky morphology as described in previous studies [29, 48] were seen (Figure 2.16 (a)); however, some (NbTi)C precipitates with a similar morphology to the Type II lamellae in HP-Nb alloys were also observed (Figure 2.16 (b)). These two (NbTi)C morphologies were confirmed to obtain the same crystal structure as the NbC precipitates in the HP-Nb alloys ($Fm\bar{3}m$), thus the same naming convention used for the NbC precipitates was used for the (NbTi)C precipitates, and the morphologies shown in Figure 2.16 (a) and (b) are referred to as Type III and Type IV morphologies respectively. In both HP-Micro alloys observed by Buchanan, the Type III (blocky) morphology was strongly dominant, with the Type IV morphology representing less than 1% of the total (NbTi)C population. Neither of the morphologies were preferentially located with respect to dendrite, grain or wall position. Comparing the Nb:Ti ratio for the two (NbTi)C morphologies showed that the titanium content in the Type IV morphology is lower than that of the Type III morphology. The undulations along the surfaces of the Type IV morphology appear to increase the total surface area relative to that of the Type III morphology, suggesting that the interfacial energy of the precipitate/matrix interface scales with the local titanium content during solidification.

Similar to the Type II morphology in the HP-Nb alloys, interfacial Cr_7C_3 was identified at the Type III/austenite and Type IV/austenite interfaces, as indicated in Figure 2.16 (a) and (b). The level of Cr_7C_3 precipitation was seen to vary between individual (NbTi)C precipitates. The interfacial Cr_7C_3 was not believed to be a part of the primary Cr_7C_3 network.

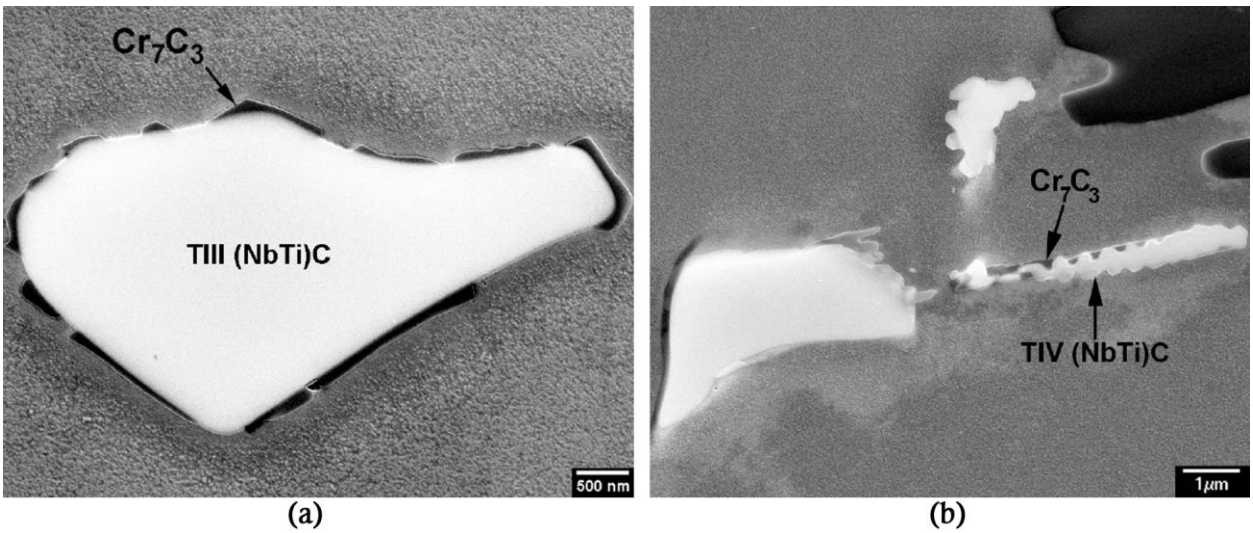

Figure 2.16 - Electron micrographs showing the morphology of the (a) Type III and (b) Type IV (NbTi)C precipitates in HP-NbTi alloys [35].

As with the HP-Nb alloys, Buchanan used deep etching in glyceregia to reveal the three-dimensional structure of the Type III and Type IV morphologies. In three-dimensions, the Type III precipitates are composed of multiple branches radiating from a common central nucleus, as shown in Figure 2.17 (a) and (b). The blocky appearance of the Type III precipitates in two dimensions (Figure 2.16 (a)) is a result of radial and longitudinal sectioning of these branches. The branching directions varied significantly between individual precipitates, indicating that the local thermal and composition gradients in the melt play a role in determining the three dimensional morphology.

Further observation of the Type III (NbTi)C precipitates in two dimensions revealed that each nucleus contained a single spherical precipitate approximately 1 - 2μm in diameter, as shown in Figure 2.18. EDS analysis suggested that these nuclei are Ti-rich spheres with aluminium oxide inclusions. The area of the (NbTi)C precipitate directly adjacent to the Ti-rich sphere was significantly enriched in titanium, and the level of titanium enrichment decreased with distance from the Ti-rich sphere. In two dimensions, multiple grains of (NbTi)C precipitate were observed to have nucleated on the Ti-rich sphere, which corresponds to multiple blocky branches radiating outwards from the Ti-rich central nucleus observed in three dimensions.

The undulations along the faces of the Type IV precipitates in two dimensions were revealed to be a result of the nodular appearance of the broad faces of the plates in three dimensions (Figure 2.17 (c)). The Type IV precipitates did not show any porosity, unlike the Type II precipitates in the HP-Nb alloys. Transitional morphologies were observed, where the precipitates exhibited attributes of both the Type III and Type IV morphologies. This is shown in Figure 2.17 (d), where a gradual transition from the Type III to Type IV morphology occurs. Through the use of EBSD, Buchanan concluded

that neither the Type III nor the Type IV morphologies likely obtained a consistent OR with the austenite matrix.

Buchanan concluded that the nucleation of both the Type III and Type IV morphologies is likely to occur in the liquid ahead of the solidifying austenite dendrites. The initial solidification of the austenite dendrites results in the rejection of niobium, titanium, carbon and nitrogen into the liquid, where aluminium oxide inclusions act as heterogeneous nucleation sites for the (NbTi)C precipitates. Multiple (NbTi)C grains nucleate from each sphere. It is believed that both the Type III and Type IV morphologies nucleate on these spheres. The higher Nb/Ti ratio in the Type IV morphology compared to the Type II morphology suggests that the (NbTi)C/liquid interfacial energy scales with the precipitate's titanium concentration. The morphology preference is believed by Buchanan to be determined by the availability of titanium in the remaining liquid during solidification. Regions with relatively high concentrations of titanium promote the formation of the Type III morphology, and regions with a comparatively lower concentration of titanium are believed to promote the Type IV morphology. The gradient in titanium concentration along the branches and the observation of precipitates transitioning from Type III to Type IV along their length (Figure 2.17 (d)) demonstrates the compositionally-induced morphology change.

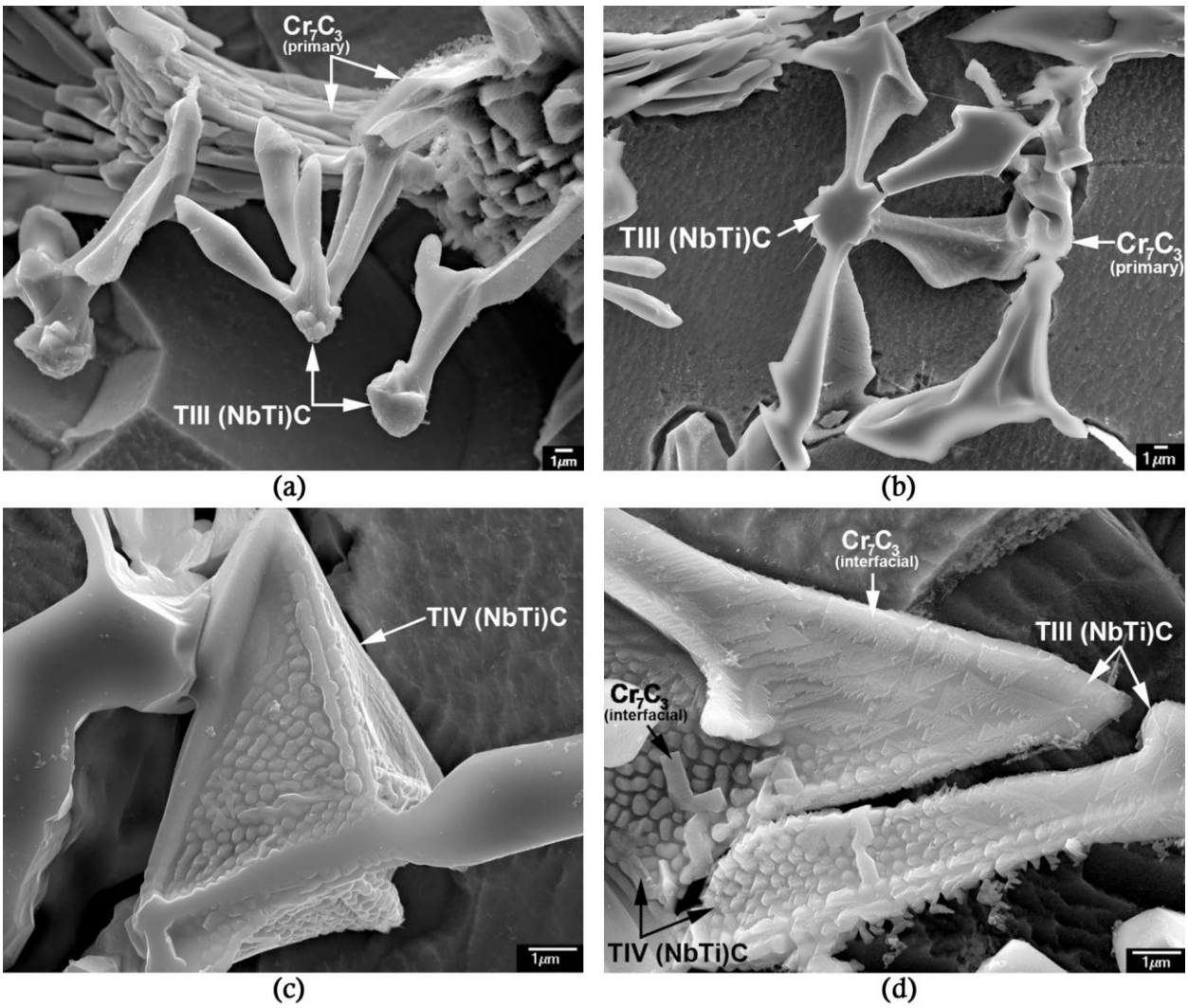

Figure 2.17 - Secondary electron micrographs showing the three-dimensional morphology of (a)-(b) Type III, (c) Type IV, and (d) mixed Type III/Type IV (NbTi)C precipitates [35].

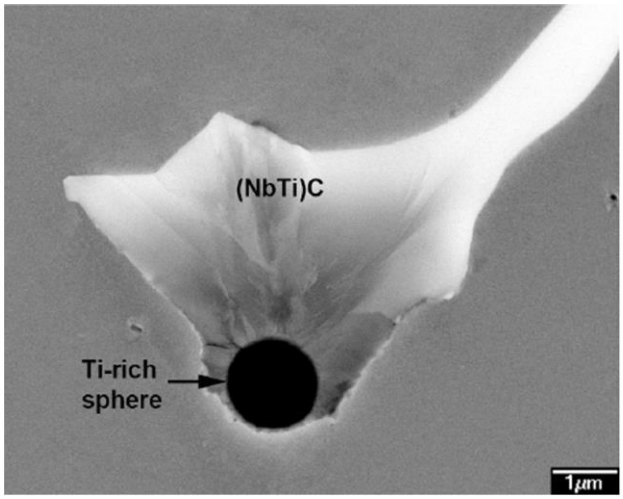

Figure 2.18 – Backscattered electron micrograph of a (NbTi)C precipitate containing a Ti-rich sphere [35].

Evolution of Microstructure during Ageing and Carburization

The HP-Micro alloys display many of the same changes seen during ageing and carburization of the HP-Nb alloys. The transformation of the primary chromium carbides from M_7C_3 to $M_{23}C_6$ occurs, as does the secondary precipitation of $M_{23}C_6$. The secondary $M_{23}C_6$ precipitates typically obtain a cuboidal morphology and a cube-cube OR with the austenite matrix, as with the HP-Nb alloys. Carbon ingress into the tube results in the transformation of $M_{23}C_6$ to M_7C_3 at the inner wall region, and the $M_{23}C_6$-to-M_7C_3 transformation front progresses into the tube wall with continued carbon supply.

The instability of NbC at elevated temperatures is also a feature of the HP-Micro alloys; however, the small additions of titanium appear to result in titanium controlling the transformation. de Almeida *et al.* [29] identified G phase in an HP-Micro alloy which had been aged for 1000 hours at 900 °C. Only partial transformation was observed, where the centre of the region remained as a (NbTi)C particle, and the outer part had transformed to G-phase. The EDS spectrum of the G-phase areas only showed Ni, Si, and Nb peaks, indicating that G-phase does not dissolve Ti. de Almeida *et al.* proposed that the transformation is an in-situ reaction controlled by the expulsion of carbon and titanium, and by the incorporation of Si and Ni. The reaction starts from the outside and continues towards the centre of the (NbTi)C particle, and thus as G-phase does not dissolve Ti then Ti controls the transformation process. To illustrate this, de Almeida *et al.* found particles of TiC in the centre of transforming precipitates (Figure 2.19).

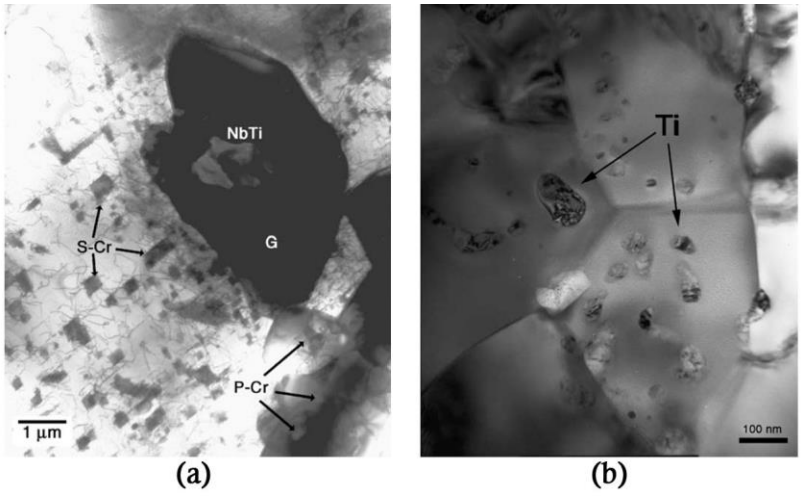

Figure 2.19 - TEM brightfield images of an HP-Micro alloy in the aged condition. (a) G-phase region, (NbTi) carbide, and primary (P-Cr) and secondary (S-Cr) precipitates indicated. (b) The G-phase region shown in (a) is illustrated, within which individual TiC particles can be seen [29].

2.4.4 Microstructural Evolution of ET45

ET45 is a recent development in the high-alloy austenitic stainless steel series, and there is little information in literature regarding its as-cast microstructure and evolution during ageing or service.

As-Cast Condition

The as-cast microstructure of ET45 alloys is reported to be similar to that of the HP-Nb and HP-NbTi alloys, consisting of an austenitic matrix with a network of primary chromium-rich and niobium-rich carbides [50-52]. Sustaita-Torres *et al.* [51] identified the chromium-rich carbides present in the as-cast condition as M_7C_3, and the niobium-rich carbides as NbC. An example of the microstructure of an as-cast ET45-type alloy is shown in Figure 2.20.

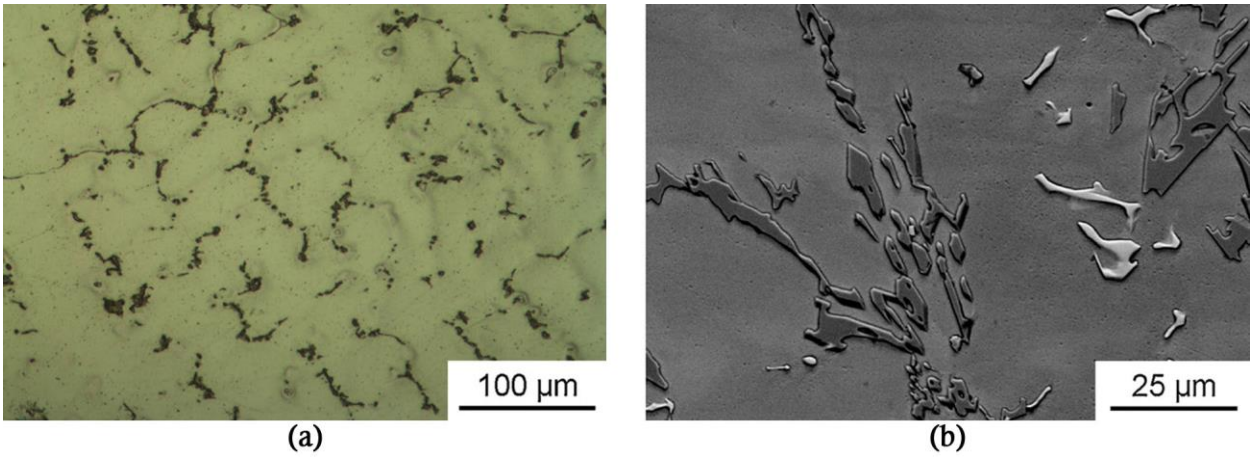

Figure 2.20 - (a) light optical micrograph and (b) backscattered electron micrograph of an as-cast ET45-type alloy [51]

Evolution of Microstructure during Ageing and Carburization

Rodriquez *et al.* [52] and Sustaita-Torres *et al.* [51] aged samples in air at 750 °C for up to 1000 hours, and observed that the microstructural changes mirrored the changes seen in HP-Nb alloys upon ageing. The M_7C_3 carbides present in the as-cast condition transformed to $M_{23}C_6$ upon ageing, and distributions of secondary $M_{23}C_6$ carbides were formed. The instability of NbC carbides at elevated temperatures persists with the ET45 alloy, with Sustaita-Torres *et al*. noting that NbC carbides had partially transformed into a nickel-niobium silicide (identified via XRD as an Nb_3Ni_2Si structure) after both 500 and 1000 hour ageing times. It was not determined whether the nickel-niobium silicide was G-phase or η-carbide.

Berghof-Hasselbächer *et al.* [50] observed G-phase along with a phase termed M_6C and rich in Cr, Ni, and Nb in some samples of ET45-type alloys exposed to temperatures of 982 – 1149 °C for up to 10,247 hours. Formation of G-phase was observed to occur at the boundary between the $M_{23}C_6$ carbides and the matrix. The M_6C phase was more frequently seen in the subsurface zones as opposed to the bulk of the samples, which may be due to depletion of the oxide-forming elements Cr and Si, or by the uptake of nitrogen. G-phase was observed over the temperature range of 982 – 1149 °C. At 1038 °C, G phase was observed after 1300 hours; however, after 3545 hours it was seen to have disappeared and been replaced by M_6C. These observations suggest that the temperature range over which G-phase is stable in ET45-type alloys differs from that observed in the HP alloy series.

The microstructure of ET45-type alloys carburized during service has been reported by Ul-Hamid *et al.* [30] to consist of a network of chromium-rich and niobium-rich carbides, along with precipitates that are comparatively rich in nickel, and have a grey appearance in backscattered electron images. An example of such a microstructure is shown in Figure 2.21. The composition of the nickel precipitates, as measured by Ul-Hamid *et al.* using EDS, is given in Table 2.3. Based on the scanning electron micrographs presented by Ul Hamid *et al*, the nickel-rich precipitates appear in both the carburized and un-carburized regions of the tube wall. It is unclear whether these are a product of ageing or carburization, or whether they were present in the as-cast structure. Although the carbide types are not identified, and there is no mention of a transformation of the chromium carbides from $M_{23}C_6$ to M_7C_3 as in carburized HP alloys, electron images presented by Ul Hamid *et al.* suggest that such a transition may be present in at least one of the ET-45-type tubes examined, as demonstrated in Figure 2.22.

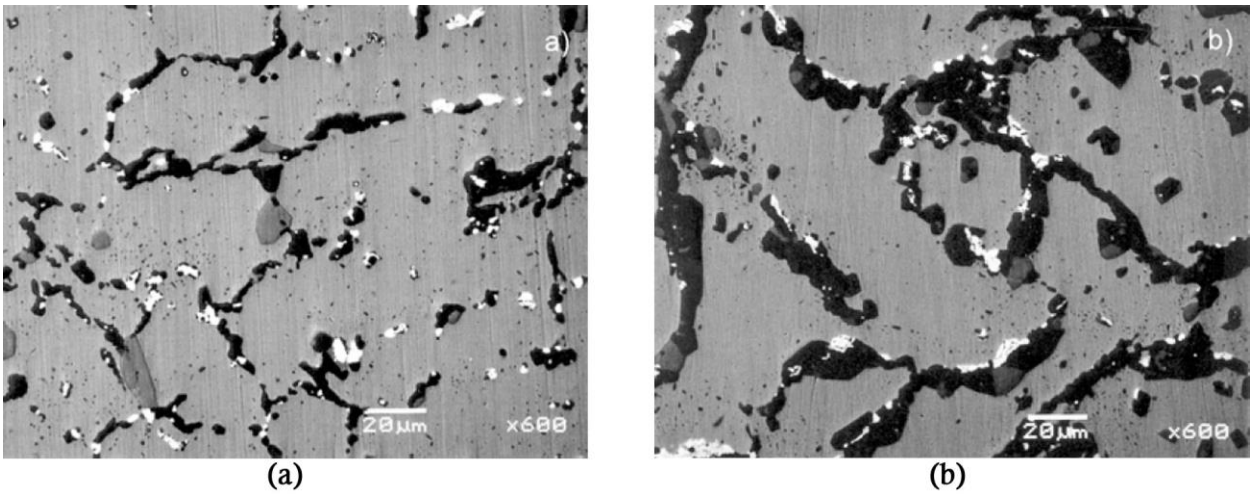

Figure 2.21 - Secondary electron micrographs of (a) un-carburized and (b) carburized regions of an ex-service ET45-type alloy pyrolysis tube [30]

Table 2.3 - Chemical composition of Ni-rich precipitates in a carburized ET45-type alloy [30]

wt.%	
Ni	63.1
Cr	19.8
Si	1.7
Fe	15.4

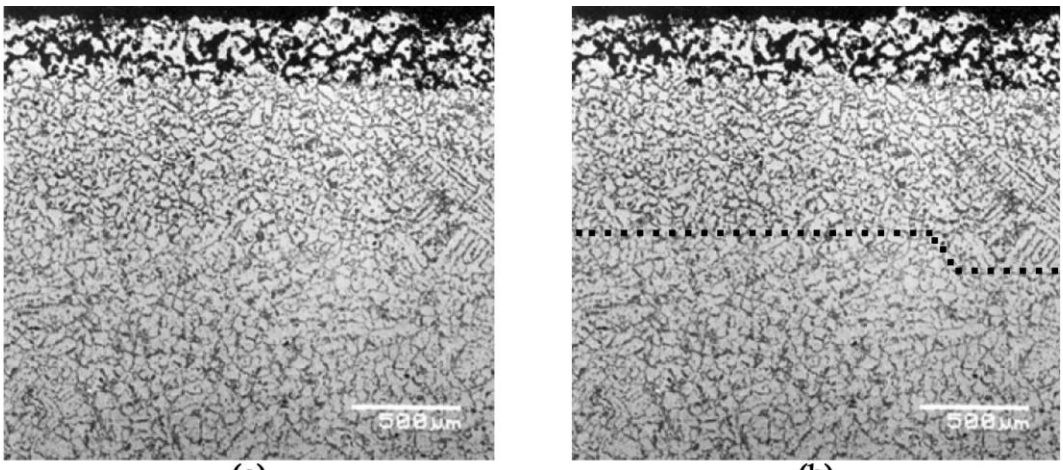

Figure 2.22 - (a) Secondary electron micrograph of a carburized ET45-type tube [30], (b) image with delineation of potential $M_{23}C_6$-to-M_7C_3 carbide transformation front.

2.5 Creep Properties and Performance

The creep properties of the HP-Nb alloy are typically greater than those of the HP alloy without additional alloying elements, as shown in Figure 2.7, and the creep properties of HP-Micro alloys are even further improved.

Improvements in the creep properties by adding niobium to the HP alloy to give HP-Nb alloys are typically attributed the fragmentation of the primary carbide network as a result of the niobium additions [29, 45-47]. de Almeida Soares *et al.* [46] compared HP alloys with varying levels of niobium content to the standard HP composition, and observed that longer rupture times and lower minimum creep rates were achieved with niobium additions.

The improvement in creep properties in the HP-Micro alloys over the HP-Nb alloys is attributed to a number of microstructural features. The addition of titanium results in further fragmentation of the primary carbide network, and the (NbTi)C carbides take on a blocky appearance, as opposed to the lamellar morphology of the NbC carbides in HP-Nb alloys. Upon ageing, the HP-Micro alloys have been observed to form a secondary precipitate network consisting of (NbTi)C and $M_{23}C_6$ precipitates, whereas the HP-Nb alloys form a secondary precipitate network consisting of solely $M_{23}C_6$ precipitates. As a result, lower minimum creep rates and longer times to rupture in the HP-Micro alloys are typically attributed to a more fragmented primary network and a finer dispersion of secondary precipitates [29, 35, 65]. In addition, the niobium rich secondary precipitates have been observed to coarsen at a significantly slower rate than the $M_{23}C_6$ secondary precipitates when aged at 1000 °C, and thus the prolonged dispersion strengthening effect of these precipitates would be expected to help maintain the superior creep resistance of the HP-Micro alloy compared to the HP-

Nb alloy [35]. Similar improvements in creep properties as a result of increased complexity in the secondary precipitate distribution were observed in the HK alloy series by Hou and Honeycombe [44].

Analysis of ex-service HP-Micro alloy reformer tubes (~940 °C, ~12 MPa, 60,000 hours) by Wahab and Kral [58, 59] revealed preferential formation of creep voids at the $M_{23}C_6$/austenite interfaces. Three-dimensional reconstructions of the ex-service material showed that all voids within the volumes inspected came into contact with $M_{23}C_6$ precipitates, whereas no voids were observed solely in contact with TiC or NbC precipitates. The highest void density occurred at the outer wall of the tube, where the grains are large, columnar grains, and the temperature is highest.

The creep properties of ET45 are reportedly higher than those of the HP-Nb alloys, and although they are not as high as those of the HP-Micro alloys the ET45 can withstand higher operating temperatures (Figure 2.7). However, aside from manufacturers data [54, 70] and that reported by Kircheiner and Woelpert [43], there is no information in the literature regarding the creep performance of ET45 tubes.

The effect of G-phase and η-carbide on creep performance is largely unknown. HK alloy tubes with niobium additions which have survived 60,000 hours of service in a reformer furnace and contain G-phase in the microstructure have been reported [28], suggesting that G-phase is not necessarily detrimental to the creep performance of these alloys.

de Almeida *et al.* [29] and Ribiero *et al.* [65] observed that, in HP-Micro alloys, the titanium additions inhibited the formation of G-phase, leading to a smaller G-phase volume fraction compared to an HP-Nb alloy aged under the same conditions. Both authors suggest that the reduced G-phase volume fraction may contribute to the HP-Micro alloy's superior creep properties, but that titanium additions also result in a finer secondary precipitate distribution and more fragmented primary carbide network, both of which have significant contributions to improvements in creep performance, and thus the contributions to creep properties are not easily separated. de Almeida *et al.* and Ribiero *et al.* noted that there is a volume expansion associated with the transformation to G-phase, causing an increased interfacial energy between the matrix and precipitate which could cause creep damage to occur preferentially at this interface.

Buchanan [35] compared an HP-Nb alloy and an HP-Micro alloy aged under the same conditions, and observed that while the size and distribution of the primary and secondary chromium carbide networks appeared relatively similar after ageing, the NbC precipitates in the HP alloy had partially transformed to the η-carbide, whereas the blocky (NbTi)C precipitates in the HP-Micro alloy remained completely stable. After creep testing the aged alloys, Buchanan noted that creep voids were preferentially located at the $Cr_{23}C_6$ and austenite interfaces, consistent with the work of Wahab and Kral [58, 59], suggesting that the NbC and η-carbide precipitates did not significantly contribute to the greater ductility of the HP-Nb alloy compared to the HP-Micro alloy.

2.6 Eddy Current Non-Destructive Testing

Eddy current non-destructive testing (NDT) is used for a wide variety of applications, including but not limited to the detection of surface and sub-surface defects, determining the thickness and electrical conductivity of coatings, and the measurement of structural features such as grain size. However, in order to avoid unnecessary detail, only the principles and literature pertaining to eddy current NDT for carburization detection will be covered in this literature review.

2.6.1 History of Eddy Current Non-Destructive Testing

The development of modern eddy current testing methods is based on discoveries made during the nineteenth century about the relationship between electricity and magnetism. Electromagnetism was first discovered in 1820 by Hans Christian Oersted, a Danish physicist and chemist. He found that electric current flowing through a wire could deflect a magnetized compass needle, thus discovering that a magnetic field can be created not only by magnetic materials, but also by a flow of current [71, 72].

In 1831, Michael Faraday, a British physicist and chemist, discovered electromagnetic induction. By conducting a series of experiments with stationary coils, he found that relative motion between a magnetic field and a conductor induces an electromotive force (emf) in the conductor, causing an induced current to flow. Thus, when the alternating magnetic field of an eddy current device's coil is brought into contact with a conductive test sample, a voltage is developed which results in a current flow in a test object. The process of inducing a current in a conductor by placing it in a time-varying magnetic field is now commonly referred to as electromagnetic induction, and it is considered to be the basis of eddy current testing systems [71, 73, 74]. Joseph Henry independently discovered electromagnetic induction in the USA at the same time as Faraday, and the unit of measure for induction, the Henry (H), is named after him.

In 1834, Heinrich Lenz, a Russian Physicist, defined Lenz's Law – the principle which defines how the properties of the test object are communicated back to the test system. Lenz's Law states that the current induced in a conductor by a changing magnetic field will be in a direction such that its magnetic field will oppose the original magnetic field. In practice, this means that the eddy currents induced in the test sample during testing develop a secondary magnetic field that cancels out a portion of the primary magnetic field (equivalent to the magnitude and phase of the secondary magnetic field) [71, 73, 74].

Eddy currents were first used for non-destructive testing in 1879. The British scientist David Hughes demonstrated how the properties of a coil change when placed in contact with materials of different conductivities and permeabilities, and thus how eddy current systems can be used to sort materials. The development of eddy current methods progressed slowly at the start of the 20th century, until the Institut de Foerster was founded in 1940 by Dr Friedrich Foerster. The Institut focussed on developing

and marketing practical eddy current testing instruments, and by the 1960's had a wide range of instruments to cover a variety of eddy current testing applications. A major contribution of the Institut de Foerster to modern eddy current testing includes the development of the impedance plane display [71]. The next major contribution to modern eddy current testing methods was the development of multi-frequency testing by Intercontrolle, a French equipment manufacturer, in 1974. Originally developed to suppress the display of undesired test variables, multifrequency testing can also optimise test conditions for variables that normally conflict (such as permeability and penetration) [71].

2.6.2 Magnetism in Materials

The force of magnetism is determined by magnetic moments – permanent dipole moments within an atom that originate from, and are proportional to, the angular momentum and spin of its electrons [73, 74].

Types of Magnetic Materials

There are a small number of crystalline materials that exhibit strong magnetic effects called ferromagnetism. All ferromagnetic materials are composed of microscopic regions called domains - regions within which all magnetic moments are aligned. Boundaries between domains with different orientations are called domain walls. In a sample that is un-magnetized, the magnetic moments in the domains are oriented randomly such that the net magnetic moment is zero. When the sample is subject to an external magnetic field, the domains within which the magnetic moments are aligned with the field grow in size at the expense of non-aligned domains (the growth of a domain only changes its boundaries). When the external magnetic field is removed, the sample may retain a net magnetization in the direction of the external field [71, 73, 74]. Examples of ferromagnetic materials are iron, carbon steel, 400 series stainless steel, and nickel [71].

Paramagnetic materials have a small but positive magnetism resulting from the presence of atoms or ions that have permanent magnetic moments. These moments interact only weakly with each other, and are randomly oriented in the absence of an external magnetic field. When a paramagnetic material is subject to an external magnetic field, its atomic moments tend to align with the field, but the alignment process must compete with thermal motion which tends to randomize the magnetic moment orientations. Upon removal of the field it may remain slightly magnetized [71, 73]. Examples of paramagnetic materials are aluminium, chromium and platinum [71].

The Curie Temperature

The Curie Temperature (T_C) is the temperature where a material's permanent magnetism changes to induced magnetism. Below the Curie Temperature, magnetic moments are aligned and the material is ferromagnetic. Above the Curie Temperature, thermal agitation is great enough to cause random orientation of the magnetic moments, the magnetic state becomes disordered, and the material becomes paramagnetic [73, 75]. The Curie Temperatures of some common magnetic materials are given in Table 2.4.

Table 2.4 - Curie Temperatures of some common magnetic materials [73, 75].

Material	Curie Temperature (°C)
Iron	770
Nickel	358
Cobalt	1130

Resistivity, Conductivity and Permeability

The electrical resistance, R, of an electrically conductive material is defined by Ohm's Law as the ratio of potential difference, or voltage, V, between the extremities of the conductor to the current, I, flowing through it, as described by Equation 2.5:

$$R = \frac{V}{I} \qquad \textbf{Equation 2.5}$$

The value of electrical resistance is dependent on the physical properties of the material as well as its shape and size, and thus electrical resistivity, ρ, is often referenced. Resistivity, or specific resistance, is independent of the geometrical characteristics of a particular sample [76, 77]. For a conductor of length l and cross-section area A, resistivity is defined by Equation 2.6:

$$\rho = \frac{RA}{l} \qquad \textbf{Equation 2.6}$$

The conductivity, σ, of a material is a value that defines how well a material can conduct electricity. The electrical conductivity of a material is influenced by many factors, including chemical composition, cold work, and heat treatments. It can be a major variable in eddy current testing, as minor variations in composition can alter the conductivity [76]. The conductivity of a material is defined as the inverse of its resistivity:

$$\sigma = \frac{1}{\rho} \qquad \textbf{Equation 2.7}$$

The extent to which a material can be magnetized is defined by its magnetic permeability – a material's ability to concentrate magnetic flux. The greater flux density obtained from a material by a given applied magnetizing force, the greater the permeability of that material [71, 77]. Magnetic permeability (μ) is a number that quantifies the degree of magnetic induction (B) of a material when a magnetic field (H) is applied:

$$\vec{B} = \mu\vec{H}$$ **Equation 2.8**

Numerical values of permeability for materials are typically reported as relative permeability (μ_r), which is the ratio of μ for the material to the permeability of air in a vacuum, $\mu_0 = 4\pi \times 10^{-7}$ H/m [71, 74, 78]:

$$\mu_r = \frac{\mu}{\mu_0}$$ **Equation 2.9**

Paramagnetic materials have a relative permeability that is equal to or slightly greater than one ($\mu_r \geq 1$) [71, 78]. Ferromagnetic materials have very high values of relative permeability; they may range from 50 to 1,000 [71, 76, 77], but are more typically in the range of 100 - 200 [77, 78].

In a similar manner to electrical properties such as conductivity, the magnetic permeability of a material is affected by changes in composition, hardness, and microstructure [76]. Small changes in the magnetic permeability of a material will have a significantly greater effect on the eddy current response than small changes in conductivity, particularly at low test frequencies[76, 78].

2.6.3 Theory of Eddy Current Non-Destructive Testing

When a coil carrying an alternating current is placed in proximity to a conductive material, secondary currents (eddy currents) will be induced in the material. The induced currents produce a secondary magnetic field which opposes the primary magnetic field surrounding the coil. The interaction between the primary and secondary magnetic fields produces a back emf (electromotive force) in the coil, and hence a change in the probe impedance [76].

Eddy currents flow in closed loops within the material. The magnitude and phase of the currents depends on a number of factors, including the magnitude of the primary magnetic field, the electrical and magnetic properties of the material, and the presence of discontinuities or dimensional changes within the material [76].

When an alternating flow of current passes through a coil there are two factors that oppose the flow of current – the ohmic resistance (R) of the coil, and the inductive reactance (X_L) of the coil. The inductive reactance of the coil is given by:

$$X_L = \omega L$$ **Equation 2.10**

where L is the inductance of the coil, and ω is the angular frequency of the alternating current, which is related to frequency, f, by:

$$\omega = 2\pi f$$ **Equation 2.11**

The inductance, L, of a coil is a measure of the opposition to any change of current through the coil. From Faraday's Law, the inductance of a coil is defined in terms of the emf generated to oppose a given change in current. The induced emf is proportional to the negative time rate of change of magnetic flux. The magnetic flux is proportional to the magnetic field, which is in turn proportional to the current in the circuit, and therefore the induced emf is proportional to the time rate of change of current, as defined by Equation 2.12:

$$emf = -L\frac{dI}{dt} \qquad \textbf{Equation 2.12}$$

The total resistance of the coil to current flow is termed the coil impedance, Z, and is given by:

$$Z = R + jX_L \qquad \textbf{Equation 2.13}$$

where:

$$j = \sqrt{-1} \qquad \textbf{Equation 2.14}$$

Combining Equation 2.13 with Equation 2.10 enables the coil impedance to be defined in terms of measurable variables:

$$Z = R + j\omega L \qquad \textbf{Equation 2.15}$$

The real and imaginary parts of the coil impedance can be displayed on an impedance plane diagram. The x axis represents the real part of coil impedance, and the y axis represents the imaginary part.

When there is no conductive test sample within range of the coil, the coil impedance is at a point of high inductance and low resistance, commonly called the "air point". The high value of inductance occurs because there is no secondary magnetic field to oppose the primary magnetic field, and low resistance occurs as the only resistance is that of the coil wire. The air point, Z_0, is defined as:

$$Z_0 = R_0 + j\omega L_0 \qquad \textbf{Equation 2.16}$$

Results are more commonly displayed on the normalised impedance plane, where the values have been normalised against the values for the coil in air. This enables the variations in coil impedance caused by the test piece and variations in system geometry to be clearly displayed without the influence of the coil properties. For the x-axis (resistance), variations in the coil wire resistance are subtracted from the total resistance (in order to display variation caused by the test piece, not the coil), and dividing by the inductive reactance of the air point:

$$R_{norm} = \frac{(R - R_0)}{\omega L_0}$$ **Equation 2.17**

The y axis (inductive reactance) is changed from a scale of the inductive reactance of the test coil, to a scale of the inductive reactance of the test coil compared to the inductive reactance of the coil in air:

$$X_{L\,norm} = \frac{\omega L}{\omega L_0}$$ **Equation 2.18**

On the normalised impedance plane, the values for the air point are $R_{norm} = 0$ and $X_{L\,norm} = 1$.

When the coil is brought into proximity to a conductive test sample, the coil impedance will change and the display will move away from the air point. The magnitude and direction of this change is dependent on a number of factors, including the geometry, conductivity and magnetic permeability of the test sample, and the geometry of the eddy current NDT system set-up [76, 78].

When a paramagnetic material is brought into proximity to the test coil, eddy currents appear, and the displacement on the normalised impedance plane is from the air point Z_0, to the point Z_1 (Figure 2.23). Resistance increases ($R_1>0$), as the test piece acts as a resistive load on the coil, due to the formation of eddy currents in the test piece dissipating power. Inductive reactance decreases ($X_{L1}<1$), as the secondary magnetic field created by the eddy currents opposes the coil's magnetic field (primary magnetic field), resulting in a weaker primary magnetic field [78]. The more conductive the test piece, the greater the cancellation of the primary magnetic field, and the further downwards the point Z_1 moves. The movement of the point Z_1 occurs on the semi-plane where $X_{Lnorm}<1$.

When the test coil is in proximity to a ferromagnetic material, the displacement on the normalised impedance plane is from the air point Z_0 to the point Z_2 (Figure 2.23). Resistance increases ($R_2>0$), and inductive reactance also increases ($X_{L2}>1$). Ferromagnetic materials, which have high values of permeability, concentrate the primary magnetic field of the coil, and this increase in primary magnetic field strength overshadows the secondary magnetic field generated by the eddy currents. Increases in magnetic permeability result in further concentration of the primary magnetic field of the coil, and inductance is increased [78]. The movement of the point Z_2 occurs on the semi-plane where $X_{Lnorm} >1$.

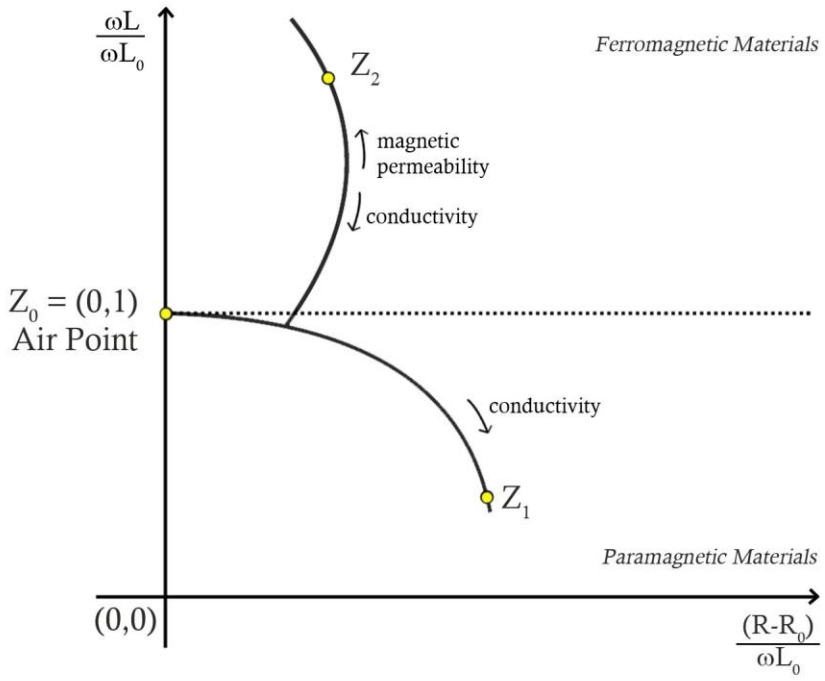

Figure 2.23 - Impedance plane response of ferromagnetic and non-ferromagnetic materials (adapted from [62]).

Lift-off is defined as the impedance change that occurs when the distance between a test coil and a test specimen changes. Inadvertent variations in the distance between the test coil and the test piece, such as operator movement, changes in coating thicknesses, or an irregular test piece surface, can cause noise signals that change or obscure the signals for which the test is being performed. The primary magnetic field is strongest near the coil, so lift-off is strongest nearest the coil. Lift-off is typically considered a source of noise, and therefore the minimisation of variations in distance between the test coil and the test piece is important [78].

Edge effects can occur when the inspection coil is located at the end of a test piece. The flow of eddy currents becomes distorted as the currents cannot flow at the edge. The distance where the edge effect is present is dependent on the test coil and test piece geometry. In order to avoid noise signals due to edge effects, inspection is typically limited near test piece edges [78].

The flow of eddy currents is not uniform throughout the volume of the test piece. Current flow is stronger at the surface, and decreases exponentially in relation to the distance from the surface. The standard depth of penetration (δ) is defined as the depth at which the eddy current density has decreased to 1/e, or approximately 37%, of the surface density, where e is the base of the natural logarithm (2.71828).

The standard depth of penetration depends on the material's conductivity, magnetic permeability and the test frequency. The standard depth of penetration, δ, for a given material and frequency is given by:

$$\delta = \sqrt{\frac{2}{\mu\omega\sigma}} \qquad \textbf{Equation 2.19}$$

Where σ is the conductivity in $1/(\Omega m)$, μ is the magnetic permeability ($\mu = \mu_r\mu_0$) and ω is the angular frequency.

Equation 2.19 demonstrates that standard penetration depth is lower when conductivity, permeability, and frequency increase. As a result, low testing frequencies are commonly used for the inspection of ferromagnetic materials due to their high permeability, to allow for greater penetration into the test piece [78].

When a test piece is less than approximately three times the standard depth of penetration, the eddy current distribution becomes distorted. For thin samples, a change in thickness will cause a change in the test coil impedance [76].

2.6.4 Eddy Current NDT for Carburization Detection

Ferromagnetic materials can, by alloying with each other or with non-ferromagnetic materials, become paramagnetic. The ferromagnetism of nickel is due to the partially filled 3d+ and 3d- electron shells being occupied by an unequal number of electrons with opposing spin, resulting in an overall magnetic moment in the material. By alloying Ni with Cr, the "holes" in the 3d electron shells become filled with Cr-valency electrons such that the resulting magnetic moment becomes zero. Above a certain Cr content a Ni-Cr alloy will be paramagnetic [17]. This is essentially why austenitic Fe-Cr-Ni alloys are paramagnetic – but the Curie Temperature, T_C, and magnetic permeability, μ, vary very strongly with the Cr/Ni+Fe ratio [17]. In the as-cast condition, the matrix of Fe-Cr-Ni alloy tubes is paramagnetic at room temperature. During service, the precipitation and growth of chromium carbides results in chromium being depleted from the austenitic matrix adjacent to the chromium carbides. With increasing carburization, the matrix composition tends towards the binary Fe-Ni composition and becomes progressively more ferromagnetic, whilst retaining the austenite crystal structure. This is accompanied by increases in magnetic permeability and the Curie Temperature [8, 10, 11, 13-15, 17, 20, 79]. Eddy current NDT techniques measure the increase in bulk magnetic permeability at room temperature that results from the progressively increasing volume of ferromagnetic material [9].

Curie Temperature data for various alloy compositions [80-82] has been compiled by Stevens *et al.* [14] and plotted on a Fe-Cr-Ni ternary diagram (Gibbs triangle), enabling the effects of chromium depletion on the magnetic behavior of the matrix at room temperature to be visualized (Figure 2.24).

The composition of the HP alloy series is very close to the boundary between paramagnetic compositions and ferromagnetic compositions, thus even a small amount of chromium depletion could result in the matrix changing from being paramagnetic at room temperature (i.e. $T_C<T_{room}$) to being ferromagnetic at room temperature (i.e. $T_C>T_{room}$) [11, 12, 14, 15, 17, 20]. It is yet to be determined if, when an ET45-type alloy is carburized, the chromium depletion in the matrix is enough to cause a paramagnetic to ferromagnetic shift, due to the high chromium content of such alloys (35wt% Cr). It is also possible that the nickel-rich precipitates that have been observed in carburized ET45-type alloys [30], but that are yet to be identified, are ferromagnetic, which could create issues in interpreting the magnetic response of these alloys.

Magnetic force microscopy (MFM) performed by Stevens *et al.* [8] on an ex-service HP alloy ethylene pyrolysis tube showed that the chromium-depleted matrix directly adjacent to the chromium carbides is ferromagnetic, and that with increasing chromium depletion these ferromagnetic regions join to form a domain structure. These findings have been replicated by Silva *et al.* [11], who also demonstrated that, at the outer wall of an ex-service HP alloy ethylene pyrolysis tube, only the regions of matrix directly adjacent to the chromium carbides are ferromagnetic. Moving further towards the inner diameter, the increased volume fraction of chromium carbides resulted in the ferromagnetic matrix regions progressively widening, leading to the entirety of the matrix at the inner wall becoming ferromagnetic.

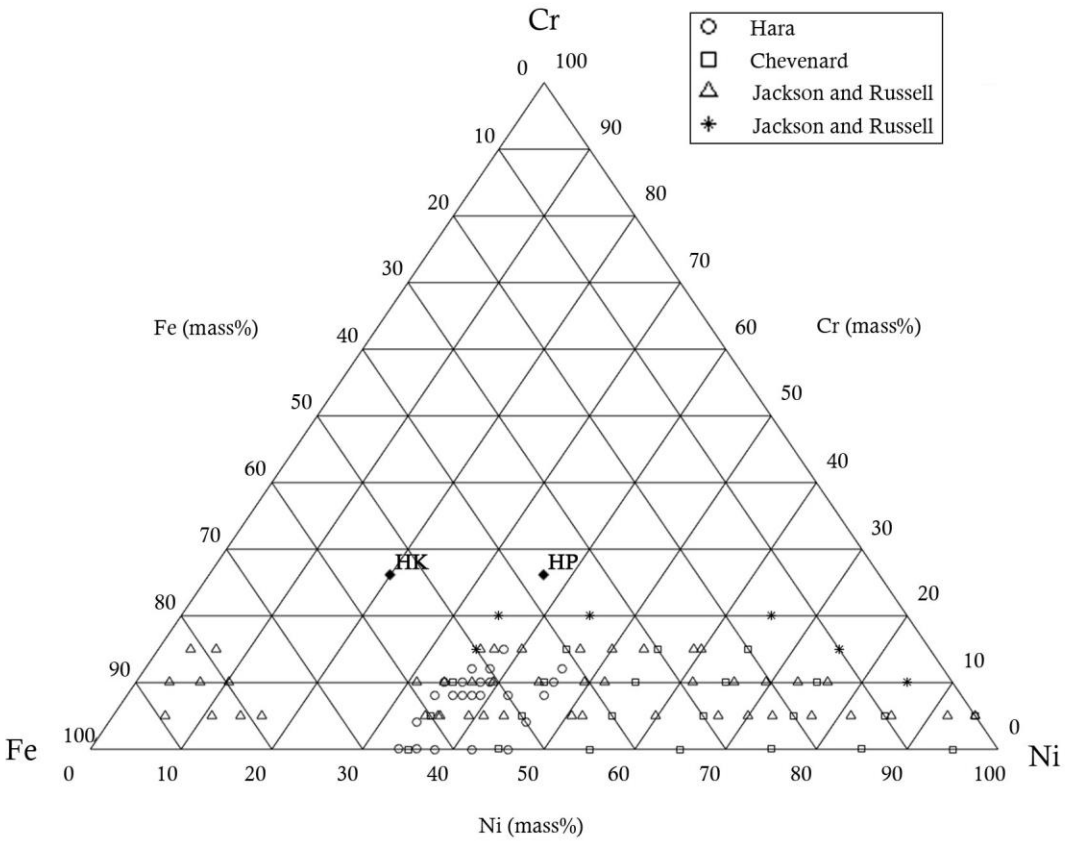

Figure 2.24 - Gibbs triangle for Fe-Cr-Ni alloys (adapted from [14]). Asterisks denote compositions that are paramagnetic at 20 °C, and open circles, squares and triangles denote compositions that are ferromagnetic at 20 °C. Black diamonds denote specific alloy compositions in the H series.

Recent work on the use of magnetic measurements to detect the extent of carburization ranges from the use of magnetic measurements relative to the magnetic response of carbon steel [20], to magnetic flux measurements [10, 12], to the use of multi-frequency eddy current probes [9, 15].

Mucek [20] used an eddy current probe to study the carburization profile of an ex-service HP40 ethylene pyrolysis tube (20 months in service). An arbitrary scale was used, with the probe calibrated to read zero in air and 100 when in contact with carbon. Low magnetic readings (~14) were seen to correspond with areas of little/no carburization, where the primary carbide network was seen to be fairly continuous, and the secondary carbide distribution remained. Increases in the magnetic readings correlated with increased primary carbide coarsening and agglomeration, combined with the dissolution of secondary carbides and a relative increase in total carbide volume fraction. The highest magnetic readings (~97) corresponded with the greatest depths of carburization (approximately 40% of the wall thickness). Matrix chromium content as low as 7.7 wt% was observed in the highly carburized areas, a significant decrease from the 27 wt% present in the as-cast condition. A small amount of matrix chromium depletion was observed in the un-carburized areas (down to 19 wt%);

however, this was attributed to the precipitation of secondary chromium carbides during service as opposed to carburization.

Mucek obtained measurements of the depth of carburization by way of polishing and etching the samples, and observing the depth of the etching band. The composition of the etchant used is not stated, and it is not possible to determine the microstructural or compositional feature that determines the regions attacked by the etchant, e.g. whether certain phases are subject to attack, or certain matrix compositions. Backscattered electron images and electron microprobe data of the composition of the phases present in the tubes analyzed indicate that two chromium carbide types are present in the carburized tubes, along with a separate chromium containing phase comparatively enriched in nickel and silicon. The crystal structures of the Cr-Ni-Si phase and the two chromium carbides are not identified, and the two chromium carbide types are not differentiated in the observation of carbide volume fraction, and thus it is not possible to determine the individual contributions to matrix chromium depletion by the three chromium-containing phases identified.

Silva *et al.* [10-12] used a combination of a ferrite magnet and a magnetoresistive sensor to measure the density of magnetic flux generated when a magnet was placed near the external surface of a carburized tube. The microstructure of a number of ex-service HP alloy ethylene pyrolysis tubes was characterized using light optical microscopy (LOM), and compared to the magnetic response. This method was able to differentiate un-carburized tubes from those with moderate carburization (defined microstructurally as increased volume fraction of carbides at the inner wall and an increase in carbide coalescence), however struggled to differentiate tubes with severe carburization (accentuated coalescence and morphological changes in the carbides at the inner wall) and extreme carburization (morphology changes in the carbides across the entire wall). In addition, LOM does not allow the various phases present in ex-service tubes (e.g. $M_{23}C_6$, M_7C_3, NbC, G-phase, η-carbide) to be easily distinguished from one another, and thus does not allow the effect of individual chromium-containing phases on the magnetic response to be determined. Therefore, SEM imaging was used by Silva *et al.* [10] along with image analysis to determine the volume fraction of chromium carbides present in the tubes for comparison with the magnetic flux measurements. The chromium carbide volume fraction was seen to be largest at the inner wall, and a reduction in chromium carbide volume fraction was observed as distance from the inner wall increased. A comparison of the magnetic flux measurements with the chromium carbide volume fractions measured across the tube wall indicated a linear correlation between magnetic flux density and the area under the volume fraction curve.

The magnetic flux density measured by Silva *et al.* gives a measure of the average magnetic permeability of the tube at the location tested. From Equation 2.8, it can be seen that the greater the magnetic flux density obtained from a material by a given applied magnetic field, the greater the magnetic permeability of the material. The area underneath the volume fraction curves is representative of an "average" volume fraction for each tube analyzed. Therefore, the higher the

average volume fraction of chromium carbides, the greater the average magnetic permeability of the material, and the greater the magnetic flux density measured. This enables the use of magnetic flux measurements as a method of detecting carburization.

Using EBSD, Silva *et al.* [11] identified the phases present in the tubes analyzed. The chromium carbides at the outer wall were identified as the $Cr_{23}C_6$ type, and at the inner wall the $Cr_{23}C_6$ carbides were observed to be replaced by the comparatively more carbon-rich Cr_7C_3 carbides. However, the carbides types are not differentiated when measuring the volume fraction of chromium carbides, i.e. the volume fraction reported is the total volume fraction of both the $Cr_{23}C_6$ and Cr_7C_3 carbides. Due to the differing ratios of chromium and carbon contained in the two carbide types identified, an overall volume fraction may not necessarily be the most accurate measurement for comparison with magnetic response. The contribution of each carbide type to the matrix chromium depletion depends on both the chromium content of the carbide as well as the individual carbide type's volume fraction. Additionally, Silva *et al.* made two dimensional measurements from SEM images, calculating the area fraction of the chromium carbides present. This data has then been presented as volume fraction, with the implicit assumption that the tube microstructure is homogenous in both the axial and longitudinal directions; however, no evidence has been offered by Silva *et al.* to show that this assumption is valid.

The use of multi-frequency eddy current probes has been a relatively recent development in carburization detection. Using a range of frequencies allows the variation in magnetic properties across the tube wall to be determined, as per Equation 2.19 low frequencies will have a high depth of penetration and will thus provide information on the properties of the material at the inner wall, whereas high frequencies will have low penetration depth and will thus provide information about the properties of the material at the outer wall.

Stevens and Trompetter [9] used an ANSYS finite element model in order to assist in the interpretation of impedance-plane outputs from multi-frequency eddy current probes. The model predicted the results of impedance scans for various combinations of ferromagnetic and paramagnetic layers in a two-layer plate. If both layers are paramagnetic (representative of a non-carburized tube), then the normalised impedance has a value of 1.0 (i.e. equal to that of the probe in air), and this decreases with increased frequency due to electrical conductivity. If the inner layer is ferromagnetic and the outer layer is paramagnetic (representative of a carburized tube), then low frequencies result in high impedance, and impedance decreases rapidly with frequency due to the lack of penetration of electromagnetic waves as the skin depth decreases. If both layers are ferromagnetic (representative of a highly carburized tube), then at low frequencies an impedance higher than the previous case is produced, and the impedance remains high with increased frequency.

Measurements of various HP alloy ex-service tubes using multi-frequency eddy current probes by Stevens and Trompetter [9] and Stevens *et al.* [15] confirm that the responses predicted by the ANSYS model are indeed what occurs with multi-frequency impedance plane scans on carburized tubes. The

normalised inductance vs. frequency plot presented by Stevens *et al.* is shown in Figure 2.25. The extremely high response of tube 6 across all frequencies indicates that both the inner and outer wall of the tube is highly carburized. The response of tube 5 is higher than that of tubes 2 and 3 at low frequencies, but they converge to a similar point at high frequencies, indicating that the outer wall of tube 5 is not as carburized as the inner wall. The inductance of tube 1 is independent of frequency and close to that of the probe in air, indicating that the tube is not carburized. These observations were corroborated by optical microscopy, hardness measurements, and vibrating sample magnetometer (VSM) measurements. XRD determined that both the $Cr_{23}C_6$ and Cr_7C_3 chromium carbide types were present [15]; however, as previously discussed, light optical microscopy does not allow for differentiation between the various chromium-containing phases that can be present in carburized tubes, and thus the contribution of individual chromium-containing phases to the magnetic response cannot be determined via LOM images alone.

Nuclear reaction analysis (NRA) measurements of carbon content by Stevens and Trompetter showed that normalised impedance typically increased with carbon content. Multi-frequency measurements on carburized tubes by Kasai *et al.* [79] also demonstrated good correlation with carbon content – those tubes with higher carbon contents displayed higher normalised probe impedances.

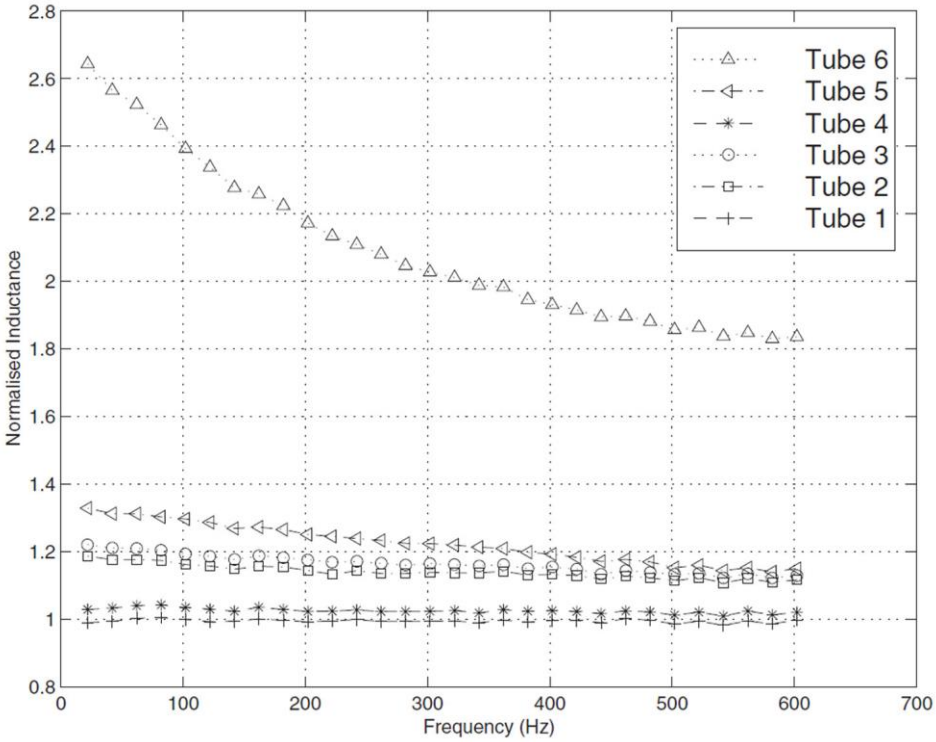

Figure 2.25 - Normalised probe inductance (L/L_0) vs frequency plot for six ex-service HP alloy ethylene pyrolysis tubes with different levels of carburization [15].

2.7 Literature Review Summary

There is a significant amount of detailed microstructural characterization of the as-cast and aged HP alloy series published in the literature, in particular the recent work completed by Buchanan [35]. However, there is little in the way of detailed microstructural characterization of carburized microstructures. A number of authors simply state the types of phases present, e.g. chromium carbides, niobium carbides, and some identify the phases present using methods such as EBSD or XRD, but beyond defining an approximate location where the $M_{23}C_6$ carbide transforms to M_7C_3, there is minimal information in the literature regarding the distributions of individual phases in carburized ethylene pyrolysis tubes. Those authors that have used image analysis to measure carbide volume fraction have done so by using the average chromium carbide volume fraction, and do not differentiate between the different chromium carbides present in the sample. The ET45-type alloys are a relatively new development, and as such there is minimal information in the widely published literature regarding as-cast, aged, and carburized microstructures of these alloys.

Over the course of this literature review, little information was found regarding the creep performance of carburized HP and ET45 type alloys outside of discussions of the potential effects of carburization on performance. There is a variety of research published on the creep performance of the as-cast and aged microstructures; however, the majority of this information pertains to long-term tests or tests to rupture, the conditions of which are not representative of the short-term thermal cycling and progressive carburization that ethylene pyrolysis tubes experience during their service life.

Multi-frequency eddy current non-destructive testing is a relatively recent development in the field of carburization detection, and as such there is minimal information regarding the relationship between the carburized microstructure and corresponding eddy current response beyond comparisons of the magnetic response to the "extent of carburization". The way that the extent of carburization has been defined in microstructural terms differs from author to author, and is sometimes not clearly defined. It has been shown by various authors that the precipitation and growth of chromium carbides during service results in the austenite matrix being depleted of chromium, leading to increasing amounts of ferromagnetic material as carburization progresses, and that increases in the volume fraction of chromium carbides leads to a higher magnetic response. However, the contribution of individual chromium carbide types, and other chromium containing-phases such as η-carbide, has not yet been determined. In addition, very little data on the matrix chromium content is reported, despite matrix chromium depletion being identified as the cause of the change in magnetic properties.

It is clear that there is a significant gap in the existing literature regarding the exact relationship between the distributions of chromium-containing phases, the chromium depletion, and the multi-frequency eddy current NDT response of carburized tubes. In addition, the creep properties of carburized microstructures are either un-tested or un-reported, which is a significant impediment to

the accuracy of remaining life estimates. In order to improve interpretation of multi-frequency eddy current NDT data, and improve the accuracy of remaining life estimates of carburized tubes, further research into these areas is necessary.

Chapter References

[1] Plehiers, P.M., Reyniers, G.C., and Froment, G.F. *Simulation of the run length of an ethane cracking furnace.* Industrial and Engineering Chemistry Research, 1990. **29**(4): p. 636-641.

[2] Chun, C.M., Desai, S., Hershkowitz, F., and Ramanarayanan, T.A. *Materials challenges in cyclic carburizing and oxidizing environments for petrochemical applications.* Materials and Corrosion, 2014. **65**(3): p. 282-295.

[3] Sundaram, K.M., Shreehan, M.M., and Olszewski, E.F. *Ethylene*, in *Kirk-Othmer Encyclopedia of Chemical Technology*. 2000, John Wiley & Sons, Inc.

[4] Wu, X.Q., Jing, H.M., Zheng, Y.G., Yao, Z.M., and Ke, W. *Coking of HP tubes in ethylene steam cracking plant and its mitigation.* British Corrosion Journal, 2001. **36**(2): p. 121-126.

[5] Jakobi, D. and Gommans, R. *Typical failures in pyrolysis coils for ethylene cracking.* Materials and Corrosion, 2003. **54**(11): p. 881-886.

[6] Shinozaki, K., Kuroki, H., Nakao, Y., Nishimoto, K., Inui, M., and Takahashi, M. *Deterioration of weldability of long-term aged HP heat-resistant cast steel containing Nb, Mo, and W.* Welding Research Abroad, 1999. **45**(4): p. 22-31.

[7] Stevens, K.J., Ingham, B., Ryan, M., Luzin, V., and Cheong, K. *Carbide composition and stress measurement in ethylene pyrolysis tubes*. in *34th Annual Condensed Matter and Materials Meeting*. 2010. Waiheke Island, New Zealand.

[8] Stevens, K.J., Parbhu, A., and Soltis, J. *Magnetic force microscopy and cross-sectional transmission electron microscopy of carburised surfaces.* Current Applied Physics, 2004. **4**(2-4): p. 304-307.

[9] Stevens, K.J. and Trompetter, W.J. *Calibration of eddy current carburization measurements in ethylene production tubes using ion beam analysis.* Journal of Physics D (Applied Physics), 2004. **37**(3): p. 501-9.

[10] da Silva, I.C., da Silva, R.S., Rebello, J.M.A., Bruno, A.C., and Silveira, T.F. *Characterization of carburization of HP steels by non destructive magnetic testing.* NDT & E International, 2006. **39**(7): p. 569-577.

[11] Silva, I.C., Rebello, J.M.A., Bruno, A.C., Jacques, P.J., Nysten, B., and Dille, J. *Structural and magnetic characterization of a carburized cast austenitic steel.* Scripta Materialia, 2008. **59**(9): p. 1010-1013.

[12] Silva, I.C., Silva, L.L., Silva, R.S., Rebello, J.M.A., and Bruno, A.C. *Carburization of ethylene pyrolysis tubes determined by magnetic measurements and genetic algorithm.* Scripta Materialia, 2007. **56**(4): p. 317-320.

[13] Stevens, K.J. and Minchington, I.E. *A portable system for through-wall carburisation detection in hydro-carbon cracking tubes*. in *NDTA Workshop 2000 - New Zealand Non Destructive Testing Association*. 2000. Rotorua, New Zealand.

[14] Stevens, K.J., Parbhu, A., Soltis, J., and Stewart, D. *Magnetic force microscopy of a carburized ethylene pyrolysis tube.* Journal of Physics D (Applied Physics), 2003. **36**(2): p. 164-8.

[15] Stevens, K.J., Tack, A.J., Thomas, C.W., and Stewart, D. *Through-wall carburization detection in ethylene pyrolysis tubes.* Journal of Physics D (Applied Physics), 2001. **34**(5): p. 814-22.

[16] Quest Integrity Group. *Ethylene Pyrolysis Tube Inspection System*. [cited 27/05/2015; Available from: http://www.questintegrity.com/services/inspection-services/ethylene-pyrolysis-tube-inspection.

[17] Lang, E. and Norton, J. *Monitoring of carburisation by the use of magnetic techniques, Part 1: Fundamental aspects and measurements on 25Cr-20Ni steels*. 1986, Commission of the European Communities, Physical Science, PETTEN, EUR 10566 EN.

[18] Schnaas, A. and Grabke, H.J. *High-temperature corrosion and creep of Ni-Cr-Fe alloys in carburizing and oxidizing environments.* Oxidation of Metals, 1978. **12**(5): p. 387-404.

[19] Christ, H.J. *Experimental characterization and computer-based description of the carburization behaviour of the austenitic stainless steel AISI 304L.* Materials and Corrosion, 1998. **49**: p. 258-65.

[20] Mucek, M.W. *Laboratory detection of degree of carburization in ethylene pyrolysis furnace tubing.* Materials Performance, 1983. **22**(9): p. 25-28.

[21] Grabke, H.J. and Wolf, I. *Carburization and oxidation.* Materials Science and Engineering, 1987. **87**(0): p. 23-33.

[22] Ramanarayanan, T.A., Petkovic, R.A., Mumford, J.D., and Ozekcin, A. *Carburization of high chromium alloys*. in *Workshop `Carburization, Metal Dusting, Carbon Deposition', 6-7 Nov. 1997*. 1998. Germany: VCH Verlagsgesellschaft.

[23] Petkovic-Luton, R. and Ramanarayanan, T.A. *Mixed-oxidant attack of high-temperature alloys in carbon- and oxygen-containing environments.* Oxidation of Metals, 1990. **34**(5-6): p. 381-400.

[24] Wolf, I. and Grabke, H.J. *A study on the solubility and distribution of carbon in oxides.* Solid State Communications, 1985. **54**(1): p. 5-10.

[25] Young, D.J. *Carburization and Metal Dusting*, in *Shreir's Corrosion*. 2010, Elsevier: Oxford. p. 272-303.

[26] Dowling, N.E. *Mechanical Behavior of Materials*. Third Edition ed. 2007: Pearson Education Inc.

[27] Schmidt + Clemens Group *Centralloy® G 4852 Material Data Sheet*. 2009.

[28] Barbabela, G.D., de Almeida, L.H., da Silveira, T.L., and Le May, I. *Phase characterization in two centrifugally cast HK stainless steel tubes.* Materials Characterization, 1991. **26**(1): p. 1-7.

[29] de Almeida, L.H., Ribeiro, A.F., and Le May, I. *Microstructural characterization of modified 25Cr-35Ni centrifugally cast steel furnace tubes.* Materials Characterization, 2003. **49**(3): p. 219-229.

[30] Ul-Hamid, A., Tawancy, H.M., Al-Jaroudi, S.S., Mohammed, A.I., and Abbas, N.M. *Carburisation of Fe-Ni-Cr alloys at high temperatures.* Materials Science Poland, 2006. **24**(2): p. 319-331.

[31] Avery, R.E. and Schillmoller, C.M. *Repair welding high-alloy furnace tubes.* Hydrocarbon Processing, 1988. **67**(1): p. 43-45.

[32] Branza, T., Deschaux-Beaume, F., Sierra, G., and Lours, P. *Study and prevention of cracking during weld-repair of heat-resistant cast steels.* Journal of Materials Processing Technology, 2009. **209**(1): p. 536-547.

[33] Allahkaram, S.R., Borjali, S., and Khosravi, H. *Investigation of weldability and property changes of high pressure heat-resistant cast stainless steel tubes used in pyrolysis furnaces after a five-year service.* Materials & Design, 2012. **33**(0): p. 476-484.

[34] Thomas, C.W., Tack, A.J., and Briggs, N. *Stress relaxation properties of alloy HP50Nb and their application to life assessment of reformer furnace tubing.* International Journal of Pressure Vessels and Piping, 1997. **70**(1): p. 59-68.

[35] Buchanan, K.G. *The Effects of Long-Term Isothermal Ageing on the Microstructure of HP-Nb and HP-NbTi Alloys - Doctoral Dissertation*. 2013, University of Canterbury: Christchurch, New Zealand.

[36] Schmidt + Clemens Group *Centralloy® HT E Material Data Sheet*. 2009.

[37] Zhang, G. and Evans, B. *Progress of modern pyrolysis furnace technology.* Advances in Materials Physis and Chemistry, 2012. **2**(4B): p. 169-172.

[38] Bennett, M.J. and Price, J.B. *A physical and chemical examination of an ethylene steam cracker coke and of the underlying pyrolysis tube.* Journal of Materials Science, 1981. **16**(1): p. 170-188.

[39] Borjali, S., Allahkaram, S.R., and Khosravi, H. *Effects of working temperature and carbon diffusion on the microstructure of high pressure heat-resistant stainless steel tubes used in pyrolysis furnaces during service condition.* Materials & Design, 2012. **34**(0): p. 65-73.

[40] Alvino, A., Lega, D., Giacobbe, F., Mazzocchi, V., and Rinaldi, A. *Damage characterization in two reformer heater tubes after nearly 10 years of service at different operative and maintenance conditions.* Engineering Failure Analysis, 2010. **17**(7–8): p. 1526-1541.

[41] Hou, W.T. and Honeycombe, R.W.K. *Structure of centrifugally cast austenitic stainless steels: Part 1 HK 40 as cast and after creep between 750 and 1000° C.* Materials Science and Technology, 1985. **1**(5): p. 385-389.

[42] Davis, J.R., (Ed). *ASM Specialty Handbook: Heat-Resistant Materials*. 1997, Materials Park, Ohio: ASM International.

[43] Kirchheiner, R. and Woelpert, P. *Niobium in centrifugally cast tubes for petrochemical applications*. in *Niobium, Science and Technology: Proceedings of the International Symposium Niobium. Orland: Minerals, Metals and Materials Society*. 2001.

[44] Hou, W.T. and Honeycombe, R.W.K. *Structure of centrifugally cast austenitic stainless steels: Part 2 Effects of Nb, Ti, and Zr.* Materials Science and Technology, 1985. **1**(5): p. 390-397.

[45] Barbabela, G.D., de Almeida, L.H., da Silveira, T.L., and Le May, I. *Role of Nb in modifying the microstructure of heat-resistant cast HP steel.* Materials Characterization, 1991. **26**(3): p. 193-197.

[46] de Almeida Soares, G.D., de Almeida, L.H., da Silveira, T.L., and Le May, I. *Niobium additions in HP heat-resistant cast stainless steels.* Materials Characterization, 1992. **29**(4): p. 387-96.

[47] Ibanez, R.A.P., de Almeida Soares, G.D., de Almeida, L.H., and Le May, I. *Effects of Si content on the microstructure of modified-HP austenitic steels.* Materials Characterization, 1993. **30**(4): p. 243-9.

[48] Caballero, F.G., Imizcoz, P., Lopez, V., Alvarez, L.F., and De Andrés, C.G. *Use of titanium and zirconium in centrifugally cast heat resistant steel.* Materials Science & Technology, 2007. **23**(5): p. 528-534.

[49] Nishimoto, K., Saida, K., Inui, M., and Takahashi, M. *Changes in microstructure of HP-modified, heat-resisting cast alloys under long-term aging. Repair weld cracking of service-exposed, HP-modified, heat-resisting cast alloys (2nd Report).* Welding Research Abroad, 2002. **48**(11): p. 1-9.

[50] Berghof-Hasselbächer, E., Gawenda, P., Schorr, M., Schütze, M., and Hoffman, J.J. *Atlas of Microstructures*: Materials Technology Institute.

[51] Sustaita-Torres, I.A., Haro-Rodríguez, S., Guerrero-Mata, M.P., de la Garza, M., Valdés, E., Deschaux-Beaume, F., and Colás, R. *Aging of a cast 35Cr–45Ni heat resistant alloy.* Materials Chemistry and Physics, 2012. **133**(2–3): p. 1018-1023.

[52] Rodríquez, J., Haro, S., Velasco, A., and Colás, R. *Aging of cast Ni-base heat resisting alloy.* International Journal of Cast Metals Research, 2004. **17**(3): p. 188-192.

[53] Schmidt + Clemens Group *Centralloy® G 4852 Micro Material Data Sheet*. 2009.

[54] Schmidt + Clemens Group *Centralloy® ET 45 Micro Material Data Sheet*. 2009.

[55] Zaghloul, M.B., Shinoda, T., and Tanaka, R. *Relation between structure and creep rupture strength of centrifugally cast HK40 steel.* Transactions of the Iron and Steel Institute of Japan, 1977. **17**(1): p. 28-36.

[56] Wahab, A.A. *Three-Dimensional Analysis of Creep Void Formation in Steam-Methane Refomer Tubes - Doctoral Dissertation*. 2007, University of Canterbury: Christchurch, New Zealand.

[57] Wu, X.Q., Jing, H.M., Zheng, Y.G., Yao, Z.M., Ke, W., and Hu, Z.Q. *The eutectic carbides and creep rupture strength of 25Cr20Ni heat-resistant steel tubes centrifugally cast with different solidification conditions.* Materials Science and Engineering: A, 2000. **293**(1–2): p. 252-260.

[58] Wahab, A.A. and Kral, M.V. *3D analysis of creep voids in hydrogen reformer tubes.* Materials Science and Engineering: A, 2005. **412**(1–2): p. 222-229.

[59] Wahab, A.A., Hutchinson, C.R., and Kral, M.V. *A three-dimensional characterization of creep void formation in hydrogen reformer tubes.* Scripta Materialia, 2006. **55**(1): p. 69-73.

[60] Buchanan, K.G. and Kral, M.V. *Crystallography and morphology of niobium carbide in as-cast HP-niobium reformer tubes.* Metallurgical and Materials Transactions A: Physical Metallurgy and Materials Science, 2012. **43**(6): p. 1760-1769.

[61] Kaya, A.A. *Microstructure of HK40 alloy after high-temperature service in oxidizing/carburizing environment. II. Carburization and carbide transformations.* Materials Characterization, 2002. **49**(1): p. 23-34.

[62] Porter, D.A., Easterling, K.E., and Sherif, M.Y. *Phase Transformations in Metals and Alloys*. 3rd ed. 2009, Boca Raton, Florida: CRC Press.

[63] Kenik, E.A., Maziasz, P.J., Swindeman, R.W., Cervenka, J., and May, D. *Structure and phase stability in a cast modified-HP austenite after long-term ageing.* Scripta Materialia, 2003. **49**(2): p. 117-22.

[64] Thomas, C.W., Stevens, K.J., and Ryan, M.J. *Microstructure and properties of alloy HP50-Nb: comparison of as cast and service exposed materials.* Materials Science and Technology, 1996. **12**(6): p. 469-475.

[65] Ribeiro, A.F., Borges, R.M.T., and de Almeida, L.H. *Phase transformation in heat resistant steel observed by STEM. (NbTi)C - NiNbSi (G-phase).* Acta Microscopica, 2002. **11**(1): p. 59-63.

[66] Shi, S. and Lippold, J.C. *Microstructure evolution during service exposure of two cast, heat-resisting stainless steels - HP-Nb modified and 20-32Nb.* Materials Characterization, 2008. **59**(8): p. 1029-1040.

[67] Voicu, R., Andrieu, E., Poquillon, D., Furtado, J., and Lacaze, J. *Microstructure evolution of HP40-Nb alloys during aging under air at 1000 °C.* Materials Characterization, 2009. **60**(9): p. 1020-1027.

[68] Laigo, J., Christien, F., Le Gall, R., Tancret, F., and Furtado, J. *SEM, EDS, EPMA-WDS and EBSD characterization of carbides in HP type heat resistant alloys.* Materials Characterization, 2008. **59**(11): p. 1580-1586.

[69] Shinoda, T., Zaghloul, M.B., Kondo, Y., and Tanaka, R. *The effect of single and combined additions of Ti and Nb on the structure and strength of centrifugally cast HK40 steel.* Transactions of the Iron and Steel Institute of Japan, 1978. **18**: p. 139-148.

[70] Kubota Metal Corporation *KHR 45A Alloy Data Sheet.*

[71] Hellier, C. *Handbook of Nondestructive Evaluation*. 2001, McGraw-Hill Professional.

[72] Dibner, B. *Oersted and the Discovery of Electromagnetism*. 1962, New York: Blaisdell Publishing Company.

[73] Serway, R.A. and Jewett, J.W. *Physics for Scientists and Engineers with Modern Physics*. 7th ed. 2008: Thomson Higher Education.

[74] Guru, B.S. and Hiziroglu, H.R. *Electromagnetic Field Theory Fundamentals*. 2004: Cambridge University Press.

[75] Jiles, D.C. *Introduction to magnetism and magnetic materials*. 1998: CRC press.

[76] Hull, B. and John, V. *Non-Destructive Testing*. 1988, London: Macmillan Education Ltd.

[77] Blitz, J., King, W.G., and Rogers, D.G. *Electrical, Magnetic and Visual Methods of Testing Materials*. 1969, London: Butterworths.

[78] García-Martín, J., Gómez-Gil, J., and Vázquez-Sánchez, E. *Non-Destructive Techniques Based on Eddy Current Testing.* Sensors, 2011. **11**(3): p. 2525-2565.

[79] Kasai, N., Ogawa, S., Oikawa, T., Sekine, K., and Hasegawa, K. *Detection of carburization in ethylene pyrolysis furnace tubes by a C core probe with magnetization.* Journal of Nondestructive Evaluation, 2010. **29**(3): p. 175-180.

[80] Jackson, L.R. and Russell, H.W. *Temperature-sensitive magnetic alloys and their uses.* Instruments, 1938. **11**(11): p. 280-282.

[81] Hara, T., Okiyama, T., and Takemoto, T. *Improvement of soft magnetic properties by Cr addition for Fe-(34-46) mass% Ni alloys.* Journal of the Japan Institute of Metals (Japan), 1996. **60**(11): p. 1136-1142 (in Japanese).

[82] Chevenard, P. *La precision en metallurgie et la metallurgie de precision.* Mem. Soc. Ing. Civ.(France), 1951. **104**: p. 1-44 (in French).

Chapter 3: Metallographic Sample Preparation for Macro- and Micro-Analysis of Ex-Service Tubes

3.1 Locations of Metallographic Samples

In order to enable comparisons between the microstructure, mechanical properties, and eddy current non-destructive testing (eddy current NDT) response of the tubes, creep samples and metallographic samples were cut from the tubes in locations which coincided with the locations at which eddy current NDT data had been collected.

Eddy current NDT data had been collected by Quest Integrity Group at a variety of angles around the tube circumferences (e.g. 0°, 90°, 180°, and 270°) and distances along the length (e.g. 20 mm, 40 mm, 60 mm, etc.). The zero points for angle and length were arbitrary and do not refer to tube orientation in the furnace.

A schematic demonstrating the typical arrangement of metallographic and creep samples is shown in Figure 3.1. A summary of the sample locations for each tube is given in Table 3.1, and a summary of the wall thicknesses at each of the metallographic sample locations in given in Table 3.2. A summary of the service conditions of the tubes from which the samples were taken can be found in Table 4.3, in Section 4.2.

Creep samples (yellow) were aligned longitudinally, such that the midsection of the sample coincided with a location where eddy current NDT data had been collected. Creep samples were taken from two locations for each tube. Metallographic samples (red) were cut from locations where eddy current NDT data had been collected, or were cut directly adjacent to the creep sample mid-sections and eddy current NDT data locations. The metallographic samples were located such that the sample face to be analyzed (green) was in the axial direction, normal to the longitudinal direction.

Due to the set locations of eddy current NDT data, and the constraints imposed by creep sample dimensions, only certain combinations of lengths and angles were able to be selected for creep and metallographic sample locations.

In order to assist in selecting locations for creep and metallographic samples, the maximum magnetic response (i.e. normalized eddy current probe inductance) at each eddy current data point was plotted as a function of angle around the tube circumference and distance along the tube length, in the form of a mesh plot. An example of a mesh plot for Tube 5 is shown in Figure 3.2. The combinations of lengths and angles selected were chosen such that regions with high magnetic response (and thus likely

high levels of carburization) as well as regions of low magnetic response (and thus likely little/no carburization) would be analyzed, in order to compare a range of microstructures, mechanical properties, and magnetic responses for each tube.

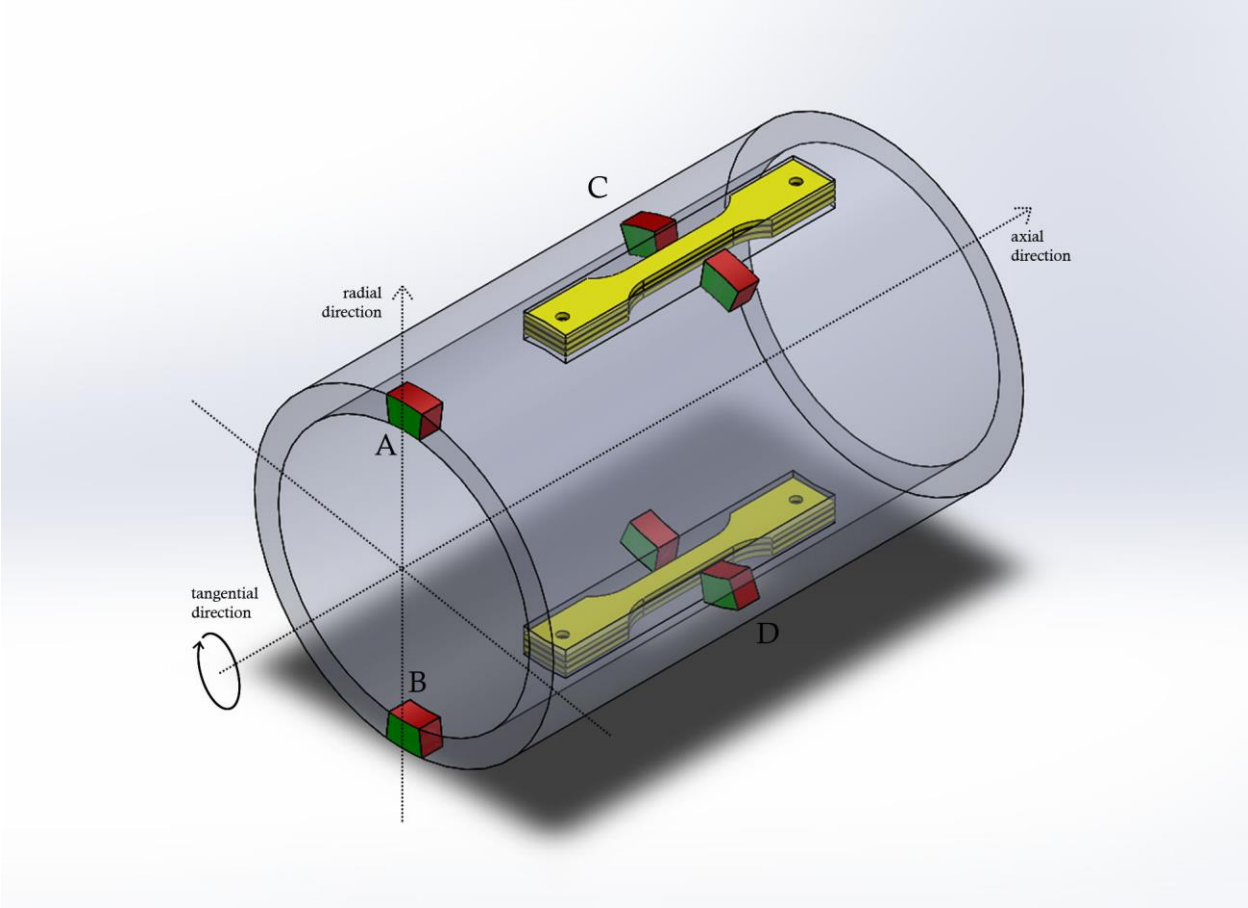

Figure 3.1 - Schematic showing typical arrangement of creep (yellow) and metallographic (red) samples in the ex-service tubes analyzed. The face of the metallographic samples analyzed is highlighted in green.

Table 3.1 - Summary of sample locations for ex-service tubes analyzed.

Tube	Location			
	A	B	C	D
1	20mm, 45°	20mm, 225°	100mm, 45°	100mm, 225°
2	180mm, 90°	180mm, 270°	100mm, 90°	100mm, 270°
3	50mm, 0°	50mm, 180°	150mm, 0°	150mm, 180°
4	100mm, 0°	100mm, 180°	200mm, 0°	200mm, 180°
5	200mm, 90°	200mm, 270°	120mm, 90°	120mm, 270°
6	160mm, 0°	160mm, 90°	80mm, 0°	80mm, 90°

Table 3.2 - Summary of tube wall thicknesses at the metallographic sample locations.

Tube	Location			
	A	B	C	D
1	7.0 mm	8.4 mm	7.9 mm	7.3 mm
2	6.9 mm	7.0 mm	7.1 mm	7.1 mm
3	7.0 mm	7.0 mm	7.2 mm	6.8 mm
4	7.1 mm	7.1 mm	7.0 mm	6.9 mm
5	7.5 mm	8.5 mm	7.9 mm	7.6 mm
6	10.4 mm	8.8 mm	10.0 mm	8.6 mm

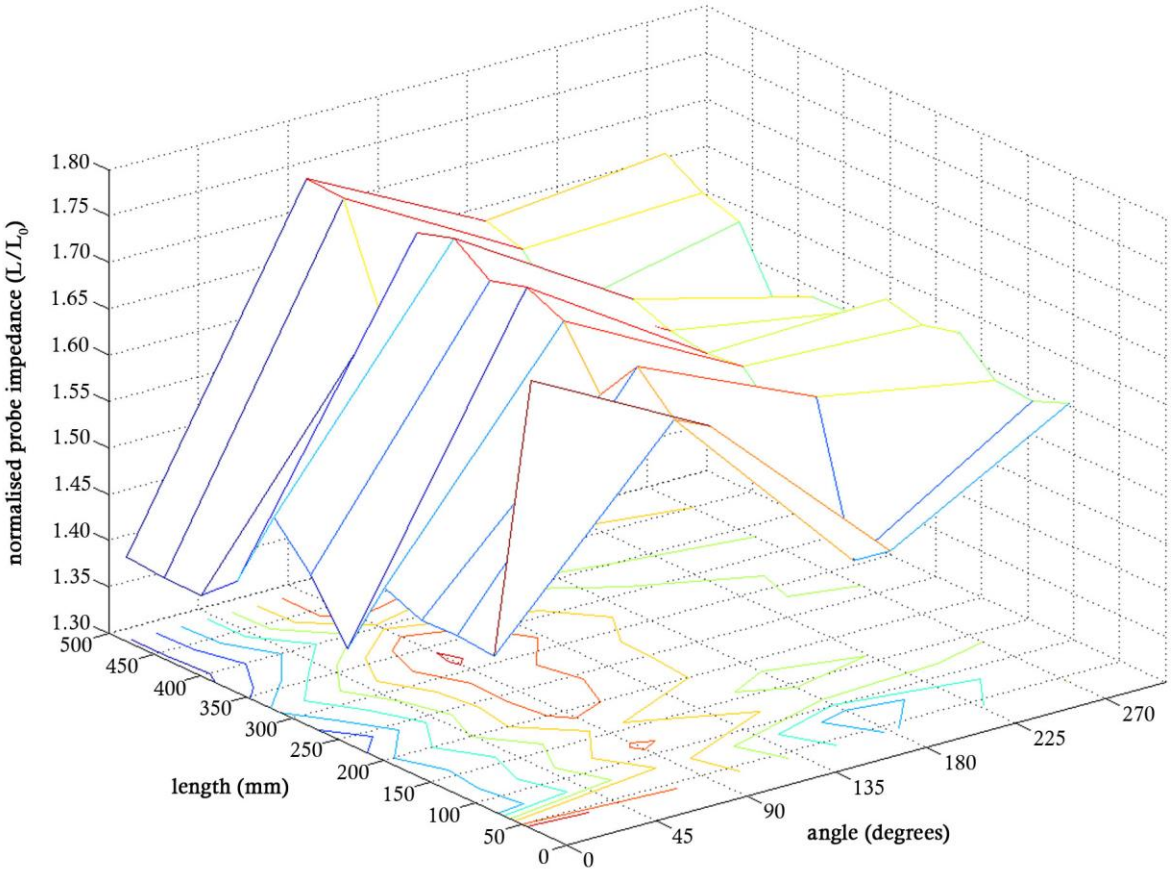

Figure 3.2 - Mesh plot of maximum normalized probe impedance as a function of distance along the tube and angle around the circumference for Tube 5.

3.2 Sample Preparation for Optical and Scanning Electron Microscopy

In order to characterize the microstructure of the ex-service ethylene pyrolysis tubes studied, numerous samples were prepared for light optical microscopy (LOM), scanning electron microscopy, and other analyses performed in a scanning electron microscope (SEM) such as energy dispersive x-ray spectroscopy (EDS) and electron backscatter diffraction (EBSD). The tube alloys can generally be polished to a surface finish acceptable for optical microscopy with relative ease; however, the preparation of high quality samples for scanning electron microscopy is typically more difficult. The difficulty arises largely due to the surface deformation induced in the material during the grinding and diamond polishing steps, which often obscures the microstructure of the sample. Extensive trial and error experimentation was necessary to define a polishing procedure that would consistently yield an acceptable surface finish. This section details the sample preparation techniques for the microstructural analysis of HP and ET45 type alloys.

3.2.1 Cutting, Mounting, Grinding and Polishing to a 3 μm Surface Finish

Metallographic samples of approximately 10 x 8 x 10 mm (arc length x tube wall thickness x depth) were cut from the tube sections using a Buehler Delta AbrasiMet® water cooled grinder. The blocks were then mounted individually in 25.4 mm diameter moulds using Buehler ProbeMet® mounting compound and a Buehler SimpliMet® 1000 automatic compression mounting system. All samples were mounted such that the through-wall axial face, normal to the longitudinal direction, would be visible.

All samples were subject to standard grinding steps, using 180, 240, 320, 400, and 600 grit silicon carbide (SiC) paper, using a Buehler Beta grinder/polisher equipped with a Vector® automated polishing head. When possible, multiple samples were polished using the automated polishing head for consistency. A pressure of 20 N was applied to each sample, while the samples rotated in a direction contra to the rotation of the grinding platen. The samples were subject to each grinding stage for 3 - 5 minutes, or until a flat surface without scratches from previous grinding stages was obtained.

Mechanical polishing, using diamond suspensions and paste in conjunction with a polishing cloth, was used to prepare the samples for OM and SEM analysis. Samples were subject to polishing steps using 9 and 3 μm Buehler MetaDi® Supreme diamond polishing suspension, in combination with a Buehler TexMet® 1000 cloth. The TexMet® 1000 cloth was chosen due to its relatively high material removal rate and ability to minimize relief between the hard carbides and the soft austenitic matrix [1]. When replacing the TexMet® 1000 cloths, it was important to give the new cloth a base of Engis Hyprez® diamond compound, and break the cloth in by polishing an unwanted sample for 1 - 2 minutes. Using a new cloth without this base typically resulted in the cloth inducing scratches on the samples greater than the scratches that could be attributed to the size of the diamond paste and/or suspension being applied to the cloth.

3.2.2 Final Polish and Etching

The final polish was carried out using either Buehler MasterMet® 2 0.02 μm or Buehler MasterMet® 0.06 μm colloidal silica in combination with a Buehler ChemoMet® polishing cloth. 20 N of force was applied to each sample, while the samples rotated in a direction contra to the rotation of the polishing platen. The time for the final polish varied depending on the nature of the subsequent analysis (e.g. LOM, SEM imaging, EBSD), as a result of the surface deformation induced during the grinding and diamond polishing stages. The remainder of this section details the final polishing procedures that proved the most successful for LOM, SEM imaging, EDS mapping, and EBSD. Where applicable, etching procedures have also been detailed.

Optical Microscopy

A final polish of 10 minutes duration was typically long enough to produce a surface which appeared free of scratches when observed under a light optical microscope in the as-polished condition. In order

to observe the precipitates present in the samples under optical microscopy, all samples were individually etched following the final polish. Samples were individually immersed and agitated in glyceregia (30 ml glycerol, 30 ml HCl, 30 ml HNO_3) for 60 – 180 seconds. The samples were thoroughly rinsed with water and ethanol prior to observation.

Electron Backscatter Diffraction (EBSD)

The length of the final polish was observed to affect the quality of the electron backscatter diffraction patterns (EBSPs) of both the austenite matrix and the chromium carbides present in the samples. A poor polish typically resulted in poor pattern quality, which subsequently created difficulties with indexing. A final polish of 60 minutes duration significantly increased the quality of the austenite EBSPs; however, the quality of the EBSPs from the chromium carbides (M_7C_3 and $M_{23}C_6$) decreased significantly. Through a process of trial and error, a final polish duration of 20 minutes was found to give the surface finish necessary such that the quality of the EBSPs from both the austenite and the chromium carbides was sufficient to allow for accurate indexing of each phase. Upon completion of the final polish, samples for EBSD analysis were subject to a short etch in glyceregia (20 seconds) in order to improve the visibility of the precipitates once the sample had been tilted in the SEM (70° from horizontal). The short glyceregia etch resulted in slight relief between the austenite matrix and precipitates, resulting in sharper edges. A comparison between etched and as-polished samples showed that the short glyceregia etch did not affect the quality of the EBSPs produced.

SEM Imaging, EDS mapping

In order to obtain high-quality SEM images, the surface deformation had to be completely removed. For those images used for image analysis, all features of interest (i.e. the precipitates) had to be clearly visible without introducing any polishing artifacts that could be mistaken as microstructural features. Potential sources of error include surface pitting, surface deformation such as scratches, staining of the surface, and excessive relief between the precipitates and the austenite matrix.

Surface deformation could generally be eliminated by increasing the polishing time; however, due to the carbides being much harder than the surrounding austenite matrix prolonged final polishes increased the level of surface relief between the carbides and the matrix. A significant amount of surface relief results in the precipitates appearing larger in the image of the cross-sectioned surface, as shown in Figure 3.3 (a). A compromise between minimization of surface relief and removal of deformation was thus necessary in determining the duration of the final polish. Several polish durations were trialed, and a final polish duration of 30 minutes was seen to give the best balance. Etching of the samples upon completion of the final polish was not performed for SEM imaging and EDS mapping, as the resulting topography of the surface induces measurements errors similar to those caused by polishing-induced surface relief, as shown in Figure 3.3(b).

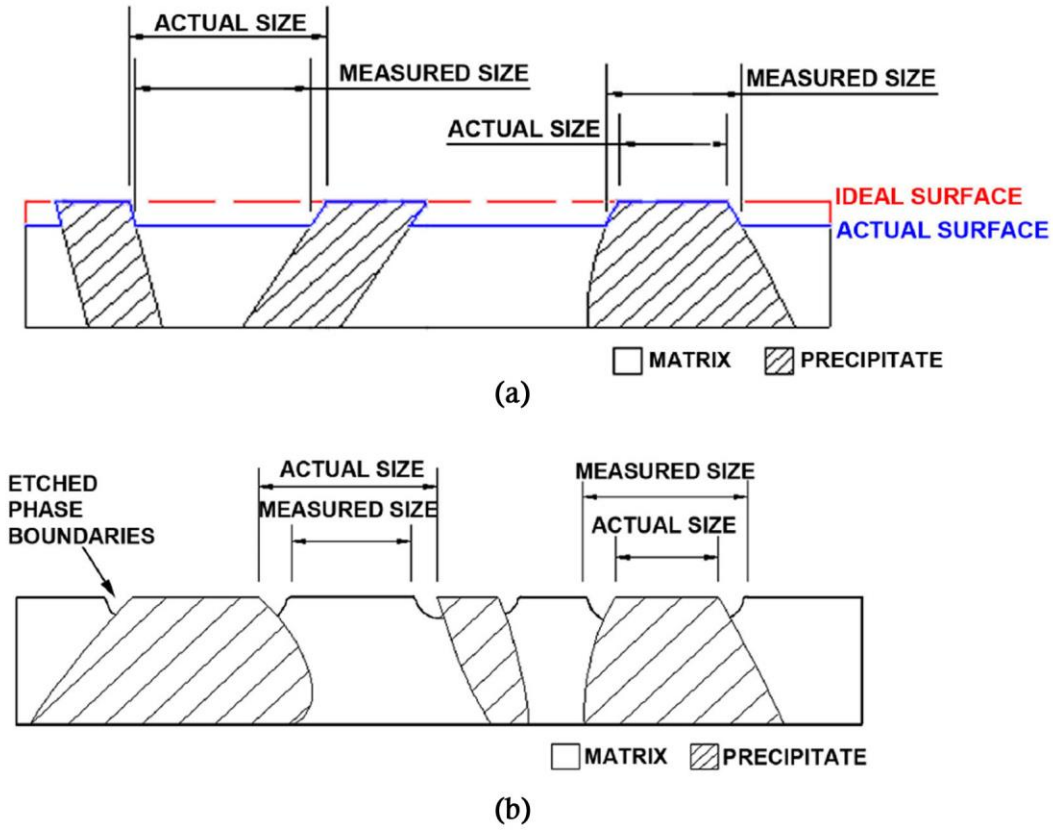

Figure 3.3 - Illustrations depicting (a) the surface relief which occurs between the soft matrix and the hard carbides during polishing, and (b) similar surface relief induced by etching [1].

3.2.3 Deep Etching for Macro- and Micro-Analysis

Deep etching was performed in order to observe the macroscopic grain structure of the tubes analyzed, and the three-dimensional morphology of the precipitate networks. For macro-analysis of grain structure, it was only necessary to grind the samples down to the 600 grit stage, as the remaining scratches and surface deformation were dissolved in the subsequent etching process. Macro-etching for grain structure analysis was performed by immersing the samples in Marbles reagent (10 grams CuSO4, 50 ml HCl, 50 ml H_2O) for 30 - 60 minutes without agitation. The samples were subsequently immersed in HNO_3 for 1-2 minutes to enhance the reflectivity of the etched surface. The surface was thoroughly rinsed with water and ethanol.

Deep etching in glyceregia was performed in order to observe precipitate networks in three dimensions. The samples were polished down to 0.02 μm so that images of the polished surface could be obtained in the SEM prior to etching, and so that the polished surface was retained and visible in the SEM after etching for ease of re-location of imaging areas. Deep etching with glyceregia was carried out with the sample set up as shown in Figure 3.4. Deep etching performed by Buchanan [1] on as-cast and aged HP alloys demonstrated that immersion of samples in a beaker of stagnant glyceregia resulted in a thin transparent film forming during etching which subsequently obscured the precipitates in the SEM. Gentle agitation with a magnetic stirrer was shown to prevent the formation

of the film without any adverse effects for the precipitate network. Having the sample offset from the center of the beaker and the stirrer, and off axis from the center of the beaker, enabled air bubbles to be avoided on the surface of the sample. After etching the samples were thoroughly rinsed in warm water and ethanol, before observation in the SEM.

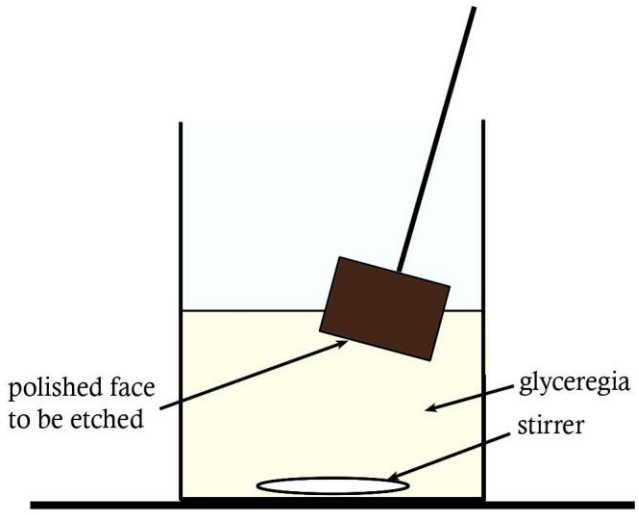

Figure 3.4 - Schematic of the apparatus used to agitate the glyceregia etchant during deep etching.

3.3 Analysis Equipment and Typical Operating Conditions

This section provides an overview of the analysis equipment and standard operating conditions used for characterization of the ex-service ethylene pyrolysis tubes analyzed.

3.3.1 Optical Microscopy

Optical microscopy was performed using a Leica DM-Inverted Research Microscope. Images were captured digitally using a Nikon Digital Sight DS-Fi1 camera and NiS Elements F (version 3.2) software.

3.3.2 Scanning Electron Microscopy

Backscattered electron (BSE) imaging and secondary electron imaging (SEI) was carried out using a JEOL 7000F field emission scanning electron microscope (SEM) equipped with a JEOL JED-2300 EDS detector. All samples were analyzed at 20 keV. This field emission SEM was used to obtain images (both backscattered and secondary electron images) of the microstructure from two-dimensional polished sections as well as images of the three-dimensional morphology of the precipitate network after samples had been subject to deep etching in glyceregia. Imaging of the three-dimensional morphology of the precipitate networks was carried out solely using secondary electrons.

Phase identification was performed using a combination of SEI imaging, EBSD, and EDS analyses. Samples were analyzed at 20 keV using a JEOL JSM 6100 SEM equipped with HKL Nordlys III EBSD detector, Oxford Instruments X-Max 50 EDS detector, and the Oxford Instruments Aztec software suite. SEI images, EDS spectra, and electron backscatter diffraction patterns (EBSPs) were collected using the Aztec software. Analysis of the composition of each phase, as provided by the EDS spectra, and comparison with the compositional information in a reference database of possible phases allowed for a list of candidate phases to be compiled. The EBSPs were then indexed using the Aztec software by comparison of the pattern with the crystal structure information in the reference database for the list of candidate phases. The reference database had been previously compiled specifically for HP alloys, by selecting known phases of similar compositions to those observed in the alloys from Pearson's crystal structure database [2]. EDS mapping was performed at 20 keV, with a dwell time of 100 μs.

Chapter References

[1] Buchanan, K.G. *The Effects of Long-Term Isothermal Ageing on the Microstructure of HP-Nb and HP-NbTi Alloys - Doctoral Dissertation*. 2013, University of Canterbury: Christchurch, New Zealand.

[2] Villars, P., (Ed). and Cenzual, K., (Ed). *Pearson's Crystal Data: Crystal Structure Database*. 2008, ASM International: Materials Park, Ohio, U.S.A.

Chapter 4: Tube Macrostructures and Phase Identification

This chapter discusses the macrostructural characterization of the ex-service ethylene pyrolysis tubes studied, in the form of compositional and grain structure analysis.

The results of phase identification in the six ex-service tubes studied will be presented, a necessary step before the distributions of the various phases across the tube walls can be discussed. A number of phase transformations occurred in the samples analysed, and although the identification of the individual phases will be discussed in this chapter, detailed discussion of the phase transformations and the distribution of the various phases across the tube walls will be presented in Chapter 5. The composition of the austenite matrix of the tubes will also not be discussed here, and will be discussed in Chapter 5.

4.1 Chemical Composition

The chemical compositions of the six tubes, as determined by inductively coupled plasma atomic emission spectroscopy (ICP-AES), are shown in Table 4.1. The samples used for ICP-AES were approximately 10 mm x 10 mm x wall thickness. For comparison, typical compositions of HP-Nb, HP-Micro, and ET45-Micro alloys are shown in Table 4.2.

Tubes 1 and 2 have the composition typical of HP-Nb alloys. The niobium content of tube 1 is higher than that of tube 2 (1.33 vs. 0.89 wt%), and tube 1 also contains more silicon (1.28 vs. 0.73 wt%). As discussed in Section 2.3, the addition of niobium to the HP alloy composition results in the partial replacement of the as-cast primary Cr_7C_3 carbide network with NbC. The relative volume fractions of the primary Cr_7C_3 and NbC carbides have been shown to be directly dependent on the niobium content of the alloy, and thus the decreased niobium content in tube 1 would likely have resulted in a lower volume fraction of NbC in the as-cast condition in comparison to tube 2 [1, 2]. The transformation rate of the NbC carbides to either G-phase or η-carbide upon exposure to elevated temperatures might be expected to be greater in tube 2 due to the higher silicon content if the two tubes were subject to solely isothermal ageing [1-4].

Tubes 3 and 4 have almost identical compositions, both of which are typical of HP-Micro alloys. The combined additions of titanium and niobium to the HP alloys composition results in the partial replacement of the as-cast primary Cr_7C_3 network with (Nb,Ti)C precipitates. Tube 5 also has a

composition typical of HP-Micro; however, in comparison to tubes 3 and 4, tube 5 contains less titanium but more niobium. The silicon content of tube 5 is similar to that of tubes 3 and 4.

Tube 6 has elevated chromium and nickel content in comparison to the other five tubes (35% Cr – 45% Ni, vs 25% Cr – 35% Ni), and also contains both niobium and titanium, typical of an ET45-Micro alloy. The niobium, titanium, and silicon content of tube 6 is similar to that of tubes 3-5.

The typical carbon content of HP and ET45 alloys is in the 0.4 - 0.5 wt% range. The carbon content of tubes 1 and 2 are significantly elevated above the typical values, likely as a result of carburization experienced during service.

Table 4.1 - Chemical composition of the six ex-service ethylene pyrolysis tubes as determined by inductively coupled plasma atomic emission spectroscopy (ICP-AES). Balance Fe.

wt%	C	Cr	Ni	Si	Mn	Nb	Ti	V	Other
Tube 1	1.61	25.50	35.60	1.28	1.23	1.33	<0.01	0.02	0.12
Tube 2	1.12	24.50	34.50	0.73	0.71	0.89	<0.01	0.03	0.06
Tube 3	0.39	24.50	33.90	1.26	1.26	0.89	0.15	0.02	0.16
Tube 4	0.41	24.40	34.00	1.25	1.25	0.90	0.14	0.02	0.17
Tube 5	0.45	25.40	34.40	1.23	1.03	1.05	0.10	0.02	0.12
Tube 6	0.46	34.50	44.90	1.14	1.06	0.97	0.13	0.01	0.10

Table 4.2 - Typical chemical compositions of HP-Nb, HP-Micro, and ET45-Micro alloys (Add. = additions, Bal. = balance).

wt%	C	Cr	Ni	Si	Mn	Nb	Ti	Zr	Rare Earths	Fe	Ref.
HP-Nb	0.40	25	35	2.0 max	2.0 max	1.5 max	-	-	-	Bal.	[5, 6]
HP-Micro	0.45	25	35	1.5	1.0	1.5 max	0.1 max	-	-	Bal.	[6-10]
ET45-Micro	0.45	35	Bal.	1.6	1.0	1.0	Add.	Add.	Add.	16	[11, 12]

4.2 Service Conditions

The service conditions of the six ex-service tubes are summarised in Table 4.3. Very little is known of the exact conditions for many of the tubes.

Table 4.3 - Summary of the known service conditions of the six ex-service ethylene pyrolysis tubes. TMT = tube mean temperature.

Tube	Tube 1	Tube 2	Tube 3	Tube 4	Tube 5	Tube 6
Type	radiant tube	radiant outlet tube	radiant Inlet tube	radiant Inlet tube	radiant tube	radiant tube
Time in service	≈ 4 years	unknown	17 months	17 months	unknown	unknown
Temperature	704 °C	TMT 982 – 1037 °C	TMT 1010 – 1080 °C	TMT 1010 – 1080 °C	unknown	unknown
Pressure	138 kPa	unknown	unknown	unknown	unknown	unknown

4.3 Macroscopic Observations

4.3.1 Grain Structure

Samples from each of the six tubes were etched in accordance with the macro-etching procedures described in Section 3.2.3, in order to observe the tube grain structures. Figure 4.1 presents the macroscopic grain structures of each of the six tubes. Depending on the cooling rate after centrifugal casting, ethylene pyrolysis tubes can exhibit either a completely columnar or a mixed equiaxed-columnar grain structure [8, 13]. High cooling rates during centrifugal casting has resulted in 100% columnar grain structures in tubes 1-5. Tube 6 displays approximately 40% equiaxed grains (inner diameter) and 60% columnar grains (outer diameter), indicating lower cooling rates were achieved during casting in comparison to tubes 1-5.

Three of the tubes (tubes 1, 2 and 5) did not respond as well to the etchant (Marbles reagent) at their inner diameters as they did at the mid- and outer-wall regions. Analyses conducted by Sun *et al.* [14-16] and Cao *et al.* [17] on the low-temperature plasma carburizing of 316 stainless steel, an austenitic alloy, have shown that the carburized layer (a layer of austenite supersaturated in carbon) is more resistant to etching with Marbles reagent than the bulk austenite. The decreased response to the etchant at the inner wall regions of tubes 1, 2 and 5 may therefore indicate carburization at the inner wall regions.

Qualitatively, tube 1 has the largest columnar grain size; however, it was not possible to take quantitative measurements of the grain size of the tubes from the images shown in Figure 4.1. The number of visible grains was seen to be dependent on the manner in which the samples were illuminated, and grains not visible in the image would typically appear to merge with an adjacent grain, therefore increasing the apparent grain size. Changing the illumination conditions, for example the illumination angle, the light source, or the number of light sources, would typically reveal previously unseen grains, but would also result in merging other grains that were previously visible. Although the images in Figure 4.1 show a significant number of the grains that were present in each sample, not all grains were able to be captured, and therefore it was considered inaccurate to measure grain size from the macro-etched samples. EBSD mapping in order to determine grain size was considered impractical due to the large grain sized observed in the samples.

The creep performance of HK and HP reformer tubes has been shown to be dictated by the grain structure of the tubes as well as the properties of the primary and secondary precipitates (e.g. the phases present, and the average, size, distribution, and volume fraction of each phase). The grain structure and the properties of the primary precipitate networks (e.g. dendrite arm spacing) are influenced by the casting conditions.

Work conducted by Zaghloul *et al.* [13] on unmodified HK alloys determined that an increase in the cooling rate during casting from 240 °C/minute to 804 °C/minute approximately doubled the dendrite arm spacing (from 45 μm to 90 μm), and also approximately halved the volume of primary precipitates (5% to 2.1%). However, the effects of the cooling rate on the creep performance of the alloy were dependent on the testing conditions – accelerated testing at 950 °C and 29.5 MPa showed no significant difference in the rupture life with respect to cooling rate, whereas accelerated testing at 1000 °C and 9.8 MPa resulted in the rupture life increasing from approximately 200 hours to 900 hours when the cooling rate was increased. Zaghloul *et al.* also determined that the size of the secondary precipitates in samples aged at 950 – 1100 ° for up to 1000 hours was also dependent on the cooling rate during casting. In general, the secondary precipitates were finer in tubes which experienced higher cooling rates during casting, regardless of the ageing temperature, which would provide a superior dispersion strengthening effect and thus contribute to an improved rupture life. However, ageing at higher temperatures or for longer times (>4500 hours) resulted in the average secondary precipitate size for all tubes to converge. As such, although the results suggest that an increased cooling rate and thus increased dendrite arm spacing may lead to an increased creep rupture life, due to the cooling rate also affecting the primary and secondary precipitate distributions it is difficult to isolate the exact effect of grain size and shape on the creep properties.

The effect of grain structure on carburization is less clear. Cross-wall grain structures consisting of columnar grains at the outer wall and fine, equiaxed grains at the inner wall have been suggested to be beneficial, as the columnar grain structure is reportedly resistant to creep while the fine equiaxed

grain structure is reportedly resistant to carburization [18]. In work focusing on the metal-dusting resistance of Alloy 800H, Grabke *et al.* [19] state that the presence of easy diffusion paths for chromium is important for the fast formation and healing of chromium-rich oxide scales, which prevent carbon diffusion into the material. Such diffusion paths – grain boundaries, sub-boundaries, and dislocations – can be provided by fine grained microstructures, and cold and/or surface work. Thus, it is possible that the 40% equiaxed – 60% columnar structure of tube 6 may provide increased resistance to carbon diffusion and thus carburization in comparison to tubes 1-5. However as the tubes are of different compositions, and have experienced different service times and conditions, it is improbable that such a hypothesis could be proven as a result of the current work.

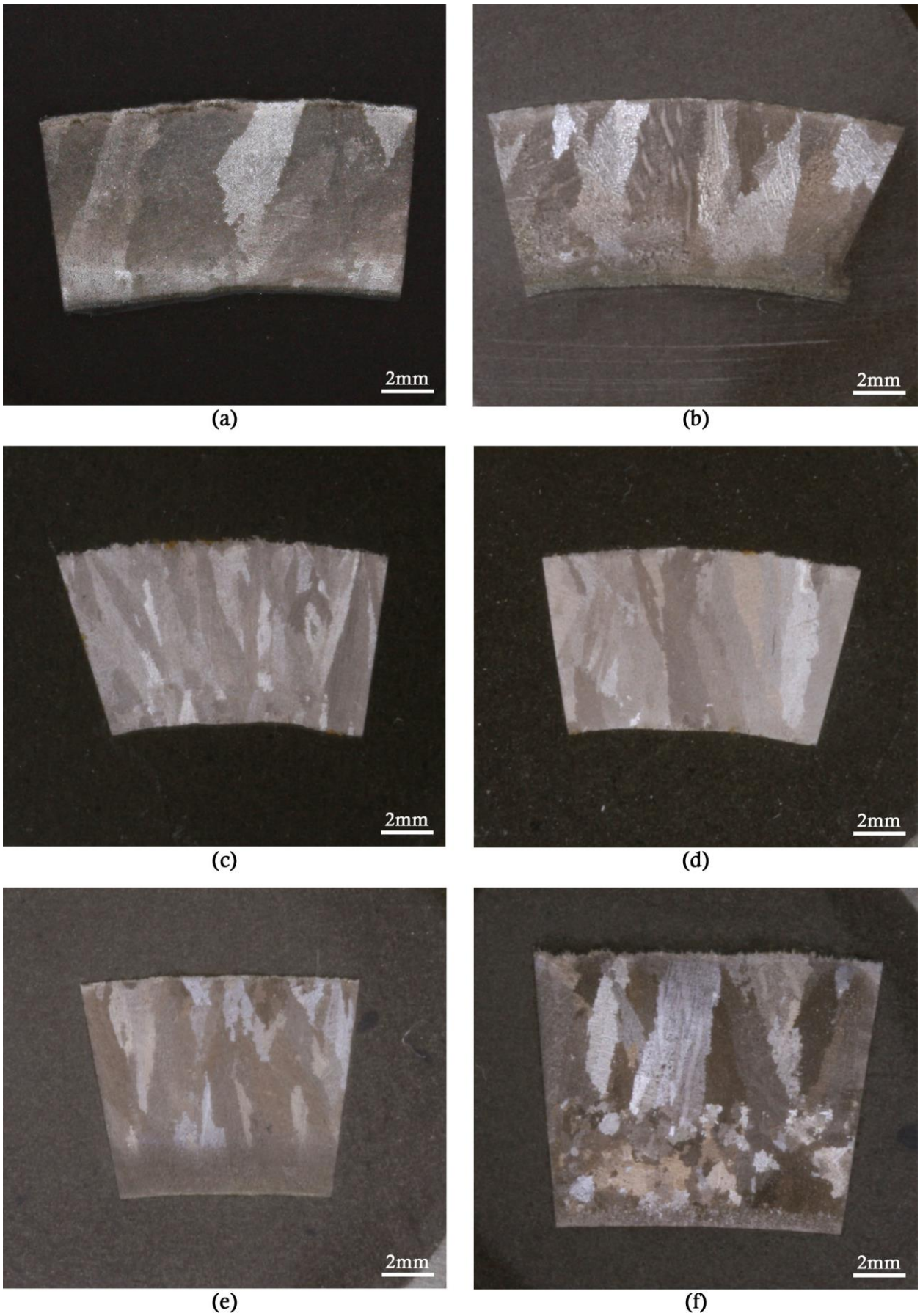

Figure 4.1 - Low magnification images showing the macrostructure of (a) tube 1, (b) tube 2, (c) tube 3, (d) tube 4, (e) tube 5, and (f) tube 6.

4.4 Comparison between Axial and Tangential Directions

As a result of the centrifugal casting process, it was expected that the macro- and microstructures of the tubes would be consistent in both the axial and tangential directions. In order to ensure that this was indeed the case, and to ensure that the microstructural characterization of the axial face would be representative of both the axial and tangential directions, analysis of the grain structure and the microstructure of both axial and tangential samples from three of the tubes was performed.

An axially-oriented sample and a tangentially-oriented sample were cut from three tubes, with the axial and tangential samples being directly adjacent to one another (Figure 4.2). Samples were first etched in accordance with the macro-etching procedure described in Section 3.2.3 in order to observe and compare the grain structure in both directions. The samples were then re-polished and etched with glyceregia in accordance with the procedure described Section 3.2.2 in order to observe and compare the microstructure in both directions.

A comparison between the macrostructures in the axial and tangential directions for tubes 2, 4, and 6 is shown in Figure 4.3. Although not all of the grains visible to the naked eye were able to be captured in the digital images (as described in Section 4.3.1), no differences were observed in the grain structure along the two directions in the three tubes analyzed.

The microstructure of tube 2 was observed to change across the wall thickness; however, the appearance at all locations was consistent across both the tangential and axial directions. A highly coarsened carbide network was observed at the mid- and outer wall regions, consisting of angular, blocky carbides, and an extremely coarsened carbide network consisting of rounded, agglomerated carbides was observed at the inner wall. A comparison between the inner-, mid-, and outer-wall microstructures of tube 2 in both directions is shown in Figure 4.4.

The microstructure of tube 4 was consistently the same at all locations across the wall thickness, in both the tangential and axial directions. A network composed of precipitates with a fine lamellar morphology was observed. A comparison between the tangential and axial microstructures of tube 4 is shown in Figure 4.5.

The microstructure of tube 6 was observed to change across the wall thickness; however, the appearance at all locations was consistent across both the axial and tangential directions (Figure 4.6). A coarse network of primary carbides was observed at the mid wall region, with the level of coarseness and agglomeration decreasing towards the outer wall. The preceding analysis confirmed the hypothesis that the macro and microstructures of the tubes are identical in both the axial and tangential directions as a result of the centrifugal casting method, and thus that microstructural characterization of the axial face is representative of the microstructure in both directions.

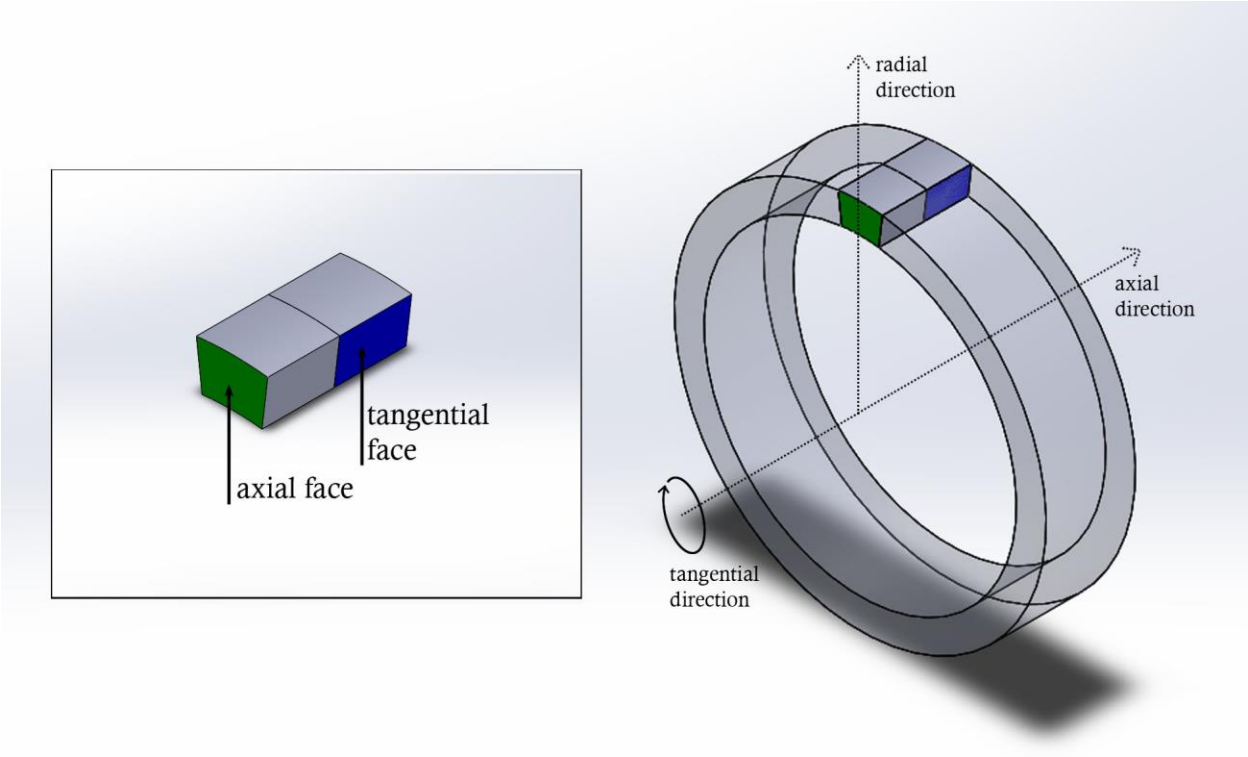

Figure 4.2 - Tube schematic indicating axial and tangential directions and faces.

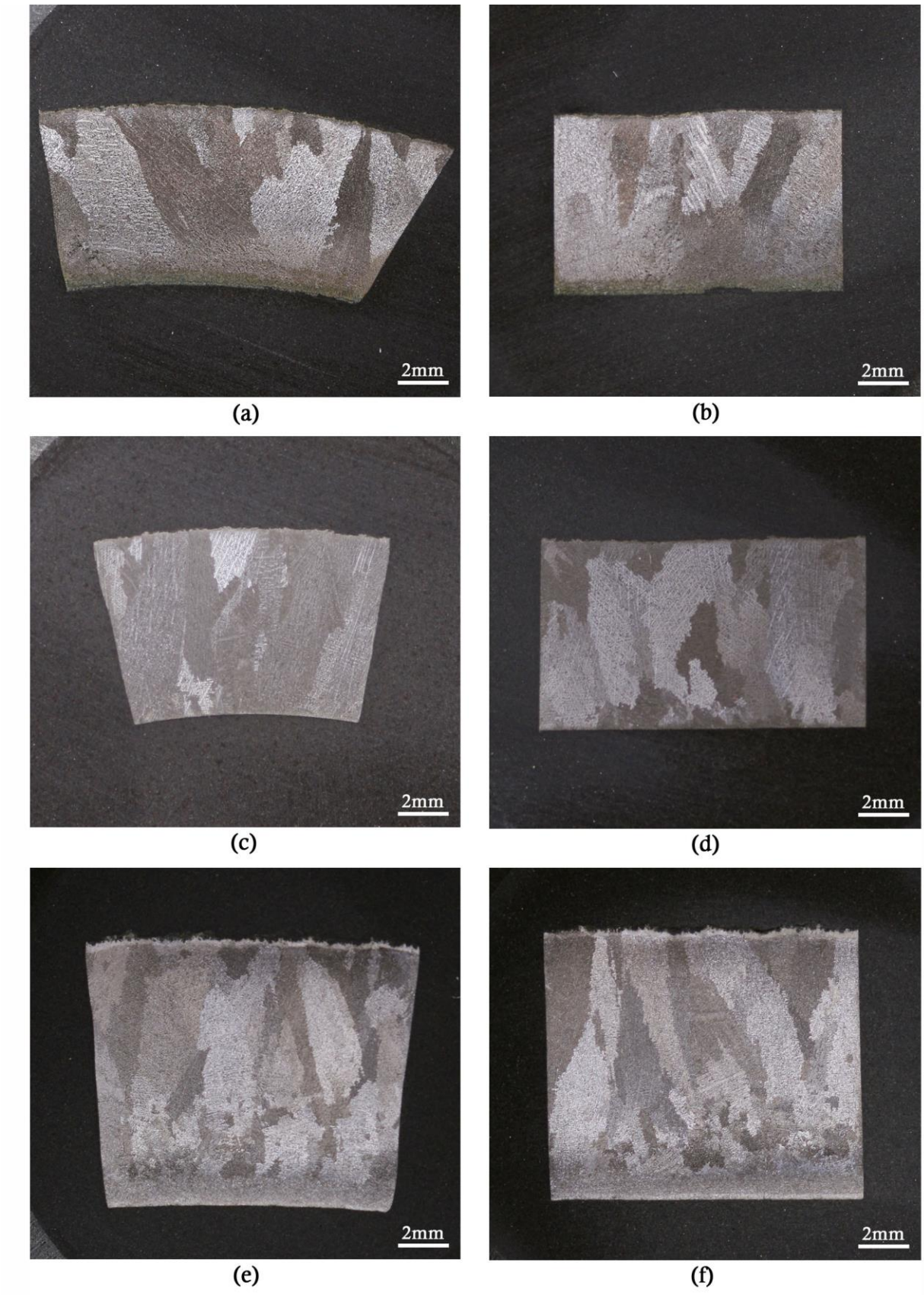

Figure 4.3 - Low magnification images showing the macrostructure of (a) tube 2, axial face, (b) tube 2, longitudinal face, (c) tube 4, axial face, (d) tube 4, longitudinal face, (e) tube 6, axial face, and (f) tube 6, longitudinal face.

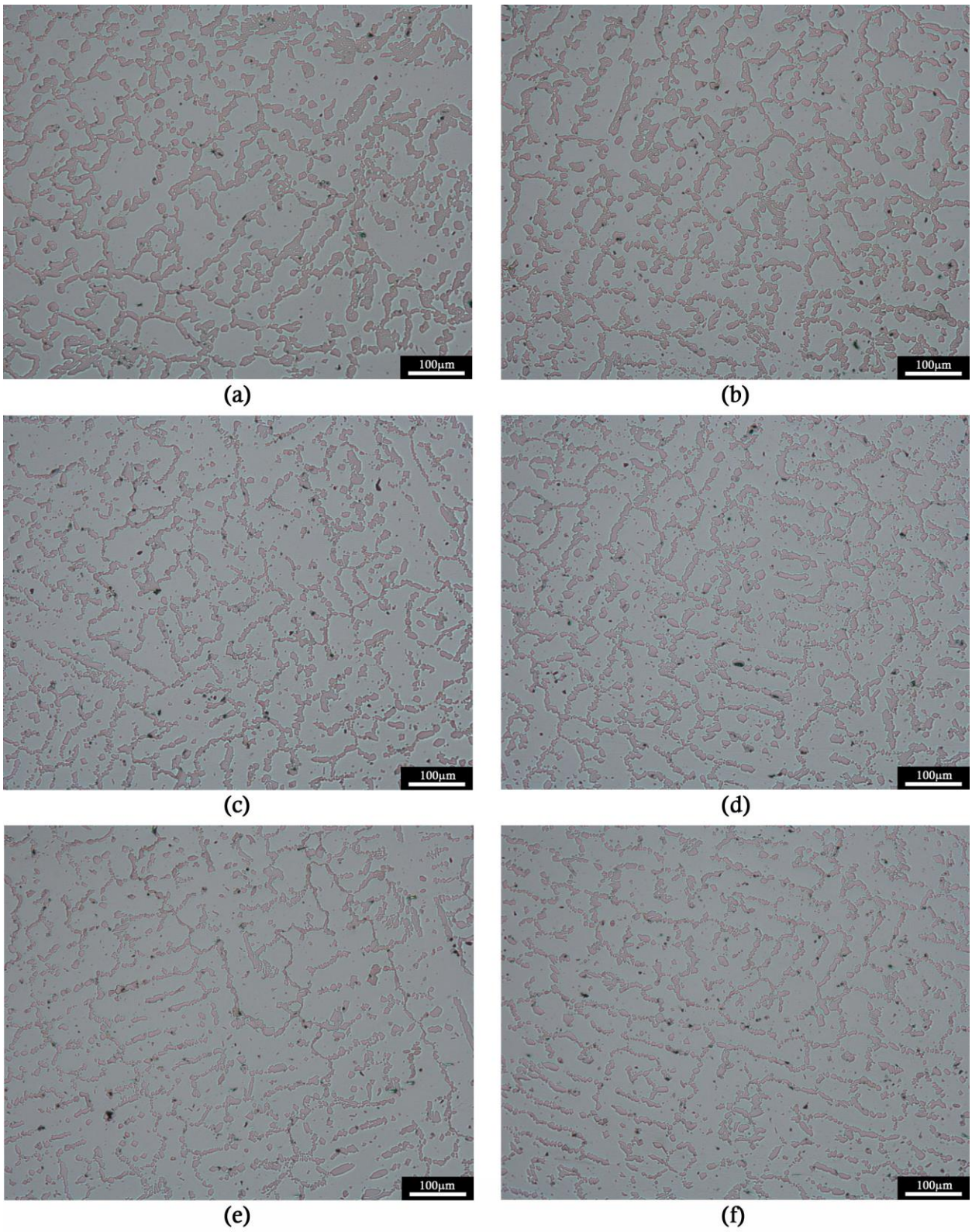

Figure 4.4 – Optical micrographs comparing the microstructure of tube 2 in the axial and longitudinal directions. (a) inner wall, axial, (b) inner wall, longitudinal, (c) mid wall, axial, (d) mid wall, longitudinal, (e) outer wall, axial, (f) outer wall, longitudinal.

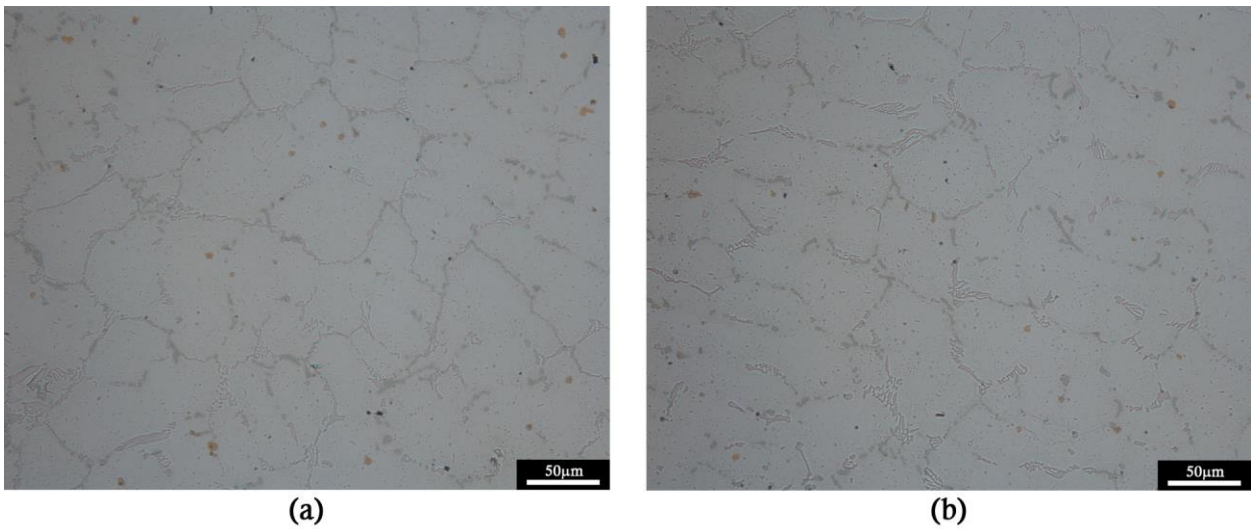

Figure 4.5 – Optical micrographs comparing representative microstructures of tube 4 in the (a) axial and (b) longitudinal directions.

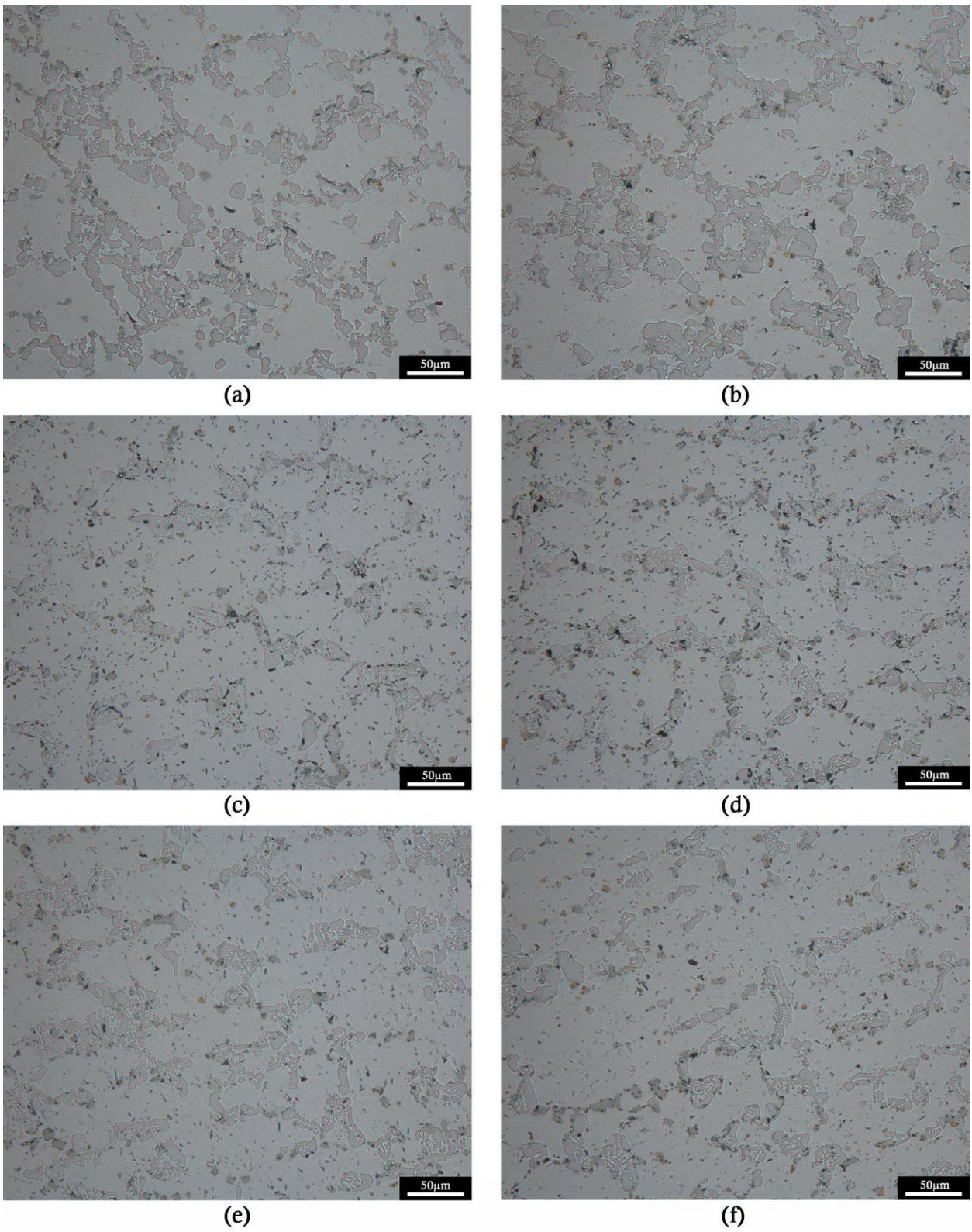

Figure 4.6 - Optical micrographs comparing representative microstructure of tube 6 in the axial and longitudinal directions. (a) inner wall, axial, (b) inner wall, longitudinal, (c) mid wall, axial, (d) mid wall, longitudinal, (e) outer wall, axial, (f) outer wall, longitudinal.

4.5 Phase Identification in Ex-Service Tubes

A database of candidate phases was constructed for the HP and ET45 alloys, by selecting known phases of similar compositions to those observed in the alloys from Pearson's crystal structure database [20] as well as phases identified in literature that are not contained in Pearson's. A summary of the phases in the database is shown in Table 4.4.

Phase identification was achieved using a combination of energy dispersive x-ray spectroscopy (EDS) and electron backscatter diffraction (EBSD). For each location of interest, the composition as determined by EDS was used to narrow down the list of candidate phases within the reference database. The electron backscatter patterns (EBSPs) were then indexed using the Oxford Instruments Aztec software by comparison with the crystal structure information in the reference database. Potential matches were ranked according to the mean angular deviation (MAD), and the correct structural match selected. The MAD is a goodness of fit parameter that expresses how well the simulated EBSP overlays the experimental EBSP, and is given in degrees specifying the angular misfit between the detected and simulated Kikuchi bands. This process was performed in multiple phase regions for each phase in each metallographic sample to confirm the identification.

The transformation of the primary NbC and (Nb,Ti)C precipitates to silicide phases upon exposure to temperatures in the range of 700 – 1050 °C is well reported in literature [1-4, 7, 9, 21, 22], as discussed in Section 2.4.2. The transformation product is typically reported as G-phase ($Ni_{16}Nb_6Si_7$), a face centered cubic ($Fm\bar{3}m$) nickel-niobium silicide; however, the diamond cubic ($Fd\bar{3}m$) chromium-nickel-niobium silicide, commonly referred to as η-carbide, has also been reported.

Due to the crystallographically similar space groups and lattice parameters of the G-phase and η-carbide crystal structures, it is not possible to positively determine the best match using EBSD analysis. There are a number of phase identification methods available that would serve to differentiate the two phases. Both selected area diffraction (SAD) analysis of thin foils and X-ray diffraction (XRD) analysis of extracted phases would enable the identification and differentiation of the face centered cubic crystal structure of G-phase and the diamond cubic crystal structure of η-carbide.

Electron diffraction patterns produced by SAD for the G-phase and η-carbide are similar along most beam directions, due to the similar space groups and lattice parameters of the two phases. There are however subtle differences that can be seen in certain beam directions that allow the two to be differentiated – one such direction is the [001] direction. Based on kinematic diffraction the {020} and {420} type reflections are forbidden for the $Fd\bar{3}m$ structure. In contrast, in the $Fm\bar{3}m$ structure of G-phase, the {200} type reflections are allowed [23-27]. Shown in Figure 4.7 (a) and (b) are simulated [001] zone axis patterns (ZAPs) for the G-phase and the η-carbide crystal structures respectively,

clearly showing the presence of {200} and {420} type reflections in the G-phase ZAP, and the absence of the same reflections in the η-carbide ZAP.

Despite the ability of SAD and XRD to differentiate between the two phases, the time-consuming nature of sample preparation for both SAD and XRD was considered prohibitive due to the large number of metallographic samples analyzed in the current project. Additionally, XRD analysis of multi-phase alloys, such as HP and ET45 alloys, can be inaccurate due to numerous peak overlaps in the spectra, and difficulty in isolating the G-phase and η-carbide structures in XRD spectra has been reported in the literature [4, 28]. However, the two phases have significantly different chromium contents (typically <5 at% in G-phase, and typically 30-35 at% in η-carbide), and thus EDS is able to be used to differentiate the two. Provided that the phase regions analysed are significantly larger than the interaction volume of the probe (~1-2 μm at 20 keV [29]) in order to avoid false contributions to the chromium content due to excitation of the chromium-rich carbides or austenite matrix, the composition as determined by EDS was considered sufficient evidence to differentiate between the two phases.

Carbon peaks (on the order of 6-20 at%) were detected in the η-carbide precipitates; however, EDS analysis at best gives a qualitative indication of the presence of carbon. It should be noted that silicides rich in chromium and nickel but free of carbon, with the same crystal structure and similar lattice parameters to that of the η-carbide precipitates have been identified in the literature [30]. Thus the η-carbide crystal structure does not necessitate the presence of carbon, and it is possible that in some cases the η-carbide could equally be classed as a silicide. The η-carbide in the present work has been labelled as such due to the indicated presence of carbon, and to be consistent with the literature to date. Further microanalysis (such as electron energy loss spectroscopy) would be necessary to quantitatively confirm the carbon content of these precipitates.

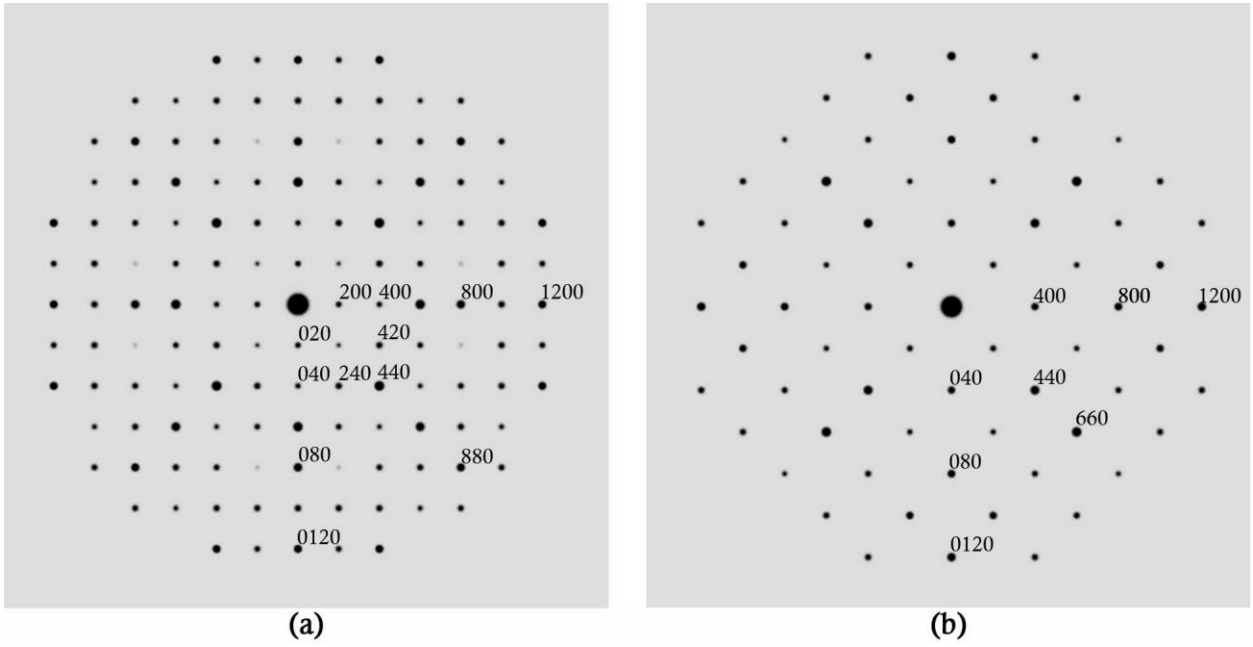

Figure 4.7 - Indexed simulated selected area diffraction patterns from the [001] zone axes of the (a) $Fm\bar{3}m$ G-phase and (b) $Fd\bar{3}m$ η-carbide crystal structures.

Table 4.4 - List of candidate crystal structures for EBSD identification of phases in HP and ET45-type ex-service ethylene pyrolysis tubes.

Phase	Crystal System	Space Group	Lattice parameters a, b, c (nm)			α, β γ (°)			Ref.
M_3C	Orthorhombic	$Pnma$	0.512	0.680	0.458	90	90	90	[31]
M_3C_2	Orthorhombic	$Pnma$	1.146	0.552	0.285	90	90	90	[4]
M_3C_2	Orthorhombic	$Cmcm$	0.285	0.926	0.697	90	90	90	[32]
M_7C_3	Hexagonal	$P6_3mc$	1.401	1.401	0.453	90	90	120	[33]
M_7C_3	Orthorhombic	$Pnma$	0.701	1.215	0.453	90	90	90	[4]
$M_{23}C_6$	Cubic	$Fm\bar{3}m$	1.065	1.065	1.065	90	90	90	[4]
NbC	Cubic	$Fm\bar{3}m$	0.44	0.44	0.44	90	90	90	[34]
Nb_2C	Hexagonal	$P6_3/mmc$	0.31	0.31	0.5	90	90	120	[4]
Nb_2C	Orthorhombic	$Pnma$	1.091	0.310	0.497	90	90	90	[35]
Nb_6C_5	Monoclinic	$C12/m1$	0.545	0.944	0.545	109.5	90	30	[4]
(Nb,Ti)C	Cubic	$Fm\bar{3}m$	0.446	0.446	0.446	90	90	90	[4]
TiC	Cubic	$Fm\bar{3}m$	0.433	0.433	0.433	90	90	90	[36]
Ti_2C	Cubic	$Fd\bar{3}m$	0.86	0.86	0.86	90	90	90	[4]
Ti_8C_5	Hexagonal	$R\bar{3}mh$	0.612	0.612	1.49	90	90	120	[4]
G-phase	Cubic	$Fm\bar{3}m$	1.1249	1.1249	1.1249	90	90	90	[4]
η-carbide	Cubic	$Fd\bar{3}m$	1.084	1.084	1.084	90	90	90	[4]
NbNiSi	Orthorhombic	$Pnma$	0.6223	0.3683	0.7088	90	90	90	[37]
$NbNiSi_2$	Tetragonal	$I4/mmm$	1.2571	1.2571	0.4988	90	90	90	[38]
$Cr_2(C,N)$	Hexagonal	$P\bar{3}1m$	0.482	0.482	0.447	90	90	120	[39]
σ-phase	Tetragonal	$P4_2/mnm$	0.880	0.880	0.454	90	90	90	[40]
MnS	Cubic	$Fm\bar{3}m$	0.522	0.522	0.522	90	90	90	[41]
Iron FCC	Cubic	$Fm\bar{3}m$	0.361	0.361	0.361	90	90	90	[42]
Iron BCC	Cubic	$Im\bar{3}m$	0.287	0.287	0.287	90	90	90	[4]

4.5.1 Tube 1

Figure 4.8 shows representative optical and scanning electron micrographs of tube 1 at the inner wall, mid wall, and outer wall regions. In all samples, the primary precipitate network was significantly coarsened across the wall of the tube in comparison to the fine lamellar groups typical of the as-cast structure. A change in the morphology of the primary chromium-rich precipitates was observed at the mid-wall region in all samples; however, the exact proximity to the inner diameter was seen to vary. On occasion a coarse distribution of secondary precipitates was observed adjacent to the primary precipitate network.

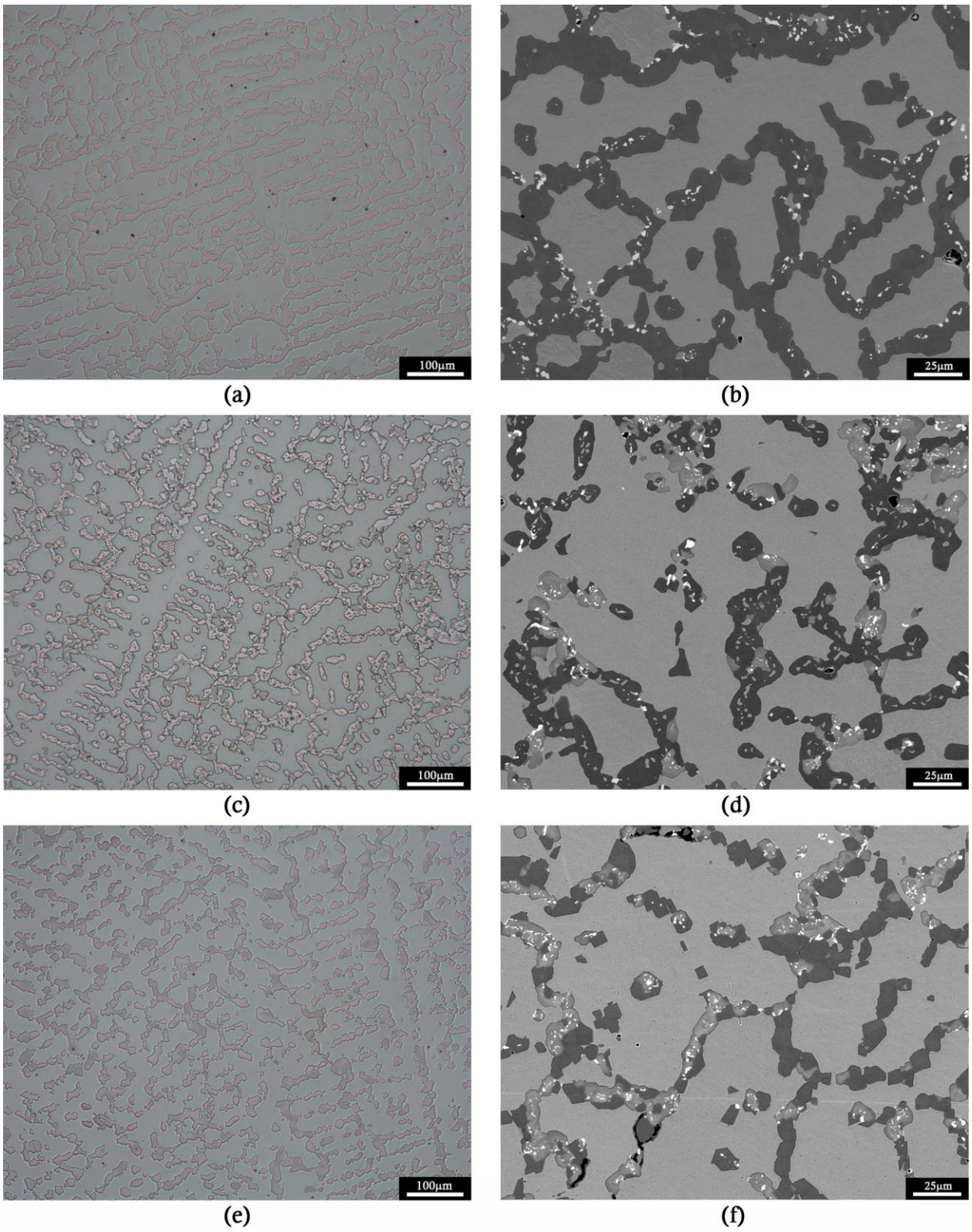

Figure 4.8 - Representative optical and backscattered electron images of the inner, mid, and outer wall regions of tube 1. (a) inner wall, optical, (b) inner wall, backscattered, (c) mid wall, optical, (d) mid wall, backscattered, (e) outer wall, optical, (f) outer wall, backscattered.

Primary Precipitate Network

Two chromium-rich precipitates were observed to compose the majority of the primary precipitate network in tube 1. A coarse and agglomerated chromium-rich carbide (B) was present at the inner wall regions, and a coarse, blocky chromium-rich carbide was present at the outer wall regions (C), as labelled in Figure 4.9, along with the matrix (A). The agglomerated chromium-rich carbide appeared darker grey in contrast to the blocky chromium-rich carbide in backscattered electron images. A band typically 150 – 350 μm thick was observed at the mid wall, where the blocky chromium-rich carbide transformed into the agglomerated chromium-rich carbide, and the two chromium-rich carbides were observed to co-exist. The distance from the inner diameter of the tube to the chromium carbide transformation front varied between samples taken from different locations in the tube (1.2 – 5.4 mm from the inner diameter).

Figure 4.10 shows the typical composition for the two primary chromium-rich carbides labeled B and C in Figure 4.9, as measured by energy dispersive x-ray spectroscopy (EDS). Both carbides were seen to contain iron (on the order of 9-13 at%) and a small amount of nickel (1-4 at%) in the metal component in addition to chromium. The total metal component (M = Cr + Fe + Ni) of carbide B was seen to be approximately 62 at%, consistent with a M_7C_3 carbide, and the total metal component of carbide C was seen to be approximately 75 at%, consistent with a $M_{23}C_6$ carbide. Figure 4.11 (a) and (c) show electron backscatter diffraction patterns (EBSPs) obtained from the two chromium-rich carbides in the primary network. Examples of the best-matching simulated crystal structures are shown in Figure 4.11 (b) and (d). The agglomerated chromium-rich carbide present at the inner wall regions of tube 2 was identified as M_7C_3 ($Pnma$), and the blocky chromium-rich carbide present at the outer wall regions was identified as $M_{23}C_6$ ($Fm\bar{3}m$). The matrix was confirmed as austenite ($Fm\bar{3}m$).

In all samples, the M_7C_3 carbides were observed to have a "porous" appearance, created due to a separate phase appearing contained within the M_7C_3 carbides when observed in cross-section. The apparent porosity was observed to decrease with increased proximity to the inner diameter of the tube, as shown in Figure 4.12. The phase that appeared contained within the M_7C_3 carbides, creating the "porous" appearance, was identified (via EDS and EBSD analyses) as austenite.

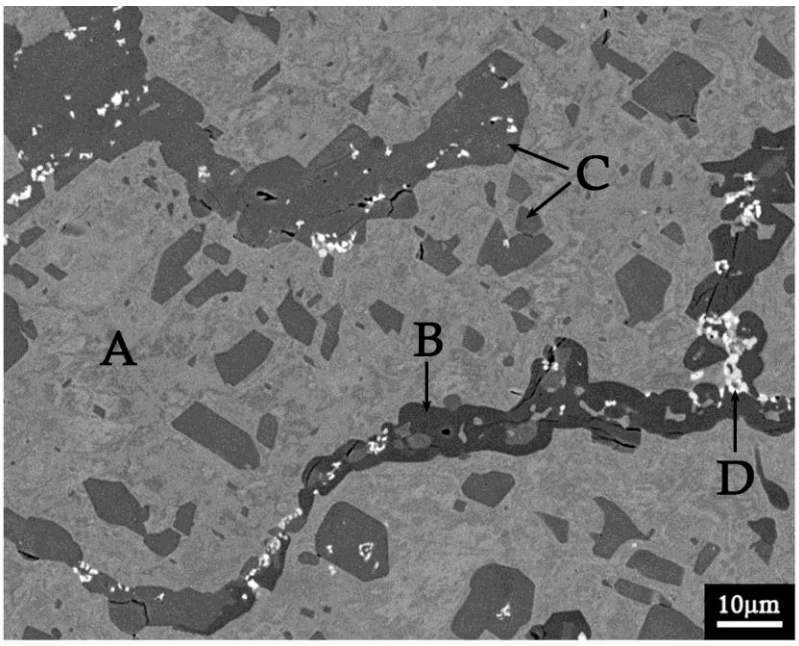

Figure 4.9 - Electron backscattered micrograph showing the matrix (A), and the primary chromium-rich (B&C) and niobium-rich (D) precipitate phases in tube 1.

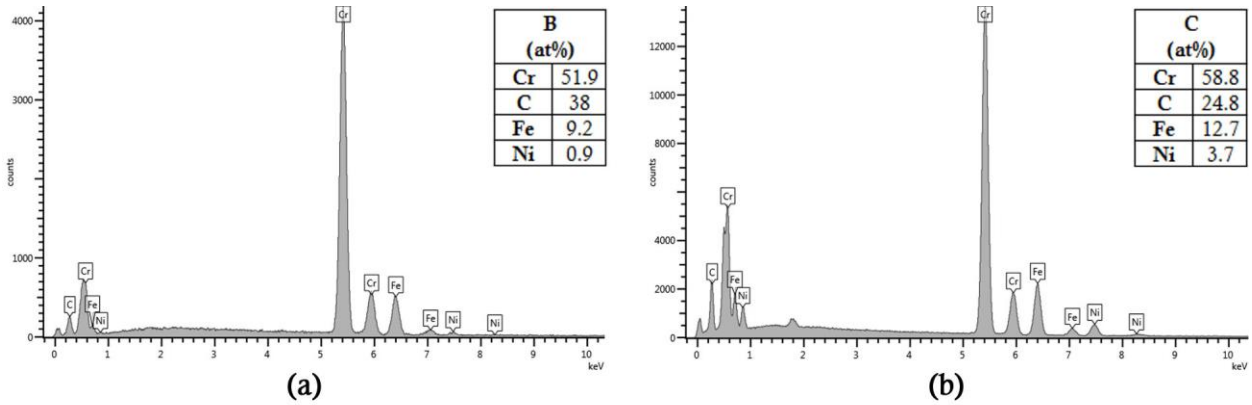

Figure 4.10 – Chemical composition of the primary chromium-rich precipitates labelled B and C in Figure 4.9, as determined by EDS.

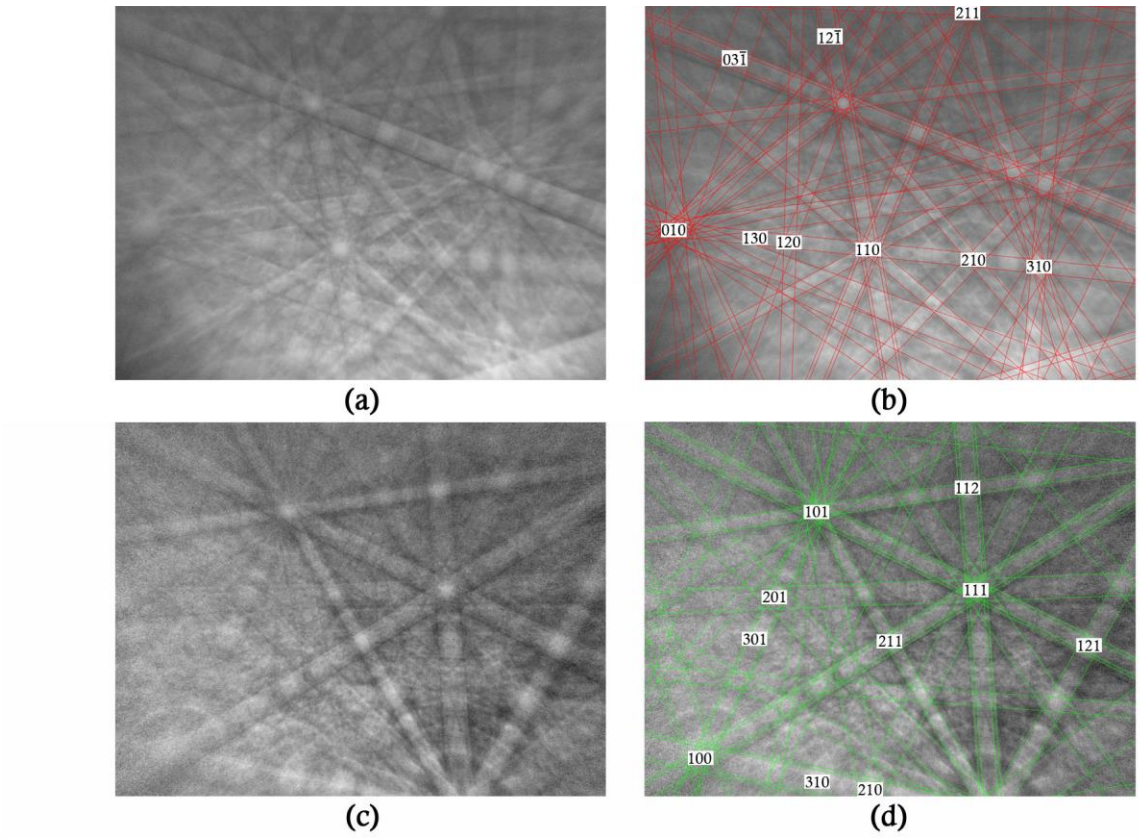

Figure 4.11 - Experimentally determined electron backscatter diffraction patterns (EBSPs) and the corresponding simulated patterns for the (a) & (b) M_7C_3, and (c) & (d) $M_{23}C_6$ crystal structures.

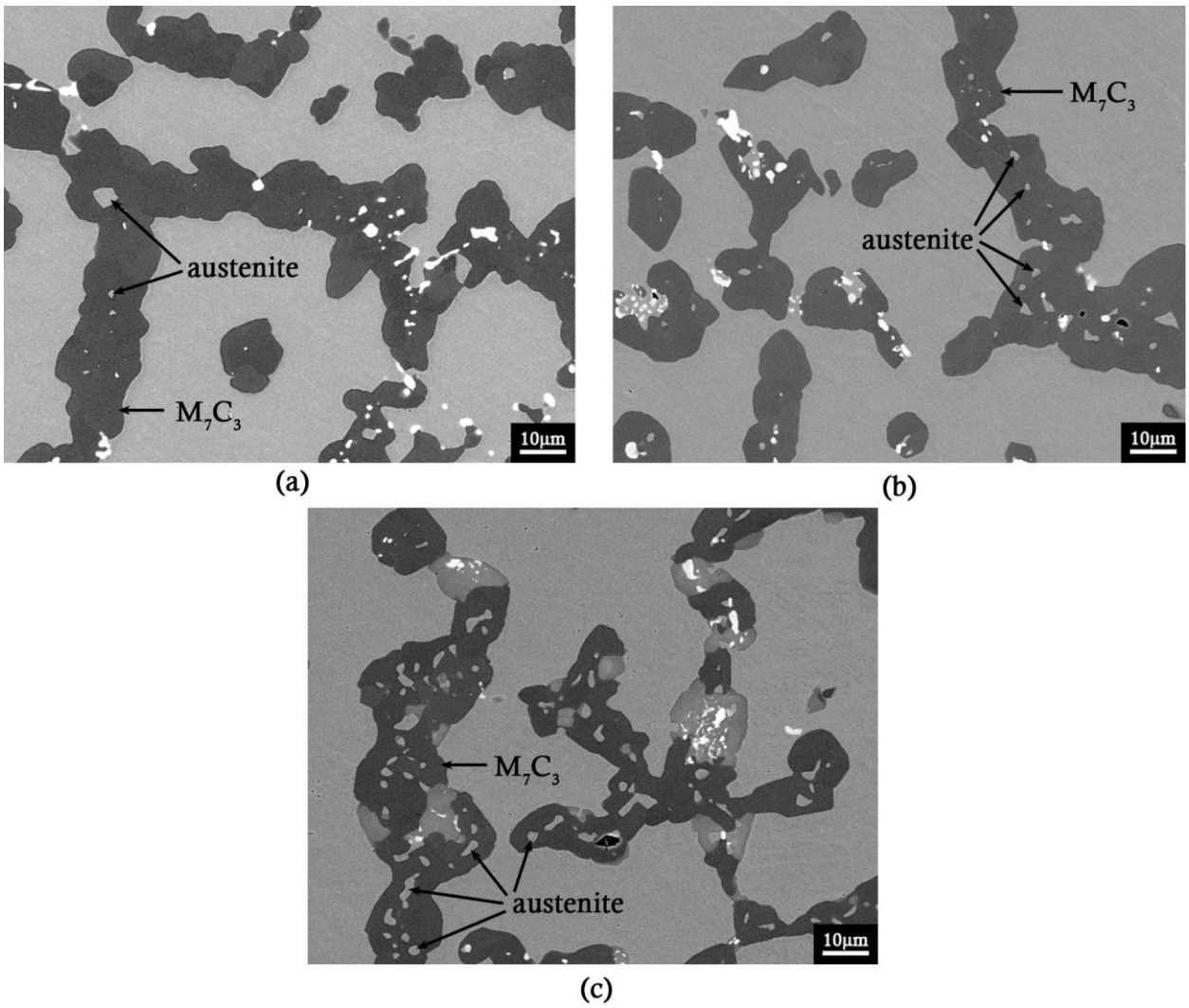

Figure 4.12 - Backscattered electron micrographs, indicating the austenite regions that appear contained within the M_7C_3 carbides, at distances of (a) 1.0 mm, (b) 3.0 mm, and (c) 5.0 mm from the inner diameter of tube 1.

Niobium-rich carbides <5 μm in diameter were observed as part of the primary network at the inner wall regions of tube 1, labelled D in Figure 4.13 (a). A representative EDS spectrum of the niobium-rich carbides in the primary network is shown in Figure 4.13 (b). An EBSP and the corresponding best-matched simulated crystal structure is shown in Figure 4.14. The EDS analyses of the niobium-rich precipitates consistently showed iron, chromium, and nickel contents on the order of 10-15 at% each; however, due to the small size of the precipitates it is expected that the iron, chromium, and nickel peaks are due to the electron beam interacting with the surrounding material (chromium-rich carbides, and chromium- iron- and nickel-rich austenite matrix). The niobium-rich carbides present in the primary network at the inner wall were subsequently identified as NbC ($Fm\bar{3}m$).

NbC carbides were also identified at the mid and outer wall regions in tube 1. In some samples the NbC carbides were observed to have transformed to a Ni-Nb-Si phase at the mid and outer wall

regions (labelled E in Figure 4.15 (a)), whereas in other samples the NbC carbides had partially transformed to a Ni-Nb-Si phase at the mid wall and a Cr-Ni-Nb-Si phase at the outer wall (labelled F in Figure 4.15 (b)). Representative EDS spectra of the Ni-Nb-Si and Cr-Ni-Nb-Si phases are shown in Figure 4.15 (c) and (d). EBSPs and the corresponding best matched simulated crystal structures are shown in Figure 4.16. The Ni-Nb-Si phase (E) was subsequently identified as G-phase ($Fm\bar{3}m$), and the Cr-Ni-Nb-Si phase (F) as η-carbide ($Fd\bar{3}m$). In those samples that contained both G-phase and η-carbide, the change between the NbC-to-G-phase and NbC-to-η-carbide transformations occurred over a very narrow band, typically ~50 μm in thickness.

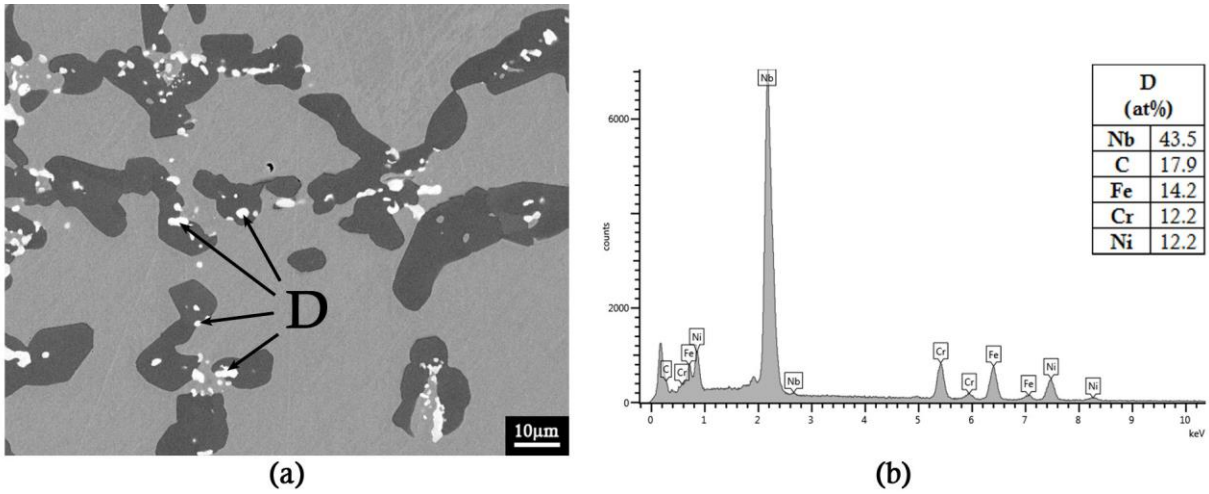

Figure 4.13 - (a) Backscattered electron micrograph showing the niobium-rich precipitates , D, observed as part of the primary network in tube 1; (b) chemical composition of the niobium-rich precipitates, as determined by EDS.

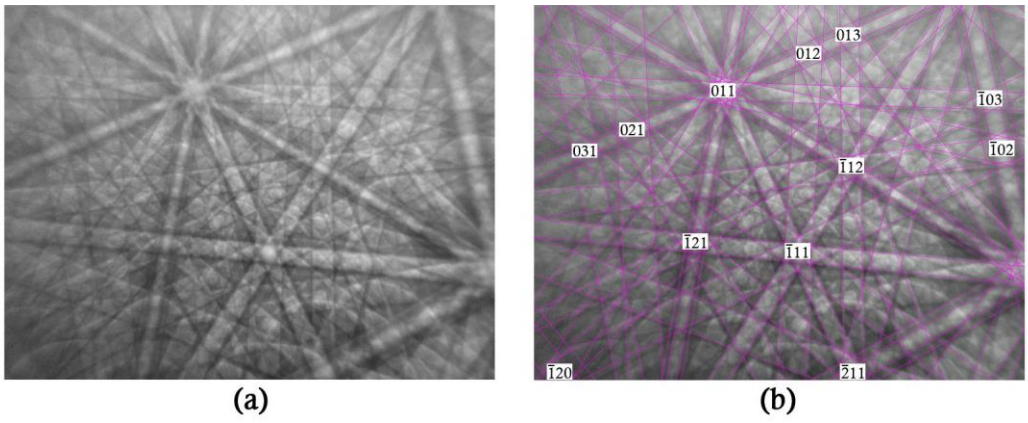

Figure 4.14 - Experimentally determined electron backscatter diffraction pattern (EBSP) and the corresponding simulated pattern for the NbC crystal structure.

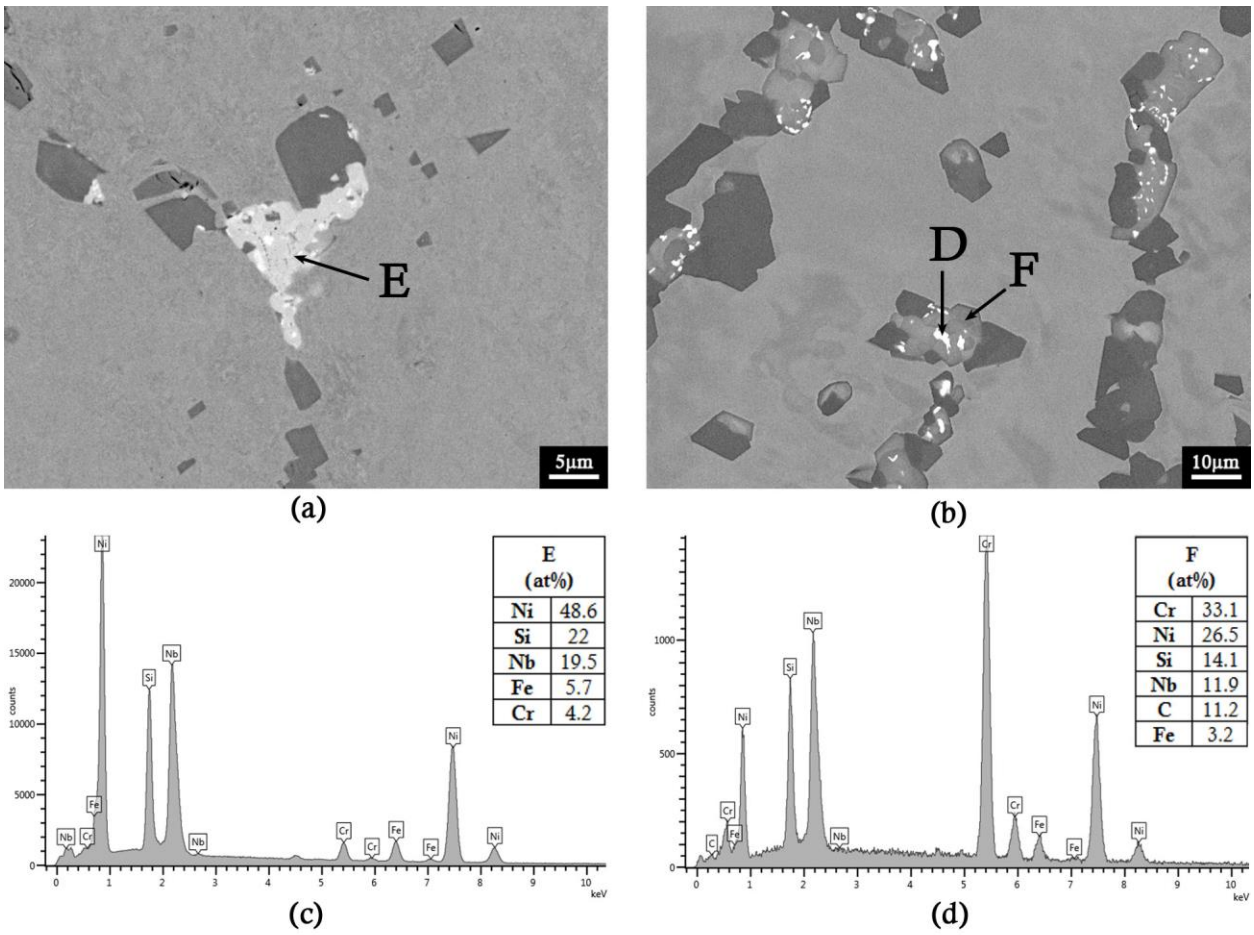

Figure 4.15 – Backscattered electron micrographs and chemical composition (as determined by EDS) of the (a) & (c) Ni-Nb-Si phase, labelled E, and (b) & (d) the Cr-Ni-Nb-Si phase, labelled F.

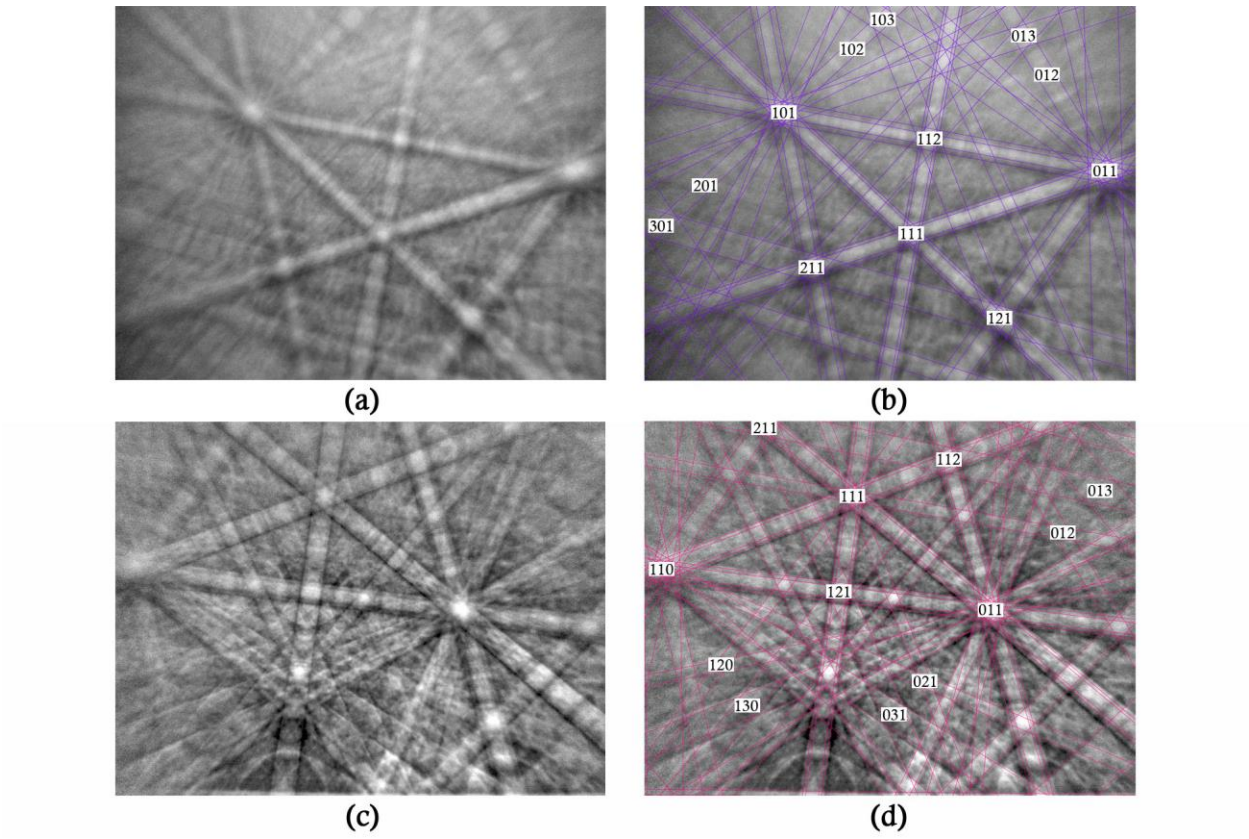

Figure 4.16 - Experimentally determined electron backscatter patterns (EBSPs) and corresponding simulated patterns for the (a) & (b) G-phase, and (c) and (d) η-carbide crystal structures.

Secondary Precipitate Network

In some samples, a coarse distribution of cuboidal, chromium-rich secondary precipitates was observed adjacent to the primary precipitate network, as shown in Figure 4.17. The presence of secondary precipitates were only present in regions of the tube wall where the primary chromium-rich carbide was $M_{23}C_6$ and typically occurred in regions where the primary $M_{23}C_6$ carbides had coarsened to a lesser extent than those shown in Figure 4.9. The secondary precipitates were subsequently identified as $M_{23}C_6$ ($Fm\bar{3}m$).

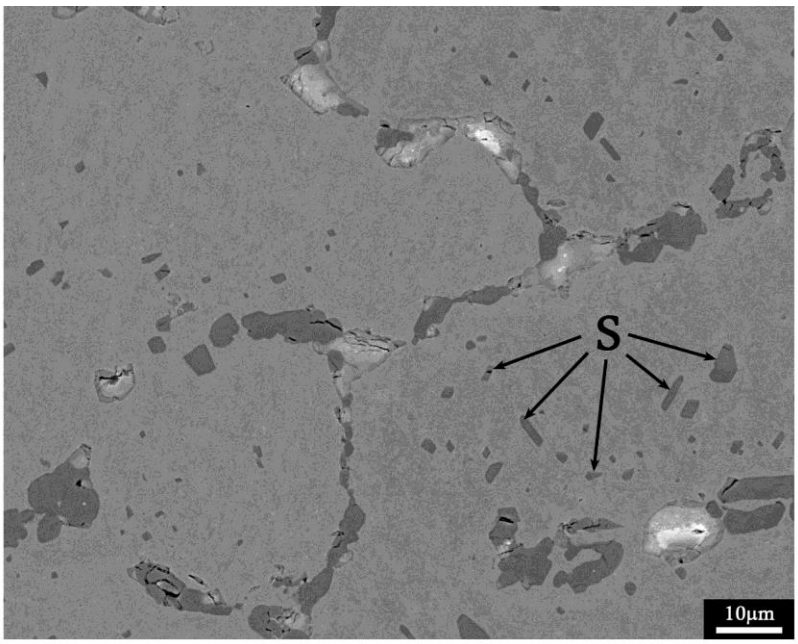

Figure 4.17 – Backscattered electron micrograph showing the chromium-rich secondary precipitates, labelled S, adjacent to the primary precipitate network in tube 1.

Nitrides

Chromium-rich carbonitrides were observed at the outer diameter region of tube 1, where they replaced the $M_{23}C_6$ carbides in the primary network. A band typically 100 – 200 μm thick was present at the outer wall, where the majority of the $M_{23}C_6$ carbides had transformed to carbonitrides, as shown in Figure 4.18. Lenticular carbonitrides were also observed to have precipitated intragranularly within this band. Individual $M_{23}C_6$ carbides which had transformed to chromium-rich carbonitrides were occasionally observed up to 500 μm further into the tube wall from the transformation front. A representative EDS spectrum of the chromium-rich carbonitrides is shown in Figure 4.19, and an EBSP and best matched simulated crystal structure shown in Figure 4.20. The chromium-rich carbonitrides were subsequently identified as $Cr_2(C,N)$ ($P\bar{3}1m$).

$Cr_2(C,N)$ carbonitrides were also occasionally observed at the $M_{23}C_6$-to-M_7C_3 carbide transformation front, where they replaced M_7C_3 carbides in the primary precipitate network (Figure 4.21). No $Cr_2(C,N)$ carbonitrides were observed in the wall between the $M_{23}C_6$-to-M_7C_3 transformation front at the mid wall, and the $M_{23}C_6$-to-$Cr_2(C,N)$ transformation front at the outer wall.

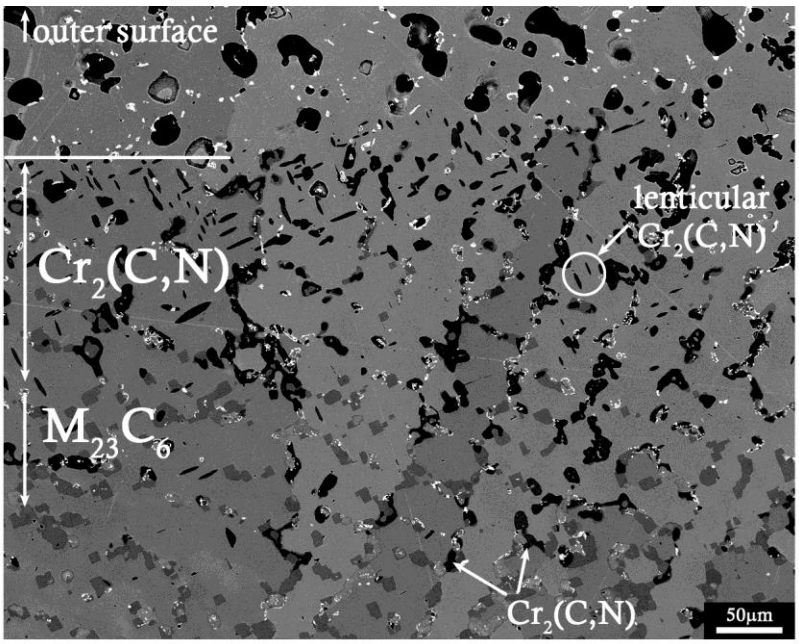

Figure 4.18 - Backscattered electron micrograph showing the transformation of $M_{23}C_6$ to $Cr_2(C,N)$ and the presence of lenticular $Cr_2(C,N)$ at the outer diameter of tube 1.

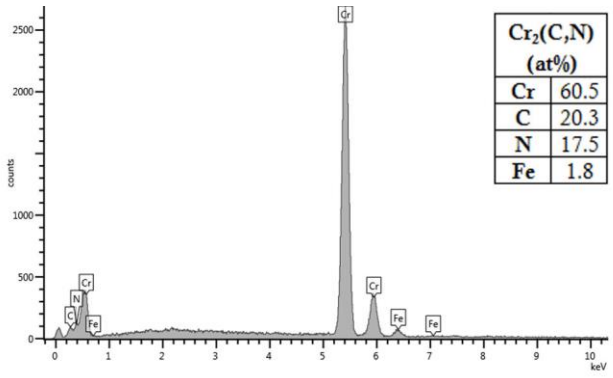

$Cr_2(C,N)$ (at%)	
Cr	60.5
C	20.3
N	17.5
Fe	1.8

Figure 4.19 - Chemical composition of the $Cr_2(C,N)$ carbonitrides, as determined by EDS.

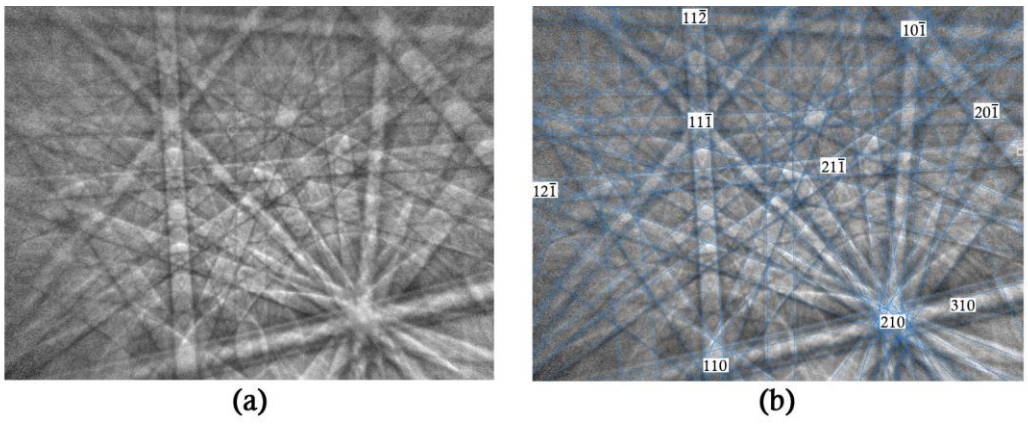

Figure 4.20 - Experimentally determined electron backscatter pattern (EBSP) and corresponding simulated pattern for the $Cr_2(C,N)$ crystal structure.

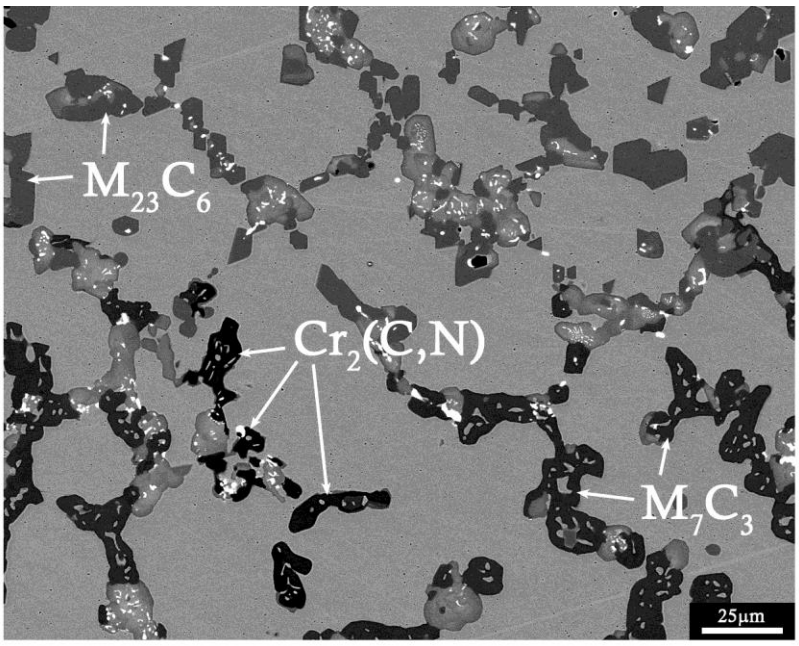

Figure 4.21 - Backscattered electron micrograph showing the presence of $Cr_2(C,N)$ at the $M_{23}C_6$-to-M_7C_3 transformation front, where it replaces the occasional M_7C_3 carbide in the primary network.

Other Phases

Inclusions rich in manganese and sulfur were observed in all samples of tube 1, as shown in Figure 4.22. The inclusions were typically <10 μm in diameter, and segregated to the inner 1.0mm of the tube wall. A representative EDS spectrum is shown in Figure 4.23, and an EBSP and best matching simulated crystal structure are shown in Figure 4.24. The inclusions were subsequently identified as MnS ($Fm\bar{3}m$). The morphologies exhibited by the MnS inclusions were observed to be similar to the Type I (globular) morphology described for MnS inclusions in cast plain carbon steels [43, 44]. The globular morphology is attributed to their precipitation as globules of liquid in the solidifying melt during casting [44], and their segregation to the inner wall is a result of the centrifugal forces during casting propelling the inclusions towards the inner diameter, due to their lower density in comparison to the liquid melt [11]. MnS inclusions in HP-Nb and HP-Micro alloys are reportedly stable with ageing [4].

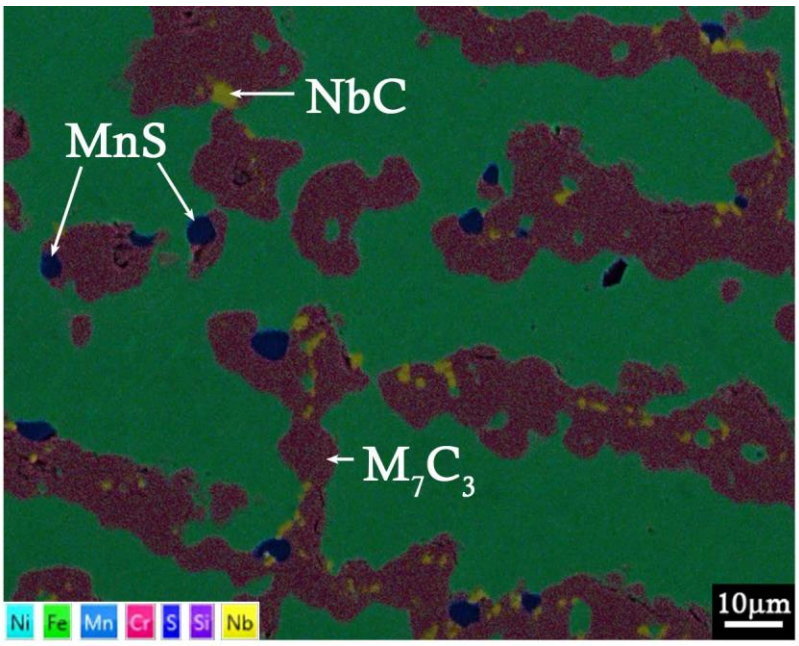

Figure 4.22 - EDS map with secondary electron micrograph underlay showing the MnS inclusions present at the inner wall region of tube 1.

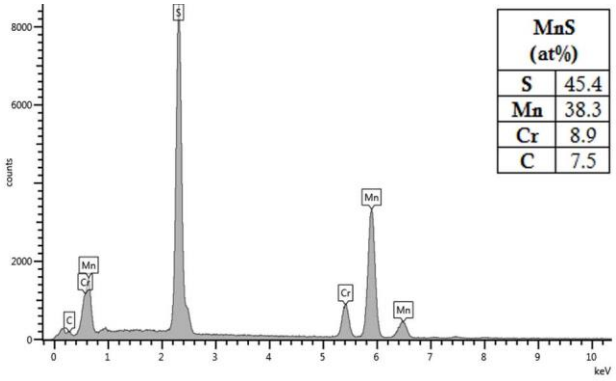

MnS (at%)	
S	45.4
Mn	38.3
Cr	8.9
C	7.5

Figure 4.23 - Chemical composition of the MnS inclusions present in tube 1, as determined by EDS.

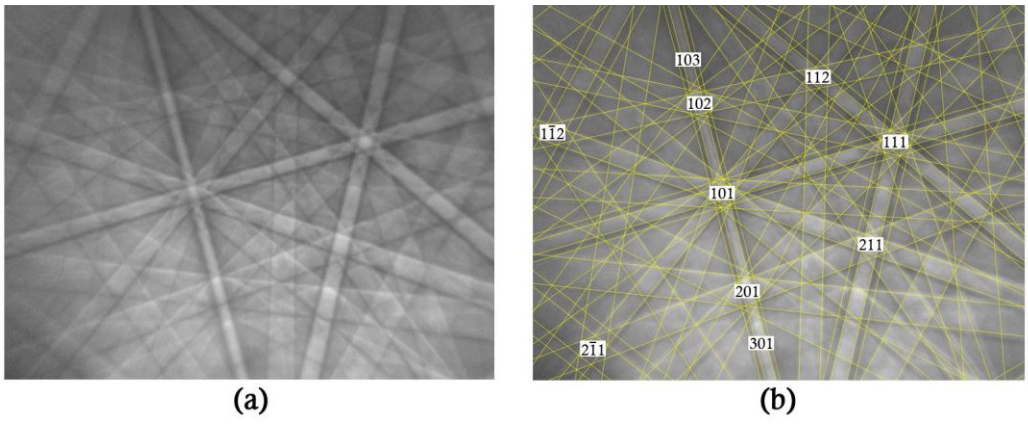

Figure 4.24 - Experimentally determined electron backscatter pattern (EBSP) and corresponding simulated pattern for the MnS crystal structure.

Inner and Outer Surfaces

Degradation at the inner and outer surfaces as a result of oxidation was evident in all samples, as shown in Figure 4.25. At the outer surface, two intermittent oxide layers were observed – a Cr-Fe-Ni-rich layer, and a Cr-rich layer. Directly beneath these layers was a chromium-free band. Within this band, the chromium-rich microconstituents located along the dendrite boundaries had completely dissolved, leaving only the NbC carbides. A thin layer of silicon oxides was observed directly between the chromium-free band and the chromium-rich oxide scale, with some silicon oxides present further into the tube wall. The thicknesses of the Cr-Ni-Fe and Cr-rich oxide layers, the depth of the chromium-depleted band, and the depth of penetration of silicon oxides were all seen to vary significantly between samples. Selective oxidation was typically observed at the inner surface, with a band within which the microconstituents along the dendrite boundaries had been transformed into chromium-rich oxides and silicon-rich oxides. The NbC carbides did not undergo oxidation, and remained present within this band. The depth of selective oxidation was also seen to vary significantly between samples.

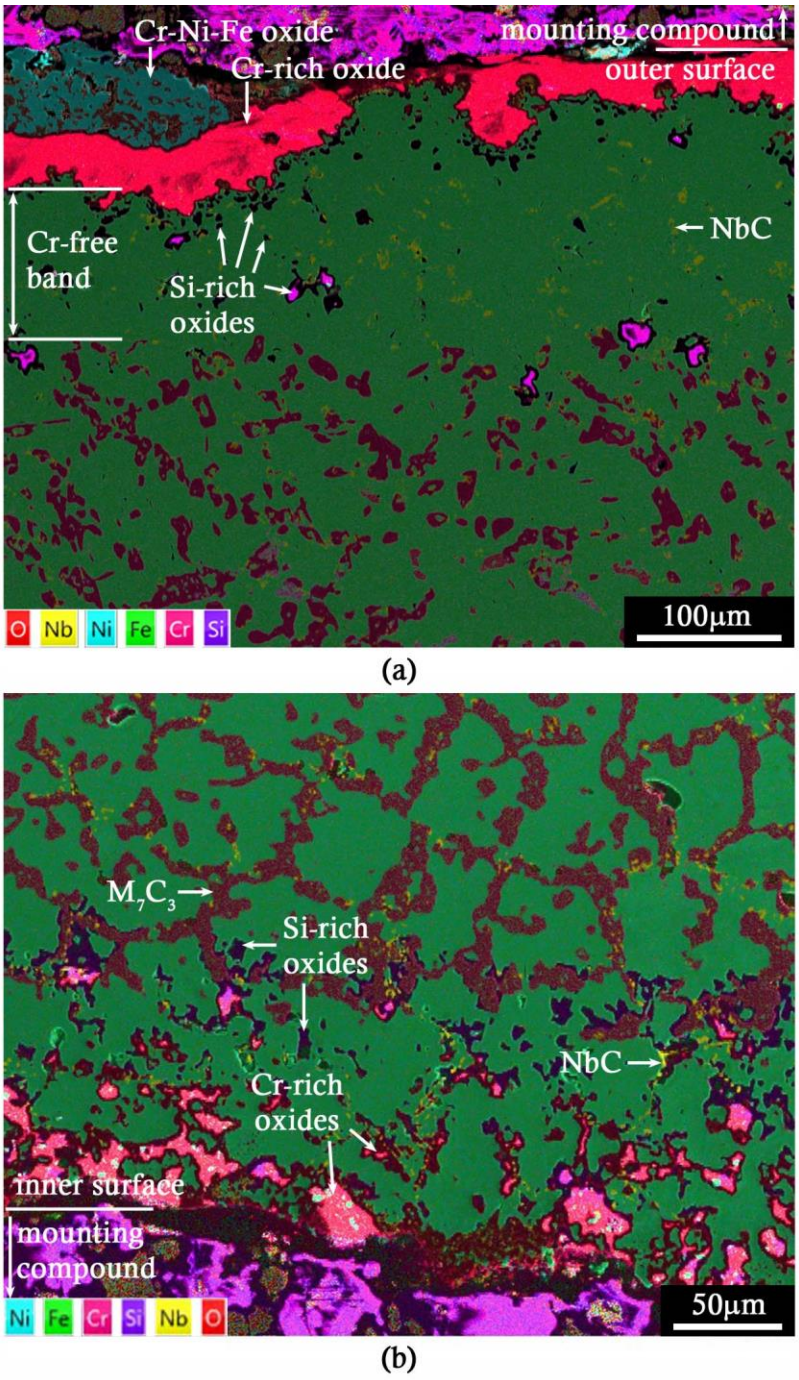

Figure 4.25 - EDS maps with secondary electron micrograph underlays showing the oxidation at the (a) outer and (b) inner surfaces of tube 1.

4.5.2 Tube 2

Figure 4.26 shows representative optical and scanning electron micrographs of tube 2 at the inner wall, mid wall, and outer wall regions. As with tube 1, the primary carbide network is significantly coarsened in comparison to the fine lamellar groups observed in typical as-cast structures. A change in the morphology of the primary chromium-rich precipitates was observed at the mid-wall region in

all samples; however, the exact proximity to the inner diameter was seen to vary. On occasion a coarse distribution of secondary precipitates was observed adjacent to the primary precipitate network.

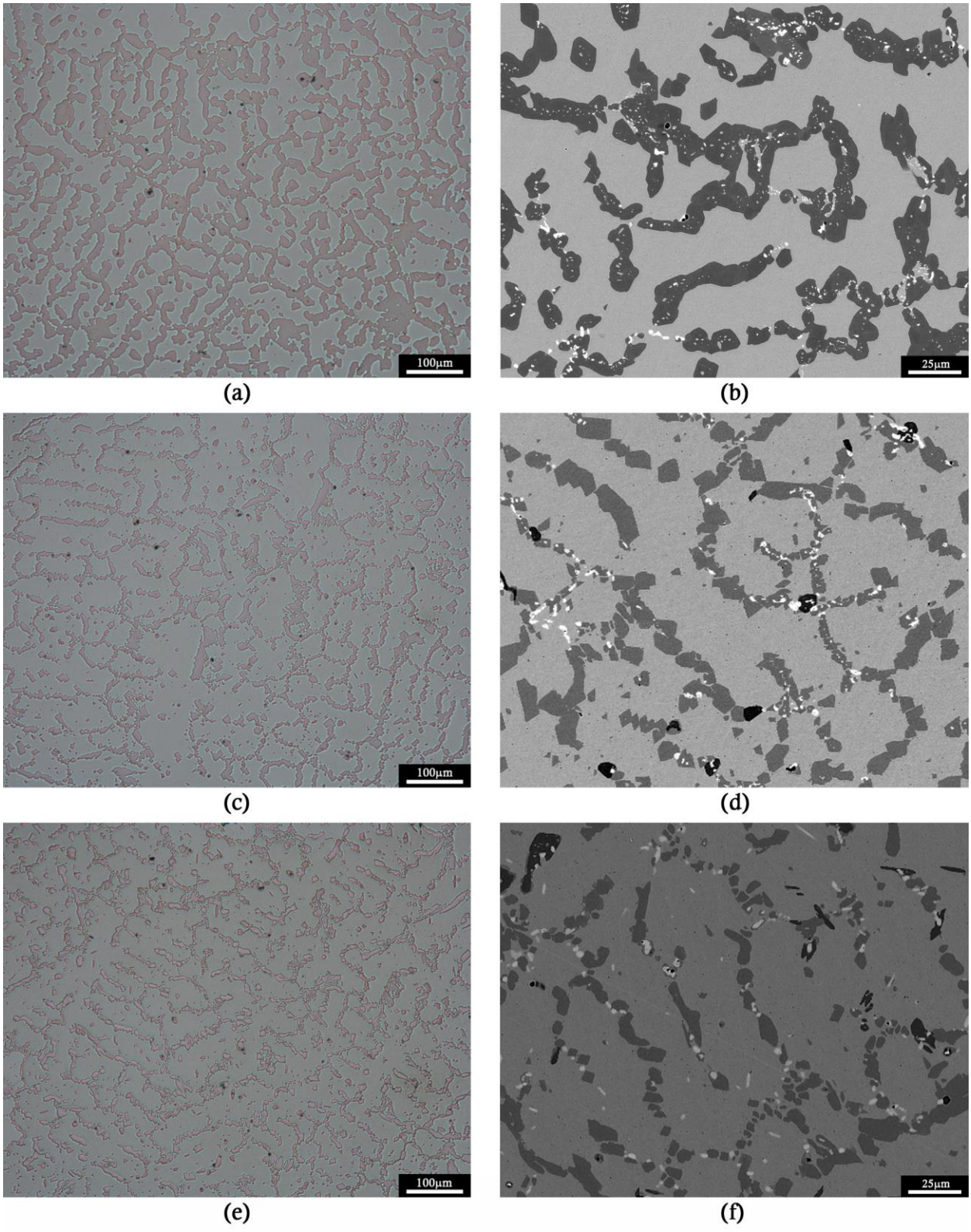

Figure 4.26 - Representative optical and backscattered electron micrographs of the inner, mid, and outer wall regions of tube 2. (a) iuner wall, optical, (b) inner wall, backscattered, (c) mid wall, optical, (d) mid wall, backscattered, (e) outer wall, optical, (f) outer wall, backscattered.

Primary Precipitate Network

As with tube 1, two chromium-rich precipitates were observed to compose the majority of the primary network in tube 2. A coarse, agglomerated chromium-rich carbide (B) was present at the inner wall regions, and a coarse, blocky chromium-rich carbide was present at the outer wall regions (C), as labelled in Figure 4.27, along with the matrix (A). The agglomerated chromium-rich carbide at the inner wall appeared darker grey in contrast to the blocky chromium-rich carbide in backscattered electron images. A band of approximately 150 – 250 μm was observed at the mid wall, where the blocky chromium-rich carbide transformed to the agglomerated chromium-rich carbide, and over which the two chromium carbides were observed to co-exist. The distance from the inner diameter of the tube to the chromium carbide transformation front varied between samples taken from different locations in the tube (2.2 – 2.9 mm from the inner diameter).

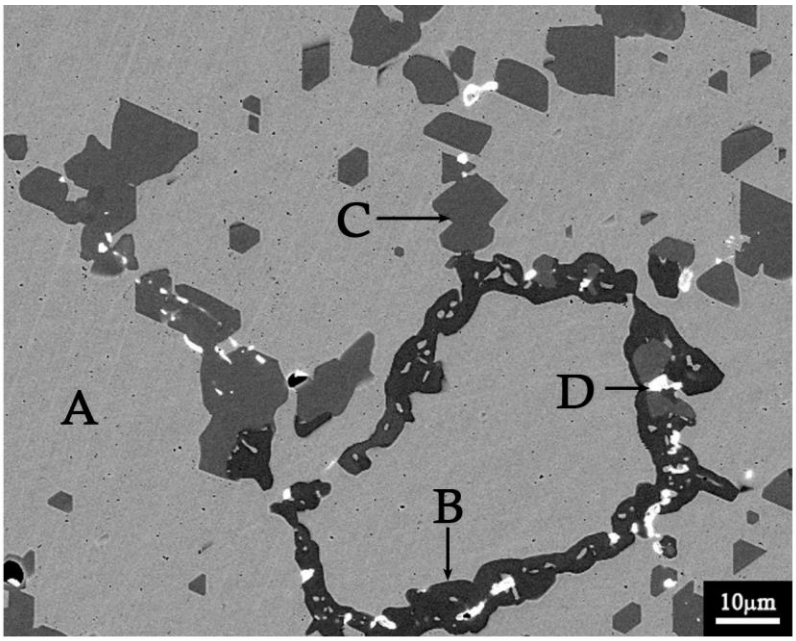

Figure 4.27 - Electron backscattered micrograph showing the matrix (A), and the primary chromium-rich (B&C) and niobium-rich (D) precipitate phases in tube 2.

The composition of the two primary chromium-rich carbides in Tube 2 were consistent with two primary chromium-rich carbides in tube 1. Both carbides were seen to contain iron (on the order of 11-12 at%) and a small amount of nickel (1-4 at%) in the metal component in addition to chromium. The agglomerated chromium-rich carbide (B) present at the inner wall regions of tube 2 was identified as M_7C_3, and the blocky chromium-rich carbide (C) present at the outer wall regions was identified as $M_{23}C_6$. The matrix was confirmed as austenite.

The M_7C_3 carbides in tube 2 displayed the same apparent porosity as the M_7C_3 carbides in tube 1, although with a finer morphology. As in tube 1, the apparent porosity of the M_7C_3 carbides decreased

with increased proximity to the inner diameter, as demonstrated in Figure 4.28. The phase contained within the "pores" was identified using EDS and EBSD as austenite.

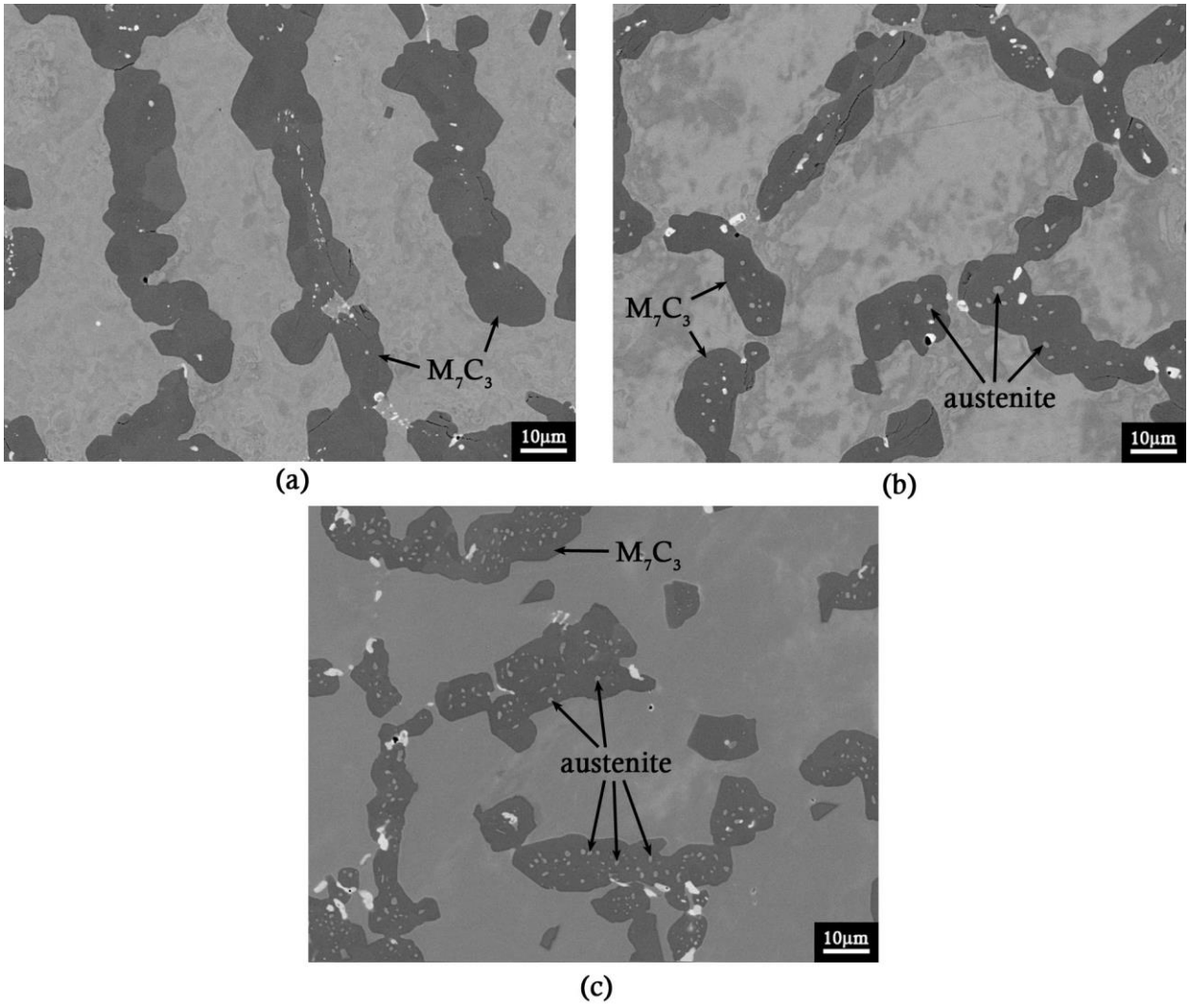

Figure 4.28 –Backscattered electron micrographs showing the small austenite regions that appear contained within the M_7C_3 carbides, at distances of (a) 1.0 mm, (b) 2.0 mm, and (c) 2.5 mm from the inner diameter of tube 2.

Niobium-rich precipitates <5 µm in diameter were observed across the whole wall of tube 2 (labelled D in Figure 4.27 and Figure 4.29). The composition of the niobium-rich precipitates in tube 2 was consistent with the NbC carbides identified in tube 1. In some samples the niobium-rich precipitates at the outer wall regions were observed to have partially transformed to a phase rich in chromium, nickel, niobium, and silicon, labelled E in Figure 4.29. The presence of the Cr-Ni-Nb-Si phase was difficult to detect in BSE images due to the small size of the phase regions; however, it was clearly visible in EDS maps due to its characteristic composition, which was consistent with the η-carbide identified in tube 1. The niobium-rich precipitates (D) were subsequently identified as NbC, and the Cr-Ni-Nb-Si phase (E) was identified as η-carbide.

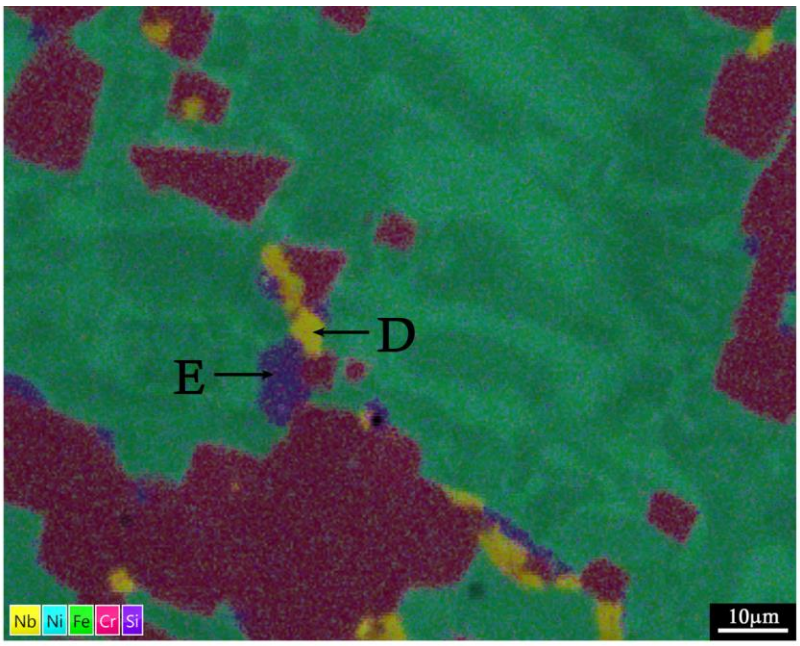

Figure 4.29 - EDS map with secondary electron micrograph underlay showing the niobium-rich precipitates, D, and the Cr-Ni-Nb-Si phase, E, in tube 3. The variation in the Fe-Cr-Ni matrix (green) is due to variation in the underlying micrograph.

Secondary Precipitate Network

In some locations, a coarse distribution of cuboidal, chromium-rich secondary precipitates was observed adjacent to the primary carbide network, as shown in Figure 4.30. This only occurred in areas of the tube wall where the primary chromium-rich precipitate was $M_{23}C_6$, and typically occurred in areas where the primary $M_{23}C_6$ carbides had not coarsened to the same extent as those shown in Figure 4.27. The composition of the secondary chromium-rich precipitates was consistent with the secondary $M_{23}C_6$ precipitates identified in tube 1, and they were subsequently confirmed as $M_{23}C_6$.

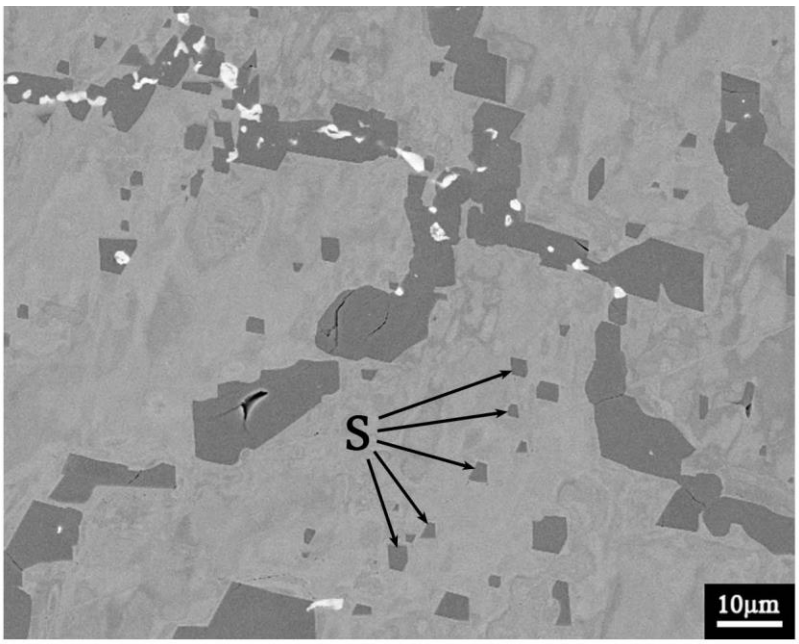

Figure 4.30 – Backscattered electron micrograph showing the chromium-rich secondary precipitates, labelled S, adjacent to the primary precipitate network in tube 2.

Nitrides

At the outer diameter of tube 2, a band approximately 100 - 150 µm thick was present within which the $M_{23}C_6$ carbides had completely transformed into a chromium-rich carbonitride, as shown in Figure 4.31. Lenticular precipitates of the same chromium-rich carbonitride were also observed intragranularly. The composition was consistent with the $Cr_2(C,N)$ precipitates identified in tube 1, and the chromium-rich carbonitride was subsequently identified as $Cr_2(C,N)$. Individual $M_{23}C_6$ carbides which had transformed into $Cr_2(C,N)$ were typically identified up to 500 µm further in to the tube wall from the edge of the $M_{23}C_6$-to-$Cr_2(C,N)$ transformation front, as indicated in Figure 4.31 (a). $Cr_2(C,N)$ was also identified at the $M_{23}C_6$-to-M_7C_3 transformation front at the mid wall of the tube, where the occasional M_7C_3 carbide had transformed to $Cr_2(C,N)$, as shown in Figure 4.32.

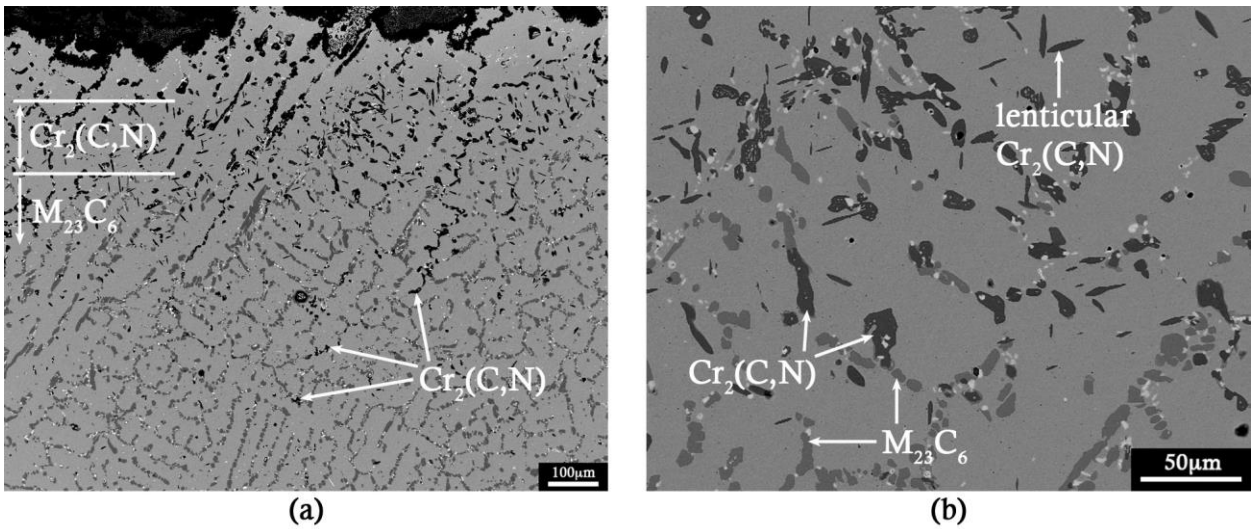

Figure 4.31 - Backscattered electron micrographs showing (a) the transformation of $M_{23}C_6$ to $Cr_2(C,N)$ at the outer diameter of tube 2; (b) lenticular $Cr_2(C,N)$ precipitates in the interdendritic regions.

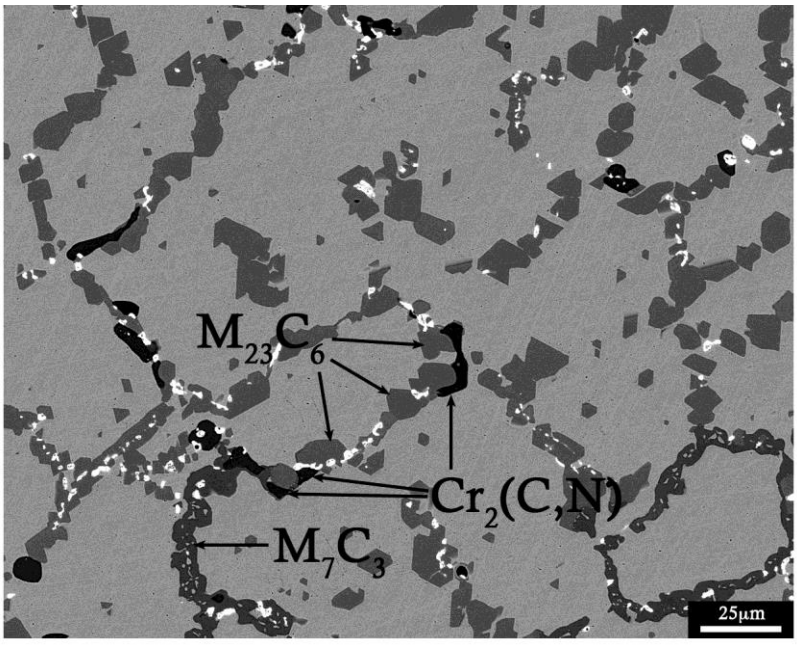

Figure 4.32 - Backscattered electron micrograph showing the presence of $Cr_2(C,N)$ at the $M_{23}C_6$-to-M_7C_3 transformation front, where it replaces the occasional M_7C_3 carbide in the primary network.

Other Phases

Inclusions <10 µm in diameter and rich in manganese and sulfur were observed at the inner wall region, typically within 1.0mm of the inner diameter. The appearance and composition was consistent with the MnS inclusions identified in tube 1 (Figure 4.22), and the inclusions were subsequently identified as MnS ($Fm\bar{3}m$).

Inner and Outer Surfaces

Degradation due to oxidation was evident at the inner and outer surfaces of all samples (Figure 4.33) and it appeared similar to the oxidation observed in tube 1. At the outer surface, intermittent Cr-Fe-Ni and Cr-rich oxide scales were observed, along with silicon-rich oxides that penetrated into the wall. A band free of chromium was seen directly beneath the oxide scales. At the inner wall, selective oxidation of the primary chromium-rich microconstituents into chromium-rich and silicon-rich oxides was observed. As with tube 1, the thicknesses of the oxide layers and the chromium free band at the outer surface, and the depth of selective oxidation at the inner surface all varied significantly between samples.

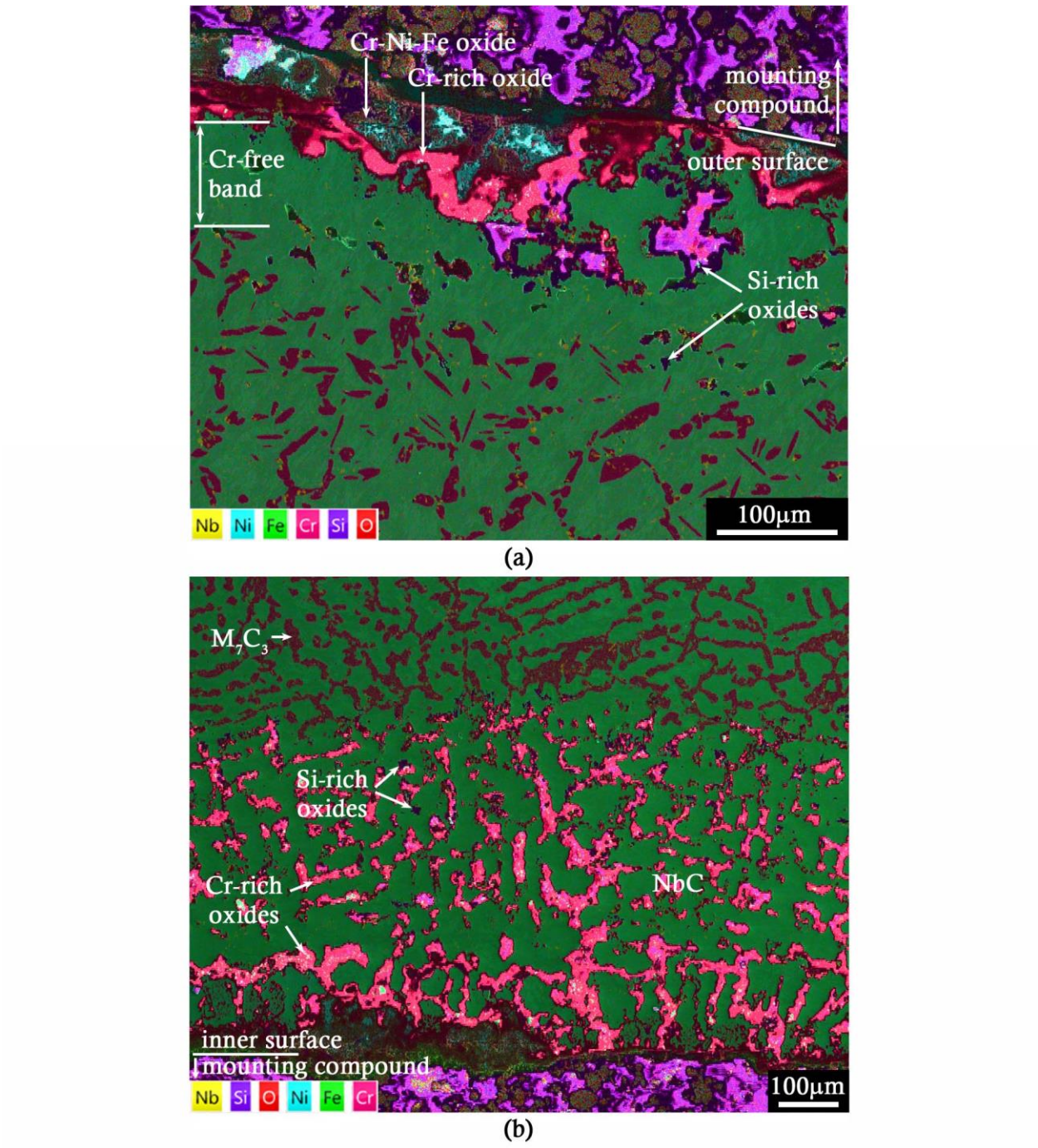

Figure 4.33 - EDS maps with secondary electron micrograph underlays showing the oxidation at the (a) outer and (b) inner surfaces of tube 2.

4.5.3 Tube 3

Figure 4.34 shows representative optical and scanning electron micrographs of tube 3. The tube microstructure appeared consistent across the wall. The primary carbide network, composed of chromium-rich and niobium-rich precipitates, had retained the fine, lamellar morphology typical of the as-cast structure, and distribution of fine, plate-like precipitates were observed intragranularly.

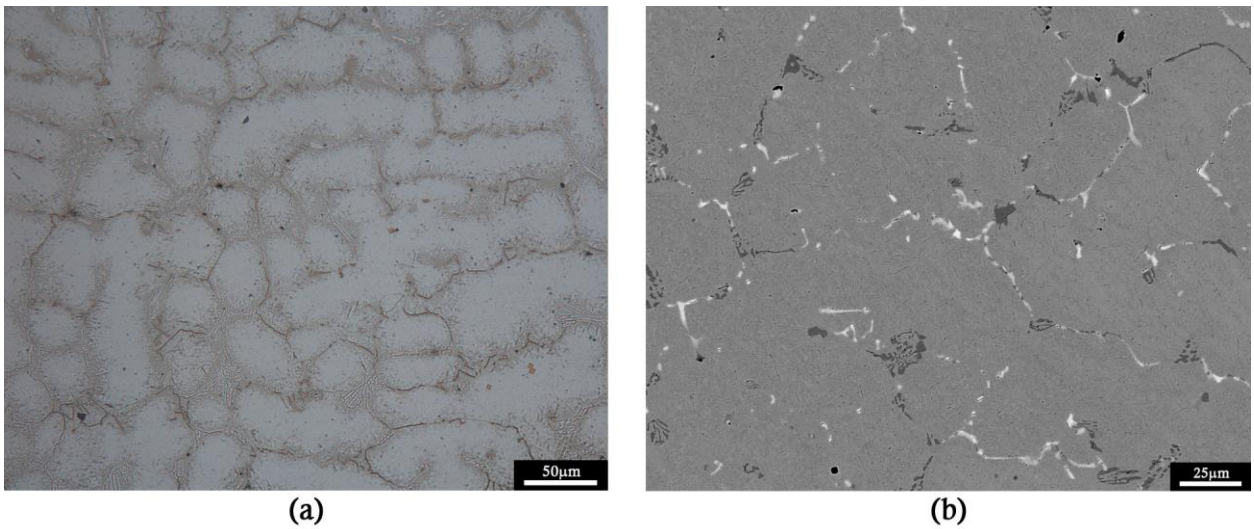

Figure 4.34 - Representative (a) optical and (b) backscattered electron micrographs of the microstructure of tube 3.

Primary Precipitate Network

Figure 4.35 shows a backscattered electron image of the matrix, A, and primary precipitate phases, B-E, in tube 3. Two phases rich in chromium were observed as part of the primary network – B and C. B appeared to be a chromium-rich carbide, and C a chromium-rich intermetallic that also contained iron, nickel, and silicon. D was observed to be a niobium-rich carbide, which also contained some titanium. It was difficult to distinguish D from E, which also contained significant amounts of niobium in addition to nickel and silicon, in the backscattered electron micrographs.

The composition of the chromium-rich carbide (B) was consistent with the $M_{23}C_6$ carbides identified in tubes 1 and 2, and the composition of the Ni-Nb-Si phase (E) was consistent with the G-phase identified in tube 1. The chromium-rich carbide (B) was subsequently identified as $M_{23}C_6$, and the Nb-Ni-Si phase (E) was identified as G-phase. The matrix was confirmed to be austenite.

A representative EDS spectrum for the Cr-Fe-Ni-Si phase is shown in Figure 4.36, and an EBSP and corresponding best matched crystal structure is shown in Figure 4.37. The Cr-Fe-Ni-Si phase (C) was subsequently identified as σ-phase ($P4_2/mnm$). A representative EDS spectrum for the Nb-Ti-rich phase is shown in Figure 4.38, and an EBSP and corresponding best matched crystal structure is shown in Figure 4.39. The Nb-Ti-rich precipitates appeared to contain nickel, chromium, silicon, and iron (~2-8 at% each), in addition to niobium (~30 at%), titanium (~12 at%), and carbon (~43 at%). However due to their small size, it is likely that the nickel, chromium, silicon and iron peaks in the EDS spectrum are a result of the electron beam interacting with the material surrounding the Nb-Ti-rich precipitate in addition to the precipitate itself. The Nb-Ti-rich phase (D) was subsequently identified as (Nb,Ti)C ($Fm\bar{3}m$).

Cuboidal precipitates rich in titanium were regularly seen intragranularly, as shown in Figure 4.40. EDS showed the precipitates contained nitrogen and carbon as well as titanium, indicting a titanium-rich carbonitride. The precipitates also contained approximately 5 at% niobium. The EBSP and closest matching simulated crystal structure of the Ti-rich phase in Figure 4.40(a) is shown in Figure 4.41. The Ti-rich precipitates were subsequently identified as Ti(C,N), a titanium carbonitride with the same crystal structure as TiC ($Fm\bar{3}m$).

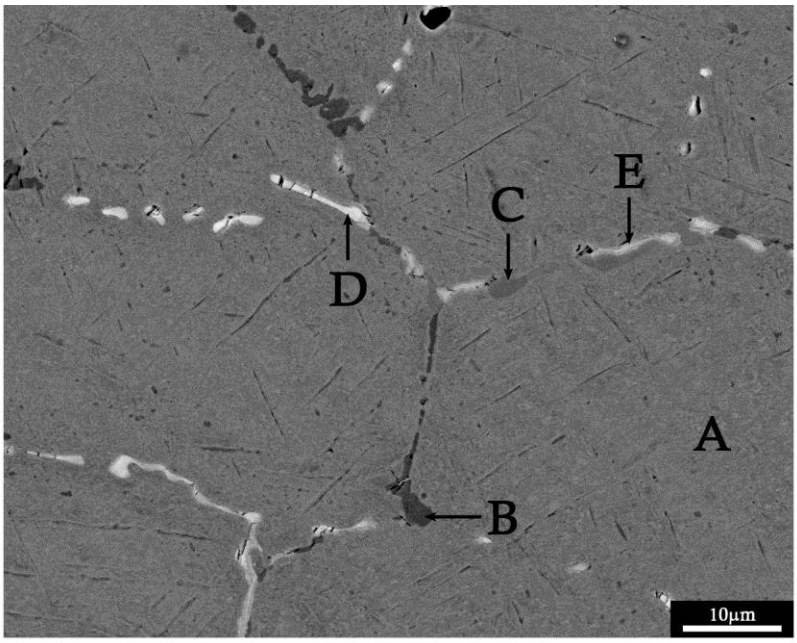

Figure 4.35 - Backscattered electron micrograph of the primary precipitates in tube 3.

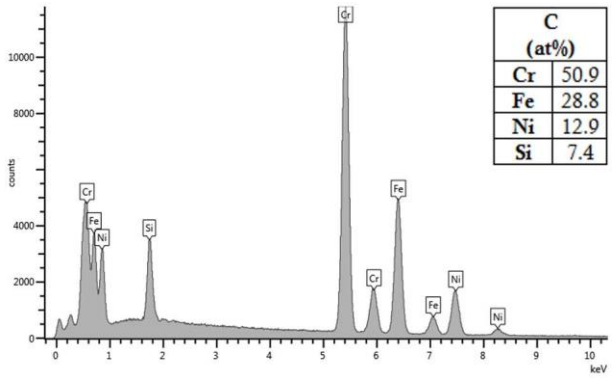

Figure 4.36 - Chemical composition of the primary Cr-Fe-Ni-Si phase, labelled C in Figure 4.35, as determined by EDS.

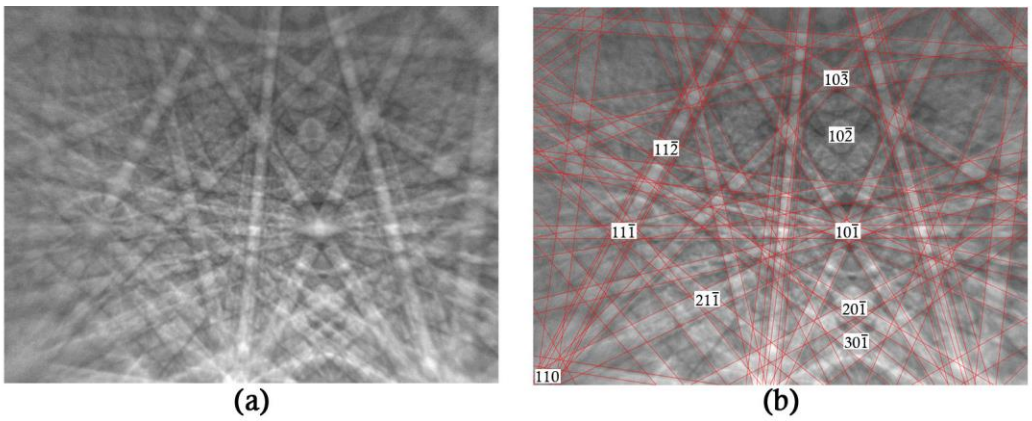

Figure 4.37 - Experimentally determined electron backscatter diffraction pattern (EBSP) and the corresponding simulated pattern for the σ-phase crystal structure.

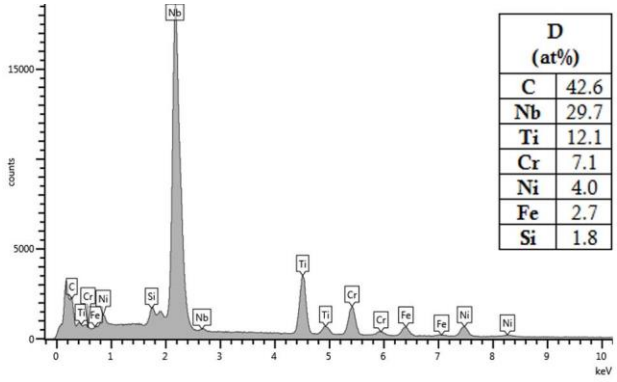

Figure 4.38 - Chemical composition of the Nb-Ti-rich precipitates, labelled D in Figure 4.35, as determined by EDS.

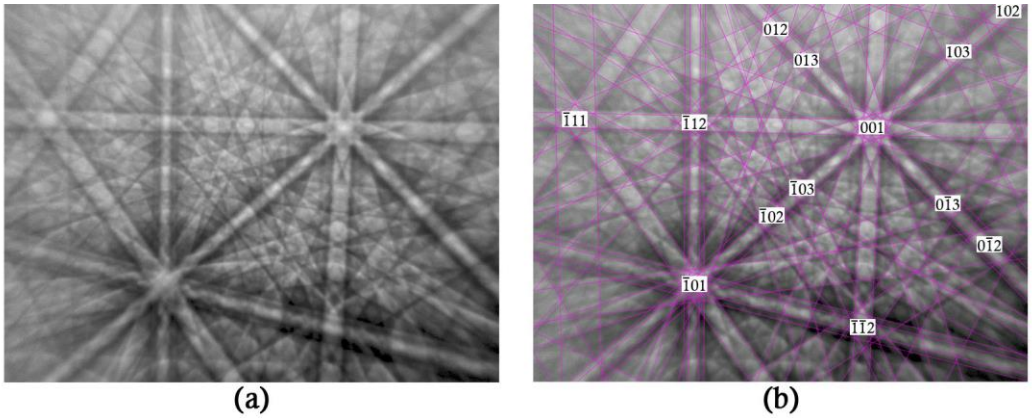

Figure 4.39 - Experimentally determined electron backscatter diffraction pattern (EBSP) and the corresponding simulated pattern for the (Nb,Ti)C crystal structure.

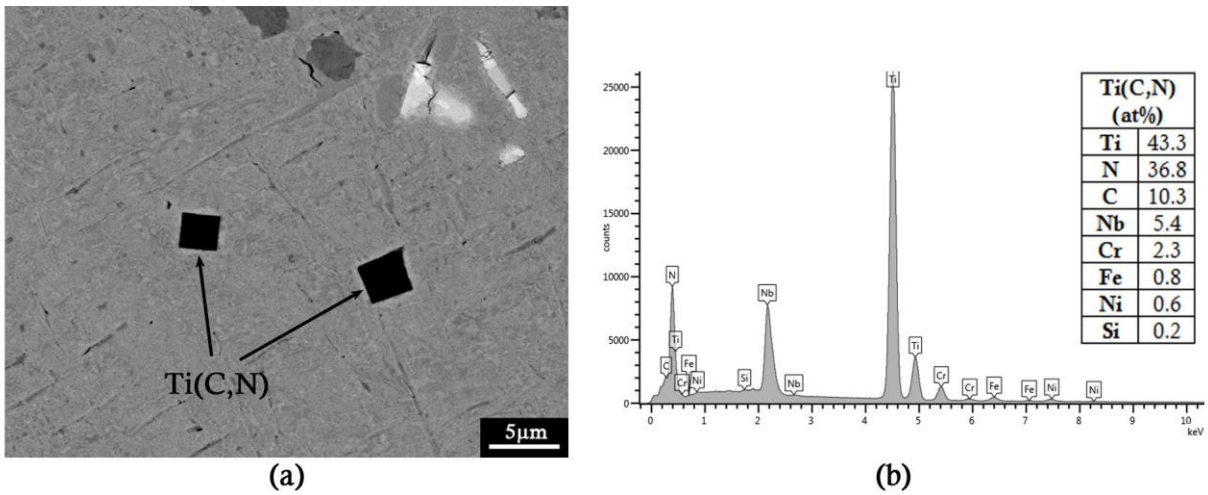

Figure 4.40 - (a) backscattered electron micrograph showing the cuboidal Ti(C,N) precipitates observed in tube 3; (b) typical composition of the Ti(C,N) precipitates, as determined by EDS.

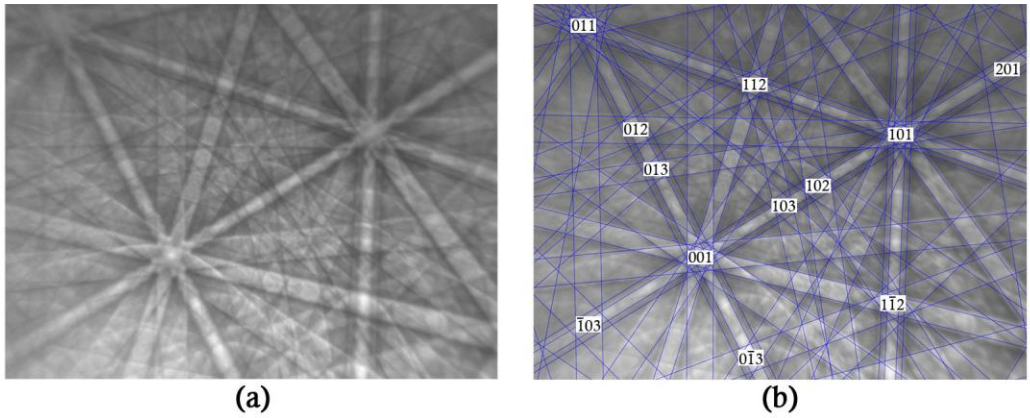

Figure 4.41 - (a) experimentally determined EBSP of the cuboidal Ti-rich precipitates in tube 3; (b) corresponding simulated pattern for the TiC crystal structure.

Secondary Precipitate Network

A distribution of secondary carbides enriched in chromium were observed in the matrix regions between the primary carbide network, as shown in Figure 4.42 (a). However, in contrast to the cuboidal, secondary $M_{23}C_6$ carbides typically observed in aged and ex-service HP-Micro tubes [8], the secondary precipitates in tube 3 were observed to have a plate-like morphology, and were present in all regions of matrix in between the primary network, not just directly adjacent to the primary network. The plate-like precipitates were seen to be rich in chromium, and also contained iron, nickel, and silicon. A typical EDS spectrum for the Cr-Fe-Ni-Si plate-like precipitates is shown in Figure 4.42 (b) – the composition was seen to be similar to the σ-phase identified in the primary network, although the chromium content of the secondary precipitates was lower (36.3 at% vs 50.9 at%), and the nickel content was increased (24.7 at% vs 12.9 at%). The plate-shaped Cr-Fe-Ni-Si secondary precipitates present in the matrix were subsequently identified as σ-phase.

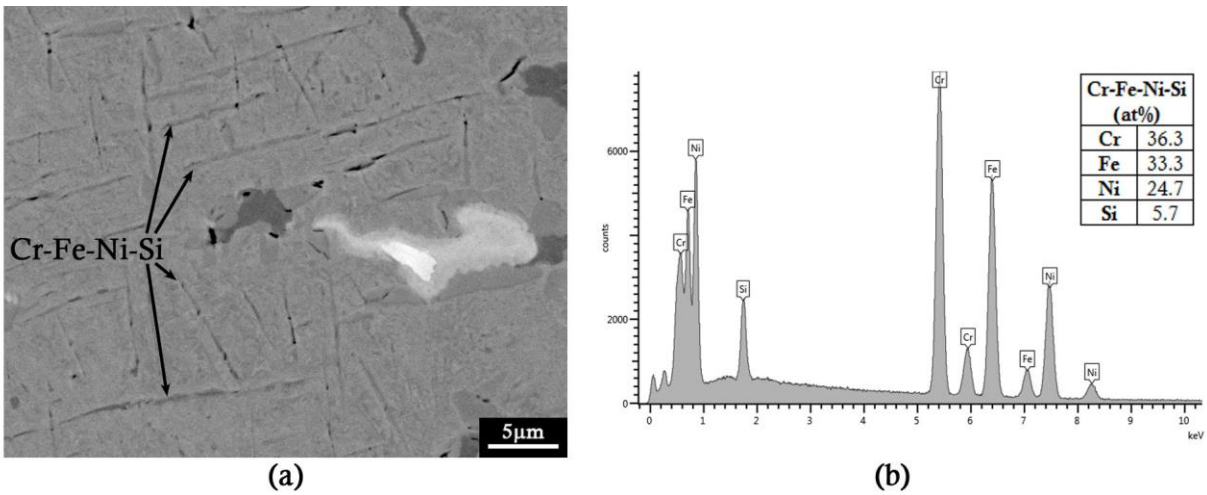

Figure 4.42 - (a) backscattered electron micrograph showing the Cr-Fe-Ni-Si precipitates with plate-like morphology in the matrix of tube 3; (b) typical composition of the Cr-Fe-Ni-Si precipitates shown in (a), as determined by EDS.

Inner and Outer Surfaces

Degradation as a result of oxidation was present at the outer diameter of tube 3, as shown in Figure 4.43 (a). Large regions of oxides rich in silicon and aluminium were observed to have penetrated into the tube wall a distance of approximately 150 µm. They did not form a continuous oxide layer, but rather appeared in sections. A thin chromium-rich oxide layer (<10 µm thick) and small sections of oxides rich in iron and nickel (<50 µm thick) were occasionally observed along the outer surface. The primary $M_{23}C_6$ and G-phase precipitates were present right up to the outer surface. Interestingly, clusters of cuboidal Ti(C,N) precipitates were seen frequently at the outer diameter, and these clusters were typically located adjacent to the Al-Si-rich oxides, as shown in Figure 4.44. At the inner diameter, the $M_{23}C_6$ carbides as well as the G-phase precipitates were observed right up to the inner surface. No chromium-rich oxide scale was present, and a minimal amount of selective oxidation by silicon was observed, with silicon oxides penetrating only ~10 µm in to the tube wall, as shown in Figure 4.43 (b).

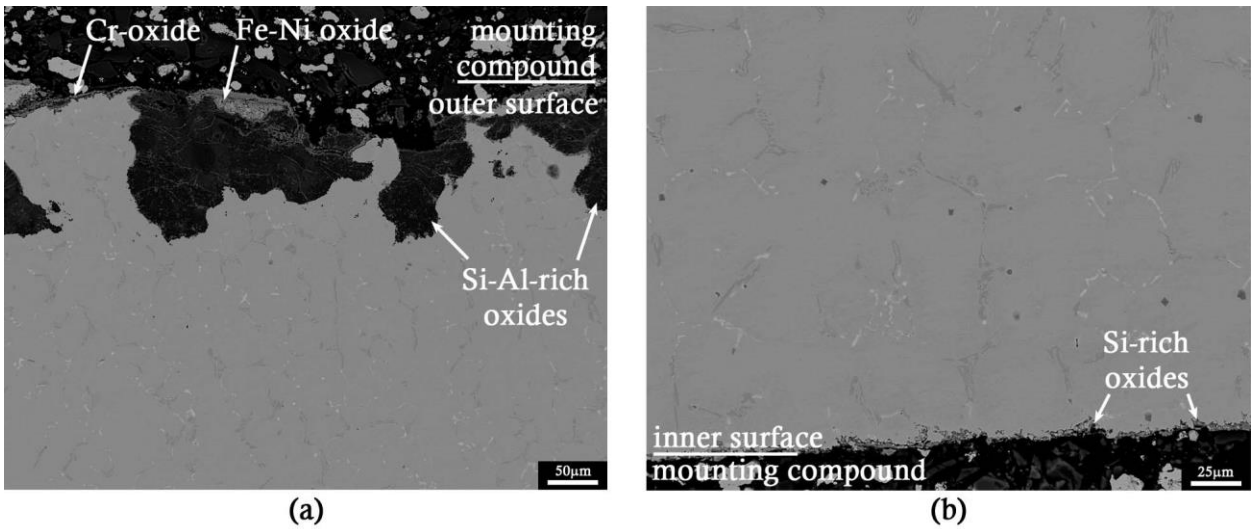

Figure 4.43 –Backscattered electron micrographs showing the degradation due to oxidation at the (a) outer and (b) inner surfaces of tube 3.

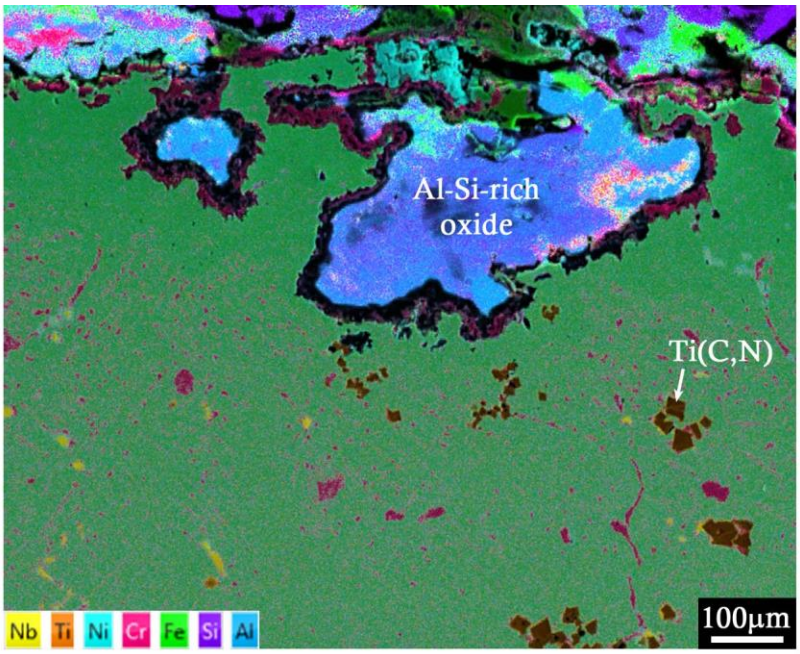

Figure 4.44 - EDS map with secondary electron micrograph underlay showing the clusters of Ti(C,N) precipitates adjacent to the Al-Si-rich oxides at the outer surface of tube 3.

4.5.4 Tube 4

Figure 4.45 shows representative optical and scanning electron micrographs of tube 4. The microstructure was observed to be consistent across the tube wall, and was composed of a primary network of fine lamellar chromium-and niobium-rich precipitates. A distribution of fine secondary precipitates was observed adjacent to the primary network.

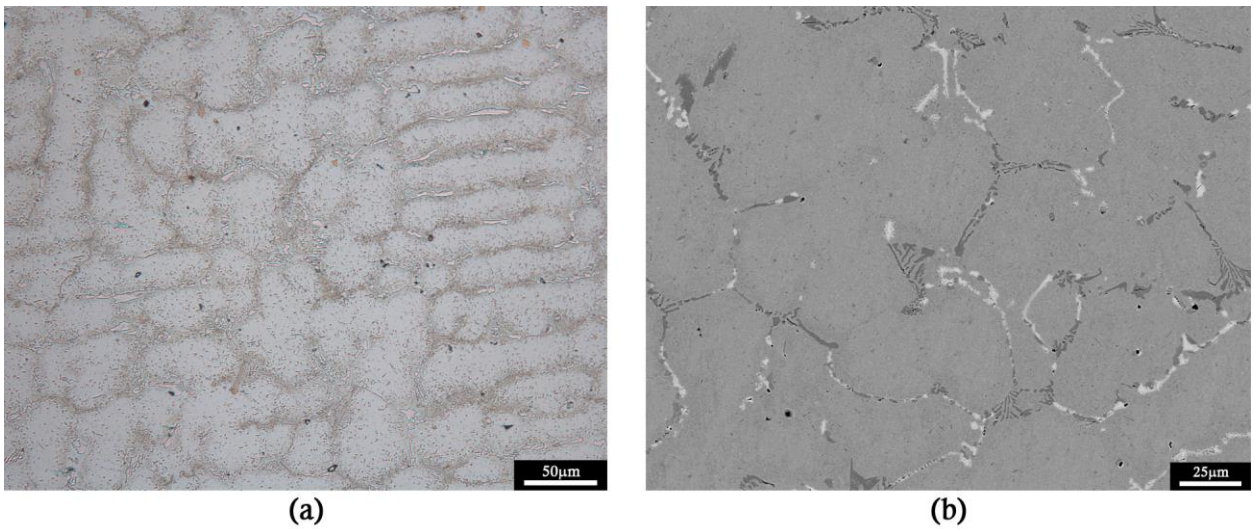

Figure 4.45 - Representative (a) optical and (b) backscattered electron micrographs of the microstructure of tube 4.

Primary Precipitate Network

The primary network in tube 4 was observed to be similar to that of tube 3, and it had retained much of the lamellar morphology typical of the primary networks observed in as-cast structures. The primary network was composed of a chromium-rich precipitate, a precipitate rich in niobium and titanium, and another niobium-rich phase which was also enriched in nickel and silicon. Figure 4.46 (a) shows a backscattered electron image of the matrix, A, and primary precipitate phases, B and C, in tube 3. The chromium-rich precipitate, B, appeared dark in the backscattered electron images in comparison to the Ni-Nb-Si phase, C, which appeared bright white due to atomic number contrast in backscattered electron images. Occasionally, small precipitates on the order of 1-2 µm in diameter (D) were observed within the Ni-Nb-Si phase (C), as labelled in Figure 4.46 (b).

The composition of the chromium-rich precipitate (B) was consistent with the $M_{23}C_6$ carbides identified in tube 1-3, and the composition of the Ni-Nb-Si phase was consistent with the G-phase identified in tubes 1-3. The chromium-rich carbide (B) was subsequently identified as $M_{23}C_6$, the Ni-Nb-Si phase (C) was identified as G-phase, and the Nb-Ti-rich phase (D) was identified as (Nb,Ti)C. The matrix was confirmed to be austenite.

Clusters of cuboidal precipitates rich in titanium were regularly observed intragranularly, as shown in Figure 4.47. The composition of the precipitates was consistent with the Ti(C,N) precipitates identified in tube 3, and the Ti-rich precipitates were subsequently identified as Ti(C,N).

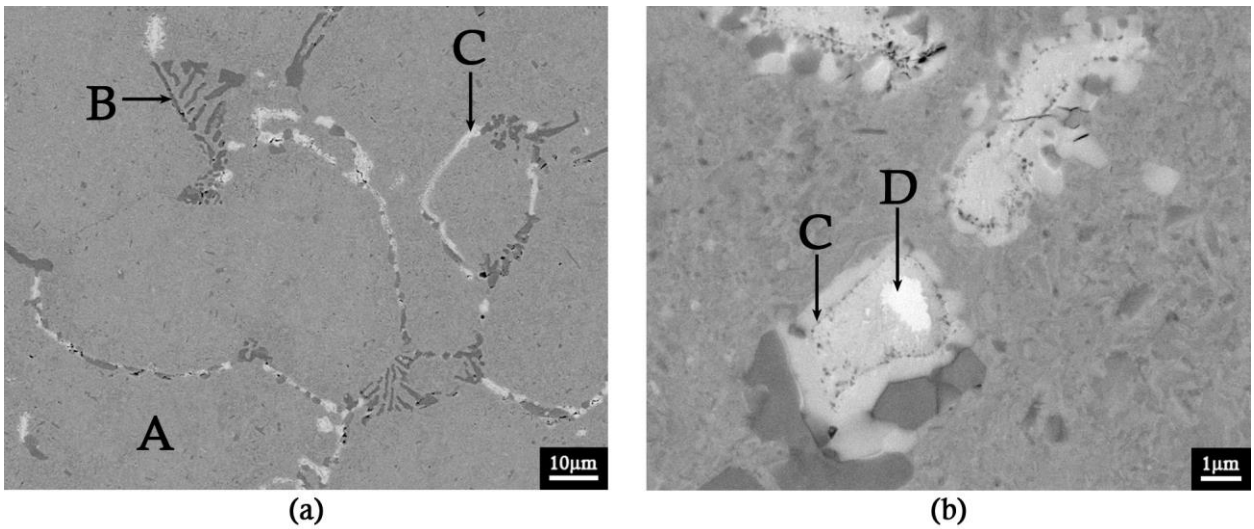

Figure 4.46 - Backscattered electron micrographs of (a) the primary precipitates in tube 4; (b) the Nb-Ti-rich precipitates within the primary Nb-Ni-Si precipitates.

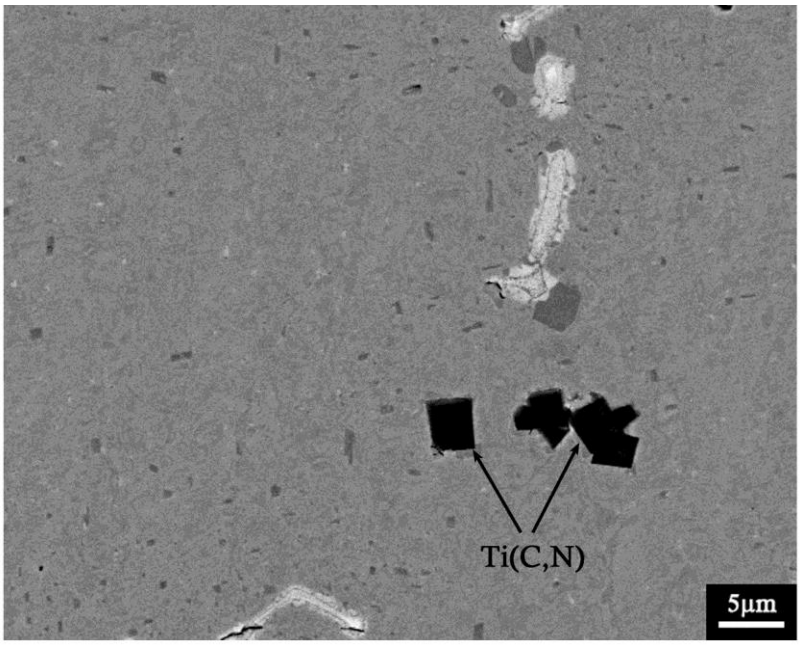

Figure 4.47 - Backscattered electron micrograph showing the clusters of cuboidal Ti(C,N) precipitates observed intragranularly in tube 4.

Secondary Precipitate Network

A fine distribution of chromium-rich precipitates was observed adjacent to the primary carbide network, as shown in Figure 4.48. The secondary precipitates displayed a cuboidal structure, and a size of <5 µm. The composition and appearance was similar to the secondary $M_{23}C_6$ carbides observed in tubes 1 and 2. The secondary Cr-rich precipitates in tube 4 were subsequently identified as $M_{23}C_6$.

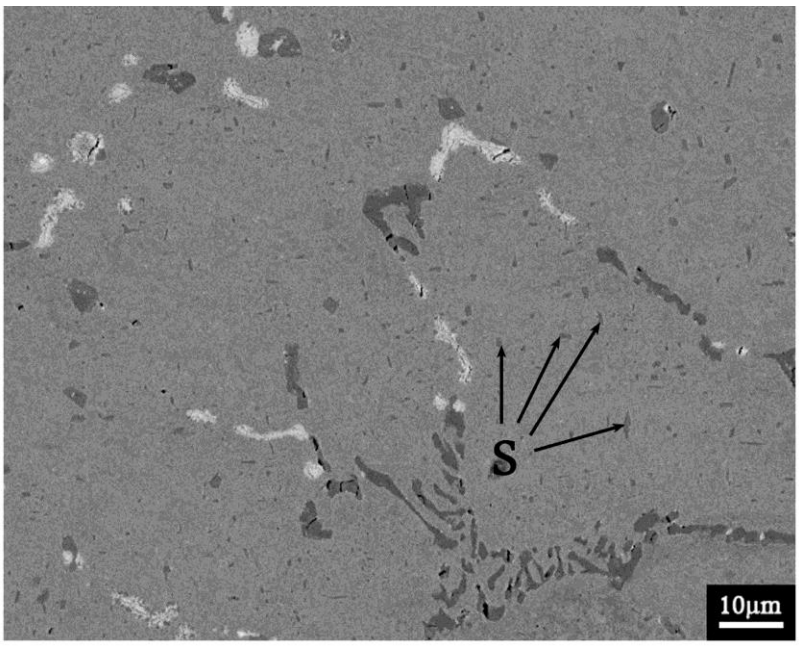

Figure 4.48 – Backscattered electron micrograph showing the secondary chromium-rich precipitates, labelled S, adjacent to the primary precipitate network in tube 4.

Inner and Outer Surfaces

Minimal degradation due to oxidation was present at the inner and outer surfaces of tube 4, as shown in Figure 4.49. No chromium-rich oxides were seen at the outer wall; however, some silicon oxides were present, penetrating approximately 100 μm in to the tube wall along dendrite boundaries. It appeared that the silicon-rich oxides had formed due to selective oxidation of the $M_{23}C_6$ on the dendrite boundaries. The G-phase precipitates were observed right up to the outer surface. Selective oxidation of the $M_{23}C_6$ carbides was also observed at the inner diameter, where they were replaced by silicon-rich oxides in a band approximately 100 μm thick. No chromium-rich oxides were observed at the inner surface.

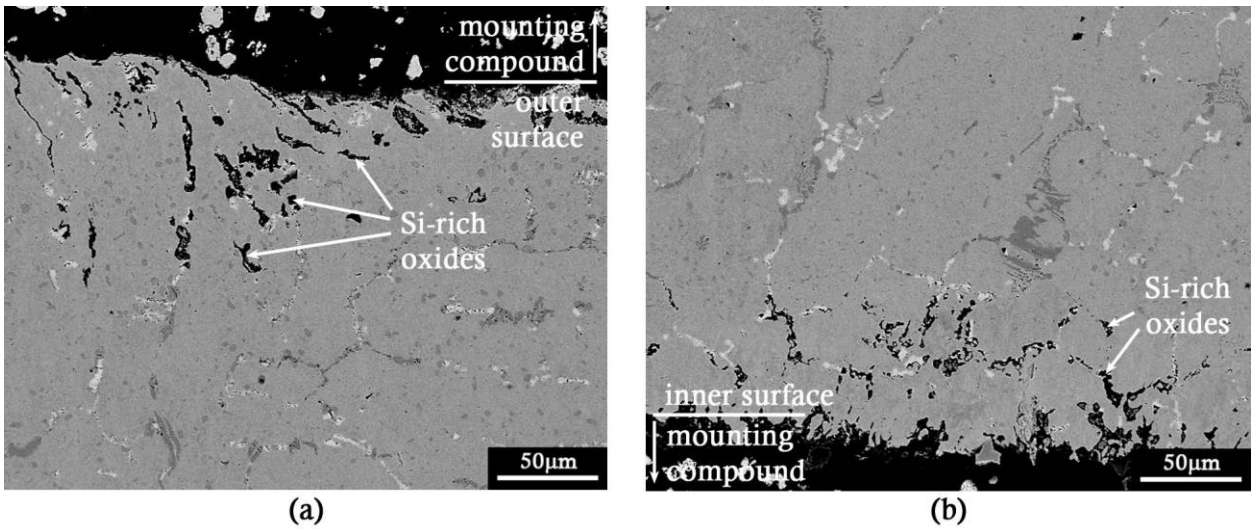

Figure 4.49 - Backscattered electron micrographs showing the silicon oxide penetration at the (a) outer and (b) inner surfaces of tube 4.

4.5.5 Tube 5

Figure 4.50 shows representative optical and scanning electron micrographs of tube 5 at the inner, mid, and outer wall regions. The primary network was observed to be coarsened at the inner diameter in comparison to the typical as-cast network, although not as coarsened and agglomerated as tubes 1 and 2. At the mid and outer wall regions the primary network was observed to be more fragmented in comparison to the inner wall, and some of the lamellar structure typical of the as-cast network had been retained. A distribution of secondary precipitates was observed in the microstructure at the mid and outer wall regions.

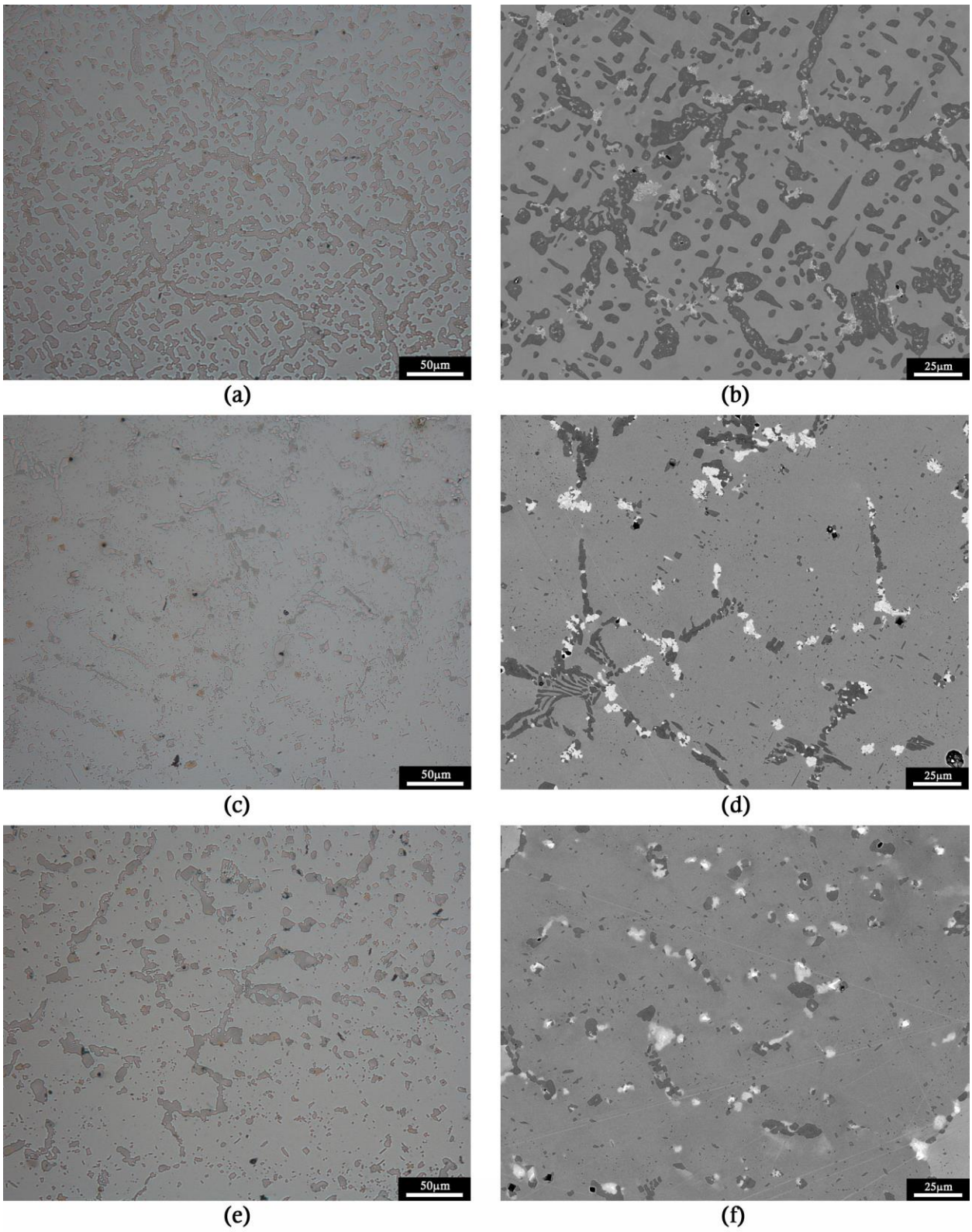

Figure 4.50 - Representative optical and backscattered electron micrographs of the inner, mid, and outer wall regions of tube 5. (a) inner wall, optical, (b) inner wall, backscattered, (c) mid wall, optical, (d) mid wall, backscattered, (e) outer wall, optical, (f) outer wall, backscattered.

Primary Precipitate Network

As with tubes 1 and 2, two chromium carbide types were observed as part of the primary precipitate network, labelled B and C along with the matrix, labeled A, in Figure 4.51. The chromium-rich carbide at the inner wall (B) was observed to be coarse and agglomerated, and appeared a darker grey in BSE images in comparison to the more angular, blocky chromium-rich carbide present at the mid and outer wall regions (C). A band typically 150 – 200 μm thick over which the blocky chromium-rich carbide transformed to the agglomerated chromium-rich carbide and over which two chromium-rich carbides co-existed was observed. The distance of the transformation front from the inner surface was observed to vary between samples taken from different locations in the tube (1.1 – 2.1 mm from the inner diameter).

The composition of the agglomerated chromium-rich carbide (B) was consistent with the M_7C_3 carbides identified in tubes 1 and 2, and the composition of the blocky chromium-rich carbide (C) was consistent with the $M_{32}C_6$ carbides identified in tube 1 and 2. The agglomerated chromium-rich carbide present at the inner wall was subsequently identified as M_7C_3, and the blocky chromium-rich carbide at the mid and outer wall was subsequently identified as $M_{23}C_6$. The matrix was confirmed as austenite.

The M_7C_3 carbides present in tube 5 exhibited a "porous" appearance, similar to that of the M_7C_3 carbides in tubes 1 and 2, as shown in Figure 4.52. However, in contrast to tubes 1 and 2, the apparent porosity of the M_7C_3 carbides in tube 5 remained relatively constant with increasing distance from the inner surface. The phase contained within the "pores" of the M_7C_3 carbides was identified as austenite, consistent with tubes 1 and 2.

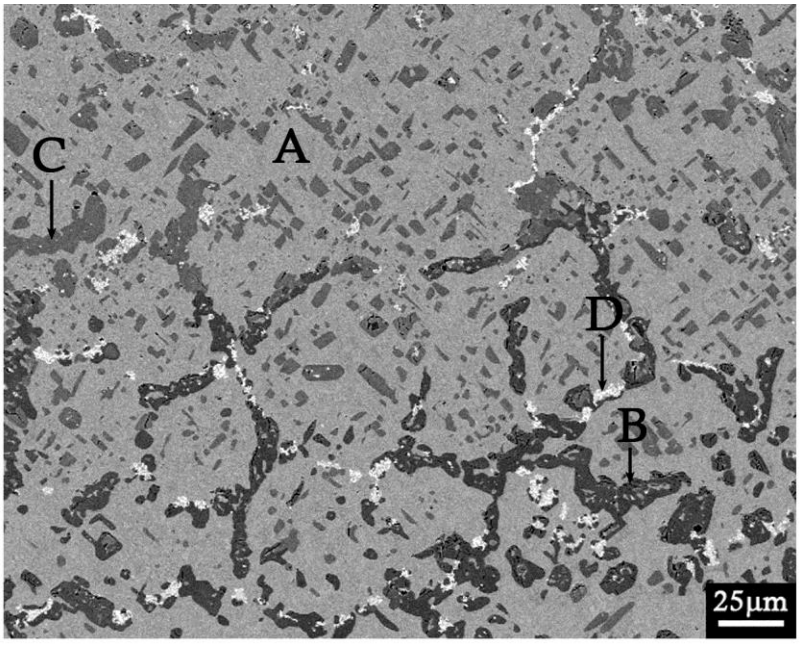

Figure 4.51 - Electron backscattered micrograph showing the matrix (A), and the primary chromium-rich (B&C) and niobium-rich (D) precipitate phases in tube 5.

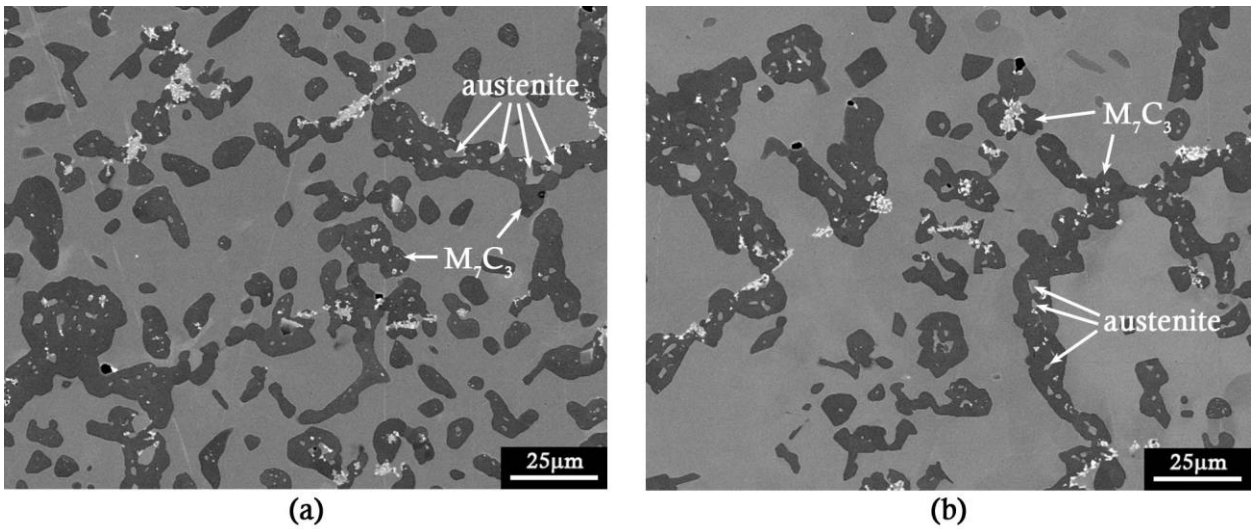

Figure 4.52 - Backscattered electron micrographs, indicating the austenite regions that appear contained within the M_7C_3 carbides, at distances of (a) 1.0 mm, and (b) 2.0 mm from the inner surface of tube 5.

Precipitates rich in niobium and titanium were observed as part of the primary network at the inner wall regions of tube 5, labelled D in Figure 4.51 , Figure 4.53, and Figure 4.54 (b). Their composition was consistent with the (Nb,Ti)C precipitates identified in tubes 3 and 4. The Nb-Ti-rich precipitates in tube 5 were subsequently identified as (Nb,Ti)C

At the mid wall of the samples, the (Nb,Ti)C precipitates were observed to have transformed almost completely to a phase rich in nickel, niobium, and silicon, labelled E in Figure 4.54 (a). At the outer wall this phase gave way to the incomplete transformation of the (Nb,Ti)C precipitates into another phase rich in chromium in addition to nickel, niobium, and silicon, labelled F in Figure 4.54 (b). The composition of the Ni-Nb-Si phase was consistent with the composition of G-phase identified in tubes 1, 3, and 4, and the composition of the Cr-Ni-Nb-Si phase was consistent with the composition of η-carbide identified in tubes 1-2. The Ni-Nb-Si phase (E) was subsequently identified as G-phase, and the Cr-Ni-Nb-Si phase (F) was subsequently identified as η-carbide. The band over which η-carbide was present was typically constrained to 1 – 1.5mm of the outer surface, and the band over which the change between the (Nb,Ti)C-to-η-carbide and (Nb,Ti)C-to-G-phase transformations occurred was very narrow, typically ~50 μm thick.

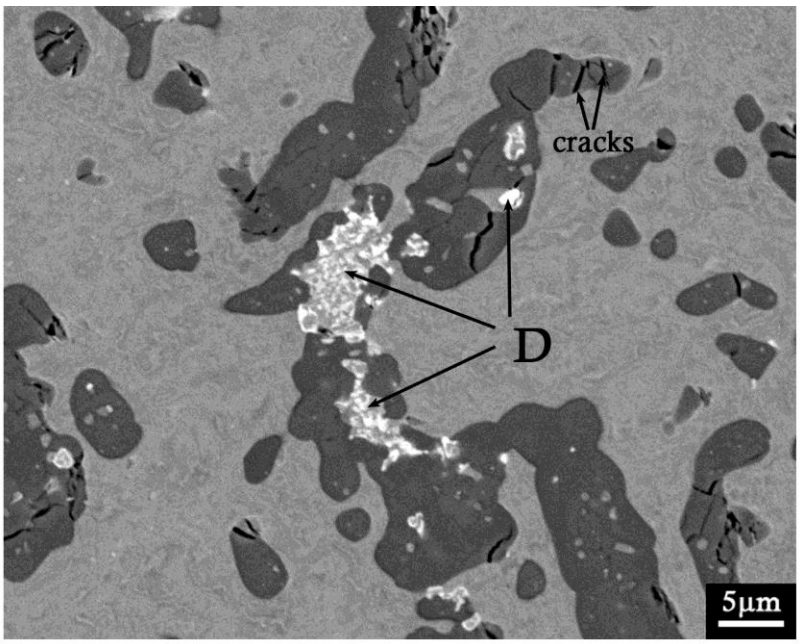

Figure 4.53 - Electron backscattered micrograph showing the primary niobium-rich precipitates (D) in tube 5. The black lines that appear in the chromium-rich carbides are cracks.

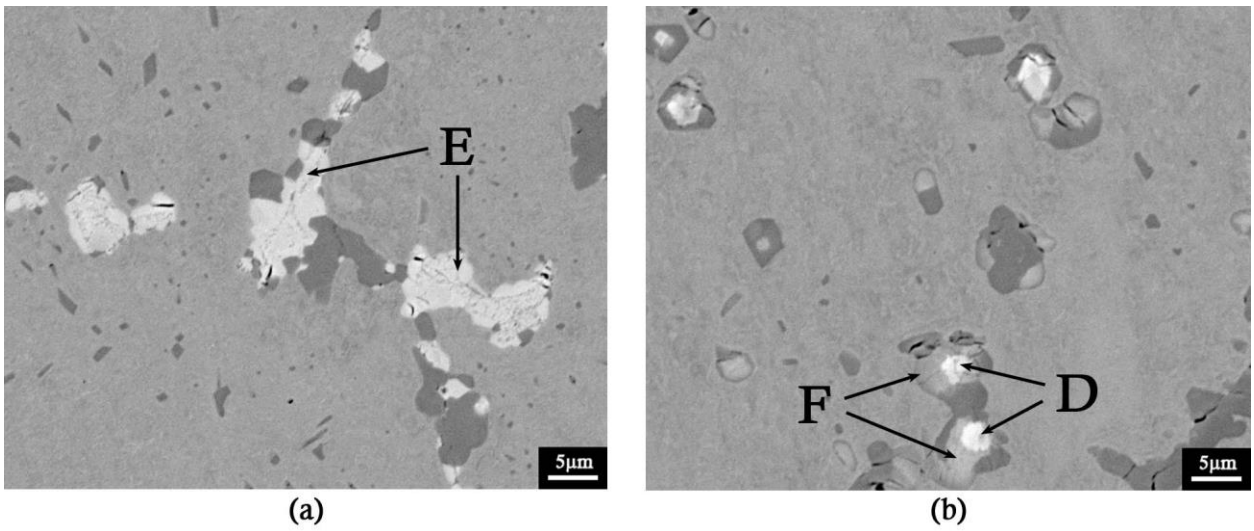

Figure 4.54 - Electron backscattered micrograph showing (a) the Ni-Nb-Si phase, labelled E, and (b) the transformation of (Nb,Ti)C, labelled D, into the Cr-Ni-Nb-Si phase, labelled F, in tube 5.

Secondary Precipitate Network

A coarse distribution of secondary chromium-rich precipitates was observed in tube 5. The secondary precipitates were only present in the mid and outer regions of the tube wall where the primary chromium carbide was $M_{23}C_6$, as shown in Figure 4.55. The precipitates displayed either a cuboidal or plate-like morphology, and were typically <5µm in size. The composition of the secondary chromium-rich precipitates was consistent with the secondary $M_{23}C_6$ precipitates observed in tubes 1, 2, and 4. The secondary chromium-rich precipitates in tube 5 were subsequently identified as $M_{23}C_6$.

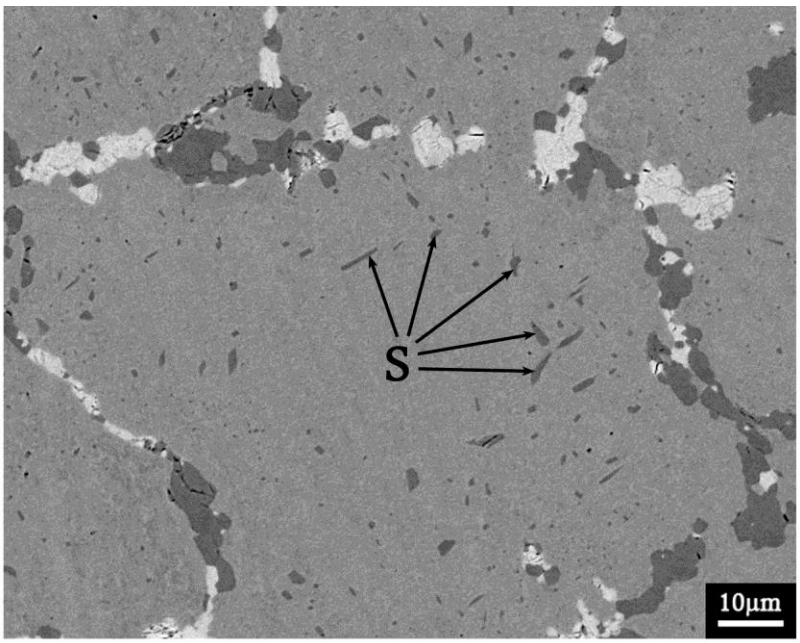

Figure 4.55 – Electron backscattered micrograph showing the secondary chromium-rich precipitates, labelled S, present adjacent to the primary network in tube 5.

Other Phases

Inclusions rich in manganese and sulfur, typically <5 μm in diameter, were observed as part of the primary network, segregated to the inner 0.5mm of the tube wall. Their composition was consistent with the MnS inclusions identified in tubes 1 & 2. The inclusions were subsequently identified as MnS.

Inner and Outer Surfaces

Degradation as a result of oxidation was evident at the inner and outer surfaces of all samples (Figure 4.56) and appeared similar to the oxidation observed at the inner and outer surfaces of tubes 1 and 2. At the outer surface, intermittent Cr-Fe-Ni and Cr-rich oxide scales were observed, as well as silicon-rich oxides that penetrated into the tube wall along dendrite boundaries. A band free of chromium-rich precipitates was present beneath the oxide scales. Within this band only silicon-rich oxides and (Nb,Ti)C precipitates were present. At the inner wall, selective oxidation of the primary rich microconstituents had occurred, and silicon-rich and chromium-rich oxides had penetrated into the tube wall along dendrite boundaries. As with tubes 1 and 2, the thickness of the oxide layers and the depth of the chromium free band at the outer surface, and the depth of selective oxidation at the inner surface, varied significantly from sample to sample.

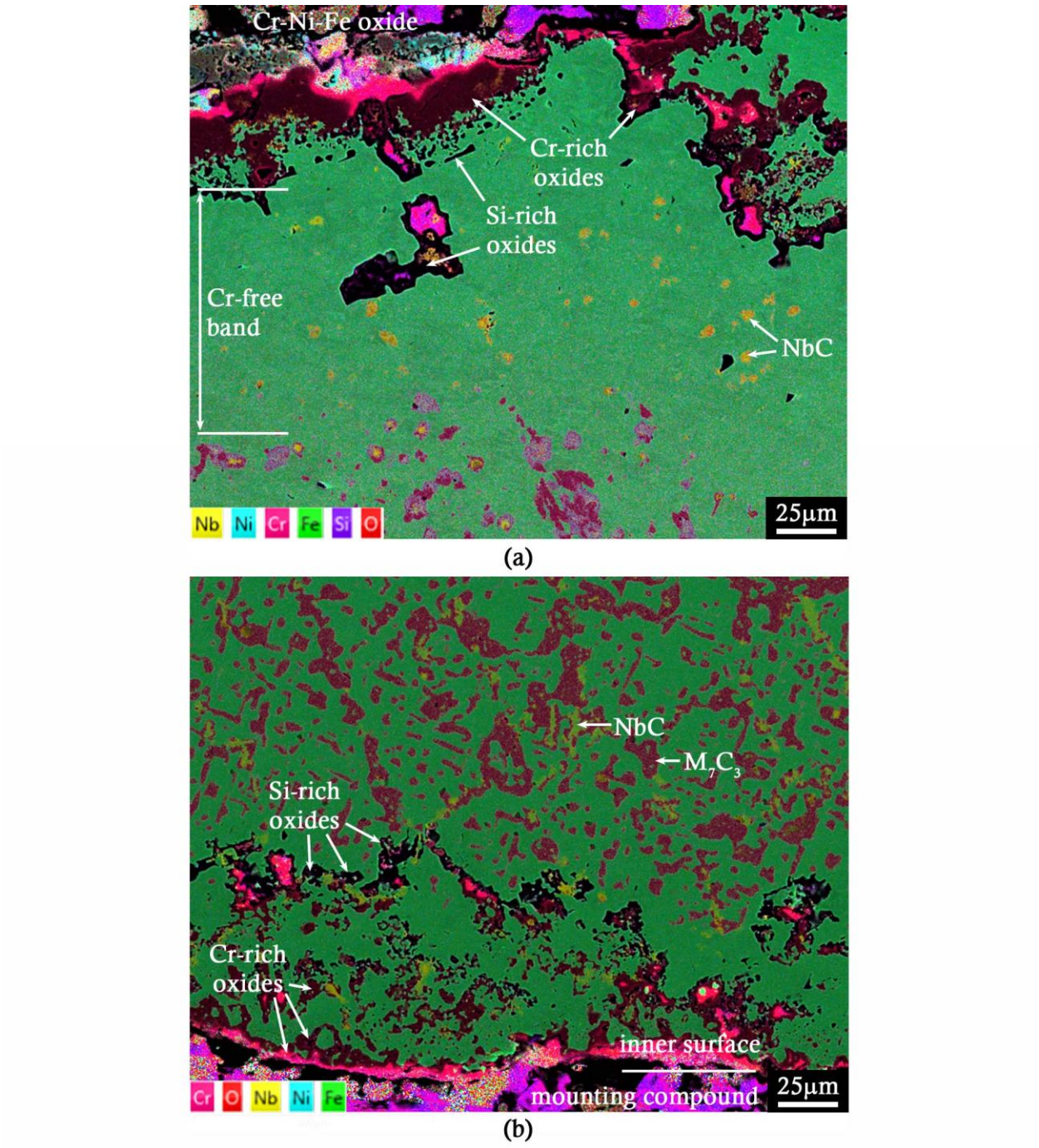

Figure 4.56 - EDS maps with secondary electron micrograph underlays showing the oxidation at the (a) outer and (b) inner surfaces of tube 5.

4.5.6 Tube 6

Figure 4.57 shows representative optical and scanning electron micrographs of tube 6 at the inner wall, mid wall, and outer wall regions. In all samples, the primary precipitate network appeared rounded and coarsened in the outer wall regions, but at the inner and mid wall regions had retained much of the lamellar morphology typical of the as-cast structure. On occasion, coarse cuboidal secondary precipitates were observed adjacent to the primary precipitate network.

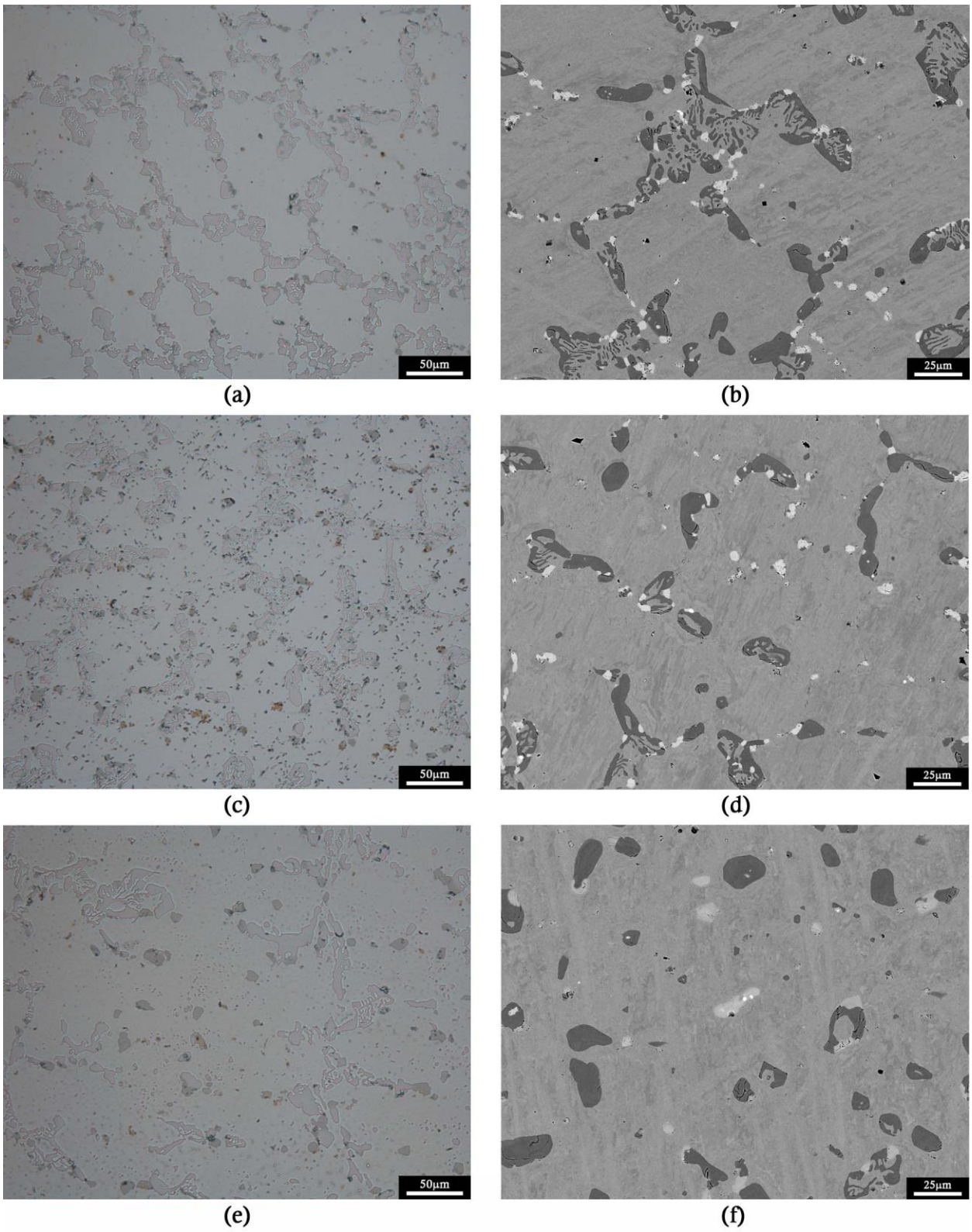

Figure 4.57 - Representative optical and backscattered images of the inner, mid, and outer wall regions of tube 6. (a) inner wall, optical, (b) inner wall, backscattered, (c) mid wall, optical, (d) mid wall, backscattered, (e) outer wall, optical, (f) outer wall, backscattered.

Primary Precipitate Network

The primary carbide network in tube 6 was composed primarily of a chromium-rich precipitate, and a phase rich in nickel, niobium, and silicon, labelled B and C respectively in Figure 4.58 (a), along with the matrix A. The chromium-rich carbide at some locations appeared rounded and coarsened, and in some parts had retained some of the lamellar morphology typical of the as-cast structure. At the outer wall regions, the Ni-Nb-Si phase gave way to a phase rich in chromium, nickel, niobium, and silicon, labelled D in Figure 4.58 (b). Round precipitates rich in niobium and titanium, approximately 1-2 μm in diameter, were observed within the Cr-Ni-Nb-Si phase regions, as labelled E Figure 4.59.

The composition of the chromium-rich precipitate (B) was consistent with the $M_{23}C_6$ carbides identified in tubes 1-5. The composition of the Ni-Nb-Si phase was consistent with the G-phase identified in tubes 1, 3, 4, and 5, and the composition of the Cr-Ni-Nb-Si phase was consistent with the η-carbide identified in tubes 1, 2, and 5. The chromium-rich carbide (B) was subsequently identified as $M_{23}C_6$, the Ni-Nb-Si phase (C) was identified as G-phase, and the Cr-Ni-Nb-Si phase was identified as η-carbide. The matrix was confirmed to be austenite. The composition of the rounded Nb-Ti precipitates located within the η-carbide phase regions was consistent with the (Nb,Ti)C carbides identified in tubes 3-5 The rounded Nb-Ti precipitates were subsequently identified as (Nb,Ti)C.

Across the entirety of the wall, cuboidal precipitates rich in titanium and with a small amount of niobium were observed isolated in the matrix. The composition and the crystal structure of the precipitates was consistent with the Ti(C,N) carbonitrides identified in tubes 3 and 4. The cuboidal Ti-rich precipitates were subsequently identified as Ti(C,N).

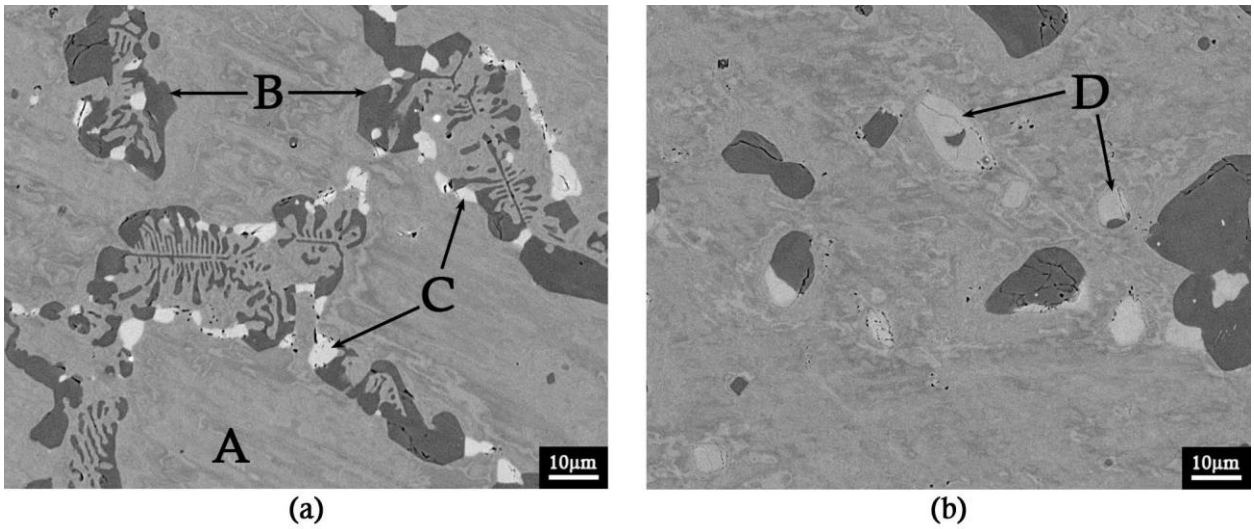

Figure 4.58 - Electron backscattered micrograph showing the matrix (A), the primary chromium-rich (B), Ni-Nb-Si (C) and Cr-Ni-Nb-Si (d) precipitates in tube 6.

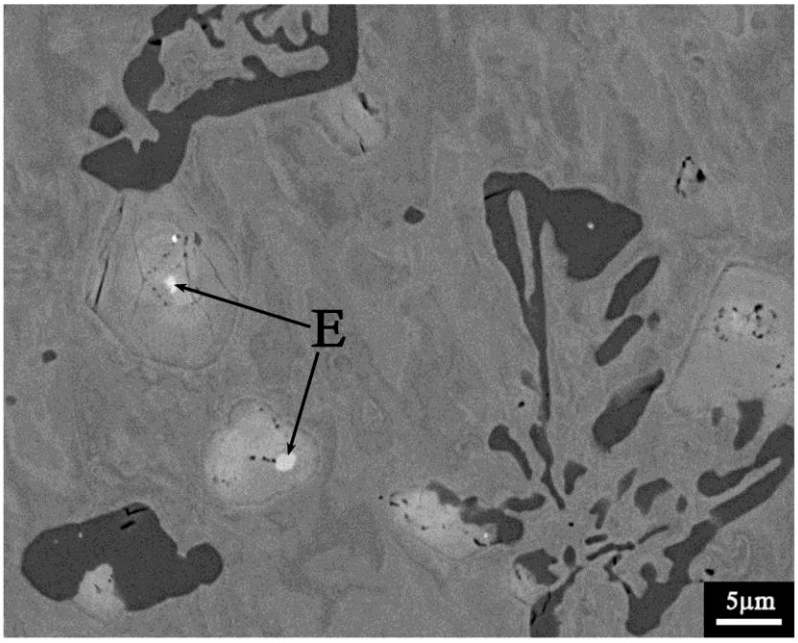

Figure 4.59 - Backscattered electron micrograph showing the niobium and titanium rich precipitates (E) present within the η-carbide phase regions in tube 6.

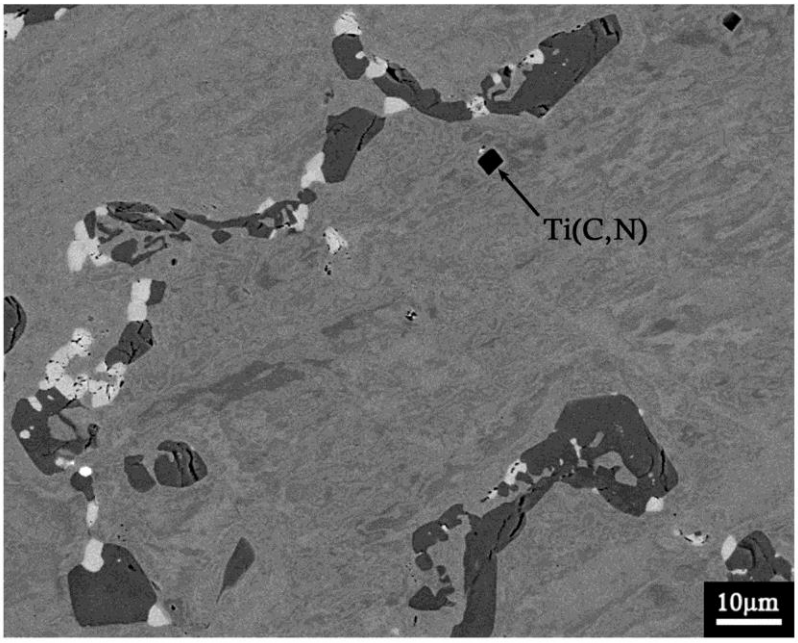

Figure 4.60 - Backscattered electron micrograph showing the cuboidal Ti(C,N) carbonitrides present in tube 6.

Secondary Precipitate Network

On occasion, a fine distribution of cuboidal, chromium-rich secondary precipitates was observed adjacent to the primary precipitate network, labelled S in Figure 4.61. The composition of the secondary chromium-rich precipitates was consistent with the secondary $M_{23}C_6$ precipitates observed

in tubes 1, 2, 4, and 5. The secondary chromium-rich precipitates in tube 6 were subsequently identified as $M_{23}C_6$.

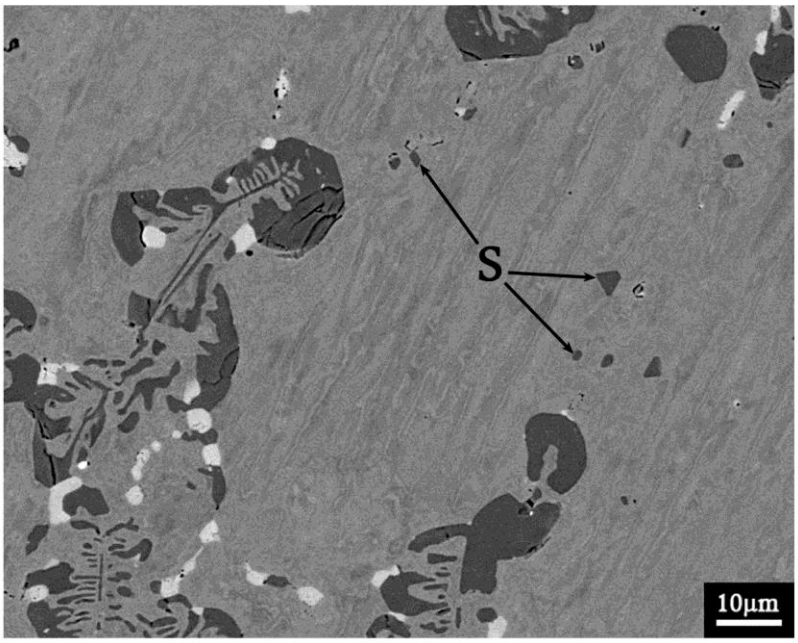

Figure 4.61 - Backscattered electron micrograph showing the chromium-rich secondary precipitates, labelled S, adjacent to the primary precipitate network in tube 6.

Inner and Outer Surfaces

The inner and outer surfaces of tube 6 showed degradation as a result of oxidation (Figure 4.62). At the outer surface, an oxide layer rich in chromium and containing some manganese was present, up to 200 µm thick in places. Directly beneath this oxide layer was a zone free of precipitates, which penetrated up to 500 µm further into the wall from the edge of the Cr- oxide layer. Within this zone, dendritic silicon-rich oxides were present. On occasion, the dendritic silicon oxides were observed to penetrate beyond the precipitate free zone, up to 800 µm into the tube wall.

At the inner surface of the tube, a thin chromium-rich oxide layer (10-20 µm thick) was present intermittently, and selective oxidation of the chromium-rich microconstituents along dendrite boundaries within approximately 80 µm of the inner surface had occurred. The chromium-rich microconstituents were replaced with silicon- and chromium-rich oxides. A zone free of precipitates was observed, approximately 200 µm thick.

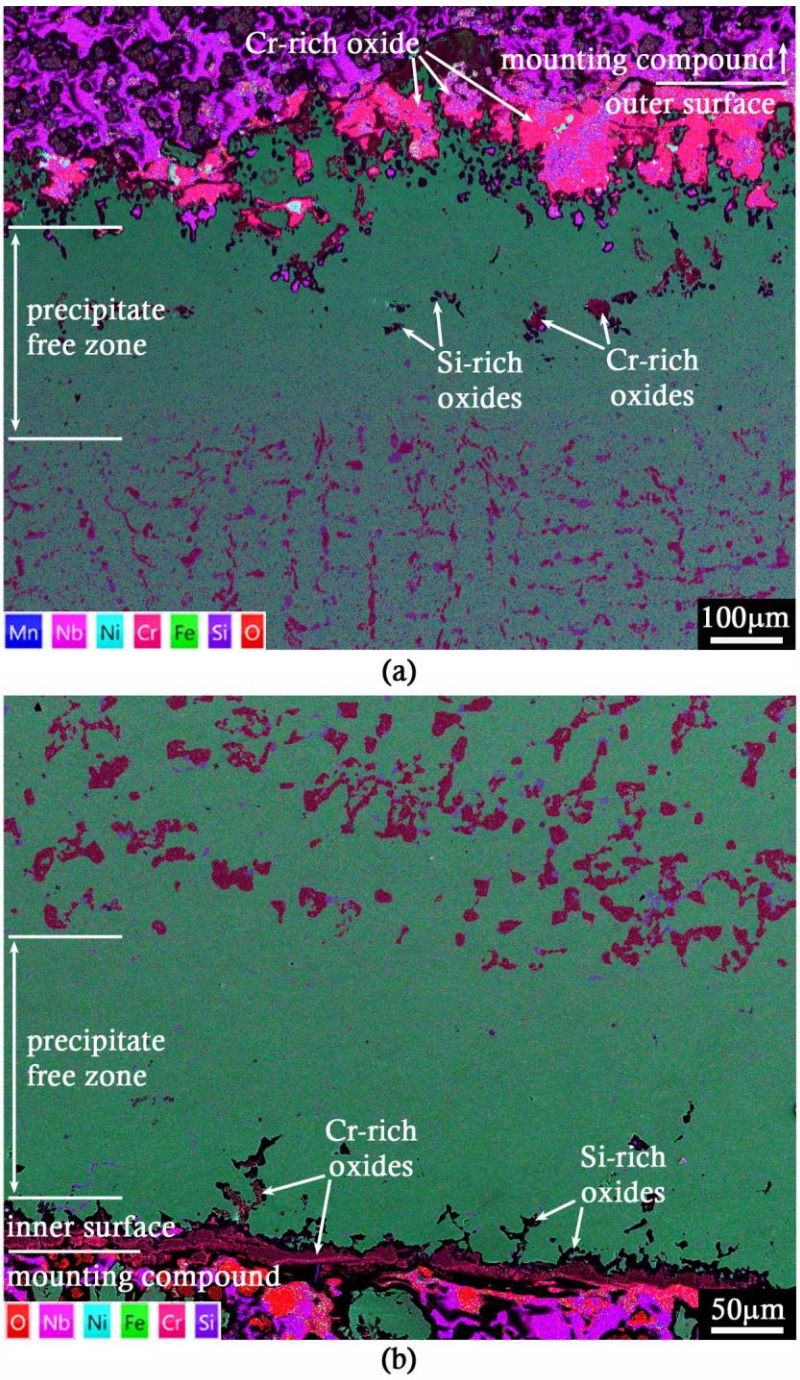

Figure 4.62 - EDS maps with secondary electron micrograph underlays showing the oxidation at the (a) outer and (b) inner surfaces of tube 6.

4.6 Apparent Porosity of M_7C_3 Carbides

In the as-cast condition, the primary chromium-rich carbide in HP-Nb, HP-Micro, and ET45-Micro alloys is typically M_7C_3. Upon ageing at temperatures above 700 °C, the M_7C_3 carbides transform to $M_{23}C_6$, with complete transformation typically occurring within the first 1000 hours [1, 2, 4]. Upon carburization, the $M_{23}C_6$ may transform back to M_7C_3 in areas with high carbon activity, as the M_7C_3 carbides have a higher carbon to metal ratio. The transformation front progresses into the tube wall

from the inner diameter as carburization progresses. The transformation of $M_{23}C_6$ to M_7C_3 was observed in three tubes (1, 2, and 5), whereas the primary chromium carbides in the remaining tubes remained as $M_{23}C_6$ across the tube wall in all samples analysed.

The chromium-rich M_7C_3 carbides present at the inner wall regions of tubes 1, 2, and 5 were observed to have a porous appearance, with the apparent porosity typically increasing with increasing distance from the inner surface. Analysis via EBSD and EDS determined that the phase that appeared contained within the M_7C_3 carbides in all three tubes was austenite. Henceforth, the austenite regions that appear contained within the M_7C_3 carbides will be termed "contained austenite".

The "porous" appearance of M_7C_3 carbides has been reported by Christ [45] to occur during carburization of a 304L type stainless steel, and by Waldenström [46] in a Fe-Cr-Ni-Mn-C alloy. Kaya [47] observed the phenomenon in an ex-service HK40 alloy ethylene pyrolysis tube, and identified the phase that appeared contained within the carbides as austenite. All three studies attribute the apparent porosity of the M_7C_3 carbides to the transformation of $M_{23}C_6$ to M_7C_3 by a eutectoid reaction during carburization. Kaya defined the transformation by Equation 1.1:

$$M_{23}C_6 \rightarrow M_7C_3 + \gamma \qquad \textbf{Equation 4.1}$$

where γ = austenite. Kaya proposed that the excess elements (presumably the metal components - Fe, Cr, and Ni) that could not be accommodated in the M_7C_3 carbides upon the transformation from $M_{23}C_6$ would form the austenite regions within the M_7C_3 carbides.

In order to further understanding of the method of formation of the contained austenite, an analysis of the orientation relationship between the contained austenite and adjacent austenite matrix was performed on a sample from tube 1, using EBSD. EBSPs were obtained from the contained austenite and the austenite matrix directly adjacent to the M_7C_3 precipitate within which they appeared to be contained. Using Oxford Instruments' Aztec software, the Euler angles (ϕ_1, ϕ_2, Φ), which describe the crystallographic orientation of a lattice with respect to a reference axis system, could then be calculated from the indexed EBSPs. The three Euler angles were used to calculate a 3x3 orientation matrix for each point of analysis. Subsequently the misorientation between any two analysis points could be calculated using the matrix operation described by Equation 4.2:

$$[A][B]^{-1} = [M] \qquad \textbf{Equation 4.2}$$

where A and B are the orientation matrices for analysis points A and B, and M is the misorientation matrix:

$$[M] = \begin{bmatrix} m_{11} & m_{12} & m_{13} \\ m_{21} & m_{22} & m_{23} \\ m_{31} & m_{32} & m_{33} \end{bmatrix}$$ **Equation 4.3**

The orientation relationship (OR) between analysis points A and B is then described by Equation 4.4:

$$\begin{aligned} [m_{11}\, m_{12}\, m_{13}]_A \quad // \quad [1 \quad 0 \quad 0\,]_B \\ [m_{21}\, m_{22}\, m_{23}]_A \quad // \quad [0 \quad 1 \quad 0\,]_B \\ [m_{31}\, m_{32}\, m_{33}]_A \quad // \quad [0 \quad 0 \quad 1\,]_B \end{aligned}$$ **Equation 4.4**

The misorientation angle, θ, and axis, [u v w], between analysis points A and B can be calculated using Equation 4.5 and Equation 4.6:

$$\theta = \cos^{-1}\left(\frac{m_{11} + m_{22} + m_{33} - 1}{2}\right)$$ **Equation 4.5**

$$[u\ v\ w] = [m_{23} - m_{32} \quad m_{31} - m_{13} \quad m_{12} - m_{21}]$$ **Equation 4.6**

The disorientation, i.e. the variant with the smallest value of θ about axis [u v w], can then be determined by considering the 24 crystallographic equivalents for the cubic crystal system [48].

A total of 65 contained austenite – austenite matrix pairs were analysed in order to determine the disorientation and the axis of rotation. Figure 4.63 shows the relative frequency of the disorientation angle. 69% of the analysed contained austenite – austenite matrix pairs had a disorientation of less than 10 degrees, which is typical of the contained austenite attaining a cube-cube OR with the austenite matrix. , i.e. $<100>_A$ // $<100>_B$, $\{100\}_A$ // $\{100\}_B$. 18% of the contained austenite – matrix pairs analysed displayed disorientations of approximately 60°, and the disorientation axes calculated for these pairs were close to [111]. A 60° rotation about a [111] axis is typical of the contained austenite attaining a twin orientation with the austenite matrix. The remaining contained austenite displayed no particular orientation relationship with the austenite matrix, indicating that no other rational orientations were obtained.

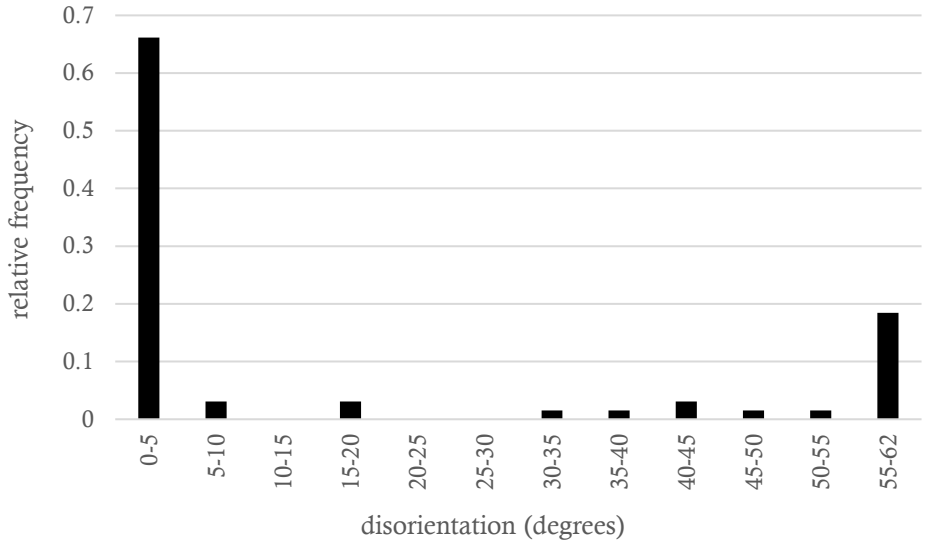

Figure 4.63 – Histogram showing the relative frequency of disorientation measured between contained austenite and the austenite matrix.

In order to observe the three-dimensional structure of the carbide network, progressive deep etching in glyceregia was performed on a separate sample from tube 1, following the procedure outlined in Section 3.2.3. As described in Section 3.2.3, glyceregia was chosen as the etchant as it has been shown to only attach austenite, leaving the carbide network intact.

The progressive deep etching revealed that areas that appeared as open austenite matrix in the as-polished condition in two dimensions became enclosed by M_7C_3 carbides beneath the plane of polish, as shown in Figure 4.64. If the plane of polish had been deeper in the sample, then these open matrix regions would have appeared contained by the M_7C_3 carbides. The progressive deep etching also revealed the three-dimensional structure of the primary chromium carbides. It was observed that, rather than being a singular grain, the M_7C_3 carbides present at the inner wall regions of tube 1 appeared to be composed of multiple equiaxed grains that were closely packed together, as shown in Figure 4.65 (a). With increasing distance from the inner surface, the frequency of appearance of regions where the grains appeared more loosely packed, as shown in Figure 4.65 (b), increased. If the plane of polish had been deeper into the sample the gaps in between the grains where the M_7C_3 was loosely packed would have appeared as austenite contained within the M_7C_3 carbides when observed in the as-polished, two dimensional condition. In contrast to the M_7C_3 carbides, the $M_{23}C_6$ carbides displayed a cuboidal morphology in three dimensions, as shown in Figure 4.66. Their three-dimensional morphology is consistent with the angular, blocky appearance when viewed in cross-section.

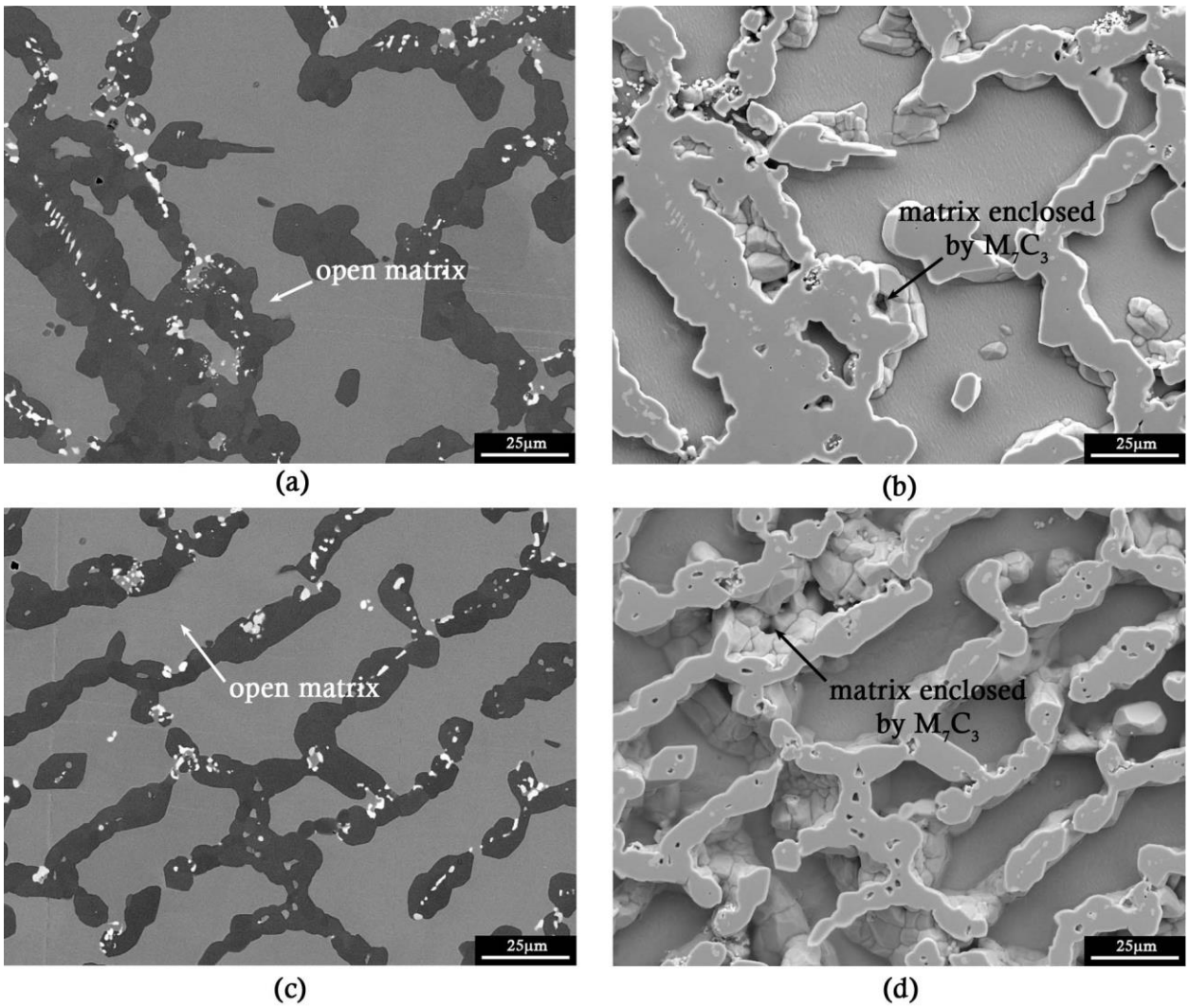

Figure 4.64 – Backscattered electron and secondary electron micrographs showing areas of austenite matrix that appear enclosed by the M_7C_3 carbides below the plane of polish in tube 1. (a) and (b) 1.0mm from the inner surface, as polished (BSE) and after 30 minutes in glyceregia (SEI) respectively. (c) and (d) 3.0mm from the inner surface, as polished (BSE) and after 120 minutes in glyceregia (SEI) respectively.

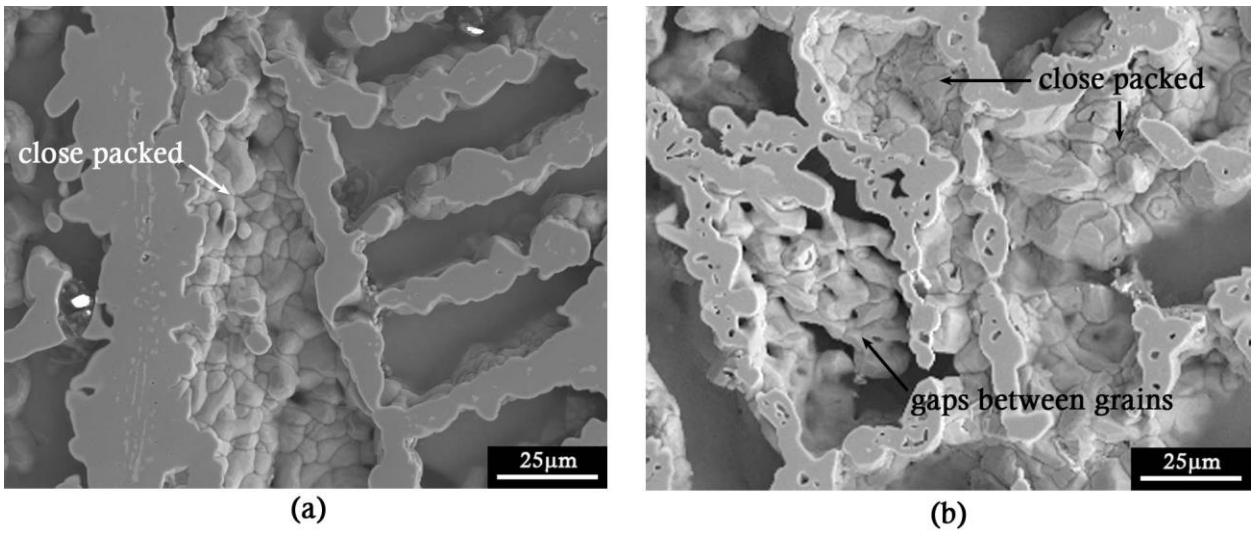

Figure 4.65 - Secondary electron micrographs showing the three-dimensional structure of the M_7C_3 carbides at (a) inner surface region and (b) close to the $M_{23}C_6$-to-M_7C_3 transformation front at the mid wall region, after 180 minutes in glyceregia.

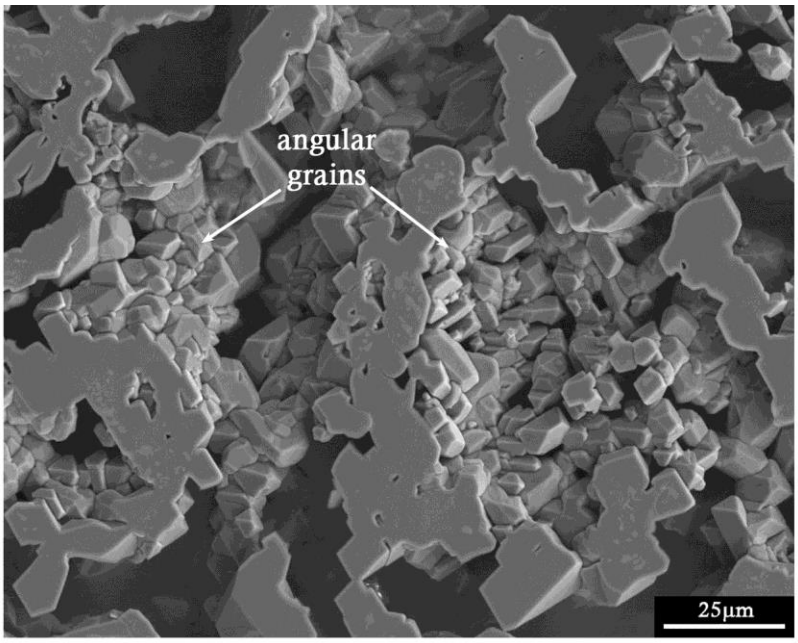

Figure 4.66 - Secondary electron micrograph showing the three-dimensional structure of the $M_{23}C_6$ carbides at the outer wall region of tube 1, after 180 minutes in glyceregia.

The space groups and lattice parameters of the M_7C_3 and $M_{23}C_6$ carbides, and of the austenite matrix, have been summarized in Table 4.4. In the as-cast condition, M_7C_3 does not have an OR with the austenite matrix, whereas the $M_{23}C_6$ carbides are typically observed to attain a cube-cube OR with the austenite matrix, both in the as-cast and aged conditions, due to having the same crystal structure and a lattice parameter almost exactly three times that of the matrix. No OR between the M_7C_3 carbides that transform from $M_{23}C_6$ as a result of carburization and the austenite matrix has been reported.

If the contained austenite regions are individual precipitates (as proposed by Kaya), then there are multiple methods by which they could have formed and attained an orientation typical of a cube-cube OR with the austenite matrix surrounding the M_7C_3 carbide within which they appear contained. If the M_7C_3 present in the carburized condition does indeed attain no rational OR with the austenite matrix, then in order to attain an orientation typical of a cube-cube OR with the austenite matrix the contained austenite regions must have nucleated either in the $M_{23}C_6$ carbides prior to their transformation to M_7C_3, or at the transformation front where M_7C_3 and $M_{23}C_6$ co-exist. Alternatively, if the M_7C_3 carbides present in the carburized condition do attain some rational OR with the austenite matrix, then the contained austenite regions may attain an orientation typical of a cube-cube OR with the austenite matrix by having M_7C_3 present at the point of nucleation.

The progressive deep etching results present an alternate method of formation of the contained austenite regions. The decomposition of $M_{23}C_6$ may begin at the $M_{23}C_6$/austenite matrix interface, with the growth of existing austenite continuing cooperatively with the growth of M_7C_3. In this case, the contained austenite regions that appear contained by the M_7C_3 carbides in two dimensions would be expected to be connected to the matrix in three dimensions, and not be individual precipitates. It is possible that the twin growth direction may be more favourable than the normal growth direction in some cases, leading to some of the contained austenite regions displaying an orientation typical of a twin OR with the austenite matrix. The contained appearance is likely the effect of observing a two-dimensional section of a complex three-dimensional network, as the location of the plane of polish has been shown to determine whether austenite regions appear as open matrix, or whether they appear enclosed within the M_7C_3 carbides when viewed in the as-polished condition. The growth of austenite occurs as a result of metal components being expelled during the transformation of $M_{23}C_6$ to M_7C_3, and as the M_7C_3 carbides coarsen, the metallic components, in particular chromium, of the austenite matrix in between the carbides are consumed. Thus, the M_7C_3 carbides appear less "porous" in areas of high carbide coarsening and agglomeration, i.e. close to the inner surface, in comparison to less coarsened areas at a greater distance from the inner surface.

4.7 Summary and Conclusions

Six ex-service ethylene pyrolysis tubes of three different alloy types were subject to macrostructural and microstructural analysis. The composition of the six tubes was analysed using ICP-AES, and it was determined that the composition of tubes 1 and 2 was consistent with HP-Nb type alloys, tubes 3, 4, and 5 were consistent with HP-Micro type alloys, and tube 6 was consistent with an ET45-Micro type alloy.

Macroscopically, each tube exhibited grain structures typical of the centrifugal casting method of manufacture. Tubes 1-5 displayed entirely columnar grain structures, whereas tube 6 was composed

of approximately 40% equiaxed grains (inner wall) and 60% columnar grains (outer wall). Microscopically, each tube was composed of a network of primary precipitates surrounded by an austenite matrix, and a number of phase transformations were observed to have occurred. The macro- and microstructures were seen to be locally consistent in both the axial and tangential tube directions. A combination of EDS and EBSD was used to identify each phase present in each tube. The phases identified in the six ex-service ethylene pyrolysis tubes are summarized in Table 4.5

The M_7C_3 carbides identified in tubes 1, 2 and 5 exhibited a "porous" appearance when observed in two dimensions, with the apparent porosity typically increasing with increasing distance from the inner surface of the tube sample. EDS and EBSD analyses were used to identify the phase regions that appeared contained within the M_7C_3 carbides, thus creating the porous appearance, as austenite. Analysis of the orientation relationship between 65 contained austenite – austenite matrix pairs, combined with progressive deep etching to observe the three-dimensional structure of the carbide network, determined that the austenite that appears contained by the M_7C_7 carbides in two dimensions is likely connected to the austenite matrix in three dimensions.

Table 4.5 - Summary of phases identified in the six ex-service ethylene pyrolysis tubes.

Phase	Tube 1	Tube 2	Tube 3	Tube 4	Tube 5	Tube 6
Austenite	matrix	matrix	matrix	matrix	matrix	matrix
M_7C_3	inner – mid wall	inner – mid wall	x	x	inner wall	x
$M_{23}C_6$ (primary)[1]	mid – outer wall	mid – outer wall	whole wall	whole wall	mid – outer wall	whole wall
$M_{23}C_6$ (secondary)	mid - outer wall in some samples	mid - outer wall in some samples	x	whole wall	mid - outer wall in some samples	on occasion
NbC	whole wall	whole wall	x	x	x	x
(Nb,Ti)C	x	x	whole wall	whole wall	inner wall, outer wall in η-carbide	outer wall in η-carbide
Ti(C,N)	x	x	whole wall	whole wall	x	whole wall
G-phase	mid wall, outer wall in some samples	x	whole wall	whole wall	mid – outer wall	mid – outer wall
η-carbide	outer wall in some samples	outer wall	x	x	outer wall	outer wall
$Cr_2(C,N)$	outer surface, carbide transition	outer surface, carbide transition	x	x	x	X
σ-phase	x	x	primary and secondary, whole wall	x	x	X
MnS	inner wall	inner wall	x	x	inner wall	x

[1] The term "primary" is typically used to refer to the interdendritic precipitates that are formed upon solidification of the HP and ET45 alloys. During exposure to elevated temperatures the primary interdendritic M_7C_3 precipitates transform to $M_{23}C_6$. Despite this transformation resulting in the interdendritic $M_{23}C_6$ precipitates not being strictly primary precipitates, using this term enables the interdendritic $M_{23}C_6$ precipitates to be distinguished from the intragranular $M_{23}C_6$ precipitates which also form during exposure to elevated temperatures.

Chapter References

[1] Barbabela, G.D., de Almeida, L.H., da Silveira, T.L., and Le May, I. *Role of Nb in modifying the microstructure of heat-resistant cast HP steel.* Materials Characterization, 1991. **26**(3): p. 193-197.

[2] de Almeida Soares, G.D., de Almeida, L.H., da Silveira, T.L., and Le May, I. *Niobium additions in HP heat-resistant cast stainless steels.* Materials Characterization, 1992. **29**(4): p. 387-96.

[3] Ibanez, R.A.P., de Almeida Soares, G.D., de Almeida, L.H., and Le May, I. *Effects of Si content on the microstructure of modified-HP austenitic steels.* Materials Characterization, 1993. **30**(4): p. 243-9.

[4] Buchanan, K.G. *The Effects of Long-Term Isothermal Ageing on the Microstructure of HP-Nb and HP-NbTi Alloys - Doctoral Dissertation*. 2013, University of Canterbury: Christchurch, New Zealand.

[5] Schmidt + Clemens Group *Centralloy® G 4852 Material Data Sheet*. 2009.

[6] Davis, J.R., (Ed). *ASM Specialty Handbook: Heat-Resistant Materials*. 1997, Materials Park, Ohio: ASM International.

[7] de Almeida, L.H., Ribeiro, A.F., and Le May, I. *Microstructural characterization of modified 25Cr-35Ni centrifugally cast steel furnace tubes.* Materials Characterization, 2003. **49**(3): p. 219-229.

[8] Caballero, F.G., Imizcoz, P., Lopez, V., Alvarez, L.F., and De Andrés, C.G. *Use of titanium and zirconium in centrifugally cast heat resistant steel.* Materials Science & Technology, 2007. **23**(5): p. 528-534.

[9] Nishimoto, K., Saida, K., Inui, M., and Takahashi, M. *Changes in microstructure of HP-modified, heat-resisting cast alloys under long-term aging. Repair weld cracking of service-exposed, HP-modified, heat-resisting cast alloys (2nd Report).* Welding Research Abroad, 2002. **48**(11): p. 1-9.

[10] Schmidt + Clemens Group *Centralloy® G 4852 Micro Material Data Sheet*. 2009.

[11] Kirchheiner, R. and Woelpert, P. *Niobium in centrifugally cast tubes for petrochemical applications*. in *Niobium, Science and Technology: Proceedings of the International Symposium Niobium. Orland: Minerals, Metals and Materials Society*. 2001.

[12] Schmidt + Clemens Group *Centralloy® ET 45 Micro Material Data Sheet*. 2009.

[13] Zaghloul, M.B., Shinoda, T., and Tanaka, R. *Relation between structure and creep rupture strength of centrifugally cast HK40 steel.* Transactions of the Iron and Steel Institute of Japan, 1977. **17**(1): p. 28-36.

[14] Sun, Y. and Bell, T. *Effect of layer thickness on the rolling-sliding wear behavior of low-temperature plasma-carburized austenitic stainless steel.* Tribology Letters, 2002. **13**(1): p. 29-34.

[15] Sun, Y. *Kinetics of low temperature plasma carburizing of austenitic stainless steels.* Journal of Materials Processing Technology, 2005. **168**(2): p. 189-194.

[16] Sun, Y. *Response of cast austenitic stainless steel to low temperature plasma carburizing.* Materials & Design, 2009. **30**(4): p. 1377-1380.

[17] Cao, Y., Ernst, F., and Michal, G.M. *Colossal carbon supersaturation in austenitic stainless steels carburized at low temperature.* Acta Materialia, 2003. **51**(14): p. 4171-4181.

[18] da Silveira, T.L. and Le May, I. *Reformer furnaces: materials, damage mechanisms, and assessment.* Arabian Journal for Science and Engineering, 2006. **31**(2): p. 99.

[19] Grabke, H., Muller-Lorenz, E., Strauss, S., Pippel, E., and Woltersdorf, J. *Effects of grain size, cold working, and surface finish on the metal-dusting resistance of steels.* Oxidation of Metals, 1998. **50**(3-4): p. 241-254.

[20] Villars, P., (Ed). and Cenzual, K., (Ed). *Pearson's Crystal Data: Crystal Structure Database*. 2008, ASM International: Materials Park, Ohio, U.S.A.

[21] Thomas, C.W., Stevens, K.J., and Ryan, M.J. *Microstructure and properties of alloy HP50-Nb: comparison of as cast and service exposed materials.* Materials Science and Technology, 1996. **12**(6): p. 469-475.

[22] Ribeiro, A.F., Borges, R.M.T., and de Almeida, L.H. *Phase transformation in heat resistant steel observed by STEM. (NbTi)C - NiNbSi (G-phase).* Acta Microscopica, 2002. **11**(1): p. 59-63.

[23] Wu, Q., Song, H., Swindeman, R.W., Shingledecker, J.P., and Vasudevan, V.K. *Microstructure of long-term aged IN617 Ni-base superalloy.* Metallurgical and Materials Transactions A, 2008. **39**(11): p. 2569-2585.

[24] Zhang, Y.G., Han, Y.F., and Chaturvedi, M.C. *TEM studies of ETA carbide precipitate particles in a DS cast Ni3Al base superalloy.* Materials Characterization, 1995. **34**(3): p. 205-212.

[25] Raghavan, M., Steeds, J.W., and Petkovic-Luton, R. *Convergent beam diffraction analysis of dispersoids in oxide dispersion strengthened alloys.* Metallurgical Transactions A, 1982. **13**(6): p. 953-957.

[26] Raghavan, M., Berkowitz, B.J., and Scanlon, J.C. *Electron microscopic analysis of heterogeneous precipitates in Hastelloy C-276.* Metallurgical Transactions A, 1982. **13**(6): p. 979-984.

[27] Tokonami, M. and Horiuchi, H. *On the space group of spinel $MgAl_2O_4$.* Acta Crystallographica A, 1980. **36**: p. 122-126.

[28] Barbabela, G.D., de Almeida, L.H., da Silveira, T.L., and Le May, I. *Phase characterization in two centrifugally cast HK stainless steel tubes.* Materials Characterization, 1991. **26**(1): p. 1-7.

[29] Goldstein, J., Newbury, D., Joy, D., Lyman, C., Echlin, P., Sawyer, L., and Michael, J. *Scanning Electron Microscopy and X-Ray Microanalysis*. 3rd ed. 2003: New York: Springer Science + Business Media Inc.

[30] Gladyshevskii, E.I. and Borusevich, L.K. *The Cr-Ni-Si ternary system.* Russian Journal of Inorganic Chemistry, 1963. **8**(8): p. 997-1000.

[31] Fruchart, D., Chaudouet, P., Fruchart, R., Rouault, A., and Senateur, J.P. *Etudes structurales de compose´s de type ce´mentite: Effet de l'hydroge`ne sur Fe3C suivi par diffraction neutronique. Spectrome´trie Mo¨ssbauer sur FeCo2B et Co3B dope´s au57Fe.* Journal of Solid State Chemistry, 1984. **51**(2): p. 246-252.

[32] Bouzy, E., Buer-Grosse, E., and Le Caër, G. *NaCl and filled Re3B-type structures for two metastable chromium carbides.* Philosophical Magazine Part B, 1993. **68**(5): p. 619-638.

[33] Berkane, R., Gachon, J.C., Charles, J., and Hertz, J. *A thermodynamic study of the chromium-carbon system.* Calphad, 1987. **11**(4): p. 375-382.

[34] Buchanan, K.G. and Kral, M.V. *Crystallography and morphology of niobium carbide in as-cast HP-niobium reformer tubes.* Metallurgical and Materials Transactions A: Physical Metallurgy and Materials Science, 2012. **43**(6): p. 1760-1769.

[35] Lönnberg, B. and Lundström, T. *Thermal expansion and phase analytical studies of Nb2C.* Journal of the Less Common Metals, 1985. **113**(2): p. 261-268.

[36] Dubrovinskaia, N.A., Dubrovinsky, L.S., Saxena, S.K., Ahuja, R., and Johansson, B. *High-pressure study of titanium carbide.* Journal of Alloys and Compounds, 1999. **289**(1–2): p. 24-27.

[37] Jeitschko, W., Jordan, A., and Beck, P.A. *V and E phase in ternary systems with transition metals and silicon or germanium.* Trans Met Soc AIME, 1969. **245**(2): p. 335-339.

[38] Markiv, V. *The crystal structures of the compounds R(M, X)2 and RMX2 in Zr-Ni-Al,*

Ti-Fe-Si, and related systems. Acta Crystallographica A, 1966. **21**: p. 84-85.

[39] Erneman, J., Schwind, M., Liu, P., Nilsson, J.O., Andrén, H.O., and Ågren, J. *Precipitation reactions caused by nitrogen uptake during service at high temperatures of a niobium stabilised austenitic stainless steel.* Acta Materialia, 2004. **52**(14): p. 4337-4350.

[40] Powell, D.J., Pilkington, R., and Miller, D.A. *The precipitation characteristics of 20% Cr/25% Ni-Nb stabilised stainless steel.* Acta Metallurgica, 1988. **36**(3): p. 713-724.

[41] Knitter, S. and Binnewies, M. *Der Chemische Transport von Mischkristallen in den Systemen MnS/ZnS, FeS/ZnS und FeS/MnS.* Zeitschrift für anorganische und allgemeine Chemie, 1999. **625**(9): p. 1582-1588.

[42] Li, F., Yang, J., Xue, D., and Zhou, R. *X-ray diffraction and Mössbauer studies of the (Fe1−xNix)4N compounds ($0 \leq x \leq 0.5$).* Journal of Magnetism and Magnetic Materials, 1995. **151**(1–2): p. 221-224.

[43] Bhadeshia, H.K.D.H. and Honeycombe, R.W.K. *Steels: Microstructure and Properties*. 3rd ed. 2006, Amsterdam, Boston: Elsevier, Butterworth-Heinemann.

[44] Krauss, G. *Steels: Processing, Structure, and Performance*. 2005, Materials Park, Ohio: ASM International.

[45] Christ, H.J. *Experimental characterization and computer-based description of the carburization behaviour of the austenitic stainless steel AISI 304L.* Materials and Corrosion, 1998. **49**: p. 258-65.

[46] Waldenstrom, M. *An experimental study of carbide-austenite equilibria in iron-base alloys with Mo, Cr, Ni, and Mn in the temperature range 1173 to 1373K.* Metallurgical Transactions A (Physical Metallurgy and Materials Science), 1977. **8A**(12): p. 1963-77.

[47] Kaya, A.A. *Microstructure of HK40 alloy after high-temperature service in oxidizing/carburizing environment. II. Carburization and carbide transformations.* Materials Characterization, 2002. **49**(1): p. 23-34.

[48] Randle, V. *The Measurement of Grain Boundary Geometry*. 1993: Institute of Physics Publications.

Chapter 5: Phase Distributions in Ex-Service Tubes

The current chapter follows on from the phase identification results presented in Chapter 4, and presents and discusses how the phases are distributed across the tube walls.

The design of an imaging and image analysis methodology was necessary in order to measure the area fractions of the various phases present in the tubes. A combination of several software programs was used, including ilastik, FIJI, and Microsoft Excel. The methodology will be discussed here.

The results of the comparison between the axial and tangential tube directions, as described in Section 4.4, showed that the tube microstructures were locally consistent in both directions. As such, although the phase fractions were measured as area fractions on the axial face, they will henceforth be referred to as volume fractions. The direction in which microstructural changes occur is the radial direction, along which the area fraction profiles were measured.

The matrix chromium concentration was also measured during the image analysis process, and the results of this will be presented.

5.1 Image Analysis Methodology

The methodology for selecting the location of creep and metallographic samples was described in Section 3.1. A summary of the metallographic sample locations in each tube and their consequent labelling was shown in Figure 3.1 and Table 3.1. The A & B and C & D samples are located at the same length along the tube respectively, and the A & C and B & D samples are located at the same angular positions respectively. The C and D samples for each tube are the samples directly adjacent to creep sample midsections.

Images were collected along radial profiles in order to measure the volume fractions of the phases in each sample, and determine how the phases were distributed across the tube walls. The analysis of volume fractions first required that the images be segmented into their discrete phases. Segmentation of the images was performed in ilastik, an interactive segmentation program [1]. Within ilastik, a classifier learns from user input (given by labels in a paint interface) and can segment an image into an arbitrary number of user-defined label classes. In this case, each phase present in the microstructure is assigned a label class. The classifier can segment based on a number of features, including color, edge, and texture descriptors. When training the classifier, ilastik can display several overlays to highlight regions where the prediction may be ambiguous, which enables the user to add extra labels where they are most needed. Once the classifier has been trained on a representative set of images, it

can be used to automatically batch process other previously unseen images. The segmentation from ilastik can be output in the form of a grayscale image, in which each label class is assigned a greyscale value (equispaced along the 0-255 greyscale range, where 0 is black and 255 is white).

Processing of the segmented images into binary images to extract volume fraction data was performed using FIJI (a distribution of the open-source image processing software ImageJ) [2]. The resulting binary image is composed of 1 and 0 values, where the phase is represented as white (1) foreground pixels, and the remaining pixels are represented as black (0) background pixels. The area fraction for each phase can then be measured by counting the number of black or white pixels in the associated binary image. Purpose-built macros were written in FIJI in order to batch process the segmented images and output the necessary data. Analysis of the data was performed using Microsoft Excel.

5.1.1 Selection of Imaging Method

Backscattered electron images (BSE images) were used extensively during the phase identification process, as atomic number contrast resulted in the majority of the phases present in the tubes being easily distinguishable from one-another. In order to use BSE images for image analysis the presence of artefacts left by the sample preparation procedures had to be avoided; however, as discussed in Section 3.2,Sample Preparation for Optical and Scanning Electron Microscopy the polishing procedures were difficult and time consuming, and a perfect polish was typically hard to achieve.

In addition, the appearance of a "watermark" effect was often visible in the austenite matrix of samples. Examples of such an effect are shown in Figure 5.1. It is currently unknown whether the watermark effect is a polishing artefact, or whether it is due to another root cause, such as a strain effect. The watermark effect was not visible until the sample was observed in the SEM, thus samples that appeared to have a good quality polish under a light optical microscope would often have to be removed from the SEM and re-polished before imaging could be performed. Segmentation in ilastik of BSE images that displayed the watermark effect was attempted, but the results were less than satisfactory. In particular, the presence of the watermark effect created difficulties in differentiating the η-carbide phase regions from the austenite matrix. The η-carbide precipitates were typically observed to have a gradient in greyscale across their cross-section when viewed with backscattered electrons due to gradients in composition, likely induced by their transformation from NbC or (Nb,Ti)C carbides. The greyscale gradient in the η-carbide precipitates was remarkably similar to the gradient in greyscale in the austenite matrix created by the watermark effect, and as a result ilastik was often unable to distinguish between the η-carbide and the austenite matrix when the watermark effect was present. Figure 5.2 (a) shows a BSE image in which both η-carbide and the watermark effect in the matrix were present. Despite multiple training iterations with the ilastik classifier, the classifier was unable to distinguish the η-carbide precipitate from the regions of austenite that exhibited the watermark effect, as shown in Figure 5.2 (b).

The G-phase, η-carbide, NbC, and (Nb,Ti)C precipitates were often difficult to differentiate without resorting to EDS analyses, as all appeared as variations of light grey or white in BSE images due to their niobium contents. This was of particular concern in samples were both G-phase and η-carbide were present, as η-carbide contains chromium and is likely to contribute to the chromium depletion of the matrix and therefore the magnetic properties of the material, whereas G-phase, NbC, and (Nb,Ti)C do not contain chromium.

Due to the inability to accurately segment all phases using BSE images, and the need for compositional data, it was decided that imaging using energy dispersive x-ray spectroscopy (EDS) mapping would be used. EDS mapping enables an area of a sample to be mapped based on the composition of the phases present. Each element is assigned a different colour, and thus each phase appears a different colour due to differences in composition. This enabled the differentiation of G-phase, η-carbide, NbC, and (Nb,Ti)C from one another. A comparison between an EDS map, and an EDS map with a secondary electron image (SEI) underlay is shown in Figure 5.3. The use of an SEI underlay was seen to improve the clarity of the edges of the precipitates and increase the colour contrast due to the slight greyscale contrast between the precipitates in the SEI image. Despite the "watermark" effect in the austenite matrix being visible in the SEI images, it was not as pronounced as in the BSE images, and it did not have an effect on the accuracy of segmentation due to the colour differences between the phases. Thus, SEI underlays were used in conjunction with the EDS maps for image analysis.

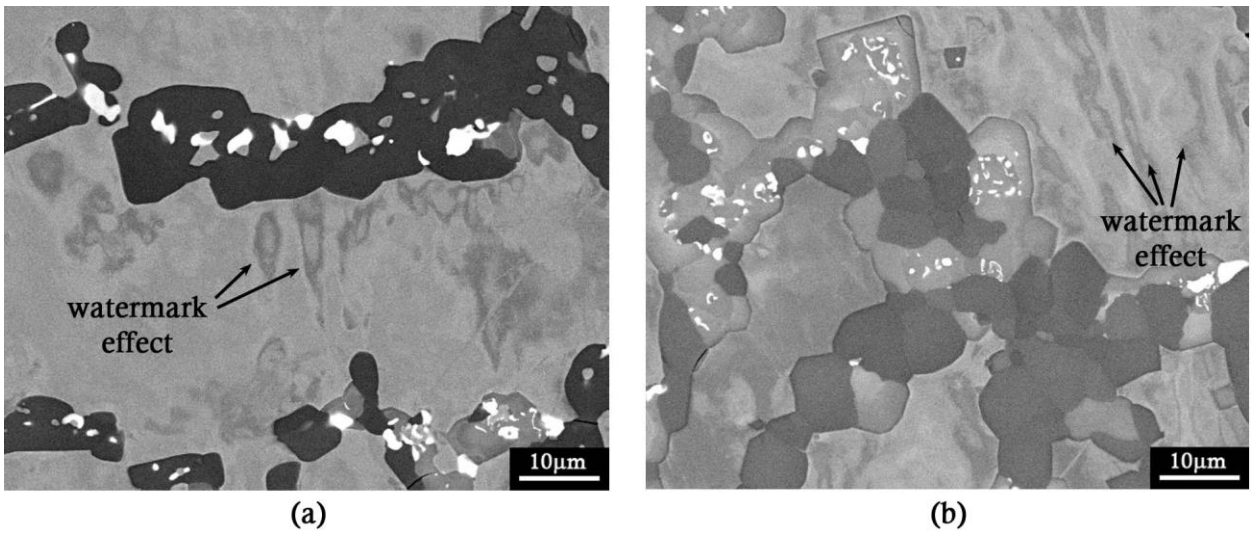

Figure 5.1 - Backscattered electron micrographs showing the watermark effect apparent in the austenite matrix.

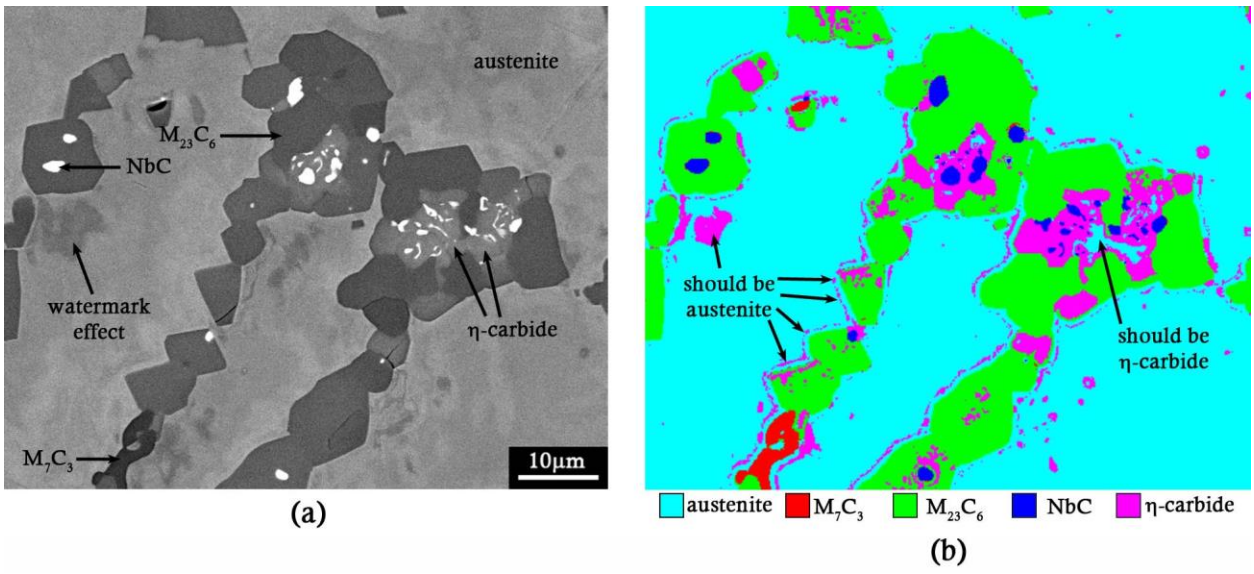

Figure 5.2 - (a) backscattered electron micrograph showing a region in which the watermark effect was present in the austenite matrix; (b) segmentation of the image in (a) in ilastik, showing errors in differentiating the austenite matrix and the η-carbide.

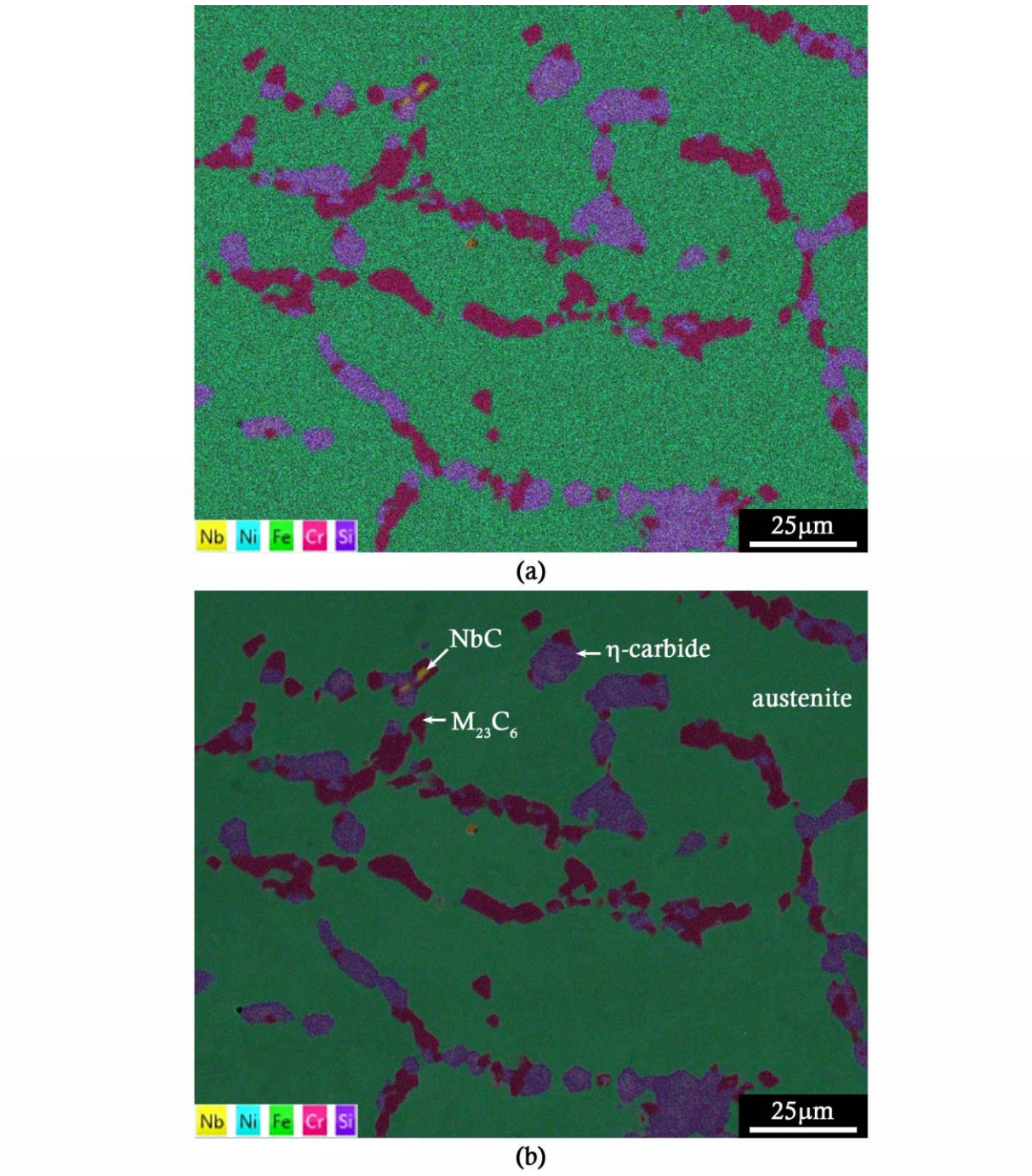

Figure 5.3 - (a) EDS map from outer wall region of tube 1, (b) same EDS map as in (a) with SEI image underlay.

5.1.2 Selection of Mapping Parameters

As the interaction volume of the electron beam is dependent on the accelerating voltage, a range of accelerating voltages was tested (5, 10, 15, and 20 keV) in order to find the optimal accelerating voltage for edge clarity. Multiple maps were taken for each keV, and the maps were then segmented in ilastik. No significant or consistent differences in the uncertainty overlays or the segmentation outputs were observed during interactive segmentation of the various map sets. 20 keV was thus chosen as the accelerating voltage, giving an interaction volume of approximately 1-2 μm [3]. A pixel dwell time of

100 μs was chosen, as it resulted in a good compromise between the quality of the maps and the collection time per map.

5.1.3 Number of Profiles

Due to each mapping profile taking on the order of 7-12 hours (depending on the wall thickness), the number of profiles had a major effect on the time to collect data. The results obtained when averaging two phase fraction profiles versus averaging three phase fraction profiles are shown in Figure 5.4 for sample 1A. The differences in the matrix chromium concentration profiles were almost indiscernible, and thus only one matrix chromium concentration profile is shown. The maximum difference in measured area fractions was approximately 4%. The difference may be due to segmentation errors, but is also likely to be a result of the inherent variability in the microstructure. The differences were not considered significant enough to justify the time necessary to map a third profile, and thus two profiles were collected per sample.

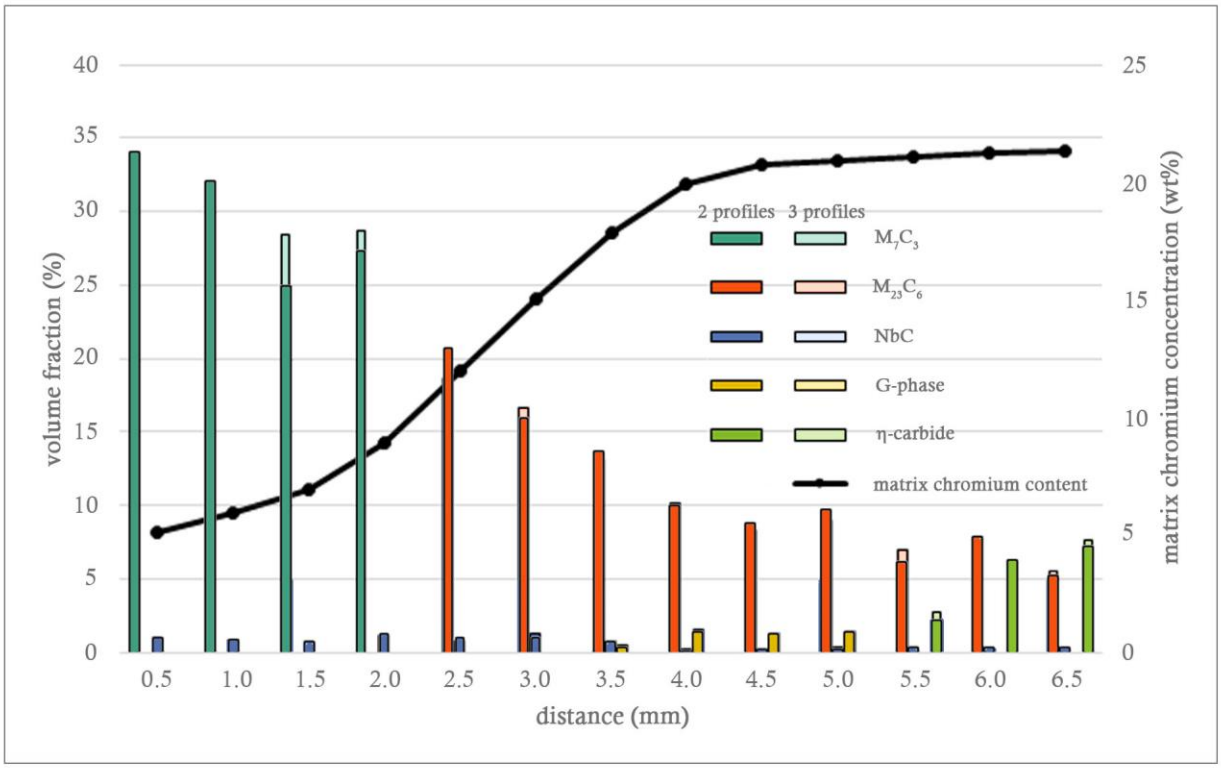

Figure 5.4 - Comparison of phase distributions for two and three averaged phase fraction profiles for sample 1A. Distance is measured from the inner diameter.

5.1.4 Creep Sample Microstructures

Due to the microstructure of the gauge length of the creep samples being unable to be observed prior to testing, it was necessary to determine if the microstructure of the material directly adjacent to the creep sample midsections was representative of the samples themselves. In order to do so, two metallographic samples were analysed – one from either side of a creep sample midsection – and the

results of both the phase distributions and the matrix chromium concentration compared. As shown in Figure 5.5, the maximum difference in area fraction for any phase was 5%. Again, this may be due to segmentation errors, but may also be a result of the inherent variability in the microstructure. The differences in the matrix chromium concentration profiles were near indistinguishable, and thus only one matrix chromium concentration profile has been presented. As the gauge length of the creep sample would be located in between the two metallographic samples, it was thus concluded that the material directly adjacent to the creep sample midsection was representative of the creep sample microstructure, and from this point forward only one metallographic sample was analysed for each creep sample location.

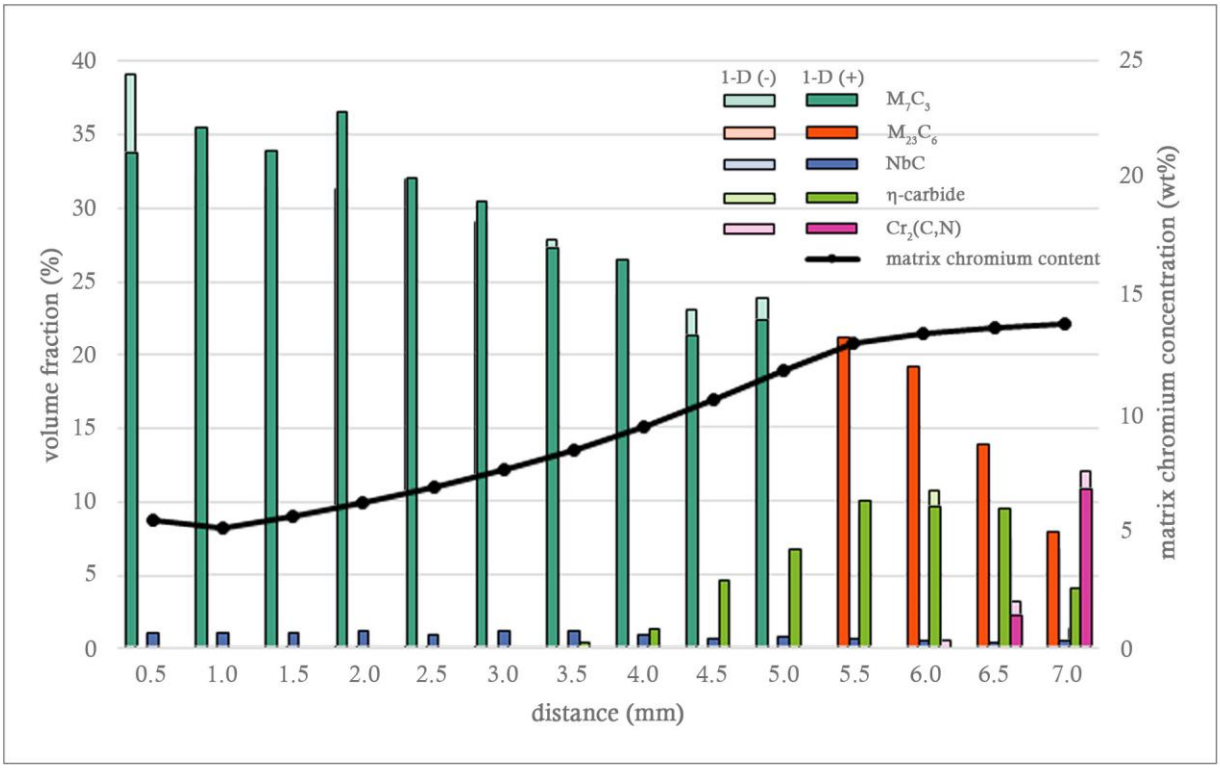

Figure 5.5 - Comparison of phase distributions for metallographic samples located either side of a creep sample mid-section for samples 1D (-) and 1D (+). Distance is measured from the inner diameter.

5.1.5 Noise Removal

The EDS maps with SEI underlay contained a reasonable amount of noise across the individual phase regions as a result of slight compositional variations, and the pixelated nature of map data. In addition, the edges of the phase regions were not always clear cut and precise, making labelling of edges when training the ilastik classifier difficult in some cases. Two edge-retaining, noise-smoothing filters were investigated, with the aim of removing noise from the image as a whole as well as smoothing edges without shifting them. ilastik has the option to display "uncertainty maps", whereby an overlay is provided of the regions in which ilastik is unsure of the classification. Therefore, a comparison between the two different filters on the segmentation in ilastik was made.

The hybrid median filter is an extension of the median filter, which is based upon moving a window (typically square) over an image and computing the output pixel as the median value of the pixels within the input window. The hybrid median filter preserves edges better than the typical square-input median filter, as the spatial directions are separately ranked. As demonstrated in Figure 5.6 for a 3x3 hybrid median filter, the median value of the horizontal and vertical pixels is calculated, the median value of the diagonal pixels is calculated, and the filtered output pixel is the median of the two median values and the value of the central pixel.

The second edge retention filter that was considered was the Kuwahara filter. The input window of the Kuwahara filter is split into four regions around the central pixel, as shown in Figure 5.7. In each of the four regions, the mean value and the variance are calculated. The filtered output pixel is the mean value of the region that has the smallest variance.

In order to compare the two filters, three EDS maps were filtered (using the same size filtering elements) and then segmented in ilastik, with the same maps used for each filter. Care was taken to ensure that the labels applied to the images during training of the classifier were as similar as possible. Although there were no significant differences in the uncertainty maps in ilastik by which to make a decision, the Kuwahara filter was seen to offer greater operator confidence when labelling edges, and thus the Kuwahara filter was chosen.

The effect of different filter sizes was compared, in order to choose the filter size that offered the best reduction in noise and smoothing of edges without removing necessary detail. The same EDS maps were filtered then segmented in ilastik, using 3x3, 5x5, 7x7, and 9x9 Kuwahara filters. The 5x5 filter was seen to offer the best balance between edge retention and loss in detail. The smaller filter did not make a significant difference in the smoothness of edges, and the larger filters resulted in significant detail being lost, particularly in small phase regions such as the niobium carbides.

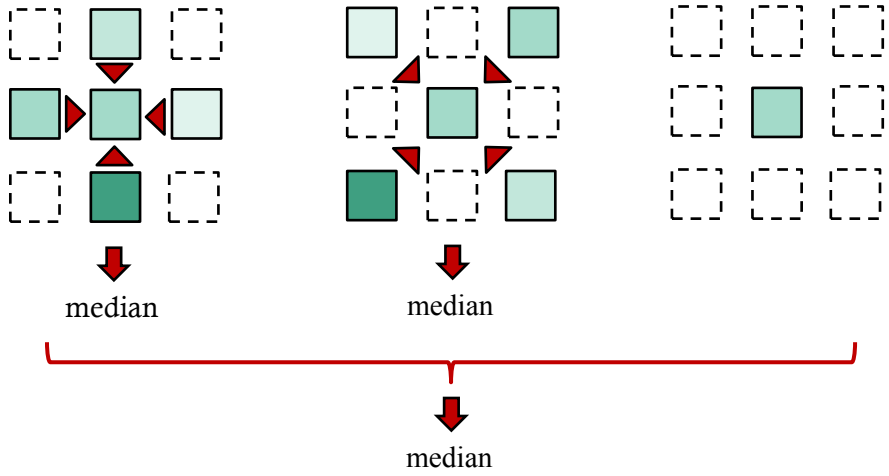

Figure 5.6 - Schematic of a 3x3 hybrid median filter.

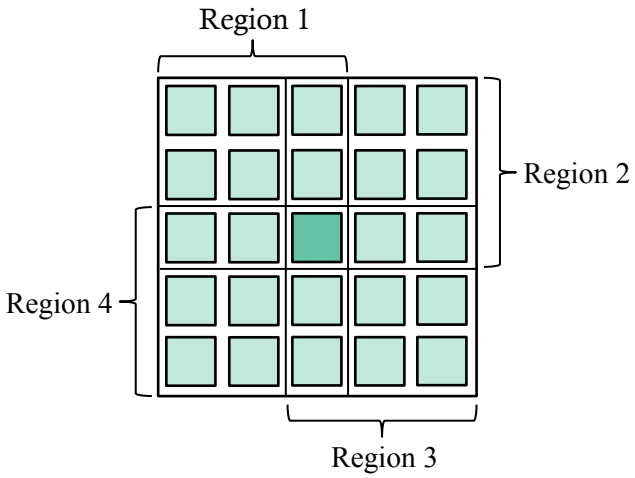

Figure 5.7 - Schematic of a 5x5 Kuwahara filter.

5.1.6 Calculation of Segmentation Errors

As previously mentioned, ilastik has the option to display "uncertainty maps" in order to identify regions where ilastik is unsure of the classification. However, the uncertainty map is given for the image as a whole and is unable to be broken down by class, thus the uncertainty or error in segmentation for each individual class (in this case, each phase) is unable to be calculated. It was observed that the uncertainties in segmentation in ilastik were typically concentrated on the interfaces between phases. With the Kuwahara filter applied, operator confidence in labelling edges was increased in comparison to the un-filtered images; however, there was still some operator uncertainty.

The uncertainty along the interfaces between phases can differ. As demonstrated in Figure 5.8 the interfaces between the three phases can be labelled – e.g. the interface between phase A and phase B has a length of $L_{A\text{-}B}$, the interface between phase A and phase C has a length $L_{A\text{-}C}$, and the interface between phase B and phase C has a length $L_{B\text{-}C}$. The width of the uncertainty along the different

interfaces may differ, e.g. the uncertainty in defining the edge along interface $L_{A\text{-}B}$ may be greater than the uncertainty defining the edge along the interface $L_{A\text{-}C}$. This was particularly visible in the EDS maps where incomplete phase transformations were observed. For example, in regions where the NbC or (Nb,Ti)C carbides had incompletely transformed to η-carbide, the interface between the NbC or (Nb,Ti)C carbides and the η-carbide was much more diffuse than the interfaces between the NbC, (Nb,Ti)C, or η-carbide with the surrounding austenite matrix.

If the width of the uncertainty is known (in pixels or microns), then, using FIJI, the binary image of the phase can first be dilated by the known width, and the difference between the dilated image and the original image calculated. The binary image can then be eroded by that same set width, and the difference in area between the eroded image and the original image can be calculated. The difference in dilation can then be set at the upper bound of the phase fraction and the difference in erosion can be set as the lower bound of the phase fraction. Dilation and erosion are binary functions, and thus require binary images. As such, the total phase interface is dilated and eroded by the same amount, rather than separate lengths of the interface having different dilation/erosion values – i.e. for phase A, $L_A = L_{A\text{-}B} + L_{A\text{-}C}$ is subject to the same amount of dilation and erosion, as opposed to having different dilation and erosion factors for $L_{A\text{-}B}$ and $L_{A\text{-}C}$. Therefore, in order to use dilation and erosion processes to calculate a measure of uncertainty in the phase fractions, the assumption needs to be made that the uncertainty is consistent along all interfaces, i.e. the uncertainty along $L_{A\text{-}B}$ is assumed to be the same as the uncertainty along $L_{A\text{-}C}$.

A purpose-built function was written in FIJI using dilation and erosion to calculate a measure of uncertainty in the phase fractions. An approximate level of uncertainty was determined based on operator confidence in labelling edges and the uncertainty maps displayed in ilastik, and a constant level of dilation and erosion was applied across all interfaces. A value of ±1 pixel was chosen as the error value for the dilation and erosion processes, as a 2 pixel width in the uncertainty map was typical of the precipitate – matrix interfaces, which constituted the majority of the interfaces. A 2 pixel width is likely a slight underestimation of the error along some precipitate – precipitate interfaces, in particular those interfaces between the niobium-rich carbides and the η-carbide, but these interfaces constituted a less significant proportion of the total interface length.

A number of other methods for calculating a measure of uncertainty were considered and discarded. Those methods based on equivalent circle radii or shape factors were considered inaccurate due to the large deviations from circular precipitates observed across the tube microstructures. In addition, due to the coarseness of the microstructures, precipitates were often observed to extend beyond the field of view, and thus calculating uncertainties based upon precipitate size or relative lengths of interfaces was not deemed feasible.

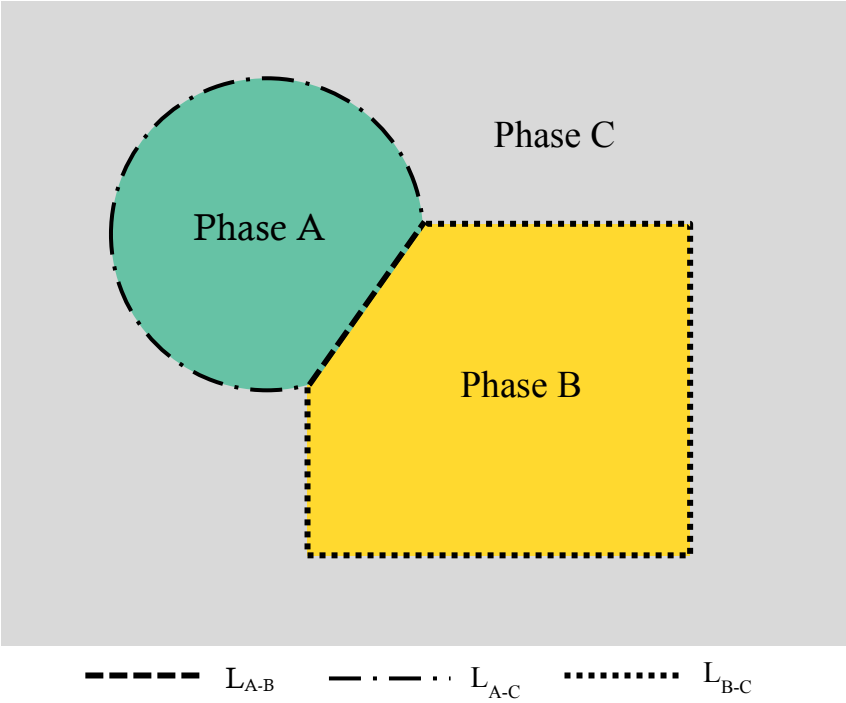

Figure 5.8 - Schematic demonstrating the interfaces between three phases, A, B, and C, with interface lengths L_{A-B}, L_{A-C}, and L_{B-C}.

The amount and way that an object grows or shrinks as a result of a dilation or erosion process depends on the structuring element used. The two most common structuring elements are the four- and eight-connected sets, N_4 and N_8, shown in Figure 5.9. When performing a dilation process, the background pixels of the image are considered in turn. The structural element is centered on a background pixel, and if at least one pixel in the structural element coincides with a foreground pixel then the center pixel is set to the foreground value. If all the pixels that coincide with the structural element are background pixels, then the pixel remains as the background value. When using a 3x3 N_8 structural element, the effect of dilation is to set any background pixel that has a neighboring foreground pixel to the foreground value. Such pixels must lie at the edges of the foreground regions, and thus the result is that the foreground regions grow by one pixel (and holes inside foreground regions shrink by one pixel). Thus, a 3x3 N_8 structural element was chosen for the dilation and erosion operations. Dilation and erosion processes can be stacked – e.g. several dilations by one pixel can be completed in order to give a total dilation of several pixels. Erosion is the dual of dilation, i.e. the dilation of an object is equivalent to the erosion of the background, and the erosion of an object is equivalent to the dilation of the background, and therefore the same process applies to erosion operations.

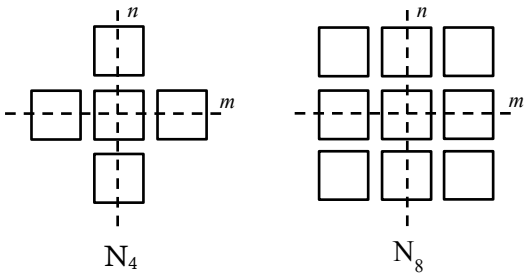

Figure 5.9 - The standard square N_4 and N_8 structuring elements, where n and m represent the dimensions of the element.

5.1.7 Measurement of Secondary Precipitate Distributions

As described in Chapter 4, all six of the ex-service tubes displayed distributions of secondary precipitates in some, if not all, of the samples analysed. In tube 3, the secondary precipitates were in the form of thin platelet σ-phase precipitates that appeared to be distributed evenly in the matrix. The secondary σ-phase platelets were typically several μm in length, but less than 1 μm wide. In tubes 1, 2, 4, 5, and 6 the secondary precipitates were in the form of small cuboidal $M_{23}C_6$ carbides, located adjacent to the primary carbide network. The size of the secondary $M_{23}C_6$ carbides varied between the tubes. In tubes with a low level of carbide coarsening (e.g. tube 4) the secondary $M_{23}C_6$ carbides were typically only a few microns wide in their largest dimension. However, even in samples from tubes with a high degree of carbide coarsening (e.g. tube 1) the largest secondary precipitates were typically only on the order of 5 μm wide in their largest dimension.

Due to the small size of the secondary precipitates, there were significant issues in representing the secondary precipitate distributions in binary form. In general, the binary representation of the secondary precipitates did not accurately represent the morphology that was observed in the electron images, both for the secondary cuboidal $M_{23}C_6$ carbides and the secondary platelet σ-phase precipitates. As well as inaccurate representation of shape, additional artefacts were introduced during segmentation of the secondary distributions. Such artefacts included under- or over-estimation of the size of the secondary precipitates, the fragmentation of individual precipitates into multiple separate precipitates in binary form, and the coalescence of individual precipitates into a single precipitate in binary form. As such, significant portions of the secondary precipitate distributions in all tubes could not be accurately captured using image analysis. Additionally, previous attempts to characterize secondary precipitate distributions in aged HP-Nb and HP-NbTi alloys by Buchanan [4] demonstrated that the exact location and distribution of the secondary precipitates with respect to the grain and dendrite boundaries can vary significantly, and that two-dimensional characterization may not necessarily be representative of the secondary distribution.

Attempted segmentation and binarisation of the secondary precipitate distributions, subsequently followed by measurement of area fractions, indicated that, despite the significant errors involved in the process, the secondary precipitate distributions likely make up < 2 % of the total volume fraction, across all samples from all tubes. For this reason, neglecting the influence of the secondary precipitates when comparing precipitate volume fractions with the matrix chromium content and the eddy current NDT response of the tubes is unlikely to greatly influence the outcome of the comparison. However, the influence of the secondary precipitate distributions is unable to be neglected when comparing the mechanical properties. The secondary carbide distribution is reported to restrict dislocation motion, and their location adjacent to the primary grain boundary network is believed to inhibit the creep deformation that is also typically concentrated in this area [5-7]. Unfortunately in this case only qualitative descriptions of the secondary precipitate distributions can be offered, as quantitative measurement using ilastik and FIJI has proven inaccurate with the current data.

5.1.8 Measurement of Matrix Composition

The composition of the austenite matrix and the changes in matrix composition across the tube walls are of interest, as it is the matrix composition that determines the bulk magnetic properties of the tube. In the as-cast condition, the austenite matrix of Fe-Cr-Ni alloys is paramagnetic at room temperature. The precipitation and growth of chromium-rich carbides results in chromium being depleted from the matrix, and the composition progressively shifts towards the binary Fe-Ni composition. Below a critical chromium content the austenite matrix shifts from being paramagnetic to being ferromagnetic at room temperature. With continued chromium depletion the amount of ferromagnetic matrix material and its relative magnetic permeability increases.

Work by Stevens *et al*. [8, 9] using magnetic force microscopy (MFM) has shown that the matrix directly adjacent to the carbides first becomes ferromagnetic, with matrix material further from the carbides becoming ferromagnetic as chromium depletion progresses. It would thus be expected that the chromium content of the matrix would be most depleted adjacent to the carbide, with increasing chromium content as distance from the carbide increased. However, as the eddy current NDT system indirectly measures the changes in the bulk magnetic permeability of the tube section, measurement of changes in the matrix chromium content on such a fine scale would not be of use when comparing the chromium content with the magnetic response. Of more interest is the change in the average or bulk matrix composition across the tube wall. As such, at each wall location that was mapped for image analysis, EDS spectra were re-constructed from the EDS map data over the largest matrix areas between the carbides, in order to obtain a measurement of the bulk composition. Care was taken to avoid capturing any secondary precipitates in the EDS area reconstruction, which could skew the composition measurement.

5.2 Phase Fractions and Phase Distributions

The phase distributions, matrix chromium content, and representative EDS maps of the microstructure are presented in Sections 5.2.1 through 5.2.6 for each sample from each of the six ex-service tubes.

The volume fractions of the MnS inclusions identified in the ex-service tubes are omitted from the results shown here. As discussed in Section 4.5.1, the morphologies exhibited by these inclusions was consistent with the Type I (globular) morphology described for MnS inclusions in cast plain carbon steels, which attain a globular morphology due to precipitating as liquid globules during casting when oxygen is present in the melt [10, 11]. Buchanan identified MnS inclusions with the same morphology in as-cast HP-Nb and HP-NbTi alloys, and observed that these inclusions remained stable with ageing. After ageing at 1000 – 1100 °C for up to 10,000 hours, the number, average size, and area fraction of the MnS inclusions were observed to remain constant [4]. The area fraction of MnS inclusions in the six ex-service tubes analysed in the current project was typically observed to remain below 1 % in all locations where they were present, and due to the likelihood of the volume fraction having remained constant during service, the impact on the microstructure in comparison to the other phases present was likely insignificant.

5.2.1 Tube 1

As described in Section 4.5.1, the microstructure of all samples from tube 1 was significantly coarsened in comparison to the typical as-cast microstructure of an HP-Nb alloy, and a number of phase transformations were observed to have occurred.

Chromium Carbides and Carbonitrides

Two chromium-rich carbides, M_7C_3 and $M_{23}C_6$, composed the majority of the primary precipitate network in all four samples from tube 1. $M_{23}C_6$ was located at the mid to outer wall regions of the samples, and M_7C_3 at the inner wall. The maximum chromium carbide volume fraction typically occurred within the 0.5mm wall region (M_7C_3 = 31 – 34 %). The chromium carbide volume fraction at the $M_{23}C_6$-to-M_7C_3 transformation front was in the range of 20 – 25 %, and this decreased progressively towards the outer wall. The minimum chromium carbide volume fraction occurred within the outer 0.5 mm of the wall thickness for all samples ($M_{23}C_6$ = 5 – 8 %). However, the distance from the inner diameter to the $M_{23}C_6$-to-M_7C_3 transformation front differed for each sample, as summarized in Table 5.1, as did the rate at which the chromium carbide volume fraction decreased with increased distance from the inner diameter. A comparison between the primary chromium carbide volume fractions in samples 1A-D is shown in Figure 5.10.

The shortest distance from the inner diameter to the $M_{23}C_6$-to-M_7C_3 transformation front was 1.25 mm, observed in sample 1B. This sample also displayed the smallest degree of chromium carbide

coarsening. This was evident both qualitatively (in the EDS map of the microstructure) and quantitatively (in the measurement of carbide volume fractions). The volume fraction of chromium carbides dropped rapidly from approximately 32 % within the 0.5 mm wall region, to below 10 % by the 2.5 mm wall region. The chromium carbide volume fraction remained in the range of 6 – 8 % for the remainder of the wall thickness.

The $M_{23}C_6$-to-M_7C_3 transformation front was located a distance of 2.3 mm from the inner diameter in sample 1A, and a distance of 3.0 mm from the inner diameter in sample 1C. The chromium carbide volume fraction in both sample 1A and 1C decreased from 32 - 34% at the 0.5 mm wall region to 20 – 25 % at the $M_{23}C_3$-to-M_7C_3 carbide transformation front; however, as the transformation front was located at a greater distance into the tube wall in sample 1C than in sample 1A, sample 1C displayed a chromium carbide volume fraction above 25 % over a greater wall thickness. In sample 1A the chromium carbide volume fraction continued to decrease across the outer wall, dropping to a value of $M_{23}C_6 \approx 5$ % within the outer 0.5 mm. The chromium carbide volume fraction in sample 1C was also observed to decrease across the outer wall, although not to the same extent as sample 1A, reaching a value of $M_{23}C_6 \approx 7$ % within the outer 0.5 mm. Qualitatively, the greater extent of carbide coarsening in sample 1C compared to 1A is evident when comparing the EDS maps presented in Figure 5.11 and Figure 5.15.

The greatest distance from the inner diameter to the $M_{23}C_6$-to-M_7C_3 transformation front was observed in sample 1D, and this sample also displayed the greatest level of carbide coarsening of all the samples from tube 1. The distance from the inner diameter to the $M_{23}C_6$-to-M_7C_3 transformation front was 5.4 mm, and the volume fraction of M_7C_3 carbides remained above 30 % within the 0 – 3.0 mm wall region, and decreased from 30 % to approximately 22 % within the 3.0 – 5.4 mm wall region. After the transformation front, the chromium carbide volume fraction dropped rapidly to a value of $M_{23}C_6 \approx 8$ % within the outer 0.5 mm. The $Cr_2(C,N)$ carbonitride was present within the outer 1.0 mm of the wall of sample 1D, where it was observed to have transformed from the $M_{23}C_6$ carbides in the primary precipitate network, as well as precipitated intragranularly in the form of lathe-shaped precipitates, as shown in Figure 5.17 (c). The volume fraction of $Cr_2(C,N)$ increased with increased proximity to the outer diameter at the expense of the volume fraction of $M_{23}C_6$ precipitates.

Secondary $M_{23}C_6$ precipitates were observed in the mid and outer wall regions of samples 1A, 1B, and 1C. No secondary precipitates were observed in sample 1D. A summary of the secondary precipitate distributions is given in Table 5.2. As discussed in Section 5.1.7, quantitative measurement of secondary precipitate size and number was not possible; however, it was evident that the secondary distribution of secondary $M_{23}C_6$ was dependent on the characteristics of the primary precipitate network. No secondary $M_{23}C_6$ precipitates were identified in the regions within which M_7C_3 was present. In the wall locations where secondary $M_{23}C_6$ precipitates were present, they were observed to be larger in size and fewer in number with increased primary $M_{23}C_6$ volume fraction, to the extent

that sample 1D, which displayed the greatest extent of primary chromium carbide coarsening, did not contain any secondary $M_{23}C_6$ precipitates.

Table 5.1 - Summary of the distance from the inner wall to the $M_{23}C_6$-to-M_7C_3 transformation front for samples from tube 1.

Sample	Positions of the $M_{23}C_6$-to-M_7C_3 transformation front (mm)
1A	2.3
1B	1.25
1C	3.0
1D	5.4

Table 5.2 - Summary of the secondary $M_{23}C_6$ precipitate distributions in samples from tube 1.

Sample	Wall region in which secondary $M_{23}C_6$ is present	Description of secondary $M_{23}C_6$ distribution
1A	2.5 - 6.5 mm	Coarse (typically ≈ 2-4 μm), relatively abundant
1B	1.5 – 8.0 mm	Fine (typically ≈ 1 μm), abundant
1C	3.5 – 7.5 mm	Very coarse (typically ≥5 μm), number of individual precipitates very low
1D	NA	No secondary $M_{23}C_6$

Niobium Carbides and Silicides

The volume fraction of the NbC carbides was observed to be < 2 % at any location in all four samples from tube 1. The transformation of NbC to η-carbide was observed in all samples, and the transformation of NbC to G-phase was observed in samples 1A and 1B. A summary of the wall regions over which the NbC-to-G-phase and NbC-to-η-carbide transformations occurred in the tube 1 samples is given in Table 5.3.

The incomplete transformation of NbC to η-carbide was observed in the mid and outer wall regions of samples 1C and 1D. The volume fraction of η-carbide was typically observed to increase with increased proximity to the outer diameter. In sample 1C, the volume fraction of η-carbide increased from ≈ 1.2 % to ≈ 9.3 % over 2.5 - 7.5mm wall region. In sample 1D, an increase from ≈ 0.3 % to ≈ 9.5 % over the 3.5 – 6.5 mm wall regions was observed. The increase in the η-carbide volume fraction was accompanied by a general decrease in the volume fraction of NbC in both samples, indicating

that the NbC-to-η-carbide transformation progressed further towards completion at the outer diameter.

The incomplete transformation of NbC to G-phase at the mid wall, accompanied by the incomplete transformation of NbC to η-carbide at the outer wall, was observed in samples 1A and 1B. G-phase was present in greater quantities, and over a greater proportion of the tube wall, in sample 1B in comparison to sample 1A. In sample 1A, G-phase composed ≈ 1.5 % of the total volume within the 3.5 – 5.0 mm wall region, whereas in sample 1B the volume fraction of G-phase was ≈ 2 - 3.6 % across the 2.0 – 7.0 mm wall region. As with samples 1C and 1D, the volume fraction of η-carbide was observed to increase with increased proximity to the outer diameter in samples 1A and 1B. In sample 1A the η-carbide volume fraction increased from ≈ 2.2 % to ≈ 7.2 % over the 5.5 – 6.5 mm wall region, and in sample 1B it increased from ≈ 4.6 % to ≈ 8.0 % over the 7.5 – 8.0 mm wall region.

Table 5.3 - Summary of the locations of the NbC-to-G-phase and NbC-to-η-carbide transformations in the tube 1 samples.

Sample	Wall region over which the NbC-to-G-phase transformation was observed	Wall region over which the NbC-to-η-carbide transformation was observed
1A	3.5 – 5.0 mm	5.5 – 6.5 mm
1B	2.0 – 7.0 mm	7.5 – 8.0 mm
1C	-	2.0 – 7.5 mm
1D	-	3.5 – 7.0 mm

Matrix Chromium Concentration

The matrix chromium concentration was observed to inversely mirror the volume fraction of chromium carbides and the η-carbide in all samples. Matrix chromium concentrations well below the total as-cast value of 25 wt% were observed at the inner wall regions. The chromium concentration of the matrix at the locations of the $M_{23}C_6$-to-M_7C_3 transformation fronts was observed to be within the range of 10-13 wt% across all samples from tube 1, as shown in Figure 5.19.

Sample 1B, the least carburized of the four samples from tube 1, displayed the greatest chromium concentration in the matrix. Despite the matrix chromium concentration reaching ≈ 7.5 wt% at the inner wall, it rapidly rose to ≈ 21 - 22 wt% and remained constant at this value for the 3.5 - 8.0 mm wall region.

The matrix chromium concentration of sample 1A was ≈ 5 wt% at the inner diameter, and this increased to a value of ≈ 21 wt% by the 4.5 mm wall region. Sample 1C displayed a matrix chromium

concentration of ≈ 6.7 wt% at the inner diameter, and although the matrix chromium concentration reached ≈ 21 wt% at the outer diameter, as in sample 1A, the increase was much more gradual across the mid wall of the sample. In sample 1A an increase in matrix chromium concentration from ≈ 7wt% to ≈ 21 wt% occurred relatively rapidly over a distance of 2.5 mm. In sample 1C the same increase occurred over a distance of 7.0 mm, and greater volume fractions for both the $M_{23}C_6$ and η-carbide precipitates were observed over this distance in comparison to sample 1A.

The most highly carburized of the four samples, sample 1D, displayed the greatest extent of matrix chromium depletion. At the inner diameter, the matrix chromium concentration was as low as 5 wt%. Although this gradually increased with increased distance from the inner diameter, the maximum matrix chromium concentration achieved was only 13.8 wt% at the outer wall.

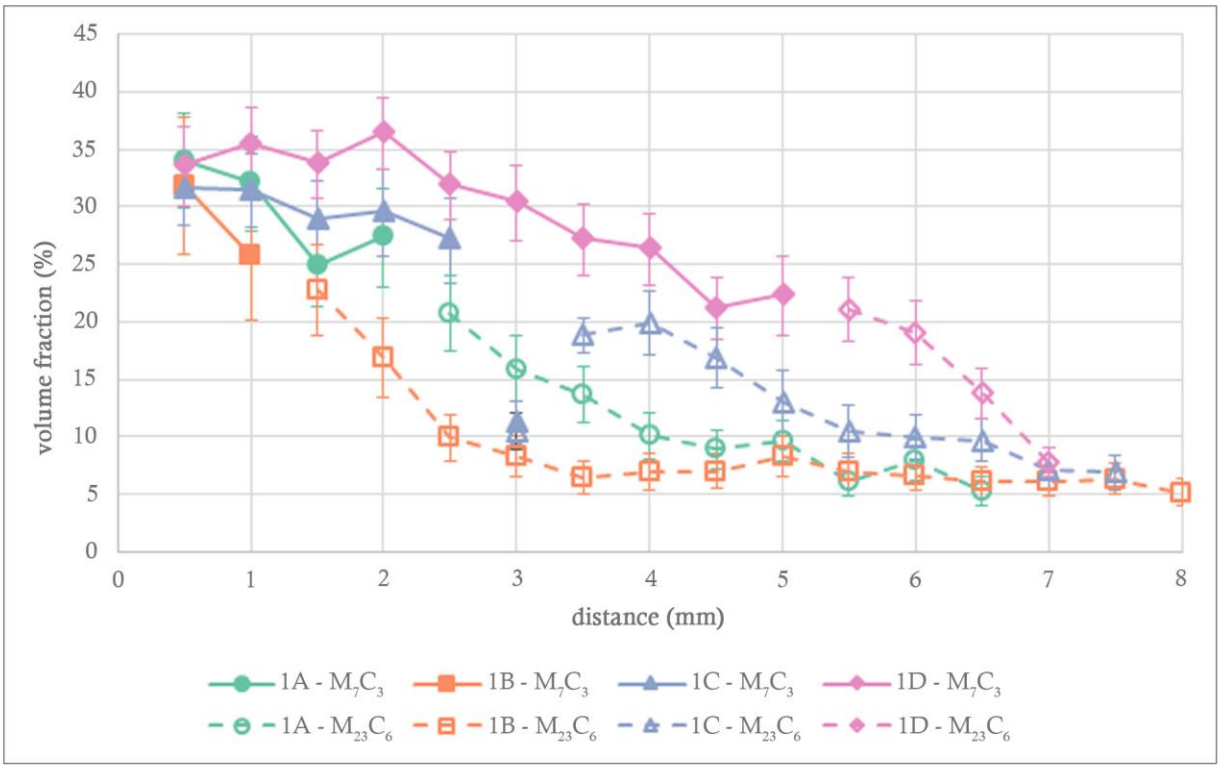

Figure 5.10 – Comparison of primary chromium carbide volume fractions in samples 1A-D. The deviation at 3.0 mm in sample 1C is due to the $M_{23}C_6$-to-M_7C_3 transformation front being located at 3.0 mm, hence both $M_{23}C_6$ and M_7C_3 are present in approximately equal quantities. Distance is measured from the inner diameter.

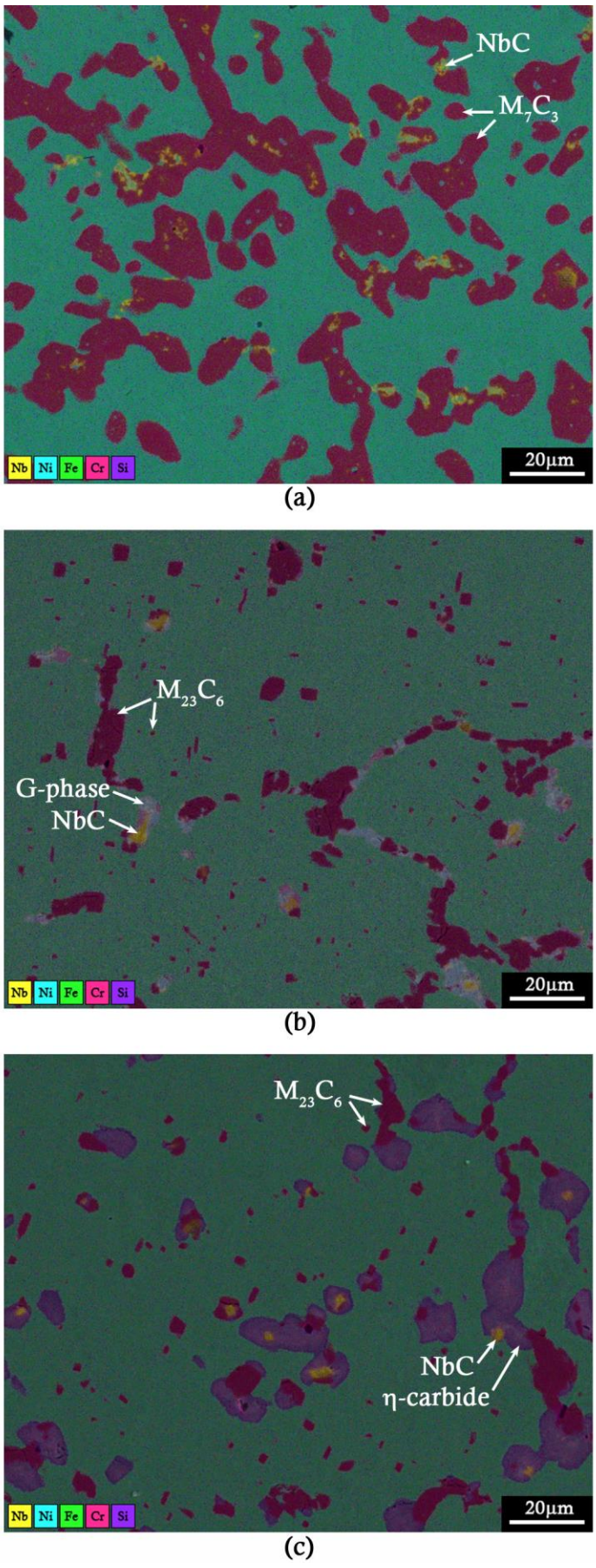

Figure 5.11 - Representative EDS maps of the microstructure in sample 1A at distances of (a) 0.5 mm, (b) 5.0 mm, and (c) 6.5 mm from the inner diameter.

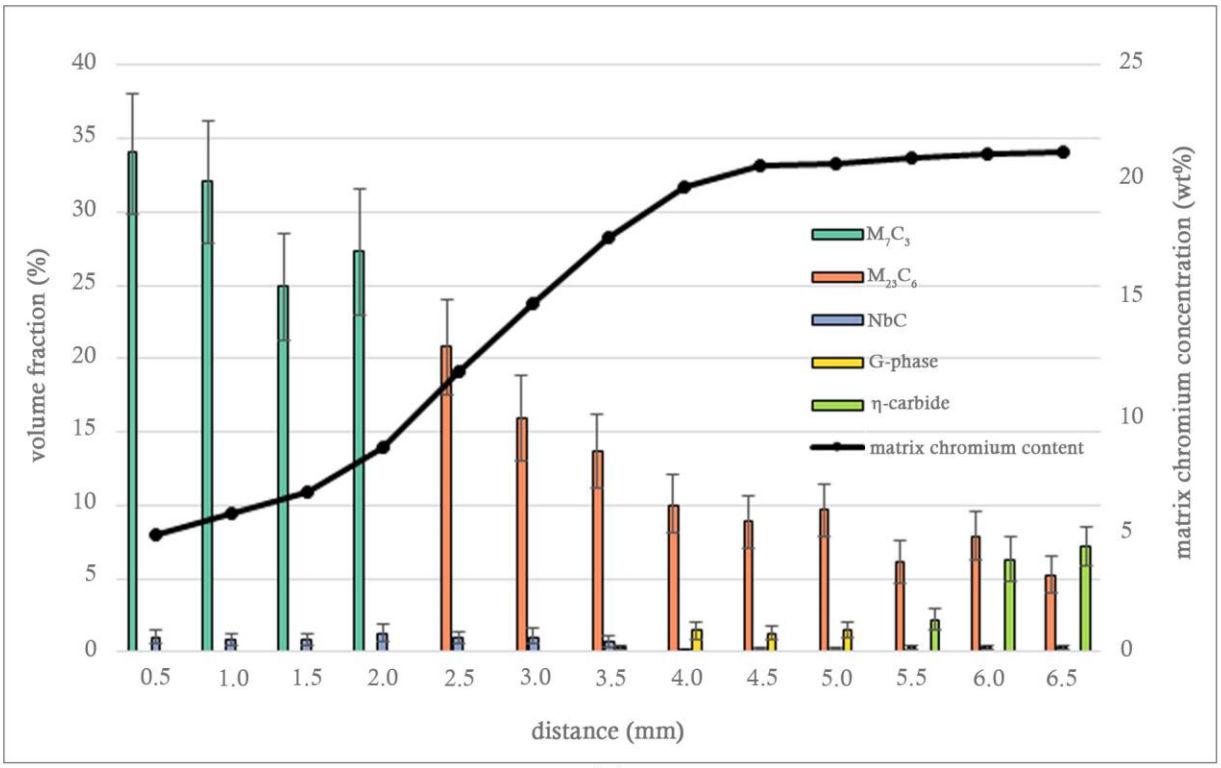

(a)

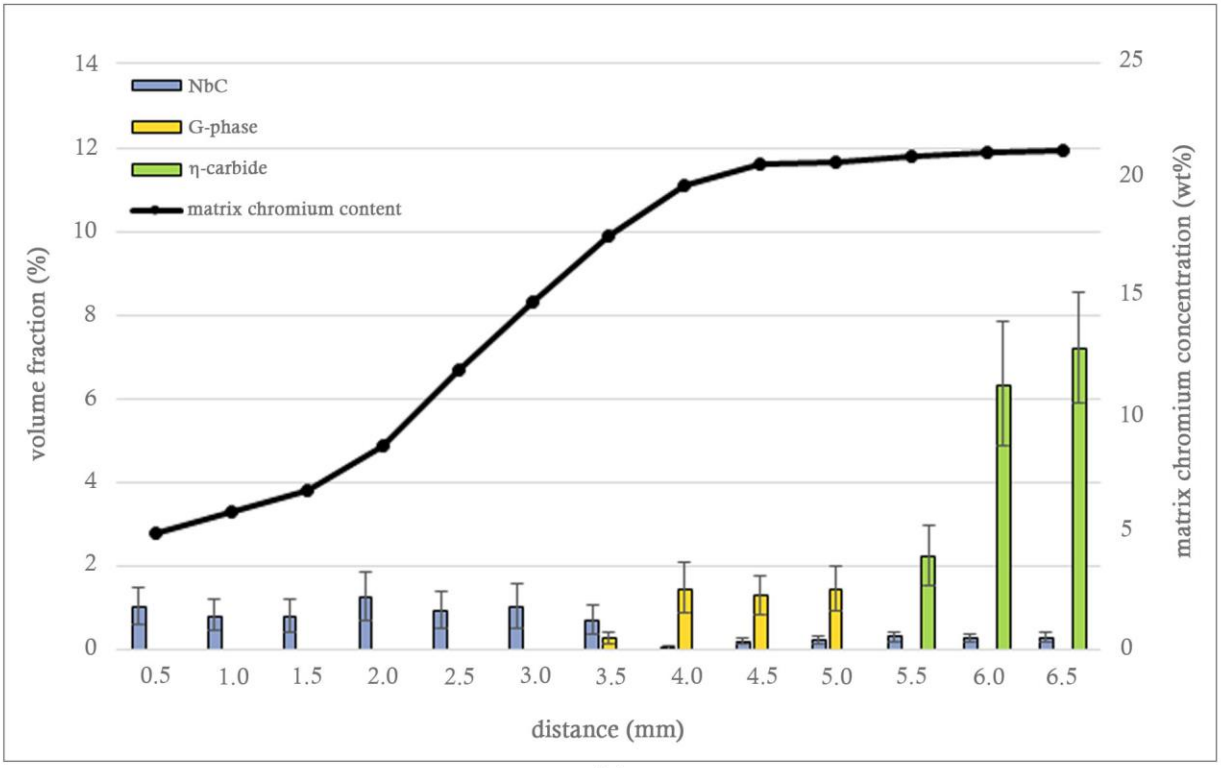

(b)

Figure 5.12 - Measured volume fractions and matrix chromium concentration in sample 1A. (a) all volume fractions, (b) minor volume fractions. Distance is measured from the inner diameter.

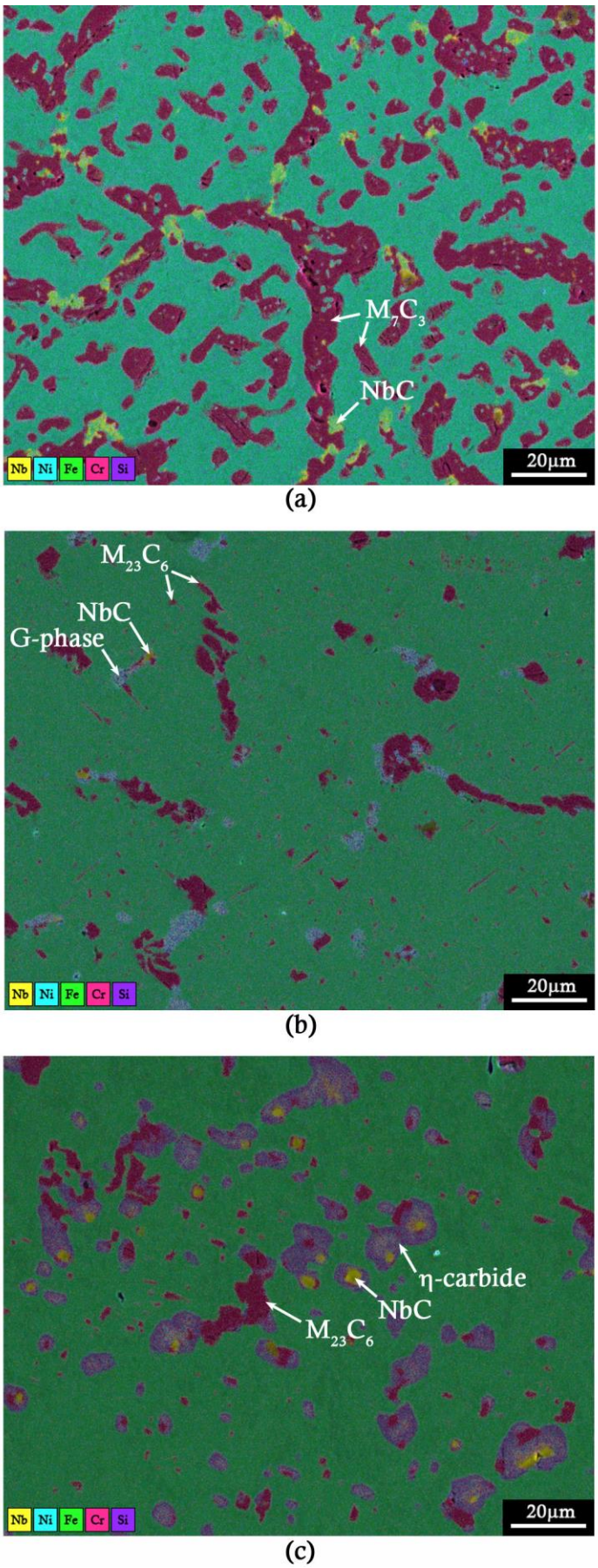

Figure 5.13 - Representative EDS maps of the microstructure in sample 1B at distances of (a) 0.5 mm, (b) 5.5 mm, and (c) 8.0 mm from the inner diameter.

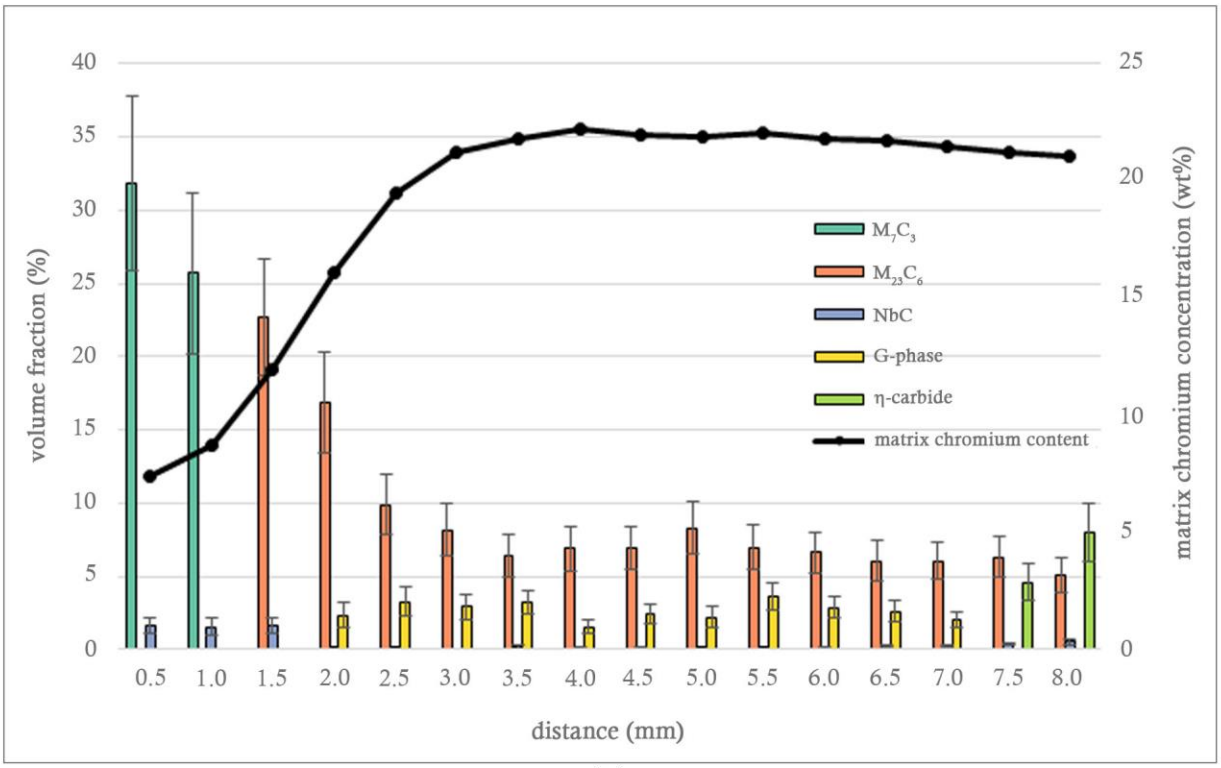

(a)

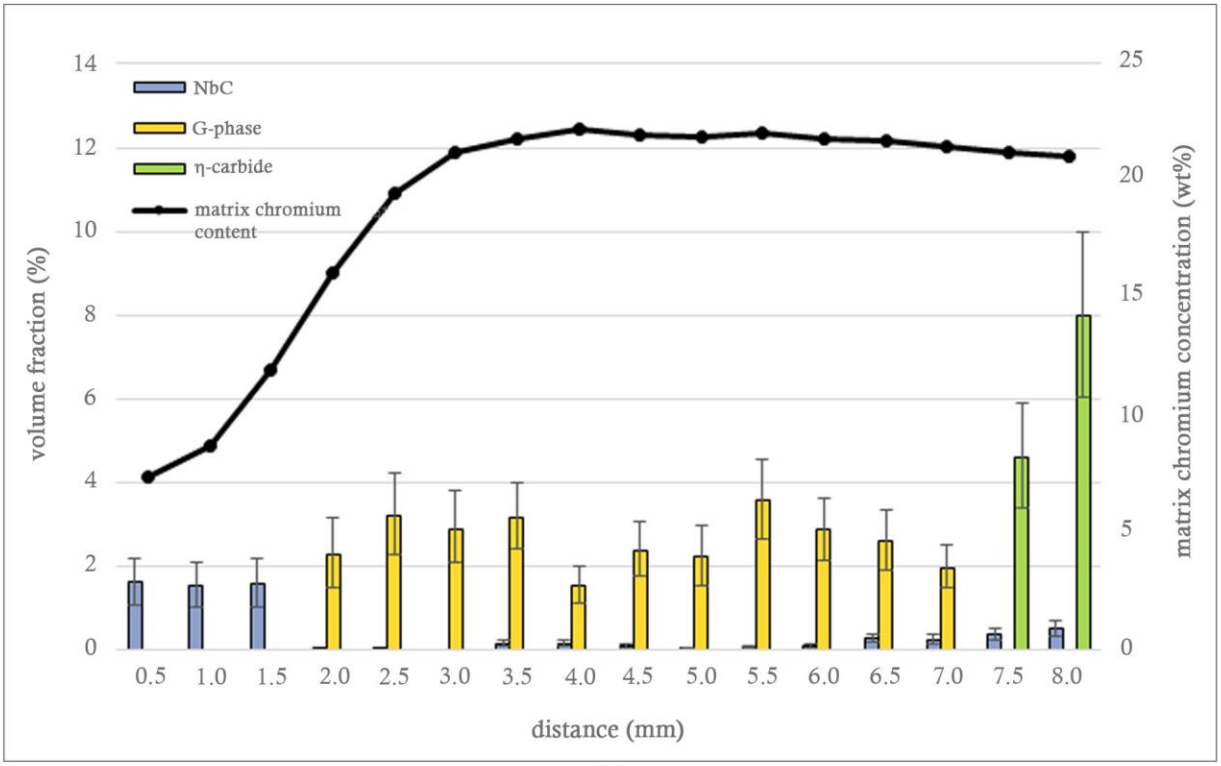

(b)

Figure 5.14 - Measured volume fractions and matrix chromium concentration in sample 1B. (a) all volume fractions, (b) minor volume fractions. Distance is measured from the inner diameter.

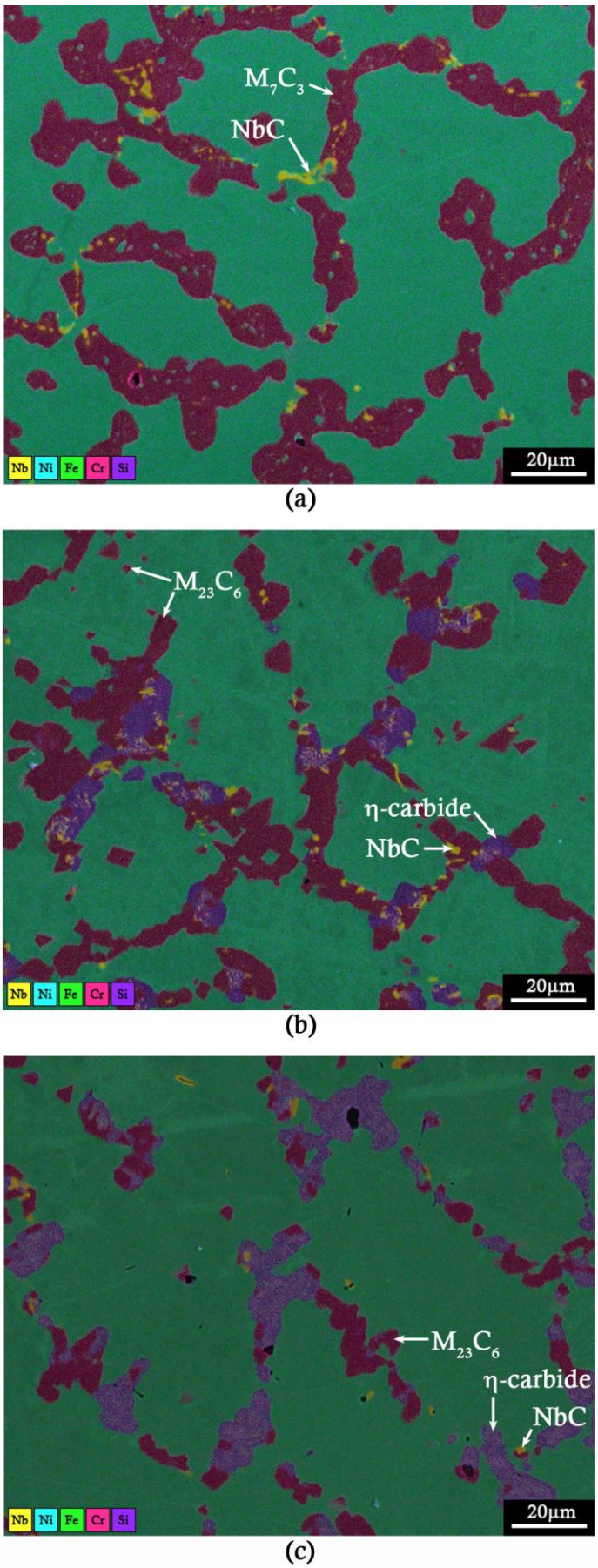

Figure 5.15 - Representative EDS maps of the microstructure in sample 1C at distances of (a) 0.5 mm, (b) 3.0 mm, and (c) 7.5 mm from the inner diameter.

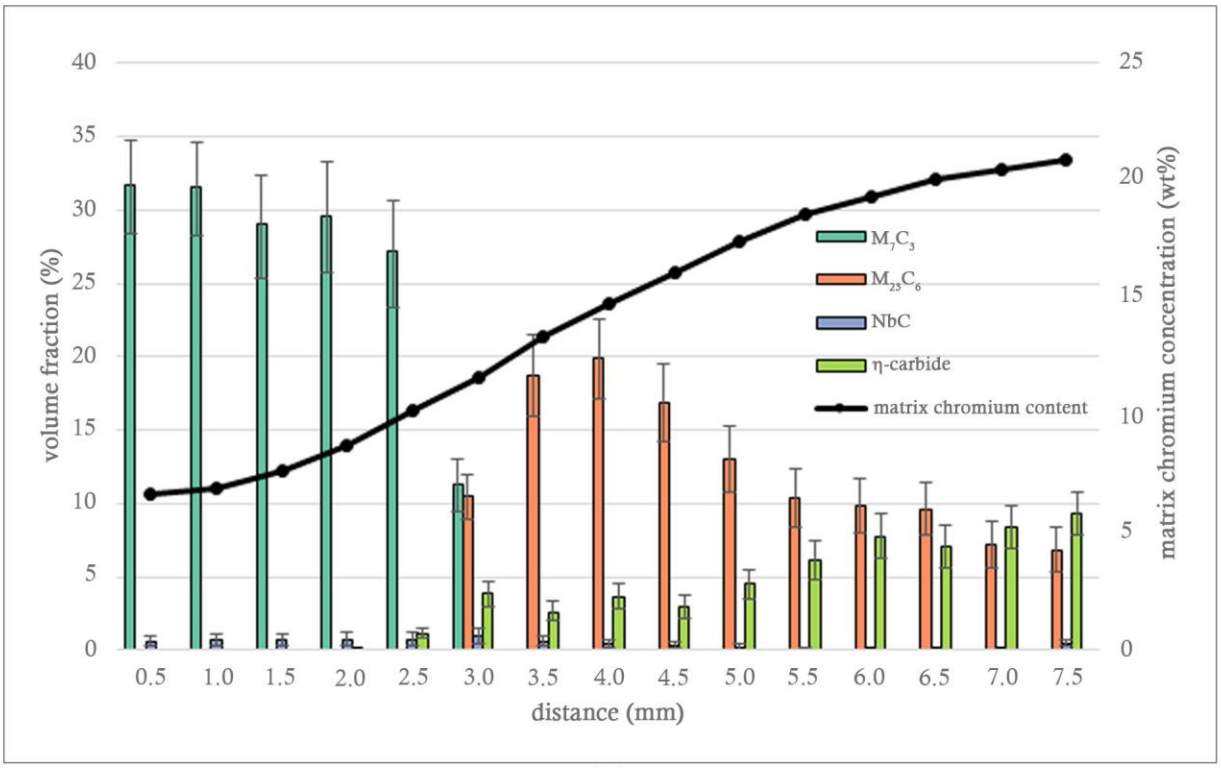

(a)

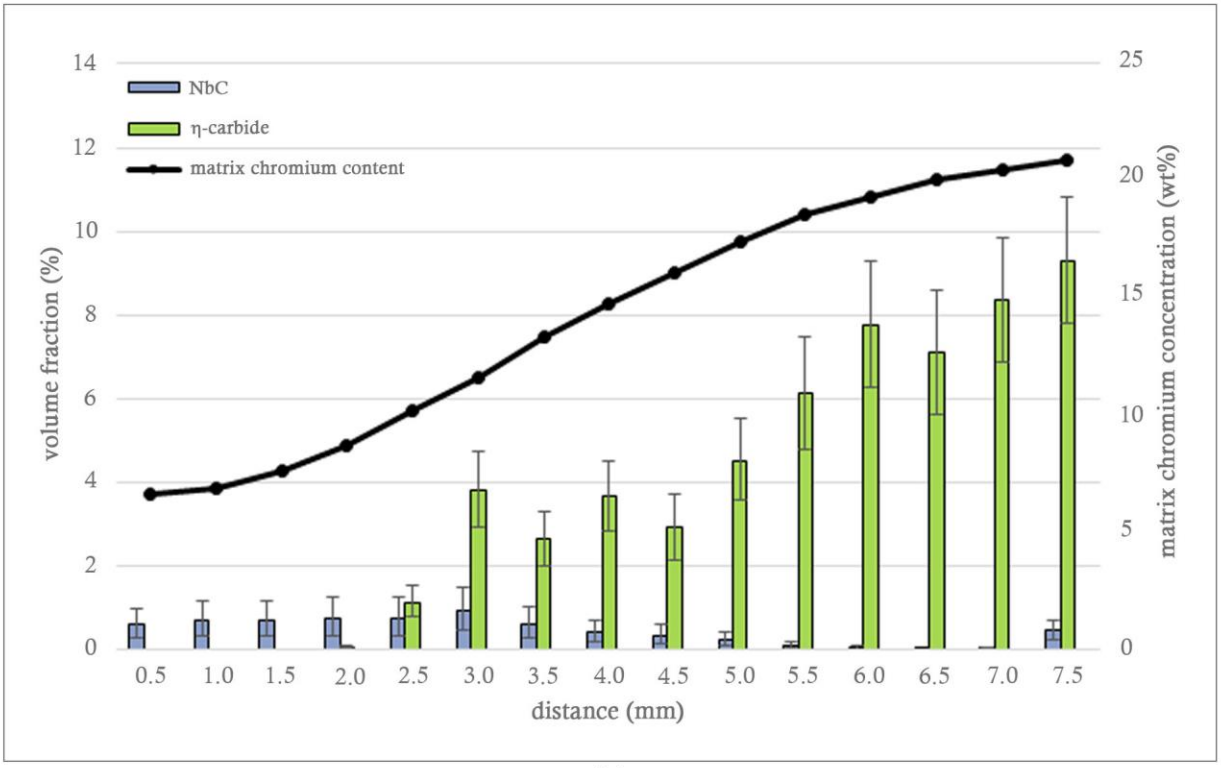

(b)

Figure 5.16 - Measured volume fractions and matrix chromium concentration in sample 1C. (a) all volume fractions, (b) minor volume fractions. Distance is measured from the inner diameter.

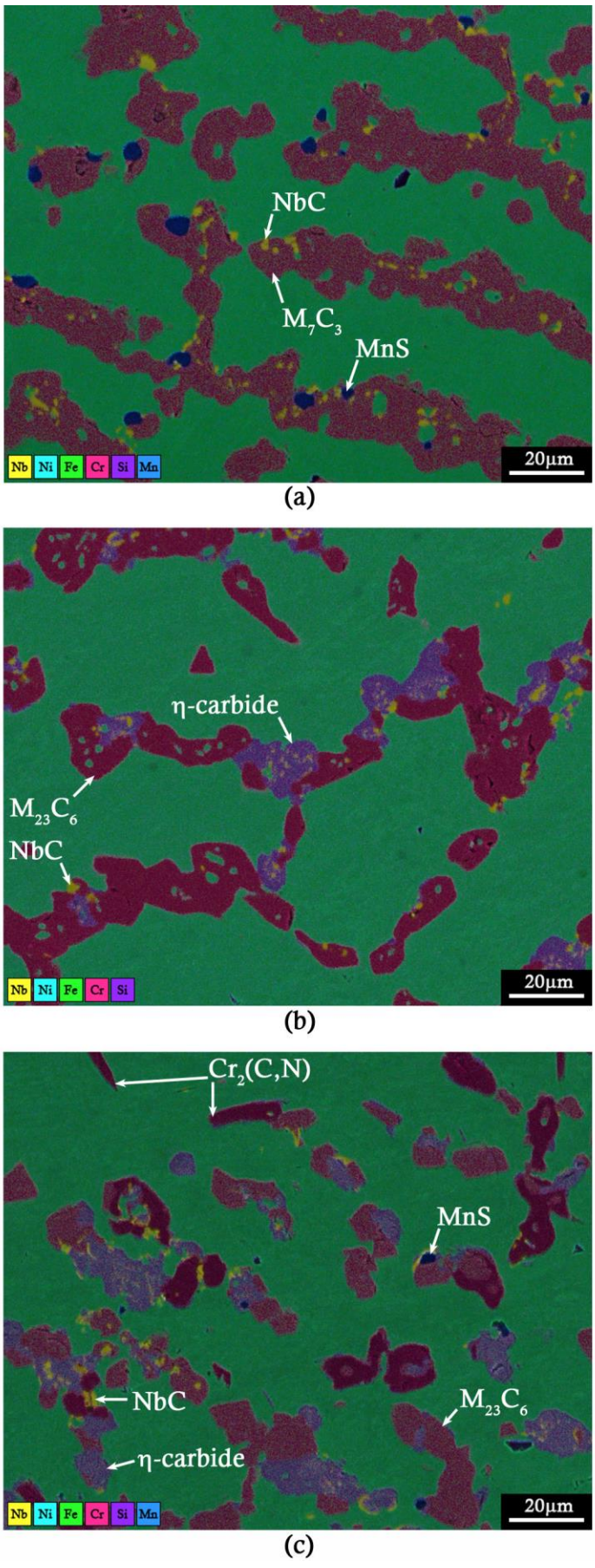

Figure 5.17 - Representative EDS maps of the microstructure in sample 1D at distances of (a) 0.5 mm, (b) 4.5 mm, and (c) 7.0 mm from the inner diameter.

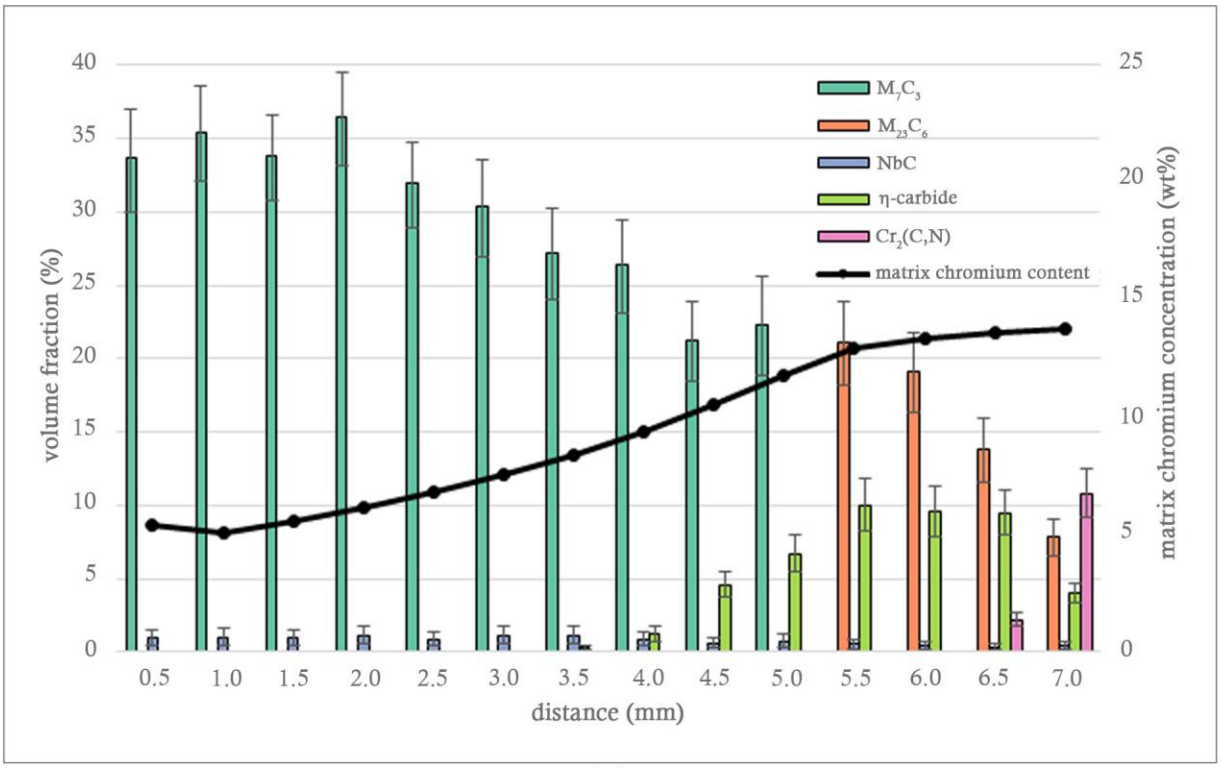

(a)

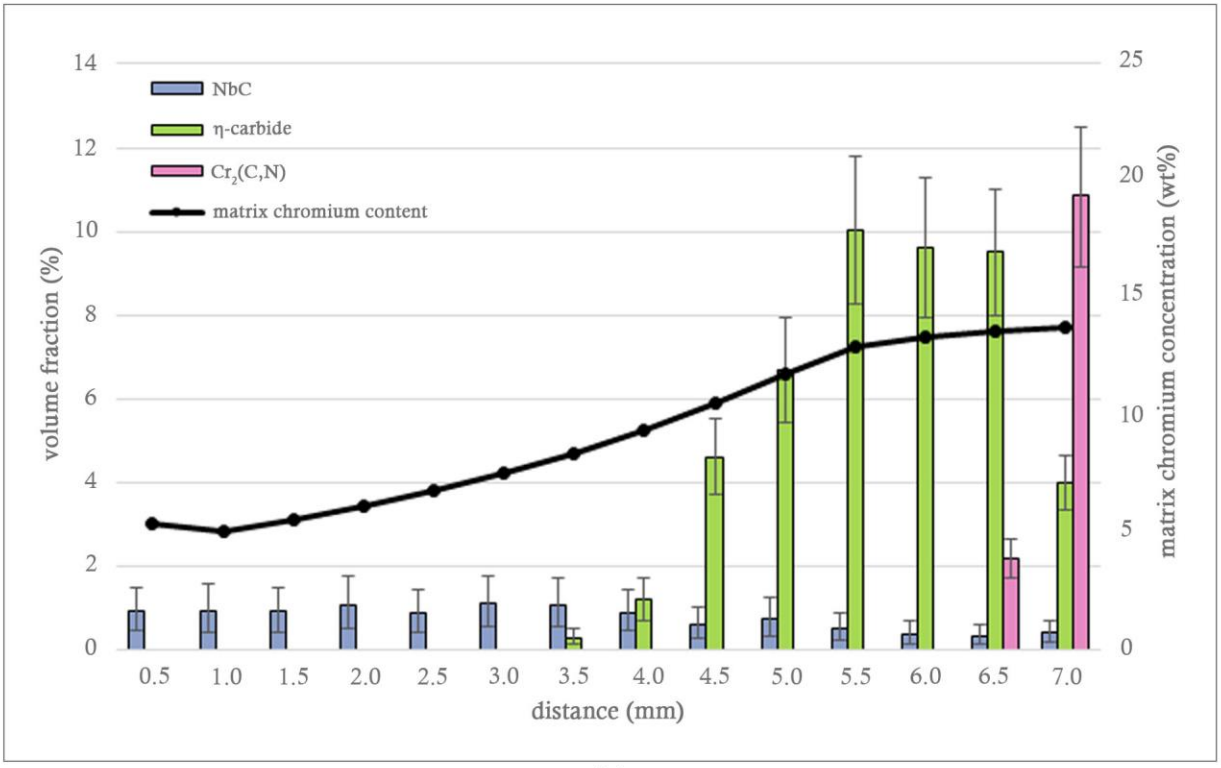

(b)

Figure 5.18 - Measured volume fractions and matrix chromium concentration in sample 1D. (a) all volume fractions, (b) minor volume fractions. Distance is measured from the inner diameter.

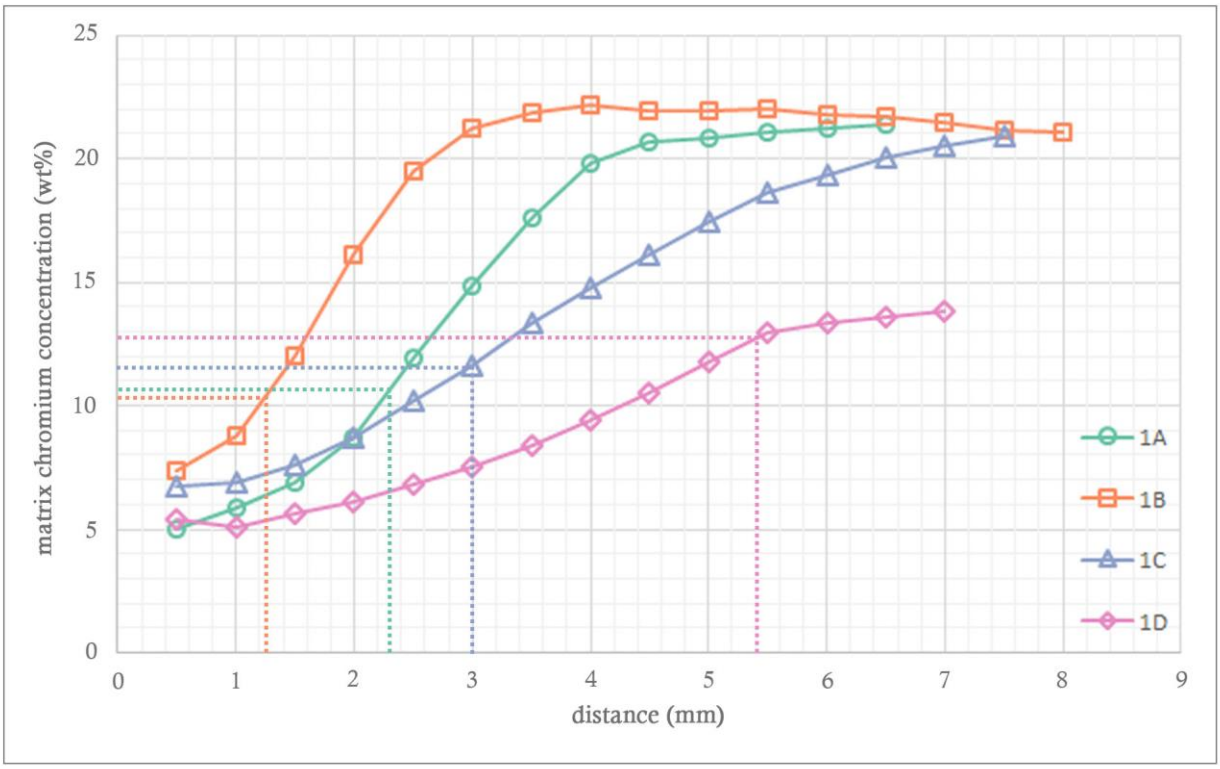

Figure 5.19 - Matrix chromium concentrations for samples 1A-D. Dashed lines indicate the positions of the $M_{23}C_6$-to-M_7C_3 transformation fronts in the corresponding colour coded sample. Distance is measured from the inner diameter.

5.2.2 Tube 2

The microstructure of tube 2 was in many respects similar to the microstructure of tube 1. All of the samples from tube 2 were observed to be significantly carburized and coarsened in comparison to the typical as-cast structure.

Chromium Carbides and Carbonitrides

As with tube 1, the majority of the primary precipitate network in tube 2 was composed of $M_{23}C_6$ (outer wall) and M_7C_3 (inner wall) chromium carbides. The microstructure of tube 2 appeared consistent across all four samples analysed. This was evident both qualitatively, by comparing the microstructures shown in the EDS maps, and quantitatively, by comparing the measured precipitate volume fractions. The $M_{23}C_6$-to-M_7C_3 transformation front occurred within the 2.0 – 3.0mm wall region in all samples, as summarized in Table 5.4. The maximum chromium carbide volume fraction occurred at the inner diameter of all samples, with the volume fraction of M_7C_3 carbides in the 0.5 – 1.0 mm wall regions in the range of 34 – 37 %. In all samples the chromium carbide volume fraction at the $M_{23}C_6$-to-M_7C_3 transformation front dropped to a value of approximately 25 %, and continued to gradually decrease towards the outer wall, reaching a value of $M_{23}C_6 \approx 13 – 17$ % by the 6.0 mm wall region. A comparison between the volume fractions of the primary chromium carbides for samples 2A-D is shown in Figure 5.20.

The volume fraction of $M_{23}C_6$ in the 6.5 mm wall regions was found to differ between samples. This coincided with a significant increase in the volume fraction of $Cr_2(C,N)$ in the same region. Small amounts of $Cr_2(C,N)$ precipitates (< 2 %) were observed to have transformed from the primary $M_{23}C_6$ precipitates in the wall regions between the $M_{23}C_6$-to-M_7C_3 transformation front and the outer diameter in all four samples; however, the greatest volume fractions of $Cr_2(C,N)$ were observed in the 6.5 mm wall region. Within this region, as well as the direct transformation of primary $M_{23}C_6$ precipitates to $Cr_2(C,N)$, lenticular $Cr_2(C,N)$ was also observed to have precipitated intragranularly, as shown in Figure 5.23 (c) and Figure 5.25 (c). The sample that displayed the greatest volume fraction of $Cr_2(C,N)$ in the 6.5 mm region displayed the lowest volume fraction of primary $M_{23}C_6$ (sample 2B, $Cr_2(C,N) \approx 11\%$, $M_{23}C_6 \approx 2.3\%$), and vice versa (sample 2D, $Cr_2(C,N) \approx 3.5\%$, $M_{23}C_6 \approx 11\%$), as is evident when comparing Figure 5.23 (c) with Figure 5.27 (c).

Secondary $M_{23}C_6$ precipitates were observed in all four samples from tube 2. A summary of the secondary precipitate distributions for each sample is given in Table 5.5. The secondary $M_{23}C_6$ precipitates were only observed in regions of the tube where the primary chromium carbide was $M_{23}C_6$. Qualitatively, the distribution in each tube was coarse (precipitates typically ≥ 5 μm in size), and the number of individual precipitates was extremely low.

Table 5.4 - Summary of the distance from the inner wall to the $M_{23}C_6$-to-M_7C_3 transformation front for samples from tube 2.

Sample	Positions of the $M_{23}C_6$-to-M_7C_3 transformation front (mm)
2A	2.5
2B	2.2
2C	2.6
2D	2.8

Table 5.5 - Summary of the secondary $M_{23}C_6$ precipitate distributions in samples from tube 2.

Sample	Wall region in which secondary $M_{23}C_6$ is present	Description of secondary $M_{23}C_6$ distribution
2A	2.5 - 6.5 mm	Very coarse (typically ≥ 5 μm), number of individual precipitates very low
2B	2.5 – 6.5 mm	
2C	3.0 – 6.5 mm	
2D	3.0 – 6.5 mm	

Niobium Carbides and Silicides

The volume fraction of NbC carbides was observed to be < 1.5 % at all locations in all four samples from tube 2. The incomplete transformation of NbC to η-carbide was observed to have occurred in the 3.0 – 6.5 mm wall regions of all four samples. The volume fraction of η-carbide remained below 1.5 % in all locations in all four samples. The NbC-to-G-phase transformation was not observed in tube 2.

Matrix Chromium Concentration

The matrix chromium concentration profiles for tube 2 were found to be consistent across the four samples, as summarised in Figure 5.29. As with tube 1, the matrix chromium concentration was seen to inversely mirror the chromium carbide volume fractions. In the 0.5 – 1.0 mm wall regions where the volume fraction of M_7C_3 was in the range of 34 – 37 %, the matrix chromium concentration was as low as 3.6 – 6 wt%. This gradually increased to a value of 10 – 12 wt% at the $M_{23}C_6$-to-M_7C_3 transformation front, before levelling out at 15 – 16.5 wt% in the 5.0 – 6.5 mm wall regions. The presence of η-carbide in such small volumes did not appear to significantly impact the chromium concentration in the matrix.

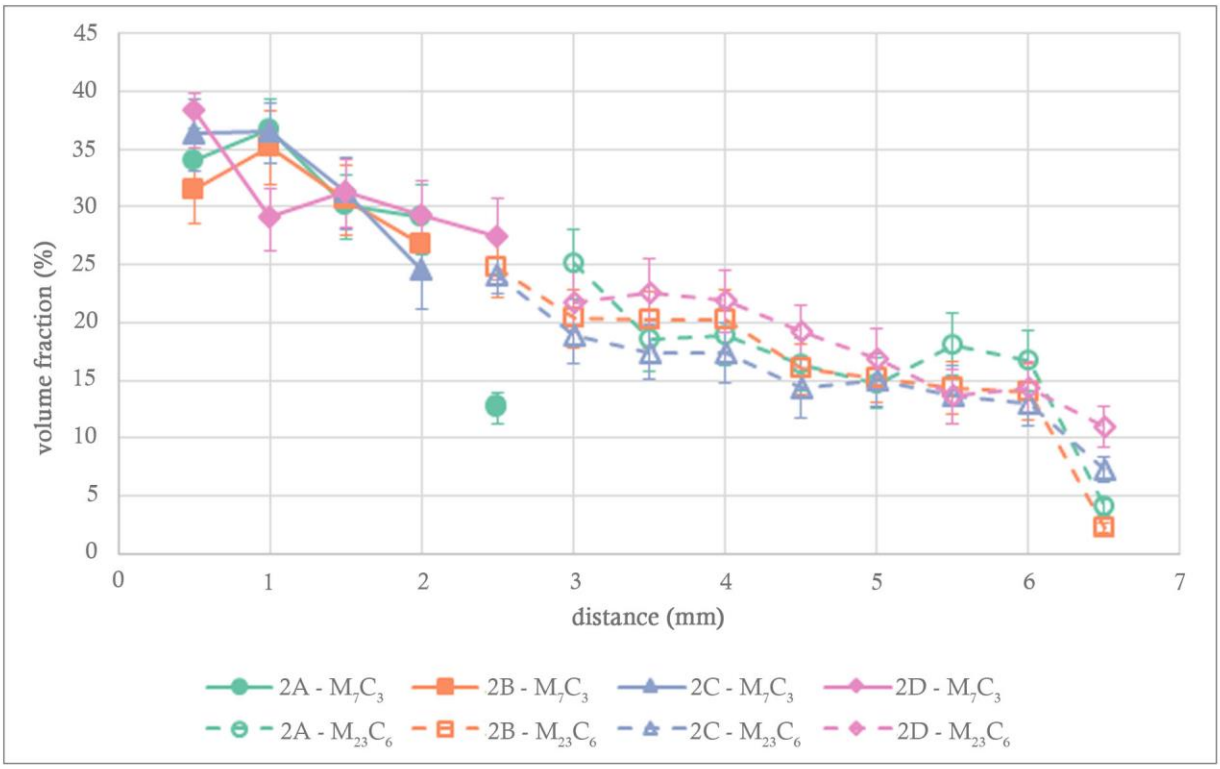

Figure 5.20 - Comparison of primary chromium carbide volume fractions in samples 2A-D. The outlier at 2.5mm in sample 2A is due to the transformation front being located at 2.5mm, hence both $M_{23}C_6$ and M_7C_3 are present in approximately equal quantities and the two data points overlap. The sum of the volume fractions of the two carbides fits the general trend. Distance is measured from the inner diameter.

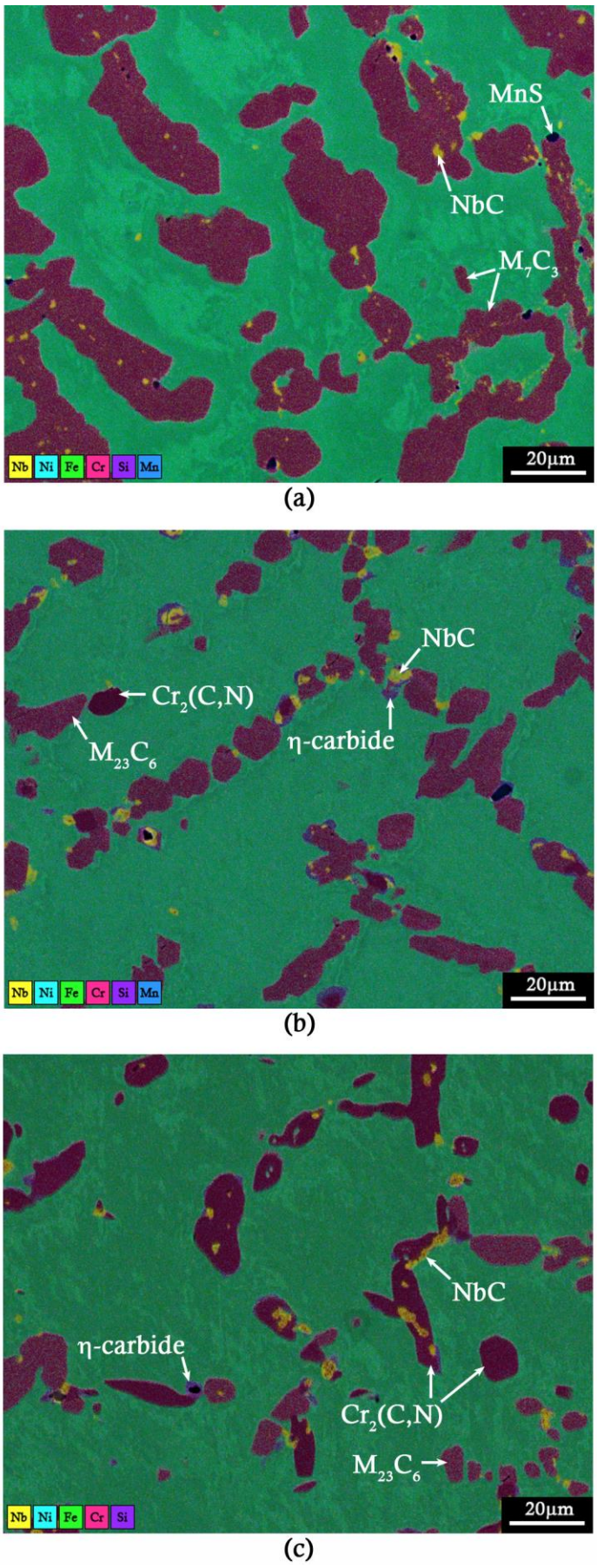

Figure 5.21 - Representative EDS maps of the microstructure in sample 2A at distances of (a) 0.5 mm, (b) 4.0 mm, and (c) 6.5 mm from the inner diameter.

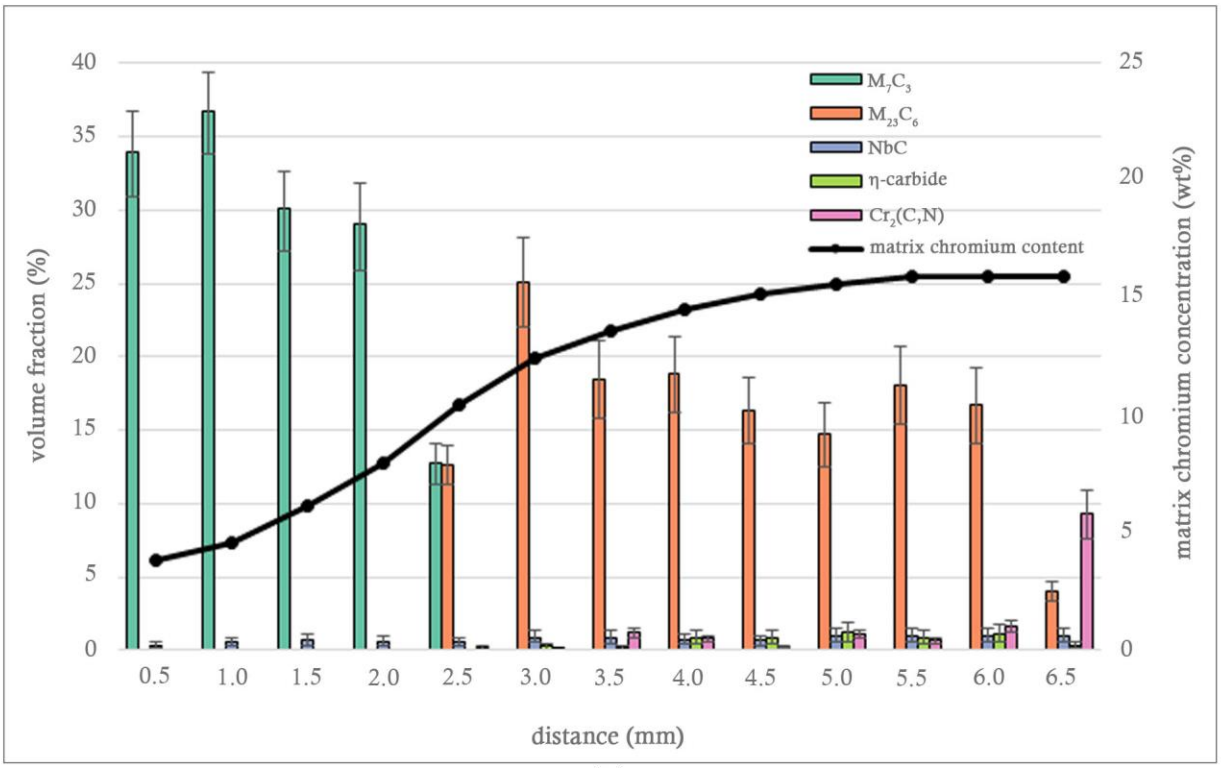

(a)

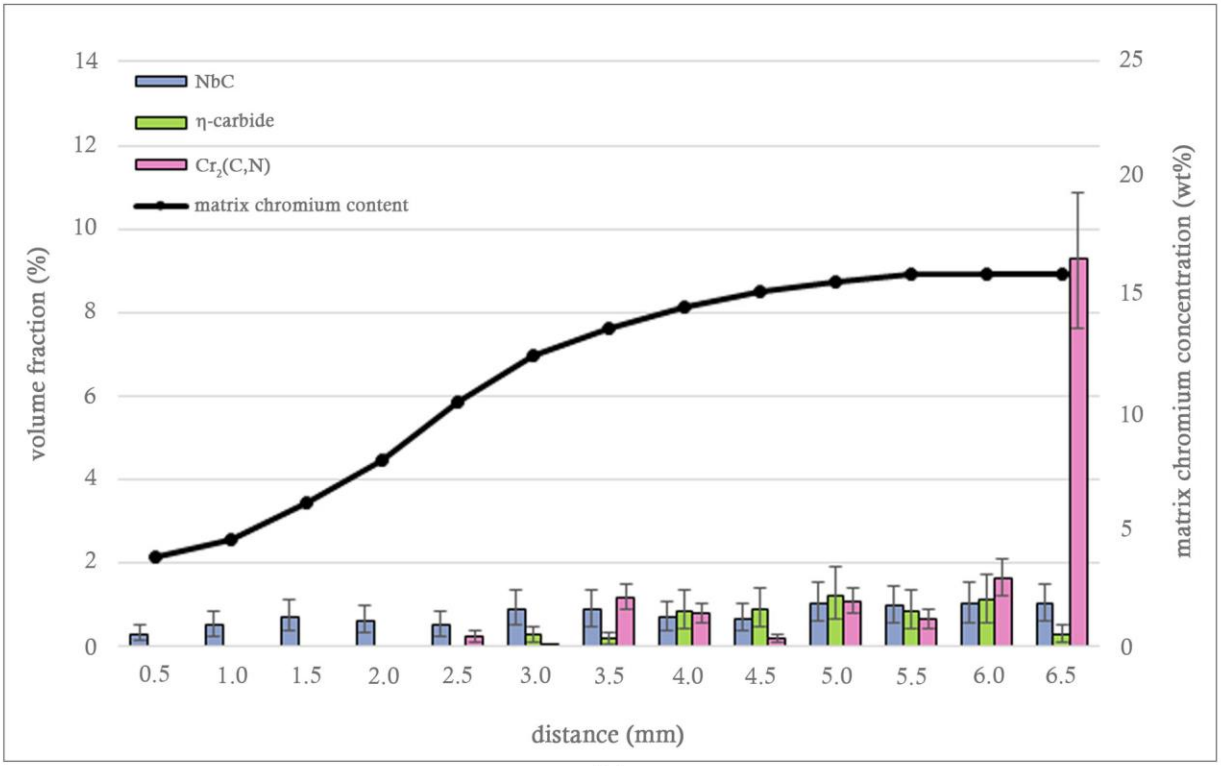

(b)

Figure 5.22 - Measured volume fractions and matrix chromium concentration in sample 2A. (a) all volume fractions, (b) minor volume fractions. Distance is measured from the inner diameter.

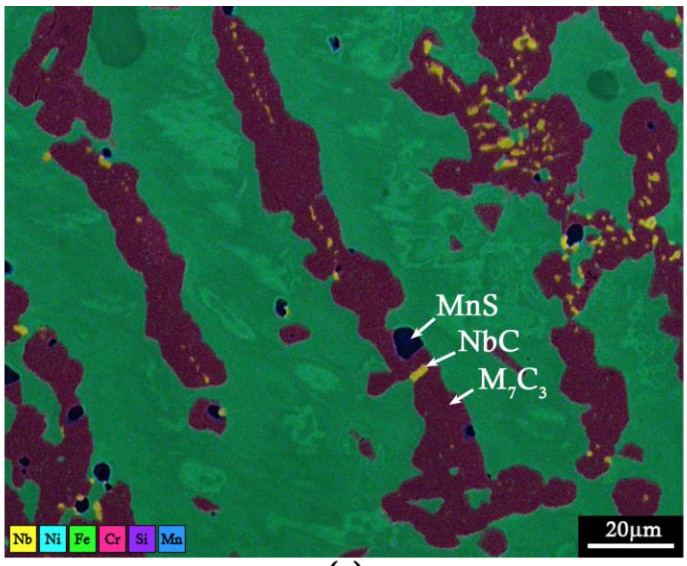

(a)

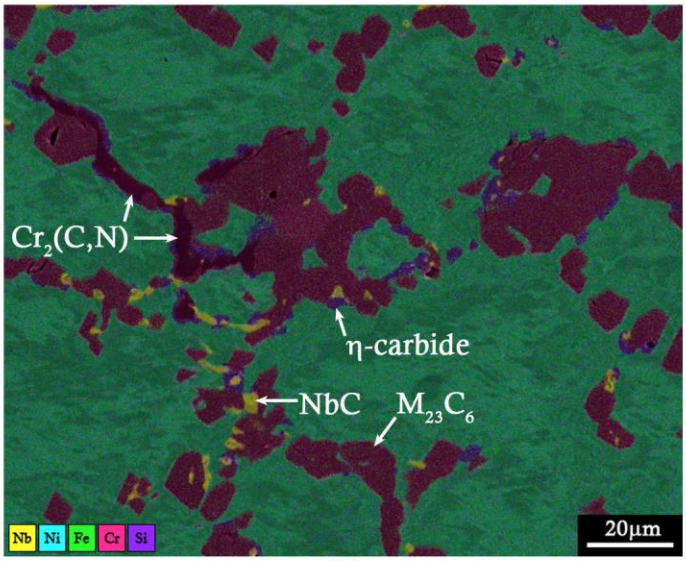

(b)

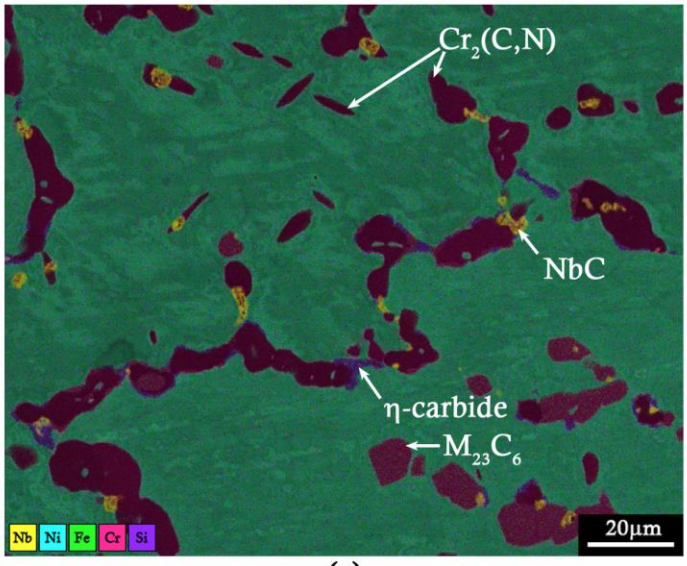

(c)

Figure 5.23 - Representative EDS maps of the microstructure in sample 2B at distances of (a) 0.5 mm, (b) 4.0 mm, and (c) 6.5 mm from the inner diameter.

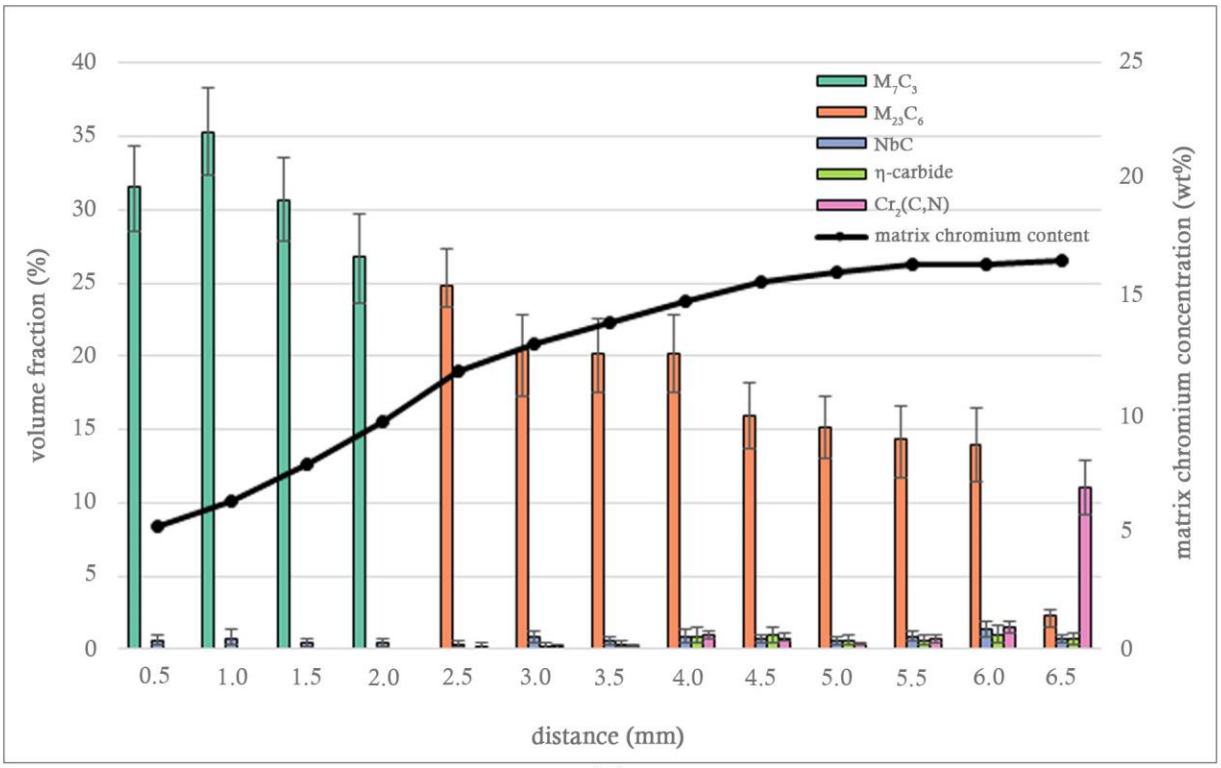

(a)

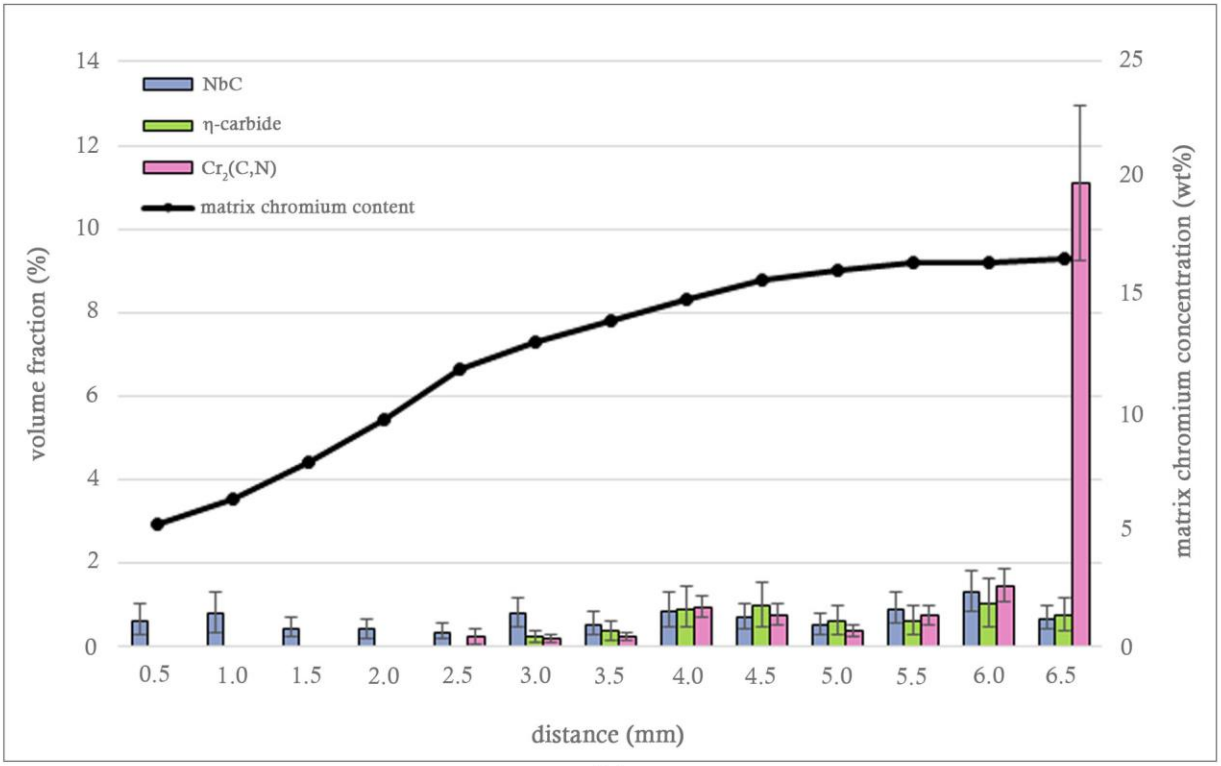

(b)

Figure 5.24 - Measured volume fractions and matrix chromium concentration in sample 2B. (a) all volume fractions, (b) minor volume fractions. Distance is measured from the inner diameter.

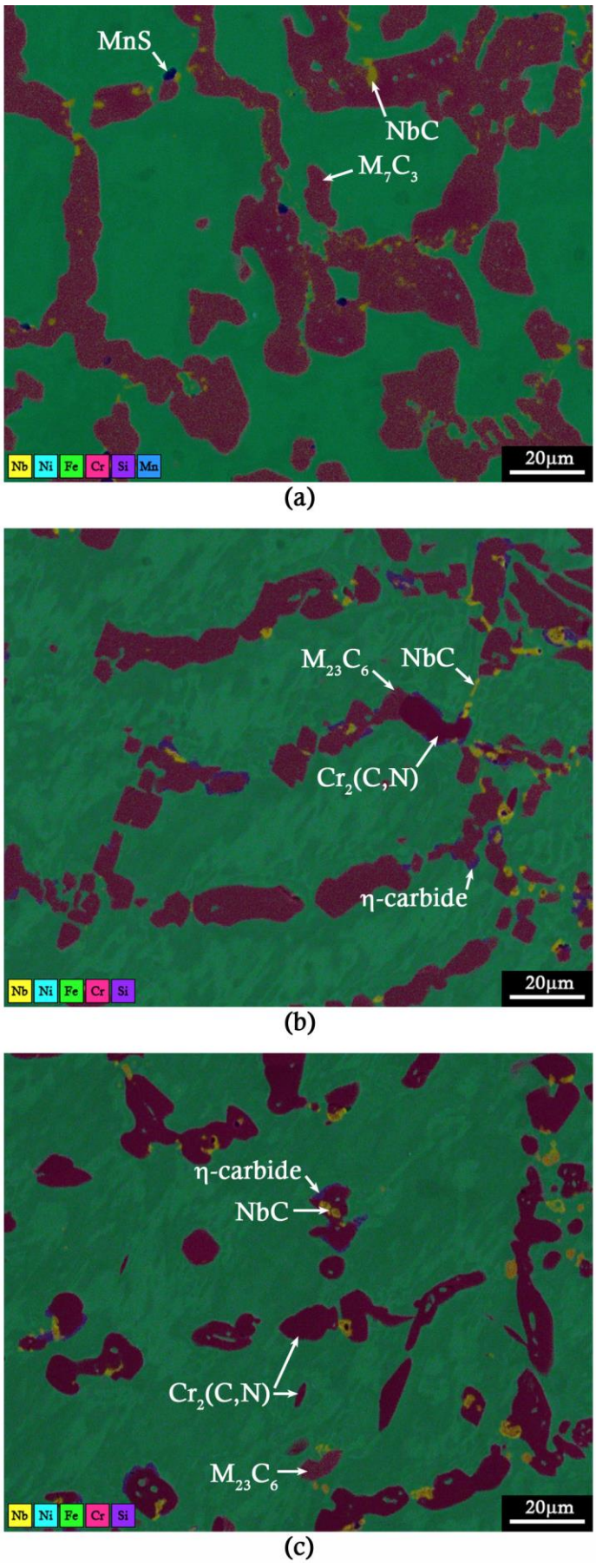

Figure 5.25 - Representative EDS maps of the microstructure in sample 2C at distances of (a) 0.5 mm, (b) 4.0 mm, and (c) 6.5 mm from the inner diameter.

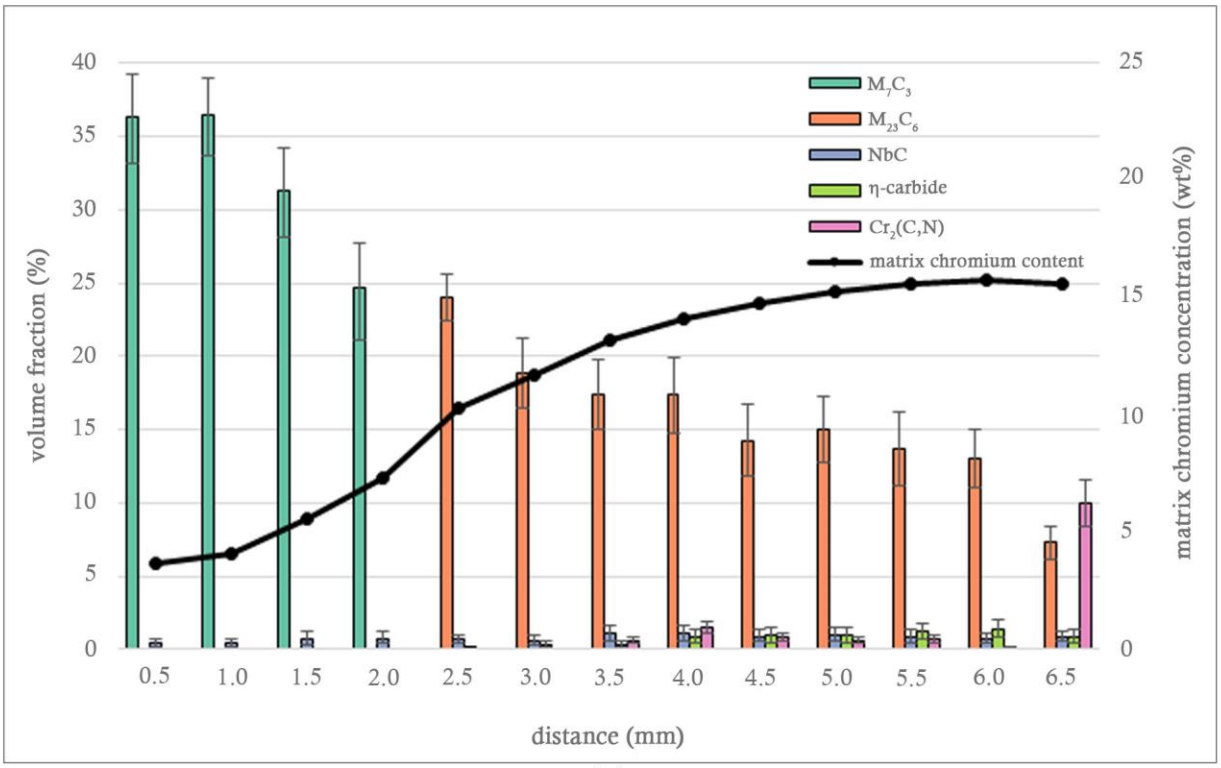

(a)

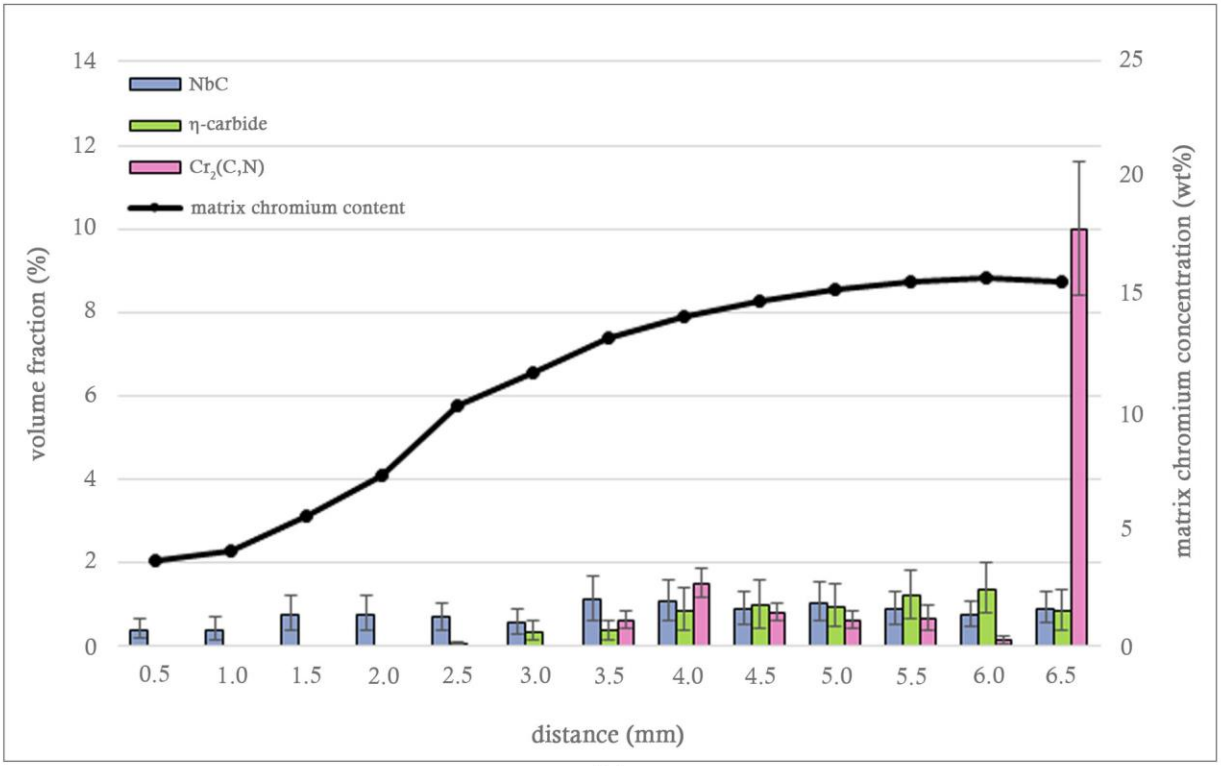

(b)

Figure 5.26 - Measured volume fractions and matrix chromium concentration in sample 2C. (a) all volume fractions, (b) minor volume fractions. Distance is measured from the inner diameter.

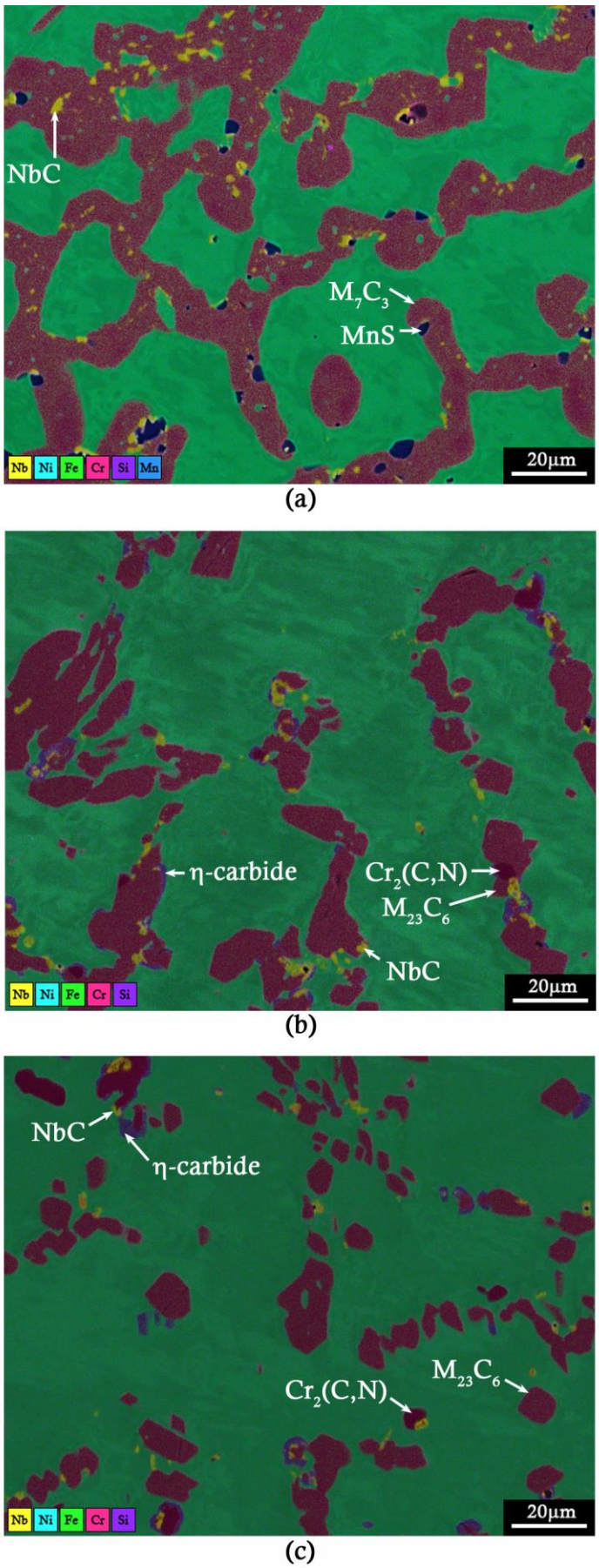

Figure 5.27 - Representative EDS maps of the microstructure in sample 2D at distances of (a) 0.5 mm, (b) 4.5 mm, and (c) 6.5 mm from the inner diameter.

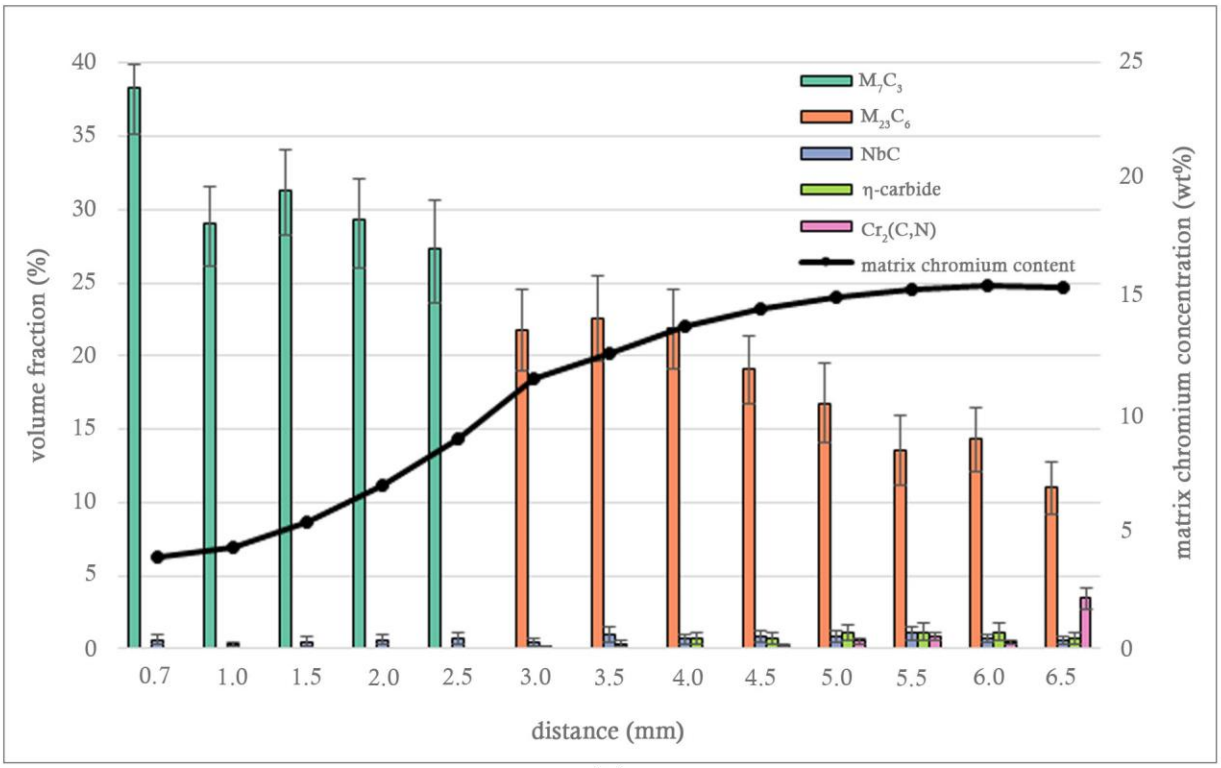

(a)

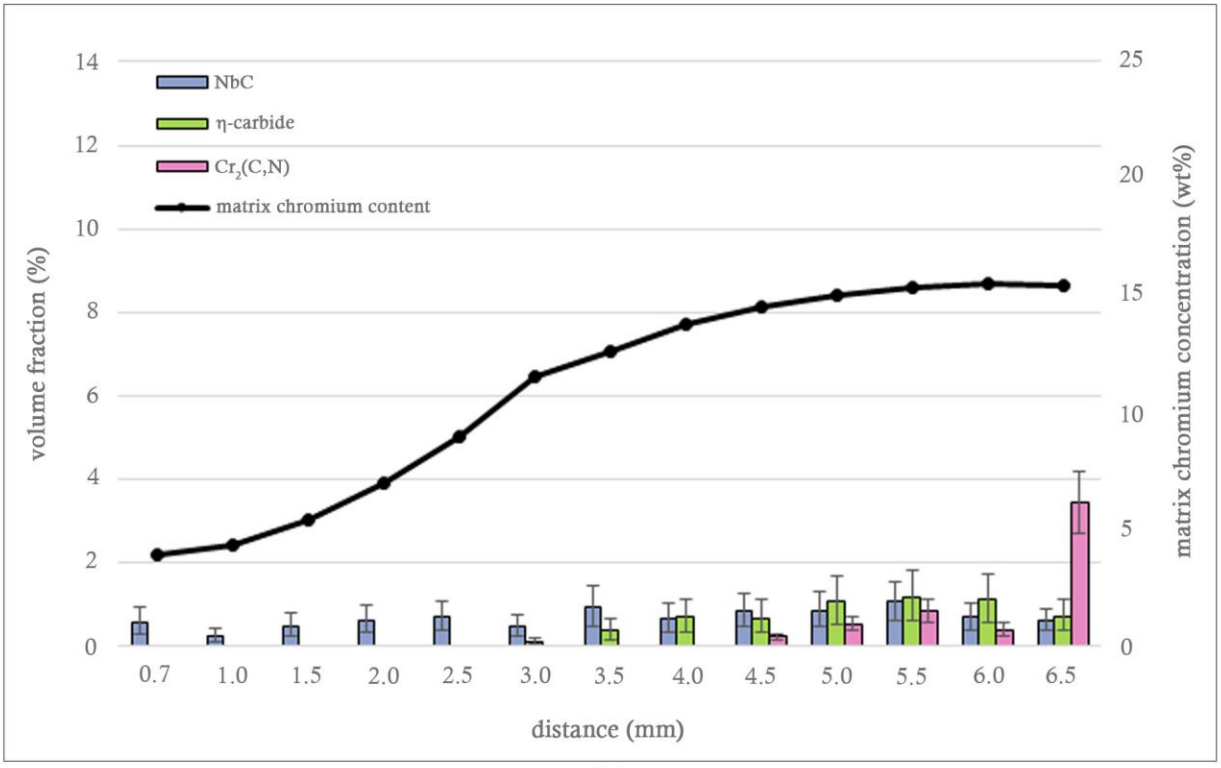

(b)

Figure 5.28 - Measured volume fractions and matrix chromium concentration in sample 2D. (a) all volume fractions, (b) minor volume fractions. Distance is measured from the inner diameter.

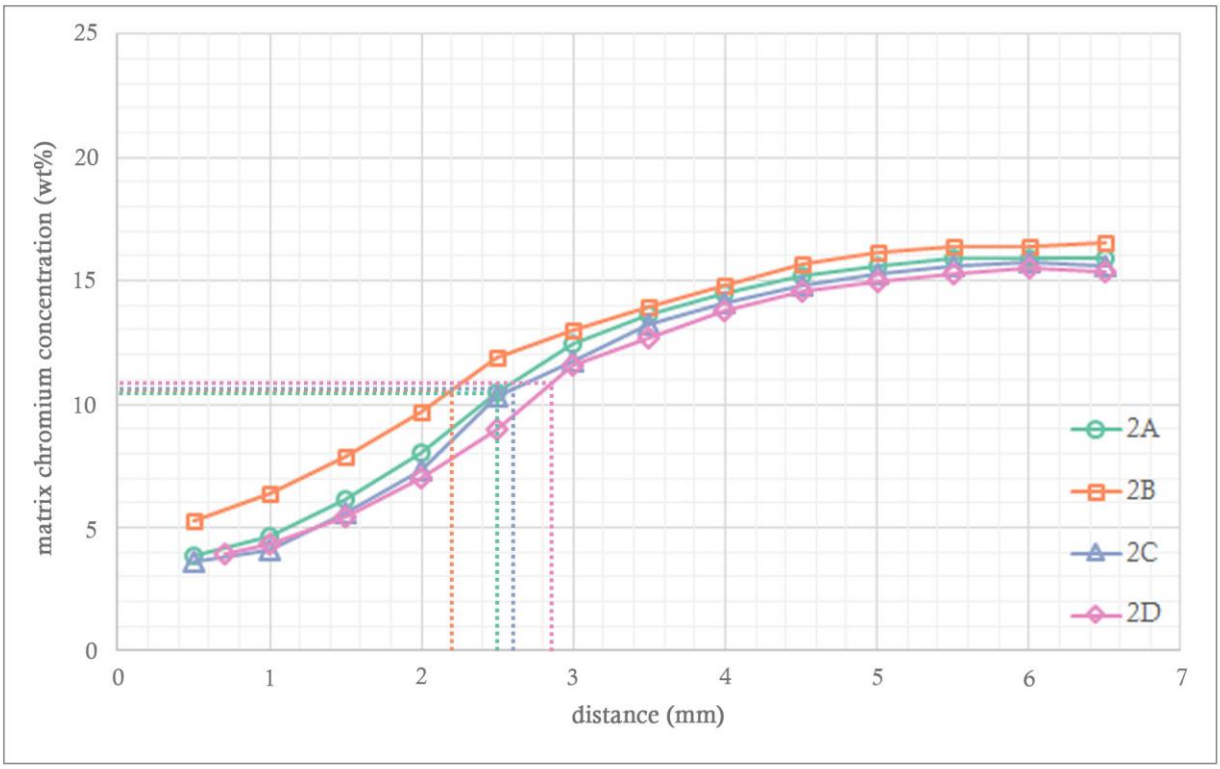

Figure 5.29 - Matrix chromium concentrations for samples 2A-D. Dashed lines indicate the positions of the $M_{23}C_6$-to-M_7C_3 transformation fronts in the corresponding colour coded sample. Distance is measured from the inner diameter.

5.2.3 Tube 3

The microstructure of tube 3 was observed to be significantly less coarsened than tubes 1 and 2. In some respects the microstructure appeared similar to the typical as-cast structure of a HP-Micro alloy, due to the primary precipitate network retaining some of the lamellar morphology.

Chromium Carbides

The primary chromium carbide in tube 3 was identified as $M_{23}C_6$, and no transformation of the $M_{23}C_6$ carbides to M_7C_3 was observed. The volume fraction of the $M_{23}C_6$ primary carbides remained consistent across all four samples from tube 3, and across the wall thicknesses of each sample, typically lying in the 1.5 – 3.0 % range. σ-phase was identified as part of the primary precipitate network, and the volume fraction of σ-phase was observed to remain consistent at ≈ 0.5 – 1.5 % for all four samples. On occasion locations were analysed where the $M_{23}C_6$ and σ-phase volume fraction was measured as lying outside the stated ranges ($M_{23}C_6$ maximum ≈ 4.2 %, σ-phase maximum ≈ 1.9%); however, due to the segmentation errors creating large error bars as a result of the small precipitate fractions in tube 3 in comparison to the highly carburized tubes, as well as the natural variance in microstructure, such outliers are unlikely to be significant.

Secondary σ-phase precipitates were observed in the matrix at all locations in all four samples from tube 3. They displayed a plate-like morphology, and were distributed throughout the matrix, not just adjacent to the primary network (as is typical of secondary distributions of $M_{23}C_6$ carbides). Although the secondary σ-phase precipitates were typically >10 μm in length they were typically <1 μm in width, and therefore quantitative measurement of their volume fraction was not possible using the current methodology.

Niobium – Titanium Carbides and Silicides

The volume fraction of the (Nb,Ti)C precipitates typically remained below 1 % at all locations in all four samples. The incomplete transformation of (Nb,Ti)C to G-phase was observed in all samples, and the G-phase volume fraction was typically in the 0.5 – 2.0 % range.

Cuboidal Ti(C,N) precipitates were present in the austenite matrix; however, these did not attain a volume fraction above 0.3 %. No other nitrides or carbonitrides were observed in tube 3.

Matrix Chromium Concentration

The matrix chromium concentration was observed to attain a value of 22 – 23 wt% at all locations in all samples analysed, as summarised in Figure 5.38. The primary $M_{23}C_6$ and σ-phase precipitates did not appear to have coarsened to the extent that a significant amount of chromium was required to be drawn from the matrix for continued growth.

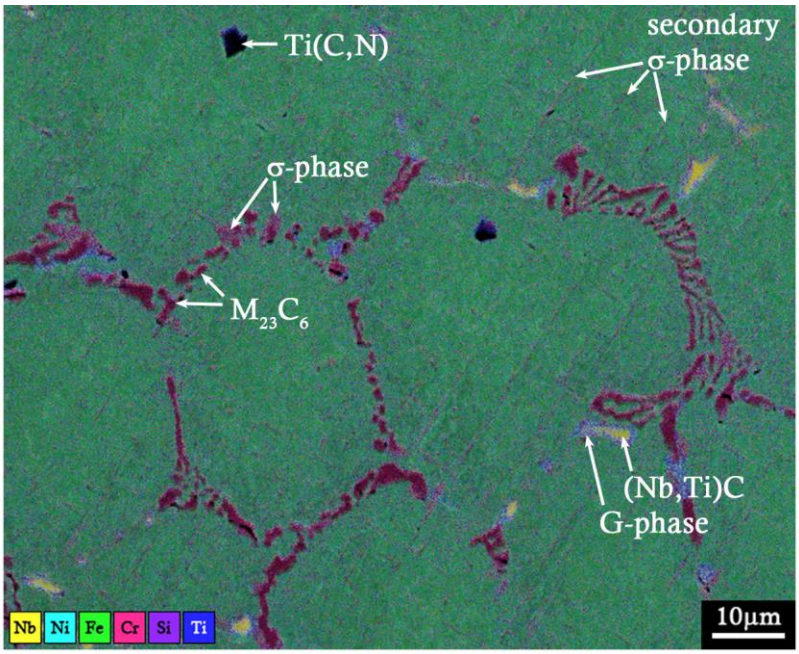

Figure 5.30 - Representative EDS map of the microstructure in sample 3A.

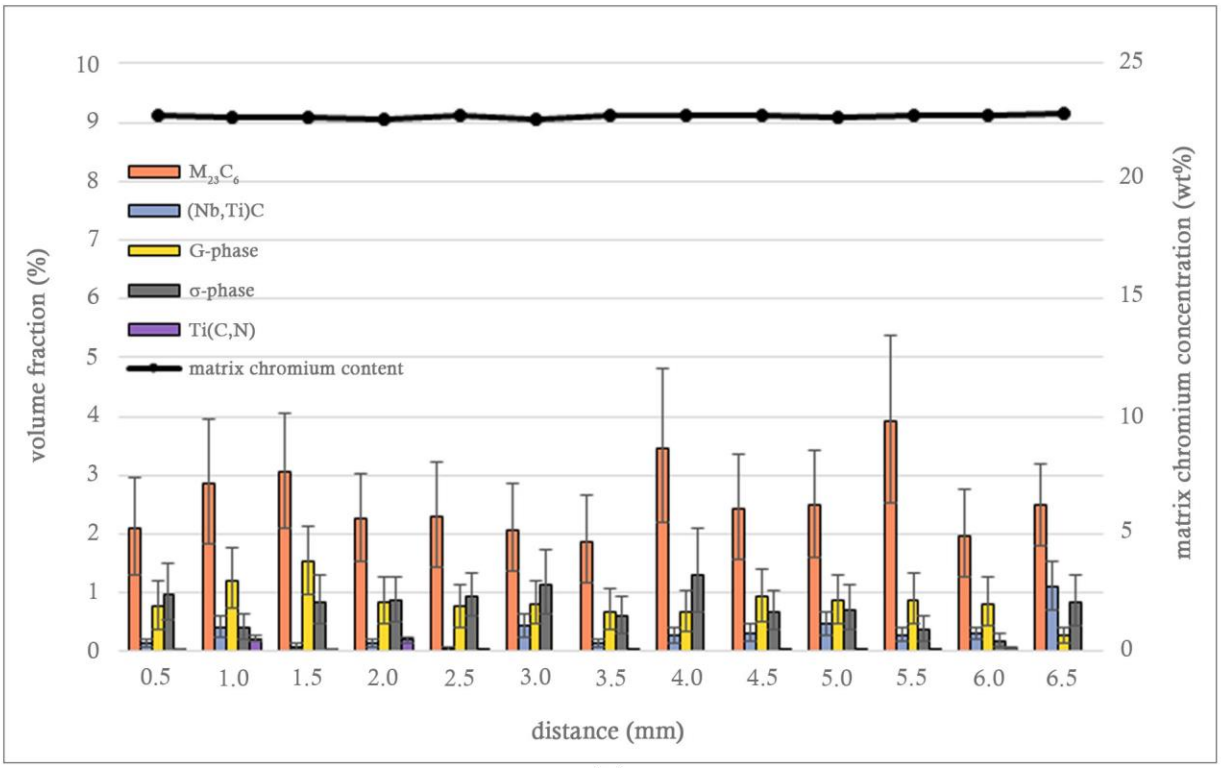

(a)

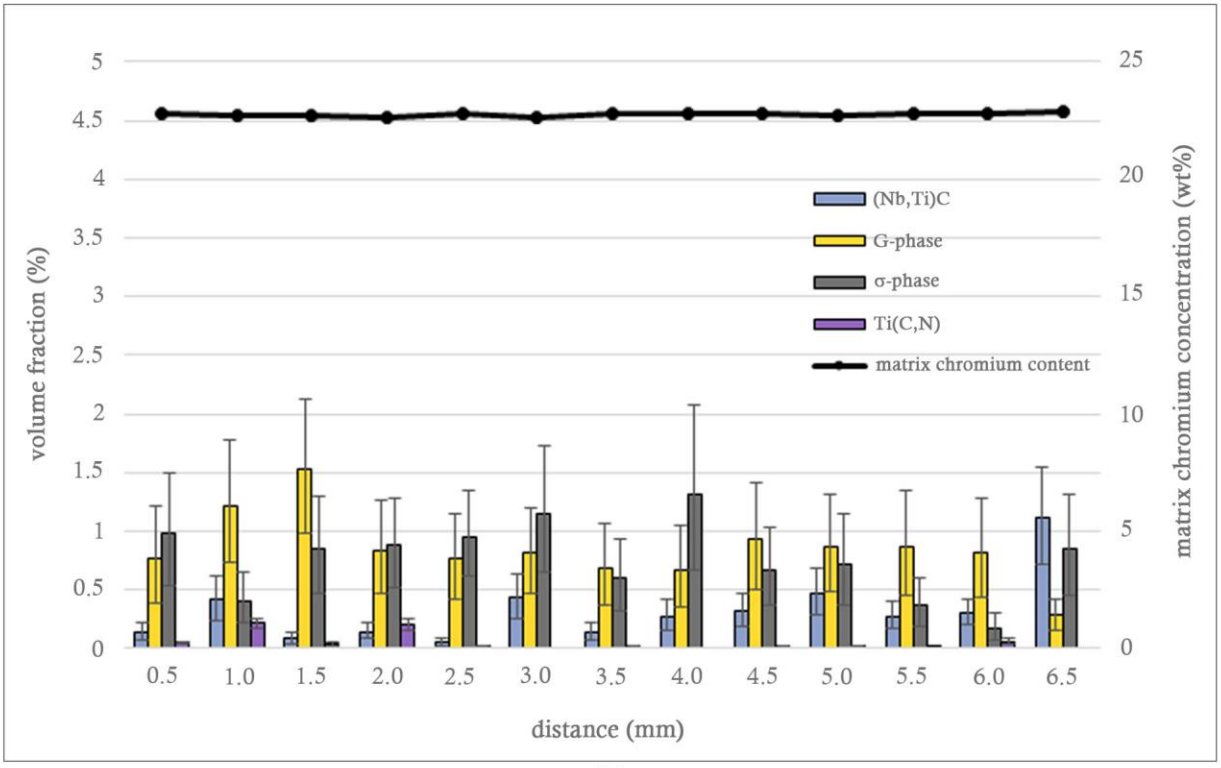

(b)

Figure 5.31 - Measured volume fractions and matrix chromium concentration in sample 3A. (a) all volume fractions, (b) minor volume fractions. Distance is measured from the inner diameter.

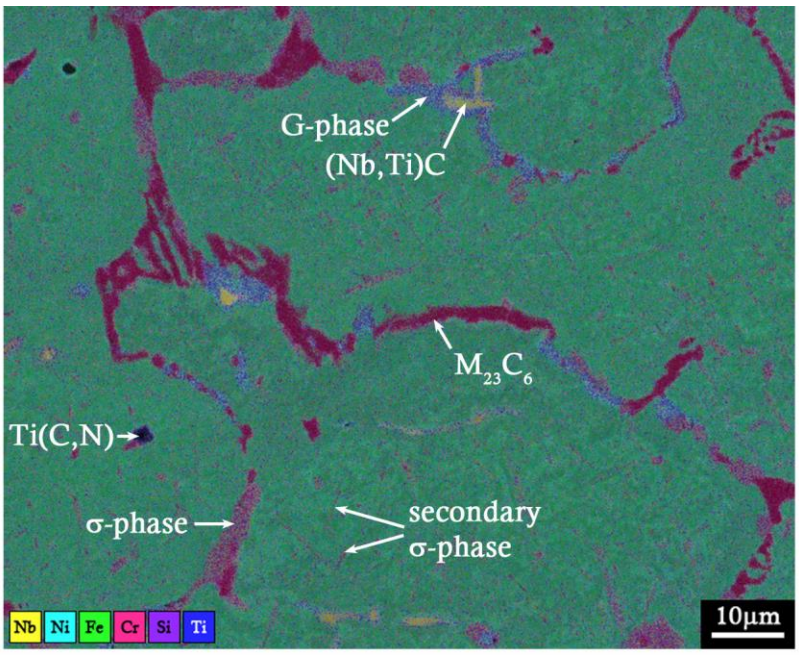

Figure 5.32 - Representative EDS map of the microstructure in sample 3B.

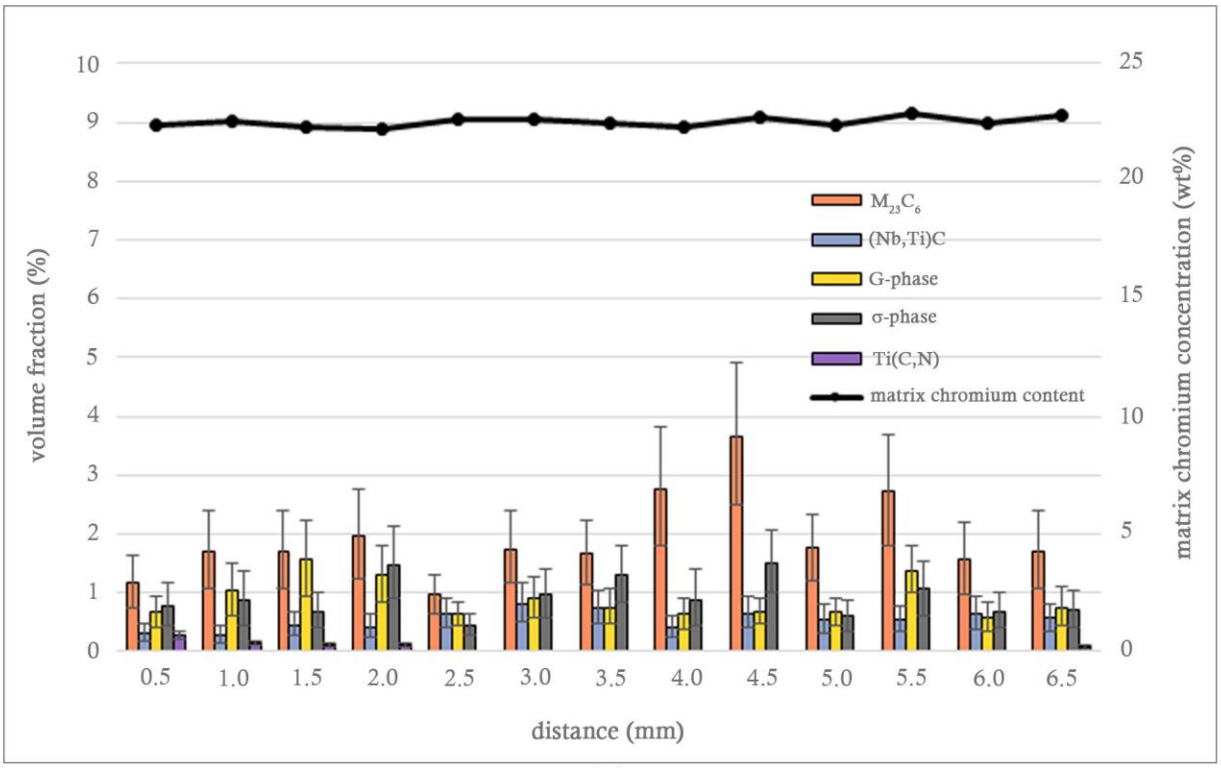

(a)

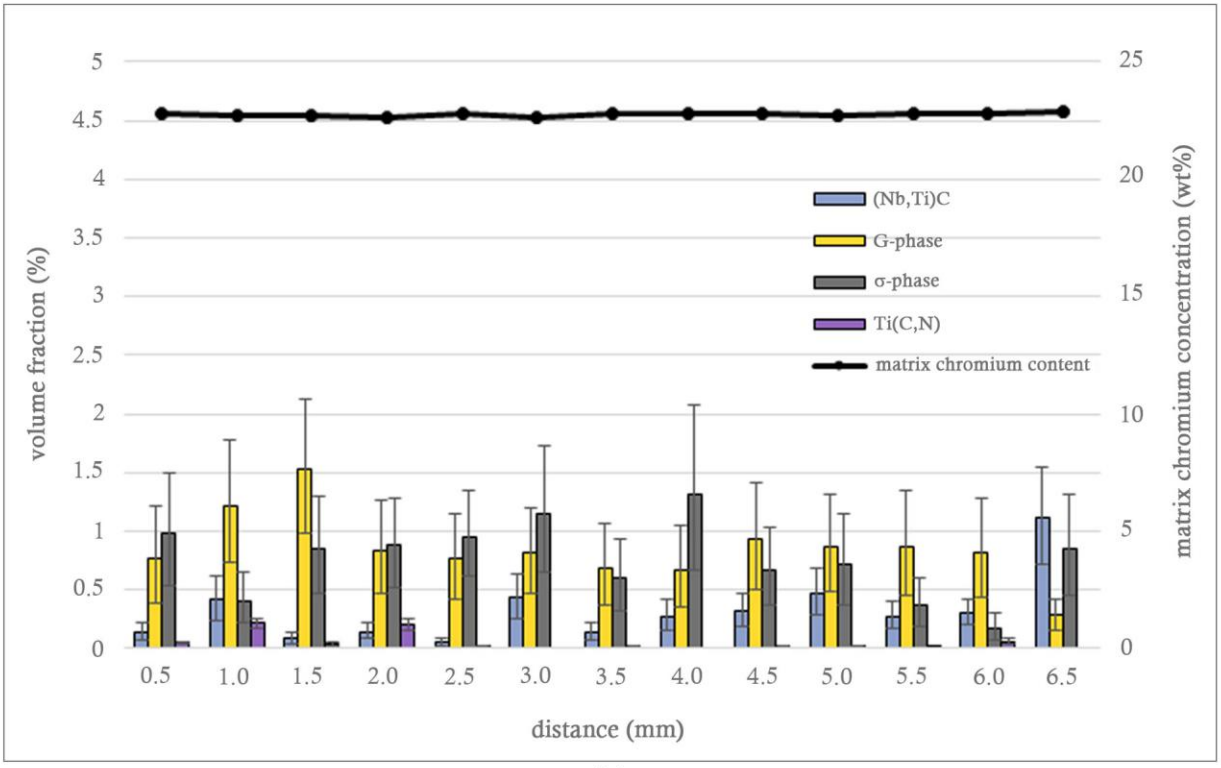

(b)

Figure 5.33 - Measured volume fractions and matrix chromium concentration in sample 3B. (a) all volume fractions, (b) minor volume fractions. Distance is measured from the inner diameter.

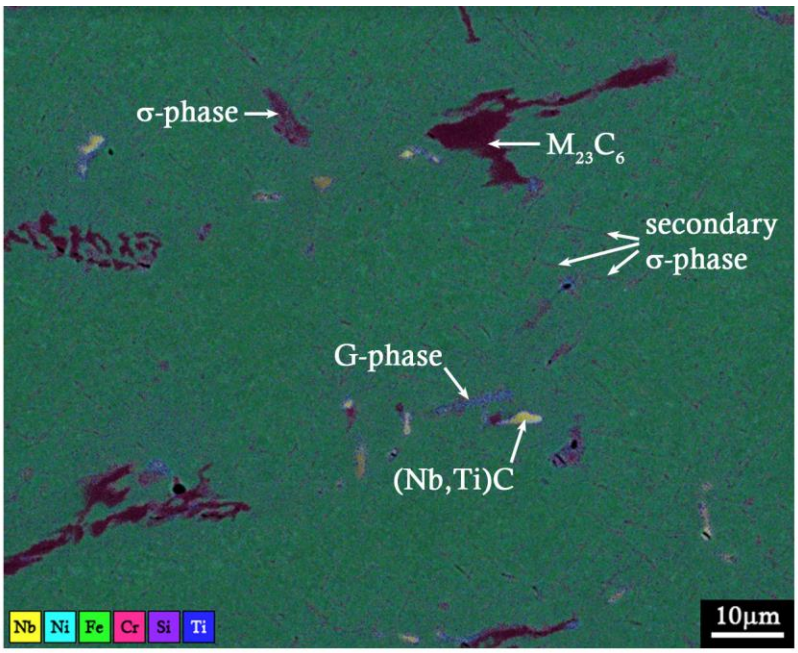

Figure 5.34 - Representative EDS map of the microstructure in sample 3C.

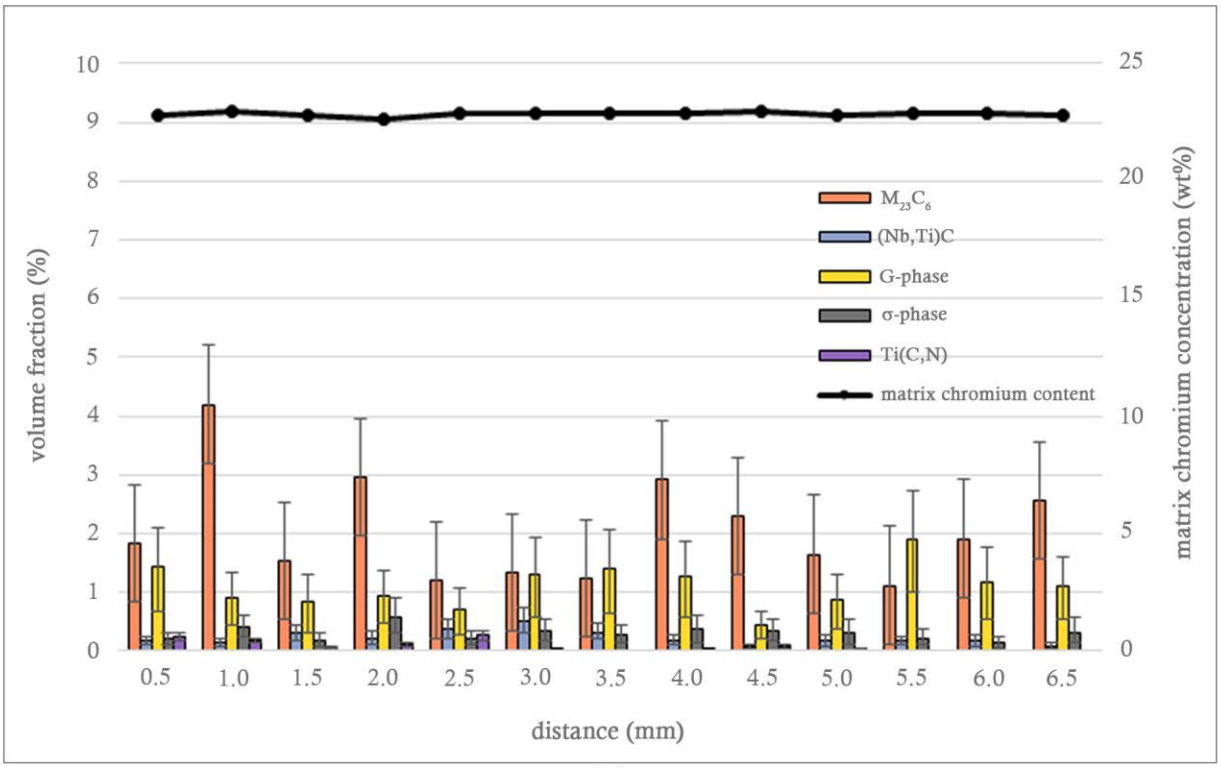

(a)

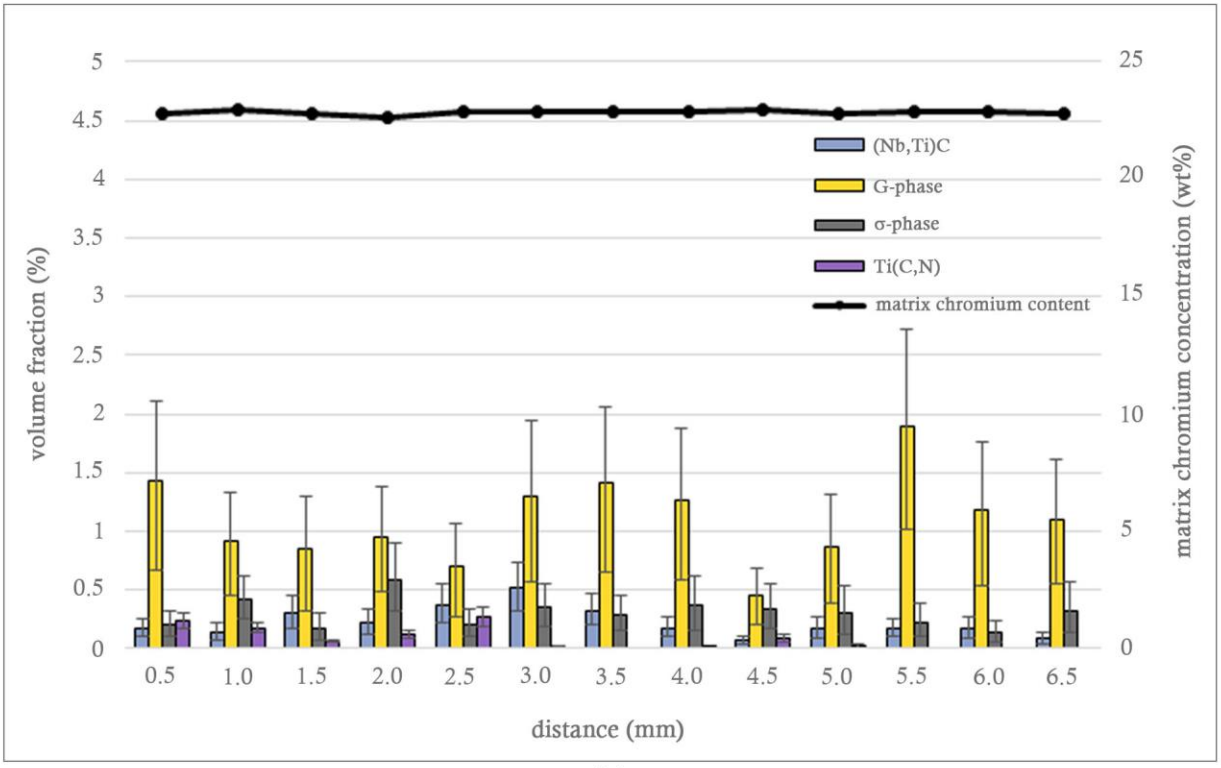

(b)

Figure 5.35 - Measured volume fractions and matrix chromium concentration in sample 3C. (a) all volume fractions, (b) minor volume fractions. Distance is measured from the inner diameter.

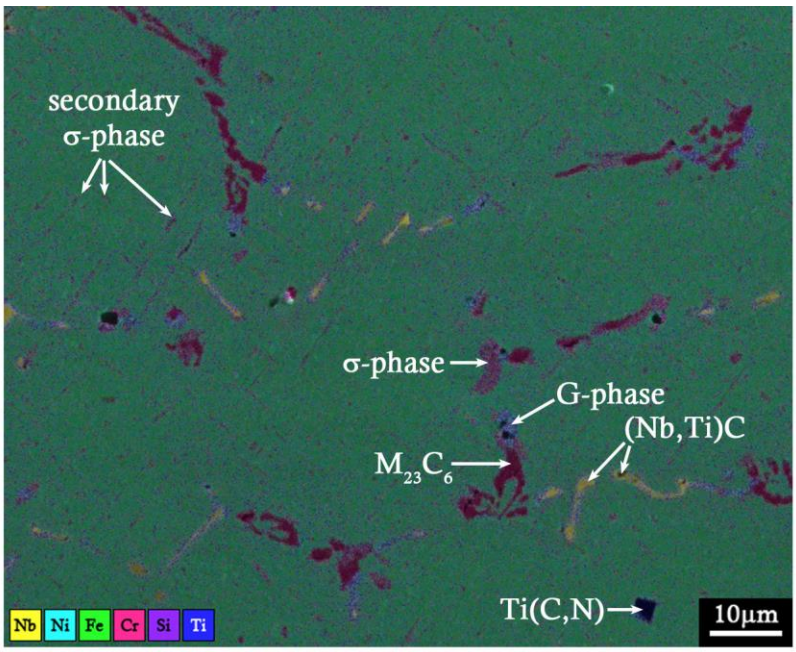

Figure 5.36 - Representative EDS map of the microstructure in sample 3D.

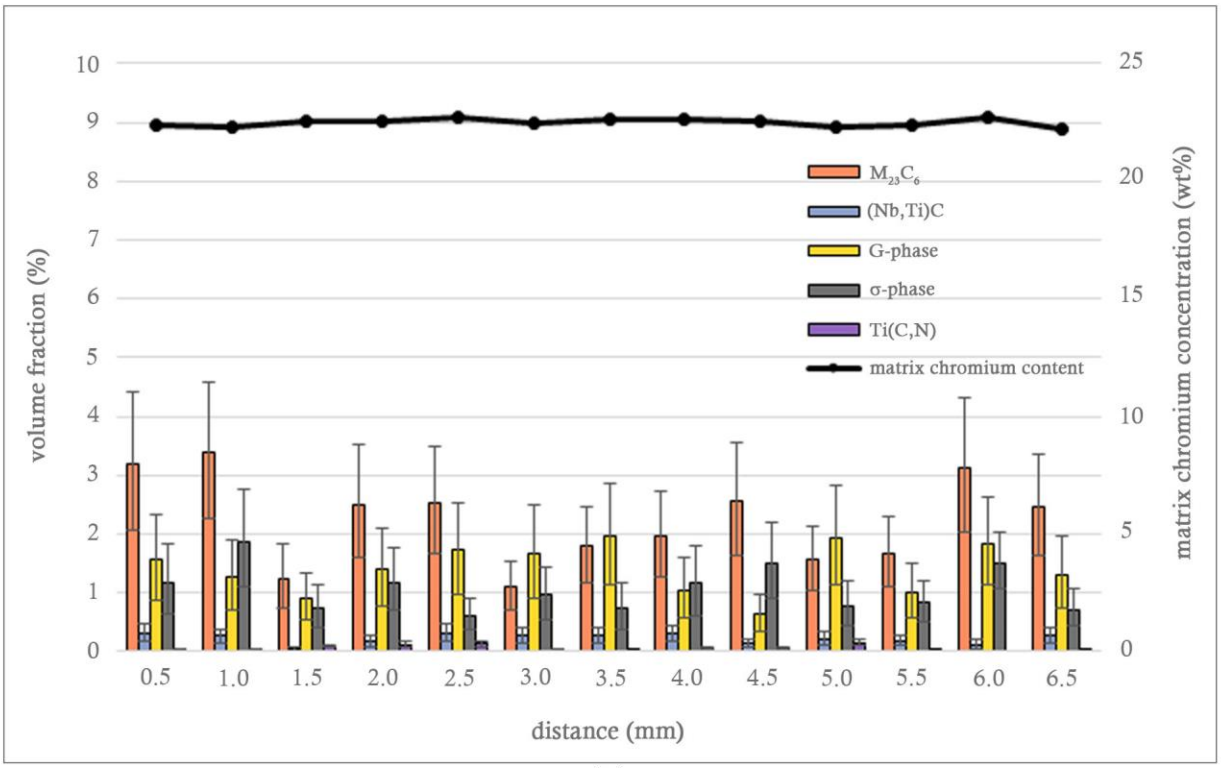

(a)

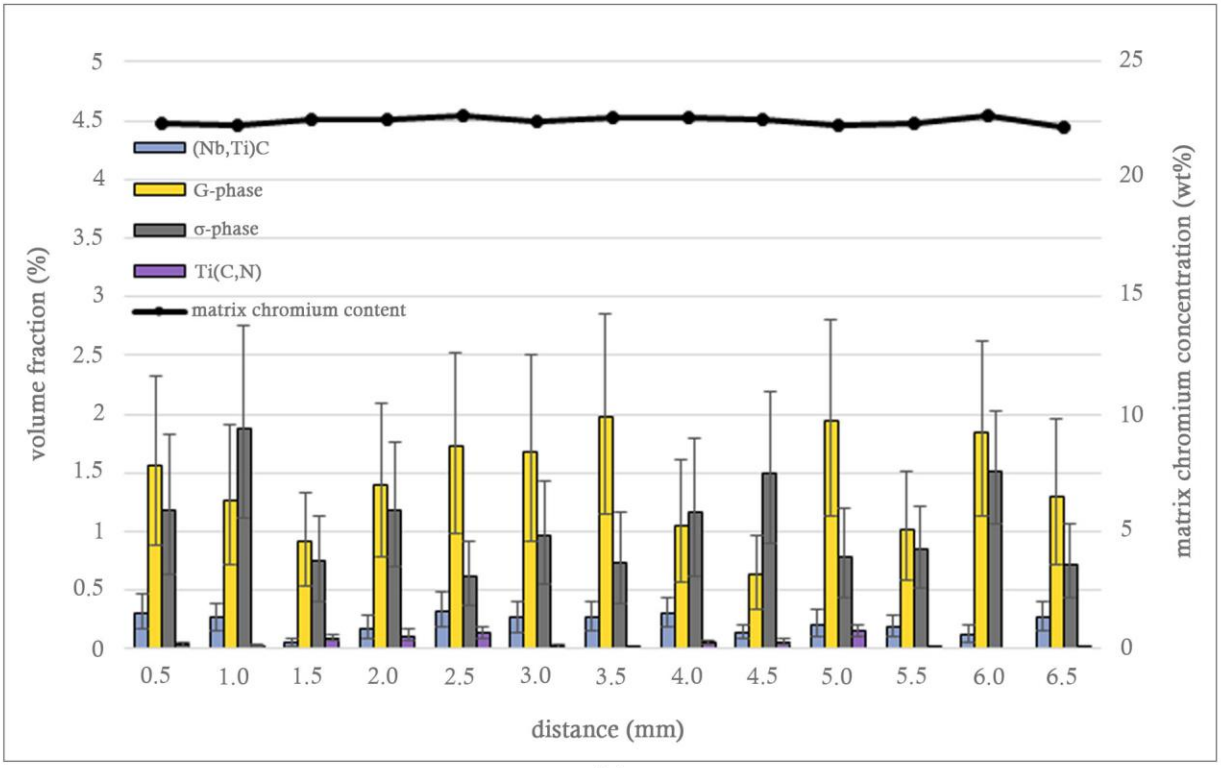

(b)

Figure 5.37 - Measured volume fractions and matrix chromium concentration in sample 3D. (a) all volume fractions, (b) minor volume fractions. Distance is measured from the inner diameter.

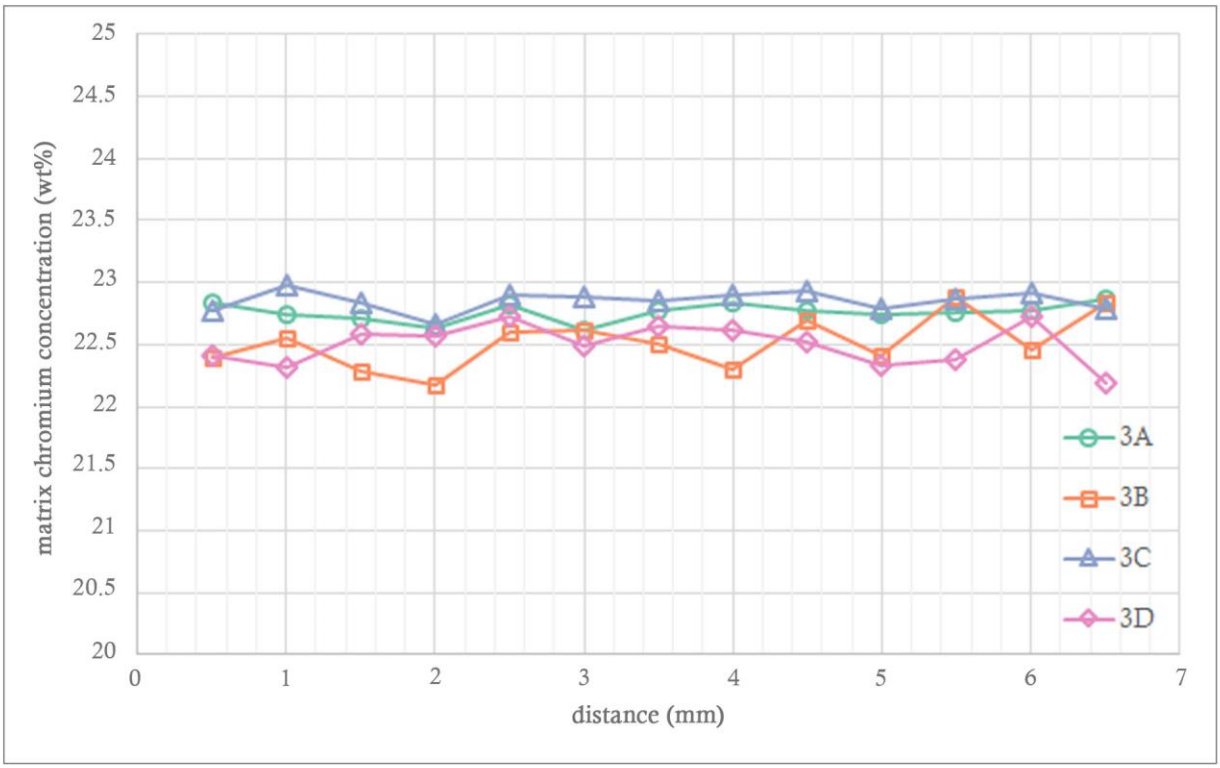

Figure 5.38 - Matrix chromium concentrations for samples 3A-D. Distance is measured from the inner diameter.

5.2.4 Tube 4

Similar to tube 3, the microstructure of tube 4 was observed to be significantly less coarsened than tubes 1 and 2, and the primary precipitate network had retained some of the lamellar morphology typical of the as-cast structure.

Chromium Carbides

The primary chromium carbide in tube 4 was identified as $M_{23}C_6$, and this was consistent across all locations in all four samples analysed, with no transformation to M_7C_3 observed. The volume fraction of primary $M_{23}C_6$ was consistently in the 3 – 6 % range across all locations in all samples. As in tube 3, there were locations where the measured volume fraction lay slightly outside this range; however, this may be a result of segmentation errors and/or inherent variations in the microstructure.

Secondary $M_{23}C_6$ precipitates were observed at all locations in all samples from tube 4. The distribution was observed to be very fine and concentrated adjacent to the primary precipitate network. The largest secondary precipitates were typically only ≈ 2 μm in their largest dimension, and the vast majority were <1 μm in size. As such, the current image analysis methodology was unable to segment the secondary precipitate network and no quantitative measurements could be made.

Niobium – Titanium Carbides and Silicides

The transformation of the (Nb,Ti)C carbides to G-phase was observed in the samples from tube 4, and the transformation appeared to be complete at almost every location analysed. (Nb,Ti)C precipitates were rarely identified within the G-phase regions. The volume fraction of (Nb,Ti)C was thus either zero, or very close to zero, at all locations. The volume fraction of G-phase was typically in the range of 1.5 – 4 %.

Ti(C,N) carbonitrides were observed on occasion in the matrix, in all samples. The volume fraction of the Ti(C,N) precipitates did not attain a value above 0.4 % at any location analysed. No other nitrides or carbonitrides were observed in tube 4.

Matrix Chromium Concentration

The matrix chromium concentration was observed to consistently remain within the range of 21 – 23 wt% at all wall locations for all samples analysed from tube 4, as summarised in Figure 5.47. As with tube 3, it did not appear that the primary $M_{23}C_6$ precipitates in tube 4 had coarsened to an extent where a significant amount of chromium was required to be drawn from the austenite matrix for continued growth.

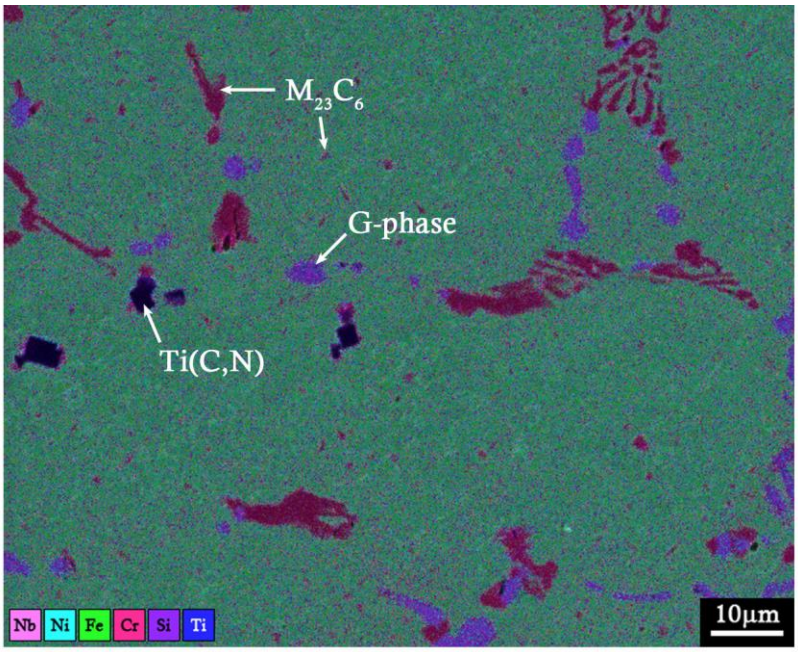

Figure 5.39 - Representative EDS map of the microstructure in sample 4A.

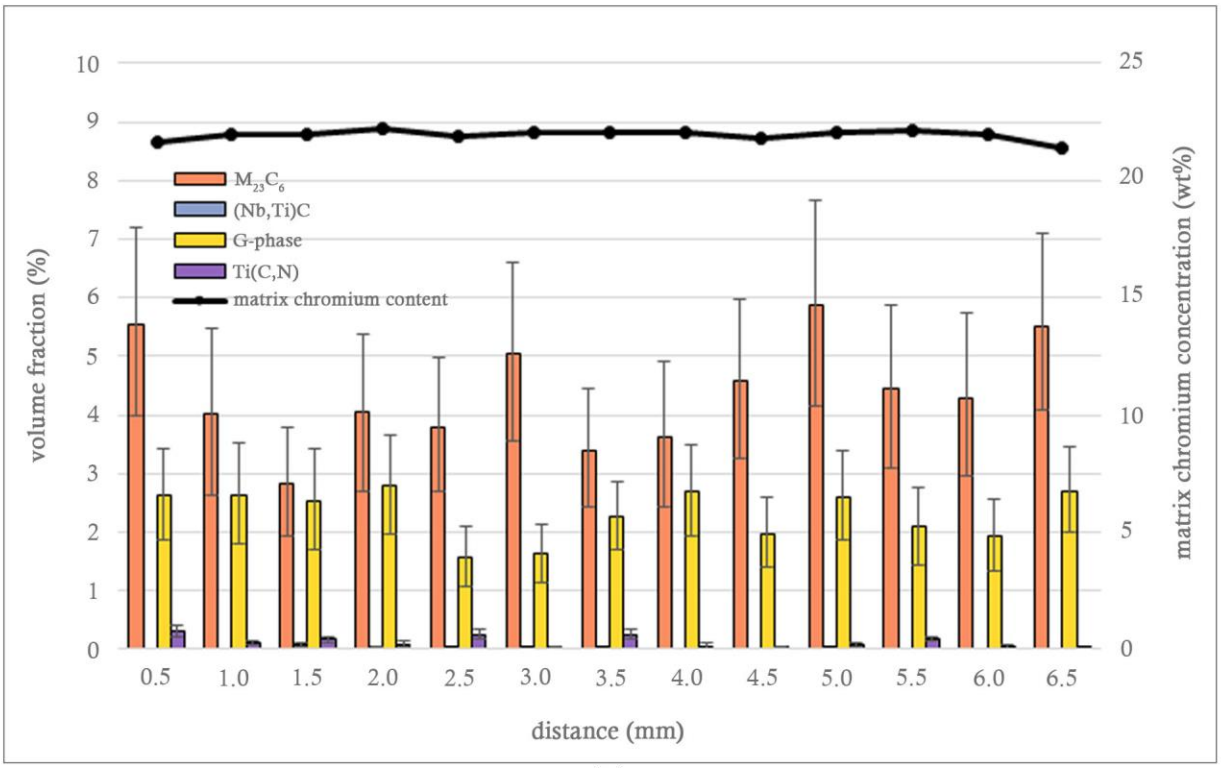

(a)

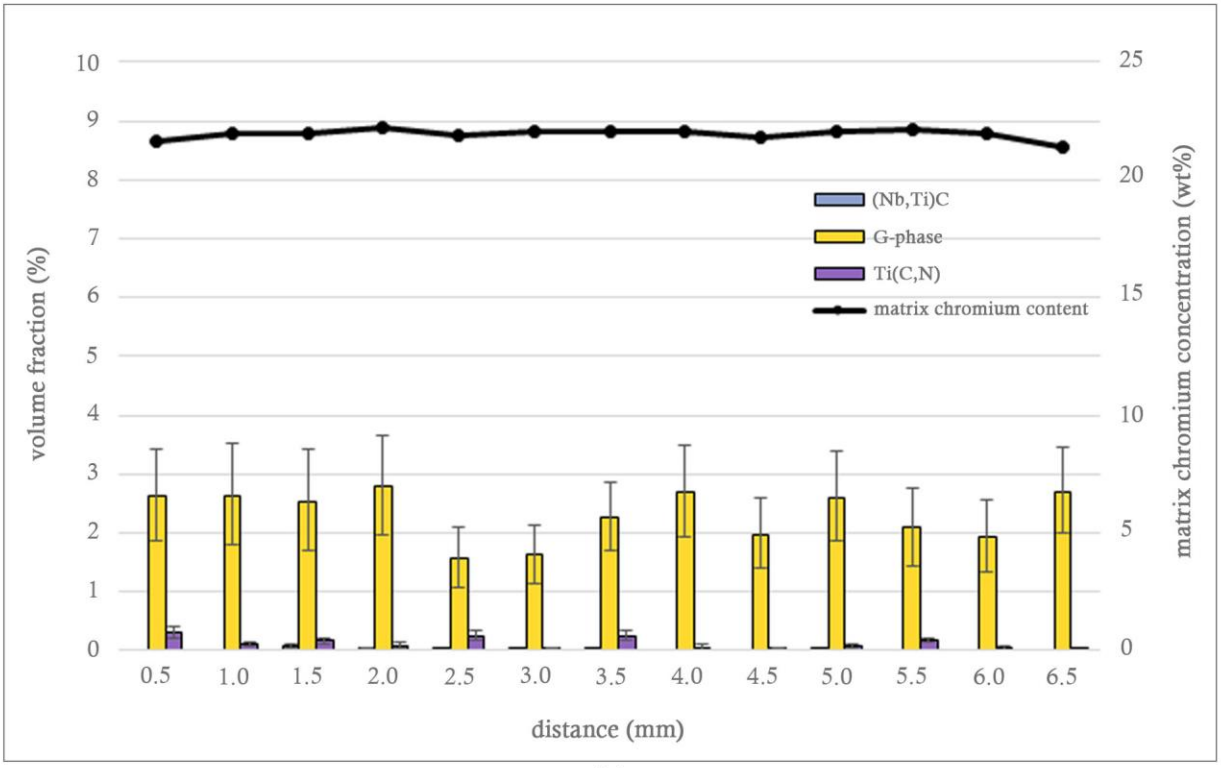

(b)

Figure 5.40 - Measured volume fractions and matrix chromium concentration in sample 4A. (a) all volume fractions, (b) minor volume fractions. Distance is measured from the inner diameter.

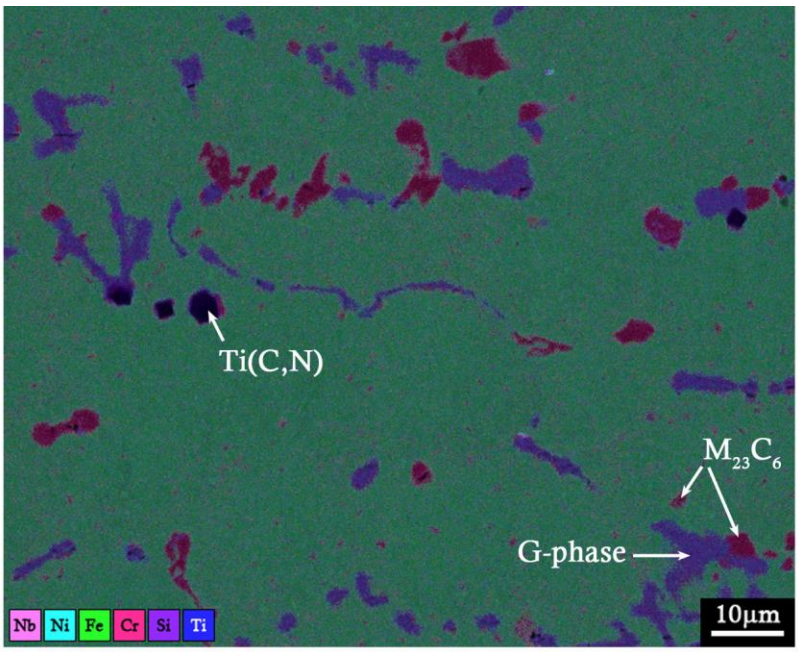

Figure 5.41 - Representative EDS map of the microstructure in sample 4B.

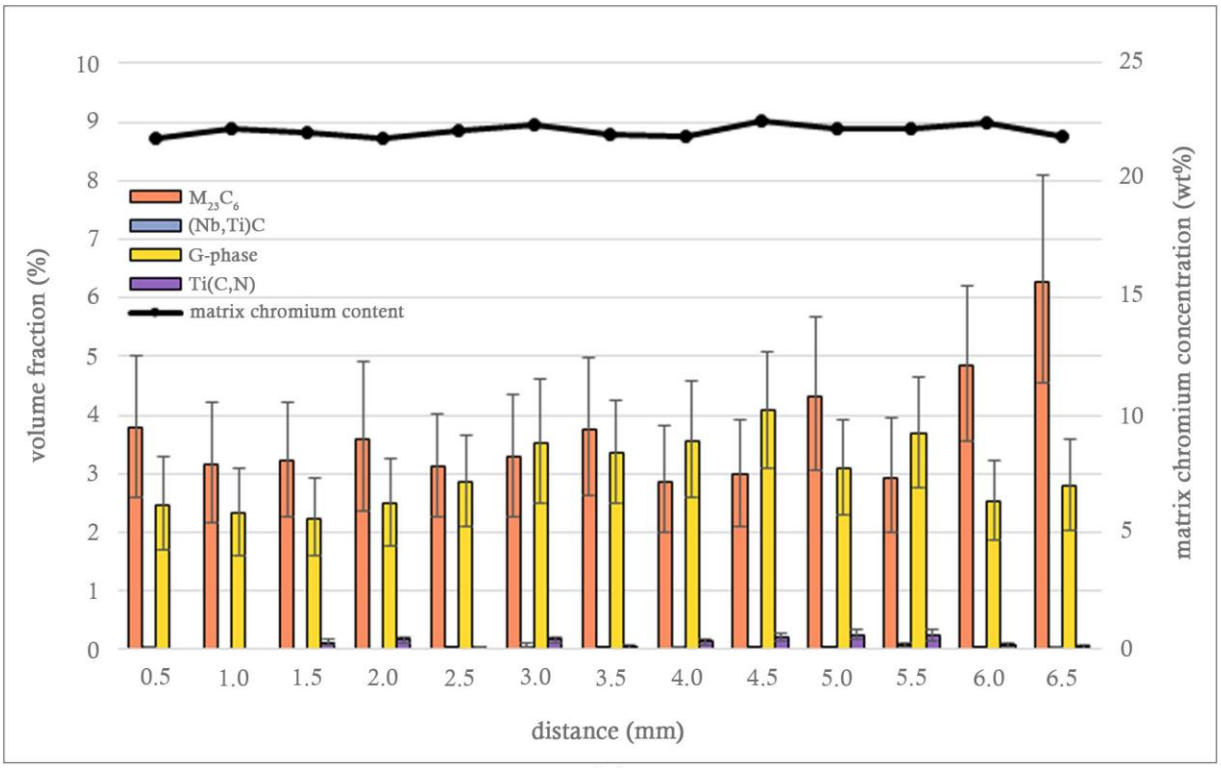

(a)

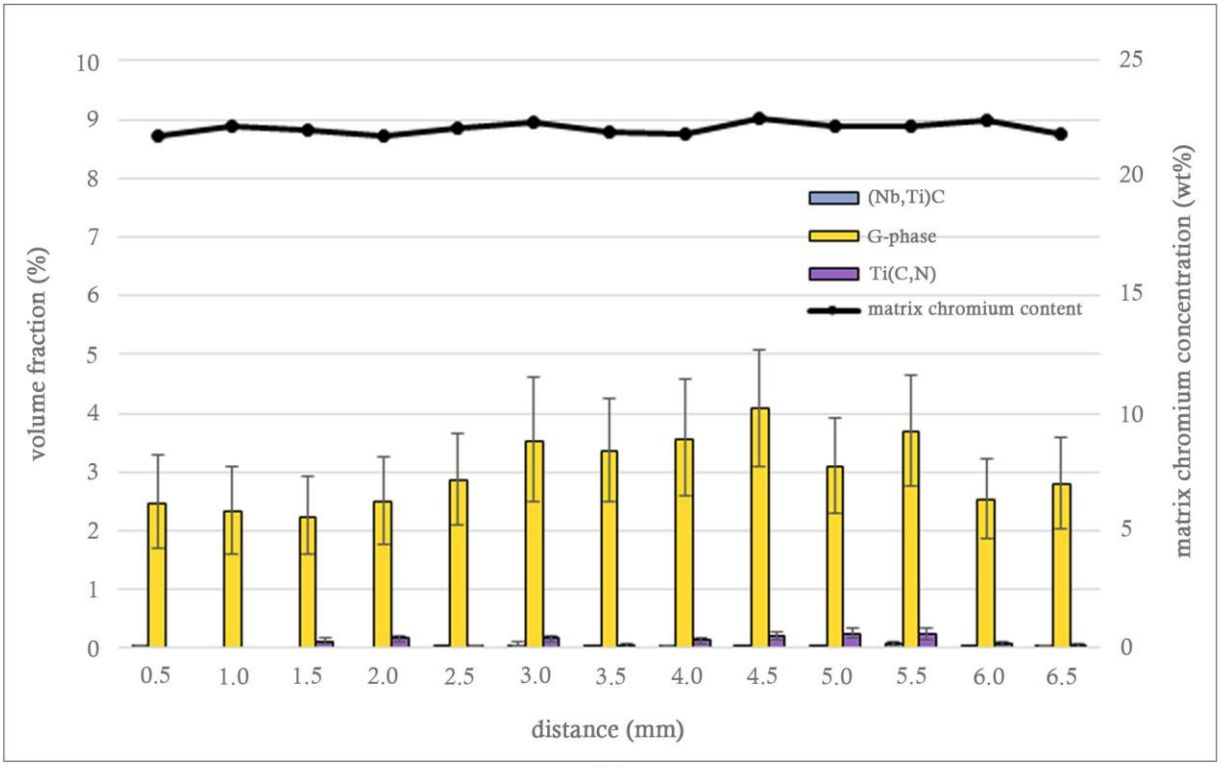

(b)

Figure 5.42 - Measured volume fractions and matrix chromium concentration in sample 4B. (a) all volume fractions, (b) minor volume fractions. Distance is measured from the inner diameter.

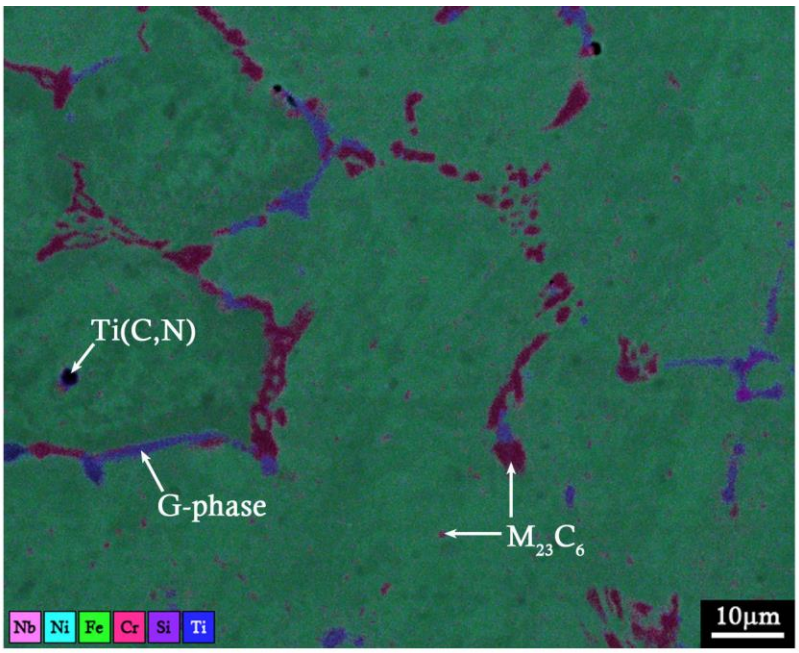

Figure 5.43 - Representative EDS map of the microstructure in sample 4C.

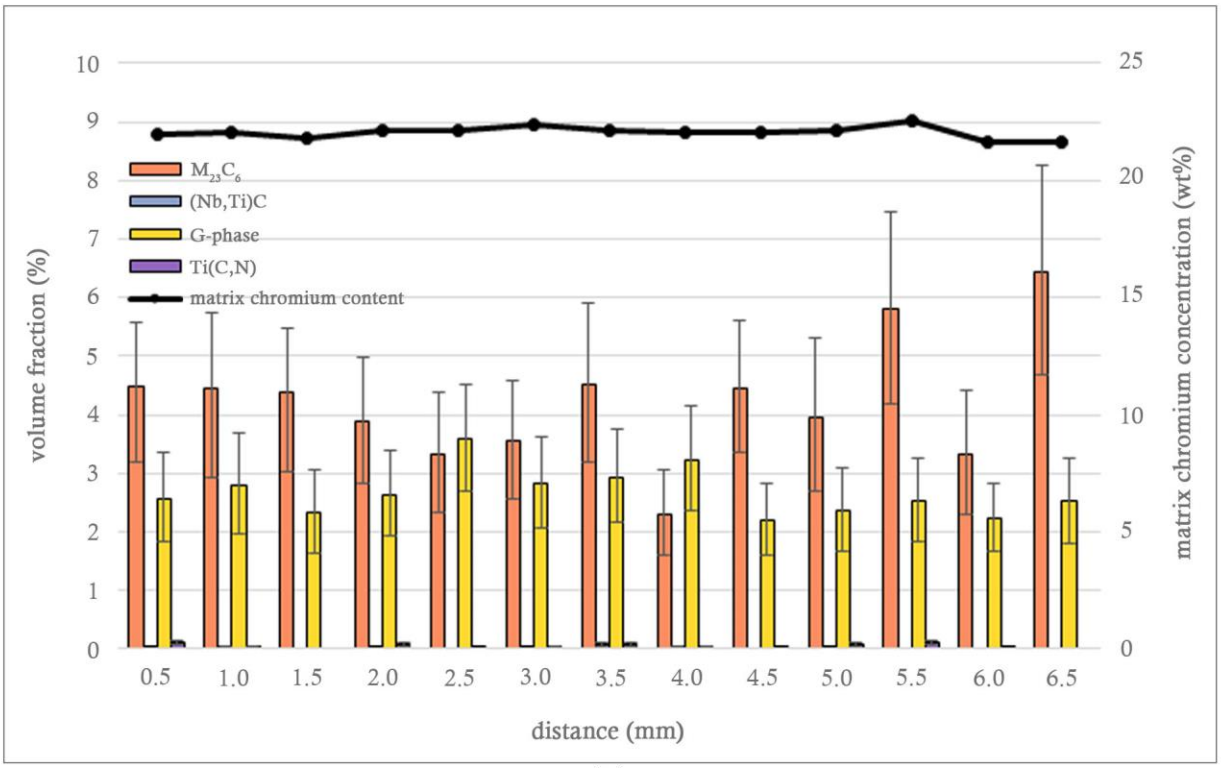

(a)

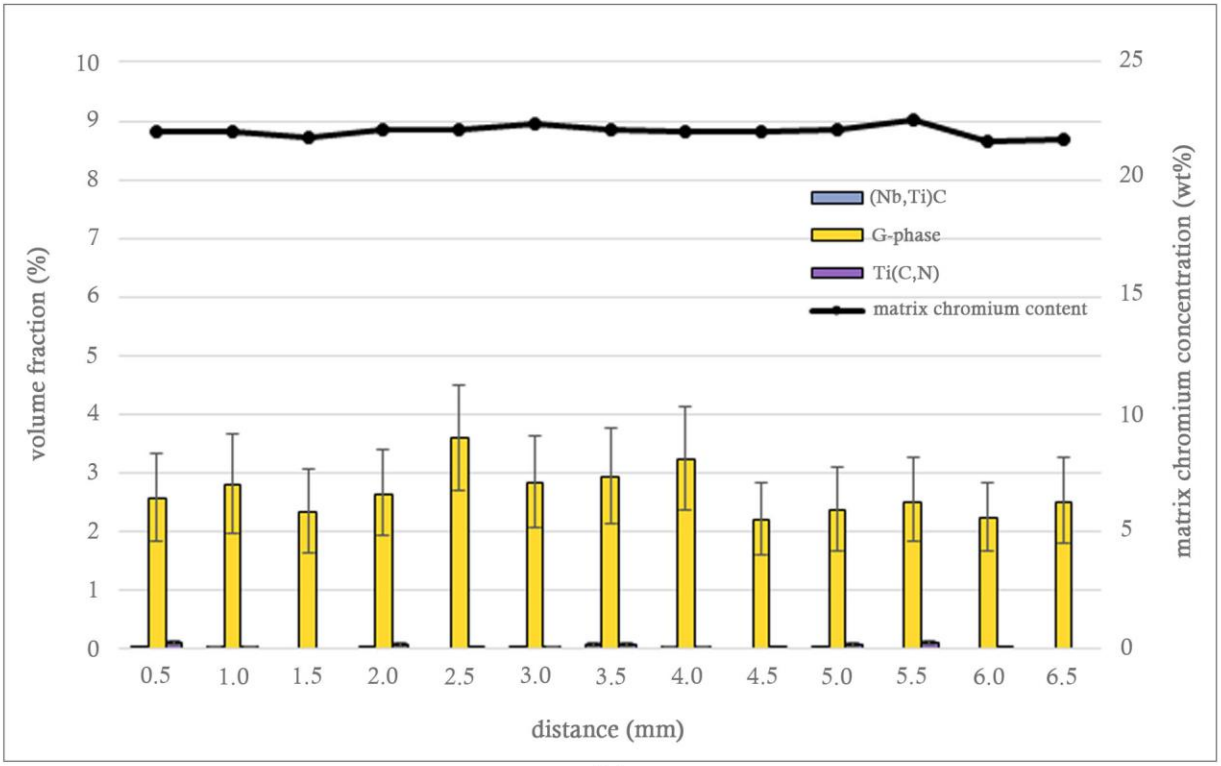

(b)

Figure 5.44 - Measured volume fractions and matrix chromium concentration in sample 4C. (a) all volume fractions, (b) minor volume fractions. Distance is measured from the inner diameter.

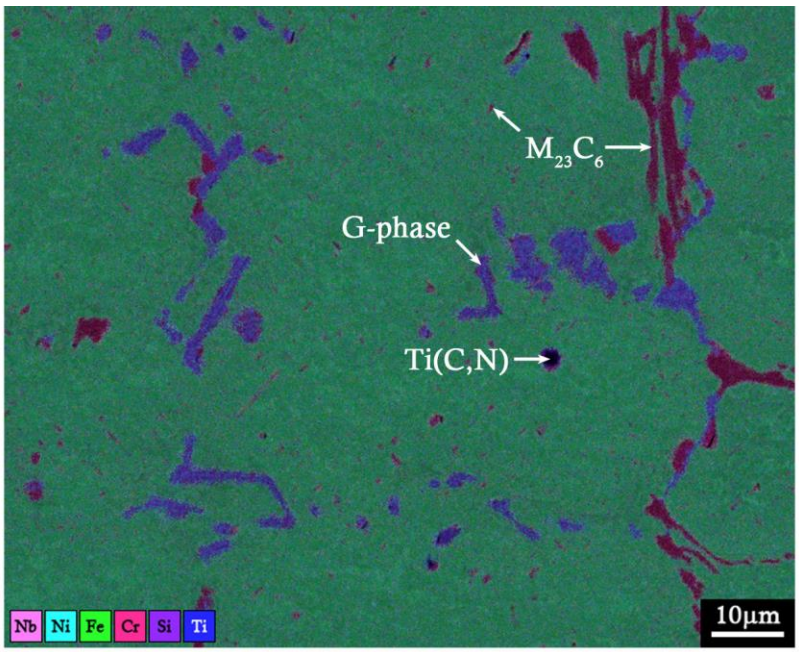

Figure 5.45 - Representative EDS map of the microstructure in sample 4D.

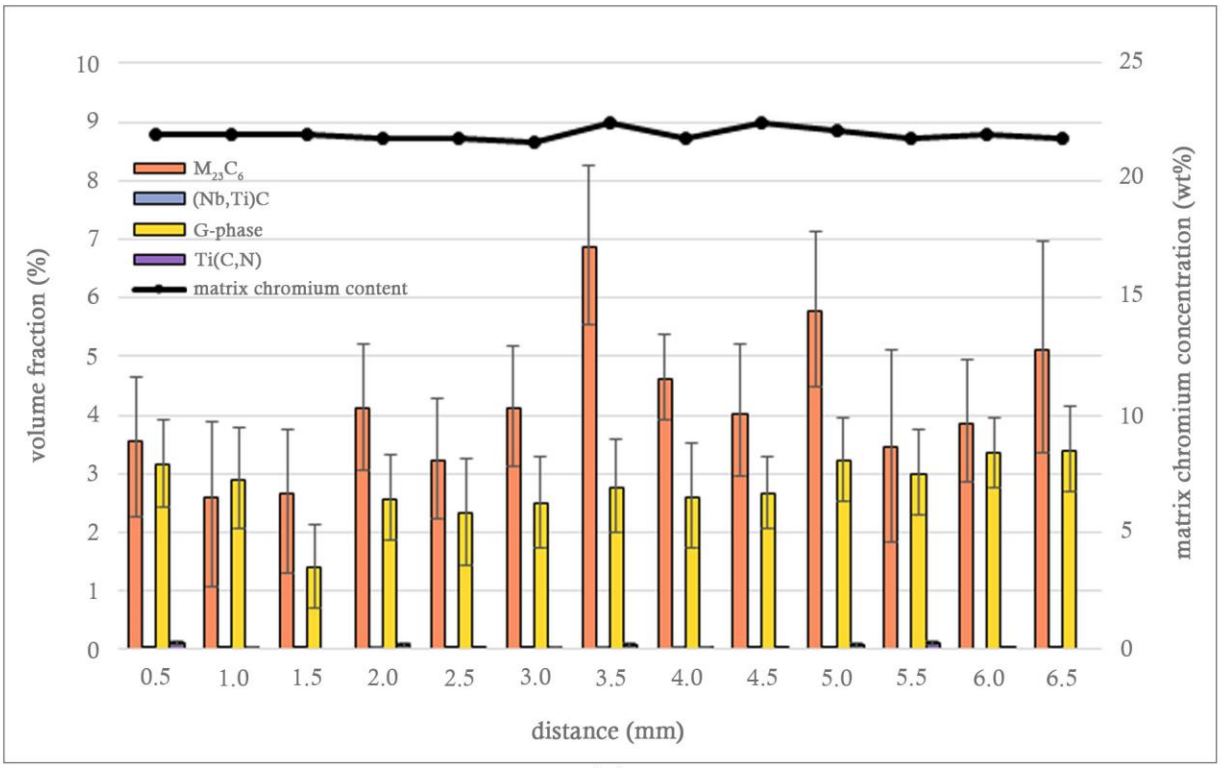

(a)

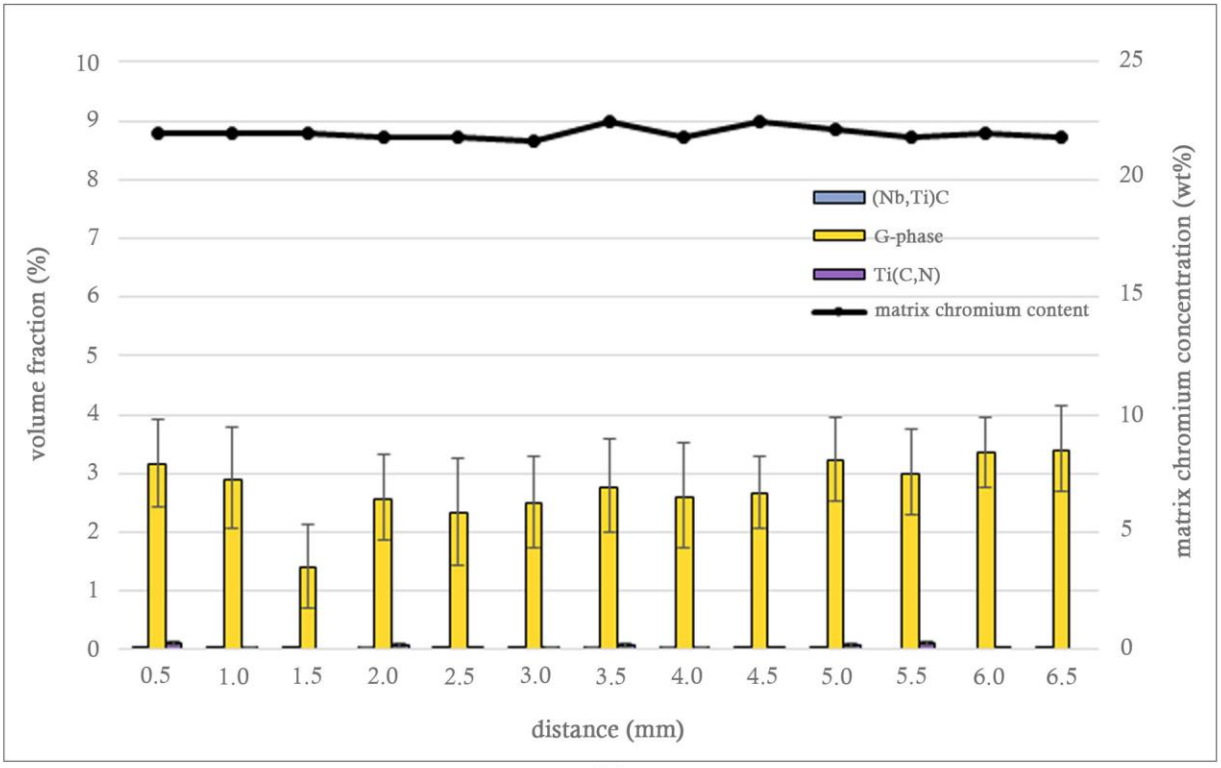

(b)

Figure 5.46 - Measured volume fractions and matrix chromium concentration in sample 4D. (a) all volume fractions, (b) minor volume fractions. Distance is measured from the inner diameter.

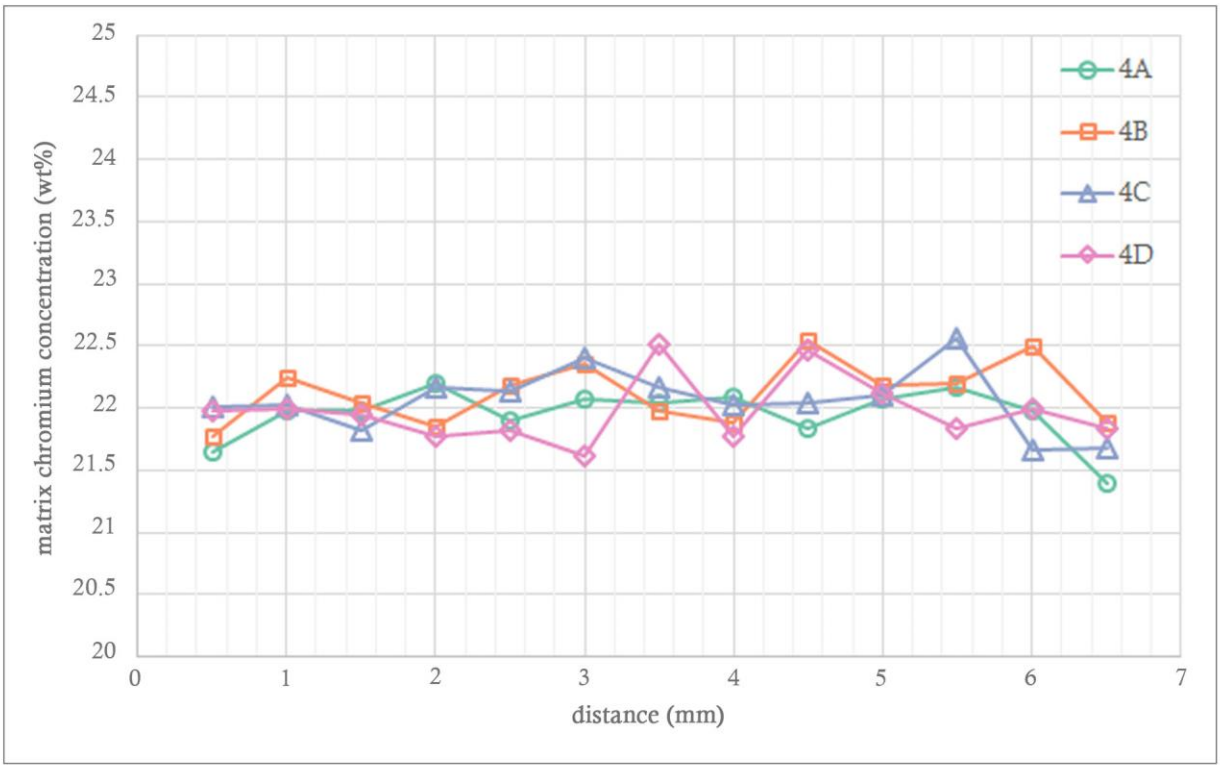

Figure 5.47 - Matrix chromium concentrations for samples 4A-D. Distance is measured from the inner diameter.

5.2.5 Tube 5

As discussed in Section 4.5.5, tube 5 displayed a moderate level of carbide coarsening and carburization.

Chromium Carbides

The majority of the primary precipitate network in tube 5 was composed of chromium carbides. $M_{23}C_6$ carbides were observed at the mid and outer wall regions of all samples, and M_7C_3 carbides at the inner wall regions. In comparing the EDS maps of the microstructure of tube 5 samples to those from tubes 1 and 2, it was evident that the tube 5 microstructure had coarsened to a lesser extent. The maximum chromium carbide volume fraction occurred within the 0.5 – 1.0 mm wall region in all four samples, in the range of $M_7C_3 \approx 26 - 31$ %. The $M_{23}C_6$-to-M_7C_3 transformation front was located within the 1.0 – 1.5 mm wall region in samples 5A, 5B, and 5C, and further from the inner diameter in sample 5D, as summarized in Table 5.6. As in tubes 1 and 2, the chromium carbide volume fraction at the transformation front was typically in the range of 20 – 25 %. In samples 5A, 5B, and 5C the chromium carbide volume fraction dropped quickly from a value of $M_{23}C_6 \approx 16.5 - 20\%$ in the 1.5 mm wall region to a value of $M_{23}C_6 \approx 5 - 8$ % by the 2.5 mm wall region, remaining constant within the 5 – 8 % range for the remainder of the wall. In sample 5D, the M_7C_3 volume fraction remained in the 25 – 30 % range up to the $M_{23}C_6$-to-M_7C_3 transformation front, and the $M_{23}C_6$ volume fraction was

observed to drop off gradually after the transformation front for the remainder of the wall thickness, down to a value of $M_{23}C_6 \approx 4$ % in the 7.0 mm wall region at the outer diameter. A comparison between the primary chromium carbide volume fractions in samples 5A-D is shown in Figure 5.48.

Secondary $M_{23}C_6$ carbides were observed in all samples from tube 5, located in the wall regions where the primary chromium carbide was $M_{23}C_6$, as summarized in Table 5.7. They were typically in the range of 2 - 5 μm in size, and relatively abundant in the mid wall regions. At the outer wall, the size of the secondary $M_{23}C_6$ tended towards the upper end of the size range, and qualitatively the number of individual precipitates appeared to decrease.

Table 5.6 - Summary of the distance from the inner wall to the $M_{23}C_6$-to-M_7C_3 transformation front for samples from tube 5.

Sample	Positions of the $M_{23}C_6$-to-M_7C_3 transformation front (mm)
5A	1.1
5B	1.25
5C	1.25
5D	2.1

Table 5.7 - Summary of the secondary $M_{23}C_6$ precipitate distributions in samples from tube 5.

Sample	Wall region in which secondary $M_{23}C_6$ is present	Description of secondary $M_{23}C_6$ distribution
5A	1.5 – 7.0 mm	Coarse (typically 2-5 μm), relatively abundant in mid wall, less so at outer wall.
5B	1.5 – 8.0 mm	
5C	1.5 – 7.5 mm	
5D	2.5 – 7.0 mm	

Niobium – Titanium Carbides and Silicides

The volume fraction of the (Nb,Ti)C carbides in tube 5 typically remained below 2 % at all locations in all samples.

In samples 5A, 5B, and 5C, the transformation of (Nb,Ti)C to G-phase was observed at the mid wall, and the incomplete transformation of (Nb,Ti)C to η-carbide was observed at the outer wall. The (Nb,Ti)C-to-G-phase transformation was noted to be extremely close to complete at all locations

where it took place. The identification of (Nb,Ti)C carbides within the G-phase regions was rare, and when they were present their volume fraction typically remained below 0.2 %. The volume fraction of G-phase was typically in the 1.2 – 3.8 % range in the locations where it was present in samples 5A, 5B, and 5C.

In sample 5A, the (Nb,Ti)C-to-η-carbide transformation occurred in the 7.0 mm wall region, and the η-carbide attained a volume fraction of ≈ 3.7 %, In sample 5C, the transformation occurred in the 7.0 – 7.5 mm wall region, with the volume fraction of η-carbide increasing from ≈ 3.3 % to ≈ 5.6 % with increased proximity to the outer surface. Sample 5B displayed the greatest volume fraction of η-carbide, with the volume fraction increasing from ≈ 5.4 % to ≈ 11.4 % over the 7.5 – 8.0 mm wall region.

In sample 5D, the incomplete transformation of (Nb,Ti)C to η-carbide was observed in the 5.0 – 7.0 mm wall region, increasing from a volume fraction of ≈ 1 % to a volume fraction of ≈ 8.5 % with proximity to the outer surface. The (NbTi)C-to-η-carbide transformation was noted to be more complete with increased proximity to the outer surface. The (Nb,Ti)C-to-G-phase transformation was not observed in sample 5D.

A summary of the locations of the (Nb,Ti)C-to-G-phase and (Nb,Ti)C-to-η-carbide transformations in the tube 5 samples is given in Table 5.8.

Ti(C,N) carbonitrides were observed on occasion in the austenite matrix in all samples from tube 5. The volume fraction of Ti(C,N) precipitates did not exceed 0.4 % at any location.

Table 5.8 - Summary of the locations of the (Nb,Ti)C-to-G-phase and (Nb,Ti)C-to-η-carbide transformations in the tube 5 samples.

Sample	Wall region over which the (Nb-Ti)C-to-G-phase transformation was observed	Wall region over which the (Nb-Ti)C-to-η-carbide transformation was observed
5A	2.0 – 6.5 mm	7.0 mm
5B	2.0 – 7.0 mm	7.5 – 8.0 mm
5C	2.0 – 6.5 mm	7.0 – 7.5 mm
5D	-	5.0 – 7.0 mm

Matrix Chromium Concentration

Samples 5A, 5B, and 5C displayed extremely similar microstructural features, and consequently also displayed nearly identical matrix chromium concentration profiles, as summarised in Figure 5.57. In

these three samples, the matrix chromium concentration was at a minimum of 7.7 wt% in the 0.5 mm wall regions, and this increased to a value of 21 – 22 wt% by the 3.0 mm wall region. The matrix chromium concentration remained in the range of 21 - 22 wt% for the remainder of the wall thickness in all three samples. In sample 5D, a minimum matrix chromium concentration of 7.7 wt% was observed in the 0.5 mm wall region, and the maximum value of 21 wt% was observed at the outer wall, as with samples 5A, 5B, and 5C. However, the slope of the matrix chromium concentration profile in between the two extreme points in sample 5D was markedly shallower than profiles of the other three samples. Sample 5D displayed greater chromium carbide and η-carbide volume fractions across larger regions of the wall thickness in comparison to the other three samples from tube 5, consistent with the reduced chromium concentration in the matrix across the mid wall region. In all samples, the matrix chromium concentration at the location of the $M_{23}C_6$-to-M_7C_3 transformation front was in the range of 10 – 12 wt%.

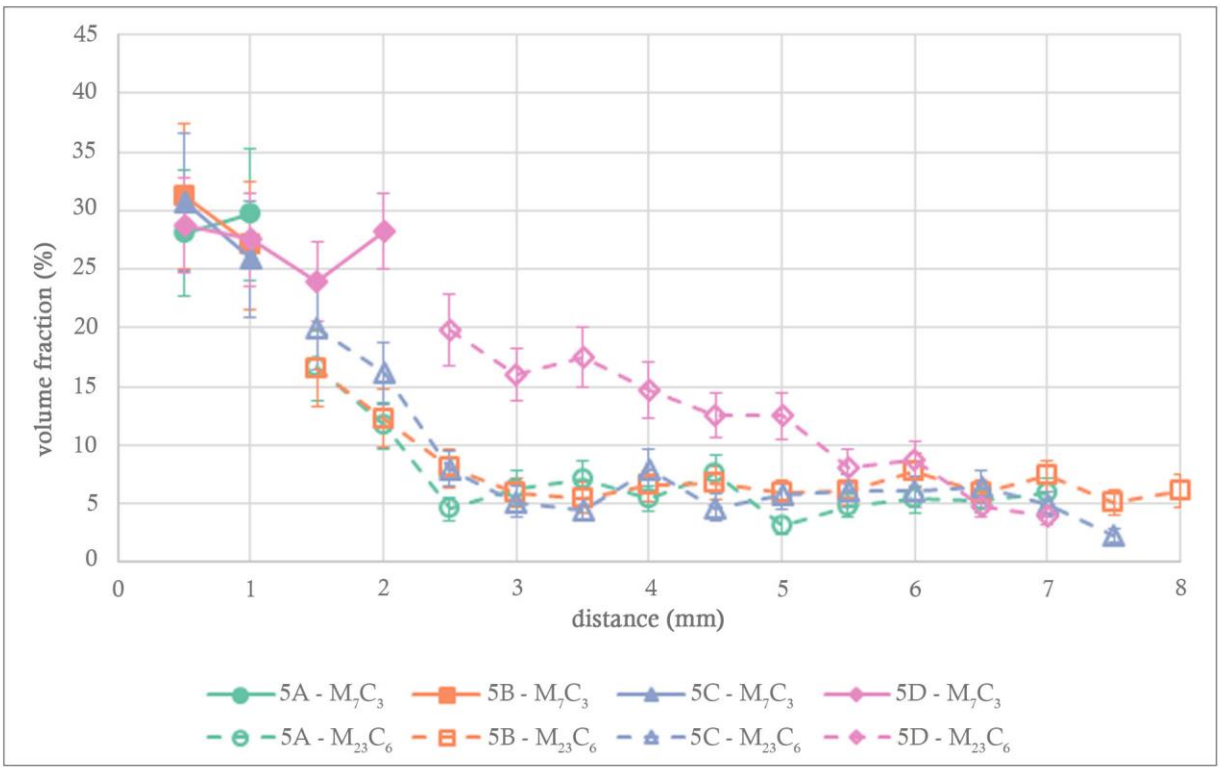

Figure 5.48 - Comparison of primary chromium carbide volume fractions in samples 5A-D. Distance is measured from the inner diameter.

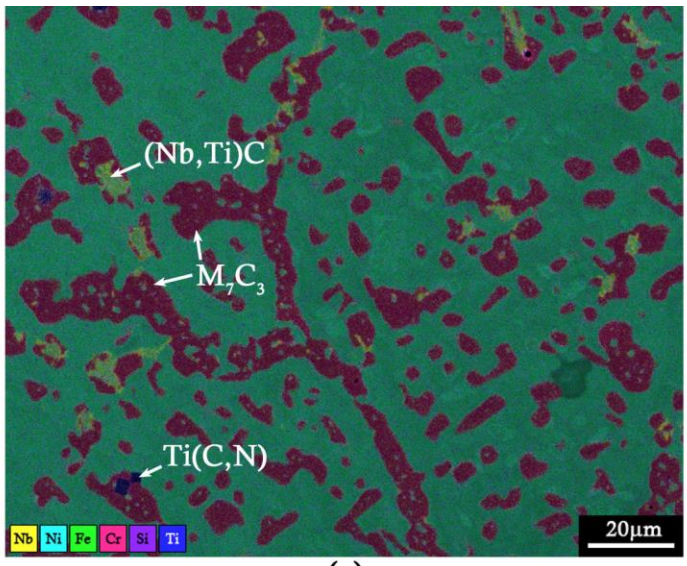

(a)

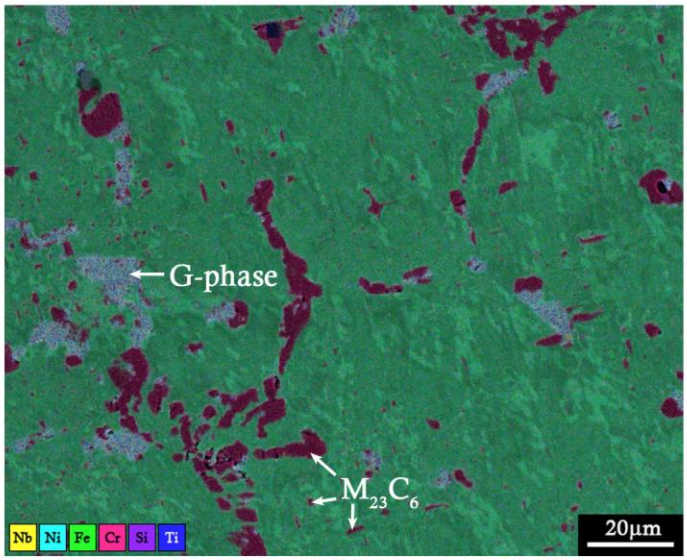

(b)

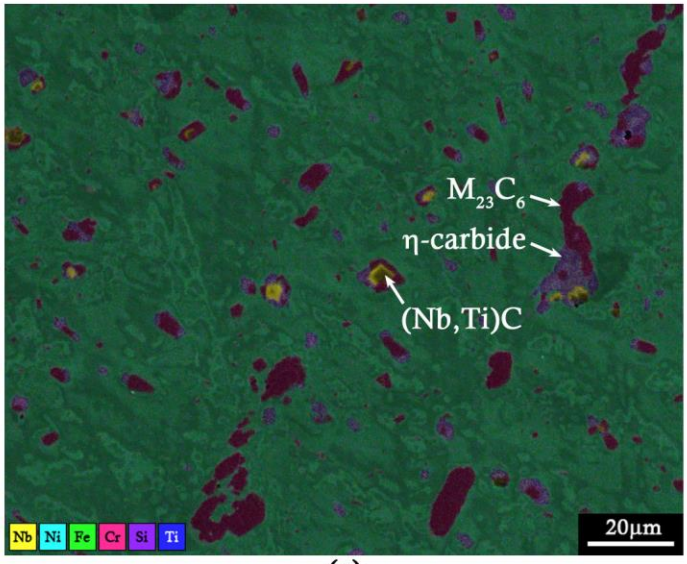

(c)

Figure 5.49 - Representative EDS maps of the microstructure in sample 5A at distances of (a) 0.5 mm, (b) 4.0 mm, and (c) 7.0 mm from the inner diameter.

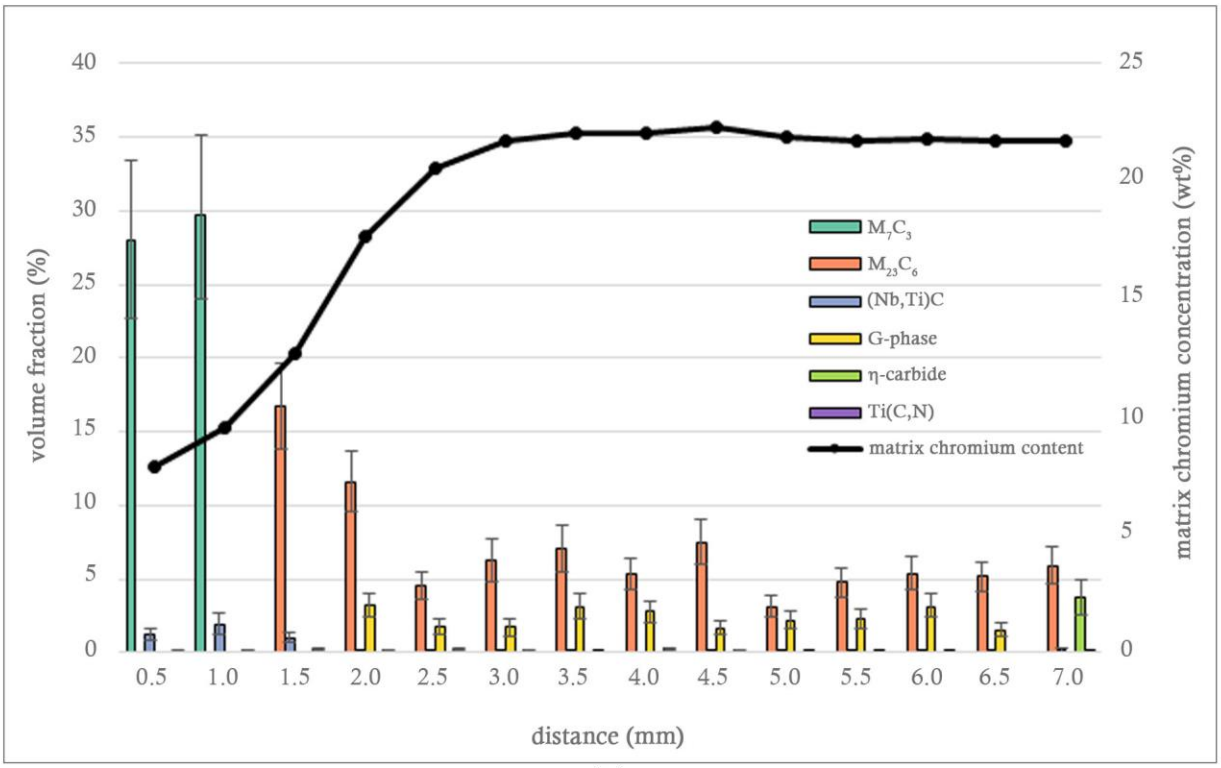

(a)

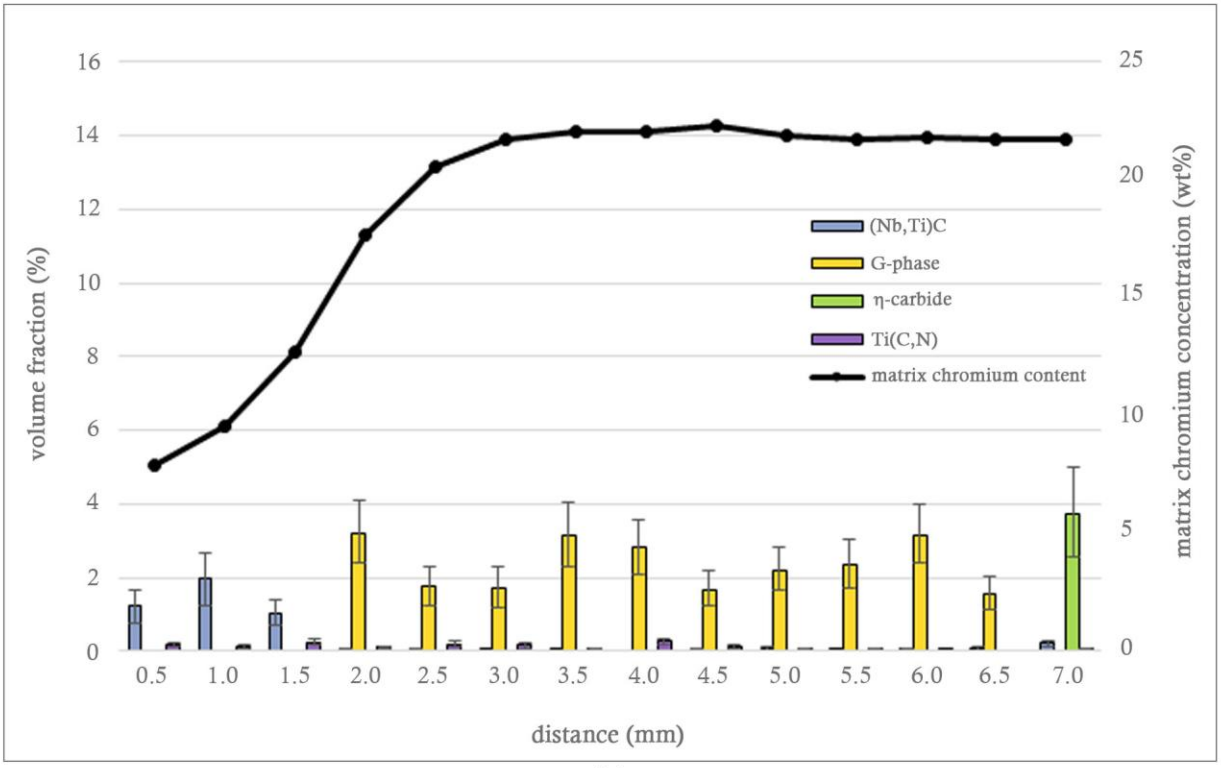

(b)

Figure 5.50 - Measured volume fractions and matrix chromium concentration in sample 5A. (a) all volume fractions, (b) minor volume fractions. Distance is measured from the inner diameter.

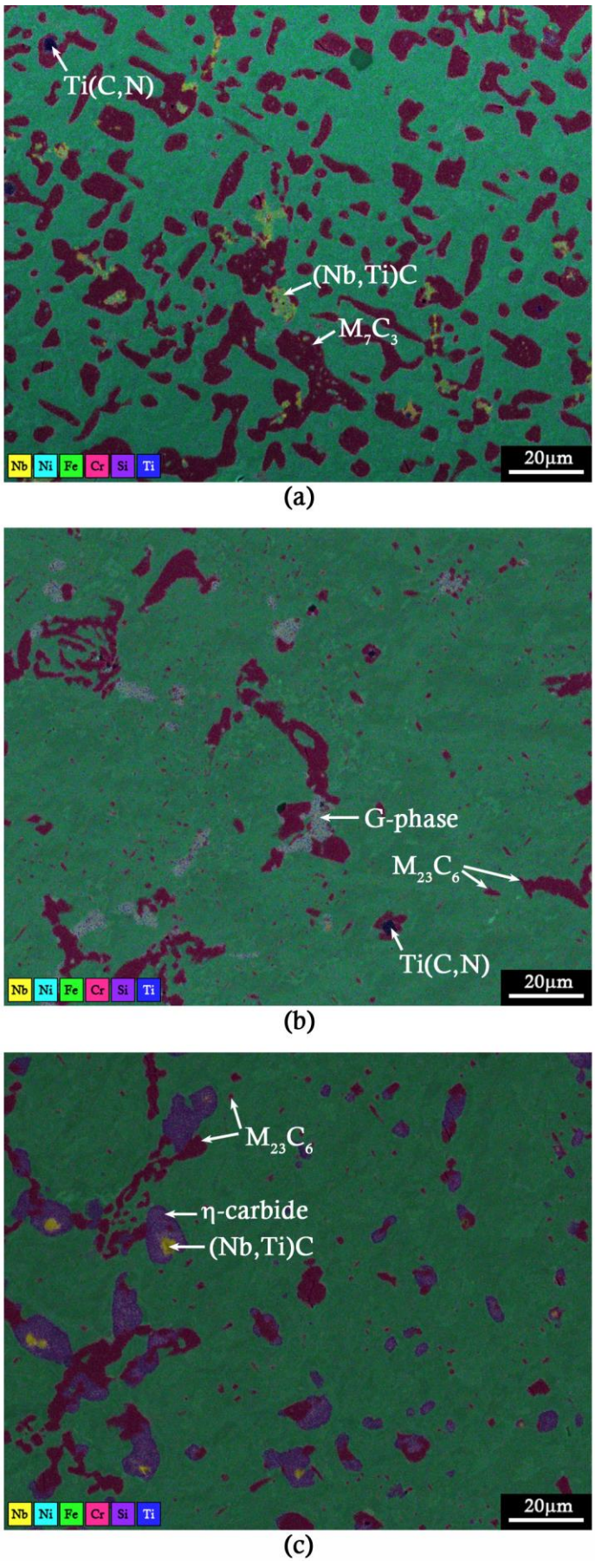

Figure 5.51 - Representative EDS maps of the microstructure in sample 5B at distances of (a) 0.5 mm, (b) 4.0 mm, and (c) 8.0 mm from the inner diameter.

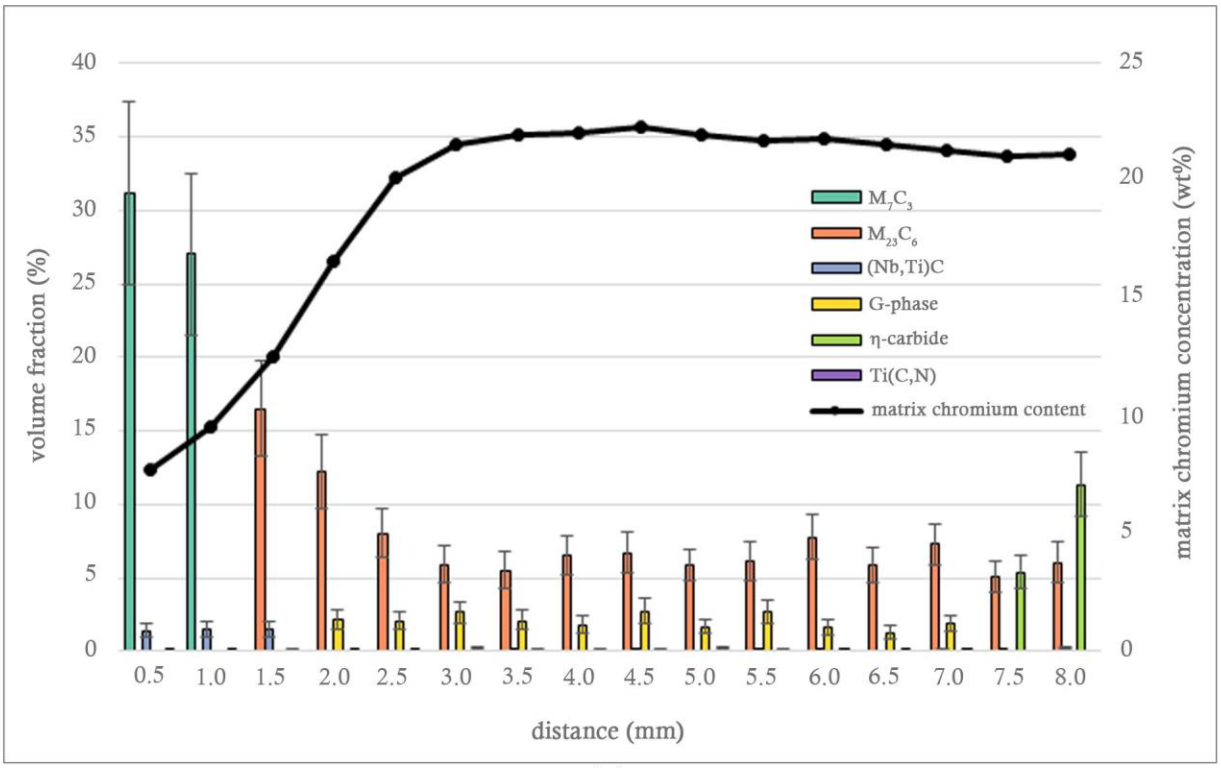

(a)

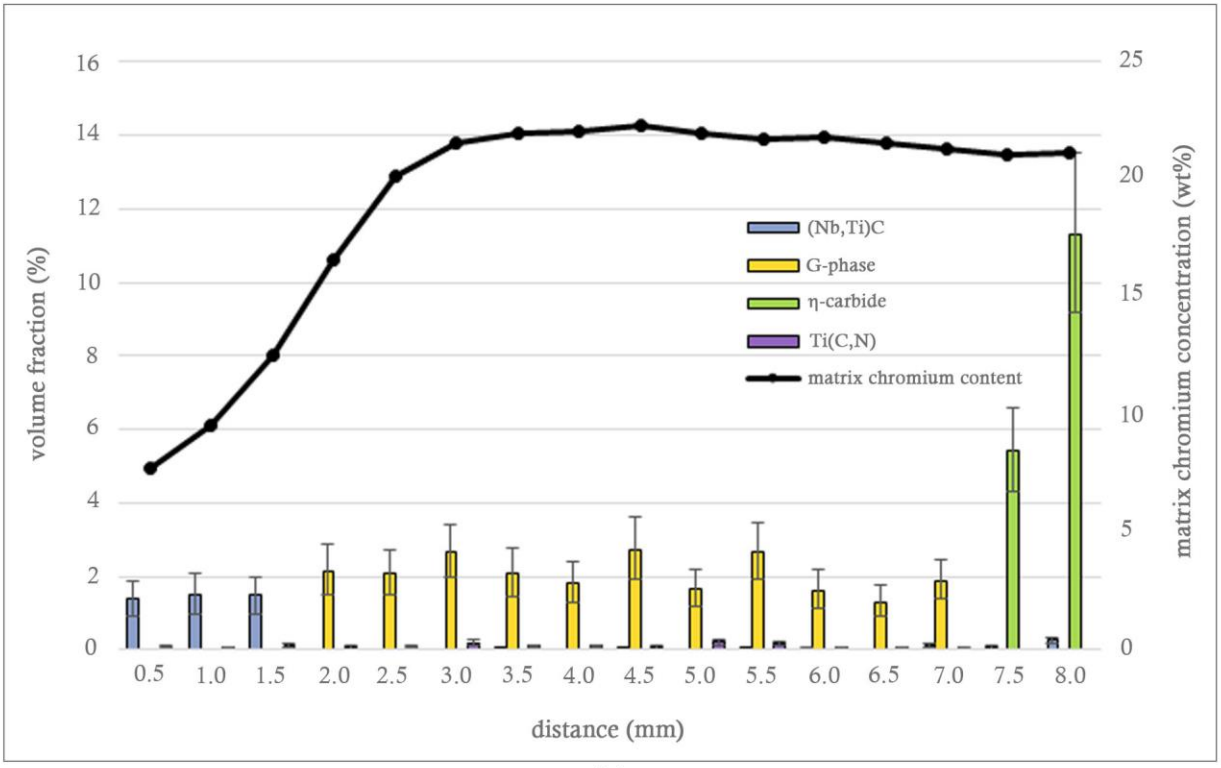

(b)

Figure 5.52 - Measured volume fractions and matrix chromium concentration in sample 5B. (a) all volume fractions, (b) minor volume fractions. Distance is measured from the inner diameter.

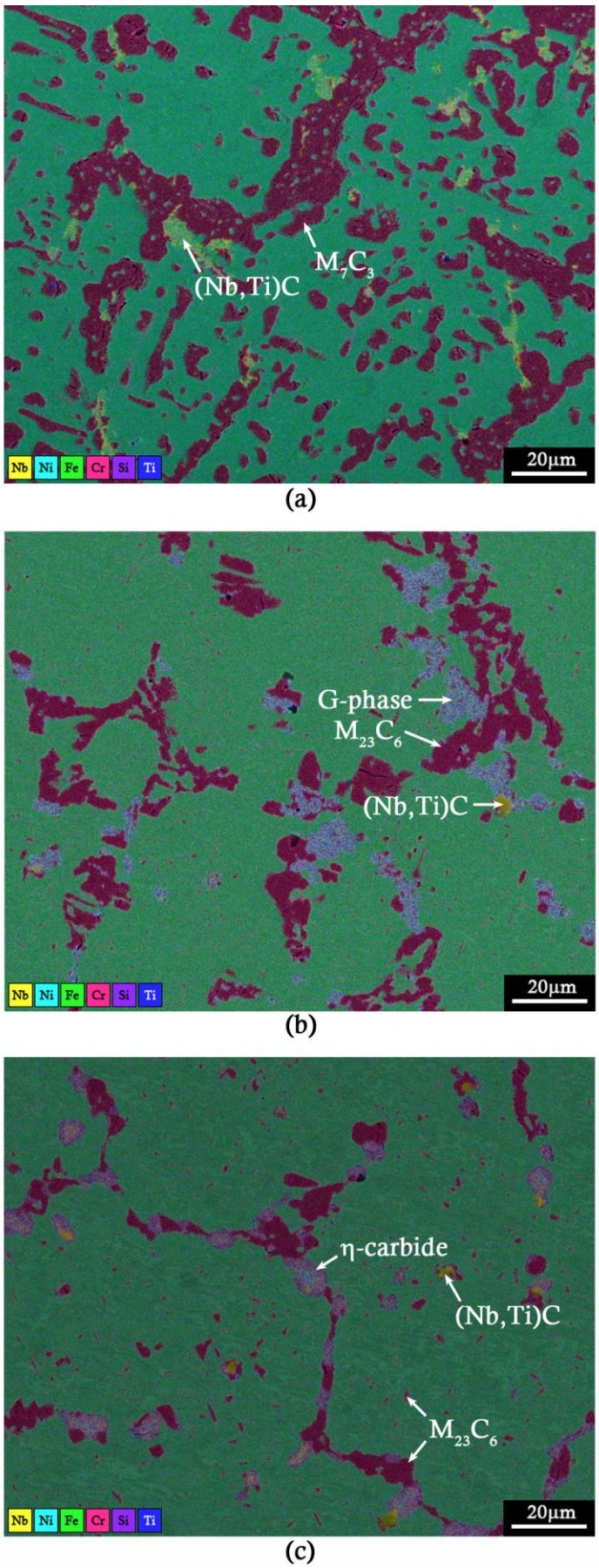

Figure 5.53 - Representative EDS maps of the microstructure in sample 5C at distances of (a) 0.5 mm, (b) 4.0 mm, and (c) 7.0 mm from the inner diameter.

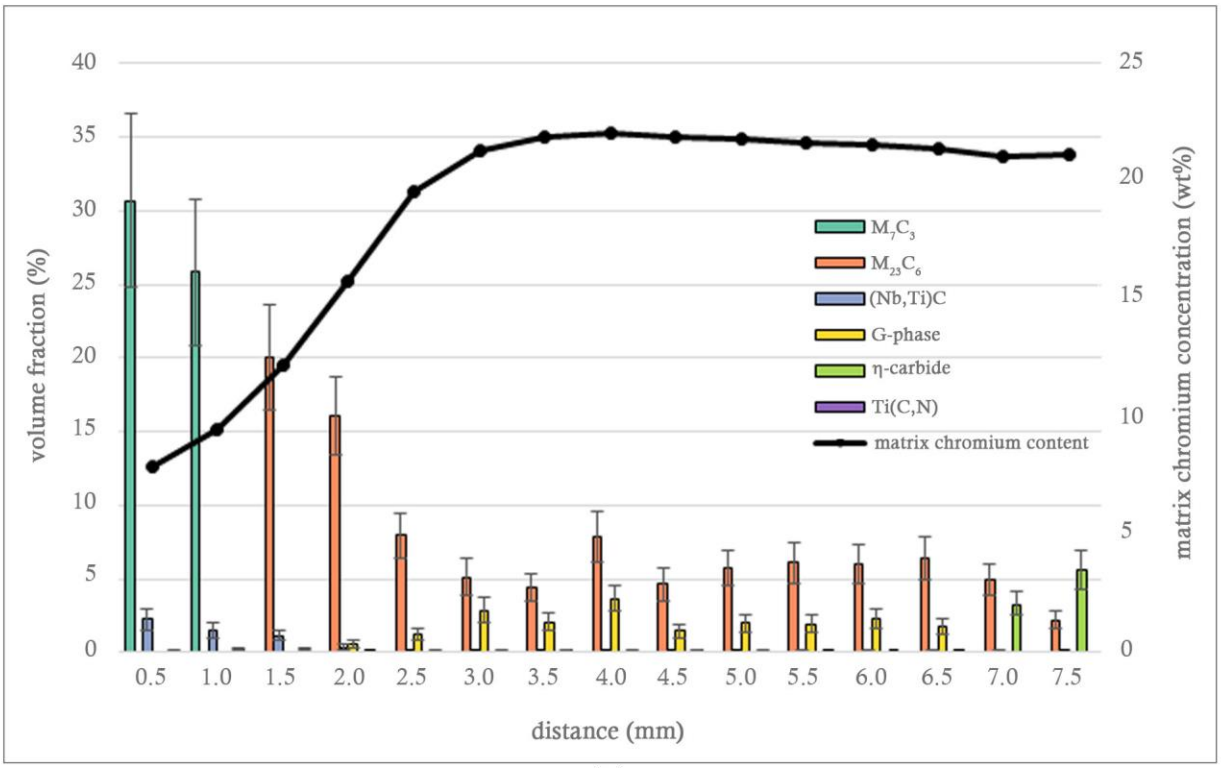

(a)

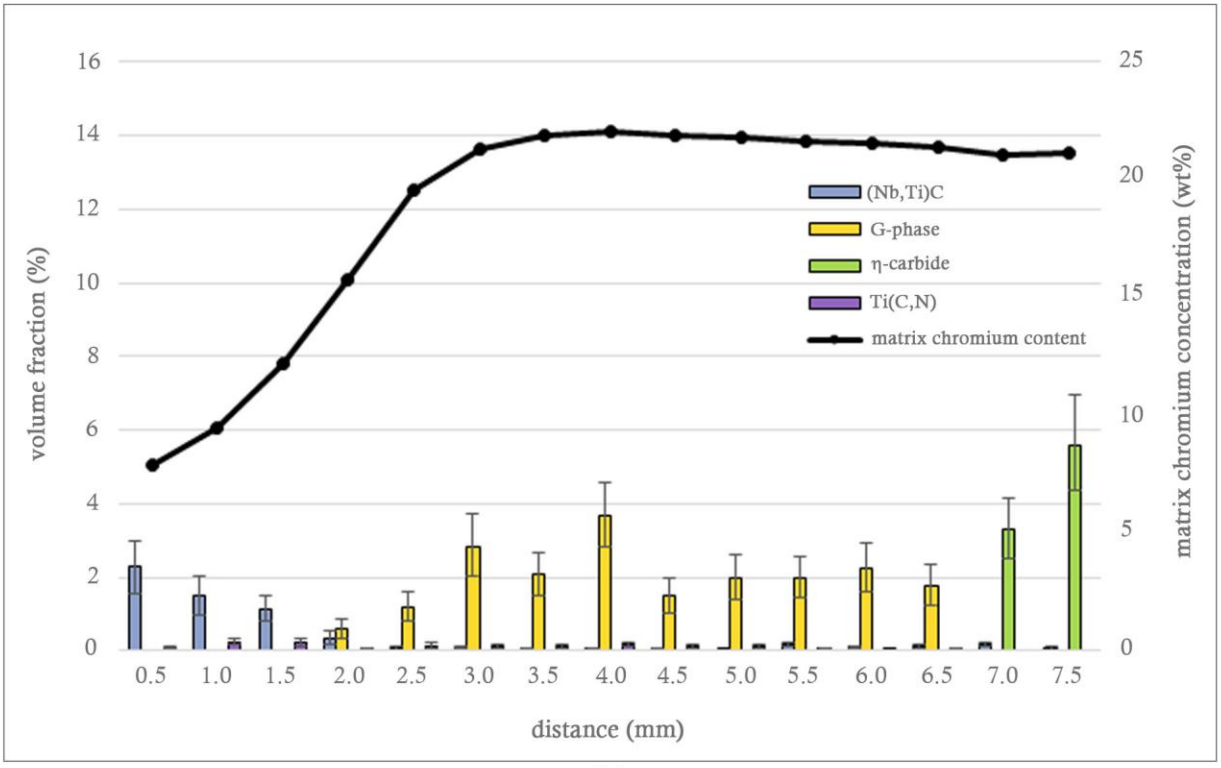

(b)

Figure 5.54 - Measured volume fractions and matrix chromium concentration in sample 5C. (a) all volume fractions, (b) minor volume fractions. Distance is measured from the inner diameter.

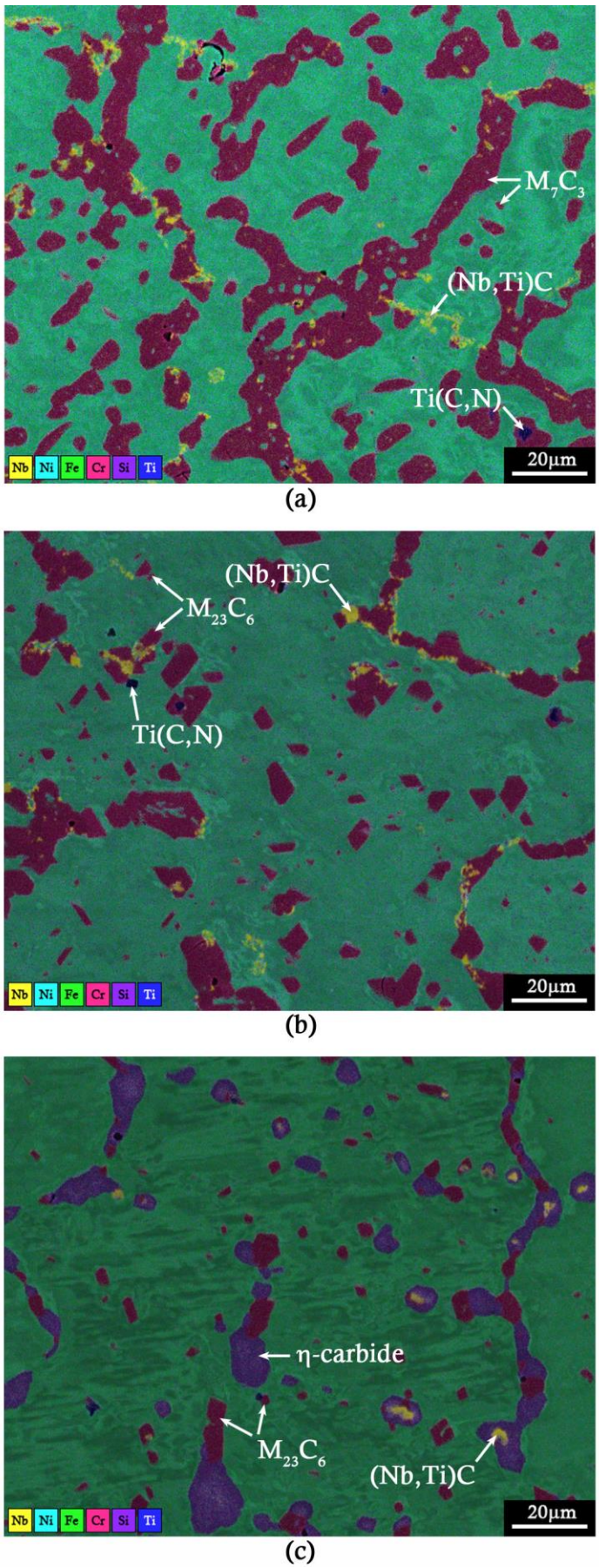

Figure 5.55 - Representative EDS maps of the microstructure in sample 5D at distances of (a) 0.5 mm, (b) 4.0 mm, and (c) 7.0 mm from the inner diameter.

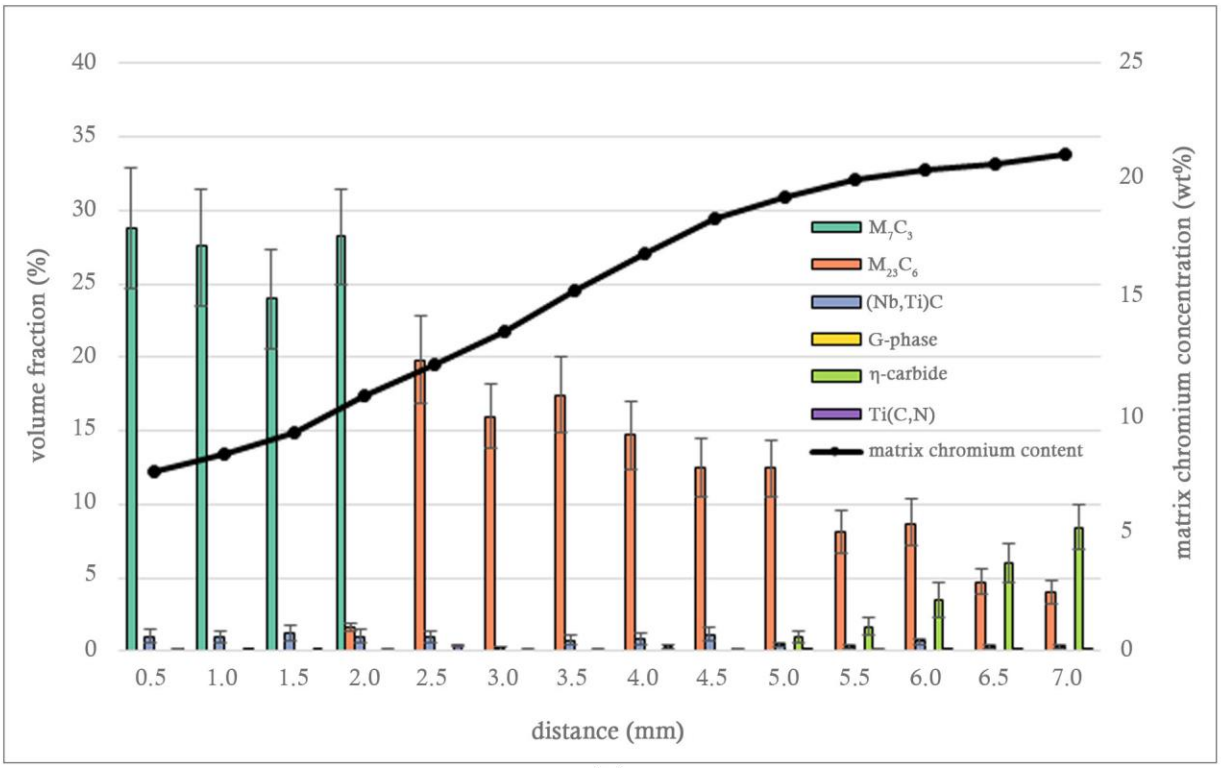

(a)

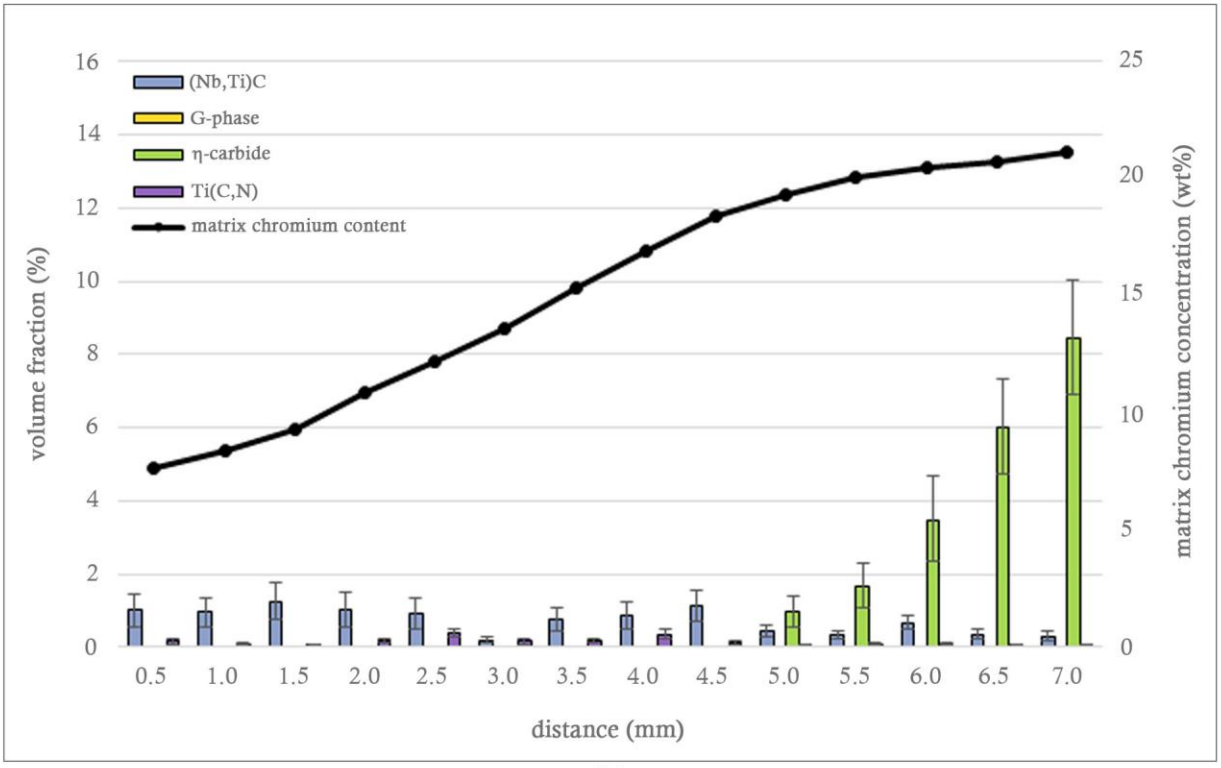

(b)

Figure 5.56 - Measured volume fractions and matrix chromium concentration in sample 5D. (a) all volume fractions, (b) minor volume fractions. Distance is measured from the inner diameter.

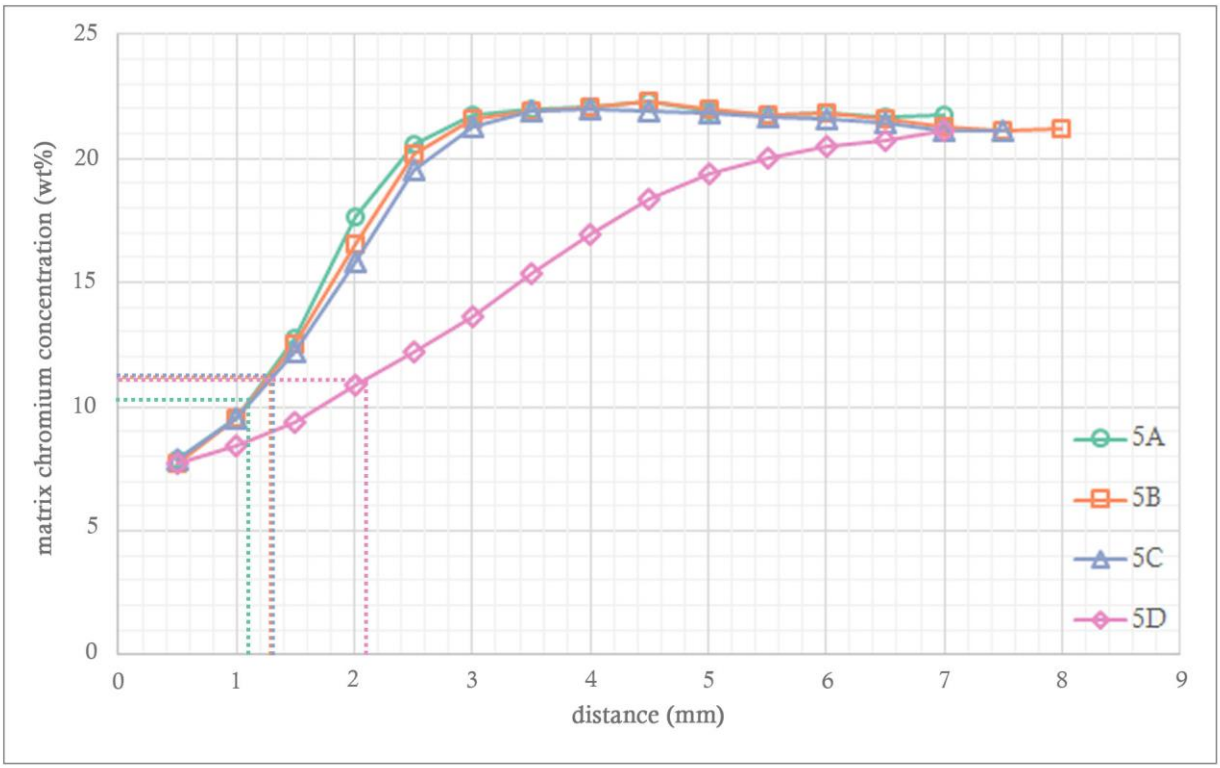

Figure 5.57 - Matrix chromium concentrations for samples 5A-D. Dashed lines indicate the positions of the $M_{23}C_6$-to-M_7C_3 transformation fronts in the corresponding colour coded sample. Distance is measured from the inner diameter.

5.2.6 Tube 6

Chromium Carbides

The majority of the primary precipitate network in tube 6 was composed of $M_{23}C_6$ chromium carbides. No transformation to M_7C_3 was observed in any of the samples from tube 6. The volume fraction of the primary $M_{23}C_6$ carbides was typically in the range of 6 - 14%. Although the volume fraction of the primary $M_{23}C_6$ carbides remained relatively consistent across the wall thicknesses of the samples in tube 6, its typical appearance changed with proximity to the outer diameter. As shown in Figure 5.62, the primary $M_{23}C_6$ precipitates at the inner wall regions had retained some of the lamellar structure typical of an as-cast ET45-Micro alloy; however, with increased proximity to the outer surface the primary $M_{23}C_6$ precipitates became more globular.

A small number of secondary $M_{23}C_6$ carbides were observed in the microstructure in the mid and outer wall regions of the samples from tube 6. When present, the secondary $M_{23}C_6$ precipitates were typically on the order of 5 μm in size, and few in number.

Niobium - Titanium Carbides and Silicides

The transformation of (Nb,Ti)C to G-phase was observed in all four samples from tube 6 at the inner and mid wall regions, and the transformation of (Nb,Ti)C to η-carbide was observed in all four samples at the outer wall regions. A summary of the wall regions over which these transformations occurred is given Table 5.9. The volume fraction of G-phase was typically in the 1.5 – 2.8 % range at all locations where the (Nb,Ti)C-to-G-phase transformation occurred. The transformation was observed to be entirely complete at almost every location analysed, and the identification of (Nb,Ti)C precipitates remnant within the G-phase regions was rare. In sample 6A, the volume fraction of η-carbide increased from a value of ≈ 2 % to a value of ≈ 3.7 % over the 8.75 – 9.5 mm wall region. Conversely, the η-carbide volume fraction in sample 6C was observed to decrease from ≈ 3 % to ≈ 2 % over the same wall region. The minimum volume fraction of η-carbide (≈ 1.8 %) was observed at the 8.0 mm wall region in sample 6B, and the maximum η-carbide volume fraction (≈ 4 %) was observed at the 8.0 mm wall region of sample 6D.

Table 5.9 - Summary of the locations of the (Nb,Ti)C-to-G-phase and (Nb,Ti)C-to-η-carbide transformations in the tube 6 samples.

Sample	Wall region over which the (Nb-Ti)C-to-G-phase transformation was observed	Wall region over which the (Nb-Ti)C-to-η-carbide transformation was observed
6A	0.5 – 8.0 mm	8.75 – 9.5 mm
6B	0.5 – 7.25 mm	8.0 mm
6C	0.5 – 8.0 mm	8.75 – 9.5 mm
6D	0.5 – 7.25 mm	8.0 mm

Matrix Chromium Concentration

The matrix chromium concentration profiles were similar for all samples analysed from tube 6, as summarised in Figure 5.66. The lowest matrix chromium concentration was observed at the 0.5 mm wall region, with values in the range of 26.5 – 28.5 wt%. For samples 6A, 6C, and 6D, the matrix chromium concentration levelled out at approximately 31.5 wt% across the mid wall regions (2.75 – 5.75 mm), before decreasing slightly to a value of approximately 30.5 wt% at the outer wall. Sample 6B displayed slightly lower values of matrix chromium concentration in comparison to the other three samples. Its matrix chromium concentration levelled out at a value of approximately 30.3 wt% in the 2.75 – 5.75 mm wall region, before decreasing slightly over the remaining wall thickness to a value of approximately 29 wt% at the outer diameter. There did not appear to be any significant microstructural features in sample 6B that would result in the matrix chromium concentration being 1 – 1.5 wt% below that of the other three samples at all locations.

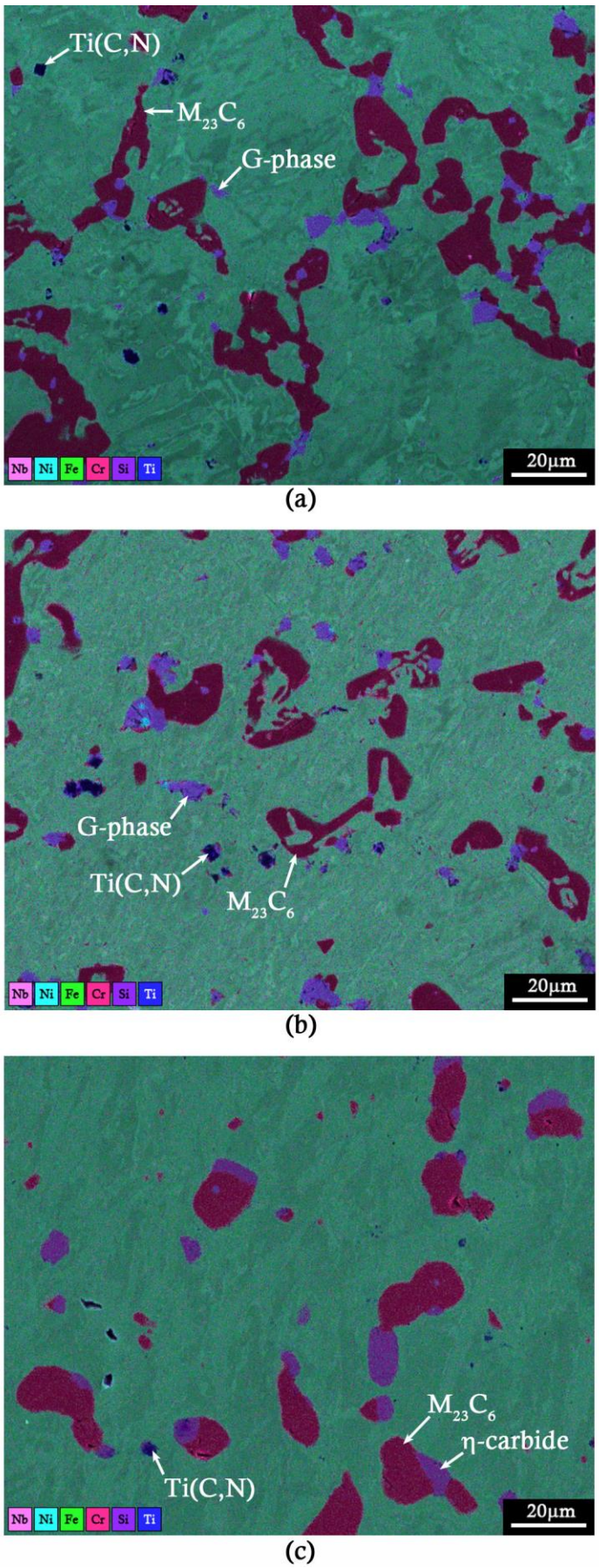

Figure 5.58 - Representative EDS maps of the microstructure in sample 6A at distances of (a) 0.5 mm, (b) 5.0 mm, and (c) 9.5 mm from the inner diameter.

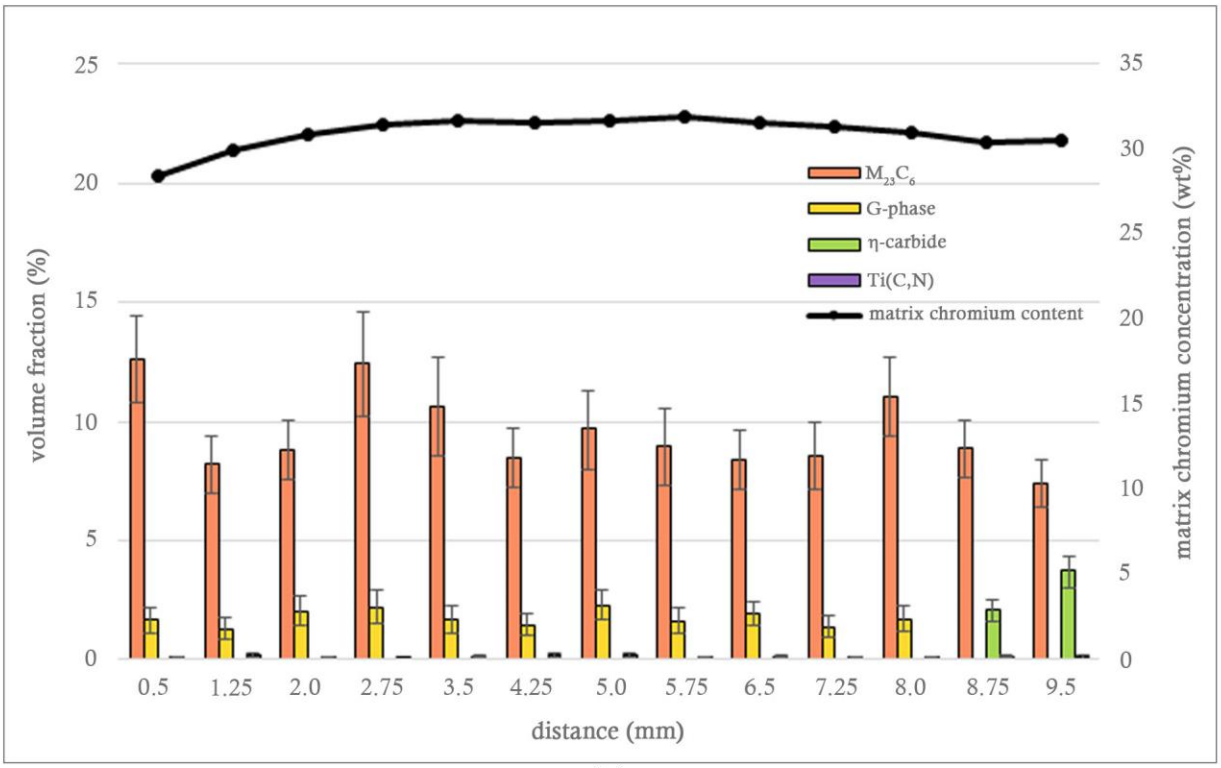

(a)

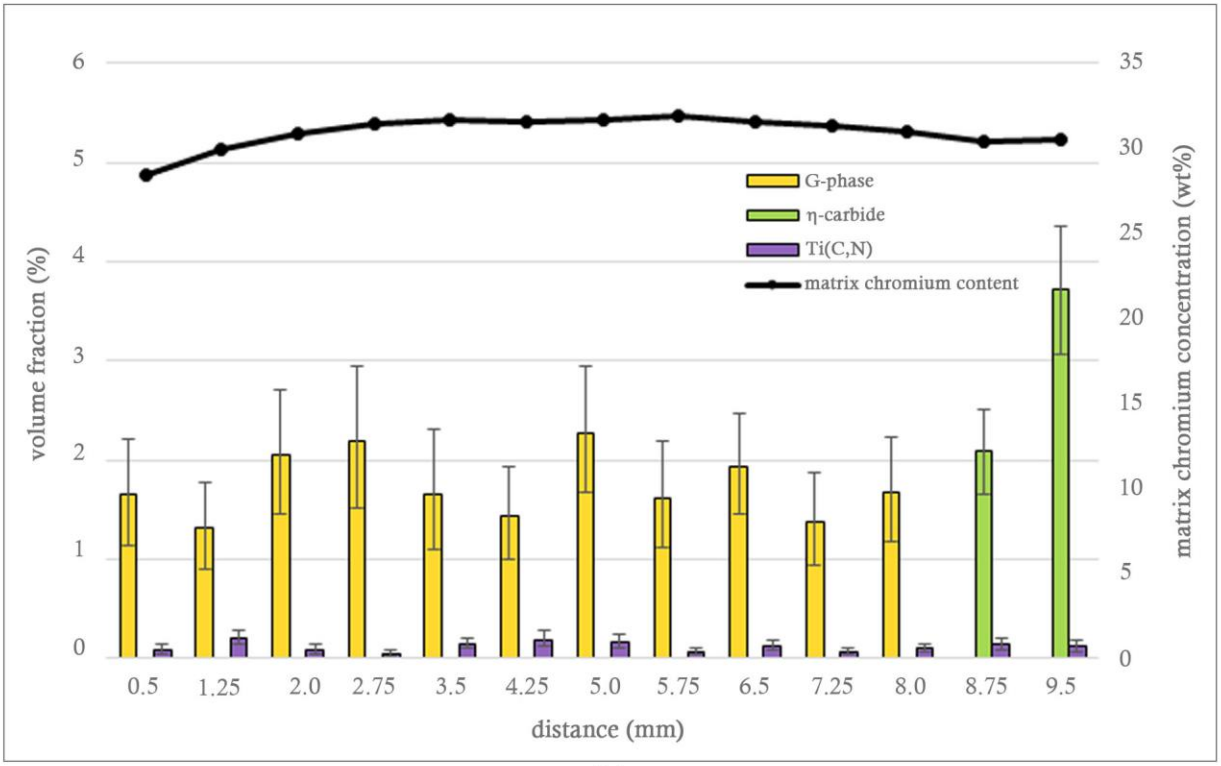

(b)

Figure 5.59 - Measured volume fractions and matrix chromium concentration in sample 6A. (a) all volume fractions, (b) minor volume fractions. Distance is measured from the inner diameter.

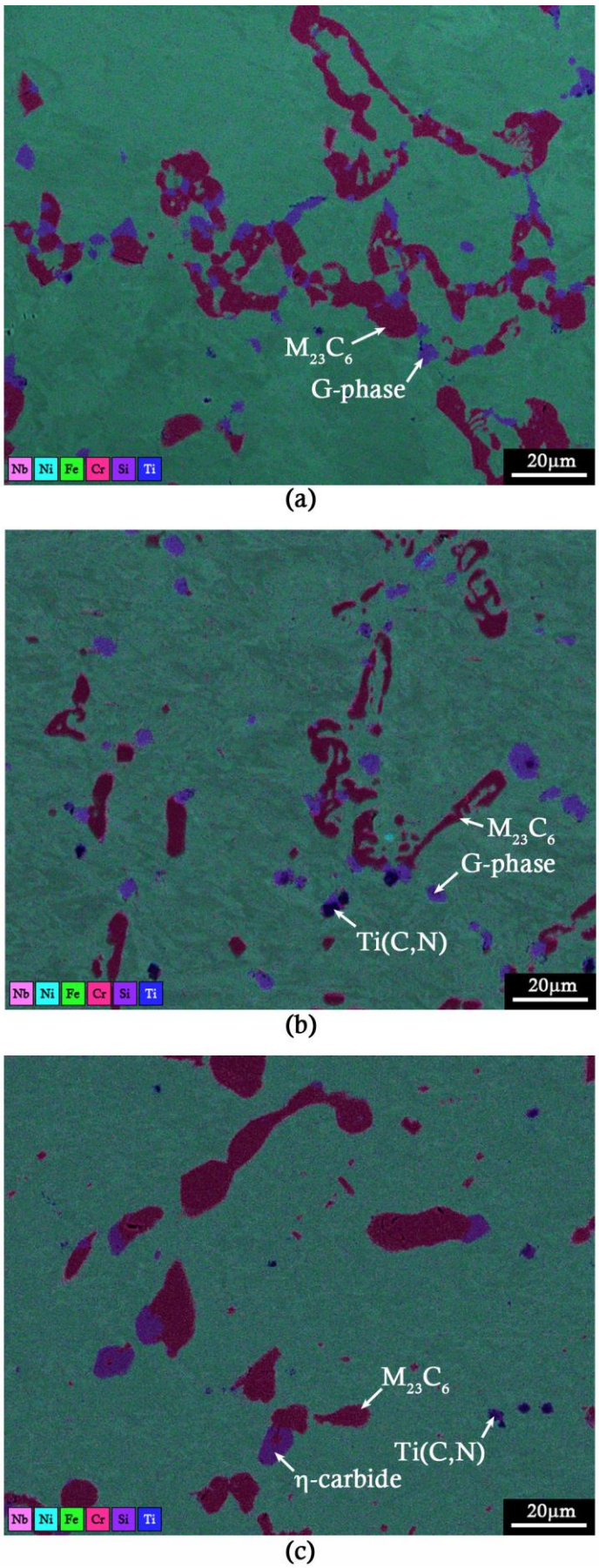

Figure 5.60 - Representative EDS maps of the microstructure in sample 6B at distances of (a) 0.5 mm, (b) 5.0 mm, and (c) 8.0 mm from the inner diameter.

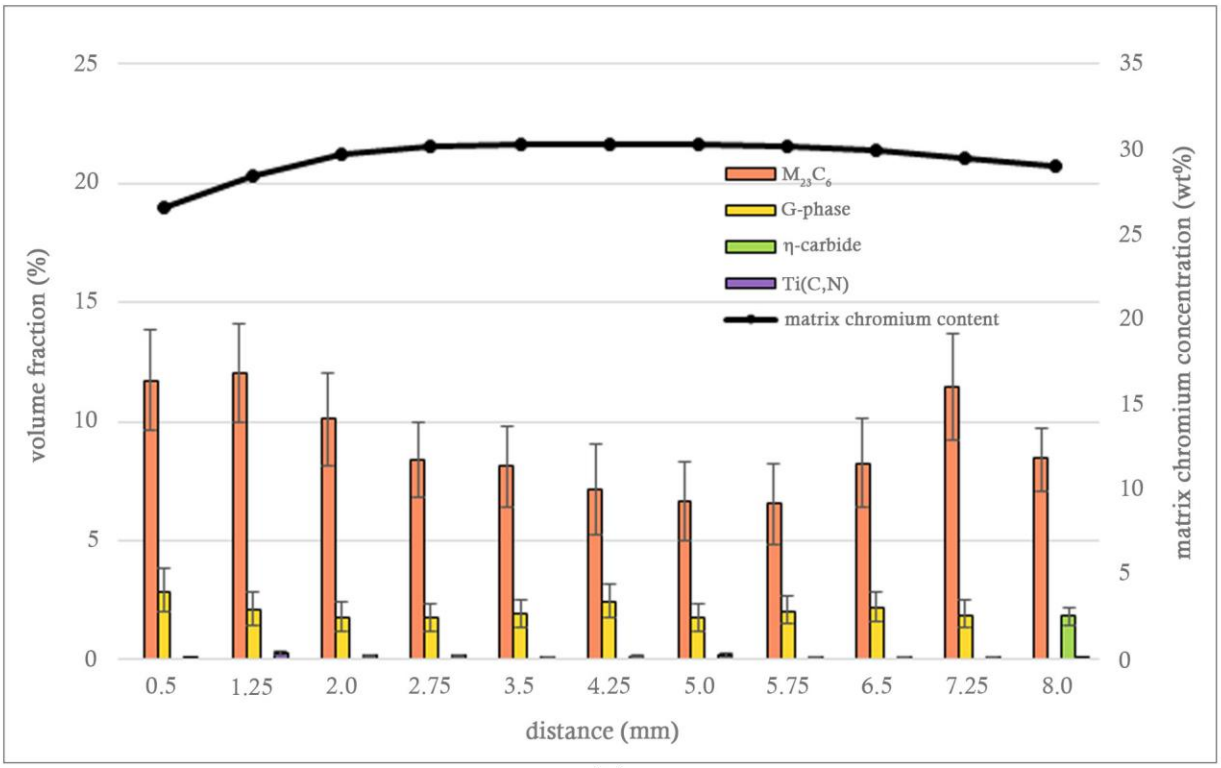

(a)

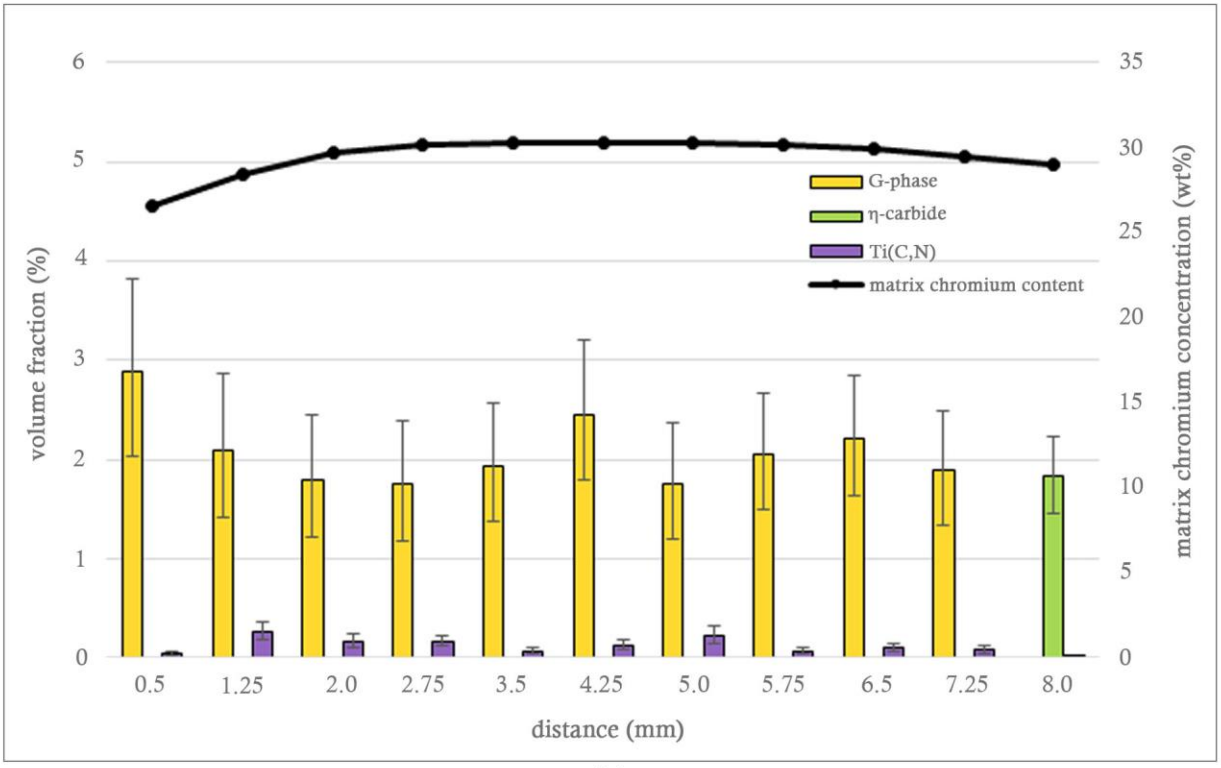

(b)

Figure 5.61 - Measured volume fractions and matrix chromium concentration in sample 6B. (a) all volume fractions, (b) minor volume fractions. Distance is measured from the inner diameter.

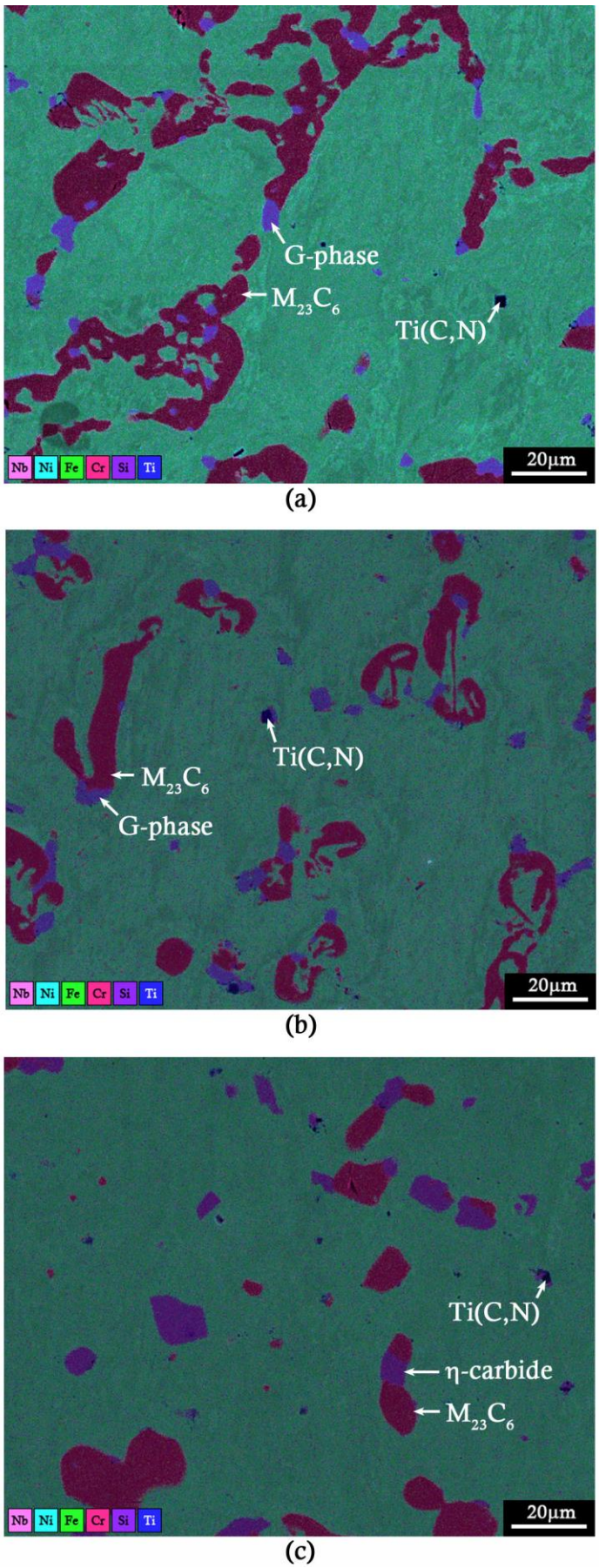

Figure 5.62 - Representative EDS maps of the microstructure in sample 6C at distances of (a) 0.5 mm, (b) 5.0 mm, and (c) 9.5 mm from the inner diameter.

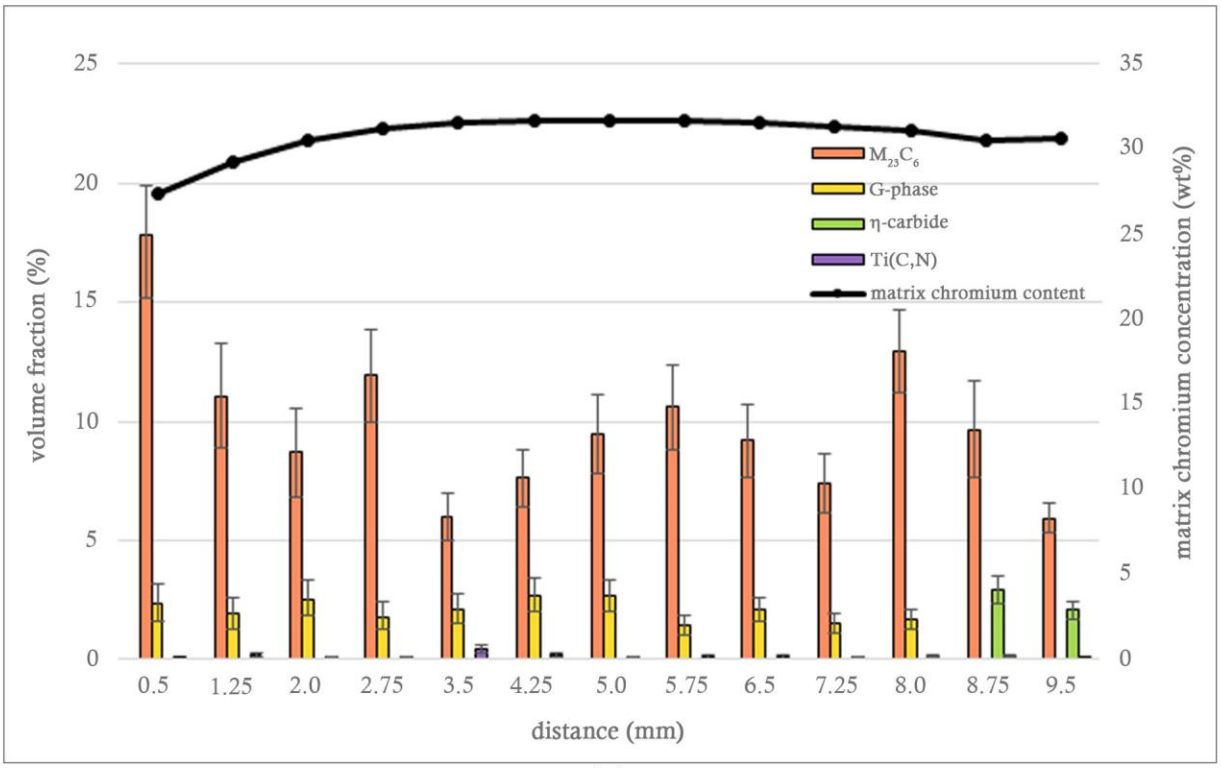

(a)

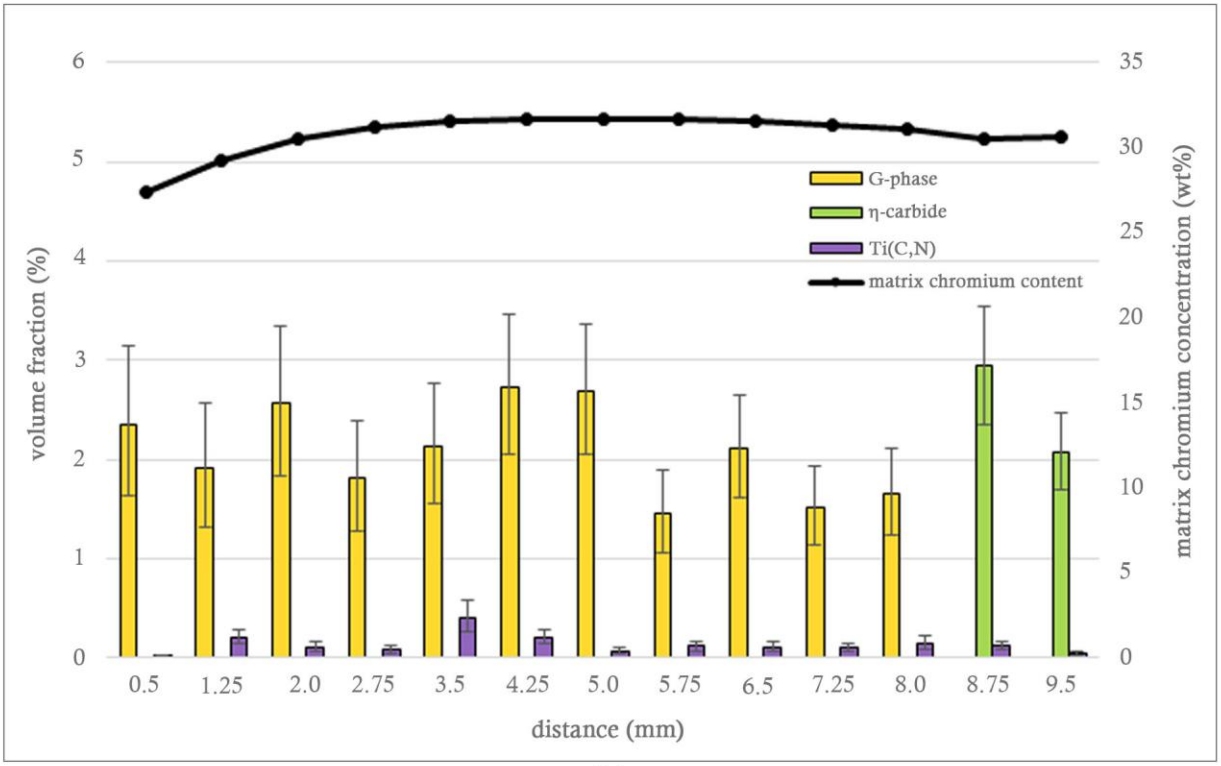

(b)

Figure 5.63 - Measured volume fractions and matrix chromium concentration in sample 6C. (a) all volume fractions, (b) minor volume fractions. Distance is measured from the inner diameter.

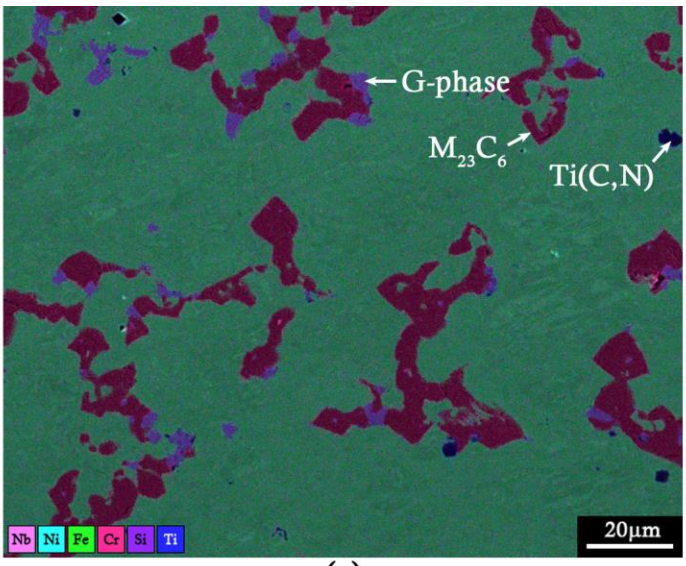

(a)

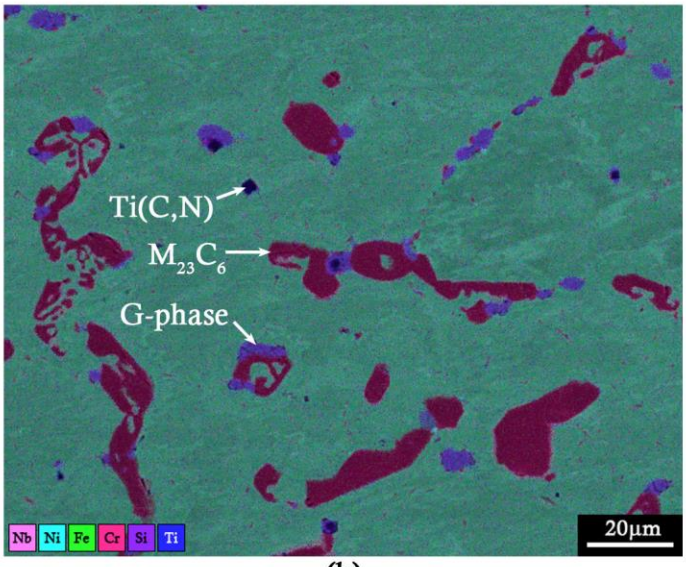

(b)

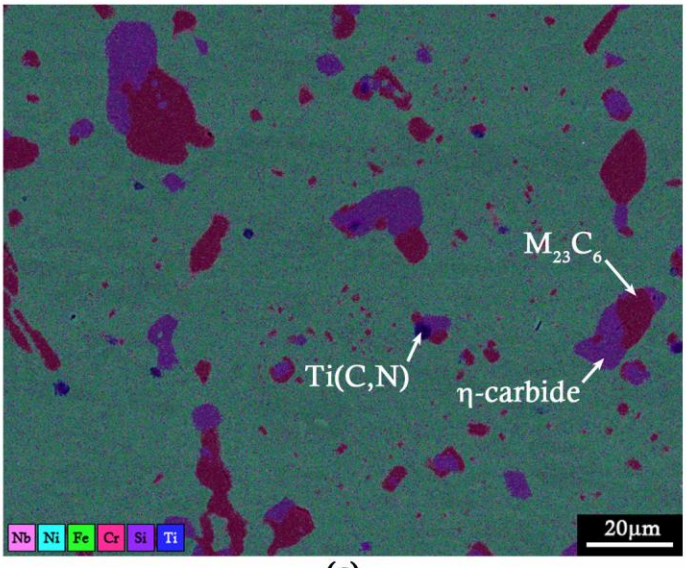

(c)

Figure 5.64 - Representative EDS maps of the microstructure in sample 6D at distances of (a) 0.5 mm, (b) 5.0 mm, and (c) 8.0 mm from the inner diameter.

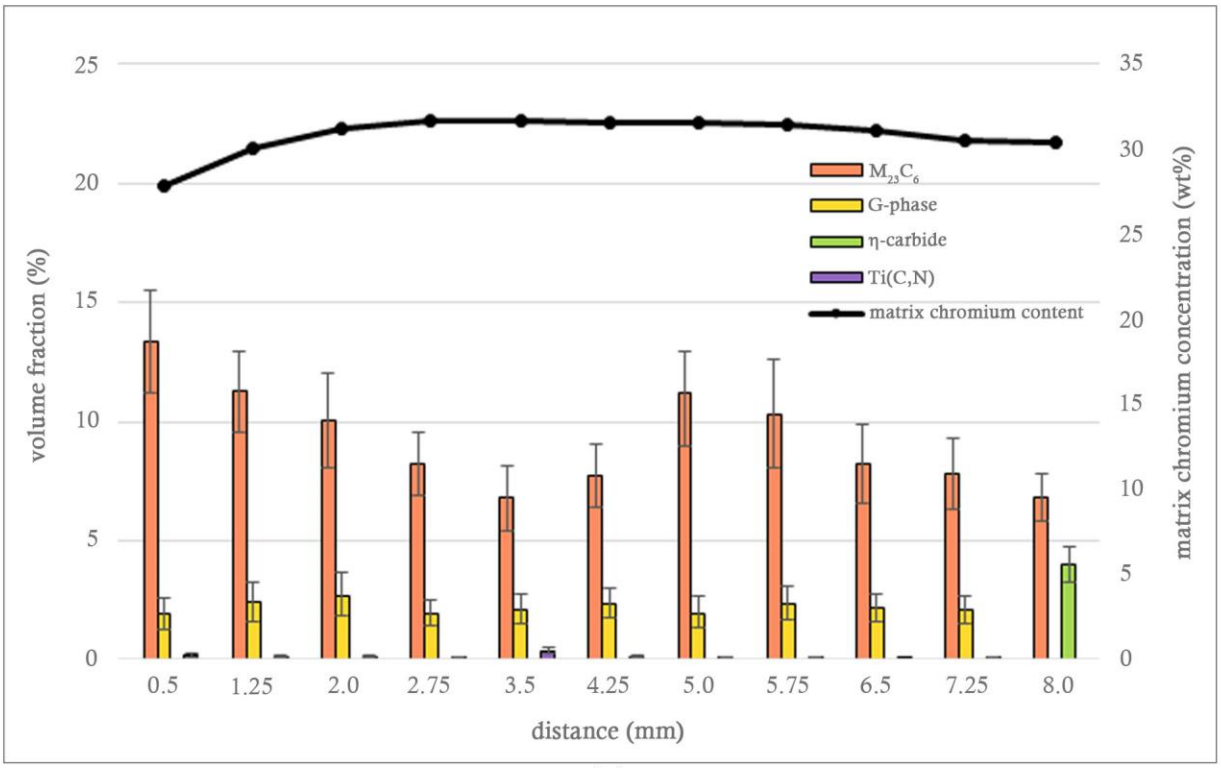

(a)

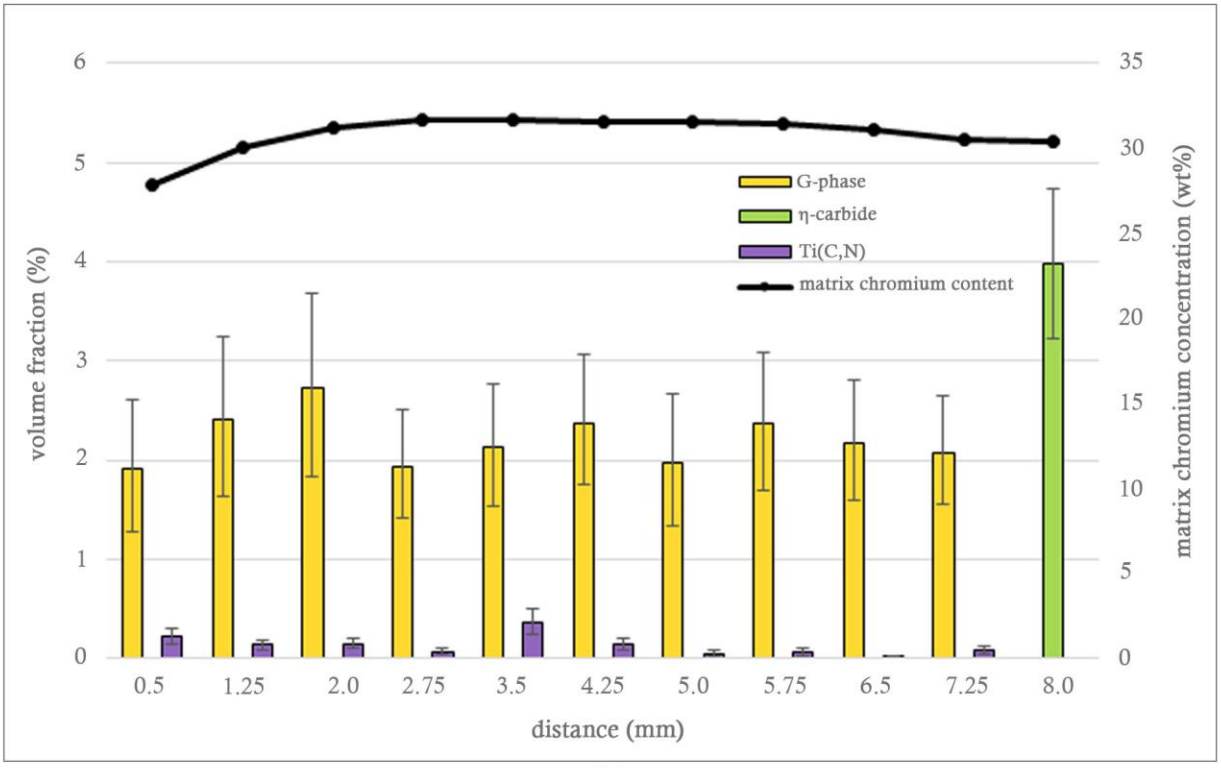

(b)

Figure 5.65 - Measured volume fractions and matrix chromium concentration in sample 6D. (a) all volume fractions, (b) minor volume fractions. Distance is measured from the inner diameter.

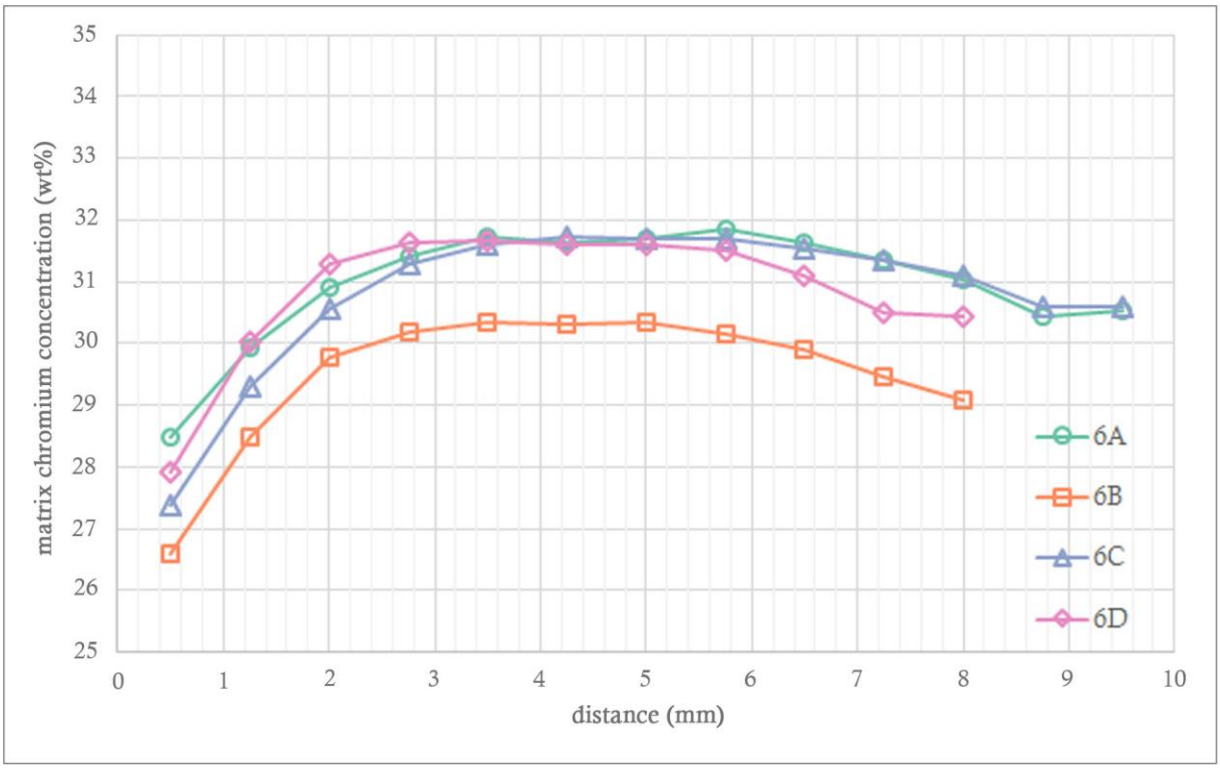

Figure 5.66 - Matrix chromium concentrations for samples 6A-D. Distance is measured from the inner diameter.

5.3 Inner and Outer Surfaces

A brief overview of the degradation as a result of oxidation at the inner and outer surfaces of the samples from each tube was given in Section 4.5. During the image analysis process to measure phase fractions, the extent of degradation was measured for the samples from each tube. The samples from tubes 3, 4, and 6 were observed to have experienced similar levels of degradation at all sample locations within the tube analysed; however, the extent of degradation in tubes 1, 2, and 5 was observed to vary between sample locations. A schematic showing the typical characteristic degradation due to oxidation at the inner and outer diameters is shown in Figure 5.67.

The oxide layers at the inner and outer diameters of the samples, when present, were observed to be intermittent in nature. The lack of continuous oxide layers may be a result of spallation due to mechanical stress as a result of thermal cycling during service, and/or spallation due to mechanical stress as a result of cooling to room temperature. Measurements of the thickness of the remaining discontinuous oxide scales were not considered accurate measurements of the extent of oxide growth during service. Bands free of chromium-rich precipitates (M_7C_3, $M_{23}C_6$, $Cr_2(C,N)$, η-carbide, and σ-phase) were evident in the sub-surface regions at both the inner and outer diameters of a majority of the samples analysed. The precipitates that did remain intact within these bands were those precipitates that did not contain chromium, such as the G-phase, NbC, (Nb,Ti)C, and Ti(C,N) precipitates. Internal oxidation (in the form of silicon-rich oxides at the outer diameter and both silicon- and chromium-rich oxides at the inner diameter) was typically observed to penetrate along dendrite boundaries up to the extent of the chromium-rich precipitate free zone. Exceptions to this were the samples from tube 6, in which the internal oxidation at the inner diameter was only seen to penetrate ≈ 50 – 100 μm into a chromium-rich precipitate free zone that was 200 – 250 μm wide. The composition of the internal silicon-rich oxides was typically consistent with SiO_2, and the composition of the internal chromium rich oxides was typically consistent with Cr_2O_3, in all samples from all tubes.

A summary of the observed oxide scales along with the widths of the bands in which chromium-rich precipitates are absent and within which internal oxidation was observed in each tube is given in Table 5.10 through Table 5.15.

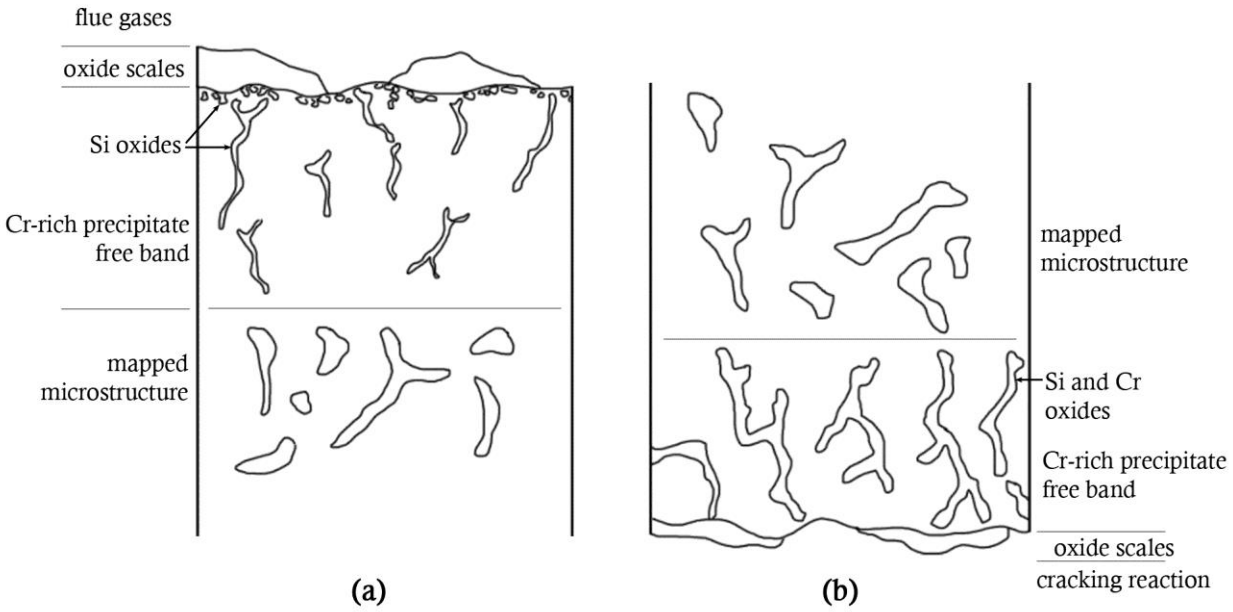

Figure 5.67 - Schematic showing the typical characteristics of degradation due to oxidation at the (a) outer diameter and (b) inner diameter of the ex-service pyrolysis tubes analysed.

Table 5.10 – Summary of degradation due to oxidation at the outer and inner diameters of tube 1.

Tube 1 - Outer Diameter			
Sample	**Oxide scale**	**Depth of Cr-rich precipitate free band.**	**Internal oxidation**
1A	Intermittent Cr-Fe-Ni and Cr oxides	≈ 250 μm	Thin layer of Si oxides beneath surface, dendritic Si oxides in Cr-rich precipitate free band.
1B		≈ 200 μm	
1C		≈ 400 μm	
1D		≈ 200 μm	
Tube 1 - Inner Diameter			
Sample	**Oxide scale**	**Depth of Cr-rich precipitate free band.**	**Internal oxidation**
1A	-	≈ 100 μm	Dendritic Si and Cr oxides in Cr-rich precipitate free band.
1B		≈ 50 - 100 μm	
1C		≈ 200 μm	
1D		≈ 350 - 400 μm	

Table 5.11 – Summary of degradation due to oxidation at the outer and inner diameters of tube 2.

Tube 2 - Outer Diameter			
Sample	**Oxide scale**	**Depth of Cr-rich precipitate free band**	**Internal oxidation**
2A	Intermittent Cr-Fe-Ni and Cr oxides	≈ 150 - 200 μm	Thin layer of Si oxides beneath surface, dendritic Si oxides in Cr-rich precipitate free band.
2B		≈ 150 - 200 μm	
2C		≈ 100 μm	
2D		≈ 200 μm	
Tube 2 - Inner Diameter			
Sample	**Oxide scale**	**Depth of Cr-rich precipitate free band**	**Internal oxidation**
2A	-	≈ 450 μm	Dendritic Si and Cr oxides in Cr- Cr-rich precipitate free band.
2B	-	≈ 450 μm	
2C	Thick Cr-Fe-Ni oxide, ≈ 150 μm	≈ 150 - 200 μm	
2D	Intermittent Cr-Fe-Ni oxide	≈ 500 μm	

Table 5.12 – Summary of degradation due to oxidation at the outer and inner diameters of tube 3.

Tube 3 - Outer Diameter			
Sample	**Oxide scale**	**Depth of Cr-rich precipitate free band**	**Internal oxidation**
3A-D	Intermittent Fe-Ni, Cr, and Si-Al oxides	None, all precipitates in primary network observed up to outer surface.	-
Tube 3 - Inner Diameter			
Sample	**Oxide scale**	**Depth of Cr-rich precipitate free band**	**Internal oxidation**
3A-D	-	≈ 20 - 60 μm	Minimal dendritic Si and Cr oxides in Cr-rich precipitate free band.

Table 5.13 – Summary of degradation due to oxidation at the outer and inner diameters of tube 4.

Tube 4 - Outer Diameter			
Sample	**Oxide scale**	**Depth of Cr-rich precipitate free band**	**Internal oxidation**
4A-D	-	≈ 80 – 100 μm	Dendritic Si oxides in Cr-rich precipitate free band.
Tube 4 - Inner Diameter			
Sample	**Oxide scale**	**Depth of Cr-rich precipitate free band**	**Internal oxidation**
4A-D	-	≈ 30 - 80 μm	Dendritic Si and Cr oxides in Cr-rich precipitate free band.

Table 5.14 – Summary of degradation due to oxidation at the outer and inner diameters of tube 5.

Tube 5 - Outer Diameter			
Sample	**Oxide scale**	**Depth of Cr-rich precipitate free band.**	**Internal oxidation**
5A	Intermittent Cr-Fe-Ni and Cr oxides	≈ 100 - 150 μm	Thin layer of Si oxides beneath surface, dendritic Si oxides in Cr-rich precipitate free band.
5B		≈ 150 - 200 μm	
5C		≈ 150 - 200 μm	
5D		≈ 200 μm	
Tube 5 - Inner Diameter			
Sample	**Oxide scale**	**Depth of Cr-rich precipitate free band**	**Internal oxidation**
5A	-	≈ 80 - 100 μm	Dendritic Si and Cr oxides in Cr-rich precipitate free band.
5B		≈ 40 - 60 μm	
5C		≈ 80 – 100 μm	
5D		≈ 80 μm	

Table 5.15 – Summary of degradation due to oxidation at the outer and inner diameters of tube 6.

Tube 6 - Outer Diameter			
Sample	**Oxide scale**	**Depth of Cr-rich precipitate free band**	**Internal oxidation**
6A-D	Intermittent Cr oxide layer	≈ 550 - 600 μm	Thin layer of Si oxides beneath surface, dendritic Si oxides in Cr-rich precipitate free band.
Tube 6 - Inner Diameter			
Sample	**Oxide scale**	**Depth of Cr-rich precipitate free band**	**Internal oxidation**
6A-D	Intermittent Cr oxide	≈ 200 - 250 μm	Dendritic Si and Cr oxides up to ≈ 50 – 100 μm deep

5.4 Phase Transformations

5.4.1 Chromium Carbide Transformations

The transformation of $M_{23}C_6$ to M_7C_3 was observed in three of the ex-service tubes analysed (tubes 1, 2, and 5). As discussed in Section 2.4.2 and Section 4.6, high amounts of carbon at the inner wall of carburized tubes drives the transformation of $M_{23}C_6$ to M_7C_3, as the M_7C_3 carbides are stable at higher carbon activities. The $M_{23}C_6$-to-M_7C_3 transformation front continues to progress into the tube wall with the continued supply of carbon from the cracking reaction at the inner diameter [12-15]. In the samples that displayed the $M_{23}C_6$-to-M_7C_3 transformation, the matrix chromium concentration at the location of the transformation front was typically observed to be in the 10 – 13 wt% range, as shown in Figure 5.19, Figure 5.29, and Figure 5.57, for tubes 1, 2, and 5 respectively. The volume fraction of chromium carbides around the location of the transformation front was typically observed to be in the range of 20 – 25 %, as shown in Figure 5.10, Figure 5.20, and Figure 5.48, for tubes 1, 2, and 5 respectively. The location of the $M_{23}C_6$-to-M_7C_3 transformation with respect to the inner diameter of the tube varied between samples, as did the degree of carbide coarsening after the transformation front.

The depth of the $M_{23}C_6$-to-M_7C_3 transformation front is often used as a measure of the extent of carburization. Analysis of the chromium carbide volume fractions indicates that the depth of the transformation front also offers a measure of the degree of carbide coarsening within the microstructure. Independent of the depth of transformation front, the wall regions between the inner diameter and the transformation front consistently displayed M_7C_3 volume fractions in the range of 25 – 35 %. In those samples in which the transformation front was located at a distance of less than 1.5 mm from the inner diameter (1B, 5A-C), the volume fraction of $M_{23}C_6$ was observed to rapidly

drop over a distance of 1 – 1.5 mm to a value of 5 – 8 % and remain within this range for the remainder of the wall thickness. In those samples in which the transformation front was located at a distance greater than 2.0 mm from the inner diameter (1A 1C-D, 2A-D, 5D), the volume fraction of $M_{23}C_6$ in the wall region between the transformation front and the outer diameter was observed to decrease at a much more gradual rate, typically not dropping below 10 % until proximity to the outer diameter was 2 mm or less.

Composition of the Primary Chromium Carbides

The composition of the primary M_7C_3 carbides changed with proximity to the inner diameter. An example of the changing composition is shown in Figure 5.68, for the carbides in sample 1D in which this phenomenon was most evident. The ratio of chromium to iron in the metal (M = Cr + Fe + Ni) component of the M_7C_3 carbides increased with increased distance into the wall from the inner diameter. The nickel component of the carbides remained constant irrespective of composition, as did the total metal component. For an M_7C_3 carbide with a formula of $(Cr_xFe_yNi_z)_7C_3$, the value of z was 0.014 irrespective of distance from the inner diameter. The ratio x:y was approximately 3.3 near the inner diameter, and approximately 7.6 close to the transformation front. The changes in the composition of the M_7C_3 carbides was greater in those samples which displayed a high volume fraction of M_7C_3 over a large region of the wall thickness in comparison to those samples in which the $M_{23}C_6$-to-M_7C_3 transformation front occurred close to the inner diameter. No such phenomenon was observed in the $M_{23}C_6$ carbides, which displayed a formula consistent with $(Cr_xFe_yNi_z)_{23}C_6$, where x = 0.783, y = 0.174, and z = 0.043, at all locations in sample 1D.

The composition of the M_7C_3 carbides is reported to be dependent on the local carbon activity of the austenite matrix, and therefore, in the ex-service tube samples, on the distance to the inner diameter. Increased carbon activity with increased proximity to the inner surface results in an increasing amount of chromium being substituted for iron [14, 16, 17]. The observations in the ex-service tubes of the M_7C_3 carbides in the most highly carburized wall regions (i.e. the wall regions with the highest M_7C_3 volume fraction) containing the lowest chromium to iron ratio are thus consistent with the literature.

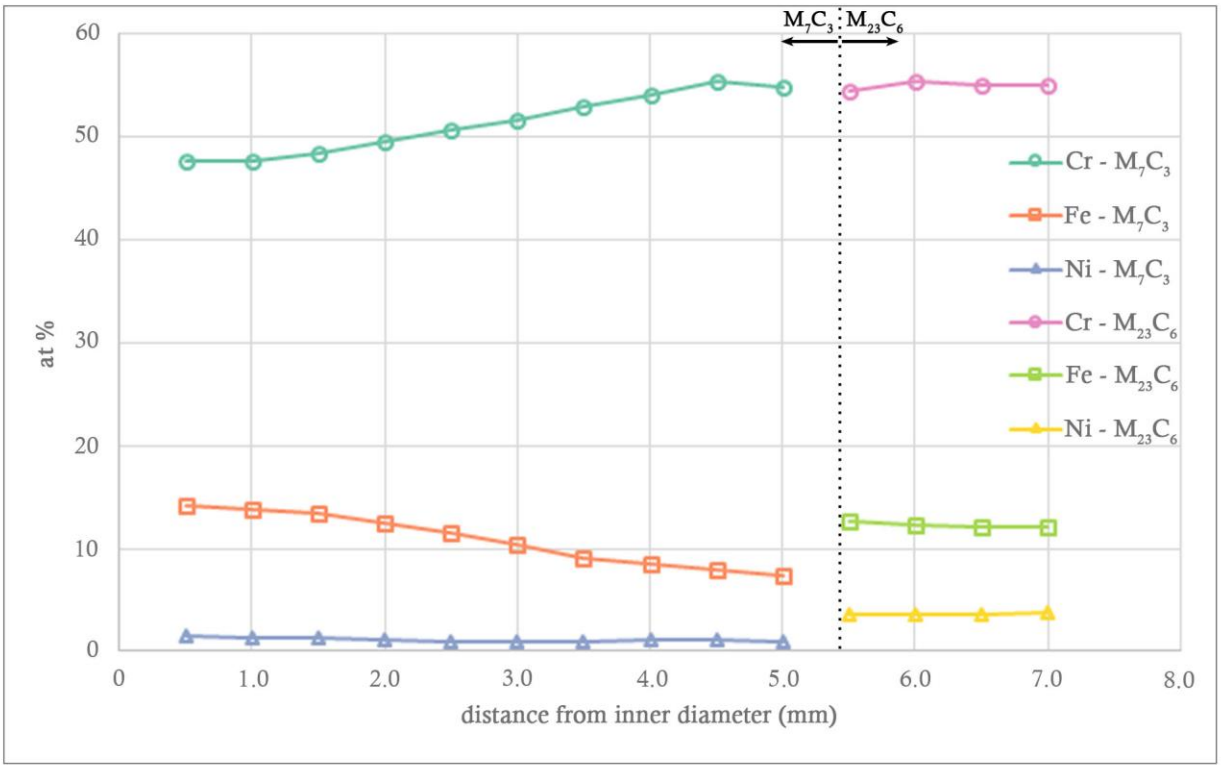

Figure 5.68 - Composition (in atomic percent) of the metal component of the M_7C_3 and $M_{23}C_6$ carbides in sample 1D, as measured by EDS. Five measurements were taken for each carbide at each location. Error bars are not shown due to high precision between the five measurements.

5.4.2 σ-Phase

σ-phase is an intermetallic phase often seen in stainless steels that have been subject to ageing at elevated temperatures. In ferritic stainless steels σ-phase is typically composed of solely iron and chromium; however, in austenitic stainless steel alloys the composition can be more complex, and it can contain nickel, manganese, silicon, and niobium in addition to iron and chromium. σ-phase forms from metastable austenite at temperatures in the range of 550 – 1000 °C [18-20]. σ-phase is typically reported to occur in close association with the chromium-rich carbides and G-phase constituents in the primary network, in laboratory aged samples [21], ex-service samples subject solely to ageing [22], and ex-service pyrolysis tubes subject to carburization [23, 24].

Haro *et al.* [21] identified σ-phase in an HK40 alloy with >2 wt% silicon, which was laboratory aged at 750 °C for 2000 hours. A nickel silicide, of formula $Ni_{31}Si_{12}$, was also identified in addition to chromium-rich $M_{23}C_6$ carbides.

Shi and Lippold [22] reported the presence of σ-phase in two HP-Nb alloy tubes that had been in service in a furnace at approximately 815 °C, one for nine years and one for 12 years. In both tubes, the σ-phase was observed to be associated with chromium-rich phases located on the dendrite

boundaries as part of the primary network. A Ni-Nb-Si-rich phase was also observed at the interdendritic sites in the ex-service HP-Nb alloys. The composition of the Ni-Nb-Si-rich phase was noted to be similar to the composition previously reported for G-phase [25]; however, the crystal structure was not confirmed.

Borjali *et al.* [24] identified σ-phase, G-phase, and $M_{23}C_6$ carbides to be present in the outer wall region of an ex-service HP-Nb pyrolysis tube with a maximum working temperature of approximately 1100°C. Based on the SEM micrographs presented, the σ-phase in the tube formed as part of the primary network, and is in close association with the $M_{23}C_6$ carbides and G-phase in the microstructure. The maximum working temperature of 1100 °C is well above the temperature range of 550 - 1000 °C over which other authors have stated σ-phase forms; however, as it is simply stated as the maximum working temperature it is possible that the tube operated at lower temperatures within the reported σ-phase formation range for a portion of its service life.

The presence of σ-phase platelets in the matrix has been reported by Tawancy *et al.* [23] to occur in an ex-service HP-Nb alloy pyrolysis furnace tube, which had been in service at approximately 850 °C for 22,000 hours. The σ-phase platelets were typically ≥10 μm long and ≤1 μm in width, and were observed to be interspersed with $M_{23}C_6$ precipitates.

Powell *et al.* [25] note that G-phase formation occurs before the formation of σ-phase, and that G-phase contains a significant amount of nickel, an austenite stabiliser. The formation of G-phase may result in the adjacent austenite regions being depletion in nickel, leading to regions of metastable austenite which could promote σ-phase formation. This argument also explains why the σ-phase regions are often observed in close association with the G-phase regions in the microstructure.

Although no secondary $M_{23}C_6$ precipitates were observed in the tube that contained σ-phase in the matrix (tube 3), the appearance of the platelet σ-phase distributed in the matrix is consistent with that reported by Tawancy *et al*. The σ-phase identified as part of the primary precipitate network was typically in contact with $M_{23}C_6$, G-phase, or both, as shown in Figure 5.69. The appearance of the σ-phase precipitates in tube 3, both as part of the primary precipitate network and as secondary precipitates in the matrix, is thus consistent with the literature. The tube mean temperature (TMT) of tube 3 during service was 1010 – 1080 °C, which lies above the 550 – 950 °C temperature range reported as the range within which σ-phase forms; however, it is consistent with the identification of σ-phase by Borjali *et al.* [24] in an ex-service pyrolysis tube that had experienced a maximum working temperature of 1100 °C during service.

The lack of σ-phase identified in the samples from tube 4 is of interest. As summarised in Table 4.3 and Table 4.2, tubes 3 and 4 were subject to the same TMT and service life and were shown to have the same composition. Despite this, there are a number of other factors that can influence the

development of microstructure of an in-service tube, in particular the furnace geometry. Shielding effects, whereby one tube shields another tube from direct radiation from the burners within the furnace, as well as the locations of the burners themselves, can cause non-uniform temperature distributions that can therefore result in non-uniform microstructural changes along the lengths of the tubes [26]. It is possible that σ-phase is present in some locations in tube 4, just not the locations analysed in the current project.

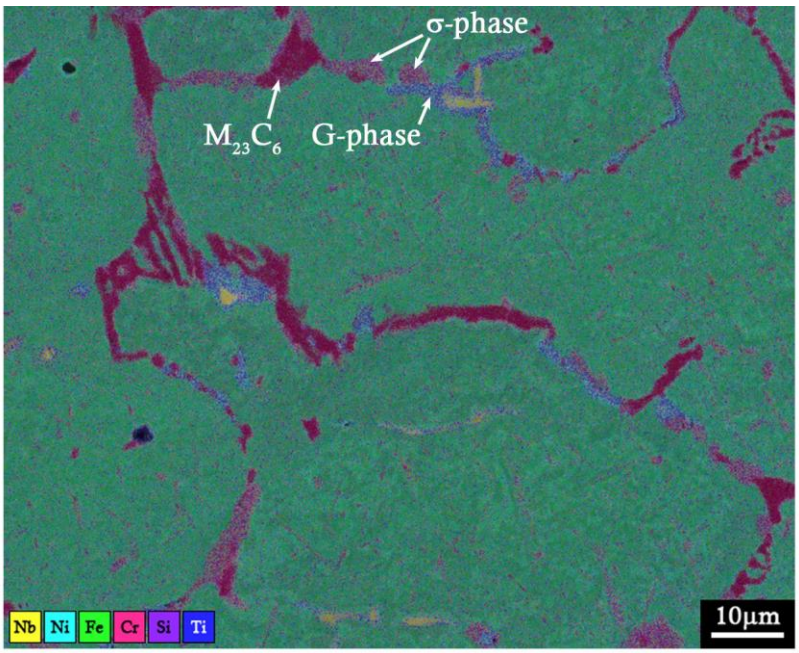

Figure 5.69 - EDS map indicating location of σ-phase adjacent to both G-phase and $M_{23}C_6$ in the primary precipitate network in sample 3B.

σ-phase is reported to result in loss of ductility and toughness at temperatures below 120 – 150 °C, but to have little effect on mechanical properties in the temperature range within which it forms [20, 22]. Provided the component operates continuously at the elevated temperature, the presence of σ-phase in the microstructure should thus have no consequence. However, impact stresses or suddenly applied high stresses upon a temperature cycle to a lower temperature can result in cracking. The presence of σ-phase in the microstructure of carburized ethylene pyrolysis tubes could therefore pose some issues. Of particular concern would be unexpected furnace shut-downs, which result in large temperature drops, especially when the furnace is near its end of run and a large coke plug at the inner diameter is a possibility. As discussed in Section 2.2.3, high stresses can be induced in the tube as result of the tube contraction being restrained by the coke plug. A highly carburized and therefore embrittled tube would be at high risk of fracture.

Reported hardness values for σ-phase, $M_{23}C_6$, and M_7C_3 are given in Table 5.16. The hardness of σ-phase is at the low end of the scale in comparison to the two chromium carbides, but still close to 1000

HV. The σ-phase could thus be expected to have an effect on the mechanical properties similar to that of the carbides. Tubes with low volume fractions of σ-phase in addition to the low volume fractions of chromium carbides, such as tube 3, may be able to survive unexpected shutdowns due to little or no carbide coarsening having taken place; however, if the σ-phase regions grow and coarsen to the same extent as the chromium carbides that have been observed in the highly carburized samples from other tubes, then the contribution to tube embrittlement and the risk of cracking would be significant.

Table 5.16 - Reported hardness values for σ-phase and the chromium-rich M_7C_3 and $M_{23}C_6$ carbides

Phase	Hardness (HV)	Reference(s)
σ-phase	940	[27]
M_7C_3	1336 – 2200	[28, 29]
$M_{23}C_6$	976 - 1650	[28-30]

5.4.3 $Cr_2(C,N)$

The formation of internal $Cr_2(C,N)$ carbonitrides was observed in sample 1D, and in all samples from tube 2. Internal nitridation as a result of exposure to the nitrogen-containing flue gases at the external surface of the tube is reported to occur during service in pyrolysis furnaces [31]; however, studies that characterize the internal nitridation of H-series alloys appear to be limited to laboratory aged samples [4, 32].

Aydin *et al.* [32] annealed samples of both HK and HP alloys in air at temperatures of 900 – 1100 °C for up to 40,000 hours. Internal nitridation of the samples was observed to begin with the transformation of the primary chromium-rich $M_{23}C_6$ carbides into chromium-rich $M_2(C,N)$ nitrides. Precipitation of platelet $M_2(C,N)$ was also observed adjacent to the primary network, but this was only observed in regions where the $M_{23}C_6$ carbides had entirely transformed to $M_2(C,N)$. Chemical analysis revealed that the $M_2(C,N)$ precipitates were almost nickel-free $Cr_2(C,N)$ precipitates, with the M component composed of approximately 85 % chromium, and the remainder being made up of mostly iron. It was also noted that the $M_{23}C_6$ carbides did not incorporate nitrogen.

The majority of the external oxide layers were observed to have spalled upon cooling; however, from the oxide layers remaining, Aydin *et al.* observed an almost pure Cr_2O_3 oxide layer in direct contact with the material with some SiO_2 inclusions, and a Cr-Mn-Fe-Ni oxide layer on the side exposed to the atmosphere. Increased annealing times saw significant internal oxidation of silicon, and the primary $M_{23}C_6$ and $M_2(C,N)$ precipitates were observed to be selectively oxidized to form SiO_2 and Cr_2O_3. A schematic of the typical structure in the sub-surface nitride zone, as presented by Aydin *et al.*, is shown in Figure 5.70. The sub-surface microstructures of tubes 1 and 2, which were discussed

in Sections 4.5.1 and 4.5.2, and Sections 5.2.1 and 5.2.2, were seen to be consistent with the schematic and the observations of Aydin *et al.*

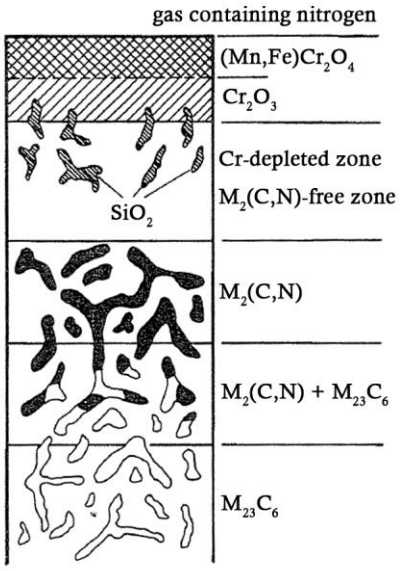

Figure 5.70 - Schematic of the typical sub-surface microstructure of an H-series alloy exposed to a nitrogen-containing gas (adapted from [32]).

The transformation of $M_{23}C_6$ to $Cr_2(C,N)$ is reported to proceed according to Equation 5.1 [32]:

$$M_{23}C_6 + 6\,N + 1\,M \rightarrow 12\,M_2(C,N) \qquad \textbf{Equation 5.1}$$

The direct transformation of $M_{23}C_6$ to $Cr_2(C,N)$ thus does not contribute significantly to chromium depletion in the matrix, as the chromium content of the $Cr_2(C,N)$ is negligibly higher than that of the $M_{23}C_6$ from which it forms. The precipitation of new, individual $Cr_2(C,N)$ precipitates may contribute to the chromium depletion of the matrix; however, as observed in Figure 5.23 (c) and Figure 5.25 (c), the volume fraction of the lenticular $Cr_2(C,N)$ that had precipitated in the matrix is qualitatively smaller than the volume fraction of the $Cr_2(C,N)$ that had transformed directly from the $M_{23}C_6$ in the primary precipitate network.

Buchanan [4] observed the effects of isothermal ageing in an air atmosphere on the microstructure of HP-Nb and HP-NbTi alloys. Two distinct zones were identified at the exposed surface, called zones A-I and A-II. Zone A-I was composed of the exposed surface and sub-surface material, and was generally consistent with the layers labelled $(Mn,Fe)Cr_2O_4$, Cr_2O_3, Cr-depleted zone, and $M_2(C,N)$-free zone in Figure 5.70.

Zone A-II was defined as the region within which the air atmosphere had caused the transformation of the primary chromium- and niobium-rich carbides into carbonitrides, and accelerated the

dissolution of the secondary precipitates. Ageing at 1000, 1050, and 1100 °C was seen to result in the transformation of the primary $Cr_{23}C_6$ precipitates into $Cr_2(C,N)$ carbonitrides in both HP-Nb and HP-NbTi alloys. The $Cr_{23}C_6$-to-$Cr_2(C,N)$ transformation was initially contained within a narrow band (<100 μm thick), but with increased ageing times the band was observed to grow uniformly towards the mid wall. The transition from $Cr_2(C,N)$ to $Cr_{23}C_6$ was typically observed to occur over a narrow band (<100 μm), within which a mixed network was present. EDS analysis of the $Cr_{23}C_6$ carbides at the transformation front showed no noticeable nitrogen peak, indicating that nitrogen is not absorbed in significant quantities by the $Cr_{23}C_6$ carbides prior to their transformation, which is consistent with the observations of Aydin *et al.* Buchanan proposed that the $Cr_{23}C_6$-to-$Cr_2(C,N)$ transformation proceeds once the local nitrogen content of the austenite matrix reaches a certain threshold (as yet unknown). The precipitates closest to the nitrogen source, i.e. the outer surface, transform first, and continued absorption of nitrogen and the diffusion of nitrogen to the mid wall results in the inwards progression of the transformation front. Additionally, Buchanan observed that on occasion $Cr_2(C,N)$ precipitates were present along columnar grain boundaries in the mid wall region of an HP-Nb alloy samples aged at 1000 °C for 10,000 hours, often up to 2.5 mm ahead of the $Cr_{23}C_6$-to-$Cr_2(C,N)$ transformation front. However, it was unknown why $Cr_2(C,N)$ precipitates would be present at such great distances ahead of the transformation front.

The internal formation of $Cr_2(C,N)$ in samples 1D and 2A-D is consistent with the observations reported for laboratory aged samples by Aydin *et al.* and Buchanan. Although it is not known why small amounts of $Cr_2(C,N)$ precipitates were present at significant distances from the $M_{23}C_6$-to-$Cr_2(C,N)$ transformation front in the tube 2 samples, further studies to determine why were not considered critical to the current project, as the direct transformation of $M_{23}C_6$ to $Cr_2(C,N)$ does not contribute significantly to the matrix chromium depletion, and the effect of carbonitrides on mechanical properties is reportedly similar to that of carbides [31].

5.4.4 The Instability of the Primary Niobium Carbides at Elevated Temperatures

As discussed in Section 2.4.2 the instability of niobium and niobium-titanium carbides at elevated temperatures is well documented in literature. From the data published in literature regarding ex-service HP-Nb and HP-NbTi alloys that had experienced ageing during service [22, 33-37], and additional studies on laboratory aged HP-Nb and HP-NbTi alloys, Buchanan [4] concluded that, in aged HP-Nb and HP-NbTi alloys the transformation product of the NbC and (Nb,Ti)C carbides is dictated by the ageing temperature.

The NbC-to-G-phase transformation is expected to be favoured at temperatures below 875 °C, whereas the NbC-to-η-carbide transformation is expected to be favoured at temperatures above 920 °C. At temperatures between 875 – 920 °C, the G-phase and η-carbide transformations occur in parallel, with the relative amounts of the two phases depending on the ageing temperature and time.

The η-carbide volume fraction would be expected to increase with ageing temperature, until the NbC-to-η-carbide transformation becomes dominant.

However, as discussed in Section 2.4.2, the stated temperature ranges are approximations based on data from a limited number of samples. Additionally, the samples from which the data was compiled had either been subject to laboratory ageing, or were taken from ex-service steam reformer tubes which undergo ageing during service but not carburization. The effects of carburization on the microstructure of pyrolysis tubes, such as the compositional gradients in the matrix across the tube wall, and the $M_{23}C_6$-to-M_7C_3 transformation, are likely to alter the temperature ranges over which the NbC-to-G-phase and NbC-to-η-carbide transformations occur in pyrolysis tubes. This is evident when comparing the known service temperatures of the tubes within which the transformation of the NbC and (Nb,Ti)C carbides to the G-phase and η-carbide occurred.

All four samples from tube 2 (TMT = 982 – 1037 °C) displayed small volume fractions of η-carbide, which is consistent with the NbC-to-η-carbide transformation being favoured at temperatures above 920 °C. The service temperature of tube 1 is recorded as 704 °C, which according to the stated temperatures ranges for aged alloys would be expected to favour the NbC-to-G-phase transformation, and be below the range in which the NbC-to-η-carbide transformation would be expected to occur. However, G-phase and η-carbide were both present in samples 1A and 1B, and solely η-carbide was present in samples 1C in 1D. Additionally, all samples from tubes 3 and 4 displayed the almost complete transformation of (Nb,Ti)C to G-phase; however, the TMT of 1010 – 1080 °C for both tubes is not consistent with the stated temperature range of G-phase stability in aged alloys being below 920°C.

Buchanan observed that exposure of samples of HP-Nb and HP-NbTi alloys to an air atmosphere during ageing promoted the transformation of the primary niobium-rich precipitates into η-carbide. The effect was dependent on both the alloy composition and the ageing temperature. In the HP-Nb alloys analysed, the NbC-to-η-carbide transformation was observed to proceed to partial completion at the mid wall independently of the air atmosphere at 1000 °C; however, when comparing the NbC-to-η-carbide transformation at the mid wall to the NbC-to-η-carbide transformation in the wall region adjacent to the air-exposed surfaces, it was observed that the rate at which the transformation occurred was accelerated by the air atmosphere. The NbC-to-η-carbide transformation had neared completion for those precipitates adjacent to the exposed surfaces, and the η-carbide regions were becoming comparable in size to the primary $Cr_{23}C_6$ precipitates.

In the HP-NbTi alloys analysed by Buchanan, the (Nb,Ti)C-to-η-carbide transformation was only observed as a direct result of the air atmosphere, and regardless of the ageing time and temperature was only observed within the affected regions at the outer wall of the samples. The lack of independent

formation of η-carbide in the HP-NbTi alloys was attributed to the increased stability of the primary niobium-rich precipitates as a result of the titanium additions. EDS analyses showed that nitrogen did not dissolve in the η-carbide, at least not to a point where it was above the limits of detection by EDS. As such, the exact component/s of the air atmosphere that influence the η-carbide transformation remain unclear.

The four ex-service pyrolysis tubes that contained η-carbide at their mid and outer wall regions (tubes 1, 2, 5, and 6) were also the tubes that displayed significant degradation at their outer surfaces as a result of oxidation (samples 1A-C, 5A-D, and 6A-D) or combined oxidation and nitridation (samples 1D, and 2A-D). The two tubes that displayed little or no degradation due to oxidation (tubes 3 and 4) only displayed the (Nb,Ti)C-to-G-phase transformation, and not the transformation to η-carbide. It is possible that the formation of η-carbide in tubes 1, 2, 5, and 6, in particular in the wall regions adjacent to the external surface, was partially due to the influence of the external flue gas atmosphere.

As discussed in Section 5.2.1, two samples from tube 1 (1C and 1D) displayed solely the NbC-to-η-carbide transformation, and not the NbC-to-G-phase transformation. In sample 1C, η-carbide was present over the 2.5 – 7.5 mm wall regions. In sample 1D, it was present over the 3.5 – 7.0 mm wall regions, and in this sample $Cr_2(C,N)$ was also present within the 6.5 – 7.0mm wall regions. In both sample 1C and 1D, a gradual decrease in the volume fraction of NbC precipitates and an increase in the volume fraction of η-carbide was observed with increased proximity to the outer diameter, indicating that the NbC-to-η-carbide transformation progressed further to completion at the outer wall regions of the tube. The NbC-to-η-carbide transformation may therefore have proceeded to partial completion in the mid wall regions of these two samples independent of the influence of the external atmosphere, and progressed further to completion at the outer wall as a result of the external atmosphere.

Samples 1A and 1B displayed the NbC-to-G-phase transformation at the mid to outer wall regions (in the 3.5 – 5.0 mm and 2.0 – 7.0 mm wall regions respectively) and the NbC-to-η-carbide transformation was observed in the outer wall regions near the external surface (in the 5.5 – 6.5 mm and 7.5 – 8.0 mm wall regions respectively. In tube 5 (an HP-Micro alloy with Ti addittions) and tube 6 (an ET45-Micro alloy with Ti additions), the (Nb,Ti)C-to-η-carbide transformation was only observed at the outermost wall locations, and the mid wall regions of the sample displayed only the (Nb,Ti)C-to-G-phase transformation. It is possible that the transformation of the NbC or (Nb,Ti)C carbides to G phase was more favourable away from the external surface, and the transformation of NbC or (Nb,Ti)C to η-carbide was more favourable close to the external surface is a result of the external atmosphere.

In tube 2 (an HP-Nb alloy), small amounts of η-carbide (< 1%) were present at all locations between the $M_{23}C_6$-to-M_7C_3 transformation front and the outer surface. Small amounts of $Cr_2(C,N)$ carbonitrides (typically < 2 %) were also present at all locations between the $M_{23}C_6$-to-M_7C_3

transformation front and the outer surface. This occurred in all four samples from tube 2. The influence of nitrogen on the formation of η-carbides in austenitic stainless steels is not well understood. A version of the η-carbide crystal structure rich in molybdenum and nitrogen has been identified in a 20Cr-25Ni-5Mo-0.2N steel after ageing for 3000 hours at 850 °C by Jargelius-Pettersson [38]. Their *et al.* [39] identified similar precipitates in a 316 stainless steel containing 0.069 wt% nitrogen that had been aged for 1 hour at 900 °C, but did not observe them after 1000 hours ageing when the nitrogen content was only 0.037 wt%. It is therefore possible that the increase in nitrogen concentration as a result of the external atmosphere may promote the formation of the niobium-rich η-carbide observed in HP and ET45-Micro alloys; however, no such similar studies were discovered in the literature for the niobium-rich η-carbide.

Nevertheless, it stands that in tubes 3 and 4, which displayed only minimal degradation due to oxidation at the external surface, only the (Nb,Ti)C-to-G-phase transformation was observed, whereas all samples from tubes 1, 2, 5, and 6 displayed either the NbC-to-η-carbide or (Nb,Ti)C-to-η-carbide transformation in the wall regions adjacent to the external surface, and in some samples further into the tube wall. This indicates that exposure to the flue gas atmosphere at the external surface of the tubes may accelerate the NbC-to-η-carbide and (Nb,Ti)C-to-η-carbide transformations.

5.5 Effect of Precipitate Phases on Matrix Chromium Concentration

The matrix chromium concentration profiles were observed to inversely mirror the volume fractions of the chromium-containing phases – in particular M_7C_3, $M_{23}C_6$, and η-carbide. However, these phases, and the other chromium-containing phases $Cr_2(C,N)$ and σ-phase, contain different amounts of chromium in comparison to each other, meaning that the same volume fraction of M_7C_3 will not draw the same amount of chromium from the matrix as the same volume fraction of η-carbide. In addition, the composition of M_7C_3 has been shown to vary with respect to distance from the wall thickness, and variations in the σ-phase and η-carbide precipitates were also observed. In order to directly compare the precipitate phase volume fractions with the chromium concentration of the austenite matrix, the composition of each phase in each location in each tube was measured using the EDS map data, and the compositions of the maximum and minimum chromium content versions of each phase extracted.

The amount of chromium drawn from the austenite matrix as a result of the formation and growth of the various chromium containing phases should be proportional to the chromium content of each phase and its volume fraction, if the total alloy chromium content and density remains constant, as shown in Equation 5.2

$$\Delta A_\gamma W_\gamma^{Cr} \rho_\gamma = -\Delta \sum_{i=1 \to n} A_i W_i^{Cr} \rho_i \qquad \textbf{Equation 5.2}$$

where A_γ is the area fraction of the austenite (γ) matrix, W_γ^{Cr} is the measured weight fraction of chromium in the austenite matrix, ρ_γ is the density of austenite, A_i is the area fraction of the precipitate phase *i*, $W_i^{Cr}$is the weight fraction of chromium in the precipitate phase *i*, and ρ_i is the density of the precipitate phase *i*. *n* is the total number of chromium-containing precipitate phases, *i*. The precipitate phases, *i*, in this case are the chromium containing precipitates M_7C_3, $M_{23}C_6$, $Cr_2(C,N)$, η-carbide, and σ-phase. Due to both area fraction and weight fraction of chromium being dimensionless quantities, the comparison is therefore between the concentration of chromium in the austenite matrix, and the total concentration of chromium in the precipitate phases (in g/cm^3). It should be noted that this mass balance fails if any significant amount of chromium is depleted from the austenite matrix to form an external chromium scale; however, the EDS maps from which compositional data was reconstructed for this analysis were well outside of any regions which were observed to be depleted of chromium as a result of external scaling.

It has been demonstrated that the $M_{23}C_6$-to-$Cr_2(C,N)$ transformation does not directly contribute to the matrix chromium depletion; however, the $Cr_2(C,N)$ precipitates nevertheless have to be accounted for in the volume fraction – concentration relationship. Their direct transformation from $M_{23}C_6$ precipitates means that they contain chromium that had been drawn from the matrix to allow the prior $M_{23}C_6$ precipitates to coarsen, and this chromium content needs to be accounted for.

If the reduction in the chromium concentration of the austenite matrix was entirely due to the formation and growth of the chromium containing phases, then plotting $A_\gamma W_\gamma^{Cr} \rho_\gamma$ against the sum of $A_i W_i^{Cr} \rho_i$ for both the minimum and maximum chromium-containing compositions of the *n* precipitate phases would be expected to give a line with a slope of -1. The densities of the austenite matrix and the precipitate phases, and the measured maximum and minimum chromium weight fractions for the precipitate phases across all six ex-service tubes are shown in Table 5.17 and Table 5.18 respectively. The composition of the precipitate phases in tube 6 was considered separately, due to the different alloy composition. Despite the composition of the $M_{23}C_6$ carbides being consistent across the locations in sample 1D, as discussed in Section 5.4.1, there were variations in the compositions of the $M_{23}C_6$ carbides observed between the six ex-service tubes.

Figure 5.71 shows the results for the HP-Nb and HP-Micro tubes (tubes 1-5). An increase in the total chromium concentration in the precipitate phases results in a decrease in the chromium concentration in the matrix. The decrease occurs in a linear fashion, and the slope is approximately -1, consistent with the hypothesis that the reduction in the matrix chromium content can be attributed to the precipitation and growth of the chromium containing precipitates M_7C_3, $M_{23}C_6$, $Cr_2(C,N)$, η-carbide, and σ-phase.

Although neither the gradient of the maximum chromium concentration line nor the gradient of the minimum chromium concentration line are exactly -1, the values for both are very close and the coefficients of determination indicate the linear fit is sound. In reality, neither the absolute maximum chromium concentration of every single phase at a single location would occur, nor would the absolute minimum – the total chromium concentration of the chromium-containing phases would be expected to lie somewhere between the maximum and minimum bounds.

The results of the same analysis for tube 6 are shown in Figure 5.72. The coefficients of determination for both the minimum chromium content and maximum chromium content in the precipitates are not as close to 1 as with the data from tubes 1-5. The number of data points for tube 6 is low in comparison to the number of data points for tubes 1-5, and additionally the range of data for tube 6 is significantly smaller due to the minimal carburization and matrix chromium depletion observed in all tube 6 samples (as discussed in Section 5.2.6). As such, it is not possible to speculate whether the deviation from a slope of -1 when comparing the chromium concentration in the matrix and precipitates in tubes 6 is a characteristic of the ET45-Micro alloys, or whether it is due to the small range of data used. A significantly larger number of ET45-Micro alloy samples would need to be analysed to confirm whether the depletion of the matrix chromium content in these alloys is directly due to the precipitation and growth of the chromium-containing precipitate phases. In particular, samples with a greater extent of carburization and microstructural coarsening (and thus more significant matrix chromium depletion) than those analysed presently, would extend the data range and allow further analysis of the relationship in ET45-Micro alloys.

Table 5.17 – Densities of the chromium – containing precipitate phases and the austenite matrix.

Phase	Density (g/cm^3)	Reference(s)
M_7C_3	6.92	[40]
$M_{23}C_6$	6.99	[40]
$Cr_2(C,N)$	6.51	[40]
η-carbide	6.54	Calculated using CrystalMaker[2]
σ-phase	7.6	[41]
austenite	8.05	[42]

Table 5.18 – Maximum and minimum weight fractions of chromium in the precipitate phases, as measured using EDS over the six ex-service tubes.

Phase	Tubes 1-5		Tube 6	
	Maximum Cr weight fraction	Minimum Cr weight fraction	Maximum Cr weight fraction	Minimum Cr weight fraction
M_7C_3	0.78	0.63	-	-
$M_{23}C_6$	0.85	0.68	0.85	0.80
$Cr_2(C,N)$	0.95	0.78	-	-
η-carbide	0.55	0.29	0.36	0.30
σ-phase	0.54	0.47	-	-

[2] CrystalMaker® version 2.3.2, CrystalMaker Software Ltd. Crystal structure simulated using parameters for η-carbide given in Table 4.4, and an M_6C composition, where M is composed of 3 Cr, 2 Ni, and 1 Si atoms.

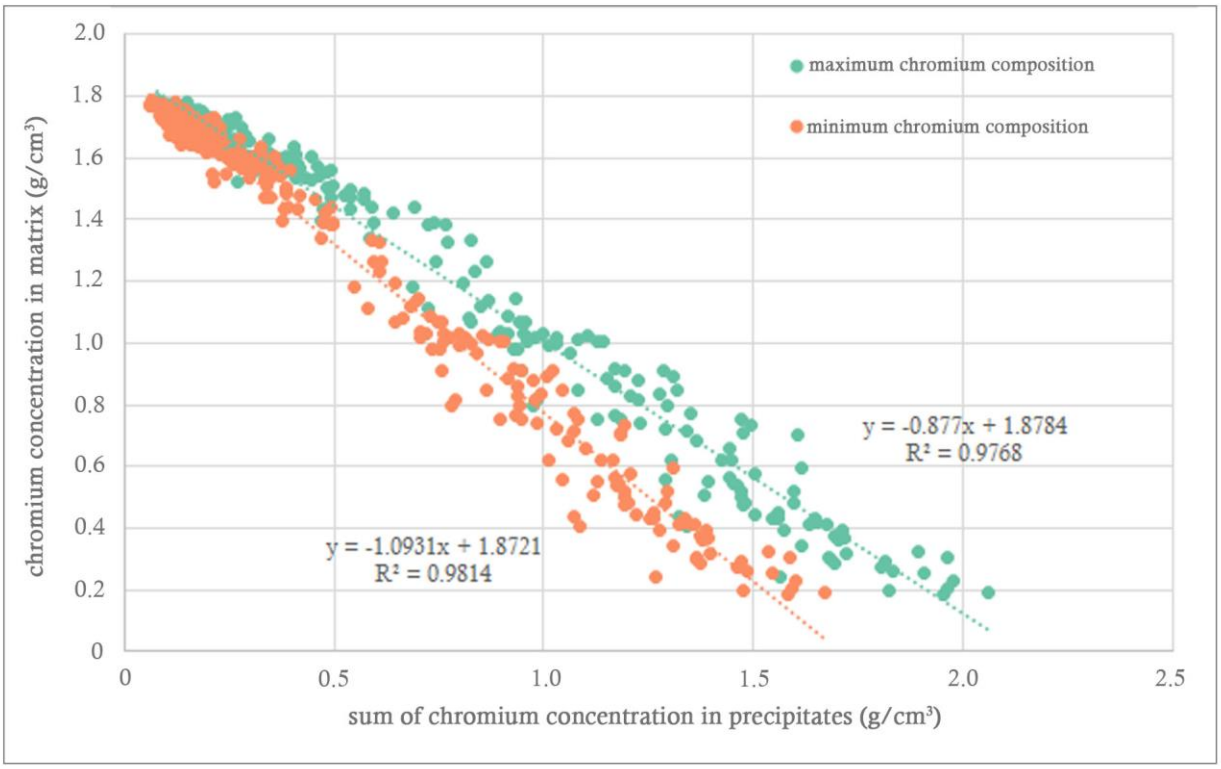

Figure 5.71 - Chromium concentration in the austenite matrix versus the sum of chromium concentration in the chromium containing precipitate phases, for tubes 1-5.

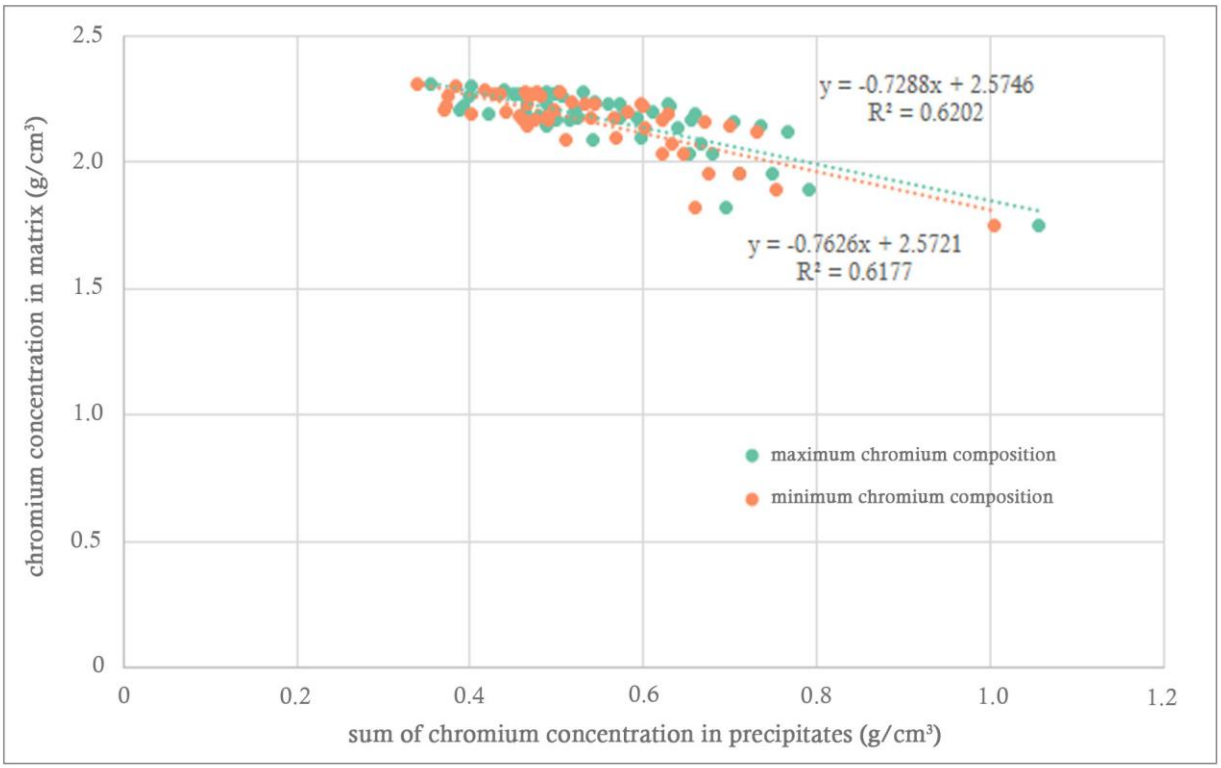

Figure 5.72 - Chromium concentration in the austenite matrix versus the sum of chromium concentration in the chromium containing precipitate phases, for tube 6.

5.6 Characterization by NACE Etching Method

Samples from each of the six ex-service tubes were selected for characterization of the depth of carburization by the chemical etching measurement method described in the NACE International Standard Test Method for Evaluation of the Carburization of Alloy Tubes used for Ethylene Manufacture [43]. The standard states that the chemical etching method described provides a means of semi-quantitatively measuring the extent of carburization in alloy tubes, whether for the purposes of comparing relative carburization resistance of alloys exposed to the standard laboratory carburization procedure, or for evaluating tubes that have been removed from operation in ethylene pyrolysis furnaces.

A sample was selected at random from each tube. The samples were prepared by grinding the surface with silicon carbide paper to 600 grit, and were then immersed in the etchant (200 ml HNO_3, 70 ml HF, 670 ml H_20) for 2 hours at room temperature. Following neutralization of the etchant and cleaning of the samples, the polished surfaces were observed. Low magnification micrographs of the surface of the samples after exposure to the etchant are shown in Figure 5.73. The samples from tubes 1, 2, and 5 displayed clear etching bands. The samples from tubes 3 and 4 did not display etching bands, and the surface appeared dull in comparison to the as-polished condition. The sample from tube 6 also did not etch, and the shiny, as-polished surface finish remained. The results are summarized in Table 5.19. The depth of the etching band was measured from the inner surface of the tube to the furthest extent of affected material.

The standard states that the etching procedure "sufficiently attacks all carbides so that a zone of carburized versus non-carburized material is visually evident". Based on the results of the etching method observed, a zone of carburized versus non carburized material is indeed visually evident, however higher magnifications micrographs (Figure 5.74) show that it is the austenite matrix within the carburized region that is attacked by the etchant, and that the carbides themselves remain unaffected.

Additional samples were taken from each of the six tubes, directly adjacent to the samples used for the NACE etching method, in order to quantify the composition of the austenite matrix. The samples were ground and polished according to the procedures described in Section 3.2. Multiple EDS spectra were taken at set intervals across the wall thickness of each sample in order to build a profile of the matrix composition. The matrix chromium concentration profiles for the six samples are shown in Figure 5.75. It was noted that the depth of the etching band, for those samples that displayed an etching band, corresponded with a local matrix chromium concentration of approximately 10 – 14 wt%. The samples from tubes 3, 4, and 6 were unaffected by the etchant, and all displayed matrix chromium concentrations well above 10 – 14 wt% across their entire wall thicknesses. The complete lack of effect of the etchant on the sample from tube 6 is likely due to its significantly higher chromium

content in comparison to the other five tubes (35 wt% as-cast versus 25 wt%). It thus appears that the etching contrast appears due to the attack of the austenite matrix when the chromium concentration falls below approximately 10 – 14 wt%. As discussed in Section 5.4.1, the matrix chromium concentration in the locality of the $M_{23}C_6$-to-M_7C_3 transformation front was observed to be in the 10 – 13 wt% range. The depth of the NACE etching band may therefore provide a simple destructive measure for quantifying the depth of the transformation front without resorting to electron microscopy.

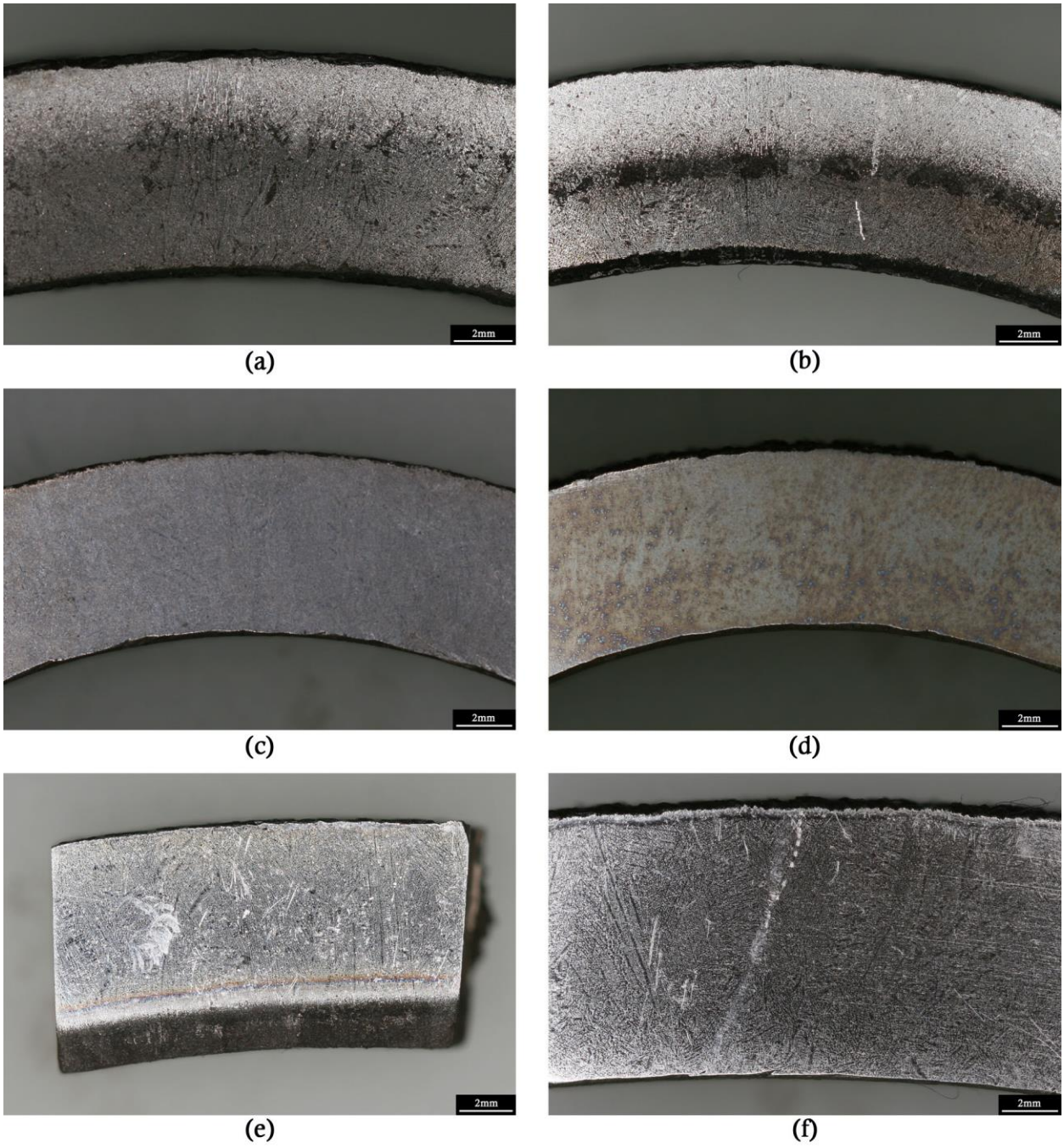

Figure 5.73 - Low magnification micrographs showing the surfaces of samples from (a) tube 1, (b) tube 2, (c) tube 3, (d) tube 4, (e) tube 5, and (f) tube 6 after exposure to the NACE International etching method.

Table 5.19 - Summary of NACE International etching method results.

Tube sample	Average depth of etching band from inner surface
1	5.1 mm
2	3.0 - 4.0 mm
3	Did not etch, dull surface.
4	Did not etch, dull surface.
5	1.7 mm
6	Did not etch, retained as-polished surface.

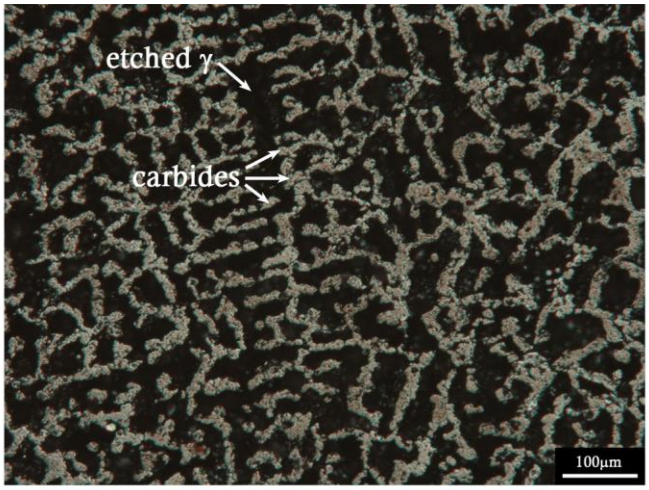

Figure 5.74 - Optical micrograph of carburized region of sample from tube 1 after exposure to the NACE International etching method (γ = austenite).

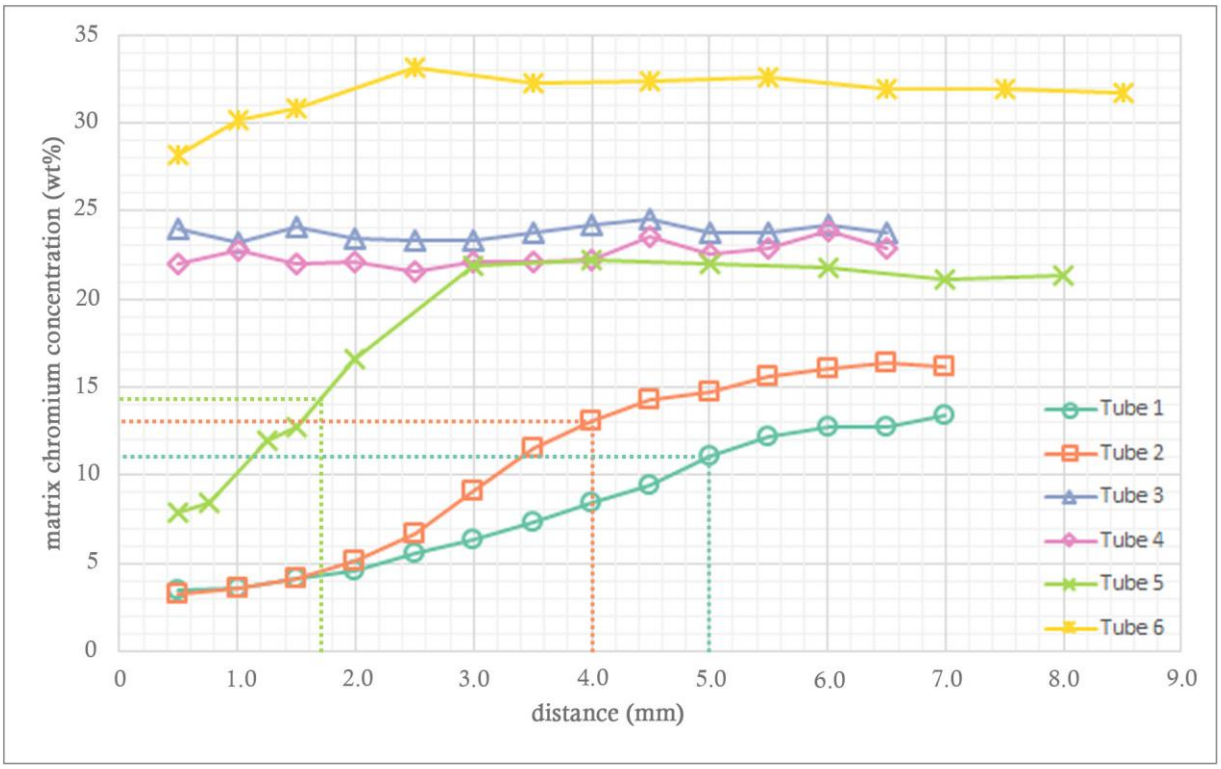

Figure 5.75 - Matrix chromium concentrations for the samples from tubes 1-6 adjacent to the NACE etching method samples. Coloured dashed lines indicate the depth of the NACE etching band for the corresponding tube. Distance is measured from the inner diameter.

5.7 Summary and Conclusions

An image analysis methodology was developed in order to measure the volume fractions of the multitude of phases present in the microstructure of the six ex-service ethylene pyrolysis tubes studied. EDS maps combined with SEI images were used in conjunction with the software programs ilastik, for automated image segmentation, FIJI, for image processing, and Microsoft Excel, for data processing and analysis.

The matrix chromium concentration at the $M_{23}C_6$-to-M_7C_3 transformation front was in the range of 10 – 13 wt% for all samples in which the transformation occurred. The location of the $M_{23}C_6$-to-M_7C_3 transformation front was seen to offer a measure of the degree of carbide coarsening:

- The chromium carbide volume fraction in the locality of the transformation front was in 20 – 25 % range for all samples in which the $M_{23}C_6$-to-M_7C_3 transformation occurred.
- Independent of the distance from the inner diameter to the transformation front, the wall regions between the inner diameter and the transformation front displayed volume fractions of M_7C_3 carbides in the 25 – 35 % range.

- When the transformation front was located less than 1.5 mm from the inner diameter, the volume fraction of $M_{23}C_6$ between the transformation front and the outer diameter rapidly dropped over a short distance of 1 – 1.5 mm to a value of 5 – 8 % and remained within this range for the remainder of the wall thickness.
- When the transformation front was located at a distance greater than 2.0 mm from the inner diameter, the volume fraction of $M_{23}C_6$ between the transformation front and the outer diameter decreased at a gradual rate, and typically did not drop below 10 % until proximity to the outer diameter was 2 mm or less.

A comparison to the results obtained using the chemical etching measurement method described in the NACE International Standard Test Method for Evaluation of the Carburization of Alloy Tubes used for Ethylene Manufacture [43] indicates that the depth of the etching band also corresponds with the $M_{23}C_6$-to-M_7C_3 transformation front in carburized tubes, and with a matrix chromium concentration of 10 – 14 wt%. The NACE etching method may therefore provide a simple, albeit destructive, measure of quantifying the depth of the transformation front, and provide a measure of the degree of coarsening, without resorting to electron microscopy. It was noted that the etchant attacks the austenite matrix in regions where the chromium concentration drops below 10 – 14 wt%, contrary to the statement of the standard that the etchant attacks carbides.

A comparison between the concentration of chromium in the austenite matrix and the total concentration of chromium in the chromium-containing precipitate phases demonstrated that, in the HP-Nb and HP-Micro alloys the precipitation and growth of the M_7C_3, $M_{23}C_6$, $Cr_2(C,N)$, η-carbide, and σ-phase precipitates directly causes the matrix chromium depletion. Due to the small amount of data available for the ET45-Micro alloy studied, it was unable to be determined whether this is also the case in ET45-Micro alloys. In order to determine whether the precipitation and growth of chromium-containing phases in the ET45-Micro alloys also directly causes the depletion of chromium in the austenite matrix a significantly larger data set including data from tubes that have experienced a greater extent of carburization than those presently analysed would be necessary.

The instability of the NbC and (Nb,Ti)C precipitates was evident in many of the tubes studied, and the transformation to G-phase, η-carbide, or a combination of the two was frequently observed; however, the temperature ranges over which the transformation occur in carburized tubes appear to differ from those tubes subject solely to ageing. The presence of η-carbide and a general trend of increases in the volume fraction in regions adjacent to the outer diameter in the samples that experienced greatest extent of oxidation is consistent with the observations of Buchanan [4] that an air atmosphere may promote the NbC-to-η-carbide and (Nb,Ti)C-to-η-carbide transformations.

One sample from tube 1 and all four samples from tube 2 displayed the direct transformation of $M_{23}C_6$ to $Cr_2(C,N)$ carbonitrides, and also the individual intragranular precipitation of lenticular $Cr_2(C,N)$

carbonitrides within the transformation band. The direct transformation of $M_{23}C_6$ to $Cr_2(C,N)$ was noted to not contribute significantly to the chromium depletion of the austenite matrix due to the two phases containing similar proportions of chromium; however, the volume fraction of $Cr_2(C,N)$ still needs to be accounted for in comparing the phase fractions to the matrix chromium concentration as the chromium it contains may have been drawn from the matrix to allow for the coarsening of the prior $M_{23}C_6$ precipitates.

Chapter References

[1] Sommer, C., Straehle, C., Kothe, U., and Hamprecht, F.A. *Ilastik: Interactive learning and segmentation toolkit*. in *2011 8th IEEE International Symposium on Biomedical Imaging: From Nano to Macro, ISBI'11, March 30, 2011 - April 2, 2011*. 2011. Chicago, IL, United states: IEEE Computer Society.

[2] Schindelin, J., Arganda-Carreras, I., Frise, E., Kaynig, V., Longair, M., Pietzsch, T., Preibisch, S., Rueden, C., Saalfeld, S., Schmid, B., Tinevez, J.-Y., White, D.J., Hartenstein, V., Eliceiri, K., Tomancak, P., and Cardona, A. *Fiji: an open-source platform for biological-image analysis.* Nat Meth, 2012. **9**(7): p. 676-682.

[3] Goldstein, J., Newbury, D., Joy, D., Lyman, C., Echlin, P., Sawyer, L., and Michael, J. *Scanning Electron Microscopy and X-Ray Microanalysis*. 3rd ed. 2003: New York: Springer Science + Business Media Inc.

[4] Buchanan, K.G. *The Effects of Long-Term Isothermal Ageing on the Microstructure of HP-Nb and HP-NbTi Alloys - Doctoral Dissertation*. 2013, University of Canterbury: Christchurch, New Zealand.

[5] Barbabela, G.D., de Almeida, L.H., da Silveira, T.L., and Le May, I. *Phase characterization in two centrifugally cast HK stainless steel tubes.* Materials Characterization, 1991. **26**(1): p. 1-7.

[6] de Almeida, L.H., Ribeiro, A.F., and Le May, I. *Microstructural characterization of modified 25Cr-35Ni centrifugally cast steel furnace tubes.* Materials Characterization, 2003. **49**(3): p. 219-229.

[7] Caballero, F.G., Imizcoz, P., Lopez, V., Alvarez, L.F., and De Andrés, C.G. *Use of titanium and zirconium in centrifugally cast heat resistant steel.* Materials Science & Technology, 2007. **23**(5): p. 528-534.

[8] Stevens, K.J., Parbhu, A., and Soltis, J. *Magnetic force microscopy and cross-sectional transmission electron microscopy of carburised surfaces.* Current Applied Physics, 2004. **4**(2-4): p. 304-307.

[9] Stevens, K.J., Parbhu, A., Soltis, J., and Stewart, D. *Magnetic force microscopy of a carburized ethylene pyrolysis tube.* Journal of Physics D (Applied Physics), 2003. **36**(2): p. 164-8.

[10] Krauss, G. *Steels: Processing, Structure, and Performance*. 2005, Materials Park, Ohio: ASM International.

[11] Bhadeshia, H.K.D.H. and Honeycombe, R.W.K. *Steels: Microstructure and Properties*. 3rd ed. 2006, Amsterdam, Boston: Elsevier, Butterworth-Heinemann.

[12] Lang, E. and Norton, J. *Monitoring of carburisation by the use of magnetic techniques, Part 1: Fundamental aspects and measurements on 25Cr-20Ni steels*. 1986, Commission of the European Communities, Physical Science, PETTEN, EUR 10566 EN.

[13] Young, D.J. *Carburization and Metal Dusting*, in *Shreir's Corrosion*. 2010, Elsevier: Oxford. p. 272-303.

[14] Grabke, H.J. and Wolf, I. *Carburization and oxidation.* Materials Science and Engineering, 1987. **87**(0): p. 23-33.

[15] Silva, I.C., Rebello, J.M.A., Bruno, A.C., Jacques, P.J., Nysten, B., and Dille, J. *Structural and magnetic characterization of a carburized cast austenitic steel.* Scripta Materialia, 2008. **59**(9): p. 1010-1013.

[16] Christ, H.J. *Experimental characterization and computer-based description of the carburization behaviour of the austenitic stainless steel AISI 304L.* Materials and Corrosion, 1998. **49**: p. 258-65.

[17] Schnaas, A. and Grabke, H.J. *High-temperature corrosion and creep of Ni-Cr-Fe alloys in carburizing and oxidizing environments.* Oxidation of Metals, 1978. **12**(5): p. 387-404.

[18] Hsieh, C.-C. and Wu, W. *Overview of Intermetallic Sigma Phase Precipitation in Stainless Steels.* ISRN Metallurgy, 2012. **2012**: p. 16.

[19] Padilha, A.F. and Rios, P.R. *Decomposition of austenite in austenitic stainless steels.* ISIJ International, 2002. **42**(4): p. 325-337.

[20] Tillack, D.J. and Guthrie, J.E. *Wrought and cast heat-resistant stainless steels and nickel alloys for the refining and petrochemical industries.* Nickel Development Institute, 1998.

[21] Haro, S., Colás, R., Velasco, A., and López, D. *Study of weldability of a Cr-Si modified heat-resisting alloy.* Materials Chemistry and Physics, 2003. **77**(3): p. 831-835.

[22] Shi, S. and Lippold, J.C. *Microstructure evolution during service exposure of two cast, heat-resisting stainless steels - HP-Nb modified and 20-32Nb.* Materials Characterization, 2008. **59**(8): p. 1029-1040.

[23] Tawancy, H.M. *Degradation of mechanical strength of pyrolysis furnace tubes by high-temperature carburization in a petrochemical plant.* Engineering Failure Analysis, 2009. **16**(7): p. 2171-2178.

[24] Borjali, S., Allahkaram, S.R., and Khosravi, H. *Effects of working temperature and carbon diffusion on the microstructure of high pressure heat-resistant stainless steel tubes used in pyrolysis furnaces during service condition.* Materials & Design, 2012. **34**(0): p. 65-73.

[25] Powell, D.J., Pilkington, R., and Miller, D.A. *The precipitation characteristics of 20% Cr/25% Ni-Nb stabilised stainless steel.* Acta Metallurgica, 1988. **36**(3): p. 713-724.

[26] Mucek, M.W. *Laboratory detection of degree of carburization in ethylene pyrolysis furnace tubing.* Materials Performance, 1983. **22**(9): p. 25-28.

[27] Davis, J.R., (Ed). *ASM Specialty Handbook: Heat-Resistant Materials*. 1997, Materials Park, Ohio: ASM International.

[28] Uglov, V.V., Khodasevich, V.V., Cherenda, N.N., Kasho, I.V., and Kutsanov, V.A. *Tribological properties of ion-implanted high-chromium steel.* Surface and Coatings Technology, 1994. **66**(1): p. 283-287.

[29] Chattopadhyay, R. *Surface wear: analysis, treatment, and prevention*. 2001: ASM international.

[30] Suprunov, V. and Freid, M.K. *Physical properties of the iron-chromium carbides (Cr, Fe) 23 C 6.* Powder Metallurgy and Metal Ceramics, 1970. **9**(12): p. 1007-1009.

[31] Jakobi, D. and Gommans, R. *Typical failures in pyrolysis coils for ethylene cracking.* Materials and Corrosion, 2003. **54**(11): p. 881-886.

[32] Aydin, I., Buhler, H.E., and Rahmel, A. *Observations concerning nitridation of refractory austenitic materials in air and combustion gases.* Materials and Corrosion 1980. **31**(9): p. 675-682. (In German).

[33] Berghof-Hasselbächer, E., Gawenda, P., Schorr, M., Schütze, M., and Hoffman, J.J. *Atlas of Microstructures*: Materials Technology Institute.

[34] Kenik, E.A., Maziasz, P.J., Swindeman, R.W., Cervenka, J., and May, D. *Structure and phase stability in a cast modified-HP austenite after long-term ageing.* Scripta Materialia, 2003. **49**(2): p. 117-22.

[35] Nishimoto, K., Saida, K., Inui, M., and Takahashi, M. *Changes in microstructure of HP-modified, heat-resisting cast alloys under long-term aging. Repair weld cracking of service-exposed, HP-modified, heat-resisting cast alloys (2nd Report).* Welding Research Abroad, 2002. **48**(11): p. 1-9.

[36] Thomas, C.W., Stevens, K.J., and Ryan, M.J. *Microstructure and properties of alloy HP50-Nb: comparison of as cast and service exposed materials.* Materials Science and Technology, 1996. **12**(6): p. 469-475.

[37] Alvino, A., Lega, D., Giacobbe, F., Mazzocchi, V., and Rinaldi, A. *Damage characterization in two reformer heater tubes after nearly 10 years of service at different operative and maintenance conditions.* Engineering Failure Analysis, 2010. **17**(7–8): p. 1526-1541.

[38] Jargelius-Pettersson, R. *Precipitation trends in highly alloyed austenitic stainless steels.* Zeitschrift für Metallkunde, 1998. **89**(3): p. 177-183.

[39] Their, H., Baumel, A., and Schmidtmann, E. *Einfluss von Stickstoff auf des Ausscheidungsverhalten des Stahles x5CrNiMol713.* Arch. Eisenhiittenw, 1969. **40**: p. 333-339.

[40] *ASM Engineered Materials Handbook*, ed. Bauccio, M. 1994, Materials Park, Ohio: ASM International.

[41] Bergman, G. and Shoemaker, D.P. *The determination of the crystal structure of the σ phase in the iron–chromium and iron–molybdenum systems.* Acta Crystallographica, 1954. **7**(12): p. 857-865.

[42] Kubota Metal Corporation *KHR 35C Alloy Data Sheet.*

[43] NACE International *NACE International Standard Test Method: Evaluation of Carburization of Alloy Tubes Used for Ethylene Manufacture*. 2006.

Chapter 6: Mechanical Performance

Vickers microhardness testing was performed on the metallographic samples from the six ex-service tubes upon completion of microstructural characterization. In addition, creep samples were machined from specific locations in the wall thickness at tube locations adjacent to the metallographic samples, to enable a direct comparison between the microstructure and creep performance. The creep samples were subject to steady state creep testing at 1025 °C and 12 MPa uniaxial stress. The current chapter presents the findings of the mechanical tests performed and discusses the relationship between microstructure and mechanical performance.

6.1 Hardness of Ex-Service Tube Samples

Hardness testing was performed on the metallographic samples upon completion of microstructural characterization, enabling a direct comparison between the hardness results and microstructural features. In addition, hardness testing of the metallographic samples taken from material adjacent to the center of the creep samples enabled comparison between the hardness results and the creep performance. A Vickers microhardness tester with a 1000 gram-force load was used to measure the hardness of the samples. In order to account for the inherent variability in the microstructure, three radial profiles were taken and then averaged for each metallographic sample to give an average radial hardness profile.

Hardness testing was not performed directly on the creep samples, but rather on the metallographic samples adjacent to the creep sample centers. The creep samples were machined from the tubes such that the centers of the gauge lengths were located where the response to eddy current non-destructive testing (eddy current NDT) had been measured, as shown in Figure 3.1, to enable a direct comparison between microstructure, mechanical properties, and magnetic response. Due to hardness indents creating stress concentrations, hardness testing was unable to be performed on the gauge section of the creep samples prior to testing without voiding the test results. A comparison between the pre-testing microstructure and hardness tests performed upon the completion of creep testing was considered inaccurate as the microstructure of the creep samples would be expected to change during the exposure to elevated temperatures during the test. Hardness testing of the grip sections of the creep samples was considered, however this was also deemed inaccurate due to the grip sections being a distance of 35 - 45 mm away from the sample centers, and thus the possibility of differences in microstructure over this distance could not be discounted. As demonstrated in Section 5.1.4, a comparison between the phase fraction distributions and matrix compositions for two metallographic

samples located either side of a creep sample center in tube 1 showed minimal difference between the two. Based on this comparison, hardness testing of the metallographic samples directly adjacent to the creep sample centers was considered the most accurate representation of the hardness of the gauge length of the creep samples.

In the three tubes that displayed the greatest extent of microstructural coarsening (tubes 1, 2, and 5), the measured hardness was seen to mirror the volume fractions of the primary chromium carbides. The maximum hardness values of 280 – 310 HV occurred in the 0.5 – 1.0 mm regions of samples 1A-D, 2A-D, and 5A-D, and corresponded with a M_7C_3 volume fraction of 28 – 38 %. At the outer wall, when the volume fraction of $M_{23}C_6$ was in the range of 5 – 8 %, the corresponding hardness was 190 – 215 HV.

In between the extremes in chromium carbide volume fraction at the inner and outer walls, the rate of decrease in the hardness profile was observed to mirror the rate of decrease in the volume fractions of the chromium carbides. For example, in sample 1B a rapid drop in the volume fraction of $M_{23}C_6$ from ≈ 22 % to the 5 – 8 % range over the 1.5 – 3.0 mm region, as shown in Figure 5.14, was accompanied by a rapid drop in hardness from approximately 260 HV to 210 HV, as shown in Figure 6.1. Sample 1C displayed a more gradual decline in hardness over the remainder of the wall in comparison to sample 1A, as shown in Figure 6.1, consistent with a correspondingly more gradual decrease in the volume fraction of chromium carbides in comparison to sample 1A (Figure 5.16 and Figure 5.12 respectively).

Although the volume fraction of $M_{23}C_6$ carbides at the outer wall region of sample 1D dropped to approximately 8 %, the hardness value remained higher than in the corresponding regions of samples 1A-C (220 – 250 HV in comparison to 200 – 215 HV). The greater hardness in the outer wall region of sample 1D is likely due to the presence of significant volume fractions of $Cr_2(C,N)$ carbonitrides (up to 11 %), which are also a hard and brittle phase and are reported to have the same effect on mechanical properties as carbides [1]. The approximate combined volume fraction of $M_{23}C_6$ and $Cr_2(C,N)$ at the 7.0 mm wall region in sample 1D was 19 %. At the outer wall of the tube 2 samples, the combined volume fraction of $M_{23}C_6$ + $Cr_2(C,N)$ was slightly lower than in 1D in the 13 – 17 % range, and the hardness was also slightly lower, in the 215 – 220 HV range. The hardness measured in regions of the tube walls where the volume fraction of primary chromium-rich precipitates is a combination of $M_{23}C_6$ and $Cr_2(C,N)$ was generally observed to be consistent with wall regions in which the same volume fraction of primary chromium-rich precipitates was composedly solely of chromium carbides. This is demonstrated in Figure 6.3 for the samples from tube 1, in which the hardness values for sample 1D, which contained $Cr_2(C,N)$ in addition to $M_{23}C_6$, are consistent within the errors of the analysis to the hardness values for samples 1A-C, which did not contain $Cr_2(C,N)$.

The hardness of samples 3A-D was typically observed to remain within the 250 – 290 HV range, as shown in Figure 6.4, and the hardness of samples 4A-D typically remained within the 210 – 250 HV range, as shown in Figure 6.5. The consistency in the measured hardness across the wall thickness of samples 3A-D and 4A-D is consistent with the relatively homogenous microstructures of the tubes, as discussed in Sections 5.2.3 and 5.2.4 respectively.

Tube 3 was observed to be composed of 1.5 – 3 % $M_{23}C_6$, 0.5 – 1.5 % σ-phase, and 0.5 – 2 % G-phase in the primary network, and also contained secondary precipitates in the form of σ-phase platelets 10 μm long and < 1 μm wide which were distributed evenly throughout the matrix. Tube 4 did not contain σ-phase, and was observed to be composed of 3 – 6 % $M_{23}C_6$, and 1.5 – 4 % G-phase. A secondary distribution of $M_{23}C_6$ precipitates, typically < 1 μm in size, was observed adjacent to the primary precipitate network in tube 4.

The effect of G-phase on the mechanical properties of HP alloys, both at room temperature and elevated temperature, is not well understood. Microhardness measurements on various microstructural constituents by Nishimoto [2] resulted in a hardness measurement for G-phase of 1050 HV, which is within the range of hardness typically reported for the M_7C_3 and $M_{23}C_6$ carbides, and 110 HV harder than reported for σ-phase, as summarised in Table 5.16. The greater volume fraction of G-phase in tube 4 in comparison to tube 3 might thus be expected to result in a greater hardness value. However, as discussed in Section 5.4.2, σ-phase is reported to result in a loss of ductility and toughness at temperatures below 120 – 150 °C, and thus the presence of σ-phase in tube 3 may be a contributing factor to the higher hardness in comparison to tube 4. The even distribution of the secondary σ-phase platelets in the matrix of tube 3 is likely to create a superior dispersion strengthening effect at room temperature in comparison to the $M_{23}C_6$ precipitates in tube 4, the distribution of which is concentrated adjacent to the primary network. As such, despite tube 3 containing a lower volume fraction of $M_{23}C_6$ carbides and G-phase, the secondary σ-phase distribution may have resulted in a higher average hardness at room temperature.

The samples from tube 6 obtained maximum hardness in the 0.5 – 1.0 mm wall region, with a value of 230 – 250 HV. For the remainder of the wall thickness the hardness was consistent in the 200 – 240 HV range. At the 9.5 mm wall position, the hardness of samples 6A and 6C was observed to sharply drop to 150 – 170 HV. The relative consistency of the hardness profiles in samples 6A-D is consistent with the relative homogeneity of the microstructures as discussed in Section 5.2.6. In comparing the typical hardness values of the tube 6 samples to the ranges of hardness values in the samples from tubes 1, 2, and 5, a hardness range of 200 – 240 HV was consistent with $M_{23}C_6$ volume fractions in the range of 6 – 16 % in tubes 1, 2, and 5.

The range of hardness values in the tube 6 samples is similar to the range of hardness values observed in the tube 3 and tube 4 samples, despite the tube 6 samples consistently displaying higher volume

fractions of primary $M_{23}C_6$ carbides (6 – 14 %, compared to 1.5 – 3 % in tube 3, and 3 – 6 % in tube 4). However, both tubes 3 and 4 displayed fine secondary precipitate distributions, whereas secondary $M_{23}C_6$ precipitates were rarely observed in tube 6. Tubes 3 and 4 may have therefore displayed a superior dispersion strengthening effects due to their secondary distributions, leading to hardness values on par with tube 6 despite lower volume fractions of primary $M_{23}C_6$ precipitates.

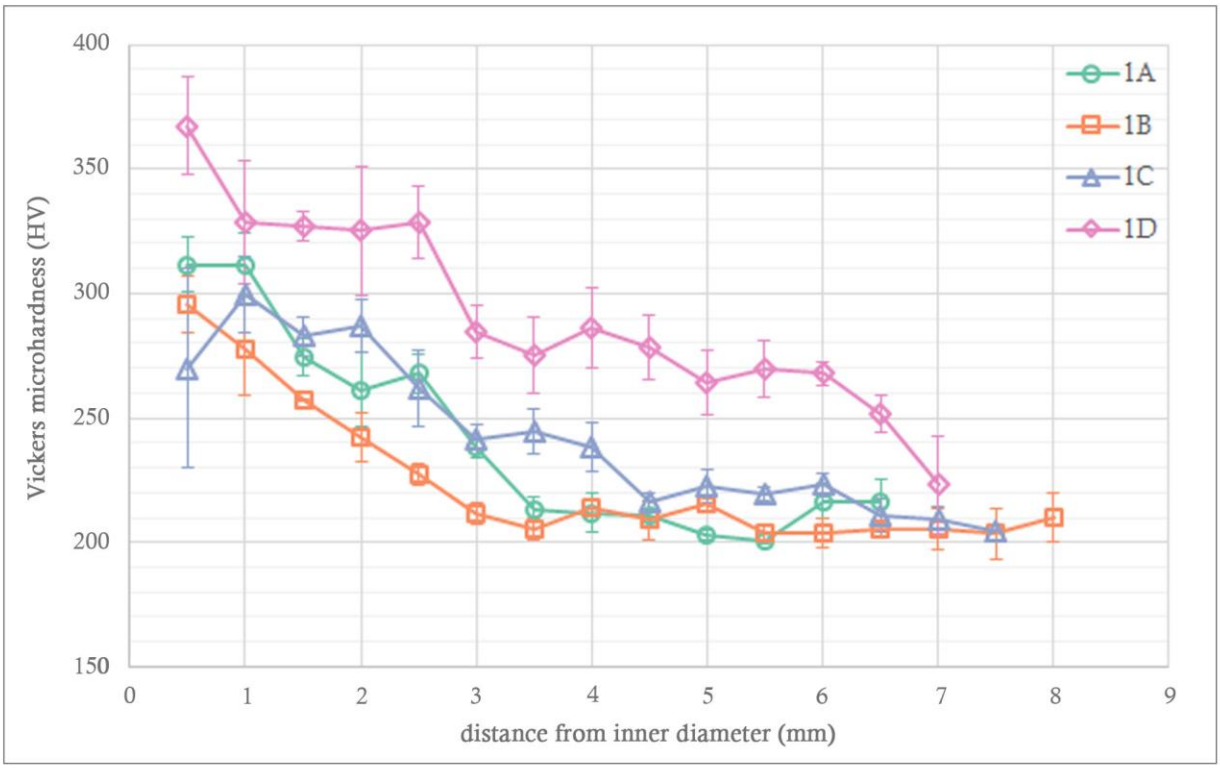

Figure 6.1 - Vickers microhardness profiles for samples 1A-D.

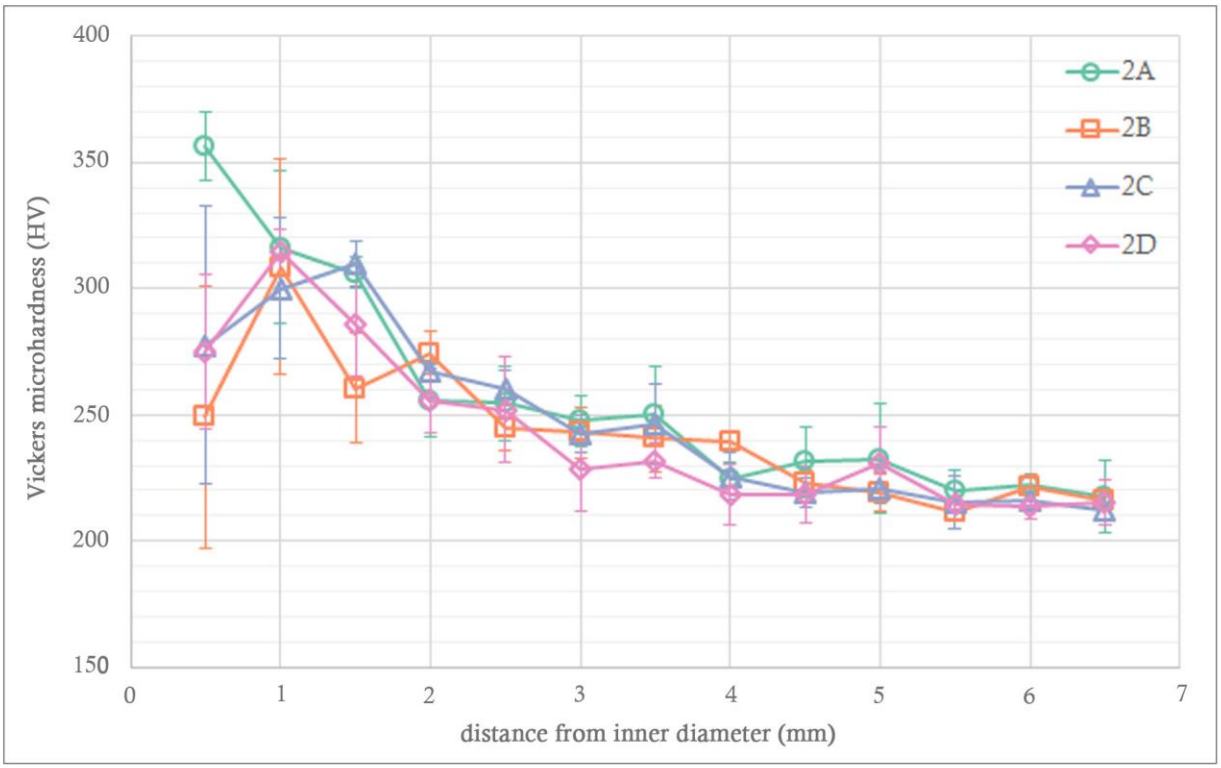

Figure 6.2 - Vickers microhardness profiles for samples 2A-D

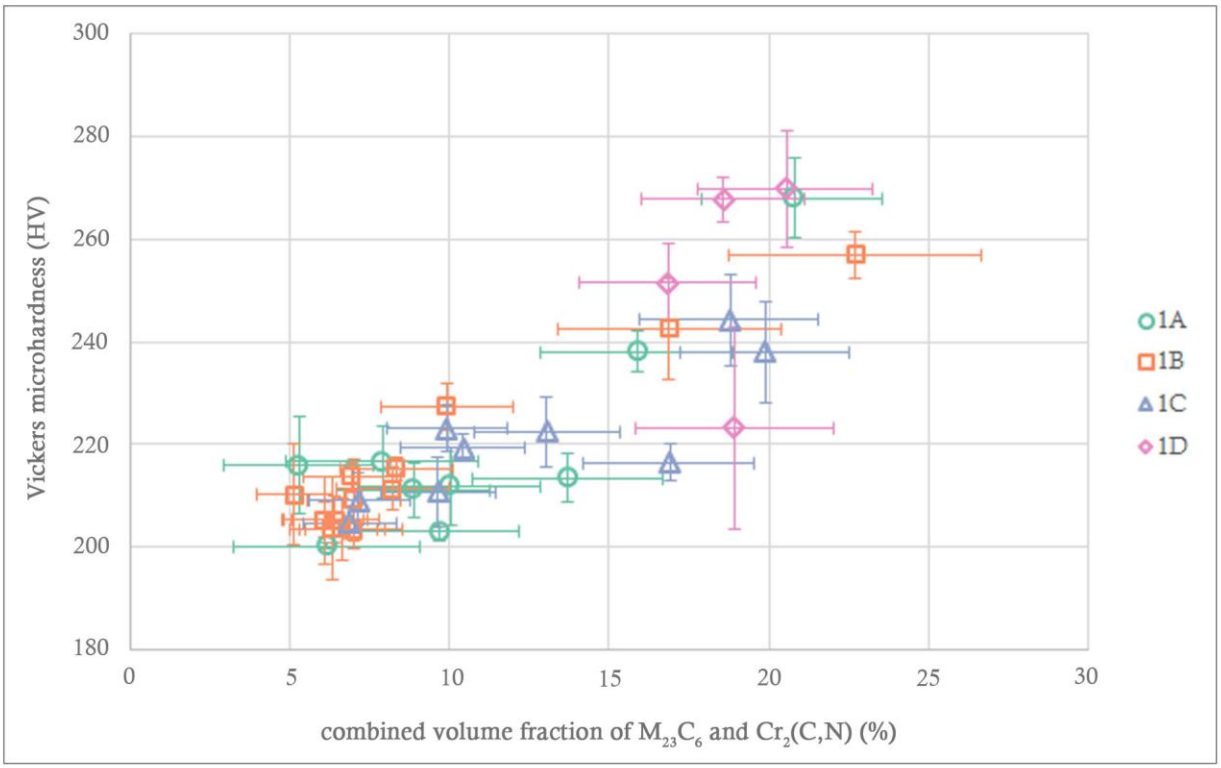

Figure 6.3 - A comparison between the Vickers microhardness and combined volume fraction of $M_{23}C_6$ and $Cr_2(C,N)$ precipitates for samples 1A-D.

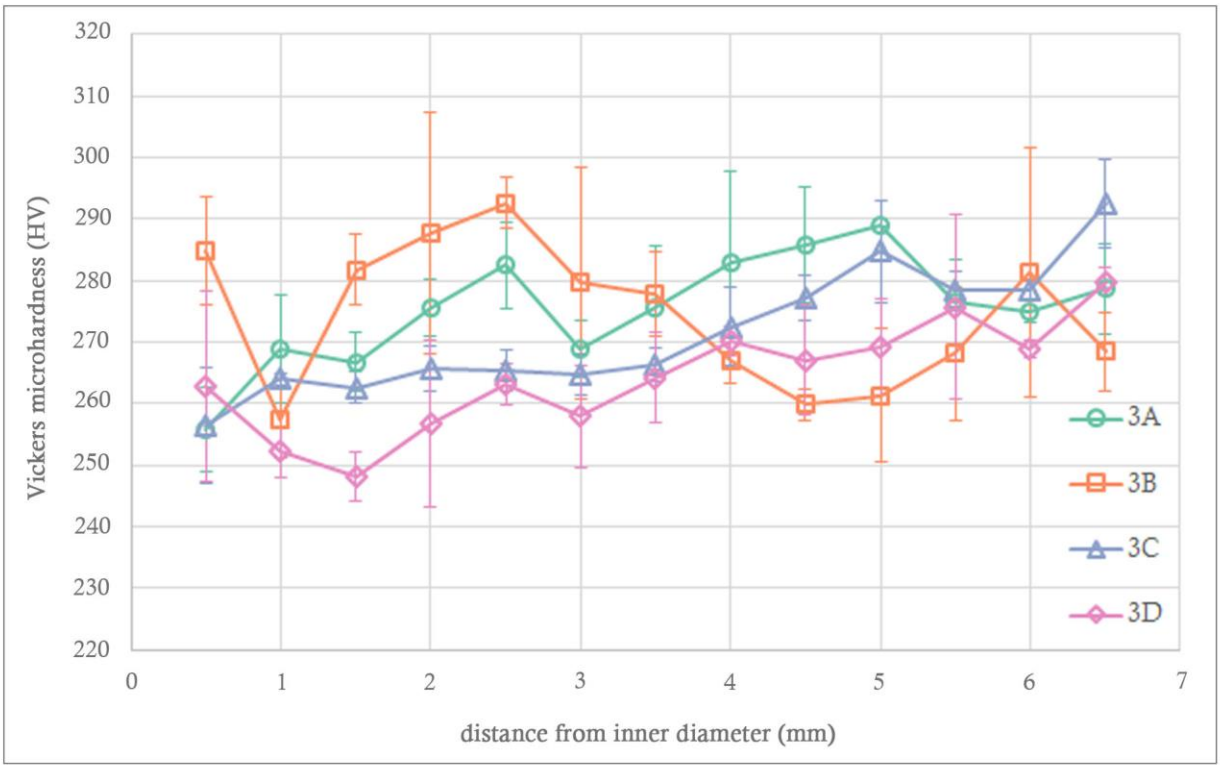

Figure 6.4 - Vickers microhardness profiles for samples 3A-D.

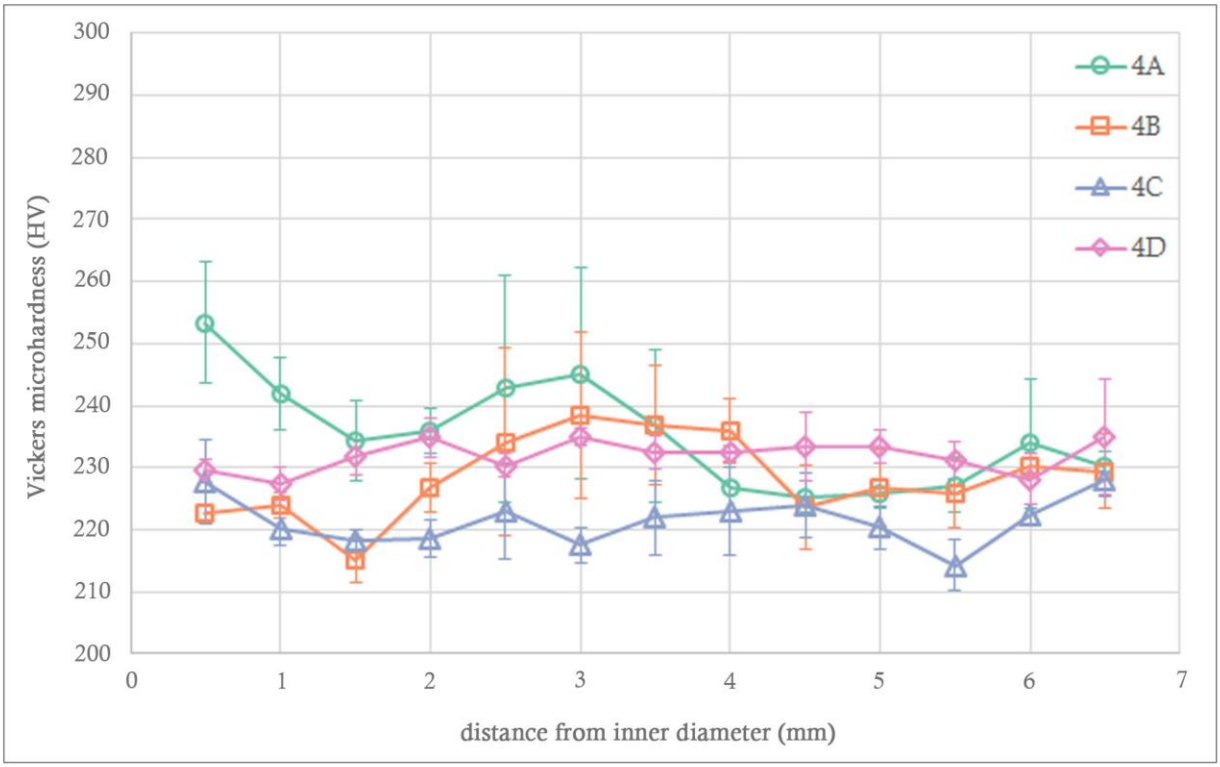

Figure 6.5 - Vickers microhardness profiles for samples 4A-D.

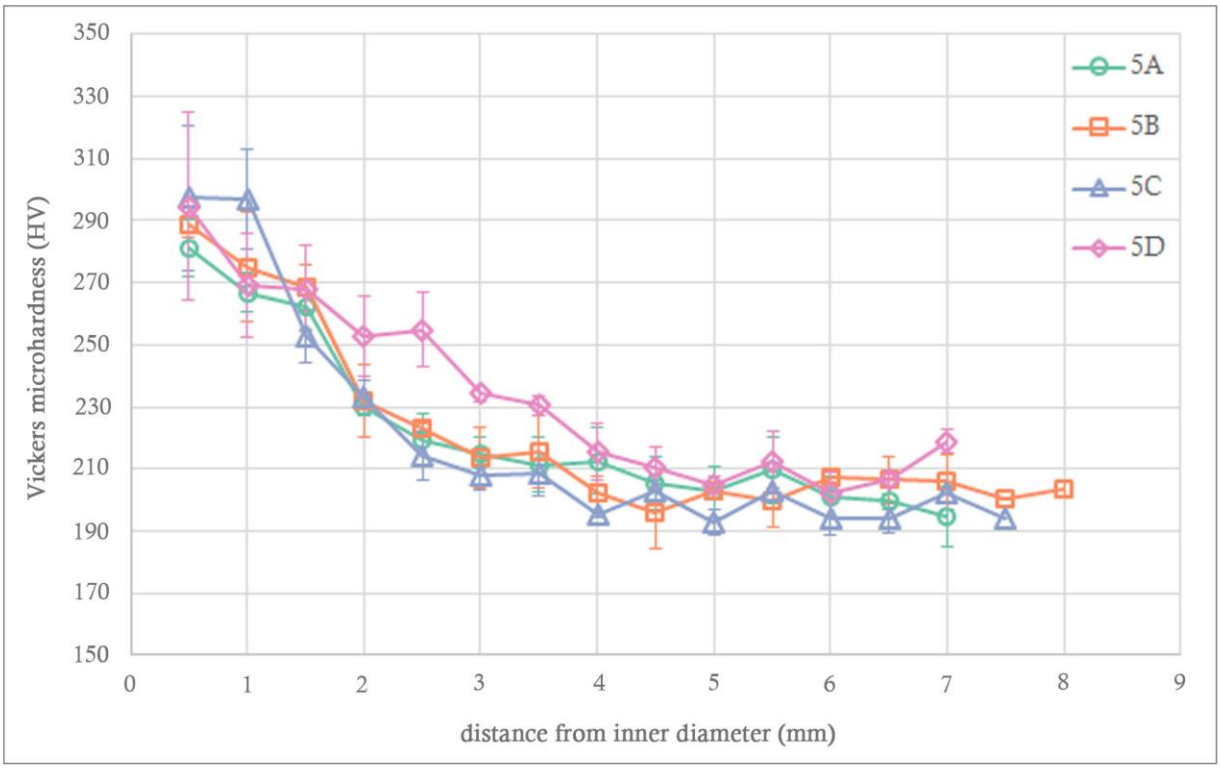

Figure 6.6 - Vickers microhardness profiles for samples 5A-D.

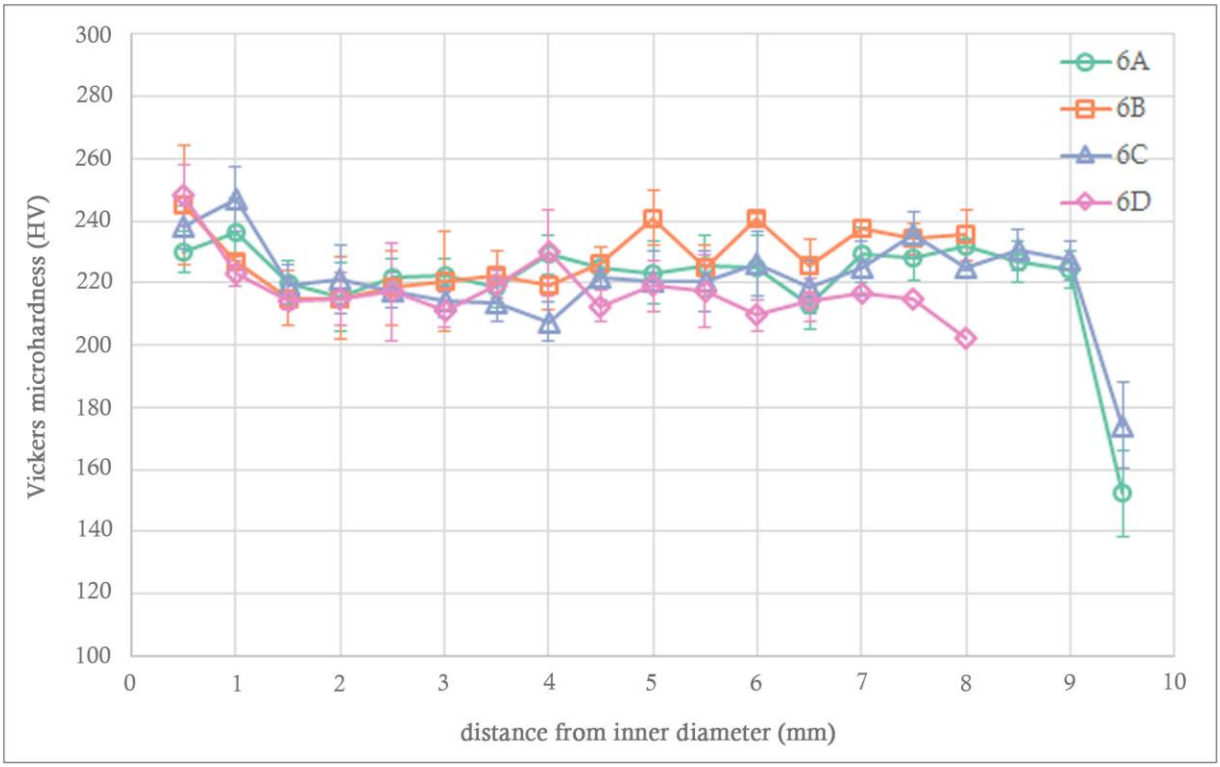

Figure 6.7 - Vickers microhardness profiles for samples 6A-D.

6.2 Creep Performance of Ex-Service Tube Samples

6.2.1 Testing Apparatuses and Conditions

Steady state creep testing of the ex-service samples was conducted at 1025 °C and 12 MPa uniaxial stress, which is within the range of conditions being tested by Quest Integrity NZL Ltd. Because of the short term nature of the thermal cycling that ethylene pyrolysis tubes experience during service, and the rapid changes that can occur in the microstructure under carburizing conditions, the steady state creep rate was deemed the most important parameter to measure. A testing time of 650 hours (approximately 27 days) was chosen to reflect the short term nature of the thermal cycles.

Testing of the creep samples was carried out using the apparatus shown in Figure 6.8. Set-up and operation of each creep test was conducted in accordance with ASTM E319 – Standard Test Methods for Conducting Creep, Creep Rupture, and Stress Rupture Tests of Metallic Materials [3]. The two creep testing apparatuses had both been previously constructed at the University of Canterbury for the purposes of steady state creep testing. Each apparatus enabled simultaneous testing of up to four creep samples in series. The creep sample and grip assemblies for the two apparatus are shown in Figure 6.9 and Figure 6.10. Three thermocouples were used for each apparatus: one to control the furnace temperature, one to record the furnace temperature, and one to record the ambient temperature of the room. The two thermocouples located in the furnace were situated such that the temperature directly adjacent to the top sample was measured.

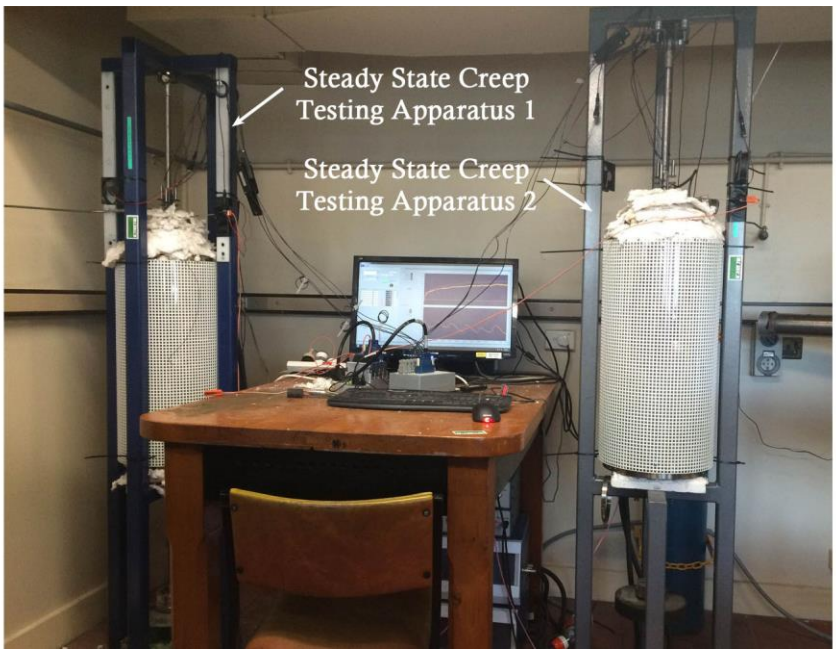

Figure 6.8 - Steady state creep testing apparatuses.

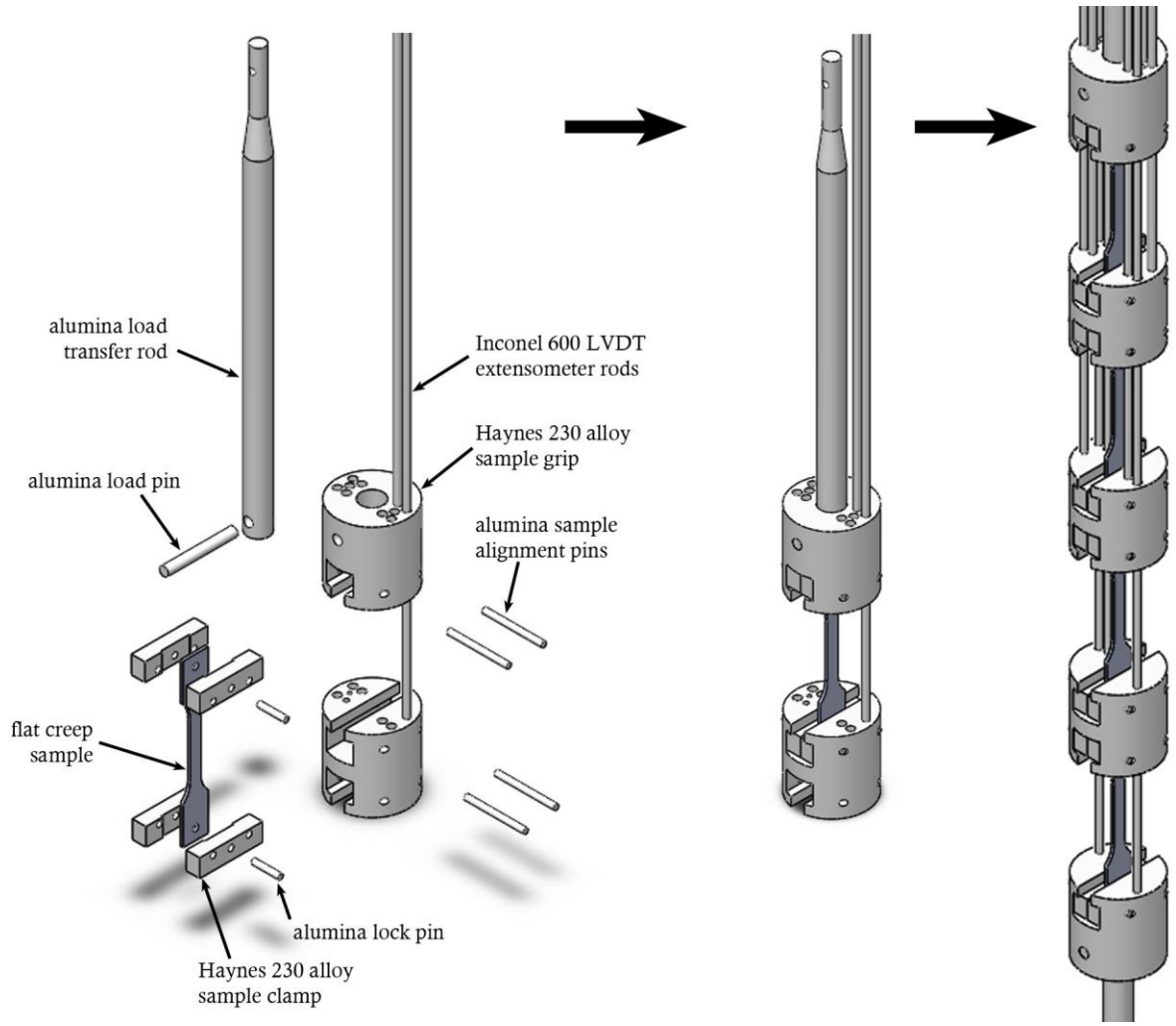

Figure 6.9 - CAD design depicting the creep sample and grip assembly for Steady State Creep Apparatus 1.

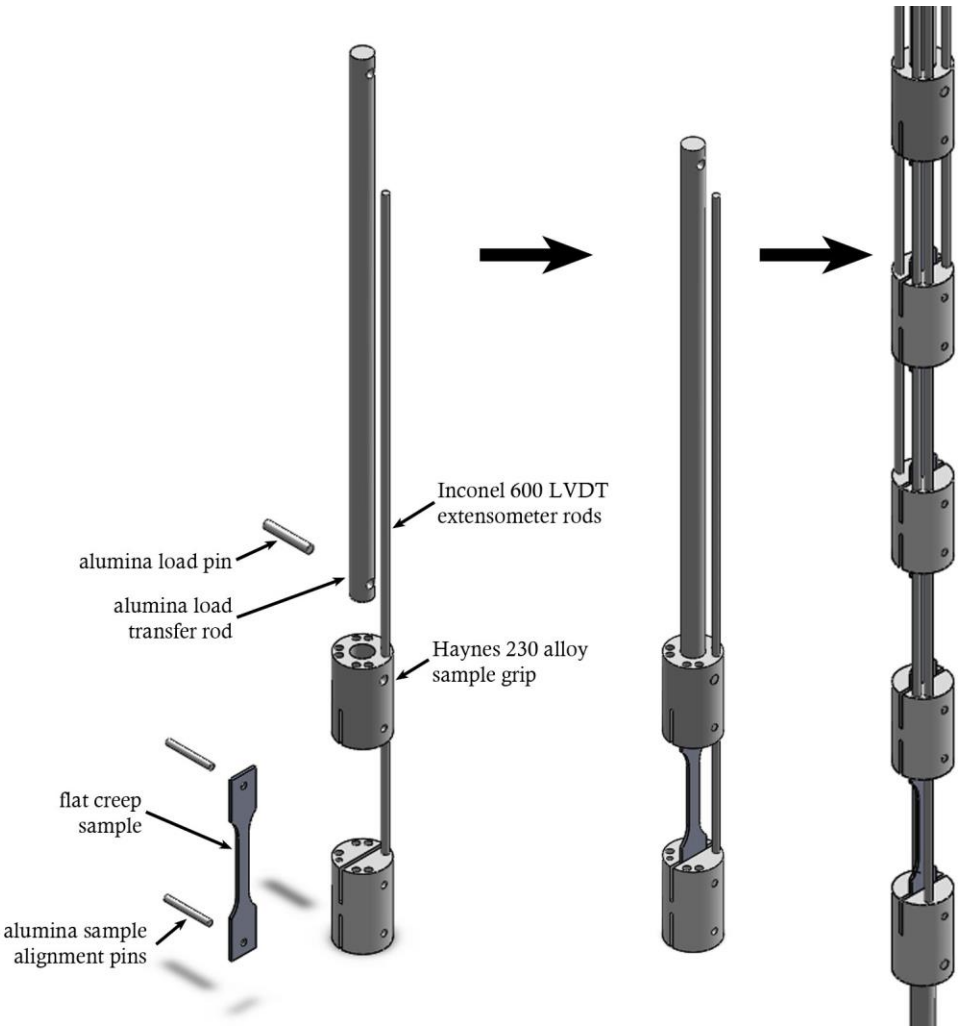

Figure 6.10 - CAD design depicting the creep sample and grip assembly for Steady State Creep Apparatus 2.

Rectangular dog-bone shaped samples were machined from the wall of the tubes, with the length of each sample running parallel to the longitudinal direction of the tube (Figure 3.1). Prior to conducting the test, the gauge length of the samples was polished using 9 μm diamond suspension. The samples were cleaned in an ethanol bath and dried before being placed in the test rig. Thin samples (1.5 mm) were used in order to determine the effects of the range of phases present in the microstructure on the creep performance of the materials. In addition, the finite element models under development at Quest Integrity NZL Ltd. use thin layers with different thermal, magnetic, and mechanical properties to make up the tube wall, and thus thin creep samples allow for the creep properties extracted to be useful inputs to the FEA models and improve the accuracy of remaining life estimation.

Heating of the samples and furnace was carried out at a rate of approximately 4.5 °C/minute. Greater rates of heating were not possible without inducing unacceptable thermal stresses in the isothermal furnace liner (heat pipe). The use of isothermal furnace liners enabled the temperature within the furnaces to remain at 1025 ± 1 °C for the duration of each test.

As specified in the standard, a total of 15 % of the test load was applied during heating to ensure that the furnace insulation did not affect the application of the full axial testing load. Prior to the application of the full testing load the samples were held at the testing temperature for 30 minutes in order to ensure that the temperature inside the furnace had normalized. The minimum time recommended in the standard is one hour, however the use of isothermal furnace liners meant that the temperature within the furnaces normalized within 15 - 20 minutes of reaching the testing temperature, making a prolonged one hour holding period unnecessary.

During the holding stage the linear variable differential transducer (LVDT) extensometers were attached to the samples. The full load was then applied to the sample-grip assembly, followed by zeroing of the LVDT extensometers. From this point onwards the extension of each sample, the furnace temperature, and the ambient room temperature were automatically appended to a .txt file at 60 second intervals using data acquisition software developed in LabVIEW. As well as recording data, the LabVIEW software also allowed for real-time monitoring of the extension of each sample and the furnace temperature, allowing the testing to be continually monitored.

6.2.2 Extracting Steady State Creep Data

Post-processing of the creep test data was performed using a combination of Microsoft Excel and a program developed in Matlab. These programs were used to plot the elongation of each sample with respect to time, and from this calculate the steady state creep rate for each sample.

The LVDT extensometer measurements exhibited some noise, typically on the order of ± 5 μm, due to fluctuations in the ambient temperature of the room. The noise was removed from the data via a moving average smoothing operation. For each data point, a range was defined according to Equation 2.19:

$$\mathrm{R}_i = \{y_{(i-n)}\ y_{(i-n+1)}\ y_{(i-n+2)} \cdots\ y_{(i+n)}\} \qquad \textbf{Equation 6.1}$$

where y_i is the extension value at time t, and 2n is the span of the data range. The span was set to 12 hours either side of the central data point in order to smooth the variations due to room temperature fluctuations. For points within 12 hours of the beginning or end of the test, the range was calculated as per Equation 6.2, where L denotes the total number of points:

$$\mathrm{R_i} = \begin{Bmatrix} y_1\ y_2 \cdots\ y_{(2i-1)} \\ y_{(2i-L)}\ y_{(2i-L+1)} \cdots\ y_L \end{Bmatrix} \begin{matrix} i < n \\ i > (L-n) \end{matrix} \qquad \textbf{Equation 6.2}$$

The smoothed data value at each point, z_i, was then calculated as the mean of the range, $\overline{\mathrm{R}}_i$.

An example creep response curve is shown in Figure 6.11, for sample 6C-M. The range of data values over which the steady state creep rate was calculated was selected by eye and adjusted in order to obtain the best fit and minimum error in the slope of the linear fit.

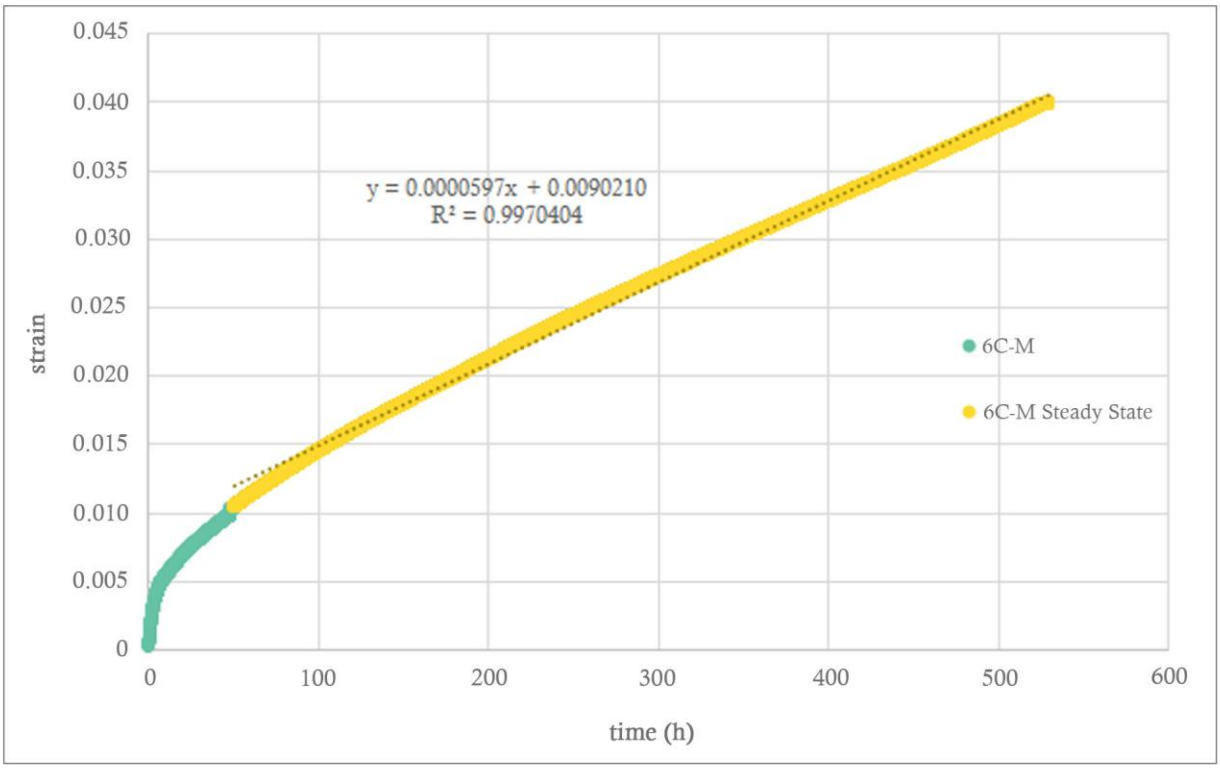

Figure 6.11 - Creep response of sample 6C-M, when tested at 1025 °C and 12 MPa uniaxial stress.

The sets of creep samples were often observed to be bowed, as a result of internal stresses released when machining the tubes. As shown in Figure 6.12 (for one of the most extreme cases observed), the inner and outer wall samples typically bowed outwards from the mid wall samples. As a result, although the primary creep response of the samples was recorded, it was likely a combination of bending and axial loading, resulting in a varying stress state along the gauge length until the sample straightened and the load became uniaxial. The calculation of the total creep strain of the samples over the test was thus considered inaccurate, as different samples displayed differing extents of bowing.

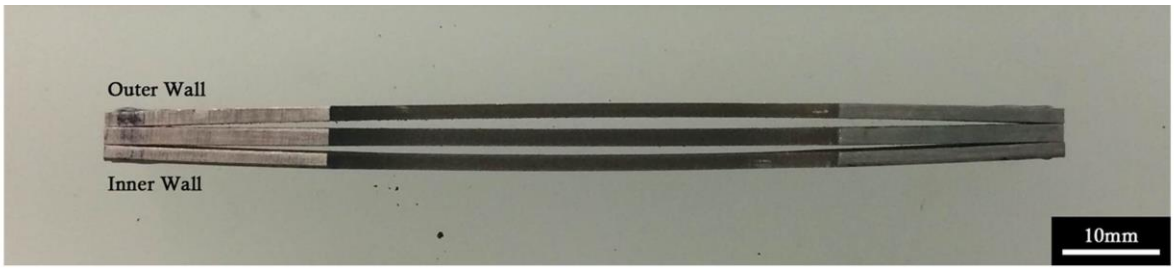

Figure 6.12 - Side view of creep samples from tube 2, bowed as a result of internal stresses released upon machining.

6.2.3 Inert Atmosphere

The creep testing rigs used for the measurement of steady state creep rates had been designed to test samples in an air atmosphere, however due to the small thickness of the creep samples tested as part of the current project (1.5 mm), the effects of oxidation and nitridation during creep testing were of concern. Due to the design of the creep testing apparatuses, it was not possible to achieve a completely inert atmosphere within the furnaces. However, it was possible to introduce a flow of inert gas, thus reducing the oxygen and nitrogen content of the furnace atmosphere.

In order to determine the effects of an air atmosphere with reduced oxygen and nitrogen content on the oxidation of ex-service alloys, short oxidation tests were run using samples from a tube with high carburization (tube 1) and a tube with low carburization (tube 3), in both air and air + argon atmospheres. Eight samples were cut from each tube, with each sample being approximately 5 mm x 7 mm x 14 mm in size. Prior to elevated temperature exposure the samples were ground and polished to a 9 μm surface finish, to be consistent with the creep samples. Four samples from each tube were aged in air, and four in an air + argon mixture, at 1025 °C, for up to 360 hours. One sample for each condition was removed from the furnace at set time intervals and air cooled. Upon completion of the ageing, the samples were sectioned, mounted, and polished, in accordance with the procedures described in Section 3.2. The samples were analysed using SEI imaging and EDS mapping. As presented in Table 4.1, ICP-AES analysis determined that tube 1 is a HP-Nb alloy, and tube 3 is a HP-Micro alloy. Both tubes contained the same amount of silicon (1.28 wt% in tube 1, 1.25 wt% in tube 3), and chromium (25.5 wt% in tube 1, 24.5 wt% in tube 3).

Two furnaces at the University of Canterbury were used for the oxidation tests – a Nabertherm box furnace for the air atmosphere test, and a Nabertherm tube furnace for the air + argon atmosphere test. The tube furnace was fitted with end caps through which an argon flow could be introduced into the tube. The flow rate of argon introduced to the tube furnace was calculated such that the partial pressures of oxygen and nitrogen were reduced to approximately ¼ of their values had no argon been present.

Macroscopic Observations

The external appearance of the aged samples after cooling in air is shown in Figure 6.13. The samples from tube 3 lost significant amounts of external scale upon cooling, and both the samples aged in air and the samples aged in the air + argon mixture were affected. Small sections of the scale were observed to spall off the surface of the samples during cooling. The resultant external appearance of the tube 3 samples was patchy, with the bulk material visible beneath an incomplete scale layer.

The external surface of the tube 1 samples appeared darkened in comparison to the polished condition prior to ageing, however no scale was apparent on the surface, nor was any scale observed to spall upon cooling.

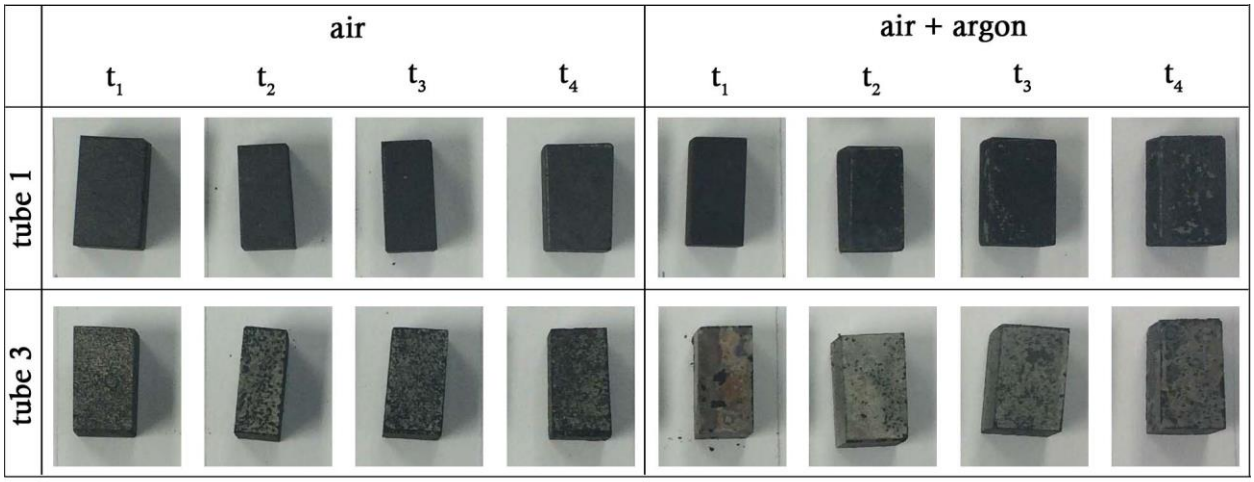

Figure 6.13 - Surfaces of samples from tubes 1 and 3 upon completion of oxidation tests.

Microscopic Observations

The microstructure at the exposed surfaces typically consisted of internal formation of silicon-rich oxides along dendrite boundaries, partially replacing the primary carbides. The depth of penetration of internal silicon oxides was generally observed to increase with exposure time. The composition of the internal silicon-rich oxides for all exposure times and atmospheres was consistent with SiO_2. At the external surface, an intermittent, fragmented scale was visible on all samples, however it was significantly more intermittent on the samples from tube 1 in comparison to those from tube 3. The composition of the external scale was consistent with Cr_2O_3, for all samples in which it was observed.

The growth of a chromium oxide scale requires the diffusion of chromium from the austenite matrix to the surface, where it then combines with oxygen. When the chromium content of the austenite matrix falls below a critical value, the continued growth of chromium oxide is no longer possible. For high carbon activity – low oxygen partial pressure environments the critical austenite chromium content value is reportedly to be approximately 10 wt% [4, 5]. As discussed in Chapter 5, the matrix chromium content in tube 1 ranges from 5 – 22 wt%, depending on volume fraction of chromium-rich phases, and the matrix chromium content in tube 2 ranges from 22 – 23 wt%. Although the furnace atmospheres used for the current oxidation tests are not entirely consistent with the high carbon – low oxygen environments reported in the literature, due to lack of a carbon-rich component, it nonetheless seems likely that the highly carburized samples of tube 1 did not contain enough chromium in the austenite matrix to form a consistent chromium oxide scale upon ageing in both the air and air + argon atmospheres. Additionally, it appears that the tube 3 samples contained enough chromium in the austenite matrix to form a chromium oxide scale during ageing in both the air and air + argon atmospheres, and this scale is what was observed to spall upon cooling of the samples.

Oxide scales can experience mechanical failure as a result of thermally induced stress. The stress is dependent on the magnitude of the temperature change (in this case a rapid change from 1025 °C to

room temperature), and the differences in the coefficients of thermal expansion (CTEs) of the oxide scale and the metal. The CTEs of Cr_2O_3 oxide and the tube alloys are summarised in Table 6.1. The CTEs of the tube alloys are much greater than that of the chromium oxide, and thus rapid cooling of the oxidized metal will have put the oxide scale in compression, leading to mechanical failure in the form of spallation. Slow cooling rates may have lessened the amount of spallation of the chromium oxide scale, however furnace constraints means that this was unable to be achieved for the current set of oxidation tests. The measurement of chromium oxide scale thickness was not considered accurate due to the significant spallation that occurred upon cooling for the tube 3 samples, and the extremely intermittent nature of scale formation in the tube 1 samples, and thus will not be presented here.

Table 6.1 - Coefficients of thermal expansion (α) for Cr_2O_3 and tube alloys at 1000°C.

Component	α (10^{-6}/K)	Reference
Cr_2O_3	7.3	[6]
HP-Nb (as-cast)	18.5	[7]
HP-Micro (as-cast)	18.5	[8]

Measurements of the depth of silicon oxide penetration were made in order to determine the kinetics of internal oxidation. The air + argon atmosphere did not appear to have a significant effect on the rate of internal silicon oxide formation in the tube 1 samples, likely due to the lack of consistent chromium oxide scale formation in both ageing atmospheres. Without a protective chromium oxide scale, oxygen will have had unimpeded access to the tube interior resulting in similar rates of internal oxidation in both the air and air + argon atmospheres. In contrast, the air + argon atmosphere appeared to have slowed the rate of silicon oxide formation in the samples from tube 3, but not completely prevented it. In the samples from tube 3, despite the observed formation of a protective chromium oxide scale in both atmospheres, the internal oxidation of silicon was typically observed to be more advanced in the sample aged solely in air in comparison to the sample aged in an air + argon atmosphere, indicating the addition of argon to the atmosphere acted to suppress the rate of internal silicon oxidation. Examples of the subsurface microstructures of samples from tubes 1 and 2 for the two atmospheres are shown in Figure 6.14.

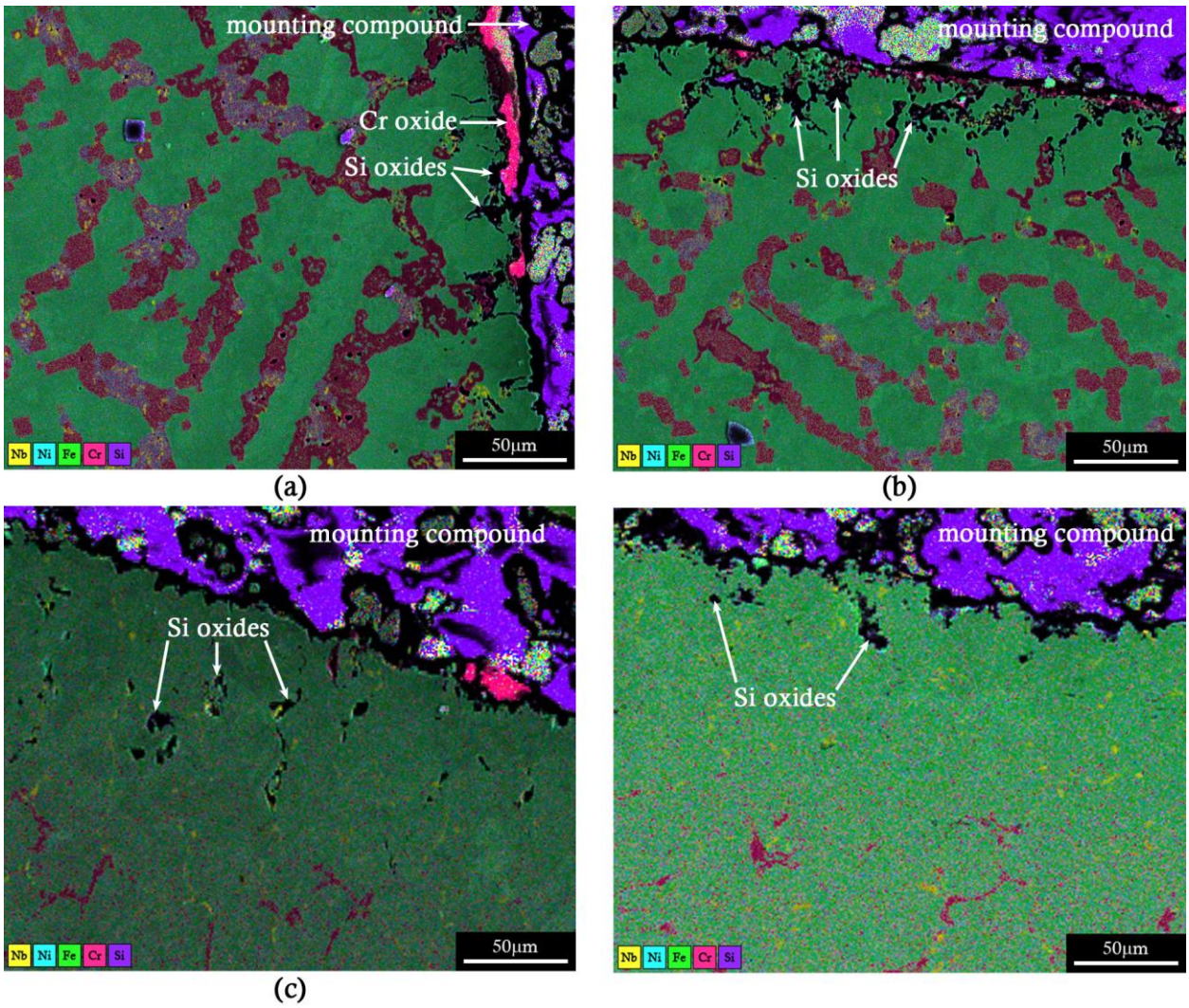

Figure 6.14 - EDS maps of the subsurface microstructures of (a) Tube 1 – Air – t_2, (b) Tube 1 - Air+ Argon – t_3, (c) Tube 3 – Air – t_4, and (d) Tube 3 – Air + Argon – t_4 samples.

If the rate of internal oxidation of silicon is predominantly influenced by the inward diffusion of oxygen, then the depth at which silicon oxides are present, with respect to time and temperature, would be expected to follow a parabolic rate law. Thus, the depth of penetration of silicon oxides as a function of exposure time can be calculated by applying Wagner's equation for parabolic kinetics [6]:

$$d^2 = k_S t \qquad \textbf{Equation 6.3}$$

where d is the penetration depth of internal silicon oxides (at constant temperature), t is exposure time, and k_S denotes the parabolic internal silicon oxidation rate constant.

Equation 6.3 can also be expressed as shown in Equation 6.4:

$$d = k_s^{1/n} t^{1/n}$$ **Equation 6.4**

where, in the case of parabolic kinetics, the value of n would equal 2. Further rearrangement enables the rate equation to be expressed as Equation 6.5:

$$\log d = \frac{1}{n}\log t + \frac{1}{n}\log k_s$$ **Equation 6.5**

Therefore, in plotting log(d) against log(t), the value of n is the reciprocal of the slope of a linear fit to the data, and if the value of n is equal to 2 then the internal oxidation of silicon can be said to obey parabolic kinetics. Figure 6.15 shows such a plot for the samples subject to air and air + argon atmospheres, using the average depths of internal oxidation of silicon. The corresponding values of n are summarised in Table 6.2.

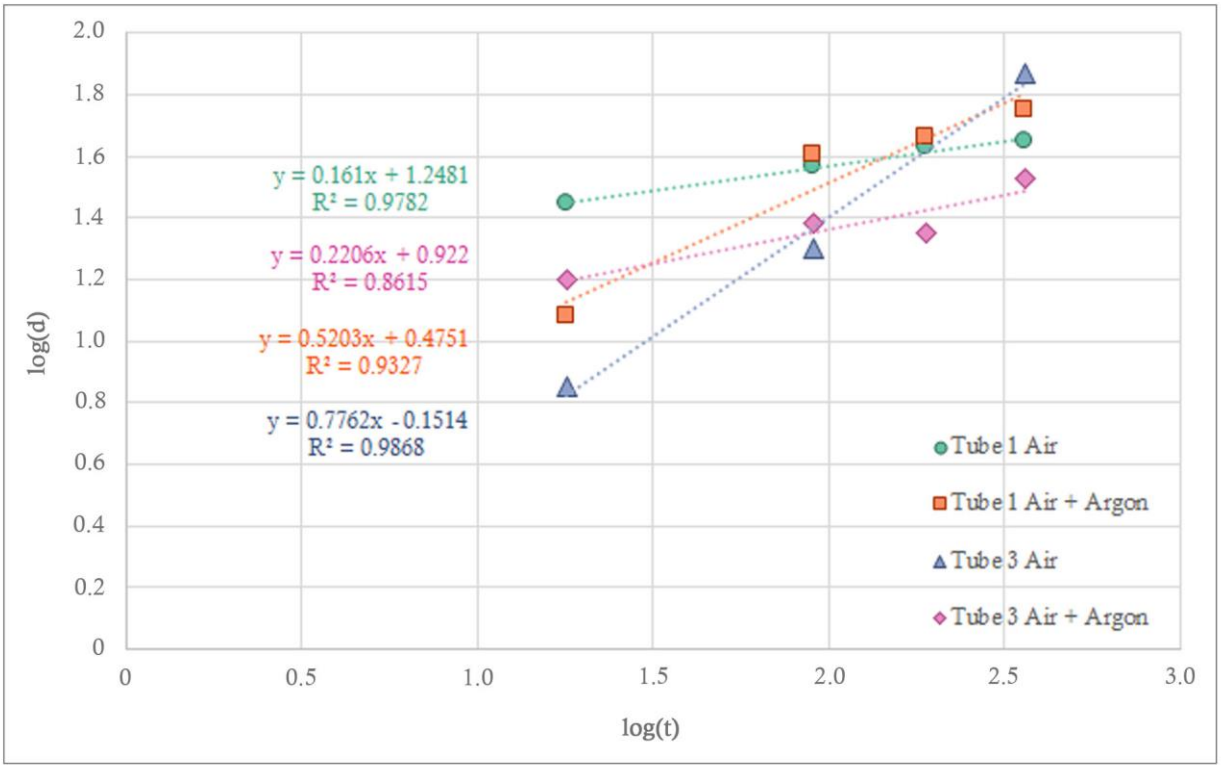

Figure 6.15 - Penetration depth of internal silicon oxides (d, measured in μm) with respect to time (t, measured in hours) in samples from tube 1 and tube 3 at 1025 °C for various atmospheres.

Table 6.2 – Values of *n* in Equation 6.5, for samples from tubes 1 and 3 aged in air and air + argon atmospheres.

Sample	*n*
Tube 1 – Air	6.21
Tube 1 – Air + Argon	1.92
Tube 3 – Air	1.29
Tube 3 – Air + Argon	4.53

The coefficients of determination for the linear fits to the data suggest that the linear fits are sound. In comparing the calculated values of *n*, it can be seen that only the sample from tube 1 that was subject to an air + argon atmosphere can be said to follow parabolic kinetics for the internal oxidation of silicon. The deviation from parabolic kinetics of internal oxidation for the tube 1 sample aged in air, and both the samples form tube 3, may be due to the complex microstructure in the subsurface of the samples. As demonstrated in Chapter 5, there are a large variety of phases present in varying quantities in the microstructure of the carburized tubes, and in addition a number of phase transformations can take place as a result of exposure to elevated temperatures and carburization. This leads to variations in the distribution of the elements across the wall thickness of the tubes, and the non-uniformity in the subsurface may account for the deviation from parabolic kinetics. Unfortunately, due to the microstructures of the samples not being characterized prior to ageing it was not possible to determine the dominant microstructural factors that may have influenced the oxidation rates in the current analysis.

On occasion, nitrides were observed in the subsurface microstructure as part of the primary carbide network. It is unknown whether these carbonitrides were a result of exposure to the furnace atmospheres, as the samples were not characterized prior to exposure. However, as discussed in Section 5.4.3, carbonitrides reportedly have the same effect on mechanical properties as carbides, and the transformation of chromium-rich carbides to chromium-rich carbonitrides does not further deplete the matrix of chromium. As shown in Figure 6.3, the hardness of areas that contained $Cr_2(C,N)$ and $M_{23}C_6$ is consistent with areas that contained a similar volume fraction of solely $M_{23}C_6$. Thus, even if the carbonitrides had formed as a result of exposure to the furnace atmospheres it is unlikely that they have any significant influence on the mechanical or magnetic properties of the samples.

Ideally, the atmosphere within the furnace of the creep testing apparatus would be entirely inert. In practice, however, this is easier said than done. An entirely inert atmosphere would require the furnace, or an enclosure around the furnace, to be completely sealed. However, as shown in Figure

6.9 and Figure 6.10, the current design of the LVDT extensometer measurement system has extension rods attached to the sample grips, which the LVDTs are then attached to outside the furnace, as their maximum operating temperature is well below 100 °C. Enabling free movement of the LVDT and load bearing rods whilst retaining a complete seal would be near impossible to achieve with the current design. A second generation of creep rig apparatus has recently been built at the University of Canterbury, removing the need to test samples in series and instead allowing four samples to be simultaneously tested with individual applied loads. The second generation design, however, uses the same method for extension measurement as the steady state apparatus, where the extension rods extend out of the furnace. Improving on the design and building a third generation of apparatus which incorporates an inert atmosphere was outside of the scope of the current project. As such, despite the minimal differences in the internal oxidation in the samples from tube 1 from a reduced oxygen atmosphere, it was nevertheless decided that an equivalent argon flow would be introduced to the steady state creep rigs in an effort to minimize the effects of oxidation and nitridation on the creep samples.

6.2.4 Steady State Creep Rate

A summary of the steady state creep rates for each of the samples tested is shown in Table 6.3, along with the corresponding average hardness. The sample name indicates the location of the midsection of the gauge length, consistent with the labelling of the metallographic samples, and is appended with either I (inner wall sample), M (mid wall sample), or O (outer wall sample). The average hardness for each sample was determined by calculating the mean of the measured hardness values over the wall regions of the adjacent metallographic sample with which the creep sample thickness corresponded. The standard error in the steady state creep rate was calculated using the "linest" function in Excel. The value of the standard error was less than 1% of the calculated steady state creep rate for all samples. Due to the small calculated error values and due to the data spanning decades of magnitude, the standard error in the steady state creep rate is not reported.

Unfortunately, due to a number of unforeseen equipment failures creating time restraints on the testing schedule, the full complement of six samples from each of the six tubes was unable to be tested. As such, the samples tested were selected so as to give a range of microstructures and levels of carburization. In analysis of the creep sample microstructures, more than one phase transformation typically occurred, and the relative importance of the phase transformations in determining differences in creep behaviour was in some cases uncertain.

Table 6.3 - Summary of steady state creep rates for the creep samples from ex-service tubes, and the corresponding hardness measured on the metallographic samples adjacent to the creep sample gauge length.

Sample	Steady state creep rate (h^{-1})	Average corresponding hardness (HV)	Standard deviation in hardness (HV)
1C-I	1.99×10^{-4}	283	18
1D-I	1.45×10^{-4}	337	27
1D-M	1.43×10^{-4}	294	25
1D-O	9.65×10^{-5}	271	16
2C-I	3.52×10^{-4}	292	25
2C-M	1.50×10^{-4}	244	16
3D-I	2.45×10^{-5}	255	12
3D-M	2.09×10^{-5}	262	7
3D-O	1.73×10^{-5}	271	10
4C-I	9.29×10^{-6}	221	6
4C-M	4.59×10^{-6}	220	6
4C-O	1.07×10^{-6}	220	6
5C-I	5.29×10^{-5}	233	26
5C-M	2.75×10^{-5}	204	8
5D-I	4.94×10^{-5}	262	16
5D-M	4.86×10^{-5}	227	10
5D-O	5.36×10^{-5}	207	8
6C-I	6.00×10^{-5}	217	10
6C-M	5.97×10^{-5}	217	12
6D-I	3.08×10^{-5}	216	10
6D-M	2.69×10^{-5}	220	12
6D-O	2.49×10^{-5}	214	7

Tubes 1 & 2

The sample that displayed the highest steady state creep rate was sample 2C-I, followed by 1C-I. Both samples displayed similar microstructures, as shown in Figure 6.16, and the volume fractions of primary M_7C_3 precipitates was similar in each (25 – 35 % in 2C-I, and 27 – 32 % in 1C-I). No distribution of secondary precipitates was observed in either tube at the locations at which these creep samples were taken. Samples 2C-I and 1C-I displayed similar hardness values, 292 and 283 HV respectively, consistent with their high level of carbide coarsening.

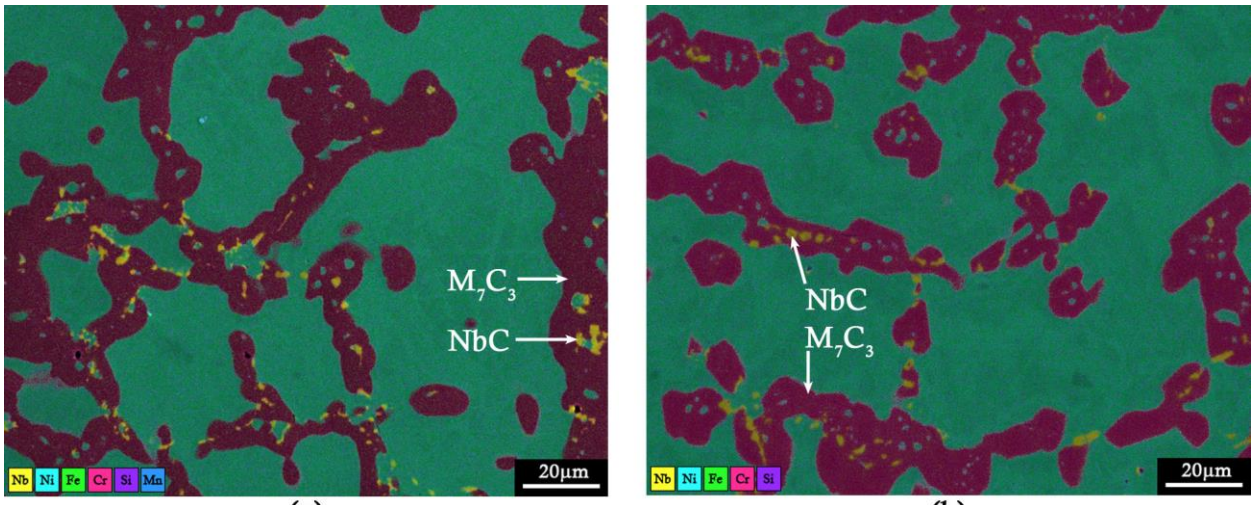

Figure 6.16 - Microstructures of creep samples (a) 1C-I and (b) 2C-I.

Samples 1D-I and 1D-M displayed similar steady state creep rates (1.45 $x10^{-4}$ /h and 1.43 x 10^{-4}/h respectively). The volume fraction of M_7C_3 in the two samples was slightly higher in 1D-I than in 1D-M (34 – 37% and 26 – 32 % respectively), which was consistent with 1D-I displaying a higher value of hardness in comparison to 1D-M (337 HV versus 294 HV). Both samples contained approximately 1 % NbC. Sample 1D-O was taken from the outer wall adjacent to sample 1D, and it was composed of 21 – 26 % $M_{23}C_6$, as well as up to 10 % η-carbide and 1 % NbC. In comparison to samples 1D-I and 1D-M, sample 1D-O displayed a lower hardness value (271 HV), consistent with the decrease in the volume fraction of chromium carbides. Sample 1D-O also displayed a lower steady state creep rate (9.65 x 10^{-5} /h).

A comparison between the microstructures of the 1D creep samples is shown in Figure 6.17. No major differences are visible in comparing the microstructures of 1D-I and 1D-M. The major differences between the microstructure of sample 1D-O in comparison to those of 1D-I and 1D-M are the presence (and lower volume fraction) of $M_{23}C_6$ as opposed to M_7C_3, and the presence of η-carbide in the primary network. The total volume fraction of precipitates is relatively similar for all three samples. The lower steady state creep rate in sample 1D-O in comparison to samples 1D-I and 1D-M, despite the total

precipitate fraction in the three samples being similar, could therefore indicate that η-carbide contributes to the creep resistance of the material.

Accelerated creep tests by de Almeida Soares *et al.* [9] on HP-Nb samples containing G-phase showed increased creep properties (i.e. lower minimum creep rate and increased time to rupture) in comparison to those aged above the upper limit of G-phase transformation, indicating that the presence of G-phase may have some beneficial effect on the creep performance. However, other studies [10, 11] that performed laboratory ageing of HP-NbTi alloys followed by creep testing on samples that contained G-phase have suggested that there is a volume change associated with the transformation of Nb-rich precipitates to G-phase that increases the precipitate's interfacial energy. The increase in energy was believed to result in preferential creep damage (e.g. creep voids) at the G-phase/austenite interface. Unfortunately, no such studies are reported for samples containing η-carbide.

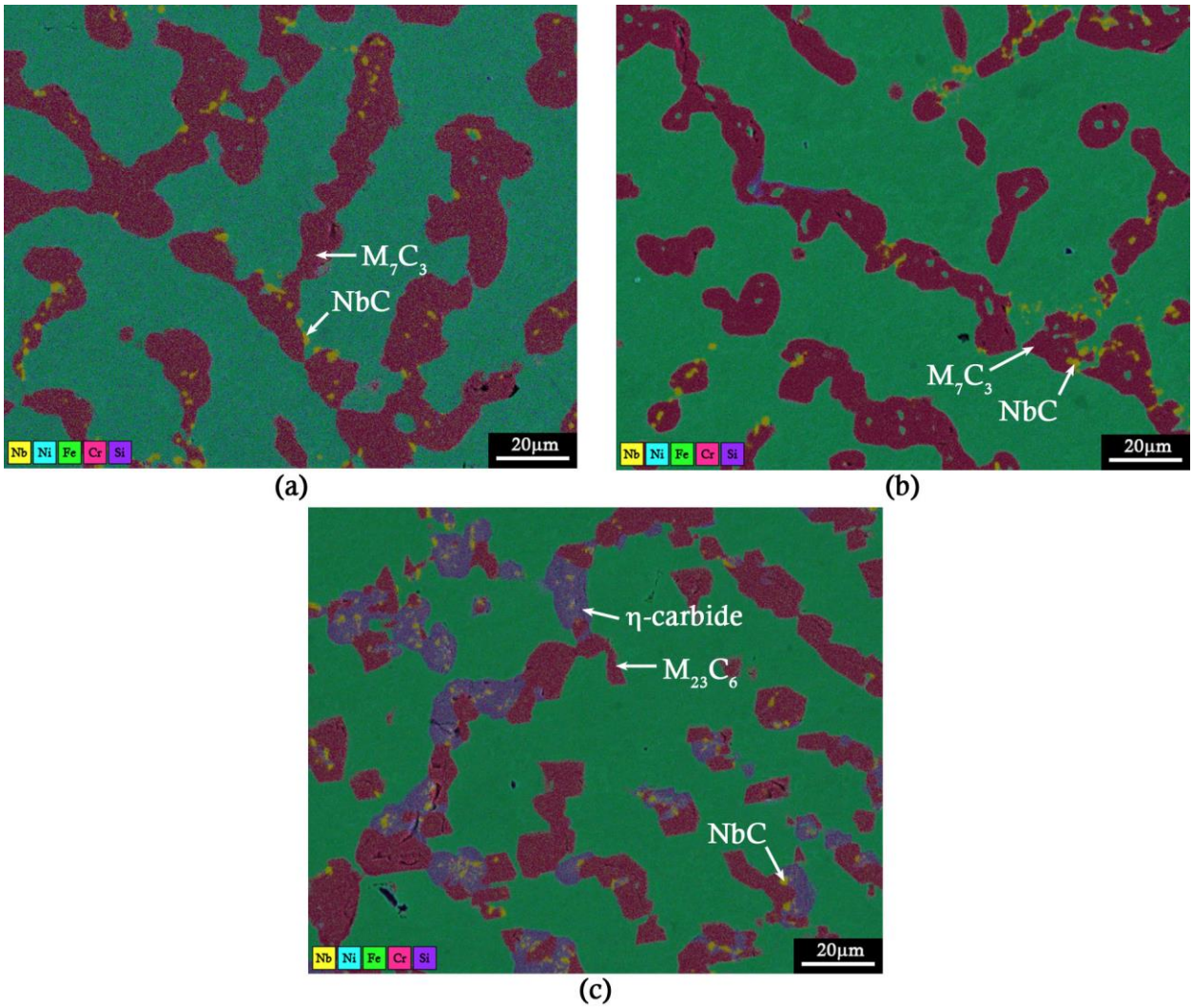

Figure 6.17 - Expected microstructures of creep samples (a) 1D-I, (b) 1D-M, and (c) 1D-O.

Sample 2C-M displayed a steady state creep rate of 1.50 x 10^{-4} /h, similar to the creep rates displayed by samples 1D-I and 1D-M. As shown in Figure 6.18, the microstructure of sample 2C-M was composed of 18 – 24 % $M_{23}C_6$, in addition to up to 1.5 % η-carbide, 1.5 % $Cr_2(C,N)$, and 1 % NbC. The average hardness of 2C-M was approximately 244 HV.

In comparing the microstructure of sample 2C-M, shown in Figure 6.18, with the microstructure of sample 1D-O, shown in Figure 6.17 (c), the morphologies of the primary $M_{23}C_6$ precipitates appear similar. The $Cr_2(C,N)$ precipitates present in sample 2C-M were observed to have transformed directly from the $M_{23}C_6$ precipitates in the primary network. In combining the volume fractions of the primary $M_{23}C_6$ and $Cr_2(C,N)$ precipitates in sample 2C-M, the total primary chromium-rich precipitate fraction (19.5 – 25.5 %) is consistent with the volume fraction of $M_{23}C_6$ in 1D-O (21 – 26 %). The main difference in microstructure between the two samples is therefore the η-carbide content, which is up to 1.5 % in 2C-M, and up to 10 % in 1D-O. 1D-O displayed a lower steady state creep rate than 2C-M (9.65 x 10^{-5} /h in comparison to 1.50 x 10^{-4} /h), again suggesting that the presence of η-carbide is not necessarily detrimental to the creep resistance of the alloy

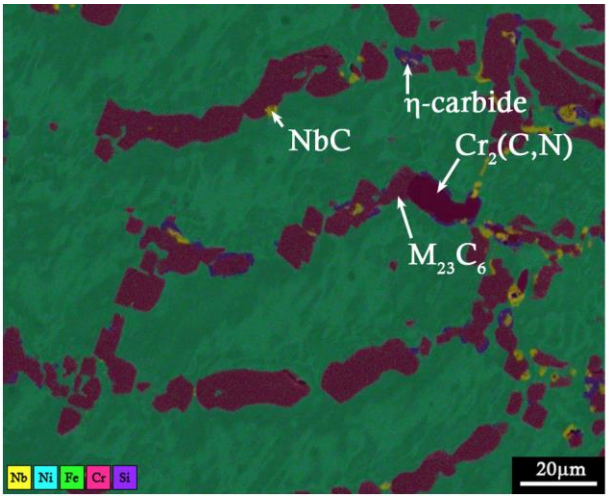

Figure 6.18 - Expected microstructure of creep sample 2C-M.

Tubes 3 & 4

The steady state creep rate of samples from tube 3 was overall higher in comparison to samples from tube 4. The average hardness of the samples from tube 3 was also higher than the average hardness of samples from tube 4 (255 - 271 HV, in comparison to ≈ 220 HV). A comparison between the microstructures of the tube 3 and tube 4 creep samples is shown in Figure 6.19.

The microstructure of tube 3 was relatively consistent across all locations, and the microstructure of each of the creep samples consisted of up to 3 % $M_{23}C_6$, up to 2 % G-phase, and up to 2 % σ-phase, all within the primary network. The volume fraction of (Nb,Ti)C carbides was <0.5 % at all locations.

A distribution of secondary σ-phase platelets, approximately 10 μm long and < 1 μm in width was present in the matrix. The volume fraction of (Nb,Ti)C precipitates was <0.5 %.

The microstructure of tube 4 was also observed to be relatively consistent across the four metallographic samples analysed. Tube 4 did not contain σ-phase, in either the primary or secondary precipitate networks. The microstructure of the tube 4 creep samples was composed of 3 – 6 % $M_{23}C_6$, and 2 – 4 % G-phase. The transformation of (Nb,Ti)C carbides to G-phase was observed to be almost entirely complete, and the volume fraction of (Nb,Ti)C carbides was <0.5 % at all locations. A fine distribution of secondary $M_{23}C_6$ precipitates, typically <1 μm in size, was observed adjacent to the primary precipitate network in all samples.

As discussed in Section 5.4.2, the presence of σ-phase in the microstructure of austenitic stainless steels is reported to result in reduced toughness and ductility at temperatures below 120 – 150 °C, but have little effect on mechanical properties in the temperature range within which it forms [12, 13]. Sourmail [14] states that, in creep resistant steels, σ-phase has a detrimental effect on the creep properties when it has precipitated on grain boundaries, but little effect on the creep properties when it has precipitated intragranularly. As such, the σ-phase precipitates in the primary network of tube 3 may reduce the creep resistance, and although the dispersion of σ-phase platelets in the matrix of tube 3 may have resulted a greater hardness being measured at room temperature in comparison to tube 4, it might not contribute to the creep resistance of the material in tube 3. In comparison, the development of a fine secondary distribution of $M_{23}C_6$ precipitates is considered to be beneficial to the creep properties of HP alloys as these precipitates reportedly restrict dislocation motion through the austenite matrix [11]. Secondary precipitates located in the vicinity of grain boundary precipitates are believed to inhibit the deformation that is typically concentrated in this area during creep [15], and creep tests of HP-Nb alloy samples that had been aged at 700 – 1100 °C for 1000 hours prior to testing have been shown to have increased creep properties compared to the as-cast condition [16]. The presence of a fine distribution of secondary $M_{23}C_6$ carbides in tube 4 may therefore contribute more to the creep resistance of tube 4 than the secondary σ-phase distribution does to the creep resistance of tube 3, leading to a reduction in the steady state creep rate in tube 4 in comparison to tube 3.

The difference in the secondary precipitate distributions was not the only difference in microstructure between tube 3 and tube 4 – tube 4 also displayed a higher volume fraction of primary $M_{23}C_6$ carbides, as well as a higher volume fraction of G-phase, in comparison to tube 3. As aforementioned, the effect of G-phase on the creep properties is not well understood, but its presence in tube 4 combined with a reduction in creep rate suggests that it is not necessarily detrimental to the creep strength. However, due to the influence of the secondary $M_{23}C_6$ precipitate distribution, the decrease in creep rate can not be attributed solely to the increase in the volume fraction of G-phase.

The steady state creep rates of the samples from tube 3 were observed to be an order of magnitude lower than the samples from tubes 1 and 2, and the creep rate of the tube 4 samples was two orders of magnitude lower, which is consistent with their significantly lower volume fractions of primary $M_{23}C_6$ precipitates, and generally lower hardness values. Qualitatively, in comparing the microstructures of tubes 3 and 4 with those of tubes 1 and 2, the primary networks appear more fragmented and less continuous due to the minimal carbide coarsening.

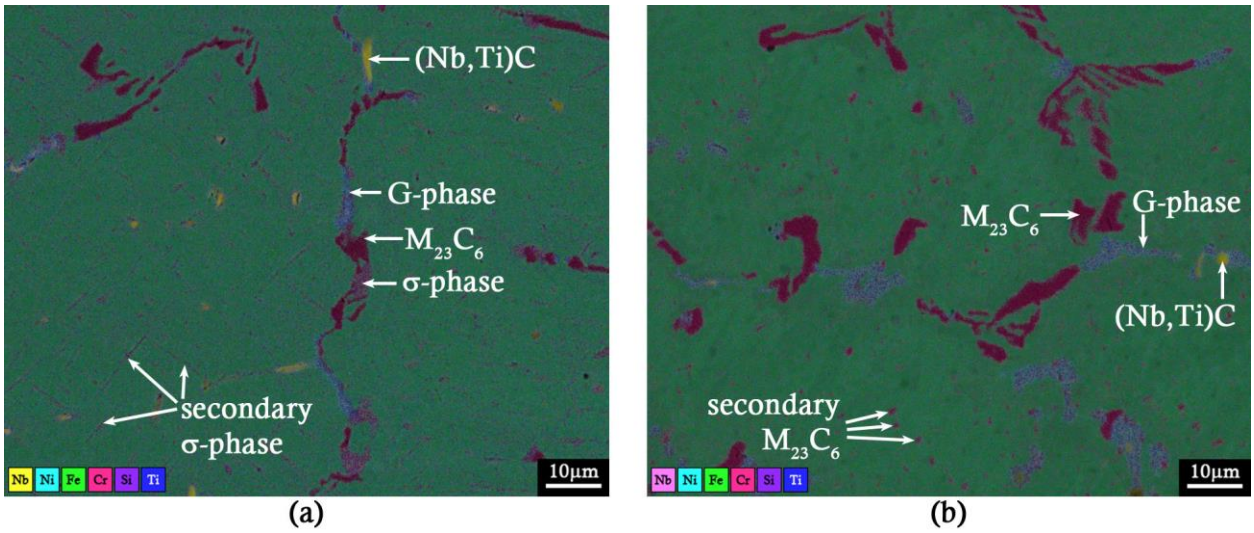

Figure 6.19 - Microstructures of creep samples from (a) tube 3 and (b) tube 4.

Tubes 5 & 6

The steady state creep rates of the samples from tube 5 and 6 were clustered within a range of 2.49 – 6.00 $x10^{-5}$ /h.

The samples 5C-I, 5D-I, 5D-M, and 5D-O displayed similar steady state creep rates, at 5.29 x 10^{-5}, 4.94 $x10^{-5}$, 4.86 $x10^{-5}$, and 5.36 $x10^{-5}$ respectively. A comparison between the microstructures of the tube 5 samples is shown in Figure 6.20. Samples 5C-I and 5D-I were taken from the most highly carburized regions of the wall in their respective locations. Sample 5C-I straddled the M_7C_3-to-$M_{23}C_6$ transformation, and thus the primary network was composed of M_7C_3 (≈ 26 %) for approximately $1/6^{th}$ of the sample thickness, and the remaining sample thickness was composed of $M_{23}C_6$ in the range of 8 – 20 %. 5C-I was also contained a small amount of G-phase, up to 1.2 %. The primary network of sample 5D-I was composed of M_7C_3 in the range of 24 – 28%. 5D-M was taken from the mid wall at location D, and the primary precipitate network was composed of $M_{23}C_6$, in the range of 15 – 17 %. The volume fraction of (Nb,Ti)C precipitates in samples 5C-I, 5D-I, and 5D-M was < 1.5 %. Sample 5D-O was taken from the outer wall of location D, which, as discussed in Section 5.2.5, was observed to contain η-carbide. The microstructure of sample 5D-O was composed of 8 – 12 % $M_{23}C_6$, with up to 3.5 % η-carbide. The volume fraction of (Nb,Ti)C in sample 5D-O was < 1%.

Sample 5C-M displayed the lowest steady state creep rate, at 2.75 x10^{-5} /h. This sample displayed the lowest volume fraction of primary chromium carbides ($M_{23}C_6$ ≈ 5 – 8 %) of the samples from tube 5. Sample 5C-M also contained G-phase, in the range of 1.2 – 4 %. The volume fraction of (Nb,Ti)C precipitates was < 0.5 % as a result of the (Nb,Ti)C-to-G-phase transformation. The microstructure of sample 5C-M is shown in Figure 6.20 (b), and qualitatively it appears significantly less coarsened than the other four samples, consistent with the quantitative measurements.

The presence of G-phase in samples 5C-I and 5C-M does not appear to have had significant adverse effects on the creep properties. The volume fraction of primary chromium carbides in sample 5C-I was relatively consistent with the primary chromium carbide volume fraction in the two other creep samples from tube 5 that displayed similar steady state creep rates (5D-I and 5D-M), indicating that the small amount of G-phase present in 5C-I (up to 1.2 %) was not necessarily detrimental to the creep properties. The volume fraction of primary chromium carbides in 5C-M was observed to be lower than in 5C-I (5 - 8 % in comparison to 8 – 20 %), however 5C-M contained a higher volume fraction of G-phase (up to 4 %, in comparison to up to 1.2 %). The reduction in creep rate in sample 5C-M when compared to the 5C-I, 5D-I, and 5D-M creep samples, despite the increase in G-phase volume fraction, may also indicate that G-phase is not necessarily detrimental to the creep resistance. However, due to the increase in G-phase volume fraction coinciding with a decrease in the volume fraction of $M_{23}C_6$, the reduction in creep rate cannot be conclusively attributed to G-phase.

The steady state creep rate of 5C-M was consistent with the steady state creep rates of the 6D-I, 6D-M, and 6D-O samples, which were in the range of 2.49 x10^{-5} – 2.75 x10^{-5} /h. The volume fractions of primary precipitates in the 6D samples were slightly higher than the 5C-M sample, containing $M_{23}C_6$ in the range of 6 – 10 % and G-phase in the range of 1.9 – 2.7 %. The average hardness of the 6D samples was 214 – 220 HV, slightly higher than the 5C-M sample (204 HV), consistent with the increased volume fraction of primary precipitates. However, such small microstructural differences do not appear to have made any significant impact on the steady state creep rate.

The steady state creep rate of the 6C samples, 6C-I and 6C-M, was slightly higher than the steady state creep rates of the 6D samples (5.97 – 6.00 x10^{-5} /h), and were more comparable to the 5D-O sample (5.36 x 10^{-5} /h). As summarised in Table 3.1, the 6C samples came from the 0° location around the tube circumference, and the 6D samples from the 90° location. A comparison between the microstructures of the creep samples from tube 6 is shown in Figure 6.21. Qualitatively, the microstructures do not appear to have any significant differences. The morphology of the primary $M_{23}C_6$ carbides is consistent across the samples, with a portion of the $M_{23}C_6$ precipitates appearing to have retained some lamellar morphology, and a portion appearing more rounded and coarsened. As discussed in Section 5.2.6, there were no major quantitative differences measured either. The slight variance in creep rate depending on the angular location suggests that there may have been differences in the microstructure between the two locations that were unable to be characterized or quantified

within the bounds of the current image analysis methodology, or that the difference in microstructure that caused the difference in creep rate was within the bounds of the errors in segmentation. However a range of 2.49×10^{-5} - 6.00×10^{-5} /h is not a significant change when compared to the steady state creep rates of the samples from tubes 1 and 2, which are an order of magnitude higher. That the steady state creep rates of the tube 6 samples are on par with those from tube 5, despite the typical volume fraction of primary $M_{23}C_6$ in the tube 6 samples being lower than the primary chromium carbide volume fraction in the majority of the tube 5 samples is consistent with reports that the creep performance of the ET45-Micro alloy is slightly inferior to that of the HP-Micro alloy [17].

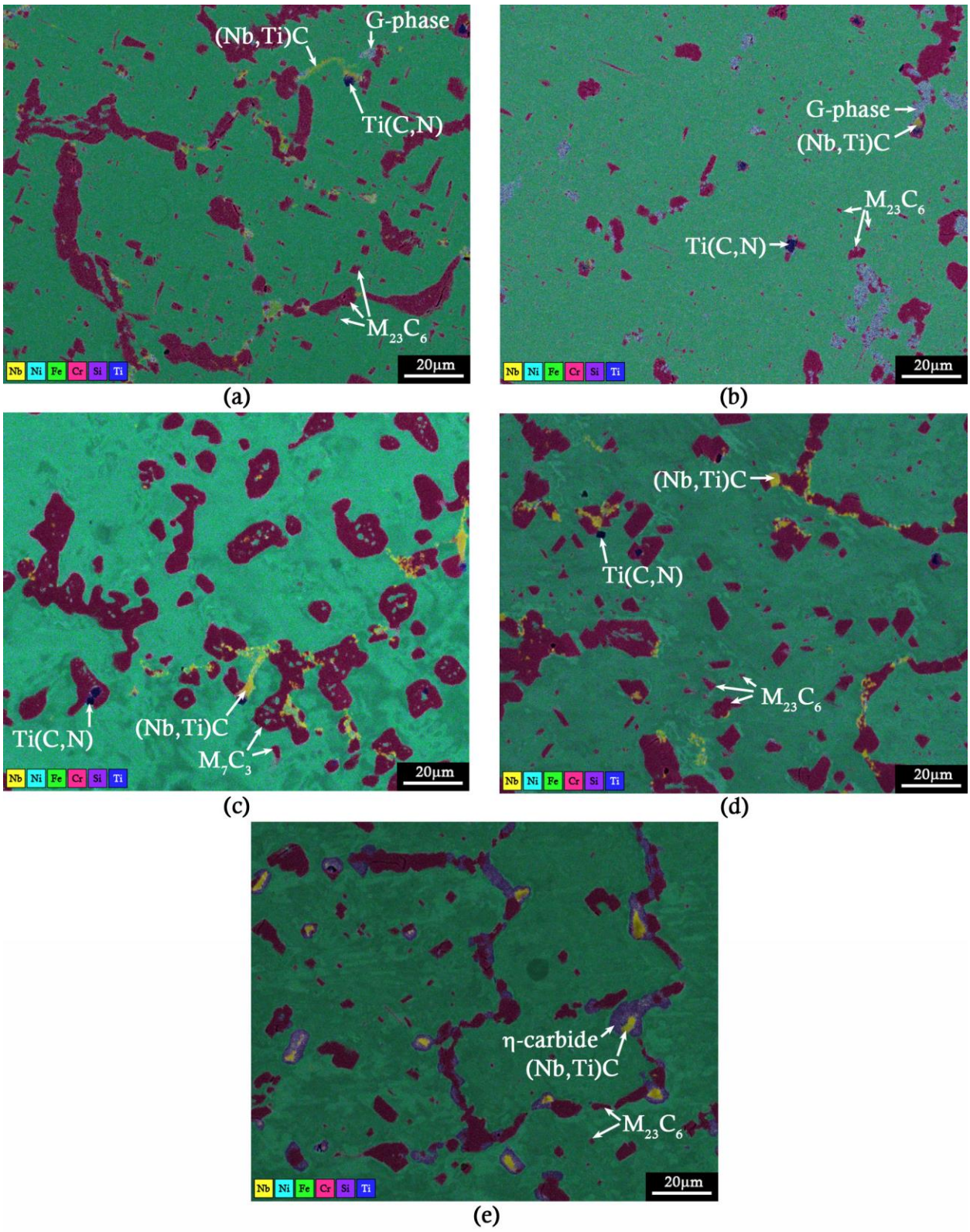

Figure 6.20 - Microstructures of creep samples (a) 5C-I, (b) 5C-M, (c) 5D-I, (d) 5D-M, and (e) 5D-O.

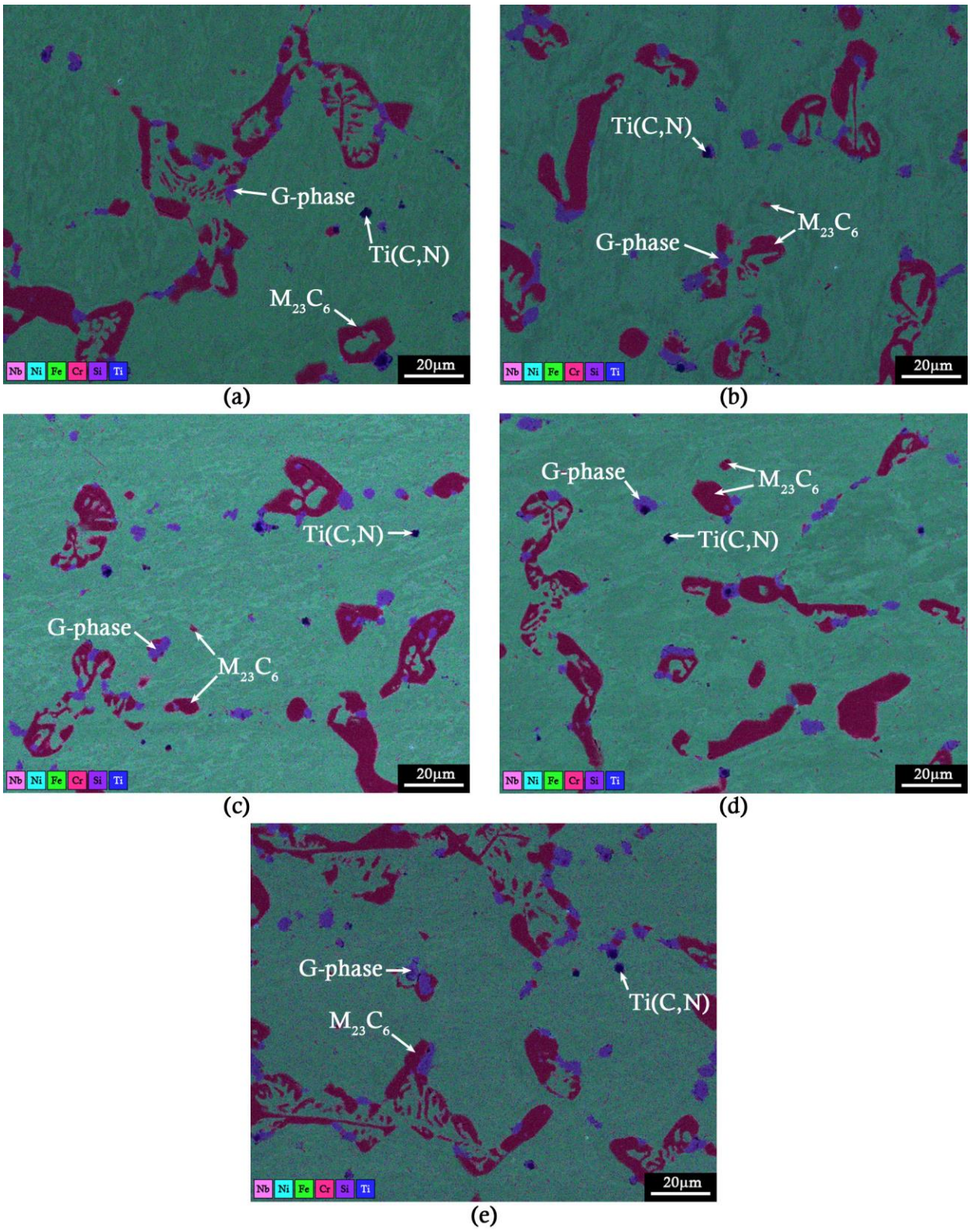

Figure 6.21 - Microstructures of creep samples (a) 6C-I, (b) 6C-M, (c) 6D-I, (d) 6C-M, and (e) 6C-O.

6.2.5 Effect of Primary Precipitate Volume Fraction on Steady State Creep Rate

As discussed in Section 6.1, the hardness of the ex-service samples was typically observed to increase with increased volume fractions of primary precipitates. Figure 6.22 shows a comparison of the average hardness of the creep samples and their measured steady state creep rates. A general trend of increased steady state creep rate with increased hardness is evident. It should be noted that the variation in the steady state creep rates of the tube 4 samples is exaggerated in this figure as a result of the logarithmic scale of the steady state creep rate axis. The hardness of the tube 3 samples is higher than would be expected based on the steady state creep rate; however, as discussed in Section 6.1, this is likely due to the distribution of fine σ-phase precipitates in the matrix of tube 3 resulting in a dispersion strengthening effect and thus elevated hardness at room temperature, whilst reportedly having little to no effect on the creep performance at elevated temperatures.

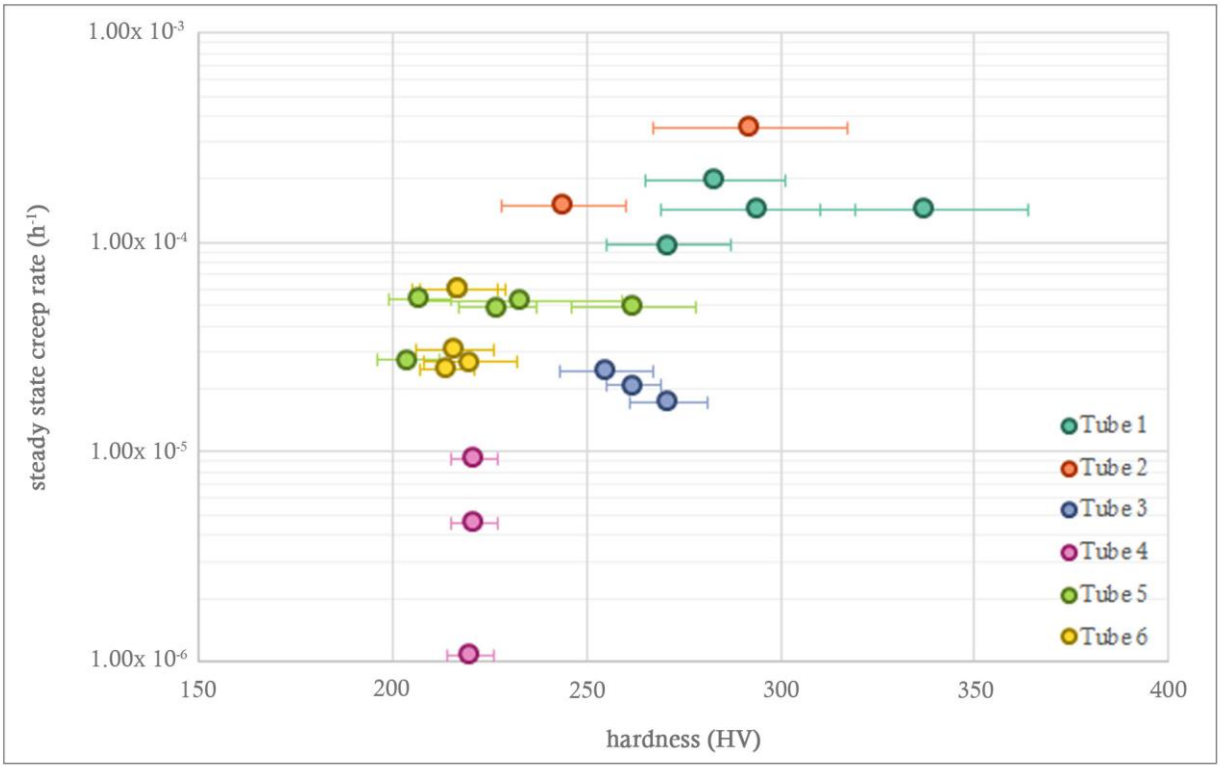

Figure 6.22 - A comparison between hardness and steady state creep rate for samples from the six ex-service tubes.

The general trend of increased steady state creep rate with increased hardness led to the consideration that the total volume fraction of primary precipitates may influence the steady state creep rate. In crystalline materials, the physical mechanisms of creep can be separated into two broad classes – diffusional flow and dislocation creep. The steady state creep rate, $\dot{\varepsilon}_{ss}$, in crystalline materials can be expressed by the general equation [18]:

$$\dot{\varepsilon}_{ss} = \frac{A_2 \sigma^m}{d^n T} e^{\frac{-Q}{RT}}$$ **Equation 6.6**

The variables that affect the steady state creep rate are the applied stress, σ, the average grain diameter, d, and the temperature, T. The coefficient A_2, the exponents m and n, and the activation energy Q are dependent on the material and the particular creep mechanism that is acting.

When dislocation processes dominate, typically at high stresses, $n = 0$ and $m \geq 3$. When diffusional processes dominate, at low stresses and high temperatures, the strain rate is approximately proportional to the applied stress and thus $m = 1$. If vacancies diffuse through the crystal lattice, the behaviour is termed Nabarro-Herring creep, and the strain rate is inversely proportional to the square of the average grain diameter ($n = 2$). If the vacancies move along grain boundaries, the behaviour is termed Coble creep. The dependence of grain size in Coble creep is inversely proportional to the cube of the average grain diameter ($n = 3$). For a given material, a deformation mechanism map can be drawn to show which deformation mechanism is dominant for a given combination of stress and temperature. Unfortunately, no such maps exist for the HK, HP, and ET45 alloys. However, given the combination of high temperature and low stress used for the current creep tests (1025 °C and 12 MPa uniaxial stress), it is likely that diffusional creep, either Nabarro-Herring or Coble creep, dominates.

The characterization of the macrostructure of the six centrifugally-cast ex-service tubes was discussed in Section 4.3. It was determined that the HP-Nb and HP-Micro tubes (tubes 1-5) were entirely composed of coarse columnar grains, and the ET45-Micro tube (tube 6) contained approximately 40% coarse equiaxed grains at the inner wall, and 60% coarse columnar grains at the outer wall. On a smaller length scale, the casting process results in a dendritic structure, with primary precipitates along the austenite dendrite and grain boundaries. As such, for the current application it might be considered that the dendrite arm spacing is analogous to the grain size, and the primary precipitates present along the dendrite boundaries analogous to precipitates along grain boundaries. In order to determine the effect of the volume fraction of primary precipitates on the steady state creep rate, then the change in area of the austenite matrix in between the dendrite arms for a given fraction of primary precipitates needs to be determined.

If the dendritic structure is approximated as a grain structure with a grain area of A_0, an equivalent circle diameter (grain diameter), of d_0, and a grain circumference C_0, then if there is continuous grain boundary precipitation with width $2s$, then the area of the grain boundary precipitate phase that is causing a reduction in the grain diameter can be approximated as:

$$A \approx C_0 s$$ **Equation 6.7**

The new area, A_1, of the matrix grain can thus be defined as:

$$A_1 = A_0 - A$$ **Equation 6.8**

If the area fraction of the grain boundary precipitate is A_f, then Equation 6.8 can be expressed as:

$$A_1 = A_0(1 - A_f)$$ **Equation 6.9**

The new grain size (equivalent circle diameter) d can thus be calculated:

$$\frac{\pi}{4}d^2 = A_0(1 - A_f)$$ **Equation 6.10**

$$d^2 = d_0^2(1 - A_f)$$ **Equation 6.11**

$$d = d_0\sqrt{(1 - A_f)}$$ **Equation 6.12**

If all variables in Equation 6.6 aside from *d* remain constant, then for diffusional creep the steady state creep rate can be expressed as being inversely proportional to the grain diameter *d* raised to the exponent *n*:

$$\dot{\varepsilon}_{ss} \propto \frac{1}{d^n}$$ **Equation 6.13**

$$\dot{\varepsilon}_{ss} \propto \frac{1}{{d_0}^n(1 - A_f)^{n/2}}$$ **Equation 6.14**

Following Equation 6.14, an increase in the volume fraction of the primary precipitate phases in the ex-service tubes would be expected to result in an increase in the steady state creep rate. Figure 6.23 shows a plot of the total volume fraction of primary precipitates in the creep samples versus the measured steady state creep rate. The total volume fraction of the primary precipitates was calculated by summing the volume fraction of primary precipitates at each location characterized, and then averaging the sum across the wall regions from which the creep samples were taken. The error bars on the total volume fraction of primary precipitates are the average of the sum of the calculated segmentation errors. All primary precipitates were included in the sums – M_7C_3, $M_{23}C_6$, NbC or (Nb,Ti)C, G-phase, η-carbide, and σ-phase. A trend of increasing steady state creep rate with increased primary precipitate volume fraction is evident.

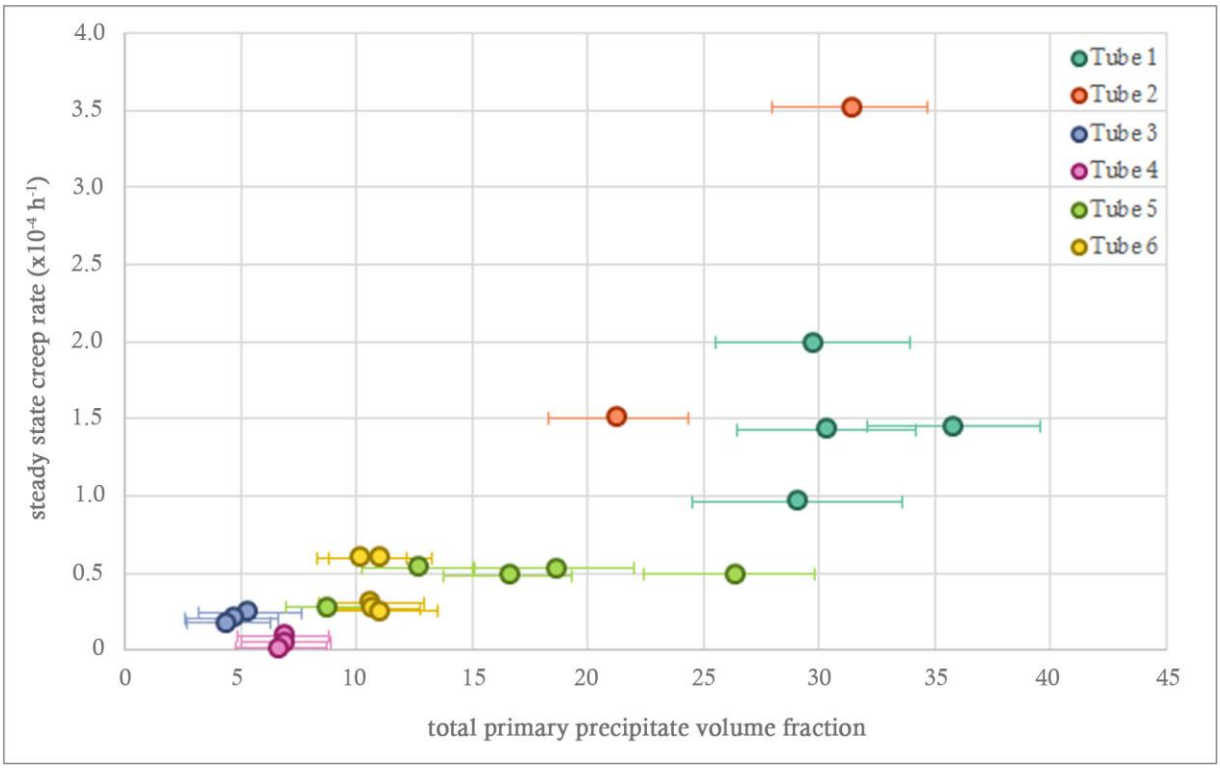

Figure 6.23 - Comparison between steady state creep rate and total primary precipitate volume fraction.

In attributing the increase in steady state creep rate to the increase in the volume fraction of primary precipitates, an inherent assumption is that the dendrite arm spacing, and thus the area of austenite matrix in between the primary precipitates, was equal for all tubes prior to service exposure and subsequent precipitate growth. However, work by Zaghloul [19] on unmodified HK alloys has shown that the dendrite arm spacing increases with increased cooling rate during the centrifugal casting process. The assumption is also made that the dendritic structure can be approximated by a grain structure. Due to the nature of a dendritic structure, the austenite dendrite arms are likely interconnected and the structure may be more complex in three dimensions than the simplified grain structure. Unfortunately, the austenite dendrite arm spacing was unable to be measured using the current microstructural data. In order to accurately segment the small phases present in the ex-service tubes analysed, relatively high magnifications were used when collecting images for the image analysis process. As such, austenite dendrite regions were typically not entirely contained in a single frame of view. Additionally, the three dimensional structure would need to be analysed in order to determine whether the simplification to a grain structure is valid, and time consuming three dimensional serial sectioning and reconstruction was well outside the scope of the current project.

Unfortunately, the preceding analysis does not allow the individual contributions of the various phases to the creep performance to be elucidated. Of particular interest are the effects of the G-phase and η-carbide silicides, however in all samples from all tubes the volume fraction of the primary chromium

carbides was consistently observed to be higher that the volume fraction of G-phase or η-carbide, and the total volume fraction of primary precipitates and therefore the relationship shown in Figure 6.23 is thus likely to be dominated by the primary chromium carbides, M_7C_3 and $M_{23}C_6$. A trend of increased creep rate with increased volume fraction of primary chromium carbides is consistent with the results discussed in Section 6.2.4. Variations in the volume fraction of G-phase or η-carbide were typically observed in tandem with variations in the volume fraction of other phases in the microstructure, and thus their individual contributions to the creep performance of the samples are unable to be determined.

6.2.6 Precipitate Network Connectivity

In visually comparing the expected microstructures of the creep samples, a trend seems to be evident whereby those samples with the highest volume fractions of primary precipitates also appear to show primary networks that qualitatively have a high level of connectivity or continuity. This is particularly evident in the inner wall samples from tubes 1 and 2, where the primary M_7C_3 carbides have coarsened and agglomerated to such an extent that the majority of them are not contained within the frame of view. In comparison, the primary carbide network in the microstructure of tube 5, which, although it contained the $M_{23}C_6$-to-M_7C_3 transformation, generally displayed lower volume fractions of primary chromium carbides, qualitatively appears more fragmented.

There are a number of image analysis methodologies for determining network connectivity, that are often applied to biological applications such as the measurement of bone structures [20] or networks of neurons [21]. Connectivity analysis typically requires an image of a network that has been skeletonised, or already has a skeletal structure. The skeleton of an object is often defined as the line representation of an object that is one pixel thick, runs through the "middle" of the object, and preserves the topology, or connectedness, of the object. Analysis of the skeleton can output data that describes the connectivity, such as the number of junctions or nodes, and the number and length of branches. Connectivity indices can then be developed from the statistics, for example the ratio of branches to junctions. Depending on the application, the analysis can be performed in 2D, as well as 3D.

Skeletonisation of the primary network in carburized samples proved no easy task. Backscattered electron images initially used for the phase identification analysis were processed using the Skeletonize3D plug-in developed for FIJI [22]. The Skeletonize plug-in is essentially a binary thinning algorithm, which iteratively erodes the surface of the object until only the skeleton is left. The results of applying the Skeletonize3D plug-in to a binary representation of the M_7C_3 carbides in a highly carburized region of a tube 1 sample is shown in Figure 6.24.

When the backscatter image was thresholded and converted to binary without filling in the "holes" in the M_7C_3 carbides, the subsequent skeleton is clearly not an ideal representation of the carbide

network, due to the erosion operation progressing from both the outer surface of the precipitate inwards, as well as from the internal surface of the holes inwards. Filling the holes during thresholding and binarising results in a skeleton that is more representative, however there are still some issues. Due to the irregular shape of the M_7C_3 carbides, there are a large number of small branches that are formed when skeletonizing precipitates with complex shapes in an attempt to preserve the morphology of the precipitates, which may result in higher than expected measurements of branch number and length, as well as the number of junctions or nodes. There are also a number of long branches that are not entirely contained within the field of view. Removal of these branches before the analysis of branch length would result in only branches with a length that can be contained within the field of view being counted, leading to a measured average branch length that is likely to be much smaller than the actual value. However, measurement of branch length for those branches that extend beyond the field of view also does not accurately represent their actual length. Analysis at lower magnifications may assist in mitigating these issues.

Additionally, the measurement of carbide network connectivity is complicated by the complex three-dimensional structure. Progressive deep etching in order to observe the three-dimensional structure of the network was performed, as discussed in Section 4.6. It was noted that rather than being a single continuous precipitate in three dimensions the carbide network appears to be composed of an agglomeration of small grains, and that precipitates that appeared disconnected from other parts of the network may well be connected in three dimensions below the plane of polish.

Measurement of connectivity by skeletonisation methods thus may not be the most accurate method by which to quantify the connectivity of the microstructure in carburized tubes, and it is apparent that three dimensional serial sectioning and reconstruction would be necessary to properly characterize the connectivity of the complex three-dimensional network. Serial sectioning using a focused ion beam (FIB) and SEM combination would allow much of the data collection to be automated, however the reconstruction and analysis is also time consuming. Analysis of precipitate network connectivity could very well be a PhD project in itself, and was considered outside the scope of the current project.

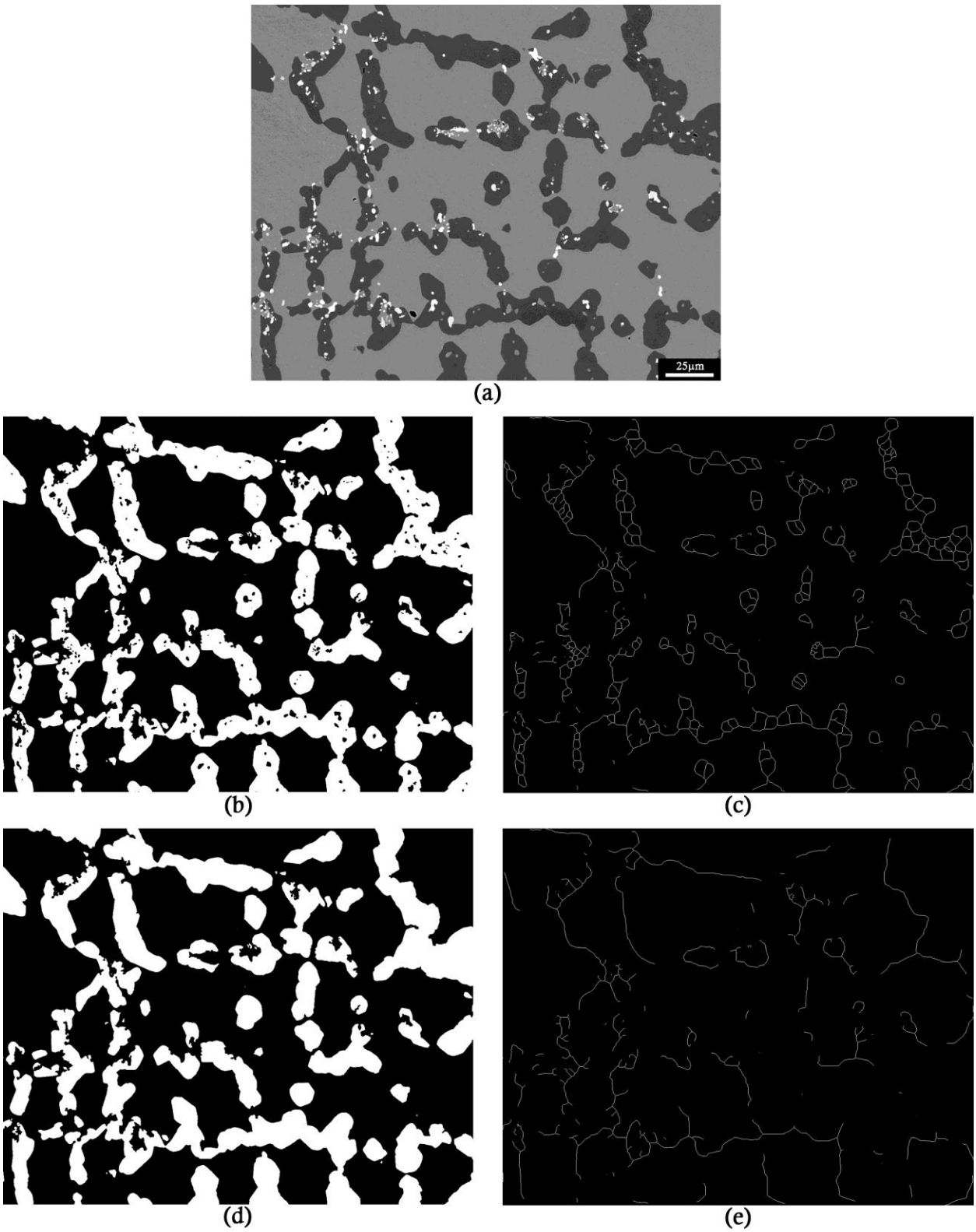

Figure 6.24 - Results of skeletonisation of M_7C_3 carbide network in a sample from tube 1. (a) Original backscattered electron micrograph, (b) thresholded and binarised micrograph with holes retained, (c) skeleton of network with holes retained, (d) thresholded and binarised micrograph with holes filled, and (e) skeleton of network with holes filled.

6.3 Summary and Conclusions

The metallographic samples from the ex-service ethylene pyrolysis tubes, for which the microstructures were characterized as described in Chapters 4 and 5, were subjected to Vickers microhardness testing. In general, the hardness at any one location was dependent on the volume fractions of the primary chromium-rich precipitates, and the presence of secondary precipitates, or lack thereof.

In the samples that displayed the greatest extent of carburization and therefore carbide coarsening, volume fractions of primary M_7C_3 carbides in the range of 28 – 38% corresponded with a hardness of 280 – 310 HV. In the regions where the primary carbides remained as $M_{23}C_6$ and the volume fraction was in the 5 – 8% range, the corresponding hardness was 190 – 215 HV. The hardness measured where the volume fraction of primary chromium-rich precipitates was a combination of $M_{23}C_6$ carbides and $Cr_2(C,N)$ carbonitrides was generally observed to be consistent with wall locations in which the same volume fraction of primary chromium-rich precipitates was made up solely of chromium-rich carbides.

The hardness of samples 3A-D was typically observed to remain within the 250 – 290 HV range, and the hardness of samples 4A-D typically remained within the 210 – 250 range. The consistency in the measured hardness across the wall thickness of samples 3A-D and 4A-D is consistent with the relatively homogenous microstructures of the tubes. The greater hardness observed in the tube 3 samples in comparison to the tube 4 samples was attributed to the superior room-temperature dispersion strengthening effect of the even distribution of secondary σ-phase precipitates in tube 3 in comparison to the secondary $M_{23}C_6$ precipitates in tube 4 which were typically concentrated adjacent to the primary precipitate network. Tube 6 was observed to display similar hardness values to tubes 3 and 4, despite containing higher volume fractions of primary $M_{23}C_6$ carbides. However, tubes 3 and 4 were observed to contain secondary precipitate distributions, whereas secondary precipitates were rarely seen in tube 6, resulting in tubes 3 and 4 having hardness values on par with tube 6 due to the dispersion strengthening effect.

Samples from each of the ex-service tubes were also subject to steady state creep testing at 1025 °C and 12 MPa uniaxial stress. The mid-section of the gauge length of the creep samples was located directly adjacent to the metallographic samples at the C and D positions of the tubes, and three thin samples were machined from the wall thickness, to enable a comparison between the characterized microstructures and the creep performance.

In general, the samples that contained the highest volume fractions of primary precipitates and displayed the highest hardness values also displayed the greatest steady state creep rates. The steady

state creep rate was determined to be proportional to the volume fraction of the primary precipitate network. The performance of the ex-service creep samples can be summarised thus:

- Highly carburized samples with primary precipitate volume fractions > 20 % displayed creep rates on the order of 10^{-4} /h
- Moderately carburized samples with primary precipitate volume fractions in the range of 6 – 20 % displayed creep rates on the order of 10^{-5} /h
- The steady state creep rate of samples that displayed little to no carburization and primary precipitate volume fractions of ≤ 6 % was seen to depend on the secondary precipitate network. The samples that contained a fine distribution of secondary $M_{23}C_6$ precipitates displayed steady state creep rates on the order of 10^{-6} /h, whereas the samples from tube 3 that contained a distribution of secondary σ-phase platelets displayed steady state creep rates on the order of 10^{-5} /h.
- The steady state creep rate of samples from the ET45-Micro tube (tube 6) was on par with the moderately carburized HP-NbTi tube (tube 5), consistent with reports that the creep properties of ET45-Micro are not improved compared to the HP-NbTi alloy.

Further analysis of the exact effects of the separate precipitate phases on the creep rates invariably resulted in more questions than answers. The effect of the G-phase and η-carbide silicides on the creep properties of Fe-Cr-Ni alloys is not well understood in the literature, and, due to the inability to directly compare varying volume fractions of these phases with performance in the current samples as a result of other microstructural variations, their exact effects remain unclear. Sample 1D-O displayed a decreased volume fraction of primary chromium carbides in comparison to samples 1D-I and 1D-M, but also contained a significant amount of η-carbide (up to 10 %), making the total precipitate volume fraction relatively consistent across the three samples. The lower creep rate displayed by sample 1D-O may therefore indicate that the η-carbide is beneficial to the creep properties of the material. Similarly, the increased volume of fraction of G-phase and lower creep rate in tube 3 in comparison to tube 4, despite a greater volume fraction of $M_{23}C_6$, may indicate that the G-phase is also beneficial to the creep performance of the material. However, tube 3 also displayed a fine distribution of secondary $M_{23}C_6$, which is reported to improve the creep resistance via dispersion strengthening, and therefore the improvement in the creep properties in tube 4 could largely be attributed to the secondary precipitates.

It was noted that connectivity or continuity of the carbide network may also play a role in creep resistance, and that the tubes with the highest volume fractions of primary precipitates could be said to qualitatively display the greatest connectivity. However, the complex nature of the precipitate network in three dimensions precluded connectivity analysis being performed within the timeframe of the current project.

The addition of argon to a furnace atmosphere in oxidation tests in order to lower the oxygen partial pressure was observed to decrease the rate of internal oxidation in those samples containing sufficient chromium to form a protective chromium oxide scale, however it did not appear to have an effect on the rate of internal oxidation in samples with significant levels of chromium depletion. In order to completely prevent oxidation during creep testing the tests would have to be conducted in an entirely inert atmosphere, however the current design of the creep testing apparatus does not allow for a complete seal to be achieved, and the design and build of new apparatus to incorporate an inert atmosphere was outside the scale of the current project. Nevertheless, a flow of argon was introduced to the furnace atmosphere in an effort to reduce the oxygen partial pressure and the rate of oxidation during the steady state creep tests.

Chapter References

[1] Jakobi, D. and Gommans, R. *Typical failures in pyrolysis coils for ethylene cracking.* Materials and Corrosion, 2003. **54**(11): p. 881-886.

[2] Nishimoto, K., Saida, K., Inui, M., and Takahashi, M. *Changes in microstructure of HP-modified, heat-resisting cast alloys under long-term aging. Repair weld cracking of service-exposed, HP-modified, heat-resisting cast alloys (2nd Report).* Welding Research Abroad, 2002. **48**(11): p. 1-9.

[3] ASTM International *E139-11: Standard Test Methods for Conducting Creep, Creep-Rupture, and Stress-Rupture Tests of Metallic Materials*. 2011.

[4] Chun, C.M., Desai, S., Hershkowitz, F., and Ramanarayanan, T.A. *Materials challenges in cyclic carburizing and oxidizing environments for petrochemical applications.* Materials and Corrosion, 2014. **65**(3): p. 282-295.

[5] Ramanarayanan, T.A., Petkovic, R.A., Mumford, J.D., and Ozekcin, A. *Carburization of high chromium alloys*. in *Workshop `Carburization, Metal Dusting, Carbon Deposition', 6-7 Nov. 1997*. 1998. Germany: VCH Verlagsgesellschaft.

[6] Young, D.J. *High Temperature Oxidation and Corrosion of Metals*. Elsevier Corrosion Series, ed. Burstein, T. 2008, Amsterdam: Elsevier.

[7] Schmidt + Clemens Group *Centralloy® G 4852 Material Data Sheet*. 2009.

[8] Schmidt + Clemens Group *Centralloy® G 4852 Micro Material Data Sheet*. 2009.

[9] de Almeida Soares, G.D., de Almeida, L.H., da Silveira, T.L., and Le May, I. *Niobium additions in HP heat-resistant cast stainless steels.* Materials Characterization, 1992. **29**(4): p. 387-96.

[10] Ribeiro, A.F., Borges, R.M.T., and de Almeida, L.H. *Phase transformation in heat resistant steel observed by STEM. (NbTi)C - NiNbSi (G-phase).* Acta Microscopica, 2002. **11**(1): p. 59-63.

[11] de Almeida, L.H., Ribeiro, A.F., and Le May, I. *Microstructural characterization of modified 25Cr-35Ni centrifugally cast steel furnace tubes.* Materials Characterization, 2003. **49**(3): p. 219-229.

[12] Shi, S. and Lippold, J.C. *Microstructure evolution during service exposure of two cast, heat-resisting stainless steels - HP-Nb modified and 20-32Nb.* Materials Characterization, 2008. **59**(8): p. 1029-1040.

[13] Tillack, D.J. and Guthrie, J.E. *Wrought and cast heat-resistant stainless steels and nickel alloys for the refining and petrochemical industries.* Nickel Development Institute, 1998.

[14] Sourmail, T. *Precipitation in creep resistant austenitic stainless steels.* Materials Science and Technology, 2001. **17**: p. 1-14.

[15] Caballero, F.G., Imizcoz, P., Lopez, V., Alvarez, L.F., and De Andrés, C.G. *Use of titanium and zirconium in centrifugally cast heat resistant steel.* Materials Science & Technology, 2007. **23**(5): p. 528-534.

[16] Ibanez, R.A.P., de Almeida Soares, G.D., de Almeida, L.H., and Le May, I. *Effects of Si content on the microstructure of modified-HP austenitic steels.* Materials Characterization, 1993. **30**(4): p. 243-9.

[17] Kirchheiner, R. and Woelpert, P. *Niobium in centrifugally cast tubes for petrochemical applications*. in *Niobium, Science and Technology: Proceedings of the International Symposium Niobium. Orland: Minerals, Metals and Materials Society*. 2001.

[18] Dowling, N.E. *Mechanical Behavior of Materials*. Third Edition ed. 2007: Pearson Education Inc.

[19] Zaghloul, M.B., Shinoda, T., and Tanaka, R. *Relation between structure and creep rupture strength of centrifugally cast HK40 steel.* Transactions of the Iron and Steel Institute of Japan, 1977. **17**(1): p. 28-36.

[20] Doube, M., Kłosowski, M.M., Arganda-Carreras, I., Cordelières, F.P., Dougherty, R.P., Jackson, J.S., Schmid, B., Hutchinson, J.R., and Shefelbine, S.J. *BoneJ: Free and extensible bone image analysis in ImageJ.* Bone, 2010. **47**(6): p. 1076-1079.

[21] Meijering, E., Jacob, M., Sarria, J.C., Steiner, P., Hirling, H., and Unser, M. *Design and validation of a tool for neurite tracing and analysis in fluorescence microscopy images.* Cytometry Part A, 2004. **58**(2): p. 167-176.

[22] Arganda-Carreras, I. *Skeletonize3D*. Available from: http://imagejdocu.tudor.lu/doku.php?id=plugin:morphology:skeletonize3d:start.

Chapter 7: Eddy Current Non-Destructive Testing

The current chapter presents the results of the eddy current non-destructive testing (eddy current NDT) performed on the six ex-service ethylene pyrolysis tubes and the relationship between the eddy current NDT response and the extent of carburization. The factors that influence the magnetic response of the tubes, including a comparison to the phase fractions and matrix compositions presented in Chapter 5, will be discussed. The composition of the austenite matrix was used to predict changes in the magnetic permeability of the austenite in each tube as a function of depth into the tube wall; subsequently, the eddy current NDT response was compared with the predictions.

The eddy current NDT data was collected by Quest Integrity NZL Ltd, using a combination of manual collection methods and the tube crawler system that has been recently developed [1]. Post-processing of the eddy current NDT data was performed both at Quest Integrity NZL Ltd and at the University of Canterbury, using a variety of Matlab programs developed for the purpose.

7.1 Composition and Magnetic Permeability

As discussed in Section 2.6.2, ferromagnetic elements can, by alloying with each other or with non-feromagnetic elements, become paramagnetic. Commercial austenitic Fe-Cr-Ni alloys are paramagnetic at room temperature, but the Curie Temperature, T_C, and the magnetic permeability, μ, vary very strongly with the Cr/Ni+Fe ratio [2].

The Curie temperature is the temperature where a material's permanent magnetism changes to induced magnetism. Below the Curie temperature, the magnetic moments in the material are aligned and the material is ferromagnetic. Above the Curie temperature, the magnetic state becomes disordered and the material becomes paramagnetic [3, 4]. Therefore, for measurements taken at room temperature, if $T_C < T_{room}$ the material is paramagnetic, and if $T_C > T_{room}$, the material is ferromagnetic.

Numerical values of magnetic permeability, μ, are typically reported as relative permeability μ_r, which is the ratio of μ of the material to the permeability of free space, $\mu_0 = 4\pi \times 10^{-7}$ H/m [5-7]:

$$\mu_r = \frac{\mu}{\mu_0} \qquad \textbf{Equation 7.1}$$

Paramagnetic materials have a relative permeability that is equal to or slightly greater than 1, whereas ferromagnetic materials have values of relative magnetic permeability in the range of slightly greater than 1 to within the thousands [5, 7-9].

During service, the precipitation and growth of chromium-rich phases results in chromium being depleted from the austenite matrix. With increasing carburization, the composition of the austenite matrix tends towards the binary Fe-Ni system, and becomes progressively more ferromagnetic, whilst retaining the austenite structure, due to increases in magnetic permeability and the Curie temperature [2, 10-16].

Curie temperature data for various alloy compositions [17-19] has been compiled by Stevens *et al.* [15] and plotted on a ternary Fe-Cr-Ni Gibbs triangle, enabling the effects of changes in composition on the magnetism of Fe-Cr-Ni alloys to be visualized, as shown in Figure 2.24. Saori and Ohta [20] measured the magnetic permeability of carbon-free Fe-Cr-Ni alloys of varying compositions and also reported the data on a ternary Fe-Cr-Ni Gibbs triangle. A ternary Fe-Cr-Ni Gibbs triangle showing the data compiled by Stevens *et al.* in addition to the data collected by Saori and Ohta is shown in Figure 7.1.

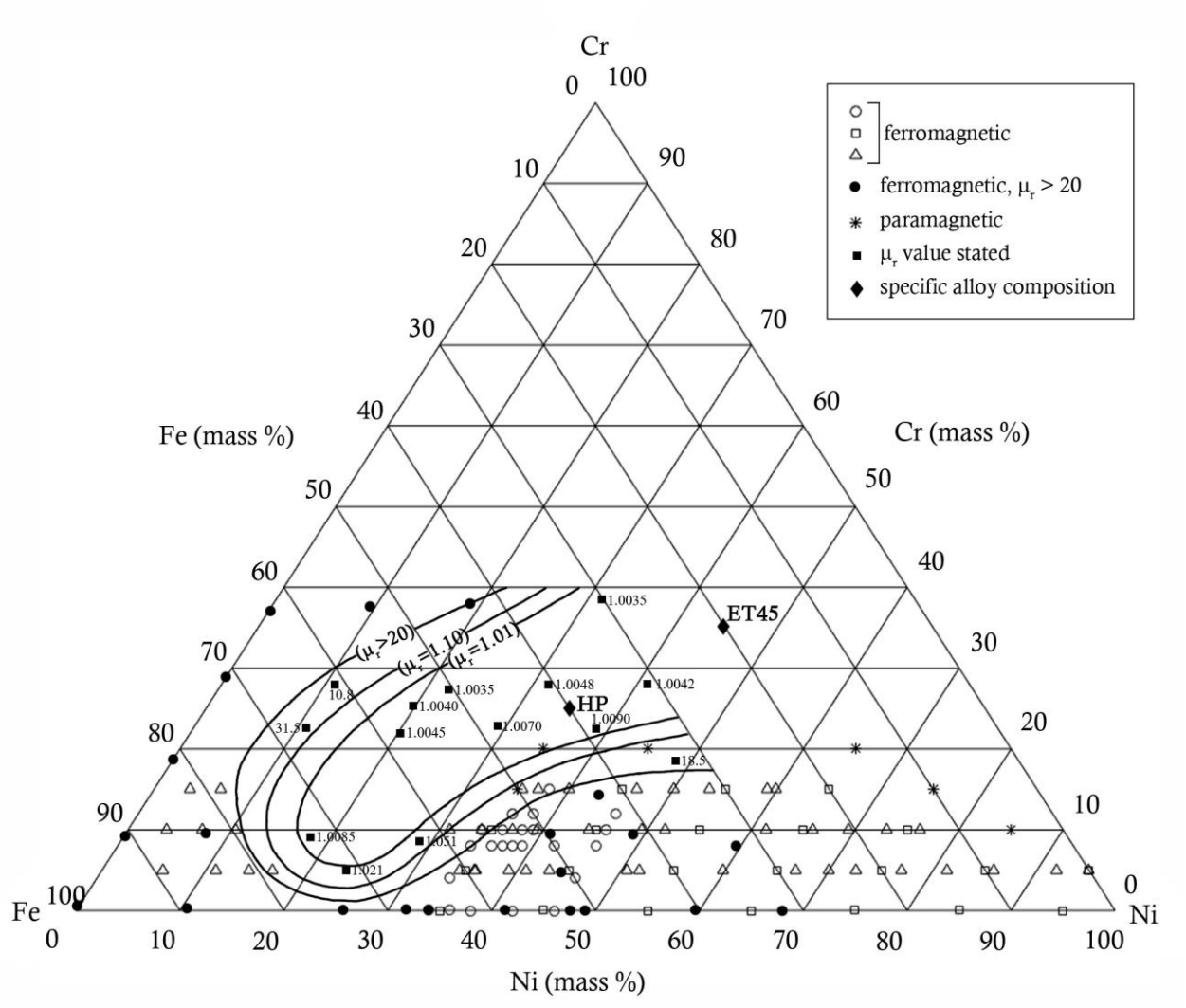

Figure 7.1 - Gibbs triangle displaying magnetic properties of various Fe-Cr-Ni compositions at room temperature. Open circles, squares, and triangles denote compositions which are ferromagnetic at room temperature, and asterisks denote compositions which are paramagnetic at room temperature (adapted

from [15]). Solid squares denote compositions for which μ_r has been measured, solid circles denote compositions for which μ_r is greater than 20, and solid lines are iso-μ_r lines (adapted from [20]).

The measurements of relative magnetic permeability collected by Saori and Ohta are seen to be consistent with the paramagnetic and ferromagnetic compositions determined by the Curie temperature data compiled by Stevens *et al*. The as-cast compositions of both the HP and ET45 alloy lie within the range of paramagnetic compositions. It can be seen the HP alloy composition is close to the boundary between paramagnetic and ferromagnetic properties, and thus even a small decrease on the order of 5 wt% in the chromium content of the alloy could significantly alter the relative magnetic permeability of the alloy. Although it is unclear exactly where the boundary between paramagnetic and ferromagnetic properties lies for the region in which chromium-depleted compositions of ET45 would be expected to be, the high chromium content of the ET45-Micro alloy means that a significant drop in the matrix chromium concentration would likely be required for the magnetic permeability to change, perhaps on the order of 10 wt% or more.

Unfortunately, the exact relative magnetic permeability values measured by Saori and Ohta are only stated when the values are below 20. For the alloy compositions where $\mu_r > 20$, the data is represented solely by a point, and no actual relative magnetic permeability value is stated. Permalloy (typically 80% Ni, 4 – 5 % Mo, balance Fe) is reported to obtain values of relative magnetic permeability of 50,000 or higher [3], so it is not inconceivable that severe chromium depletion of the austenite matrix in carburized Fe-Cr-Ni alloys could result in values of relative magnetic permeability significantly higher than 20. If a twenty-fold increase in μ_r occurs due to a drop in matrix chromium concentration from 18 to 15 wt%, then the values for μ_r for matrix chromium compositions less than 15 wt% would be expected to increase significantly as matrix chromium concentration increases.

Based on the locations of the matrix compositions of the ex-service tubes as plotted on the Gibbs triangle (to be shown in Sections 7.1.1 through 7.1.6), a matrix chromium content above 18 wt% results in $\mu_r < 1.10$, and a matrix chromium concentration of 15 wt % or less results in $\mu_r > 20$. Matrix chromium concentrations in-between 15 and 18 wt% would display values of relative magnetic permeability in the range $1.10 < \mu_r < 20$.

7.1.1 Tube 1

The matrix chromium concentration for samples 1A-D is shown in Figure 7.2 and the corresponding locations on the Gibbs triangle in Figure 7.1 are shown in Figure 7.3 (a) – (d). Of the four samples from tube 1, sample 1D displayed the greatest extent of matrix chromium depletion, with the composition of the matrix across the entire wall lying in the $\mu_r > 20$ region. Approximately 4.1 mm of sample 1C, 1.9 mm of 1B, and 3.4 mm of 1A lay within the $\mu_r > 20$ region. A summary of the

amount of material in each magnetic region, both in absolute distance and relative to the sample wall thickness, is shown in Table 7.1.

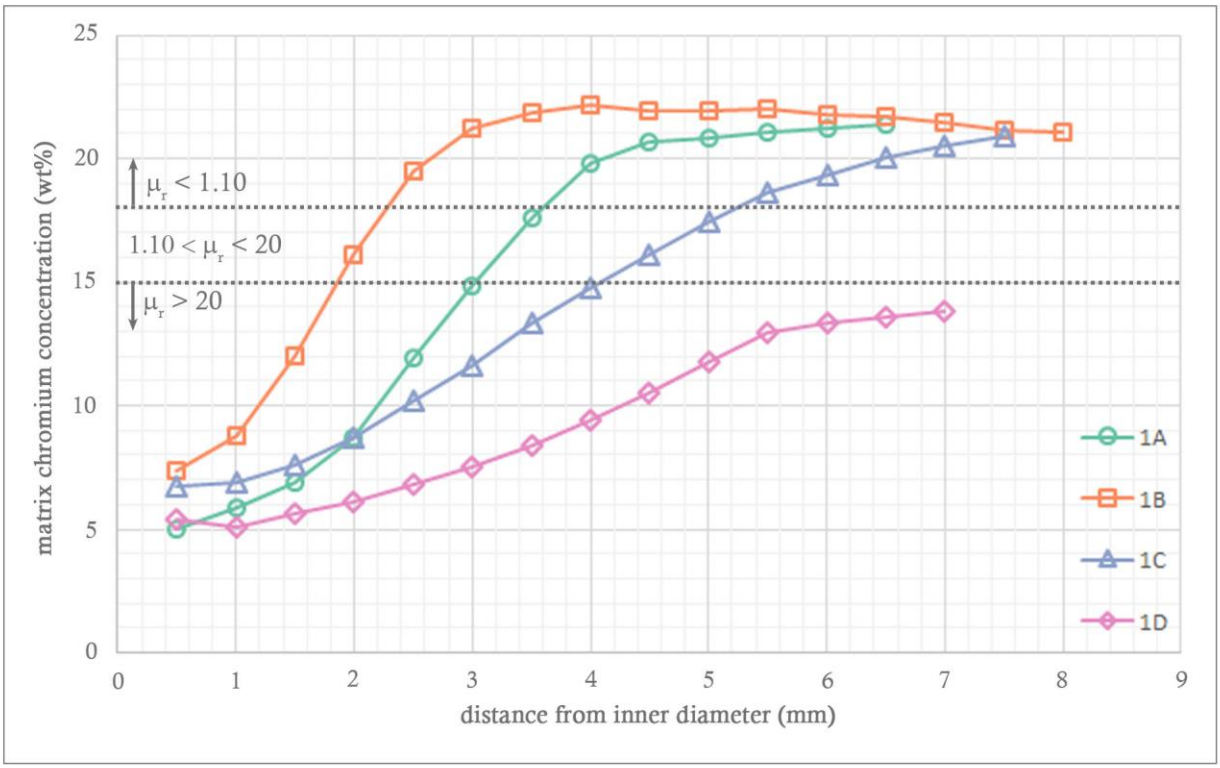

Figure 7.2 - Matrix chromium concentration in samples 1A-D, as measured by EDS.

Table 7.1 - Summary of wall thickness fractions within various magnetic regions for samples 1A-D

Sample	$\mu_r > 20$	$1.10 < \mu_r < 20$	$\mu_r < 1.10$
1A (t ≈ 7.0 mm)	3.4 mm (≈ 49 %)	0.6 mm (≈ 9 %)	3.0 mm (≈ 42 %)
1B (t ≈ 8.4 mm)	1.9 mm (≈ 23 %)	0.4 mm (≈ 5 %)	6.1 mm (≈ 72 %)
1C (t ≈ 7.9 mm)	4.1 mm (≈ 52 %)	1.1 mm (≈14 %)	2.7 mm (≈ 34 %)
1D (t ≈ 7.3 mm)	7.3 mm (≈ 100 %)	-	-

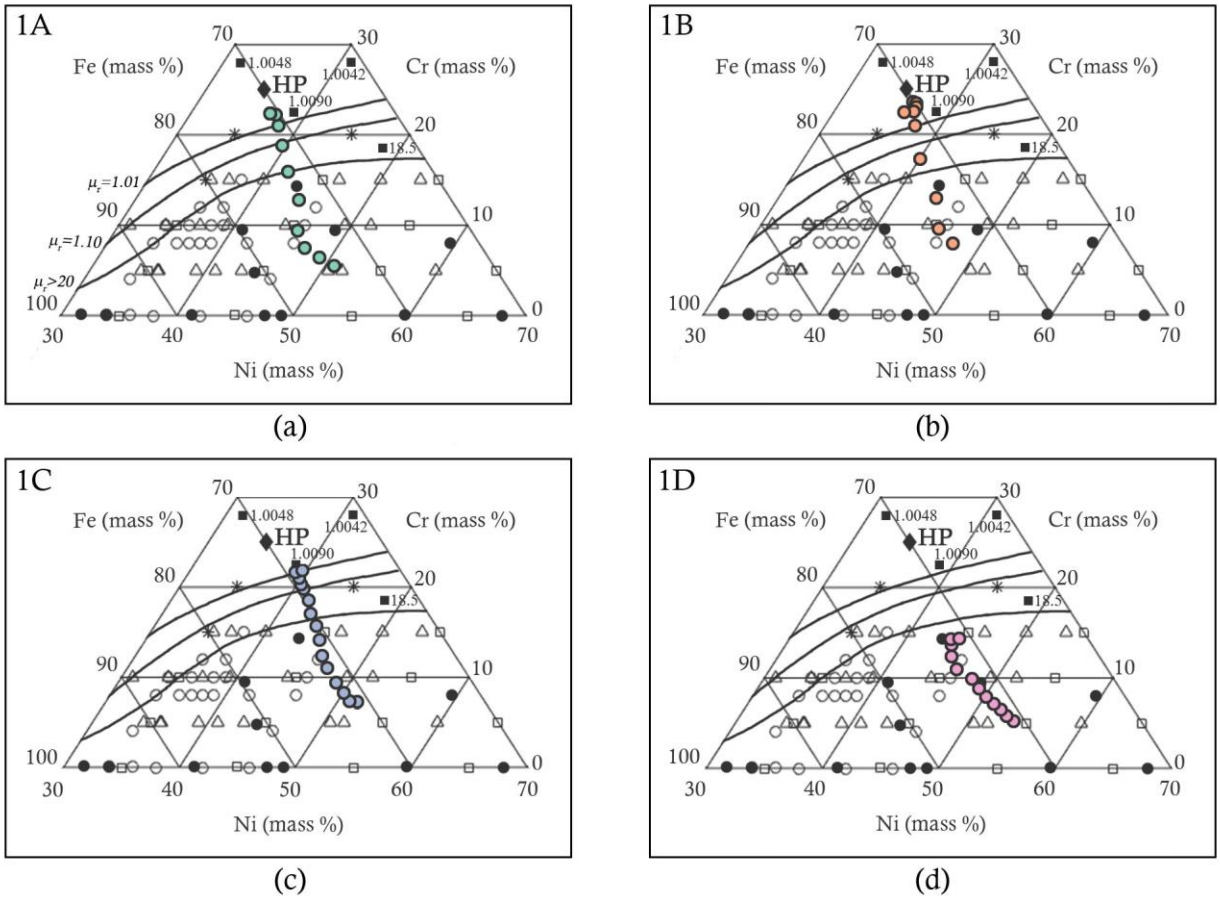

Figure 7.3 - Matrix chromium concentration and magnetic permeability on a section of the Gibbs triangle, for samples (a) 1A, (b) 1B, (c) 1C, and (d) 1D. Iso-μ_r lines are labelled in (a).

7.1.2 Tube 2

The matrix chromium concentration was seen to be relatively consistent across all samples from tube 2, and due to all samples having similar wall thicknesses both absolute and proportional measures of the various regions of magnetic permeability were similar. Samples 2A, C, and D contained 4.5 – 4.9 mm of matrix material that fell within the $\mu_r > 20$ region, equating to 64 – 69 % of the wall thickness. The exception was sample 2B, which displayed chromium concentration values 1 – 1.5 wt% above those in samples 2A, C, and D at all locations. As such, sample 2B displayed only 4.0 mm of material that lay within the $\mu_r > 20$, equating to approximately 57 % of the wall thickness. The composition of the remainder of the wall thickness in all four samples from tube 2 lay within the $1.10 < \mu_r < 20$ range, as summarised in Table 7.2.

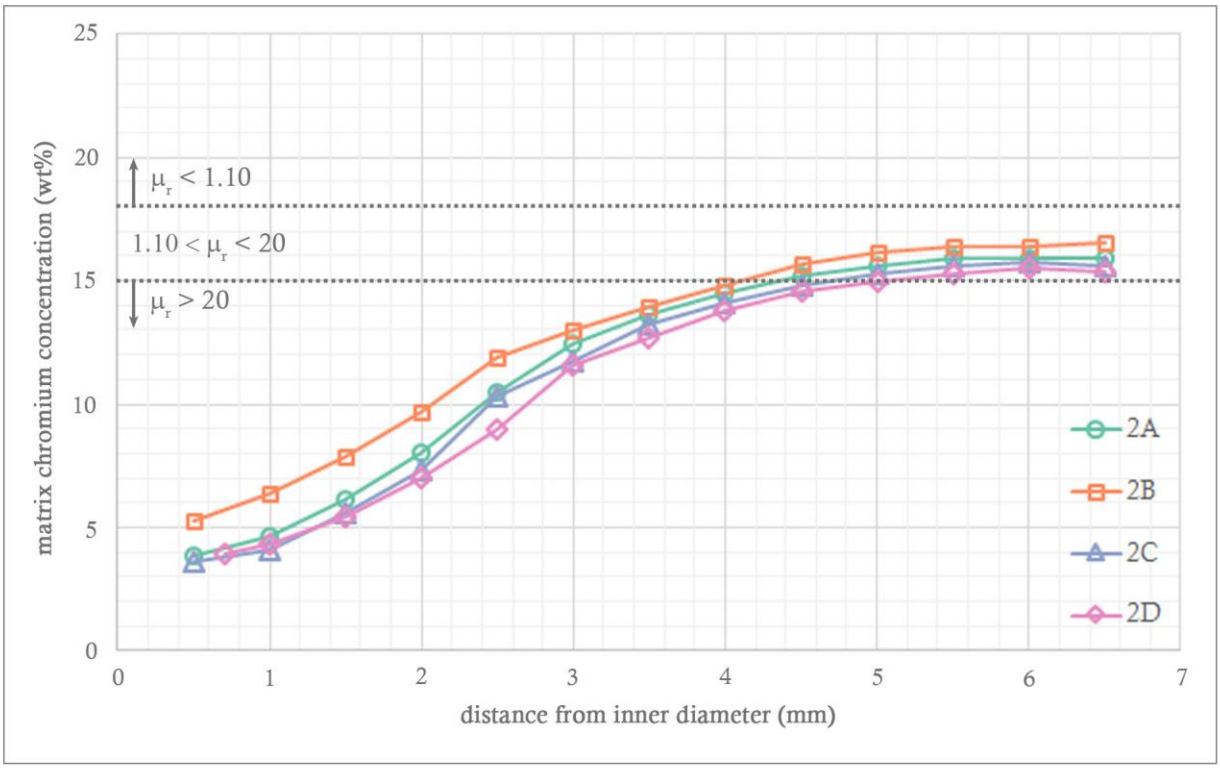

Figure 7.4 - Matrix chromium concentration in samples 2A-D, as determined by EDS.

Table 7.2 - Summary of wall thickness fractions within various magnetic regions for samples 2A-D

Sample	$\mu_r > 20$	$1.10 < \mu_r < 20$	$\mu_r < 1.10$
2A (t ≈ 7.0 mm)	4.5 mm (≈ 64 %)	2.5 mm (≈ 36 %)	-
2B (t ≈ 7.0 mm)	4.0 mm (≈ 57 %)	3.0 mm (≈ 43 %)	-
2C (t ≈ 7.1 mm)	4.6 mm (≈ 65 %)	2.5 mm (≈ 35 %)	-
2D (t ≈ 7.1 mm)	4.9 mm (≈ 69 %)	2.2 mm (≈ 31 %)	-

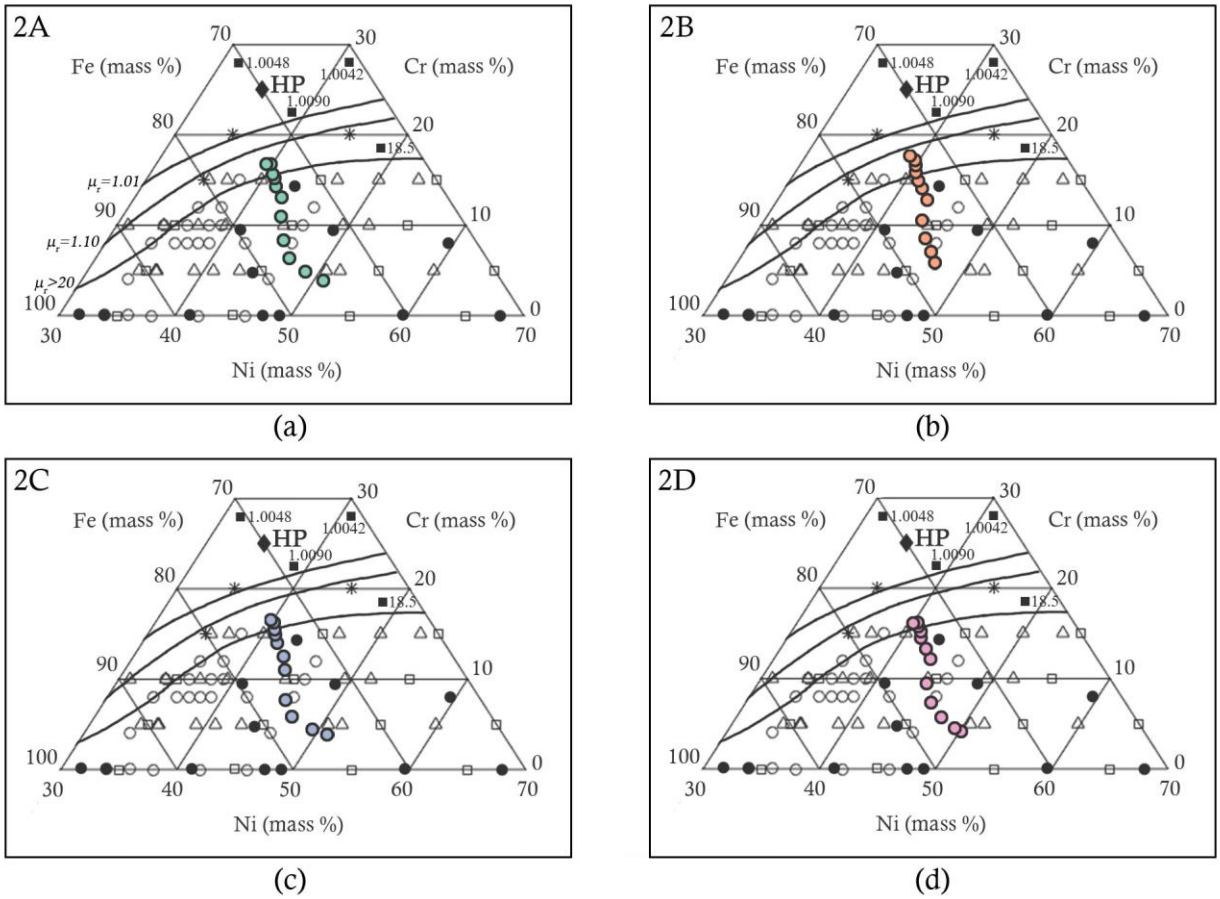

Figure 7.5 - Matrix chromium concentration and magnetic permeability on a section of the Gibbs triangle, for samples (a) 2A, (b) 2B, (c) 2C, and (d) 2D. Iso-μ_r lines are labelled in (a).

7.1.3 Tube 3

The matrix chromium concentration in tube 3 was seen to lie within the range of 22 – 23 wt% for all locations in all samples, as shown in Figure 7.6. As such, all material in the tube 3 samples remained contained within the paramagnetic $\mu_r < 1.10$ region, as summarised in Table 7.3.

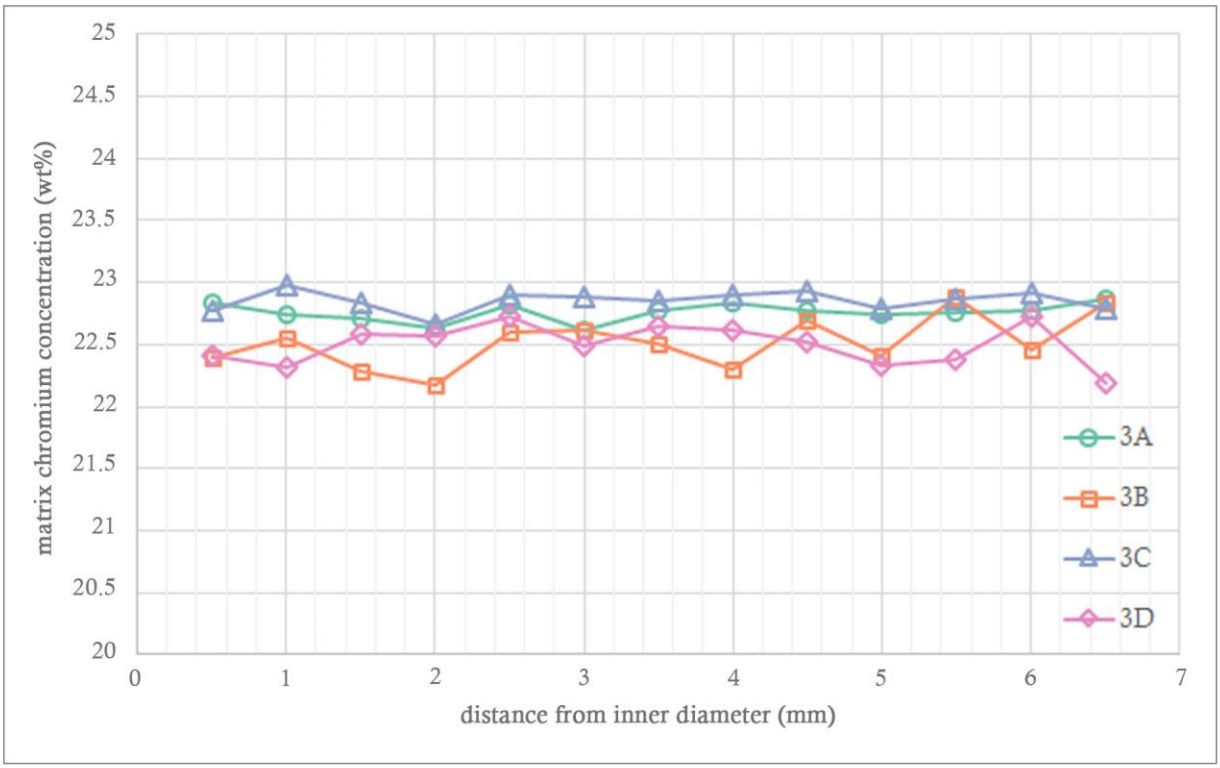

Figure 7.6 - Matrix chromium concentration in samples 3A-D, as determined by EDS.

Table 7.3 - Summary of wall thickness fractions within various magnetic regions for samples 3A-D

Sample	$\mu_r > 20$	$1.10 < \mu_r < 20$	$\mu_r < 1.10$
3A (t ≈ 7.0 mm)	-	-	7.0 mm (100 %)
3B (t ≈ 7.0 mm)	-	-	7.0 mm (100 %)
3C (t ≈ 7.2 mm)	-	-	7.2 mm (100 %)
3D (t ≈ 6.8 mm)	-	-	6.8 mm (100 %)

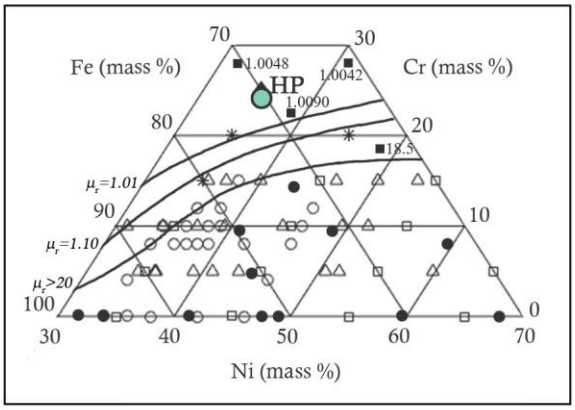

Figure 7.7 - Matrix chromium concentration and magnetic permeability on a section of the Gibbs triangle, for tube 3. The composition of all samples at all locations was contained within the green circle. Iso-μ_r lines are labelled.

7.1.4 Tube 4

As with tube 3, the matrix chromium concentration of tube 4 was seen to have little variance, as shown in Figure 7.8, and typically remained within the range of 21.5 – 22.5 wt % at all locations for all samples. As such, all material in the tube 4 samples remained contained within the paramagnetic $\mu_r < 1.10$ region, as summarised in Table 7.4.

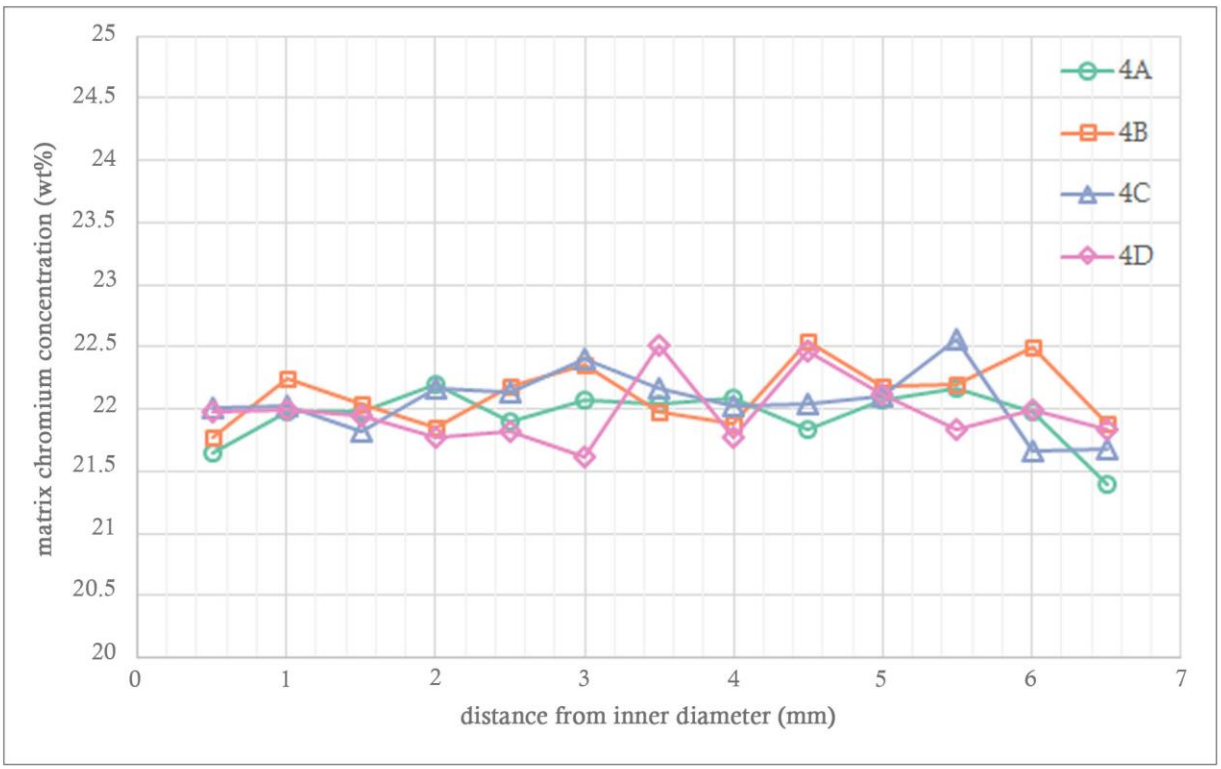

Figure 7.8 - Matrix chromium concentration in samples 4A-D, as determined by EDS.

Table 7.4 - Summary of wall thickness fractions within various magnetic regions for samples 4A-D

Sample	$\mu_r > 20$	$1.10 < \mu_r < 20$	$\mu_r < 1.10$
4A (t ≈ 7.1 mm)	-	-	7.1 mm (100 %)
4B (t ≈ 7.1 mm)	-	-	7.1 mm (100 %)
4C (t ≈ 7.0 mm)	-	-	7.0 mm (100 %)
4D (t ≈ 7.0 mm)	-	-	7.0 mm (100 %)

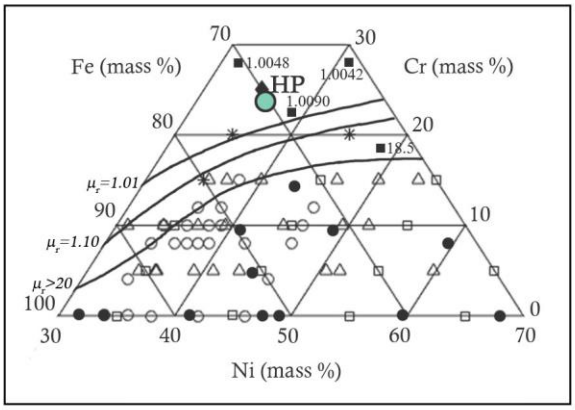

Figure 7.9 - Matrix chromium concentration and magnetic permeability on a section of the Gibbs triangle, for tube 4. The composition of all samples at all locations was contained within the green circle. Iso-μ_r lines are labelled.

7.1.5 Tube 5

The matrix chromium concentration in tube 5 was observed to be consistent across samples 5A-C. These three samples contained 1.7 – 1.9 mm of material that lay within the $\mu_r > 20$ region. Differences in the wall thicknesses resulted in the proportional amount of material within the $\mu_r > 20$ region varying from 21 – 24%, as summarized in Table 7.5. Very little material was expected to have a composition within the $1.10 < \mu_r < 20$ range (0.3 – 0.4 mm, or 4 – 5 %), and the remainder of the wall thickness in samples 5A-C was expected to remain in the paramagnetic region.

Sample 5D displayed a greater extent of matrix chromium depletion than samples 5A-C. This was reflected in the amount of ferromagnetic material in the sample, with 3.4 mm (45 % of the wall thickness) lying within the $\mu_r > 20$ region. Sample 5D also contained more material within the $1.10 < \mu r < 20$ region, approximately 1.0mm (13 % of the wall thickness) in comparison to 0.3 – 0.4 mm (4 – 5 %) in samples 5A-C. As such, only the outer 3.2 mm (42 %) of the wall thickness of sample 5D was expected to remain in the paramagnetic region.

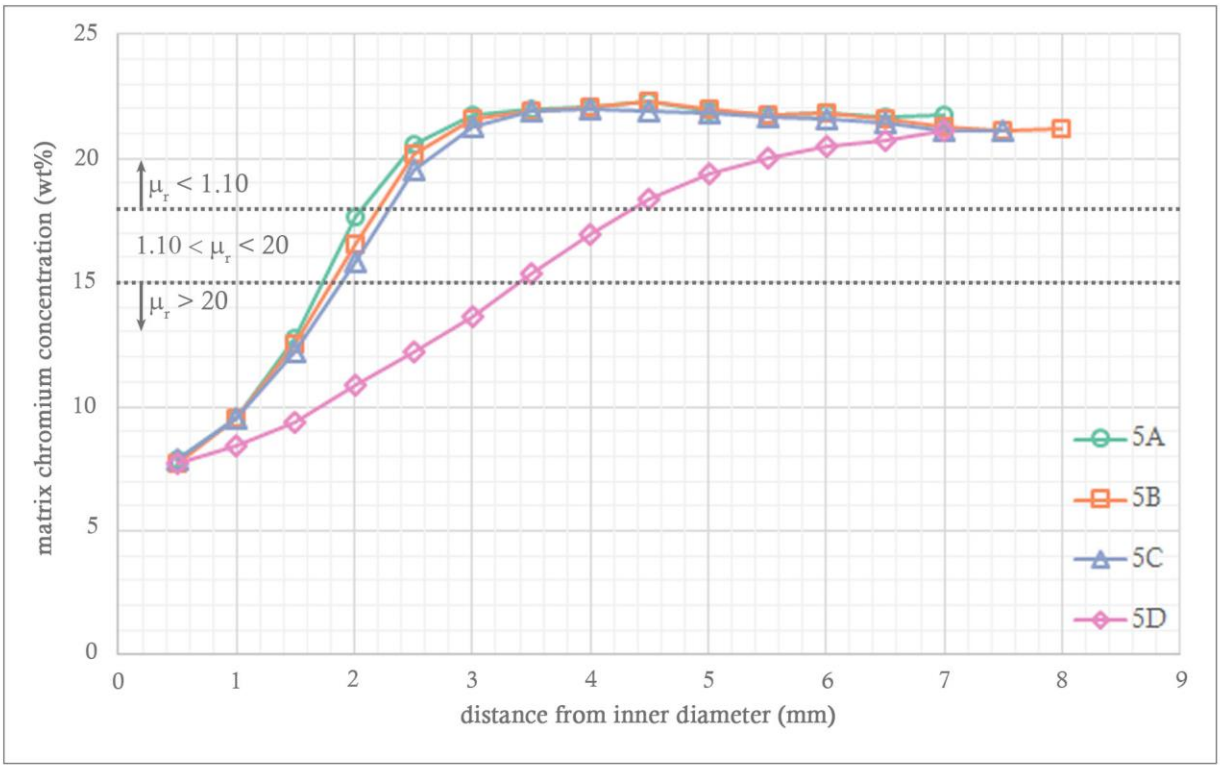

Figure 7.10 - Matrix chromium concentration in samples 5A-D, as determined by EDS.

Table 7.5 - Summary of wall thickness fractions within various magnetic regions for samples 5A-D

Sample	$\mu_r > 20$	$1.10 < \mu_r < 20$	$\mu_r < 1.10$
5A (t ≈ 7.5 mm)	1.7 mm (≈ 23 %)	0.3 mm (≈ 4 %)	5.5 mm (≈ 73 %)
5B (t ≈ 8.5 mm)	1.8 mm (≈ 21 %)	0.4 mm (≈ 5 %)	6.3 mm (≈ 74 %)
5C (t ≈ 7.9 mm)	1.9 mm (≈ 24 %)	0.4 mm (≈ 5 %)	5.6 mm (≈ 71 %)
5D (t ≈ 7.6 mm)	3.4 mm (≈ 45 %)	1.0 mm (≈ 13 %)	3.2 mm (≈ 42 %)

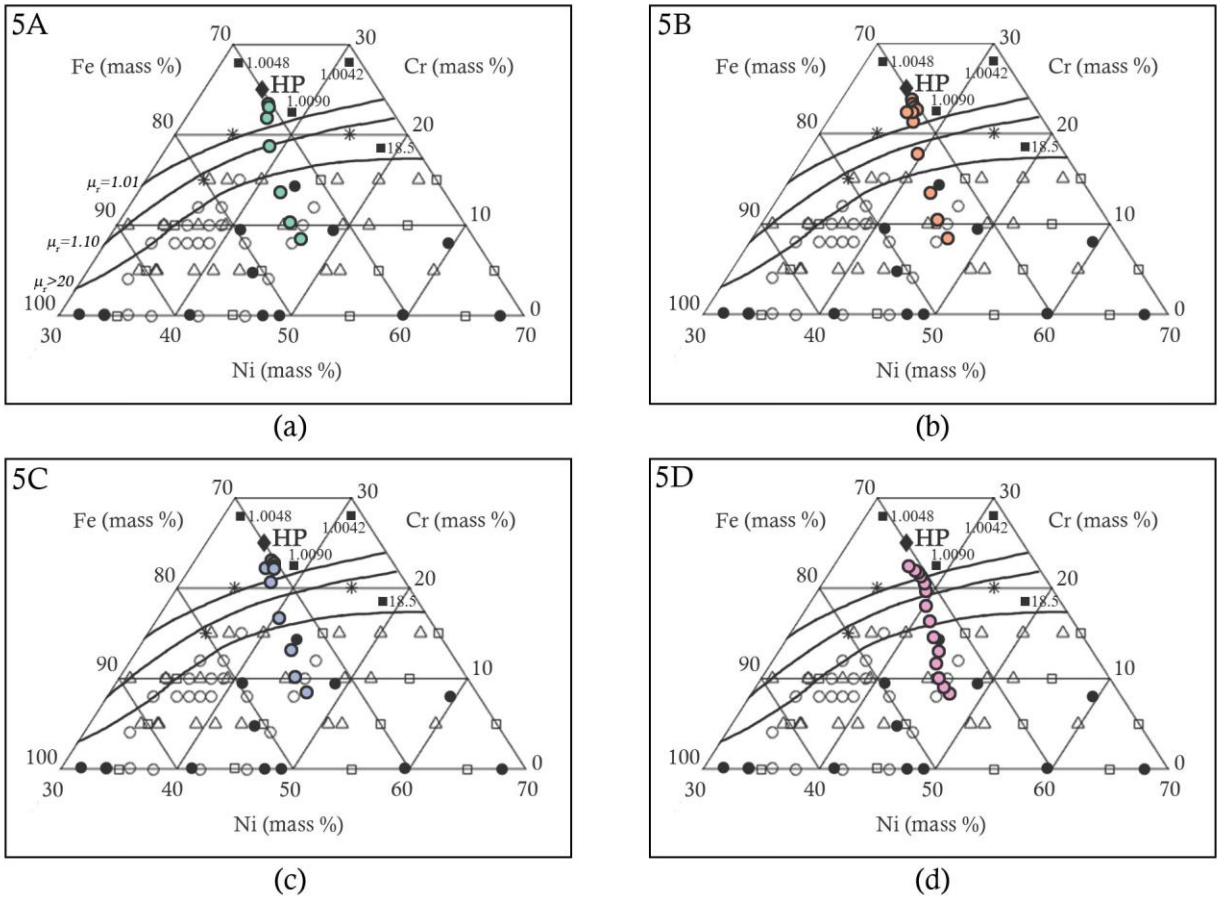

Figure 7.11 - Matrix chromium concentration and magnetic permeability on a section of the Gibbs triangle, for samples (a) 5A, (b) 5B, (c) 5C, and (d) 5D. Iso-μ_r lines are labelled in (a).

7.1.6 Tube 6

Although the exact boundary between paramagnetic and ferromagnetic behaviour is not known for the region in which the composition of the 35%Cr-45%Ni alloys lie, due to the high-chromium high-nickel composition of the ET45-Micro alloy and the relatively minimal chromium depletion of the matrix (Figure 7.12), all locations in all samples from tube 6 were expected to remain within the paramagnetic $\mu_r < 1.10$ region, as summarised in Table 7.6.

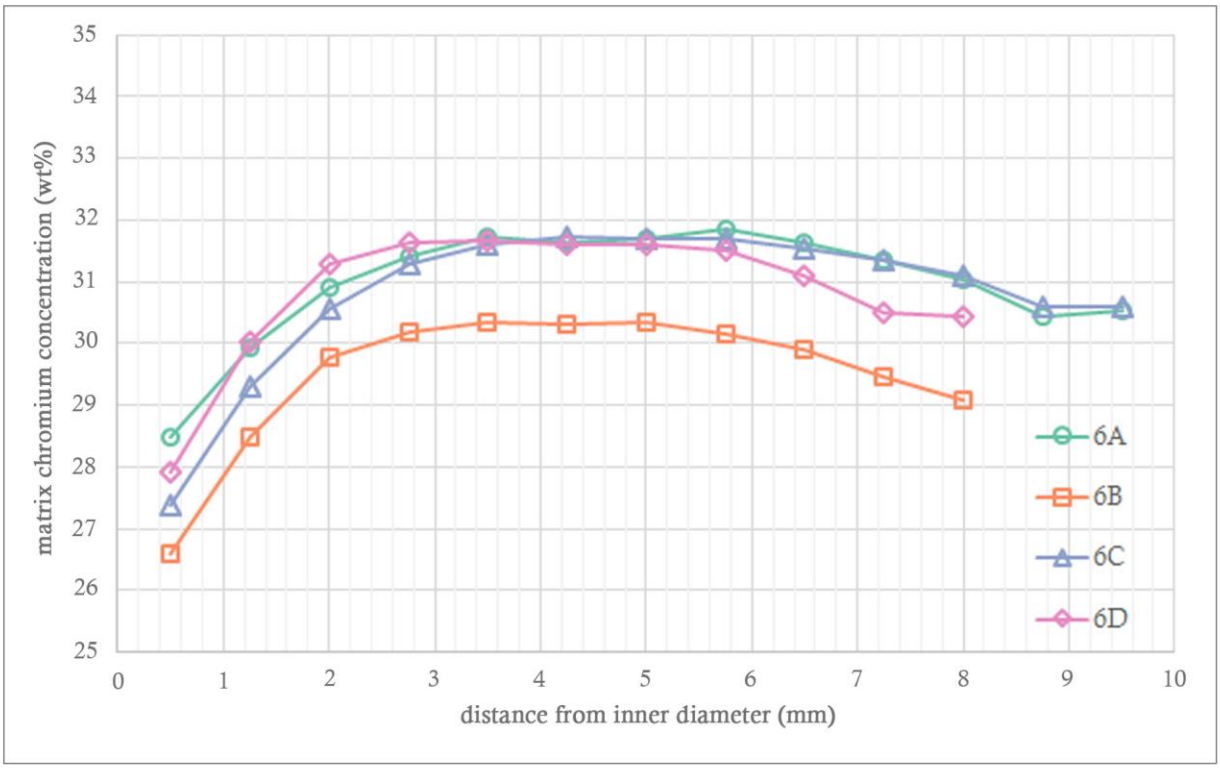

Figure 7.12 - Matrix chromium concentration in samples 6A-D, as determined by EDS.

Table 7.6 - Summary of wall thickness fractions within various magnetic regions for samples 6A-D

Sample	$\mu_r > 20$	$1.10 < \mu_r < 20$	$\mu_r < 1.10$
6A (t ≈ 10.4 mm)	-	-	10.4 mm (100 %)
6B (t ≈ 8.8 mm)	-	-	8.8 mm (100 %)
6C (t ≈ 10.0 mm)	-	-	10.0 mm (100 %)
6D (t ≈ 8.6 mm)	-	-	8.6 mm (100 %)

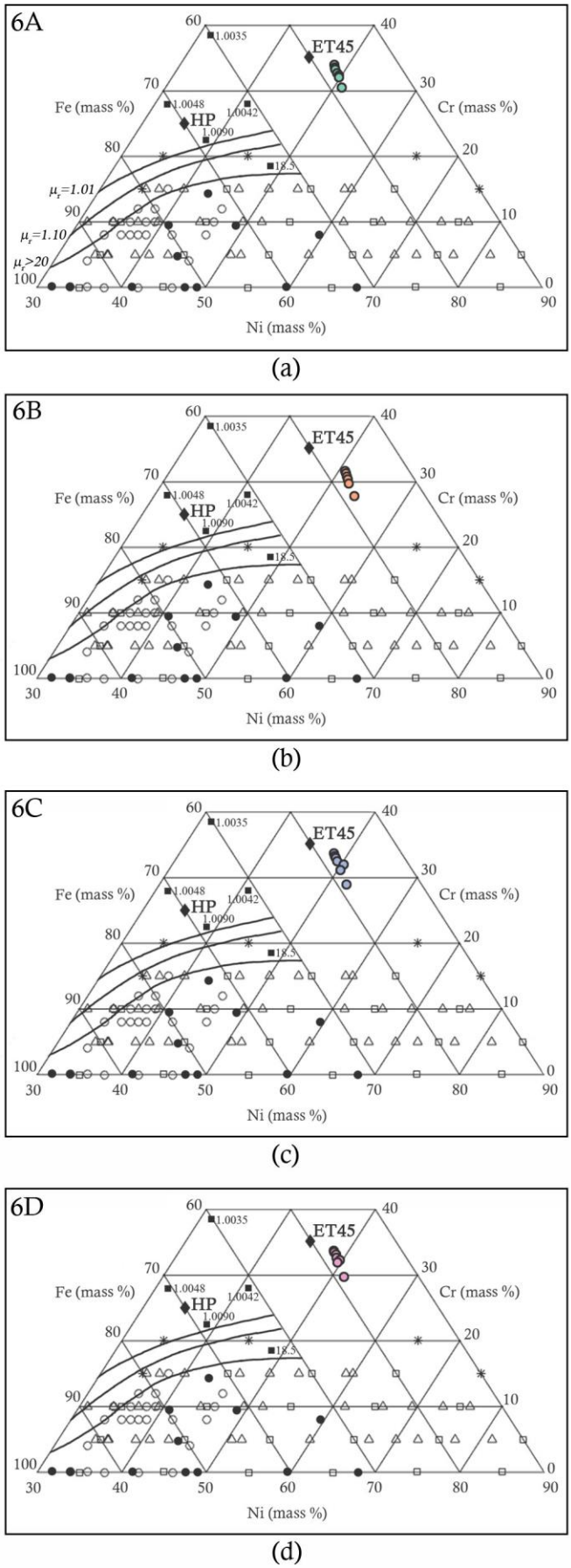

Figure 7.13 - Matrix chromium concentration and magnetic permeability on a section of the Gibbs triangle, for samples (a) 6A, (b) 6B, (c) 6C, and (d) 6D. Iso-μ_r lines are labelled in (a).

7.2 Eddy Current NDT Response

The eddy current NDT data was collected by Quest Integrity NZL Ltd, using a combination of manual collection methods and the tube crawler system that has been recently developed [1]. The manual inspection system and the tube crawler inspection system both use cylindrical coil probes. Prior to each measurement run, the instrumentation was allowed to warm up, and the response of the probe in air was then logged. Single measurements at each combination of longitudinal and angular positions were then made, with the longitudinal measurements at one angular location taken before progressing around the tube to the next angular location. However, due to the collection of the eddy current NDT data being performed by Quest Integrity NZL Ltd, the author does not know the sequence in which the measurements were taken, and how many angular locations were measured for each calibration of the probe response in air. Tubes 1 and 2 were measured using the crawler inspection system, whereas tubes 5 and 6 were measured using the manual inspection system. The 0° locations in tubes 3 and 4 were measured using the manual inspection system, and the remaining angular locations were measured using the crawler inspection system.

7.2.1 Depth of Eddy Current Penetration

As discussed in Section 2.6.3, the flow of eddy currents is not uniform through the thickness of the test piece. The eddy current flow is strongest at the surface, and decreases exponentially with distance from the surface. The standard depth of penetration, δ, is defined as the depth at which the density of eddy currents has reduces to $1/e$, or approximately 37%, of the surface density. The standard depth of penetration is dependent on the conductivity and magnetic permeability of the material, as well as the test frequency, as described by Equation 2.19. The standard depth of penetration is seen to decrease when conductivity, magnetic permeability, and frequency increase. As such, materials with high magnetic permeability are typically tested at low frequencies to allow for greater penetration into the test piece.

The high frequency response is therefore representative of the magnetic properties of the outer wall of the samples, as at high frequencies the depth of penetration into the sample wall from the outer surface will be low, as demonstrated schematically in Figure 7.14. The interpretation of the low frequency response of the samples is more complex. At low frequencies the eddy currents are able to penetrate a greater depth into the tube wall. However, the eddy currents do not only form at the maximum penetration depth, but are present in the material right through the sample wall up to the maximum penetration depth. As such, the low frequency response of the samples will be a combination of the magnetic properties for all material within which the eddy currents have formed, and not just the properties of the material at the maximum penetration depth.

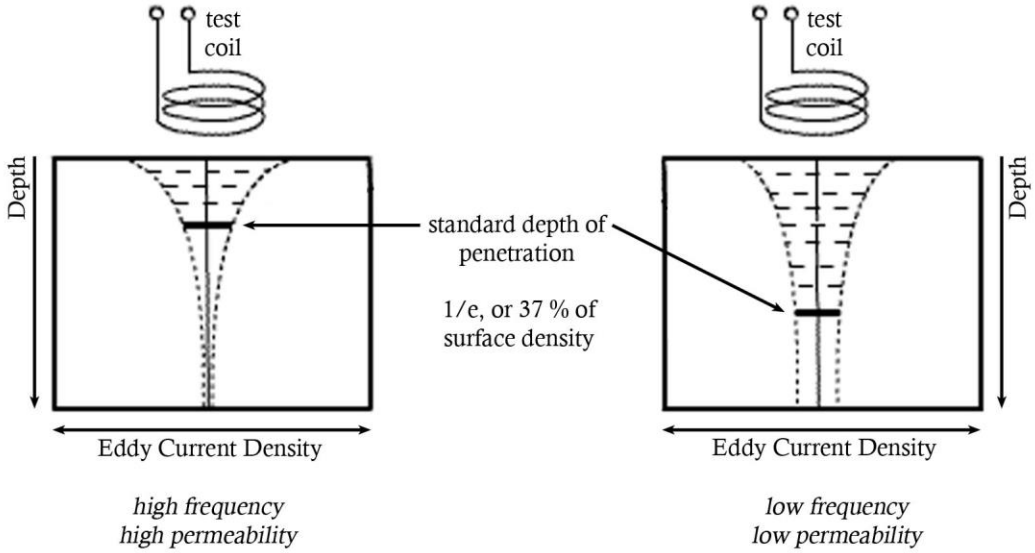

Figure 7.14 - Schematic demonstrating the depth of eddy current penetration with differences in frequency and magnetic permeability, for a cylindrical coil probe (adapted from [21]).

The normalised impedance plane, upon which the eddy current NDT response is observed, was presented in Figure 2.23. As discussed in Section 2.6.3, when the test probe is in proximity to a ferromagnetic material, both the probe inductance and probe resistance increase. The probe inductance increases as the primary magnetic field of the probe is concentrated. In an ideal case, only the inductance of the probe would increase and there would be no increase in resistive loss. In reality, increases in resistance are observed to accompany increases in inductance due to increased amounts of energy being dissipated to align the magnetic moments to the field [22].

7.2.2 Tubes 1 and 2

1D displays the highest response of the samples from tube 1 (Figure 7.15). As shown in Figure 7.3 (d), the matrix chromium concentration in sample 1D indicates that the entire wall thickness of the sample is in the ferromagnetic region of the Fe-Cr-Ni permeability diagram, with a relative magnetic permeability greater than 20 at all locations. As such, the sample shows elevated probe inductance at all frequencies. The relatively shallow slope in the high frequency range in Figure 7.15 is consistent with the very slight changes in matrix chromium concentration from 13 – 14 wt% at the outer 2 mm of the sample wall, as shown in Figure 7.2, and these points correspondingly being clustered in approximately the same region of the Cr-Fe-Ni Gibbs diagram in Figure 7.3 (d). The significant increase in normalised inductance up to a value of 1.86 at the lowest test frequency is consistent with a drop in the matrix chromium concentration at the inner wall of sample 1D to 5 wt%, and the spread of the inner wall points across the μ_r >20 ferromagnetic region as shown in Figure 7.3 (d). The range of normalised inductance values was seen to be 0.3.

The normalized inductance versus frequency response of sample 1A is overall lower in comparison to 1D, and the range of inductance values is also decreased (0.1 compared to 0.3). As summarised in Table 7.1, approximately 49 % of the wall thickness of sample 1A was expected to have a relative magnetic permeability above 20, with the remaining 51 % of the wall thickness displaying a magnetic permeability below 20. Despite the matrix chromium concentration at the inner wall of sample 1A reaching as low as 5 wt%, as in sample 1D, the value of normalised inductance displayed by sample 1A at low frequencies is significantly lower than that displayed by sample 1D (1.4 in comparison to 1.86). A slight decrease in normalised inductance in sample 1A is seen as frequency is increased, dropping to approximately 1.3 at high frequencies. The relatively consistent response across the high frequency range is consistent with sample 1A displaying matrix chromium concentration in the 20 – 21 wt% range over the outer 2.5mm of the wall thickness, and these values correspondingly being clustered together in the $\mu_r < 1.10$ region of the Fe-Cr-Ni Gibbs triangle, as shown in Figure 7.3 (a).

The greater normalised inductance response at high frequencies in sample 1D in comparison to sample 1A is likely due to the outer wall of sample 1D having a relative magnetic permeability above 20, whereas in sample 1A, 0.6 mm (9 %) of the wall thickness is expected to be in the $1.10 < \mu_r < 20$ range, and the remaining 3.0 mm (42 %) of the wall thickness is expected to have a relative magnetic permeability less than 1.10. The decreased range of normalised inductance values in sample 1A in comparison to sample 1D is likely due to the averaging effect of eddy currents as penetration depth into the tube wall increases (with decreased test frequency). At the lowest test frequency in sample 1A, the response will be a combination of 49 % ferromagnetic material, and 51 % paramagnetic material, where as in sample 1D the lowest frequency response is a combination of the entirely ferromagnetic wall.

The responses of samples 1B and 1C were not as expected. Sample 1C displayed a greater extent of matrix chromium depletion across the tube wall, but not quite to the same extent as sample 1D. Based on the matrix chromium concentration, the inner 4.1 mm (52 %) of the tube wall was expected to have a relative magnetic permeability above 20, and the remaining 3.7 mm (48 %) of the tube wall was expected to have a relative magnetic permeability below 20. As such, the normalised inductance response of sample 1C was expected to be slightly higher than that of sample 1A, and to have a slightly increased range of values. As shown in Figure 7.15, this was not the case, and the response of sample 1C was significantly lower in comparison to sample 1A, and with a reduced range in normalised probe inductance values (0.04 in comparison to 0.1).

Sample 1B displayed the smallest extent of carburization and carbide coarsening of all the samples from tube 1, and therefore displayed the greatest concentration of chromium in the matrix, The matrix chromium concentration was observed to be approximately 7 wt% at the inner wall, but this rapidly increased and remained at a value of 21 – 22 wt% for the majority of the wall thickness. Based on the matrix composition, only 1.9 mm (23 %) of the wall thickness of sample 1B was expected to have a

magnetic permeability above 20, and the remaining 6.5 mm (77 %) was expected to have a relative magnetic permeability below 20. As such the normalised impedance response of sample 1B was expected to be well below the response of the other three samples from tube 1, and to have a very small rage of normalised impedances; however, as can be seen in Figure 7.15 this was again not the case, and the response was similar to that of sample 1A.

The microstructure of tube 2 was seen to be consistent across the four samples analysed, and as such they displayed similar matrix chromium concentration profiles, as shown in Figure 7.4. In comparing the matrix chromium profiles to those of the samples from tube 1, it was expected that the magnetic response of the tube 2 samples would lie in between the response of samples 1D and 1A. As shown in Figure 7.15, this was the case for samples 2B, 2C, and 2D.

The normalised inductance profiles for samples 2B and 2D displayed an elevated response, and a wide range of values. The maximum normalised inductance at the lowest test frequency attained a value of approximately 1.7, and this dropped to a value of 1.45 – 1.46 at the highest test frequency. The range of normalized inductance values displayed by samples 2B and 2D was thus 0.24 – 0.25. In comparison to sample 1D, in which the matrix was seen to be ferromagnetic across the entire wall, samples 2B and 2D were expected to contain 4.0 mm (57 %) and 4.9 mm (69 %) ferromagnetic material with relative magnetic permeability above 20. The remainder of the wall thickness in samples 2B and 2D stayed within the permeability range $1.10 < \mu_r < 20$.

The normalised inductance values for sample 2C were observed to be in-between those of samples 1A and 1D, as expected. However, the range in normalised inductance was lower than the range displayed by samples 2B and 2D (0.1 in comparison to 0.24 – 0.25), and the values were also lower, with the maximum value being 1.45 and dropping to 1.35 at the outer wall. The matrix chromium concentration measurements from sample 2C indicated that 4.6 mm (65 %) of the wall thickness should be composed of ferromagnetic material with a relative magnetic permeability above 20, and that the remainder of the wall thickness should remain in the $1.10 < \mu_r < 20$, which would have been expected to result in a response near identical to that of samples 2B and 2D.

The normalised inductance response of samples 2A was well below what was expected based on the matrix chromium concentration. The wall thickness of 2A was expected to be composed of 4.5 mm (69 %) of material with a relative magnetic permeability greater than 20, and the remaining 2.5 mm (36 %) of the wall thickness was expected to be in the $1.10 < \mu_r < 20$ range. This is almost identical to sample 2C. However, sample 2A displayed a decreased range in normalised inductance values (0.03 compared to 0.1), and the overall normalised inductance values remained low in the range of 1.17 – 1.2.

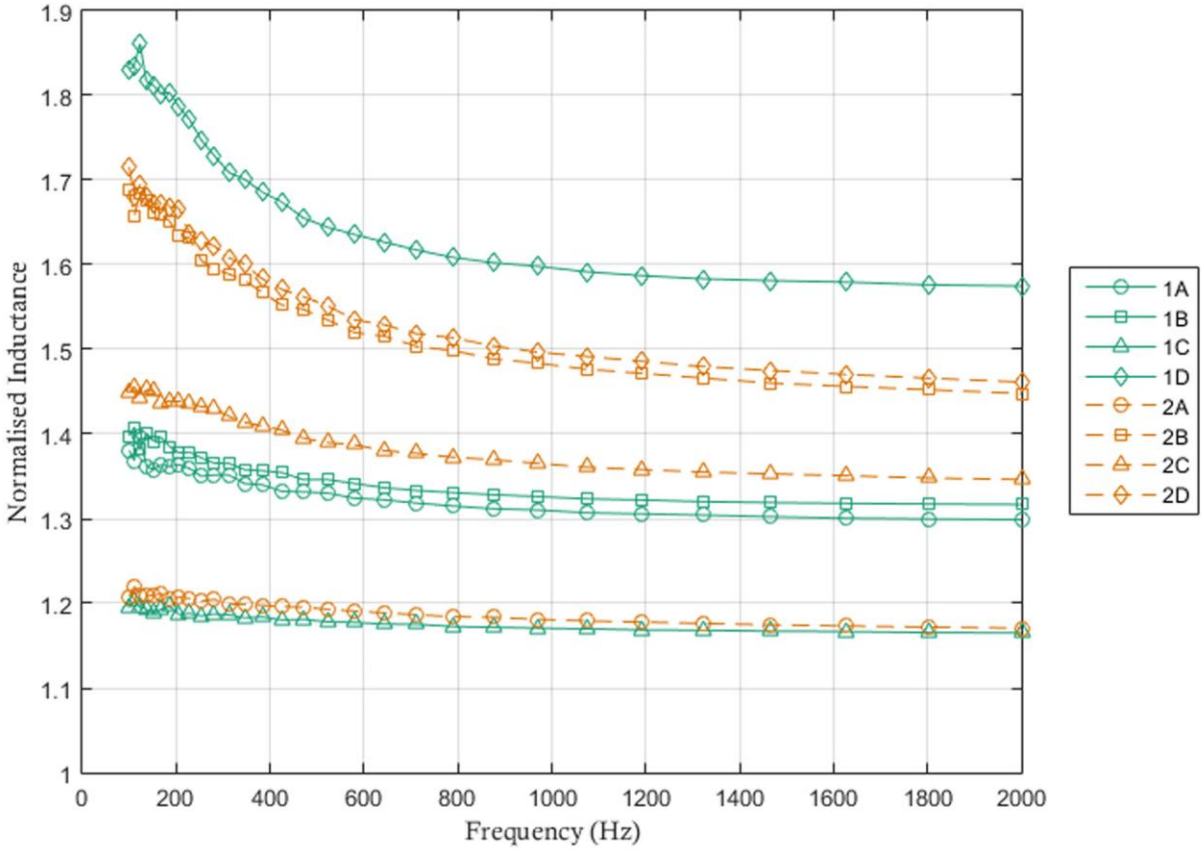

Figure 7.15 - Normalised probe inductance versus test frequency response for tubes 1 and 2.

7.2.3 Tubes 3, 4, and 6

It was observed that the data point at the highest test frequency deviated on occasion from the general trend in the remainder of the data, as can be seen for samples 3B, 3D, 4B, and 4D in Figure 7.16. If it was an artefact of the test probe, then the deviation would be expected to occur at all measurement locations, and not just on occasion. However, it also does not seem to correlate with microstructural features, such as the degradation at the outer diameter due to exposure to flue gases. Quest Integrity NZL Ltd has not reported observing this deviation in recent tests. Despite not knowing why the deviation at the highest test frequency occurs on occasion, the points at the highest test frequency that deviate significantly from the general trend in the data are displayed on the plots but omitted in the data analysis.

The microstructure of tube 3 was seen to display minimal coarsening of the primary chromium-rich precipitates, and despite the precipitation of σ-phase there was not a significant amount of matrix chromium depletion. The microstructure and matrix chromium concentration profiles were observed to be consistent across the four samples analysed, and the minimal matrix chromium depletion (as shown in Figure 7.6) was expected to result in the matrix in all locations in all samples to remain in the μ_r <1.10 range, as demonstrated in Figure 7.7. This was reflected in the eddy current NDT response. As shown in Figure 7.16, the normalised inductance of all four samples remained

consistently low, and the variation of normalised inductance with frequency was minimal, remaining within the range of 1.01 – 1.05 across all frequencies for all samples. This is consistent with the relatively homogenous microstructure and predicted lack of ferromagnetic material.

As with tube 3, the microstructure of tube 4 was seen to display minimal coarsening of the primary $M_{23}C_6$ precipitates. Aside from a fine distribution of $M_{23}C_6$ precipitates that was expected to compose < 2 % of the total volume fraction, no other chromium-rich phases were identified. The matrix chromium concentration was observed to remain within the 21.5 – 22.5 wt% range at all locations in all samples, as shown in Figure 7.8, and as a result the matrix at all locations in all samples was expected to remain in the $\mu_r < 1.0$ range, as demonstrated in Figure 7.9. The normalised inductance response with respect to test frequency for tube 4 is shown in Figure 7.16. The response of samples 4A and 4C was as expected – very little change in normalised inductance with frequency, and a low overall normalised inductance in the range of 1.02 – 1.08, consistent with the response of the tube 3 samples

The elevated response of samples 4B and 4D was unexpectedly high. The normalised inductance values of sample 4B ranged from 1.3 at low frequencies to 1.25 at high frequencies, and the values for sample 4D ranged from 1.23 at low frequencies to 1.19 at high frequencies. The range in normalised inductance values was thus 0.05 for 4B, and 0.04 for 4D, higher than the range in values of 0.01 displayed by samples 4A and 4C. Samples 4A and 4C were taken from the same angular location on the tube (0°), and the samples 4B and 4D from the opposite side (180°). The deviation of samples 4B and 4C from the expected response, as displayed by samples 4A and 4C, may therefore be a result of errors incurred during the collection of the eddy current NDT data.

The range of normalised inductance values for samples 6A, 6B, and 6D was as expected – a range of < 0.02, consistent with the entire wall thickness of the samples remaining within the paramagnetic regions of the Fe-Cr-Ni Gibbs triangle shown in Figure 7.13. The response of sample 6C showed a slightly greater range of values of normalised inductance (0.04), and the position on the normalised inductance scale was well elevated above the other three samples (a maximum of 1.3, in comparison to ≤ 1.1), as shown in Figure 7.16.

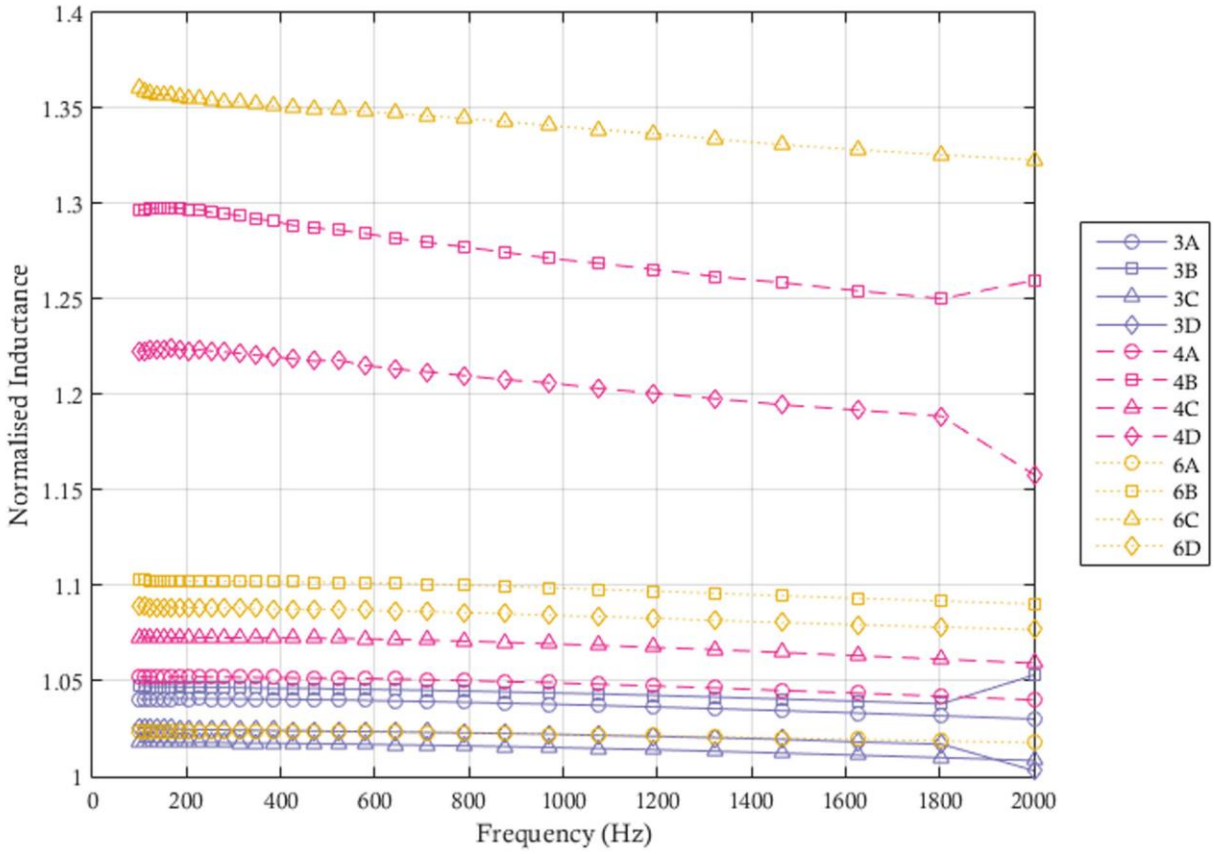

Figure 7.16 - Normalised probe inductance versus test frequency response for tubes 3, 4, and 6.

7.2.4 Tube 5

The matrix chromium concentration profiles in samples 5A-C were observed to be very similar, and as a result the amount of ferromagnetic material in each sample was expected to be similar, as summarised in Table 7.5, with slight variations due to the variations in wall thickness between the samples. Samples 5A-C were expected to contain 1.7 – 1.9 mm (21 – 24 %) of material with a relative magnetic permeability greater than 20. 0.3 – 0.4 mm (4 – 5%) of the tube wall was expected to have a relative magnetic permeability in the $1.10 < \mu_r < 20$ range, and the remaining 5.5 – 6.3 mm (71 – 74%) of the wall thickness in each sample was expected to remain in the paramagnetic region, as shown in the Fe-Cr-Ni Gibbs triangles in Figure 7.11 (a) – (c). In comparison to samples 5A-C, sample 5D displayed a greater extent of matrix chromium depletion across the tube wall. The matrix chromium concentration at the inner wall of sample 5D dropped to 7.7 wt%, as with samples 5A-C; however, due to larger chromium carbide volume fractions the increase up to approximately 21 wt% at the outer diameter was observed to occur more gradually than samples 5A-C, as shown in Figure 7.10. As a result, sample 5D was expected to contain an increased amount of ferromagnetic material in comparison to samples 5A-C. The inner 3.4 mm (45 %) of the wall thickness in sample 5D was expected to have a relative magnetic permeability greater than 20, and 1.0 mm (13 %) to fall within the $1.10 < \mu_r < 20$ range. The remaining 3.2 mm (42 %) of the wall thickness was expected to remain

in the paramagnetic region, as shown in Figure 7.11 (d). In comparison to samples from tubes 1 and 2, the response of samples 5A-C was expected to be very similar to that of sample 1B, as the matrix chromium concentration profiles and thus the amount of matrix material in each of the magnetic regions was expected to be near identical. However, as shown in Figure 7.17, the magnetic response of the samples from tube 5 appeared to be dependent more on sample location than microstructure and matrix chromium concentration.

As summarised in Table 3.1, Sample 5A and 5C came from the 90° angle of tube 5, at lengths of 200 mm and 120 mm respectively, whereas samples 5B and 5D came from the 270° location, also at lengths of 200 mm and 120 mm respectively. Although the range of normalized inductance values was similar for the two angular locations, at approximately 0.05 – 0.07, the samples from the 90° location displayed an overall normalised inductance response with a value of 0.1 higher than the samples from the 270° location. Sample 5D displayed a response on par with samples 5A-C, despite being expected to display a greater range in normalized inductance values and an overall greater normalized inductance response.

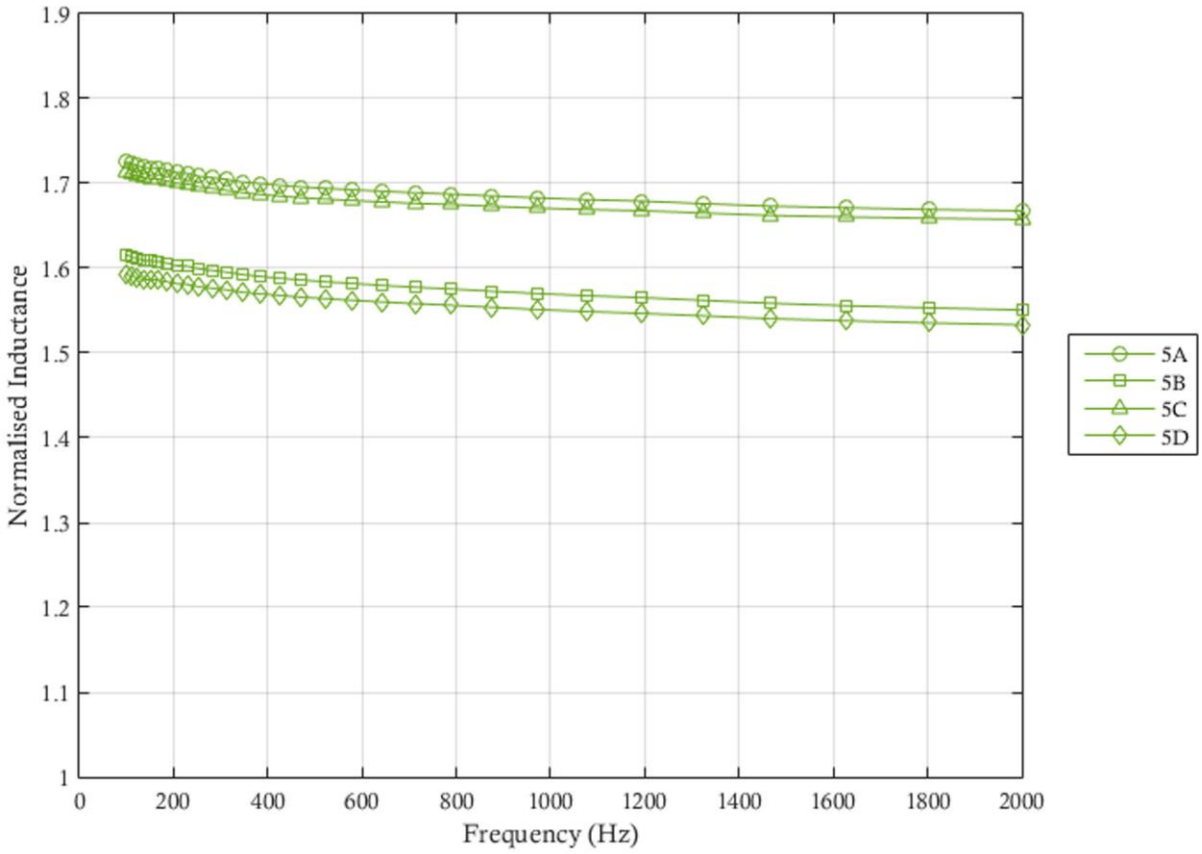

Figure 7.17 - Normalised probe inductance versus test frequency for tube 5.

7.2.5 Interpretation of Results and Deviation from Expected Response

As discussed in Section 2.6.4, impedance plane analysis by Stevens and Trompetter [23] and Stevens *et al*. [14] using a finite element model and measurement of carburized tubes determined the varying expected responses of tubes depending on the level of carburization. It was determined that a tube highly carburized across the whole wall would display a normalised probe inductance across all frequencies, well elevated above the response in air. A tube with a high level of carburization at the inner diameter but a low level of carburization at the outer would display a moderate normalised probe inductance at low frequencies, but this would decrease at high frequencies. A tube with little or no carburization would display a low normalised probe inductance independent of frequency. The response of samples 1A, 1D, 2B, 2D, 3A-D, 4A, 4C, 6A, 6B, and 6D were consistent with these observations. A summary of the magnetic response of these samples is shown in Table 7.7. The minimum and maximum normalised probe inductance values reported are the absolute minimum and maximum values, and the range reported is the difference between the minimum and maximum values. Figure 7.18 displays comparisons between the range in normalised inductance, the maximum value of normalised inductance, and the wall thickness in which $\mu_r > 20$, for all samples.

Table 7.7 - Summary of magnetic response of tube samples in descending order, for those samples where the magnetic response was consistent with the predictions based on the matrix chromium concentration.

Sample	Wall thickness in which $\mu_r > 20$	Range in normalised probe inductance	Minimum normalised probe inductance	Maximum normalised probe inductance
1D (t ≈ 7.3 mm)	7.3 mm (100 %)	0.3	1.56	1.86
2D (t ≈ 7.1 mm)	4.9 mm (69 %)	0.25	1.45	1.7
2B (t ≈ 7.0 mm)	4.0 mm (57 %)	0.24	1.46	1.7
1A (t ≈ 7.0 mm)	3.4 mm (49 %)	0.1	1.3	1.4
6B (t ≈ 8.8 mm)	0 mm (0 %)	0.01	1.09	1.10
6D (t ≈ 8.6 mm)	0 mm (0 %)	0.01	1.08	1.09
4C (t ≈ 7.0 mm)	0 mm (0 %)	0.01	1.06	1.07
4A (t ≈ 7.1 mm)	0 mm (0 %)	0.01	1.04	1.05
3B (t ≈ 7.0 mm)	0 mm (0 %)	0.01	1.04	1.05
3A (t ≈ 7.0 mm)	0 mm (0 %)	0.01	1.03	1.04
3D (t ≈ 6.8 mm)	0 mm (0 %)	0.01	1.02	1.03
6A (t ≈ 10.4 mm)	0 mm (0 %)	0.01	1.02	1.03
3C (t ≈ 7.2 mm)	0 mm (0 %)	0.01	1.01	1.02

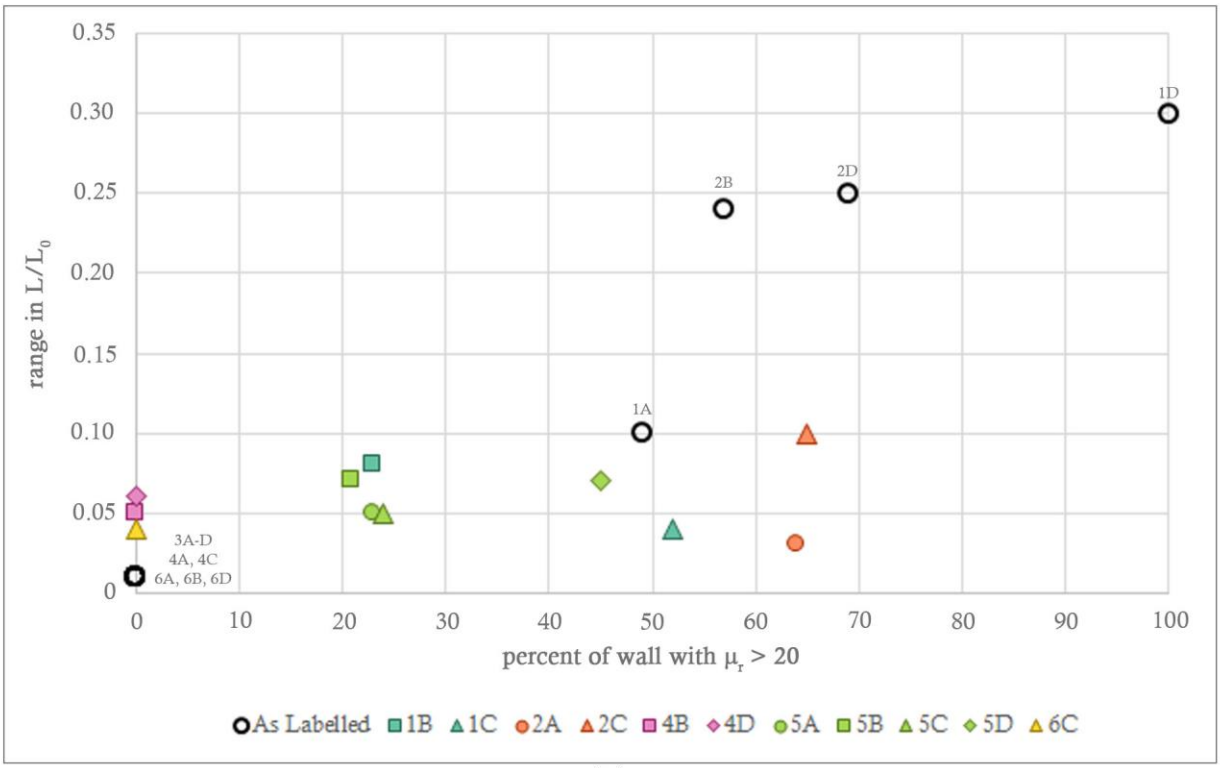

(a)

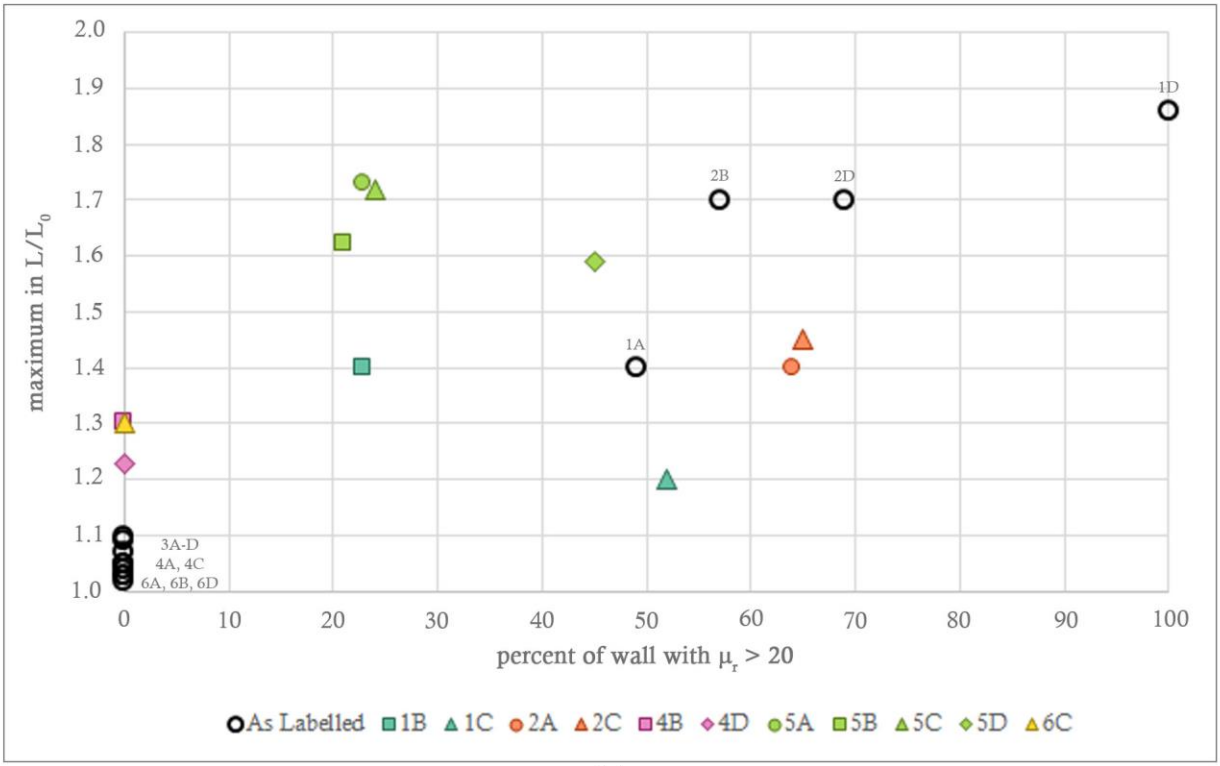

(b)

Figure 7.18 - Comparison between the (a) range and (b) maximum value of normalised probe inductance with the percent of the wall for which $\mu_r > 20$, for all samples. Those samples for which the magnetic response was as predicted are represented by open black circles and labelled. Those samples for which the magnetic response deviated from the predicted response are shown as filled shapes as specified in the legend.

Sample 1D displayed a matrix composition that lay entirely within the $\mu_r > 20$ range, and consequently displayed the highest normalised probe inductance, with a maximum value of 1.85, and the response remained high across the high test frequencies consistent with the high level of carburization and chromium depletion observed across the wall thickness. Samples 2B and 2D, which displayed similar matrix chromium concentrations as 1D at the inner wall but only 64 – 69% of their wall thicknesses within the $\mu_r > 20$ region displayed a slightly smaller range in normalised probe inductance values (0.24 – 0.25, in comparison to 0.3 in 1D) and at a lower point on the normalised inductance axis. These samples achieved a maximum normalised probe inductance of 1.7. Sample 1A, which also displayed the same matrix chromium concentration at the inner diameter, but only 49 % of the wall within the $\mu_r > 20$ range displayed a corresponding decrease in range of normalised inductance values (only 0.1) and a lower value of maximum normalised probe inductance (1.45). The tube 3, 4, and 6 samples that displayed little chromium carbide coarsening and consequently matrix compositions entirely within the paramagnetic range displayed minimal changes in the normalised probe inductance with frequency. As shown in Figure 7.18, the range of normalised probe inductance values and the maximum normalized probe inductance value both display a general trend where both increase when the amount of material in the tube with compositions in the $\mu_r > 20$ range increases.

There were a significant number of magnetic response results that were not as predicted based on the measured matrix compositions and the magnetic permeability data shown in Figure 7.1. As discussed in Section 2.6.3, there are a number of factors that can influence the normalised inductance plane response of a material. The conductivity of a material (i.e. its ability to conduct electricity) is seen to vary with changes in composition; however, small variabilities in magnetic permeability are reported to have a greater effect on the eddy current response than small changes in electrical conductivity. This is reported to be particularly true at low test frequencies [9]. In the case of carburized tubes, the lowest test frequencies are used to measure the response in the most highly carburized regions that will have undergone the greatest changes in composition, but also the greatest changes in magnetic permeability, so the changes in electrical conductivity are unlikely to significantly change the eddy current response.

The samples from the ex-service tubes displayed variations in wall thickness, both between samples from the same tube and between the different tubes. If the wall thickness is less than approximately three times the standard depth of penetration, the distribution of eddy currents in the material can become distorted, with the extent of distortion varying with the change in thickness, as demonstrated schematically in Figure 7.19. If the test sample is thin enough, a change in thickness will therefore result in changes in the coil impedance due to the change in the distribution of the eddy currents. However, despite the samples from tube 2 displaying very similar wall thicknesses and being expected to contain approximately the same amount of ferromagnetic material and thus display a similar normalised probe inductance, there was variation in the response between the samples. Additionally,

the sample from tube 6 that displayed a normalised probe inductance higher than the other three tube 6 samples had a wall thickness that was in the middle of the range for the tube six samples. It thus appears that distortions in the eddy current distribution due to variances in wall thickness are not the culprit for the deviations from expected response observed in the current samples.

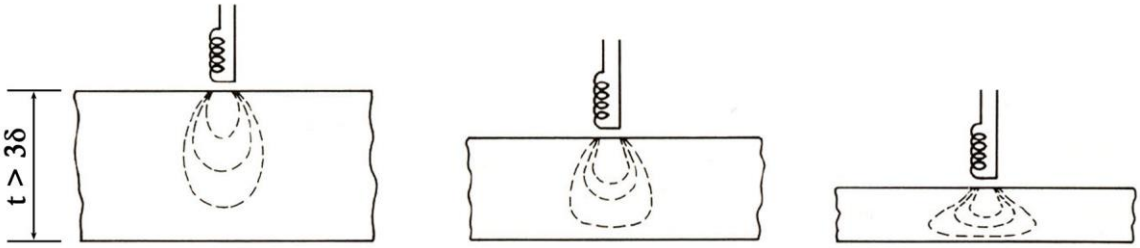

Figure 7.19 - Schematic demonstrating the distortion of an eddy current distribution in thin samples (adapted from [9]).

One of the most likely candidates for the deviation from the expected response is lift off. As discussed in Section 2.6.3, lift off is defined as the impedance change that occurs when the distance between the test probe and the test piece changes. As the distance between the probe and the test piece decreases, the eddy current density increases, and therefore there will be an increased change in the probe inductance with respect to the probe values in air. In samples such as those from tubes 3, 4, and 6 that display a low normalised probe inductance due to low magnetic permeability, the effect of lift off on the probe inductance may overshadow the features of interest – i.e. any slight changes in probe impedance due to microstructural variance. Minimisation in the variation in distance between the probe and the test piece is therefore important, but can be difficult to achieve during inspection, especially when the test piece surface is curved as with a tube. As such, the elevated response of samples 4B, 4D, and 6D (in both range and maximum normalised inductance, as shown in Figure 7.18) may be a result of unintentional changes in the lift off when data was collected. However, whilst the effects of variances in lift off may have an effect on the normalised probe inductance of alloy compositions with low values of relative magnetic permeability, the exact changes in normalised probe inductance have not been quantified. A series of experiments on as-cast tubes or tubes with little to no carburization in which the lift off was systematically varied and the subsequent changes in probe inductance recorded would enable confirmation of whether the elevated normalised probe inductance values displayed by samples 4B, 4D, and 6D are due to lift off, or whether they are due to some as yet unknown factor. The development of the carburization crawler by Quest Integrity will go some ways to limiting variances in lift off, as the automated movement removes operator error in positioning the test probe, and enables a consistent distance between the test probe and the tube to be maintained.

The lack of known values for the relative magnetic permeability of Fe-Cr-Ni alloys in the region of low chromium concentrations in the austenite matrix complicates the interpretation of the results from

the moderately and highly carburized tubes (1, 2, and 5). The values of relative magnetic permeability for the wall regions of these tubes where the matrix chromium concentration is below 15 wt% are unknown, but based on the rapid increase in relative magnetic permeability from 1.10 to 20 with a drop in matrix chromium concentration from 18 to 15 wt%, the change in relative magnetic permeability associated with a drop from 15 wt% to 5 wt % would be expected to be significant. As such, it is difficult to determine whether changes in probe inductance as a result of lift-off are big enough to overshadow the changes in probe inductance as a result of increased magnetic permeability, in particular in the tube 5 samples that display moderate levels of carburization and thus only moderate amounts of ferromagnetic material, and tube 1 and 2 samples that display high levels of carburization and thus significant amounts of ferromagnetic material.

As shown in Figure 7.18, the range of normalised inductance values for sample 1B could be considered reasonable in comparison to other samples, however its maximum value was higher than expected. Both the range and the maximum normalised inductance were considerably lower than expected for sample 1C. The range for samples 2A and 2C was lower than might be expected based on the matrix chromium concentration, but their maximum normalised inductance values could be considered reasonable in comparison to other samples. Conversely, the range for samples 5A-C could be considered reasonable in comparison to the other samples, but their maximum values of normalised inductance were higher than expected based on their matrix chromium concentrations. Sample 5D displayed values for the range and maximum normalised inductance that appeared relatively consistent with the general trend for a sample with 5D's amount of ferromagnetic material, however as shown in Figure 7.17 it displayed the same response as sample 5B despite containing significantly more ferromagnetic material. It was considered that the depth (in mm) from the outer surface of the samples to the point where μ_r increased above 20 may have better correlated with the magnetic response than the percent of the wall region in which $\mu_r > 20$. However, comparing these measurements with the magnetic response provided no further insight into why some samples deviated from the predicted response.

In addition to lift-off experiments on as-cast tubes, lift-off experiments on tubes with varying levels of carburization would enable the effect of lift-off on the response of tubes with ferromagnetic material to be better understood, despite the current lack of knowledge of relative permeability values for tubes with significant levels of chromium depletion in the austenite matrix. However, knowledge of the relative magnetic permeability values for matrix compositions with low chromium concentration would also assist in enabling simulation of the additive nature of the response as the test frequency decreases and penetration into the tube wall increases. As described by Equation 2.19, the standard depth of penetration of the eddy currents decreases when frequency, conductivity, and magnetic permeability increase. With knowledge of the magnetic permeability for a wider range of low-chromium compositions, the standard depth of penetration with respect to frequency could be

simulated or calculated based on the matrix chromium concentration at various wall locations, and a better understanding of the relationship between test frequency and wall position could be achieved.

Measurements of magnetic permeability of cast Fe-Cr-Ni alloys within the chromium-depleted austenite composition range would require the casting of a number of alloy compositions. The wide range of Fe-Cr-Ni compositions tested by Saori and Ohta [20] would not be necessary - focusing the compositions along the matrix chromium concentration profiles plotted on the Fe-Cr-Ni Gibbs triangles for tubes 1 and 2 (Figure 7.3 and Figure 7.5 respectively) would be the most appropriate for the current application.

Eddy Current NDT Response and Creep Performance

Difficulties arise in comparing the creep performance of the carburized microstructures to the eddy current NDT response due to the large number of unknowns present in the magnetic response analysis. In general, those tubes that displayed microstructures that were consistent across the tube wall (tubes 3, 4, and 6) and primary precipitate volume fractions up to 20 % displayed steady state creep rates on the order of 10^{-6} to 10^{-5} /h. These tubes did not display significant depletion of chromium in the austenite matrix, and subsequently typically displayed a low range in normalised inductance values (0.01), and a maximum value ≤ 1.10. The tubes that displayed primary precipitate volume fractions above 20 % displayed steady state creep rates on the order of 10^{-4} /h (tubes 1 and 2). These tubes contained significant amounts of ferromagnetic matrix material (49 – 100 % of the wall thickness) as a result of the depletion of chromium in the austenite matrix, and consequently typically displayed a greater range in normalised inductance values (0.24 – 0.1) and significantly higher maximum normalised inductance values (1.4 – 1.86) in comparison to the tubes with creep rates on the order of 10^{-4} to 10^{-5} /h. A comparison between the creep performance and the eddy current NDT response of the tube 5 sample is not possible due to the significant deviations in the magnetic response from that predicted based on the matrix compositions of this tube.

A more in-depth analysis of the relationship between creep performance and the magnetic response of the various carburized microstructures would be enabled if data on the relative magnetic permeability of the low-chromium austenite compositions was available. As previously mentioned, this would enable the standard depth of penetration with respect to the test frequency to be calculated based on the matrix chromium concentration. From this, a better understanding of the relationship between the test frequency and wall position could be achieved, and the frequency ranges and thus the portion of the response that corresponds with the wall positions of the creep samples could be determined and analysed.

7.3 Summary and Conclusions

The concentration of chromium in the matrix of the samples of the six ex-service tubes was measured by reconstructing spectra from EDS map data, and compared to the magnetic permeability data compiled for Fe-Cr-Ni alloys by Stevens *et al.* [15] and [20] and Saori and Ohta. When the matrix chromium concentration remained above 18 wt%, the relative magnetic permeability of the tubes was seen to remain with the paramagnetic region, with a value of $\mu_r < 1.10$. When the matrix composition dropped below 15 wt% chromium, the relative magnetic permeability was seen to increase above 20, and become ferromagnetic. For matrix chromium concentrations in the 15 – 18 wt% range, the relative magnetic permeability was seen to be in the range of $1.10 < \mu_r < 20$, slightly ferromagnetic. Due to such a rapid increase in relative magnetic permeability from 1.10 to 20 with a drop in matrix chromium concentration of only 3 wt%, depletion of the matrix chromium concentration to values as low as 5 wt%, as seen in the inner wall regions of the most highly carburized tubes, would be expected to be accompanied by significant increase in relative magnetic permeability. Unfortunately, data values for the $\mu_r > 20$ region are not available in the literature.

The response of samples 1A, 1D, 2B, 2D, 3A-D, 4A, 4C, and 6A-C was seen to be consistent with the simulated and observed responses of Stevens and Trompetter [23] and Stevens *et al.* [14]. Sample 1D, which contained the greatest amount of ferromagnetic material, was observed to display the largest range in normalised probe inductance values (0.3) and the highest normalised probe inductance values overall (a maximum of 1.86). With decreasing amounts of ferromagnetic material, the range in inductance values decreased, as did the overall normalized probe inductance values. Those samples that were predicted to contain no ferromagnetic material displayed very low normalized inductance values, ≤ 1.10, that were relatively independent of the test frequency.

The increase in range with increased amounts of ferromagnetic wall region is likely due to the eddy current response at low frequencies (and therefore greater penetration depths) being a combination of the magnetic response across all the wall locations in which eddy currents are present. An increase in the proportion of the wall region that displays ferromagnetic properties would result in an increased normalised probe inductance over a wider range of depth, and therefore test frequencies. With progressively greater chromium depletion, the extent of ferromagnetism displayed by the material would be expected to progressively increase, i.e. an increase in the value of relative magnetic permeability. Thus, the regions at the inner wall that display the greatest values of relative magnetic permeability will concentrate the primary magnetic field of the test probe to a greater extent than the regions with a lower value of magnetic permeability slightly further into the tube wall. This results in an increase in the normalised probe inductance at the lowest test frequencies as the lowest test frequencies correspond with the greatest depths of penetration.

Lift off, i.e. variance in the distance between the test probe and the test piece, was seen to potentially affect the response of those samples that displayed low values of relative magnetic permeability across the wall thickness. Increased proximity of the probe to the surface of the test piece results in increased eddy current density, and therefore an increased probe inductance relative to the probe in air. Such variations in probe inductance due to lift off may overshadow the small variations in magnetic properties in those samples that are predicted to contain little or no ferromagnetic material. Measurements of the change in probe inductance with variation in the distance between the test probe and the sample surface on tubes with little or no carburization would provide a means of quantifying the effects of lift off.

The lack of knowledge of the values of relative magnetic permeability for matrix chromium contents below 15 wt% makes it difficult to determine the reason that some samples displayed magnetic responses that were not consistent with their predicted magnetic properties. Magnetic permeability measurements of Fe-Cr-Ni alloys within the range of the matrix chromium compositions in the $\mu_r >$ 20 regions of tubes 1 and 2 would enable a greater understanding of the eddy current response of tubes that are predicted to contain large amounts of ferromagnetic material, and why some of the predicted responses did not come to fruition. Additionally, with the direct contribution of the volume fraction of the chromium containing phases in the carburized tubes to the matrix chromium depletion being confirmed, analysis of solely the matrix composition for prediction of magnetic response allows the time-consuming step of microstructural characterization to be removed from the process. Knowledge of the relative magnetic permeability values for low-chromium compositions, coupled with the use of solely EDS measurements of matrix composition, would allow for a much wider range of carburized samples to be analysed and compared with the normalised probe inductance response in a rapid and more accurate manner.

In general, the tubes that displayed steady state creep rates on the order of 10^{-5} to 10^{-6} /h contained less than 20 % volume fraction of primary precipitates, displayed minimal chromium depletion in the austenite matrix, and subsequently typically displayed a low range in normalised inductance values (0.01) and a low maximum normalised inductance value (≤1.10). The tubes that displayed steady state creep rates on the order of 10^{-4} /h contained greater than 20 % volume fraction of primary precipitates, displayed significant amounts of matrix chromium depletion and thus contained significant amounts of ferromagnetic material. As a result, these tubes typically displayed a greater range in normalised inductance (0.24 – 0.1) and higher maximum normalised inductance (1.4 – 1.86) in comparison to the tubes with creep rates on the order of 10^{-5} to 10^{-6} /h. Knowledge of the relative magnetic permeability of the low chromium austenite compositions would enable the regions of the magnetic response that correlate with the creep sample wall positions to be determined, and a more in-depth analysis of the relationship between creep rate and magnetic response to be performed.

Chapter References

[1] Quest Integrity Group. *Ethylene Pyrolysis Tube Inspection System*. [cited 27/05/2015; Available from: http://www.questintegrity.com/services/inspection-services/ethylene-pyrolysis-tube-inspection.

[2] Lang, E. and Norton, J. *Monitoring of carburisation by the use of magnetic techniques, Part 1: Fundamental aspects and measurements on 25Cr-20Ni steels*. 1986, Commission of the European Communities, Physical Science, PETTEN, EUR 10566 EN.

[3] Jiles, D.C. *Introduction to magnetism and magnetic materials*. 1998: CRC press.

[4] Serway, R.A. and Jewett, J.W. *Physics for Scientists and Engineers with Modern Physics*. 7th ed. 2008: Thomson Higher Education.

[5] García-Martín, J., Gómez-Gil, J., and Vázquez-Sánchez, E. *Non-Destructive Techniques Based on Eddy Current Testing.* Sensors, 2011. **11**(3): p. 2525-2565.

[6] Guru, B.S. and Hiziroglu, H.R. *Electromagnetic Field Theory Fundamentals*. 2004: Cambridge University Press.

[7] Hellier, C. *Handbook of Nondestructive Evaluation*. 2001, McGraw-Hill Professional.

[8] Blitz, J., King, W.G., and Rogers, D.G. *Electrical, Magnetic and Visual Methods of Testing Materials*. 1969, London: Butterworths.

[9] Hull, B. and John, V. *Non-Destructive Testing*. 1988, London: Macmillan Education Ltd.

[10] Mucek, M.W. *Laboratory detection of degree of carburization in ethylene pyrolysis furnace tubing.* Materials Performance, 1983. **22**(9): p. 25-28.

[11] Kasai, N., Ogawa, S., Oikawa, T., Sekine, K., and Hasegawa, K. *Detection of carburization in ethylene pyrolysis furnace tubes by a C core probe with magnetization.* Journal of Nondestructive Evaluation, 2010. **29**(3): p. 175-180.

[12] da Silva, I.C., da Silva, R.S., Rebello, J.M.A., Bruno, A.C., and Silveira, T.F. *Characterization of carburization of HP steels by non destructive magnetic testing.* NDT & E International, 2006. **39**(7): p. 569-577.

[13] Silva, I.C., Rebello, J.M.A., Bruno, A.C., Jacques, P.J., Nysten, B., and Dille, J. *Structural and magnetic characterization of a carburized cast austenitic steel.* Scripta Materialia, 2008. **59**(9): p. 1010-1013.

[14] Stevens, K.J., Tack, A.J., Thomas, C.W., and Stewart, D. *Through-wall carburization detection in ethylene pyrolysis tubes.* Journal of Physics D (Applied Physics), 2001. **34**(5): p. 814-22.

[15] Stevens, K.J., Parbhu, A., Soltis, J., and Stewart, D. *Magnetic force microscopy of a carburized ethylene pyrolysis tube.* Journal of Physics D (Applied Physics), 2003. **36**(2): p. 164-8.

[16] Stevens, K.J., Parbhu, A., and Soltis, J. *Magnetic force microscopy and cross-sectional transmission electron microscopy of carburised surfaces.* Current Applied Physics, 2004. **4**(2-4): p. 304-307.

[17] Chevenard, P. *La precision en metallurgie et la metallurgie de precision.* Mem. Soc. Ing. Civ.(France), 1951. **104**: p. 1-44 (in French).

[18] Hara, T., Okiyama, T., and Takemoto, T. *Improvement of soft magnetic properties by Cr addition for Fe-(34-46) mass% Ni alloys.* Journal of the Japan Institute of Metals (Japan), 1996. **60**(11): p. 1136-1142 (in Japanese).

[19] Jackson, L.R. and Russell, H.W. *Temperature-sensitive magnetic alloys and their uses.* Instruments, 1938. **11**(11): p. 280-282.

[20] Saori, M. and Ohta, S. *Carburization and its prevention in ethylene cracking furnace tubes*. in *Proceedings of 3rd JIM International Symposium: High Temperature Corrosion of Metals and Alloys (Japan Institute of Metals).* 1982. Lake Yamanaka, Jpn: Japan Inst of Metals.

[21] NDT Education Resource Center. [cited January 2016]; Available from: https://www.nde-ed.org/EducationResources/CommunityCollege/EddyCurrents/Physics/depthcurrentdensity.htm.

[22] Shull, P.J. *Nondestructive evaluation: theory, techniques, and applications*. 2002: CRC press.

[23] Stevens, K.J. and Trompetter, W.J. *Calibration of eddy current carburization measurements in ethylene production tubes using ion beam analysis.* Journal of Physics D (Applied Physics), 2004. **37**(3): p. 501-9.

Chapter 8: Summary and Concluding Remarks

The primary objective of the current project was to characterize in detail the microstructures of ex-service ethylene pyrolysis tubes, and determine the microstructural features that influence the mechanical and magnetic properties. The information gained is to be used in improving the microstructural and materials data inputs into finite element models that simulate the service conditions and stresses experienced by various pyrolysis furnace geometries over multiple thermal cycles, and to also improve the interpretation of the eddy current non-destructive testing response and how it relates to the features in the carburized microstructure and subsequent mechanical properties, in order to improve the accuracy of remaining life estimates.

8.1 Summary of Achievements

8.1.1 Characterization of Microstructure of Ex-Service Pyrolysis Tubes

An image analysis methodology was developed using EDS mapping combined with automated image segmentation and processing in order to quantify the volume fractions of the various phases present in ex-service ethylene pyrolysis tubes, and the resultant composition of the austenite matrix. Four samples each from six ex-service pyrolysis tubes with varying amounts of carburization were analysed.

A number of phase changes were observed to have occurred in the ex-service tubes. The $M_{23}C_6$-to-M_7C_3 transformation occurred in the three tubes that displayed the greatest extent of primary carbide coarsening, and the $M_{23}C_6$-to-$Cr_2(C,N)$ transformation was identified at the mid and outer wall of some of the samples as a result of exposure to a nitrogen-containing atmosphere at the outer surface. The instability of the NbC and (Nb,Ti)C precipitates at elevated temperatures was widely observed, with the transformation to G-phase and/or η-carbide occurring in many samples. The precipitation of both primary and secondary σ-phase was identified in one of the tubes.

The matrix chromium concentration in the locality of the $M_{23}C_6$-to-M_7C_3 transformation front was observed to be in the range of 10 – 13 % for all samples in which this transformation occurred. The location of the transformation front was also seen to offer a measure of the degree of carbide coarsening. The primary chromium carbide volume fraction in the locality of the $M_{23}C_6$-to-M_7C_3 transformation front was in the range of 20 – 25% for all samples in which the transformation occurred. Independent of the distance of the transformation from the inner diameter, the wall regions in between the inner diameter and the transformation front contained M_7C_3 carbides with volume fractions of 25 – 35 %. When the transformation front was located a distance less than 1.5 mm from the inner diameter, the volume fraction of $M_{23}C_6$ carbides between the transformation front and the

outer wall rapidly dropped to 5 – 8 % and remained within this range for the remainder of the wall thickness. When the transformation front was located at a distance greater than 2 mm from the inner diameter the volume fraction of $M_{23}C_6$ carbides between the transformation front and the outer surface decreased at a more gradual rate, and typically did not drop below 10 % until the proximity to the outer diameter was less than 2 mm.

The detailed microstructural characterization has highlighted that the depletion of chromium in the matrix, while primarily being affected by the precipitation and growth of primary chromium-rich carbides during carburization, also depends on the occurrence, or lack thereof, of other phase transformations in which chromium-rich precipitates are formed, and the extent to which these transformations occur. Both the η-carbide and σ-phase have been shown to contribute to the depletion of chromium in the austenite matrix. Despite a number of the phase transformations that occur during service having previously been observed in similar alloys subject solely to ageing, the range of times and temperatures over which they occur in carburized tubes is not well understood. In particular, the temperature ranges over which the transformation of the primary NbC or (Nb,Ti)C carbides to the G-phase and/or η-carbide silicides occur in carburized tubes appear to differ significantly to alloys subject solely to ageing. The transformation of NbC and (Nb,Ti)C carbides to η-carbide was identified in many of the tube samples analysed. The volume fraction of η-carbide was typically observed to increase with increased proximity to the outer surface, indicating that exposure to an air atmosphere at the outer diameter of the tubes during service may promote the NbC-to-η-carbide and (Nb,Ti)C-to-η-carbide transformations. The tube mean temperature (TMT) of the tube that contained σ-phase was observed to be outside of the range of σ-phase formation typically reported in the literature, but consistent with the operating temperatures of other ex-service tubes reported to contain σ-phase. The presence of σ-phase ethylene pyrolysis tubes could be a significant issue if the tubes become highly carburized are subject to extreme temperature drops (such as during unexpected shutdowns), due to the embrittling effect of σ-phase below operating temperatures.

The combined volume fraction of M_7C_3 and $M_{23}C_6$ carbides, $Cr_2(C,N)$ carbonitrides, σ-phase intermetallics, and η-carbide silicides was seen to directly correlate with the chromium depletion of the austenite matrix. In the HP-Nb and HP-Micro tubes, and increase in the amount of chromium concentrated in the primary precipitates resulted in a corresponding decrease in the chromium concentration in the austenite matrix. The decrease occurred in a linear fashion with a slope of approximately -1, and thus the reduction in chromium in the austenite matrix in HP-Nb and HP-Micro alloys can be directly attributed to the precipitation and growth of the chromium-containing precipitates during service exposure. Due to the small range of microstructures studied for the ET45-Micro alloys, it was not possible to speculate whether such a phenomenon also occurs in these alloy types. Analysis of a significantly larger number of samples over a range of more highly carburized

microstructures would be necessary to determine the relationship between chromium rich precipitates and the matrix chromium concentration in ET45-Micro alloys.

Analysis of samples from the six ex-service tubes following the chemical etching method described in the NACE International Standard Test Method for Evaluation of the Carburization of Alloy Tubes used for Ethylene Manufacture indicates that the etching method may offer a simple destructive measure for quantifying the depth of the $M_{23}C_6$-to-M_7C_3 transformation front. It was observed that the extent of the etching band corresponded with the location of the $M_{23}C_6$-to-M_7C_3 transformation front in the carburized tubes analysed. It was determined that the etchant attacks the austenite matrix in regions where the chromium concentration drops below 10 – 14 wt%, contrary to the statement of the standard that the etchant attacks the carbides.

8.1.2 Effects of Microstructure on Creep Performance

The metallographic samples from the ex-service ethylene pyrolysis tubes were subjected to microhardness testing. In addition, samples from each of the ex-service tubes were subject to steady state creep testing at 1025 °C and 12 MPa uniaxial stress. In general, the samples that contained the highest volume fractions of primary precipitates and displayed the highest hardness values also displayed the greatest steady state creep rates. The steady state creep rate was determined to be proportional to the volume fraction of the primary precipitate network.

Highly carburized samples that contained primary precipitate volume fractions > 20 % displayed creep rates on the order of 10^{-4} /h, and moderately carburized samples that contained primary precipitate volume fractions in the range of 6 - 20 % displayed creep rates on the order of 10^{-5} /h. For samples that displayed little to no carburization and primary precipitate volume fractions of ≤ 6 % the steady state creep rate was seen to be dependent on the secondary precipitate network. Samples that contained a fine distribution of secondary $M_{23}C_6$ precipitates displayed steady state creep rates on the order of 10^{-6} /h, whereas samples that contained a distribution of secondary σ-phase platelets displayed steady state creep rates on the order of 10^{-5} /h. The ET45-Micro samples were not observed to show superior creep performance to the HP-Micro samples, consistent with the statements in the literature.

Further analysis of the effects of the various phases present in the ex-service tubes on the steady state creep rates invariably resulted in more questions than answers. Comparisons between samples that contained η-carbide with those that did not, and comparisons between samples that contained G-phase with samples that did not, or between samples that contained varying amounts of G-phase, indicated that the η-carbide and G-phase silicides may be beneficial to the creep resistance of the alloys. However, the variations in the volume fractions of the η-carbide and G-phase silicides were typically accompanied by other microstructural variations, such as differences in primary chromium carbide volume fraction or the presence of secondary precipitates distributions, and thus the effects of

the η-carbide and G-phase precipitates on the steady state creep rates of carburized tubes were unable to be separated from other microstructural features.

8.1.3 Effects of Microstructure on Magnetic Response

The quantification of the compositions of the matrix from the EDS map data enabled the magnetic properties and eddy current NDT response of the ex-service samples to be predicted based on magnetic permeability data published for Fe-Cr-Ni alloys in the literature. It was determined that when the matrix chromium concentration remained above 18 wt% the relative magnetic permeability of the material remained within the paramagnetic ($\mu_r < 1.01$) range. When the matrix chromium concentration dropped below 15 wt%, the relative magnetic permeability was seen to increase above 20, and the material became ferromagnetic. For matrix chromium concentrations in the 15 – 18 % range, the relative magnetic permeability was seen to be in the range of $1.10 < \mu_r < 20$.

Those samples that contained primary precipitate volume fractions > 20% and therefore contained the greatest amounts of ferromagnetic material in the $\mu_r > 20$ region displayed the greatest range in normalised probe inductance values (0.3), and also the highest normalised probe inductance values overall (up to 1.86). The creep samples from these tube locations displayed steady state creep rates on the order of 10^{-4} /h. With decreasing primary precipitate volume fractions and therefore decreasing amounts of ferromagnetic material, the range in normalised inductance values decreased, as did the overall normalised inductance value. Those samples that, based on the concentration of chromium in the matrix, were expected to be composed of entirely paramagnetic material displayed low normalised inductance values (≤ 1.10) that were relatively independent of the test frequency. The creep samples from these tube locations displayed steady state creep rates on the order of 10^{-5} – 10^{-6} /h. The increase in the range of normalised inductance values with increased amounts of ferromagnetic material is likely due to the eddy current response at low frequencies, and therefore greatest penetration depths, being a combination of the magnetic response of all the ferromagnetic material across the wall up to the depth of eddy current penetration.

The magnetic response of some of the samples analysed deviated from the response predicted by the matrix chromium concentration. Changes in normalised inductance due to lift off (i.e. the variance in distance between the probe and test sample), may have overshadowed the changes in normalised inductance due to slight variations in microstructure in those tubes that were predicted to contain little to no ferromagnetic material. For a number of other samples the reasoning behind the deviations from expected response was unable to be determined.

The lack of data values for relative magnetic permeability when the matrix chromium concentration drops below 15 % is a hindrance to the analysis of the magnetic response data, and the comparison between magnetic response and creep sample microstructures. If a twenty-fold increase in relative magnetic permeability occurs due to a drop in matrix chromium concentration from 18 to 15 wt%,

then the values of relative magnetic permeability for matrix chromium compositions less than 15 wt% would be expected to increase significantly as matrix chromium concentration increases, however the true extent is not known. Further testing to measure the relative magnetic permeability of Fe-Cr-Ni alloys within the regions of the low chromium concentration austenite compositions is necessary in order to enable a greater understanding of the relationship between test frequency and wall position, and improve the interpretation of the magnetic response data.

8.2 Concluding Remarks

The primary objective of the current research was to characterize the microstructure, mechanical performance, and magnetic response of carburized ethylene pyrolysis tubes, with the aim of improving the materials data inputs into finite element models for simulation of service conditions, and to improve the interpretation of the eddy current non-destructive testing response of in-situ tubes, in order to improve remaining life estimates.

Extensive quantitative characterization of phase distributions in ex-service ethylene pyrolysis tubes has provided insight into the wide range of phases present and phase transformations that can occur during service. It has been shown that the primary chromium-rich carbides are the main contributors to the depletion of chromium in the austenite matrix, but that other phase transformations that occur during service, such as the transformation of NbC or (Nb,Ti)C to η-carbide, and the precipitation of σ-phase, also contribute. The depletion of chromium in the austenite matrix of HP-Nb and HP-Micro tubes was demonstrated to be directly proportional to the concentration of chromium in the primary precipitate network.

The matrix chromium concentration was compared to available data for magnetic permeability in order to predict the amount of ferromagnetic material in each sample. Increases in the amount of ferromagnetic material resulted in both increases in overall normalised probe inductance and increases in the range of normalised probe inductance. The analysis demonstrated that measurement of the magnetic permeability of Fe-Cr-Ni compositions with chromium concentrations below 15 wt% in the range of the chromium-depleted matrix material would enable more accurate interpretation and better insight into the relationship between chromium concentration and magnetic response.

The precipitation and growth of the primary precipitate network was shown to be the main contributor to the reduction in creep resistance of the carburized tubes. The steady state creep rate was determined to be dependent on the volume fraction of the primary precipitate network, with highly carburized tubes displaying steady state creep rates an order of magnitude higher than moderately carburized tubes, and up to two orders of magnitude higher than tubes with little or no carburization. The steady state creep testing results indicated that the η-carbide and G-phase precipitates may contribute to the creep resistance of the alloys, however this was unable to be definitively confirmed.

8.3 Future Work

8.3.1 G-phase and η-carbide Transformations

Although the temperature ranges over which the transformation of NbC and (Nb,Ti)C precipitates to the G-phase and/or η-carbide silicides have been partially reported in the literature, comparisons between the known service conditions of the ex-service pyrolysis tubes from which the present samples were taken to the ranges reported in the literature indicated that the temperature ranges over which the transformations occur in carburized tubes are likely significantly different to those for tubes subject solely to ageing. Detailed analysis of further ex-service pyrolysis tube samples with known service conditions is necessary to further define the temperature range over which these transformations occur. Additionally, such analysis would assist in determining the extent to which the atmosphere at the external surface of the tube affects the microstructure, in particular the NbC or (Nb,Ti)C to η-carbide transformation.

8.3.2 Quantitative Measurement of Secondary Precipitate Distributions

Characterization and quantification of the secondary precipitate distributions in the ex-service tubes was unable to be completed accurately using the current image analysis methodology. Their small size relative to the primary precipitates led to significant errors in segmentation and binarisation, and previous studies have shown that their position with respect to the grain and dendrite boundaries can vary significantly. Serial section of samples that contain secondary precipitate distributions using a focused ion beam (FIB) combined with SEM imaging is necessary to accurately characterize and compare secondary precipitate distributions.

8.3.3 Characterization of Primary Precipitate Network Connectivity

In comparing the creep performance of the various ex-service microstructures it was noted that those samples that displayed the highest volume fractions of primary chromium carbides and thus the highest creep rates also qualitatively displayed high levels of connectivity and continuity in the primary precipitate network. Three dimensional serial sectioning and reconstruction of the primary precipitate network may provide a method by which the network connectivity can be quantified.

8.3.4 Creep Testing in Inert Atmosphere

A comparison between samples subject to short term ageing in an air atmosphere to samples subject to short term ageing in an air + argon atmosphere determined that a reduced oxygen partial pressure resulted in a decreased rate of internal silicon oxide formation in samples containing enough chromium to form a protective chromium oxide layer, but had no effect on the rate of internal oxidation in samples with significant chromium depletion. In order to fully prevent oxidation during creep testing an entirely inert atmosphere would be ideal, however a complete seal is not possible with the current generations of creep testing apparatus due to the design of the load application and LVDT

rods. A re-design for the next generation of creep testing apparatus will be necessary if an inert atmosphere is to be incorporated.

8.3.5 Magnetic Permeability Measurements

There is a lack in magnetic permeability data for Fe-Cr-Ni alloys with chromium concentrations below 15 wt% for the range of compositions represented by the carburized samples. Measurement of magnetic permeability of cast Fe-Cr-Ni alloys with compositions within this range would enable a greater insight into the extent of ferromagnetism displayed at the inner diameter of the highly carburized tubes, and simulation or calculation of the depth of eddy current penetration based on the measured matrix chromium compositions.

Appendix A: Publications

During the course of the research, two journal papers were published. Both papers are attached in the current appendix.

McLeod, A.C.; Bishop, C.M.; Stevens, K.J. and Kral M.V. (2015) *Microstructure and Carburization Detection in HP Alloy Ethylene Pyrolysis Tubes,* Metallography, Microstructure and Analysis, 4 (4): 273-285.

McLeod, A.C; Bishop, C.M.; Stevens, K.J. and Kral, M.V. (2016) *Microstructural Characterization and Image Analysis in Ex-Service HP alloy Stainless Steels Tubes for Ethylene Pyrolysis,* Metallography, Microstructure and Analysis, 5(3); 178-187.

Metallogr. Microstruct. Anal. (2015) 4:273–285
DOI 10.1007/s13632-015-0210-8

TECHNICAL ARTICLE

Microstructure and Carburization Detection in HP Alloy Pyrolysis Tubes

A. C. McLeod[1] · C. M. Bishop[1] · K. J. Stevens[2] · M. V. Kral[1]

Received: 22 March 2015 / Revised: 4 June 2015 / Accepted: 7 June 2015 / Published online: 25 June 2015

Abstract A highly carburized HP40-Mod alloy ethylene pyrolysis tube was characterized by means of scanning electron microscopy with backscatter electron imaging, electron back-scattered diffraction, energy dispersive spectroscopy, and etching using the NACE International Standard Test Method for evaluation of carburization of ethylene pyrolysis tubes. The response of the tube to eddy current non-destructive testing was measured using the carburization crawler under development at Quest Integrity NZL Ltd. The matrix was significantly depleted of chromium, as low as 4 wt% Cr at the inner wall. $M_{23}C_6$ carbides transformed to M_7C_3 at the inner wall region and NbC carbides partially transformed to the chromium-rich η-carbide at the outer wall region, both of which likely contributed to the chromium depletion of the matrix. The present results indicate that the NACE etchant attacks the austenitic matrix where chromium content is below approximately 12wt%. A comparison to other ex-service tubes indicates that matrix chromium content and the location of the $M_{23}C_6/M_7C_3$ transformation front are useful microstructural characteristics for interpreting eddy current NDT response.

✉ M. V. Kral
milo.kral@canterbury.ac.nz

[1] Department of Mechanical Engineering, University of Canterbury, Private Bag 4800, Christchurch 8140, New Zealand

[2] Quest Integrity NZL Ltd, Part of the Quest Integrity Group, Gracefield Research Centre, 69 Gracefield Road, PO Box 38-096, Lower Hutt 5045, New Zealand

Keywords Scanning Electron Microscopy · Steels · Phase transformations · Metallography

Introduction

Ethylene is used extensively in the production of plastics, cabling, and automotive products, and is typically produced by the thermal cracking (pyrolysis) of more complex hydrocarbons, such as naphtha or ethane, at 700–1100 °C inside a tube in a pyrolysis furnace. In order to provide the corrosion resistance and creep strength necessary to withstand such harsh operating conditions, the heat resisting (H-series) centrifugally cast, austenitic stainless steels are typically used for pyrolysis tubes [1, 2].

Carburization is one of the major degradation mechanisms of pyrolysis tubes [3]. High carbon potentials at the inner diameter due to the cracking reaction and high tube temperatures result in the diffusion of carbon into the tubes, where it combines with chromium and other carbide-forming elements to grow existing carbides and create new ones [4, 5]. The carbides undergo chemical and morphological changes, initially coarsening and coalescing, followed by phase transformation [4].

Internal carbide precipitation results in considerable volume increases, changes in thermal expansion coefficient of the carburized zone, and embrittlement. The result is a reduction in ductility as well as increase in internal stresses, adversely affecting the creep properties and the ability of the tube to withstand thermal cycling [2, 5–8].

Consequently, there is interest in non-destructive testing (NDT) methods to evaluate the level of carburization of tubes in situ. Carbide precipitation and the segregation of elements in HP alloy tubes result in a change in the magnetic properties of the carburized region, allowing

carburization to be detected non-destructively using eddy current techniques [6, 7, 9]. However, the eddy current systems require calibration using ex-service pyrolysis tubes that have had their microstructure, mechanical properties, and magnetic response characterized [6, 9].

This paper presents the results of detailed microstructural characterization of a highly carburized ex-service ethylene pyrolysis tube. The purpose of the paper is to determine whether there are certain microstructural features or compositional variations (e.g., chromium depletion) that dictate the eddy current NDT response of ex-service tubes.

Materials and Methods

An ex-service HP40-Mod alloy ethylene pyrolysis tube was examined. It had spent approximately 4 years in service, at 20 psig and 1300 °F (138 kPag and 704 °C). The typical as-cast composition of an HP40-Mod alloy is given in Table 1 [10]. The tube had an outer diameter of 100 mm, and an average wall thickness of 7.7 mm.

A ring approximately 10-mm thick was cut from the tube, and a metallographic sample approximately 8 × 10 mm was sectioned and mounted in order to observe the through-wall face. The sample was ground on SiC paper at 180, 240, 320, 400, and 600 grit, then polished with 9 and 3 μm diamond suspension. A final polish to a 0.02-μm finish was achieved using colloidal silica. Prior to electron back-scattered diffraction (EBSD) analysis, the sample was etched in glyceregia for 10 s, in order to increase the visibility of the precipitates. The composition of the glyceregia was 30 ml of glycerol, 30 ml of hydrochloric acid, and 10 ml of nitric acid.

Phase identification was carried out using a JEOL JSM 7000 field emission scanning electron microscope (FE-SEM), equipped with a JEOL JED-2300 energy dispersive x-ray spectroscopy (EDS) system, and a JEOL 6100 SEM, equipped with an Oxford HKL Channel 5 EBSD system. A combination of back scatter electron (BSE) imaging, EDS, and EBSD was used to identify the precipitate phases present in the tubes and determine their locations across the tube wall. BSE images were taken at set intervals across the tube wall, with multiple EDS spectra taken for each phase at each location. The appearance of each phase in the BSE images and the composition determined by EDS were used to produce a list of candidates for each phase. Crystal structure was then confirmed using EBSD.

The chromium depletion of the matrix was measured using EDS. The spectra were taken at a distance of approximately 10 μm from primary chromium carbides. In the highly carburized region of the sample, 10 μm was approximately the distance at which a point in the matrix was equidistant from surrounding chromium carbides.

Table 1 Typical Composition of an HP40-Mod alloy [10]

Wt%	C	Cr	Ni	Nb	Si	Mn	Fe
HP-40-Mod	0.4	25	35	1.5	1.5	1.5	Bal.

Progressive deep etching was used in order to gain an understanding of the three-dimensional structure of the carbide network. The sample was imaged in BSE mode at multiple locations in the as-polished condition, and the same locations were imaged in SEI mode after 15, 30, 60, 120, and 180 min etching using glyceregia. Glyceregia was chosen as the etchant as in HP alloys it only etches away austenite, leaving the carbide network intact [10].

The etching method described in the NACE International Standard Test Method for evaluation of carburization of ethylene pyrolysis tubes [11] was used to semi-quantitatively measure the extent of carburization in the ex-service tube. The etchant was composed of 200 ml of nitric acid, 70 ml of hydrofluoric acid, and 670 ml of distilled water. The etching sample was taken from the sectioned ring, adjacent to the metallographic sample. Upon completion of the etching, the sample was observed under an Olympus SZH10 stereo-optical microscope.

Precipitate—matrix orientation relationships were analyzed using EBSD. EBSD patterns (EBSPs) were obtained from the precipitates and the austenitic matrix directly adjacent to each precipitate. The Euler angles (φ_1, φ_2, Φ) that describe the crystallographic orientation with respect to a reference axis system were calculated from the indexed EBSPs. The Euler angles were used to calculate an orientation matrix for each point of analysis, and then the misorientation between the two points was calculated. The disorientation (i.e., the variant with the smallest rotation angle θ about the rotation axis [u v w]) was then calculated by considering symmetry operations, e.g., the 24 crystallographic equivalents for the cubic system [12].

The eddy current NDT response of the ex-service tube was measured using the eddy current NDT carburization crawler that is being developed by Quest Integrity NZL Ltd. The system uses cylindrical coils to probe the tube with variable frequency electromagnetic waves, and measures the changes in coil properties (i.e., inductance, resistance), which differ depending on the level of carburization of the tube.

Results and Discussion

Macrostructure

Figure 1 shows the through-wall grain structure of the tube. Centrifugally cast HP alloy tubes display either a completely columnar structure or a mixed columnar-equiaxed structure, depending on the centrifugal casting conditions

Fig. 1 Low-magnification image showing the through-wall grain structure of the ex-service tube (etchant: Marbles reagent)

(for example, the pouring temperature and the cooling rate) [13–15]. The 100% columnar structure of the ex-service tube indicates a high cooling rate induced during casting.

Phase Identification

A number of different phases were present across the wall thickness of the ex-service tube, including carbides, carbonitrides, and silicon-rich phases. A schematic of the tube wall summarizing the locations of interest and the phases identified is shown in Fig. 2.

Chromium Carbides

The microstructure across the tube wall consisted of an austenitic matrix with a network of coarse chromium-rich carbides and niobium-rich carbides. The chromium-rich carbides in the 0.4–5 mm region of the tube wall were identified as M_7C_3 (where M = Fe, Cr, Ni), and those in the 5–7.2 mm region were identified as $M_{23}C_6$. The niobium-rich carbides were identified as NbC.

The progression of the microstructure in the 0.4–5 mm region of the tube wall is shown in Fig. 3. The ratio of Cr to Fe in the M_7C_3 carbides increased as the distance into the tube wall from the inner diameter increased, as shown in Fig. 4. The Ni content remained constant at 1–2 at.%.

M_7C_3 is formed by the conversion of $M_{23}C_6$, as a result of the increasing C/Cr ratio at the inner wall region due to carbon diffusion from the inner diameter [5]. The composition of the M_7C_3 depends on the local carbon activity [16, 17], and thus, in the ex-service tube, on the distance from the inner diameter. The main metal component of M_7C_3 is Cr, but with increasing carbon activity an increased amount of iron is substituted for chromium [17–19].

The $M_7C_3/M_{23}C_6$ transformation front was located at a distance of approximately 5 mm from the inner diameter of the tube. The $M_{23}C_6$ carbide had a medium gray contrast in the BSE images, as shown in Fig. 5. The transition between

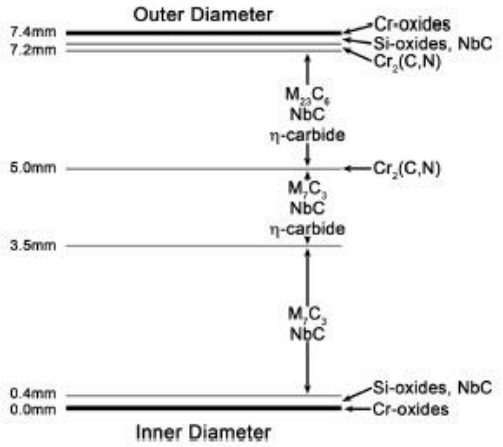

Fig. 2 Schematic of the tube wall summarizing the locations of the phases identified

M_7C_3 and $M_{23}C_6$ occurred over a very narrow range, with a band of approximately 200 μm in width where both M_7C_3 and $M_{23}C_6$ were present.

The appearance of the M_7C_3 carbides changed across the wall, with a separate phase appearing to be encapsulated, or contained, within the M_7C_3, giving a "porous" appearance in two dimensions. The contained phase was present in the carbides across the 0.4–5 mm wall region, but appeared to become more prevalent as distance from the inner diameter increased, as evidenced in Fig. 3. The M_7C_3 carbides at a distance of 5 mm into the tube wall appear significantly more "porous" than those closer to the inner diameter. EDS and EBSD analysis identified the contained phase as austenite.

The "porous" appearance of the M_7C_3 carbides, without identifying the phase present inside the carbides, was previously reported by Christ [17] to occur during carburization of a 304L type stainless steel, and by Waldenström [20] in a Fe–Cr–Ni–Mn–C alloy. Kaya [4] also observed this phenomenon in an ex-service HK40 alloy ethylene pyrolysis tube, identifying the phase present inside the M_7C_3 carbides as austenite. All three studies attribute the "porous" appearance of the M_7C_3 carbides to its transformation from $M_{23}C_6$ by a eutectoid reaction during carburization, with Kaya defining the transformation as $M_{23}C_6 \rightarrow M_7C_3 + \gamma$ (where γ = austenite).

Kaya proposed that the excess elements (presumably Fe, Cr, and Ni [18], as M_7C_3 has a lower ratio of M to C) that cannot be accommodated in the M_7C_3 carbides upon the transformation from $M_{23}C_6$ would form the austenite phase regions in the M_7C_3 carbides, and that these austenite regions may nucleate on the $M_{23}C_6/M_7C_3$ transformation

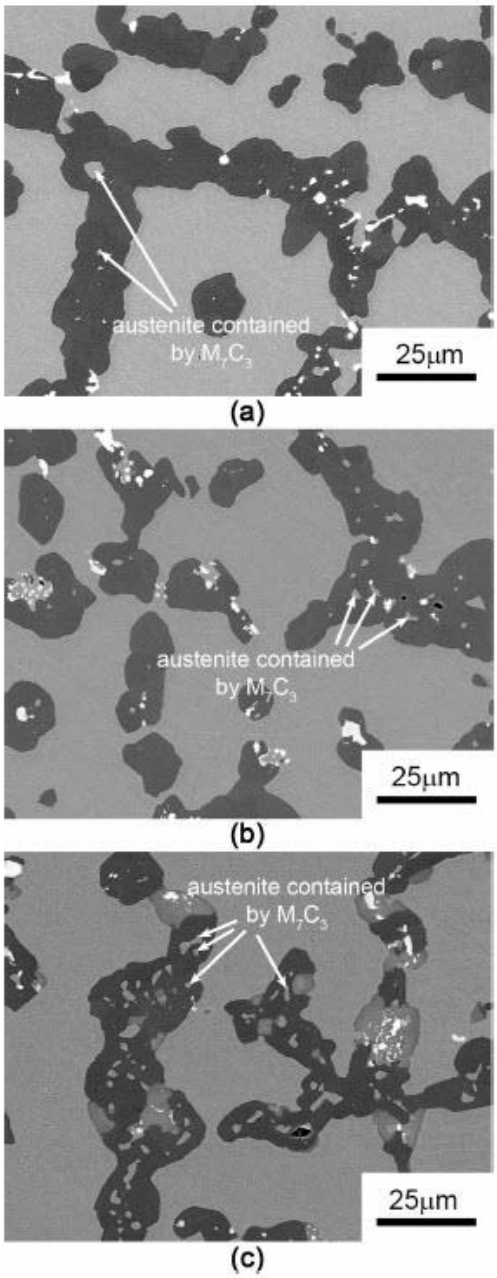

Fig. 3 BSE micrographs of the microstructure at (**a**) 1.0 mm, (**b**) 3.0 mm, and (**c**) 5.0 mm from the inner diameter

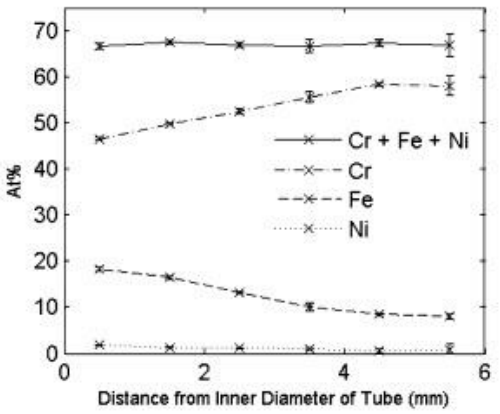

Fig. 4 Change in composition of the M_7C_3 carbides with distance from the inner diameter. Results from three EDS spectra were averaged at each location

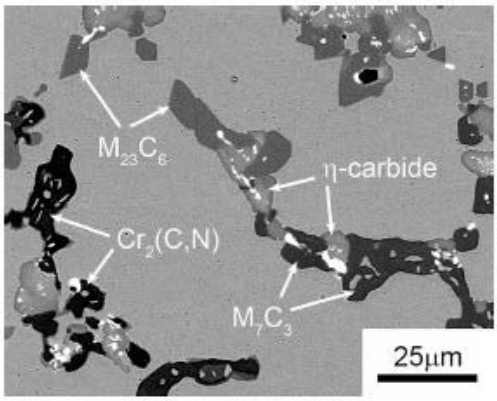

Fig. 5 BSE micrograph indicating the phases present at the M_7C_3/$M_{23}C_6$ transformation front

front, or alternatively behind the moving front on the defects present in the M_7C_3 carbides.

EBSD analysis of 65 contained austenite–matrix pairs enabled the disorientation between the contained austenite regions and the adjacent austenitic matrix to be calculated. Figure 6 shows the relative frequency of the disorientation angle. 69% of the analyzed contained austenite pairs had a disorientation of less than 10°, typical of a cube–cube orientation with the austenitic matrix. 18% of the analyzed pairs displayed disorientations close to 60°, and the calculated disorientation axes for these pairs were close to [111]—typical of a twin orientation. The remaining contained austenite displayed no particular orientation

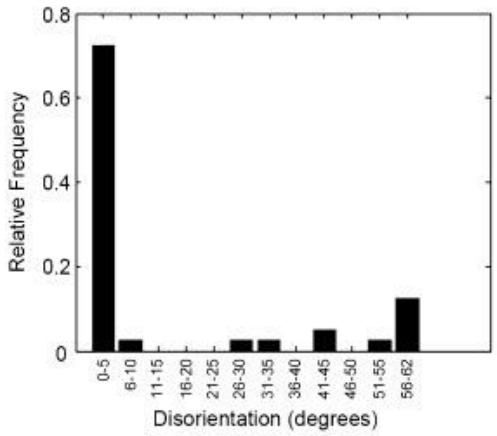

Fig. 6 Relative frequency of angle of disorientation for contained austenite—austenitic matrix pairs

relationship with the austenitic matrix, indicating that no other rational orientations were obtained.

Progressive deep etching (Fig. 7) revealed that areas that appeared as open matrix in the as-polished condition became enclosed by M_7C_3 carbides beneath the plane of polish. If the plane of polish was further down into the sample, these regions would have appeared as austenite contained within the M_7C_3 carbides. Even though the carbide network may have appeared disconnected in the as-polished condition, the deep etch revealed that the carbides have a high level of connectivity in three dimensions.

Near the inner diameter of the tube, the M_7C_3 carbides appeared to be composed of many rounded grains which were very closely packed. Closer to the $M_7C_3/M_{23}C_6$ transformation front, there were regions where the M_7C_3 grains were closely packed, but also regions where the grains were more loosely packed, as shown in Fig. 8. If the plane of polish had been further down in the sample, the gaps in between the grains in the loosely packed regions would have appeared as austenite contained by M_7C_3 carbides in two dimensions. In contrast to the M_7C_3 carbides, the $M_{23}C_6$ carbides appeared to be composed of many closely packed angular grains, as shown in Fig. 9.

The space groups and lattice parameters of the M_7C_3 and $M_{23}C_6$ carbides, and of austenite, are summarized in Table 2 [15, 21]. In the as-cast condition, M_7C_3 does not have an orientation relationship with the austenitic matrix [19]. The $M_{23}C_6$ carbides are typically observed to have a cube–cube orientation relationship with the matrix [19, 22], the same crystal structure and a lattice parameter almost exactly three times that of the matrix. No orientation relationship between the M_7C_3 carbides that transform from $M_{23}C_6$ as a result of carburization and the matrix has been reported.

Based on the orientation results and information in literature, there are a number of possible options for the formation of the austenite regions that appear contained by the M_7C_3 carbides:

- If the austenite regions are individual precipitates separate from the matrix:
  - If M_7C_3 in the carburized condition has no rational OR with the austenitic matrix, then the austenite regions must have nucleated in $M_{23}C_6$ or at the transformation front. A schematic portraying how this may occur at the transformation front is seen in Fig. 10(a).
  - If M_7C_3 in the carburized condition does have a rational OR with the matrix, the austenite regions may gain an OR by having M_7C_3 present at the point of nucleation. Nucleation could occur at or behind the transformation front.
- The decomposition of $M_{23}C_6$ may begin at the $M_{23}C_6$/austenite interface with growth of existing austenite cooperatively with M_7C_3. In this case, the austenitic regions that appear contained by the M_7C_3 carbides would be expected to be connected to the matrix in three dimensions. It is possible that the twin growth direction may be more favorable than the normal growth direction in some cases. A schematic of how the austenite matrix may grow cooperatively with M_7C_3 is shown in Fig. 10(b).

From the deep etching results, it seems more likely that the austenite regions that appear contained by the M_7C_3 carbides are connected to the matrix in three dimensions, as opposed to being individual precipitates separate from the matrix. The gaps in between the M_7C_3 carbide grains after deep etching appear more prevalent closer to the transition than at near the inner diameter, as do the austenite regions that appear contained by the carbides in the as-polished condition. It is possible that the contained austenite regions are the gaps in between the grains, and appear contained by the M_7C_3 carbides due to sectioning effects.

Cr–Ni–Nb–Si Rich Phase

In the 3.5–7.2 mm region of the wall, a phase rich in silicon, nickel, niobium, and chromium was observed, with a light gray contrast in BSE images in comparison to the darker gray chromium carbides. The average composition measured by EDS is shown in Fig. 11. The Cr–Ni–Nb–Si rich phase appeared to be transformed from NbC, and the area covered by this phase appeared to increase as distance from the inner diameter increased.

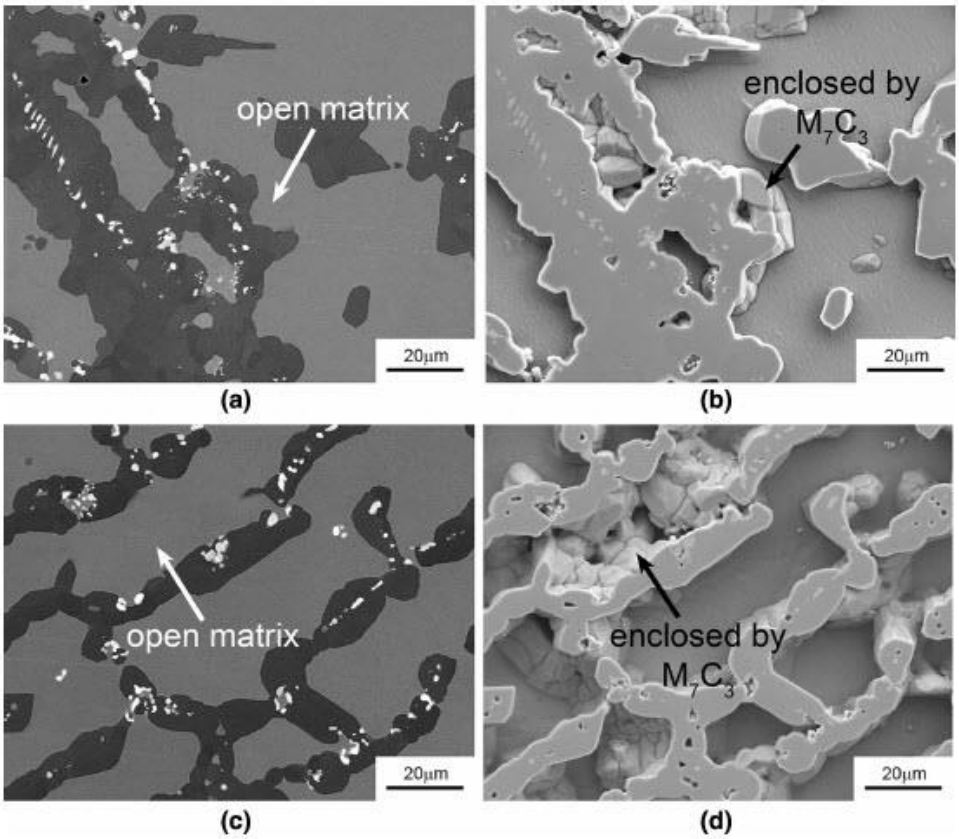

Fig. 7 M_7C_3 carbides (**a**) and (**b**) 1.0 mm from the inner diameter, as polished (BSE) and after 30 min in glyceregia (SEI) respectively. (**c**) and (**d**) 3.0 mm from the inner diameter, as polished (BSE) and after 120 min in glyceregia (SEI) respectively

The instability of NbC precipitates at temperatures of 700–1050 °C has been well reported in the literature [1, 22–27]. The product of the transformation is generally identified as G-phase, which has a commonly reported composition of $Ni_{16}Nb_6Si_7$, and an FCC structure with a lattice parameter of 1.12 nm [1, 23, 24].

The transformed phase identified in the ex-service tube contained Nb, Ni, and Si. However, it also contained a significant amount of chromium (determined by EDS as 42.5 at.%), and the Ni content was significantly lower (32.5 at.%), than the values typically reported for G-phase (approximately 55 at.%).

Another phase, the diamond cubic η-carbide, has also been identified in ex-service HP–Nb reformer tubes and aged HP–Nb alloy [10, 22, 25–27]. The typical composition of the transformed phase in the ex-service pyrolysis tube closely resembled the reported compositions. Despite ambiguity in the EBSD analysis due to the similar space groups and lattice parameters of G-phase and η-carbide, the comparison between the composition of the transformed phase (Fig. 11) to reported values was considered sufficient evidence to identify the transformed phase in the ex-service tube as η-carbide, as opposed to G-phase. As η-carbide contains a significant amount of chromium, it is likely that the NbC-to-η-carbide transformation contributes to the chromium depletion of the matrix.

The current literature on the NbC-to-G-phase and NbC-to-η-carbide transformations in HP–Nb alloys is constrained to ex-service reformer tubes [8, 22, 25–27] and a limited number of laboratory-aged studies [1, 23–25]. Based on the available literature and data from laboratory-aged HP–Nb alloys, Buchanan [10] concluded that the NbC-to-G-phase and NbC-to-η-carbide transformations in aged HP–Nb alloys are dictated by the aging temperature.

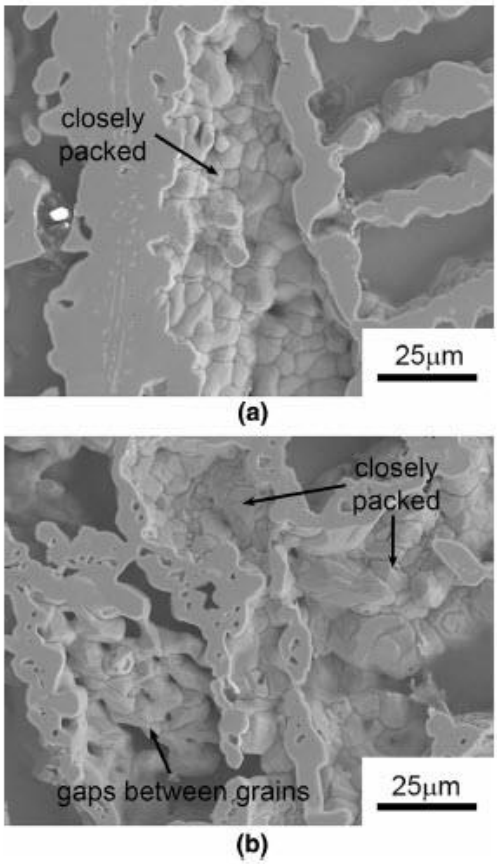

Fig. 8 SEI images of M_7C_3 carbides at (**a**) inner diameter region and (**b**) inner diameter side of the $M_7C_3/M_{23}C_6$ transition after 180 min in glyceregia

At temperatures below 875 °C the NbC-to-G-phase transformation dominates. Between 875 and 920 °C, the NbC-to-G-phase and NbC-to-η-carbide transformations can occur in parallel, and the η-carbide volume fraction is expected to increase with aging temperature until the NbC-to-η-carbide transformation becomes dominant, up to an upper limit of 1050 °C above which NbC carbides are stable.

As a result of carburization during service, the pyrolysis tube has a continual composition gradient across the tube wall (both for the austenitic matrix and the M_7C_3 carbides), and has a phase transformation front where $M_{23}C_6$ transforms to M_7C_3, along with microstructural changes (such as the instability of NbC) associated with long term aging. There is also significant coarsening of the carbides in

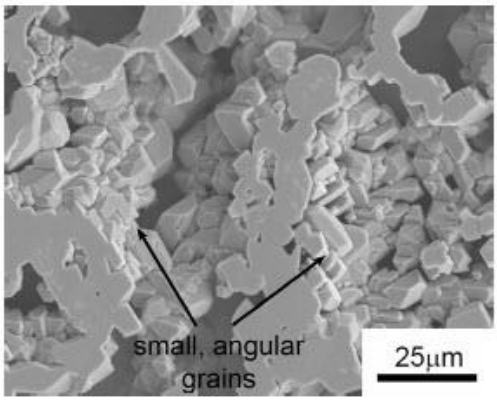

Fig. 9 SEI image of $M_{23}C_6$ carbides on the outer diameter side of the $M_7C_3/M_{23}C_6$ transition, after 180 min in glyceregia

highly carburized areas of the tube wall. The combination of these factors creates significantly different conditions within the pyrolysis tube compared to ex-service reformer tubes and laboratory-aged alloys. It is highly likely that the difference in conditions results in the temperature ranges over which the NbC-to-G-phase and NbC-to-η-carbide transformation occur in pyrolysis tubes to differ from those seen in the ex-service reformer tubes and laboratory aged alloys. This is evidenced by the ex-service pyrolysis tube's service temperature of 704 °C, along with the presence of η-carbide and lack of G-phase in the microstructure.

Inner and Outer Oxide Scales, Carbonitrides

At the inner diameter of the tube, a chromium-rich oxide scale with a depth of 100 μm was present. Inwards of the chromium oxide scale, a band of dendritic silicon oxides 250–300-μm thick penetrated into the tube (Fig. 12). Within this band, no chromium-rich precipitates were found, with only NbC carbides identified.

An oxide scale was also present at the outer diameter, with a layer composed of chromium oxides and silicon oxides 100–150-μm thick. The silicon oxides penetrated into the tube across a band 200–300-μm thick. This band was also free of chromium-rich precipitates (Fig. 13) with only NbC carbides present.

The presence of a chromium-rich oxide scale results in the depletion of chromium in the matrix adjacent to the scale, leading to a Cr-depleted zone free of chromium-rich precipitates. The Cr- and Si-rich oxide scales and the chromium precipitate free zone that were observed at the inner and outer diameters of the ex-service tube are consistent with observations of HP alloys exposed to oxidizing and carburizing environments at elevated temperatures [28, 29].

Table 2 Space groups and lattice parameters of relevant chromium carbides and the austenitic matrix [15, 21]

Phase	Space group	Lattice parameter
M_7C_3	Pnma	$a = 0.453$ nm, $b = 0.701$ nm, $c = 1.21$ nm
$M_{23}C_6$	Fm3m	$a = 1.066$ nm
Austenite	Fm3m	$a = 0.366$ nm

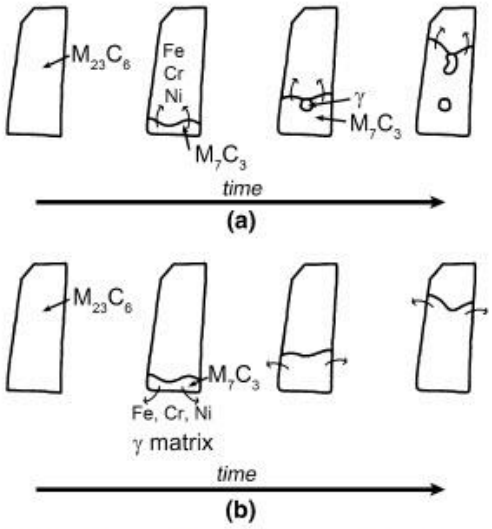

Fig. 10 (**a**) Schematic of how austenite may precipitate as individual precipitates at the $M_7C_3/M_{23}C_6$ transformation front, (**b**) schematic of how the austenite matrix may grow cooperatively with M_7C_3 at the $M_7C_3/M_{23}C_6$ transformation front

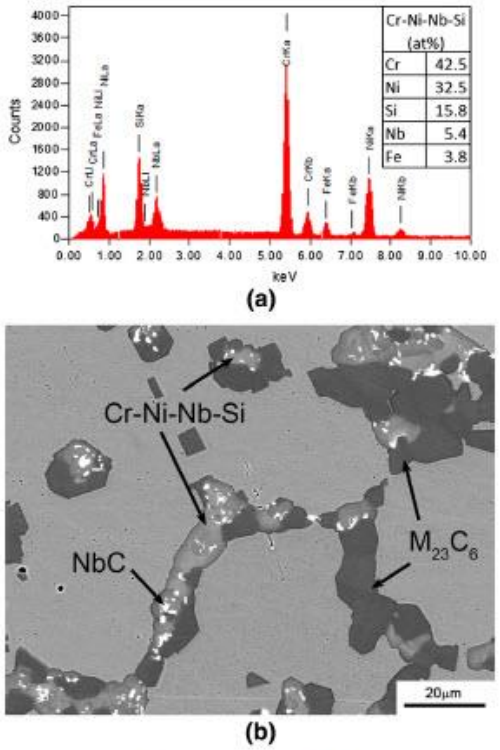

Fig. 11 (**a**) typical composition of the Cr–Ni–Nb–Si rich phase as determined by EDS, (**b**) BSE micrograph showing the transformation of NbC to a Cr–Ni–Nb–Si rich phase

Inwards from the chromium-rich precipitate free zone at the outer diameter, the $M_{23}C_6$ carbides in the carbide network transformed into a different chromium-rich precipitate, which had a blocky appearance and a darker contrast in BSE images compared to the medium gray $M_{23}C_6$ carbides. Lath-shaped precipitates of the same contrast were observed to have precipitated intragranularly. Both the lath-shaped precipitates and the blocky precipitates transformed from $M_{23}C_6$ were identified as $Cr_2(C,N)$, a carbonitride. It appeared that the majority of the $M_{23}C_6$ within a narrow band of <200 μm had transformed into $Cr_2(C,N)$, with some of the $M_{23}C_6$ carbides further into the tube having also transformed into $Cr_2(C,N)$ (Fig. 13). The transformation of $M_{23}C_6$ to $Cr_2(C,N)$ and the precipitation of $Cr_2(C,N)$ at the outer diameter of the tube occurs due to the exposure of the tube's outer surface to the flue gases present in the furnace during service. Nitrogen diffusion into the tube results in the precipitation of $Cr_2(C,N)$ and the conversion of $M_{23}C_6$ to $Cr_2(C,N)$, which can then continue to grow by uptake of chromium and nitrogen [3]. The changes in materials properties due to nitriding are very similar to those due to carburization—in both cases precipitates are formed, internal volume is increased, and the matrix is depleted of chromium [3].

$Cr_2(C,N)$ precipitates were also identified at the $M_7C_3/M_{23}C_6$ transformation front. They appeared to take the place of the M_7C_3 carbides in the network, as indicated in Fig. 5, and were not seen anywhere else in the mid-wall region of the sample. It is currently unknown why $Cr_2(C,N)$ precipitates are present at such a distance from the $M_{23}C_6/Cr_2(C,N)$ transformation front, and why they are not present anywhere else in the region between the $M_7C_3/M_{23}C_6$

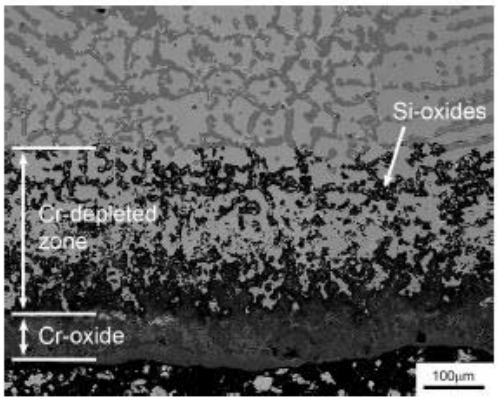

Fig. 12 BSE micrograph of oxide scale at inner diameter

transformation front and the outer diameter. However, due to the similar effects on mechanical properties of nitrides and carbides [3], it is unlikely that the replacement of some carbides by carbonitrides in the inner wall has any significant effect on the tube properties.

Chromium Depletion in the Matrix and the Paramagnetic to Ferromagnetic Change

In the as-cast condition, HP alloy tubes are paramagnetic. The precipitation and growth of chromium carbides causes chromium depletion in the austenitic matrix. With increasing carburization, the matrix composition tends toward the binary Fe–Ni composition, and the matrix becomes progressively more ferromagnetic [2, 5, 7, 30–32].

The change in matrix chromium content, measured at a distance of 10 µm from the primary chromium carbide network, is shown in Fig. 14. The matrix chromium content is significantly below the typical as-cast chromium content of 25 wt%, particularly at the inner wall region. The location of the $M_7C_3/M_{23}C_6$ transformation front corresponded with a matrix chromium content of 11–12 wt%.

The change in matrix composition across the tube wall has been plotted on the ternary Fe–Cr–Ni diagram (Fig. 15) along with data representing the paramagnetic and ferromagnetic compositions (determined by the Curie temperature) [33–35]. As seen in Fig. 15, the matrix composition is in the ferromagnetic region across the entire tube wall. Although the $M_7C_3/M_{23}C_6$ transformation front, which is sometimes used as a measure of the depth of carburization [5], is only located at a distance of approximately 5 mm from the inner diameter, the large, blocky $M_{23}C_6$ carbides in the 5–7.2 mm wall region and the regions of chromium-rich η-carbide in the 3.5–7.2 mm wall region have likely

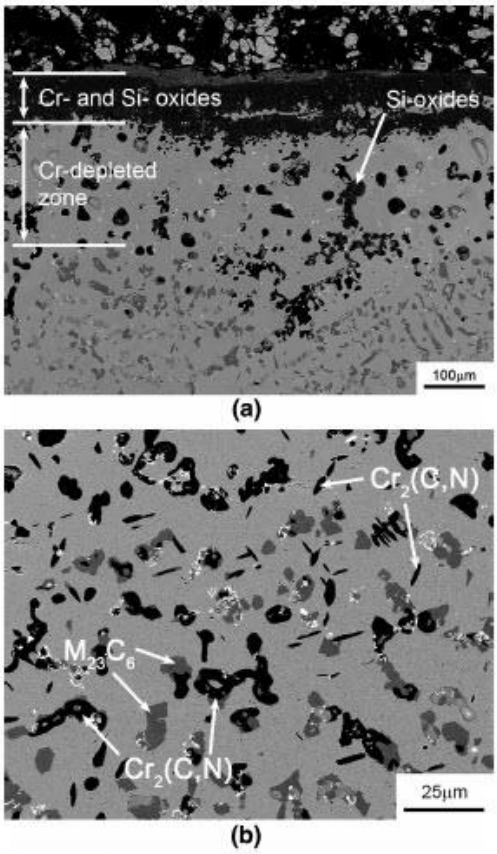

Fig. 13 BSE micrographs of the outer diameter indicating (**a**) the Cr-depleted zone, and (**b**) intragranular $Cr_2(C,N)$ and the transformation of $M_{23}C_6$ into $Cr_2(C,N)$

contributed to the chromium depletion of the matrix at the outer wall region, leading to a matrix composition that is ferromagnetic at room temperature.

NACE Etching Method

A dark etching band was clearly seen on the sample that was subjected to the NACE etching method (Fig. 16a). The etching band extended a depth of 5–5.5 mm from the inner diameter, which the standard states indicates the depth of the carburized region [11].

The location where the matrix chromium content reached 11–12 wt% corresponded with both the location of the $M_7C_3/M_{23}C_6$ transformation front (approximately 5 mm from the inner diameter) and the edge of the NACE etching band.

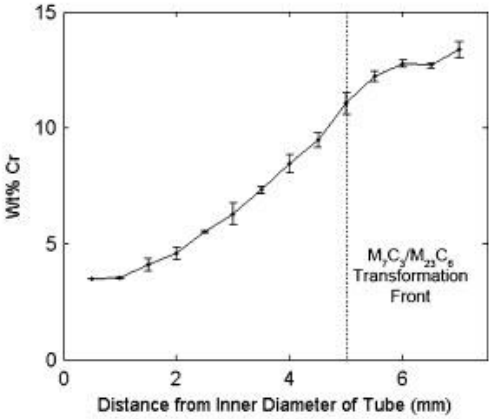

Fig. 14 Chromium content of the matrix across the tube wall, as determined by EDS. Results from three EDS spectra were averaged at each location

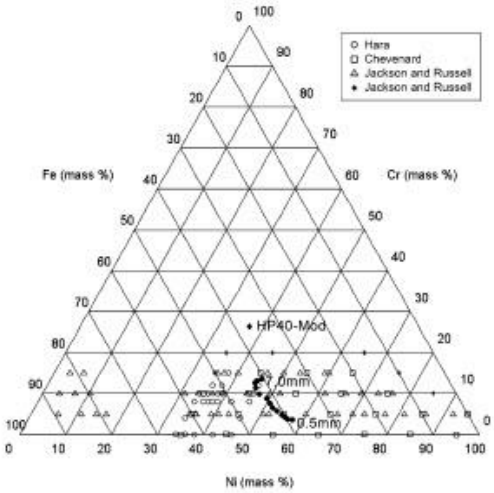

Fig. 15 Ternary Fe–Cr–Ni diagram showing the changes in matrix composition of the ex-service tube. Typical as-cast condition of HP40-Mod is denoted by a solid diamond. Matrix compositions are denoted by solid circles, and labeled with distance (mm) from the inner diameter. Asterisks denote compositions that are paramagnetic at room temperature. Open circles, squares, and triangles denote compositions that are ferromagnetic at room temperature

Two other ex-service HP alloy ethylene pyrolysis tubes (tubes B and C) were also subjected to the NACE etch for comparison with the ex-service tube for which the microstructure has been characterized (tube A).

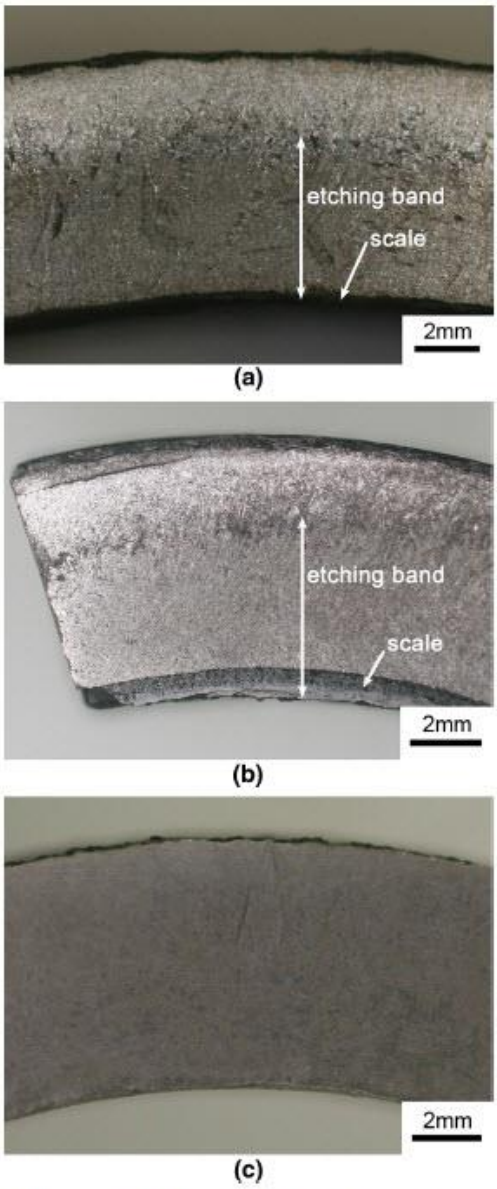

Fig. 16 Sections of (**a**) tube A, (**b**) tube B, and (**c**) tube C after being subjected to the NACE etching method

The microstructure of tube B appeared very similar to tube A with regards to phases present and morphologies. However, tube B did not contain η-carbide or G-phase, and

the $M_7C_3/M_{23}C_6$ transition occurred closer to the inner diameter (4 mm). The microstructure of tube C appeared similar to that of as-cast HP alloys, however, the NbC carbides appeared to have fully transformed into G-phase.

The etching results for tubes B and C are shown in Fig. 16(b) and (c), respectively. It was seen that tube B displayed an etching band as a result of the NACE etch, however, it was not as well-defined as that of tube A, and did not extend as far into the tube wall. The etched surface of tube C appeared dull compared to the as-polished condition but was otherwise unaffected by the NACE etchant.

It should be noted that the NACE standard states that the contrast is achieved by the attack of carbides, however, the present results indicate that the contrast is due to attack of the austenitic matrix where the chromium content falls below approximately 12 wt%.

Eddy Current NDT Response

The eddy current NDT response of tubes A, B, and C, as measured by the carburization crawler under development at Quest integrity NZL Ltd, is shown in Fig. 17, where the normalized probe inductance is plotted against frequency. Tube A displays the highest normalized probe inductance across all frequencies, ranging from 1.83 at low frequencies to 1.57 at higher frequencies. A high normalized probe inductance across all frequencies indicates that the entire tube wall is highly carburized, which is consistent with the matrix of tube A being ferromagnetic across the entire tube wall as indicated by the matrix composition profile. The slight drop in normalized probe inductance at high frequencies indicates the outer wall region is carburized to a slightly lesser extent than the inner wall, which is consistent with microstructural observations and the NACE etch results.

Tube B displays the same trend in normalized probe inductance as tube A, albeit at a slightly lower range, indicating that tube B is less carburized than tube A, which is consistent with the $M_7C_3/M_{23}C_6$ transition occurring closer to the inner diameter in tube B, and the lack of η-carbide to contribute to the chromium depletion. The normalized probe inductance for tube B ranges from 1.72 at low frequencies to 1.50 at high frequencies. The eddy current response of tube B indicates carburization to a lesser extent than tube A, and correlates well to the NACE etch results.

Tube C exhibits a constant normalized probe inductance of 1.02 across all frequencies. An un-carburized tube would be expected to have a normalized probe inductance below that of the probe in air, i.e., <1. The response of tube C indicates that there is little or no carburization. Tube C did not respond to the NACE etchant, and did not display a chromium carbide transition in the microstructure, which is consistent with little or no carburization, however, slight carbide coarsening may have caused chromium depletion in the matrix, leading to a normalized inductance value slightly greater than 1.

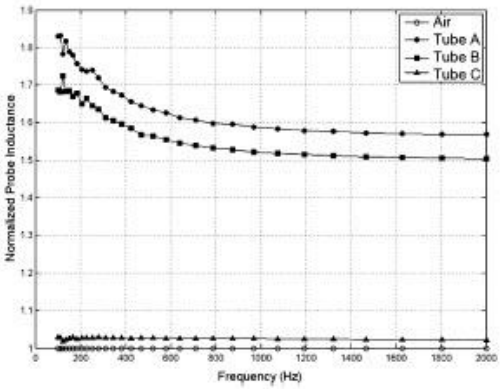

Fig. 17 Eddy current NDT response (normalized probe inductance vs. frequency) of tubes A, B, and C

Conclusions

- Three important phase transformations were identified in the ex-service HP alloy tube:
  - $M_{23}C_6$ transformed to M_7C_3, with the transformation front located a distance of approximately 5 mm from the inner diameter.
  - $M_{23}C_6$ transformed to $Cr_2(C,N)$ at the outer diameter of the tube, as a result of exposure of the tube's outer surface to flue gases during service. $Cr_2(C,N)$ carbonitrides were also observed at the $M_7C_3/M_{23}C_6$ transformation front, appearing to take the place of M_7C_3 carbides, but their presence at the transformation front is currently unexplained.
  - NbC transformed to η-carbide in the 3.5–7.2 mm region of the wall. η-carbide was identified rather than G-phase due to significant differences in the chromium and nickel content between the two phases. As η-carbide contains a significant amount of chromium, it is likely that the NbC-to-η-carbide transformation contributes to the chromium depletion of the matrix. Although there is information in literature regarding the temperature ranges over which the NbC-to-G-phase and NbC-to-η-carbide transformations occur in HP-Nb alloys, the conditions under which these data were collected differ significantly from the carburizing conditions experienced by pyrolysis tubes in service, so are not directly comparable.

- The M_7C_3 carbides appeared to contain a separate phase, identified as austenite. EBSD analysis on contained austenite–matrix pairs determined that 69% of the pairs obtained an orientation typical of a cube–cube orientation, and 18% obtained an orientation typical of a twin orientation. Deep etching in glyceregia showed the M_7C_3 carbides appeared to be composed of many rounded grains, and that regions of austenite that appeared as open matrix in the as-polished condition would have appeared enclosed by the M_7C_3 carbides had the plane of polish been deeper into the sample. It seems likely that the austenite regions that appear contained by the M_7C_3 carbides are actually connected to the matrix in three dimensions, and may appear contained as a result of sectioning effects.
- The edge of the NACE etching band corresponds to the $M_{23}C_6/M_7C_3$ transformation front, which corresponded with a matrix chromium content of approximately 12 wt%. Rather than attack of carbides, it appears that the NACE etch contrast occurs due to attack of the austenitic matrix where the chromium content falls below approximately 12 wt%.
- Severe chromium depletion of the matrix was seen across the tube wall, but particularly near the inner diameter region where the matrix chromium content dropped as low as 4 wt%. A comparison with Curie Temperature data indicated that the matrix is ferromagnetic across the entire tube wall.
- The present results indicate that the eddy current method is able to detect and measure carburization non-destructively.

Acknowledgments The authors gratefully acknowledge the financial support of Quest Integrity NZL Limited, and the Ministry of Science and Innovation of New Zealand (now administered by Callaghan Innovation) under contract QINZ1001. Thanks to Charles Thomas and Andy Saunders-Tack of Quest Integrity NZL Ltd for their continued support.

References

1. G.D. de Almeida Soares, L.H. de Almeida, T.L. da Silveira, I. Le May, Niobium additions in HP heat-resistant cast stainless steels. Mater. Charact. **29**, 387–396 (1992)
2. I.C. Silva, J.M.A. Rebello, A.C. Bruno, P.J. Jacques, B. Nysten, J. Dille, Structural and magnetic characterization of a carburized cast austenitic steel. Scripta Mater. **59**, 1010–1013 (2008)
3. D. Jakobi, R. Gommans, Typical failures in pyrolysis coils for ethylene cracking. Mater. Corros. **54**, 881–886 (2003)
4. A.A. Kaya, Microstructure of HK40 alloy after high-temperature service in oxidizing/carburizing environment. II. Carburization and carbide transformations. Mater. Charact. **49**, 23–34 (2002)
5. E. Lang, J. Norton, Monitoring of carburisation by the use of magnetic techniques, Part 1: fundamental aspects and measurements on 25Cr-20Ni steels, Commission of the European Communities, Physical Science, PETTEN, EUR 10566 EN, 1986
6. K.J. Stevens, W.J. Trompetter, Calibration of eddy current carburization measurements in ethylene production tubes using ion beam analysis. J. Phys. D **37**, 501–509 (2004)
7. K.J. Stevens, A.J. Tack, C.W. Thomas, D. Stewart, Through-wall carburization detection in ethylene pyrolysis tubes. J. Phys. D **34**, 814–822 (2001)
8. S. Shi, J.C. Lippold, Microstructure evolution during service exposure of two cast, heat-resisting stainless steels—HP-Nb modified and 20-32Nb. Mater. Charact. **59**, 1029–1040 (2008)
9. K.J. Stevens, A. Parbhu, J. Soltis, Magnetic force microscopy and cross-sectional transmission electron microscopy of carburised surfaces. Curr. Appl. Phys. **4**, 304–307 (2004)
10. K.G. Buchanan, The effects of long-term isothermal ageing on the microstructure of HP-Nb and HP-NbTi alloys, Doctoral Dissertation, University of Canterbury, Christchurch, 2013
11. NACE International, NACE International Standard Test Method: Evaluation of Carburization of Alloy Tubes Used for Ethylene Manufacture, 2006
12. V. Randle, *The Measurement of Grain Boundary Geometry* (Institute of Physics Publications, Philadelphia, 1993)
13. X.Q. Wu, H.M. Jing, Y.G. Zheng, Z.M. Yao, W. Ke, Z.Q. Hu, The eutectic carbides and creep rupture strength of 25Cr20Ni heat-resistant steel tubes centrifugally cast with different solidification conditions. Mater. Sci. Eng. A **293**, 252–260 (2000)
14. F.G. Caballero, P. Imizcoz, V. Lopez, L.F. Alvarez, C.G. De Andrés, Use of titanium and zirconium in centrifugally cast heat resistant steel. Mater. Sci. Technol. **23**, 528–534 (2007)
15. K.G. Buchanan, M.V. Kral, Crystallography and morphology of niobium carbide in as-cast HP-niobium reformer tubes. Metall. Mater. Trans. A **43**, 1760–1769 (2012)
16. A. Schnaas, H.J. Grabke, High-temperature corrosion and creep of Ni-Cr-Fe alloys in carburizing and oxidizing environments. Oxid. Met. **12**, 387–404 (1978)
17. H.J. Christ, Experimental characterization and computer-based description of the carburization behaviour of the austenitic stainless steel AISI 304L. Mater. Corros. **49**, 258–265 (1998)
18. H.J. Grabke, I. Wolf, Carburization and oxidation. Mater. Sci. Eng. **87**, 23–33 (1987)
19. D.J. Young, *High Temperature Oxidation and Corrosion of Metals* (Elsevier, Amsterdam, 2008)
20. M. Waldenstrom, An experimental study of carbide-austenite equilibria in iron-base alloys with Mo, Cr, Ni, and Mn in the temperature range 1173 to 1373K. Metall. Trans. A **8A**, 1963–1977 (1977)
21. P. Villars, K. Cenzual (ed.), Pearson's Crystal Data: Crystal Structure Database, ASM International, Materials Park, OH (2008)
22. E.A. Kenik, P.J. Maziasz, R.W. Swindeman, J. Cervenka, D. May, Structure and phase stability in a cast modified-HP austenite after long-term ageing. Scripta Mater. **49**, 117–122 (2003)
23. R.A.P. Ibanez, G.D. de Almeida Soares, L.H. de Almeida, I. Le May, Effects of Si content on the microstructure of modified-HP austenitic steels. Mater. Charact. **30**, 243–249 (1993)
24. L.H. de Almeida, A.F. Ribeiro, I. Le May, Microstructural characterization of modified 25Cr-35Ni centrifugally cast steel furnace tubes. Mater. Charact. **49**, 219–229 (2003)
25. K. Nishimoto, K. Saida, M. Inui, M. Takahashi, Changes in microstructure of HP-modified, heat-resisting cast alloys under long-term aging. Repair weld cracking of service-exposed, HP-modified, heat-resisting cast alloys (2nd Report), Welding Research Abroad, **48**, 1–9 (2002)
26. C.W. Thomas, K.J. Stevens, M.J. Ryan, Microstructure and properties of alloy HP50-Nb: comparison of as cast and service exposed materials. Mater. Sci. Technol. **12**, 469–475 (1996)
27. E. Berghof-Hasselbächer, P. Gawenda, M. Schorr, M. Schütze, J.J. Hoffman, Atlas of Microstructures, Materials Technology Institute

28. D. Oquab, N. Xu, D. Monceau, D.J. Young, Subsurface microstructural changes in a cast heat resisting alloy caused by high temperature corrosion. Corros. Sci. **52**, 255–262 (2010)
29. R. Voicu, E. Andrieu, D. Poquillon, J. Furtado, J. Lacaze, Microstructure evolution of HP40-Nb alloys during aging under air at 1000°C. Mater. Charact. **60**, 1020–1027 (2009)
30. K.J. Stevens, A. Parbhu, J. Soltis, D. Stewart, Magnetic force microscopy of a carburized ethylene pyrolysis tube. J. Phys. D **36**, 164–168 (2003)
31. M.W. Mucek, Laboratory detection of degree of carburization in ethylene pyrolysis furnace tubing. Mater. Perform. **22**, 25–28 (1983)
32. I.C. da Silva, R.S. da Silva, J.M.A. Rebello, A.C. Bruno, T.F. Silveira, Characterization of carburization of HP steels by non destructive magnetic testing. NDT E Int. **39**, 569–577 (2006)
33. L.R. Jackson, H.W. Russell, Temperature-sensitive magnetic alloys and their uses. Instruments **11**, 280–282 (1938)
34. T. Hara, T. Okiyama, T. Takemoto, Improvement of soft magnetic properties by Cr addition for Fe-(34-46) mass% Ni alloys. J. Jpn Inst. Metals **60**, 1136–1142 (1996). **(in Japanese)**
35. P. Chevenard, La precision en metallurgie et la metallurgie de precision. Mem. Soc. Ing. Civ. (France) **104**, 1–44 (1951). **(in French)**

Metallogr. Microstruct. Anal.
DOI 10.1007/s13632-016-0274-0

TECHNICAL ARTICLE

Microstructural Characterization and Image Analysis in Ex-Service HP Alloy Stainless Steel Tubes for Ethylene Pyrolysis

A. C. McLeod[1] · C. M. Bishop[1] · K. J. Stevens[2] · M. V. Kral[1]

Received: 11 January 2016 / Revised: 24 February 2016 / Accepted: 28 March 2016

Abstract Carburization is the major degradation mechanism of the HP alloy stainless steel tubes used for ethylene pyrolysis. Due to the changes in the microstructure and magnetic properties of the heat-resistant HP grade (Fe-Cr-Ni) alloy tubes over their service life, the level of carburization can be detected non-destructively using eddy current methods. In the current project, the microstructure of a carburized ex-service Nb-modified HP alloy tube has been characterized via image analysis. The phase fractions and phase distributions have been measured in order to determine the microstructural features that contribute to the eddy current non-destructive testing response, to assist in improving the accuracy of remaining life estimates. Issues in differentiating the large number of phases were encountered when using electron backscattered images for image analysis, and thus, energy-dispersive x-ray spectroscopy maps have been used, in combination with the software programs ilastik, for automated image segmentation, and FIJI, for image processing. The chromium depletion of the austenite matrix of the tube, and thus the magnetic response, was observed to be predominantly influenced by the volume fraction of M_7C_3 and $M_{23}C_6$ chromium carbides, with potential contribution from the chromium-containing η-carbide intermetallic. Carbonitrides of the type $Cr_2(C,N)$ were seen to have negligible impact. A comparison between microstructures and magnetic response has determined that eddy current non-destructive testing can detect and measure carburization.

Keywords Metallography · Scanning electron microscopy · Quantitative microscopy · Steels · Electron microscopy

This article is an invited paper selected from presentations at the 2015 Microscopy & Microanalysis Conference, held August 2–6, 2015 in Portland, Oregon, USA, and has been expanded from the original presentation.

✉ M. V. Kral
milo.kral@canterbury.ac.nz

[1] Department of Mechanical Engineering, University of Canterbury, Private Bag 4800, Christchurch 8140, New Zealand

[2] Quest Integrity NZL Ltd, Part of the Quest Integrity Group, Gracefield Research Centre, 69 Gracefield Road, PO Box 38-096, Lower Hutt 5045, New Zealand

Introduction/Background

Ethylene is used extensively in the production of plastics, cabling, and automotive products, and is typically produced by the thermal cracking (pyrolysis) of more complex hydrocarbons (such as naphtha or ethane) at 950–1100 °C inside stainless steel tubes in an ethylene pyrolysis furnace. In order to provide the corrosion and creep resistance necessary to withstand the severe operating conditions, the heat-resisting (H-series) centrifugally cast austenitic stainless steels are typically used for pyrolysis tubes. The most common variants in use are the HP alloys (25%Cr–35%Ni) and ET45 alloys (35Cr–45%Ni) [1–3]. The section of the furnace in which the pyrolysis reaction occurs is composed of hundreds of vertically oriented tubes. The feedstock is combined with steam and passes through the tubes, which are externally heated by burners. The number of tubes, and the tube lengths, diameters, and wall thicknesses are dependent on the total production rate of ethylene required and the residence time of the feedstock within the tubes. As such, there are many different furnace designs implemented in industry, and ethylene pyrolysis tubes can therefore come in many different lengths, diameters, and wall thicknesses. Variations in wall thickness

Published online: 11 April 2016

can also be present along the length of an ethylene pyrolysis tube due to the centrifugal casting process.

Carburization is the main contributor to the failure of ethylene pyrolysis tubes. High carbon concentrations present at the inner diameter of the tubes due to the cracking reaction and the elevated service temperature result in the diffusion of carbon into the tubes. The carbon combines with chromium and other carbide-forming elements to grow existing carbides and create new ones. This leads to increases in internal volume, a loss in weldability, and a reduced ability to withstand thermal cycles [2, 4–8].

Knowing the level of carburization of an in-situ tube can assist in establishing and improving remaining life estimates based on Finite Element Modeling, thermography, and fracture mechanics. Carbide precipitation and the segregation of elements in HP alloy tubes results in a change in the magnetic properties of the carburized region, enabling the level of carburization to be detected non-destructively using eddy current probes [6] and a tube crawler system [9, 10]. However, the eddy current system requires calibration on ex-service tubes that have had their microstructure, mechanical properties, and magnetic response characterized [6].

The growth of chromium-rich carbides and other chromium-containing phases due to carburization results in a depletion of chromium in the austenite matrix. In the as-cast condition, the Fe–Cr–Ni austenite matrix is paramagnetic, but as carburization progresses, it tends toward the binary Fe–Ni system and becomes progressively more ferromagnetic, while retaining the austenite structure [5, 6, 11–13]. The change in the bulk magnetic permeability of the tube as a result of the progressive increase in the amount of ferromagnetic material is measured by the eddy current system. As such, the volume fractions of phases that contribute to the chromium depletion of the austenite matrix and the distributions of these phases across the tube walls are of interest.

This paper discusses the development of microstructural features of ex-service ethylene pyrolysis tubes, along with the methodology being utilized in the current project for the characterization of volume fractions and phase distributions. The volume fraction and phase distribution results are presented for two samples taken from a single ex-service tube and compared to the magnetic response at the sample locations, in order to determine the microstructural features that contribute to the eddy current non-destructive testing (eddy current NDT) response.

Microstructural Features of Ex-Service Tubes

The tube studied in this paper is an ex-service HP-Nb alloy stainless steel ethylene pyrolysis tube. The chemical composition of the tube, as determined by inductively coupled plasma atomic emission spectroscopy (ICP-AES), is shown in Table 1, along with a comparison to the typical HP–Nb composition. Although other tube alloys are in use in the industry, for example, the HP-Mod alloys (HP alloy with combined niobium and titanium additions, sometimes with rare earth additions) and the ET45 alloys (35%Cr–45%Ni), only the microstructural developments relevant to the HP–Nb alloy studied here will be discussed.

Two samples were taken from the tube for analysis. Samples locations were selected such that they coincided with locations at which the eddy current NDT response had been measured. The two samples were taken from the same side of the tube, at a distance of 80 mm apart. The tube had a service life of approximately 4 years.

As-Cast Structure

In the as-cast condition, the microstructure of a typical HP-Nb alloy consists of an austenitic matrix with alternating interdendritic groups of primary chromium-rich and niobium-rich carbides. The primary niobium-rich carbides are typically NbC, and the primary chromium-rich carbides are typically M_7C_3 (where M = Cr, Fe, Ni); however, $M_{23}C_6$ carbides have been identified as the primary chromium-rich carbide in the as-cast condition in HP–Nb alloys where the niobium content is greater than 1.97 wt% [3, 14–16]. The primary carbide network is typically reported to obtain a lamellar or "Chinese Script" morphology. Representative optical and backscattered electron (BSE) micrographs of the microstructure of an as-cast HP-Nb alloy are shown in Fig. 1. The as-cast microstructure is typically observed to be consistent across the wall thickness.

Aged and Carburized Structure

Exposure of the HP-Nb alloys to temperatures above 700 °C results in the primary M_7C_3 carbides transforming to the more stable $M_{23}C_6$ carbide. The transformation is typically observed to be complete within the first 1000 h of exposure [3, 15, 17]. During prolonged aging (>1000 h), the primary $M_{23}C_6$ coarsens.

Carbon diffusion into the tube results in chromium (a strong carbide former) being pulled from the austenite matrix to grow the existing chromium-rich carbides and precipitate new ones. With continued carbon diffusion, the primary network continues to coarsen and coalesce, eventually becoming an almost continuous network. Two chromium carbide types are typically observed in ex-service ethylene pyrolysis tubes. Initially, $M_{23}C_6$ is present across the entire wall; however, in regions of the tube wall with a high carbon concentration (i.e., the inner wall regions), the $M_{23}C_6$ carbides transform to M_7C_3, due to M_7C_3 being more stable at higher C activity [2, 8, 18, 19].

Table 1 Chemical composition of the ex-service HP-Nb alloy ethylene pyrolysis tube determined by ICP-AES, and the typical composition of an HP-Nb alloy

wt%	C	Cr	Ni	Si	Mn	Nb	Ti	V	Cu	Al	P	Fe
Ex-service HP-Nb tube	1.61	25.50	35.60	1.28	1.23	1.33	<0.01	0.02	0.05	0.03	0.04	Bal.
Typical HP-Nb alloy	0.4–0.5	24–28	34–37	1.5	1.5	1.5 max	–	–	–	–	–	Bal.

Bal. balance

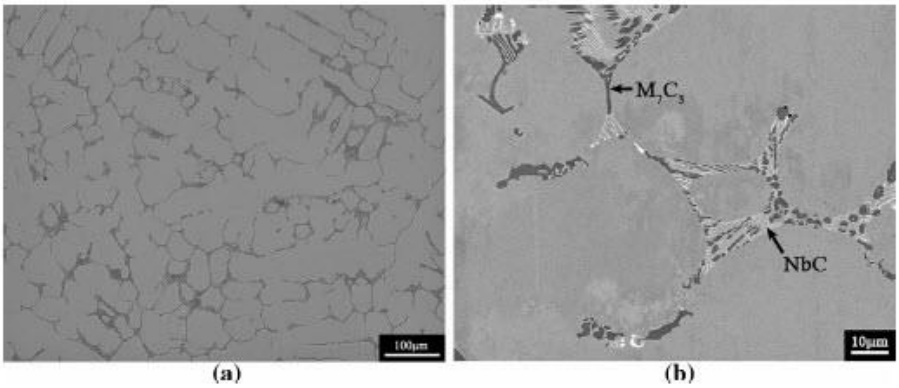

Fig. 1 Representative (**a**) optical and (**b**) backscattered electron micrographs of the microstructure of an as-cast HP-Nb alloy. Etchant for optical image—glyceregia

The $M_{23}C_6$-to-M_7C_3 transformation front progresses into the tube wall with the continual supply of carbon from the cracking reaction at the inner diameter of the tube.

A fine distribution of secondary carbides (typically $M_{23}C_6$) forms in the austenite matrix upon exposure to elevated temperatures, and the distribution is typically located adjacent to the primary carbide network [15–17]. Prolonged exposure to elevated temperatures results in Ostwald ripening of the secondary precipitate distribution, leading to their dissolution in favor of the primary network [17].

Exposure of the HP-Nb alloys to elevated temperatures can, depending on the silicon and niobium content, result in the transformation of the primary NbC precipitates to one of two intermetallic phases—G-phase, a Ni–Nb–Si intermetallic, or η-carbide, a Cr–Ni–Nb–Si intermetallic. The instability of the NbC precipitates at elevated temperatures is well documented in the literature [3, 14, 17, 20–23].

Exposure of HP-Nb alloys to air or flue gas atmospheres can result in the diffusion of nitrogen into the tube wall, resulting in the formation of carbonitrides near the outer surface. The transformation of $M_{23}C_6$ to the chromium-rich carbonitride $Cr_2(C,N)$ within a defined band can occur, and on occasion individual lathe-shaped $Cr_2(C,N)$ precipitates are observed intragranularly within the transformation band [17, 24]. Additionally, it has been reported that exposure to air atmospheres may accelerate the rate of transformation of NbC precipitates to η-carbide in regions near the exposed surfaces [17].

Image Analysis Methodology

In the current project, metallographic samples have been sectioned from locations in an ex-service tube that coincide with locations where the eddy current NDT response has been measured. Each metallographic sample is imaged along multiple radial profiles in order to identify the phases present, measure phase volume fractions, and characterize the phase distributions across the tube walls.

The analysis of phase fractions and phase distributions first requires that the image be segmented into its constituent phases. Segmentation of the images into discrete phases was performed in ilastik, an interactive segmentation program [25]. The ilastik classifier can segment the image into a number of pre-defined label classes, after learning from user input in the form of labels applied in a paint-like interface. In this case, each label class

corresponds to an individual phase that could be present in the tube microstructure. ilastik can differentiate between classes based on a number of features, including color, edge, and texture descriptors. Once the classifier has been trained on a set of representative images, ilastik can automatically batch process large numbers of previously unseen images.

Processing of the segmented images into binary images and extraction of the volume fraction information was performed using purpose-written macros in FIJI (a distribution of the open-source image processing software ImageJ). Analysis of the data was performed using Microsoft Excel.

Backscattered electron images were used extensively during the phase identification process, as the atomic number contrast enabled the majority of the phases present in the microstructure to be easily differentiated. In order to be able to use BSE images for image analysis, the presence of polishing artifacts had to be avoided during the sample preparation; however, the polishing procedure was typically difficult and time consuming, and a perfect polish was hard to achieve. A "watermark" effect was often observed in the austenite matrix of the samples, when observed both in BSE mode and with secondary electrons. Figure 2 shows the watermark effect as observed in BSE mode, in sample 2. It is currently unknown whether this is a polishing artifact, or whether it is due to another cause such as strain effects in the austenite matrix. Segmentation in ilastik of images from samples that displayed the watermark effect was attempted; however, the results were less than satisfactory. In particular, the presence of the watermark effect caused significant issues in differentiating the η-carbide phase regions from the austenite matrix. In BSE images, the η-carbide regions typically have a greyscale gradient due to compositional differences across the phase region. The watermark effect in the austenite matrix resulted in similar gradients in greyscale in the matrix and led to ilastik being unable to differentiate the two phases.

Additionally, the G-phase, η-carbide, and NbC precipitates were often difficult to differentiate from the BSE images alone, as all appeared as variations of light gray or white in the images. This was of particular concern in samples where the η-carbide was present, as of the three niobium-containing phases, η-carbide is the one that contains chromium and thus has the potential to affect the magnetic properties of the sample.

Due to the inability to accurately segment all phases in BSE images, and the need for compositional data to assist in phase differentiation, it was decided that energy-dispersive spectroscopy (EDS) maps would be used for the image analysis instead. The compositional differences between the phases enabled accurate segmentation in ilastik, and EDS spectra could be reconstructed from the map data in order to determine the variation in the chromium content of the matrix across the tube wall.

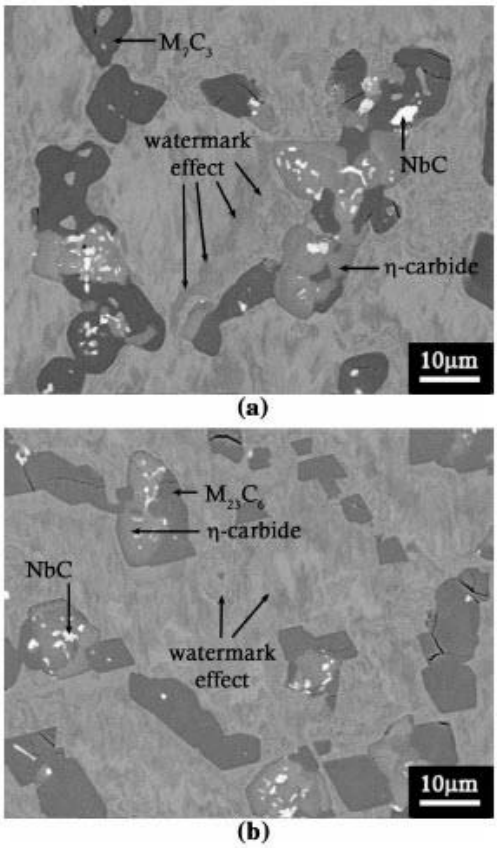

Fig. 2 Backscattered electron images showing the "watermark" effect apparent in the austenite matrix in sample 2

Results and Discussion

Area Fraction Versus Volume Fraction

Due to ethylene pyrolysis tubes being manufactured by a centrifugal casting process, it was expected that the macro- and microstructures of the ex-service tube studied would be consistent in both the tangential (around the tube circumference) and axial (along the tube length) directions within a localized area. Analysis of the grain structure and the microstructure of an axial and a tangential sample located adjacent to each other confirmed this hypothesis. As such,

although the phase fractions have been measured as area fractions on the axial face, the consistency in the macro- and microstructure allows the volume fraction to be inferred as being equal to the area fraction. The phase fractions will thus be presented as volume fractions.

Chromium Carbide Volume Fraction

Representative low-magnification (optical) and high-magnification (BSE) micrographs of the microstructure across the wall thickness of samples 1 and 2 are shown in Figs. 3 and 4, respectively. In comparison to the typical as-cast structure shown in Fig. 1, the microstructure of the ex-service tube displayed a high level of primary carbide coarsening at all locations observed. Sample 1 represents a comparatively low level of carburization for this tube, and sample 2 represents a comparatively high level of carburization.

For both samples, the maximum chromium carbide volume fraction occurred at the inner diameter and was in the range of 32–33%. The chromium carbide volume fraction at the $M_{23}C_6$-to-M_7C_3 transformation front was observed to be in the 20–25% range for the two samples, and this decreased to a minimum of 5–8% at the outer wall. However, the distance of the $M_{23}C_6$-to-M_7C_3 transformation front from the inner diameter differed between the samples, and the distribution of the chromium carbides across the tube walls varied greatly between the two samples, as shown in Figs. 5 and 6.

Sample 1 was observed to have the smallest degree of carburization and carbide coarsening, with the transformation front located a distance of approximately 1.3 mm into the tube wall and a chromium carbide volume fraction of less than 10% across the majority of the tube wall. Sample 2 was seen to be more highly carburized. The transformation front was located at a distance of approximately 5.4 mm from the inner diameter, and the chromium carbide volume fraction remained high across the whole wall.

$Cr_2(C,N)$ carbonitrides were observed within a band approximately 1 mm thick at the outer wall of sample 2. It appeared that they had directly transformed from the $M_{23}C_6$ carbides. On occasion, lenticular $Cr_2(C,N)$ precipitates were also observed to have precipitated intragranularly within the transformation band. The presence of $Cr_2(C,N)$ thus resulted in a decrease in the volume fraction of $M_{23}C_6$. The maximum volume fraction of $Cr_2(C,N)$ precipitates at the outer wall of sample 2 was approximately 10%.

Instability of NbC

The volume fraction of NbC carbides present was typically below 1.5% at any location in either of the samples. In sample 2, the transformation of NbC to the η-carbide intermetallic was observed at the mid and outer wall regions. In sample 1, the NbC carbides were observed to have almost completely transformed to the G-phase intermetallic at the mid-wall regions, and almost completely transformed to the η-carbide intermetallic within 1–1.5 mm of the outer surface. The volume fraction of G-phase was relatively consistent across the locations in which it was observed; however, in both samples, the volume fraction of η-carbide tended to increase with increased proximity to the outer surface—this may be due to the flue gas atmosphere present at the outer surface accelerating the NbC-to-η-carbide transformation rate [17].

Contribution of Phases to Chromium Depletion

The matrix chromium concentration profiles were typically observed to inversely mirror the chromium carbide volume fraction profiles—decreases in the chromium carbide volume fraction corresponded with increases in the matrix chromium content. The matrix chromium content was significantly lower than the typical as-cast chromium content of 25 wt%, in regions with a high volume fraction of chromium carbides. In both the samples, the matrix chromium content was in the range of 5–7 wt% at the inner wall, where the volume fraction of M_7C_3 carbides was in the 32–33% range. The matrix chromium content at the $M_{23}C_6$-to-M_7C_3 transformation front was observed to be approximately 12 wt% in both samples.

Sample 1 displayed a significant increase in the matrix chromium content with increased proximity to the outer surface, reaching a maximum matrix chromium content of approximately 21 wt%. A slight decrease was observed near the outer surface, which may be due to the NbC-to-η-carbide transformation in this region further depleting the matrix of chromium. The chromium content of the η-carbide observed in the samples was determined to be 40–45 at%, and although it does not contain as much chromium as the M_7C_3 (max 70 at%) and $M_{23}C_6$ (max 79 at%) carbides, in sample 1, it attains volume fraction comparable to that of the $M_{23}C_6$ carbides and thus may contribute to the chromium depletion of the surrounding matrix.

Sample 2 displayed high volume fractions of the M_7C_3 and $M_{23}C_6$ carbides across the whole sample and also contained significant amounts of the chromium-containing η-carbide intermetallic at the outer wall regions, and as a result, the matrix chromium content remained below 14 wt%, even at the outer surface.

The $Cr_2(C,N)$ carbonitrides present at the outer wall of sample 2 do not appear to have a significant effect on the chromium depletion of the austenite matrix. The lack of

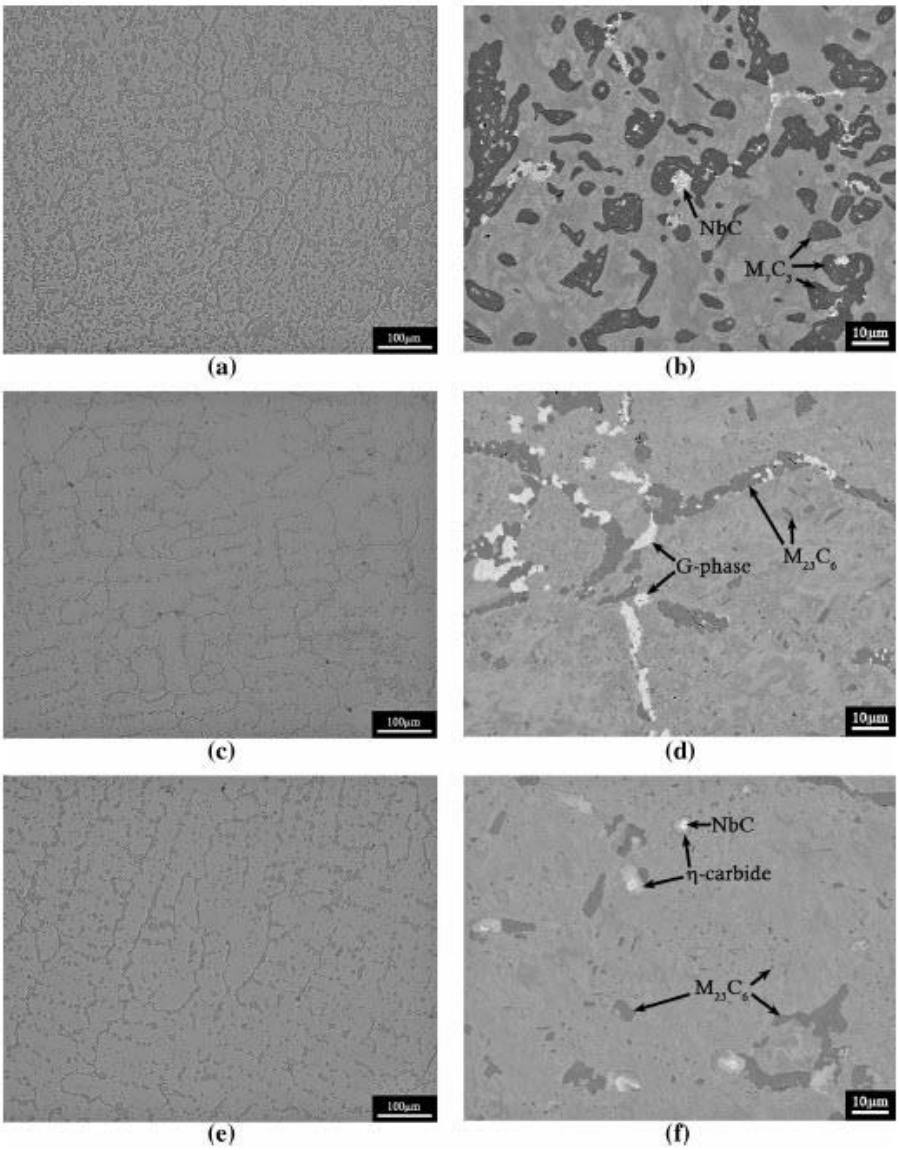

Fig. 3 Representative (**a**), (**c**), and (**e**) optical and (**b**), (**d**), and (**f**) backscattered electron micrographs of the microstructure of sample 1 at the (**a**) and (**b**) 1.0 mm (inner), (**c**) and (**d**) 3.0 mm (mid), and (**e**) and (**f**) 7.5 mm (outer) wall positions. Etchant for optical images—glyceregia

effect is likely due to the majority of the $Cr_2(C,N)$ precipitates present transforming directly from $M_{23}C_6$ carbides already present in the microstructure. Aydin et al. [26] report that the transformation occurs according to Eq. 1:

$$M_{23}C_6 + 6N + 1M = 12M_2(C,N), \quad (1)$$

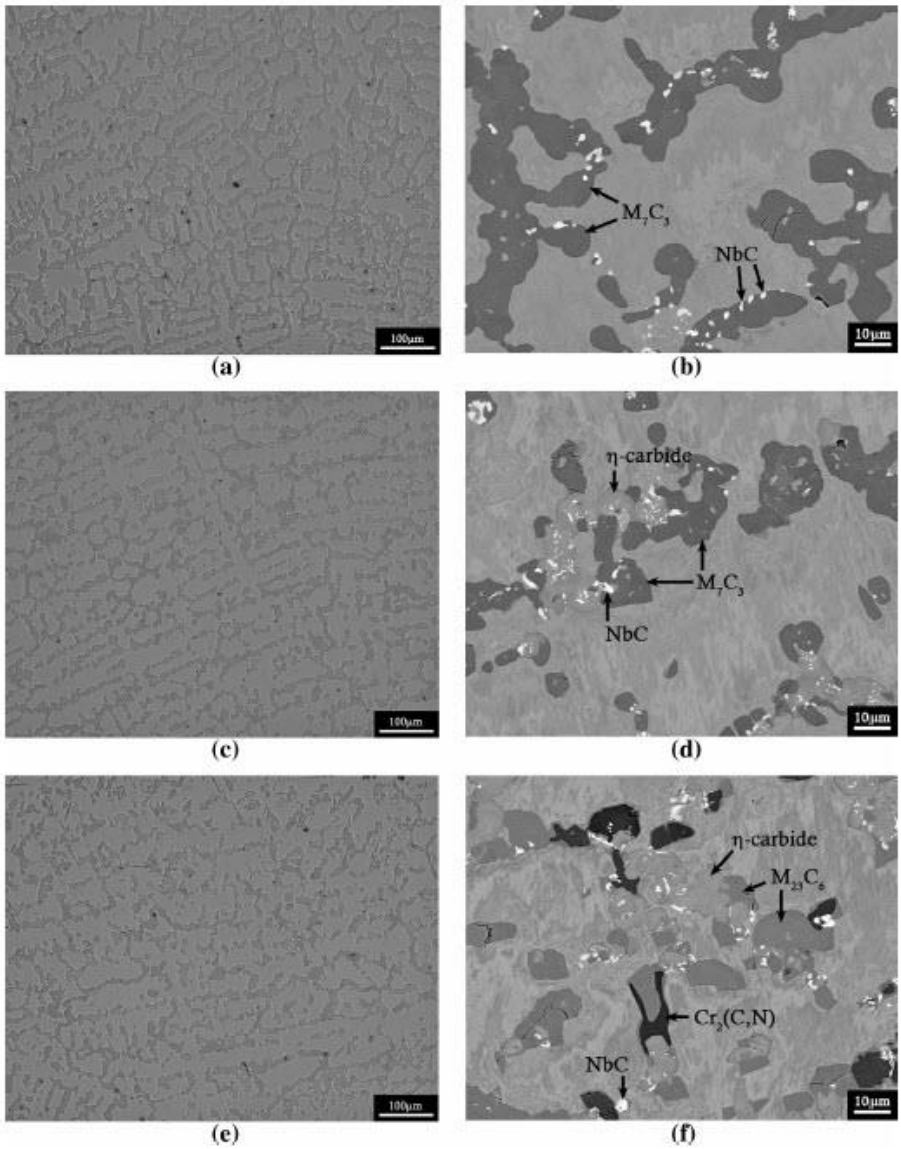

Fig. 4 Representative (**a**), (**c**), and (**e**) optical and (**b**), (**d**), and (**f**) backscattered electron micrographs of the microstructure of sample 2 at the (**a**) and (**b**) 1.0 mm (inner), (**c**) and (**d**) 5.0 mm (mid), and (**e**) and (**f**) 7.0 mm (outer) wall positions. Etchant for optical images—glyceregia

and thus, the chromium content in the transformed $Cr_2(C,N)$ precipitates is negligibly higher than that in the $M_{23}C_6$ precipitates from which they formed, and there is very minimal chromium depletion of the surrounding matrix as a result.

Magnetic Response

Curie temperature data for various alloy compositions have been compiled by Stevens et al. [12] and plotted on the Fe–Cr–Ni Gibbs triangle, enabling the effects of chromium

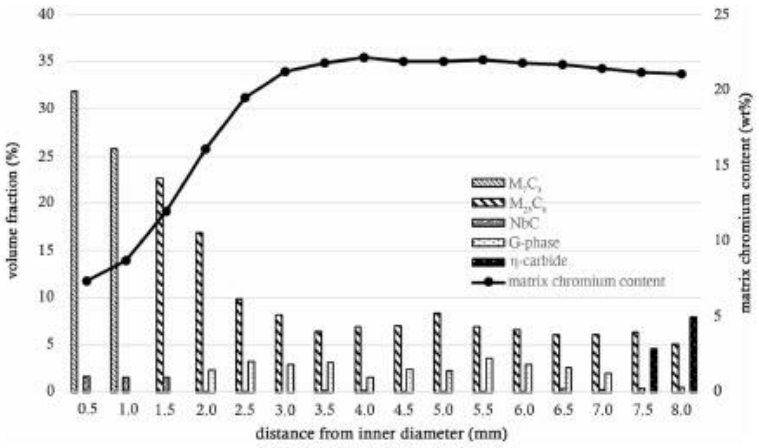

Fig. 5 Phase fractions and distributions in sample 1

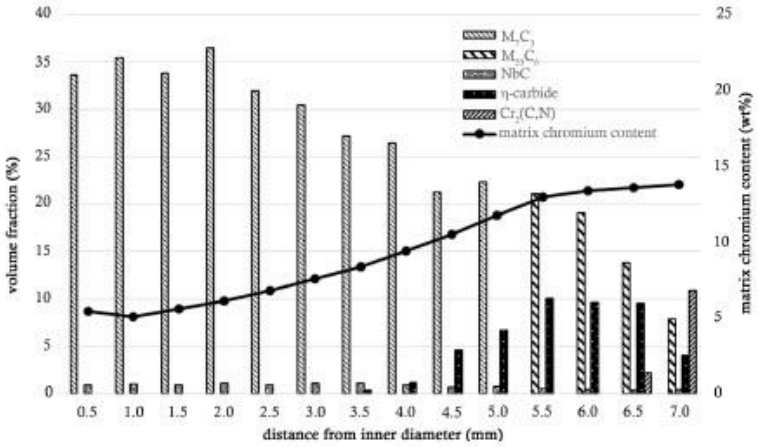

Fig. 6 Phase fractions and distributions in sample 2

depletion on the magnetic behavior of the matrix at room temperature to be visualized. Based on the Curie data, it can be seen that Fe–Cr–Ni matrix compositions with approximately 15 wt% chromium or less are ferromagnetic at room temperature. Comparing the matrix chromium content profiles of samples 1 and 2 to the data presented in Fig. 7 indicates that the matrix of sample 2 is ferromagnetic across the entire wall, whereas the matrix in the inner 24% of the wall of sample 1 is ferromagnetic, and the remainder is paramagnetic.

Figure 8 displays the eddy current NDT response of the two samples. The response has been normalized against the response of the probe in air, in order to remove the influence of the probe properties from the results. Multi-frequency scans enable the magnetic response across the tube wall to be determined, as low frequencies have a high depth of penetration and thus provide information on the material properties at the inner wall, and high frequencies have a low depth of penetration and thus provide information on the material properties at the outer wall. Both the samples 1 and 2 exhibit magnetic responses significantly elevated above the response of the probe in air.

Sample 2 exhibits the highest normalized probe inductance across all frequencies, ranging from 1.87 at low frequencies to 1.57 at high frequencies. The elevated normalized probe inductance across all frequencies corresponds with the matrix of sample 2 being ferromagnetic across the entire wall as determined by the matrix chromium content. Sample 1 exhibits a normalized inductance that ranges from 1.40 at low frequencies to 1.31 at high

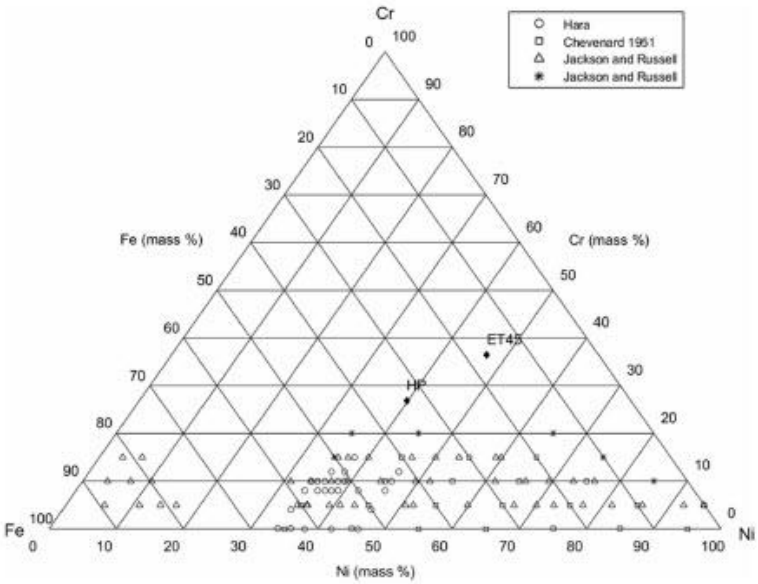

Fig. 7 Gibbs triangle for Fe–Cr–Ni alloys (adapted from [12]). *Asterisks* denote the compositions that are paramagnetic at 20 °C, and *open circles*, *squares*, and *triangles* denote the compositions that are ferromagnetic at 20 °C. *Black diamonds* denote specific alloy compositions

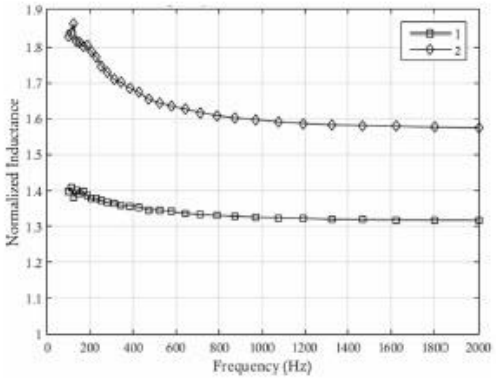

Fig. 8 Normalized probe inductance versus frequency plot for the two samples studied

frequencies, lower than the response of sample 2 but still significantly elevated above the response of the probe in air. The response of sample 1 indicates that it is carburized to a lesser extent than that of sample 2, which is consistent with sample 1 generally displaying lower chromium carbide volume fractions across the wall.

The difference between the low and high frequency values of normalized impedance in sample 2 when compared to sample 1 may be due to the greater extent of matrix chromium depletion at the inner wall region. A reduction in the chromium content leads to an increase in the value of magnetic permeability, and due to ferromagnetic materials concentrating the magnetic field of the eddy current probe, an increase in magnetic permeability results in increased probe inductance [27]. Although the matrix chromium content of both samples is 5–7 wt% at the inner surface, in sample 1, this rises rapidly, whereas in sample 2, the matrix chromium content remains low. As such, even though the inner wall regions in both samples are ferromagnetic, the matrix within the inner wall region of sample 2 is likely to have higher values of magnetic permeability in comparison to the matrix within the inner wall region of sample 1. The significantly elevated inductance displayed by sample 2 at low frequencies is likely due to the higher levels of magnetic permeability through the wall as a result of the greater extent of chromium depletion.

Summary/Conclusions

A "watermark" effect was observed in BSE images of the austenite matrix of a carburized ex-service ethylene pyrolysis tube. It is currently unknown whether this is a polishing artifact or due to another cause such as strain effects; however, it presented difficulties in differentiating the matrix from the η-carbide intermetallic when using BSE for image analysis.

Image analysis using a combination of ilastik, FIJI, and Microsoft Excel software has been successfully used to

process EDS maps of carburized microstructures and extract phase volume fraction data.

The chromium depletion of the austenite matrix, and thus the magnetic properties of the material, has been shown to be predominantly influenced by the volume fraction of the M_7C_3 and $M_{23}C_6$ chromium carbides. The $Cr_2(C,N)$ carbonitride does not have a significant effect on the chromium depletion due to its direct transformation from $M_{23}C_6$. The η-carbide intermetallic may contribute to the chromium depletion; however, analysis of further samples containing this intermetallic is required to confirm this.

A comparison between the magnetic responses of two samples with different levels of carburization has shown that the eddy current method is able to detect and measure carburization non-destructively. The more highly carburized sample displayed a greater magnetic response overall due to greater carbide volume fractions and thus greater matrix chromium depletion. Its significantly elevated inductance at low frequencies is likely due to higher levels of magnetic permeability through the tube wall as a result of the greater extent of chromium depletion.

Acknowledgments The authors gratefully acknowledge the financial support of Quest Integrity NZL Ltd and the Ministry of Science and Innovation of New Zealand (now administered by Callaghan Innovation) under contract QINZ1001. The authors thank Charles Thomas and Andy Saunders-Tack of Quest Integrity NZL Ltd for their continued support.

References

1. R. Kirchheiner, P. Woelpert, Niobium in centrifugally cast tubes for petrochemical applications, in *Niobium, Science and Technology: Proceedings of the International Symposium Niobium, Orland: Minerals, Metals and Materials Society*, 2001
2. I.C. Silva, J.M.A. Rebello, A.C. Bruno, P.J. Jacques, B. Nysten, J. Dille, Structural and magnetic characterization of a carburized cast austenitic steel. Scr. Mater. **59**(9), 1010–1013 (2008)
3. G.D. de Almeida Soares, L.H. de Almeida, T.L. da Silveira, I. Le May, Niobium additions in HP heat-resistant cast stainless steels. Mater. Charact. **29**(4), 387–396 (1992)
4. S. Shi, J.C. Lippold, Microstructure evolution during service exposure of two cast, heat-resisting stainless steels—HP-Nb modified and 20–32Nb. Mater. Charact. **59**(8), 1029–1040 (2008)
5. K.J. Stevens, A.J. Tack, C.W. Thomas, D. Stewart, Through-wall carburization detection in ethylene pyrolysis tubes. J. Phys. D (Appl. Phys.) **34**(5), 814–822 (2001)
6. K.J. Stevens, W.J. Trompetter, Calibration of Eddy current carburization measurements in ethylene production tubes using ion beam analysis. J. Phys. D (Appl. Phys.) **37**(3), 501–509 (2004)
7. D. Jakobi, R. Gommans, Typical failures in pyrolysis coils for ethylene cracking. Mater. Corros. **54**(11), 881–886 (2003)
8. E. Lang, J. Norton, *Monitoring of carburisation by the use of magnetic techniques, Part 1: Fundamental aspects and measurements on 25Cr–20Ni steels*. Commission of the European Communities, Physical Science, PETTEN, EUR 10566 EN, 1986
9. K.J. Stevens, A.C. McLeod, C.W. Thomas, A. Saunders-Tack, B. de Lorenzo, *Inspection and remnant life assessment of ethylene cracker tubes*, in *Ethylene Middle East Technology Conference*, Bahrain, 2014
10. Quest Integrity Group, *Ethylene Pyrolysis Tube Inspection System* (2015), http://www.questintegrity.com/services/inspection-services/ethylene-pyrolysis-tube-inspection. Accessed 27 May 2015
11. I.C. da Silva, R.S. da Silva, J.M.A. Rebello, A.C. Bruno, T.F. Silveira, Characterization of carburization of HP steels by non destructive magnetic testing. NDT E Int. **39**(7), 569–577 (2006)
12. K.J. Stevens, A. Parbhu, J. Soltis, D. Stewart, Magnetic force microscopy of a carburized ethylene pyrolysis tube. J. Phys. D (Appl. Phys.) **36**(2), 164–168 (2003)
13. K.J. Stevens, A. Parbhu, J. Soltis, Magnetic force microscopy and cross-sectional transmission electron microscopy of carburised surfaces. Curr. Appl. Phys. **4**(2–4), 304–307 (2004)
14. R.A.P. Ibanez, G.D. de Almeida Soares, L.H. de Almeida, I. Le May, Effects of Si content on the microstructure of modified-HP austenitic steels. Mater. Charact. **30**(4), 243–249 (1993)
15. G.D. Barbabela, L.H. de Almeida, T.L. da Silveira, I. Le May, Role of Nb in modifying the microstructure of heat-resistant cast HP steel. Mater. Charact. **26**(3), 193–197 (1991)
16. L.H. de Almeida, A.F. Ribeiro, I. Le May, Microstructural characterization of modified 25Cr-35Ni centrifugally cast steel furnace tubes. Mater. Charact. **49**(3), 219–229 (2003)
17. K.G. Buchanan, *The Effects of Long-Term Isothermal Ageing on the Microstructure of HP-Nb and HP-NbTi Alloys—Doctoral Dissertation*. (University of Canterbury, Christchurch, 2013)
18. D.J. Young, Carburization and metal dusting, *Shreir's Corrosion* (Elsevier, Oxford, 2010), pp. 272–303
19. H.J. Grabke, I. Wolf, Carburization and oxidation. Mater. Sci. Eng. **87**, 23–33 (1987)
20. A.F. Ribeiro, R.M.T. Borges, L.H. de Almeida, Phase transformation in heat resistant steel observed by STEM. (NbTi)C NiNbSi (G-phase). Acta Microsc. **11**(1), 59–63 (2002)
21. C.W. Thomas, K.J. Stevens, M.J. Ryan, Microstructure and properties of alloy HP50-Nb: comparison of as cast and service exposed materials. Mater. Sci. Technol. **12**(6), 469–475 (1996)
22. E.A. Kenik, P.J. Maziasz, R.W. Swindeman, J. Cervenka, D. May, Structure and phase stability in a cast modified-HP austenite after long-term ageing. Scr. Mater. **49**(2), 117–122 (2003)
23. E. Berghof-Hasselbächer, P. Gawenda, M. Schorr, M. Schütze, J.J. Hoffman, *Atlas of Microstructures* (Materials Technology Institute, 2008)
24. R. Voicu, E. Andrieu, D. Poquillon, J. Furtado, J. Lacaze, Microstructure evolution of HP40-Nb alloys during aging under air at 1000 °C. Mater. Charact. **60**(9), 1020–1027 (2009)
25. C. Sommer, C. Straehle, U. Kothe, F.A. Hamprecht, Ilastik: interactive learning and segmentation toolkit, in *2011 8th IEEE International Symposium on Biomedical Imaging: From Nano to Macro, ISBI'11*, March 30, 2011–April 2. (IEEE Computer Society, Chicago, 2011)
26. I. Aydin, H.E. Buhler, A. Rahmel, Observations concerning nitridation of refractory austenitic materials in air and combustion gases. Mater. Corros. **31**(9), 675–682 (1980). **(In German)**
27. J. García-Martín, J. Gómez-Gil, E. Vázquez-Sánchez, Non-destructive techniques based on Eddy current testing. Sensors **11**(3), 2525–2565 (2011)